NATIONAL TECHNICAL UNIVERSITY OF ATHENS

SCHOOL OF NAVAL ARCHITECTURE AND MARINE ENGINEERING

MARINE STRUCTURES DIVISION

Determination of failure criteria and incorporation in FE codes for the simulation of ship's hull in extreme loading conditions

J.N. Marinatos

PhD thesis

September 2015

European Union
European Social Fund

OPERATIONAL PROGRAMME
EDUCATION AND LIFELONG LEARNING
investing in knowledge society
MINISTRY OF EDUCATION & RELIGIOUS AFFAIRS
MANAGING AUTHORITY

NSRF 2007-2013
programme for development
EUROPEAN SOCIAL FUND

Co-financed by Greece and the European Union

Determination of failure criteria and incorporation in FE codes for the simulation of ship's hull in extreme loading conditions

J.N. Marinatos

NATIONAL TECHNICAL UNIVERSITY OF ATHENS
SCHOOL OF NAVAL ARCHITECTURE AND MARINE ENGINEERING
MARINE STRUCTURES DIVISION
SEPTEMBER 2015

Supervisor

Professor M. Samuelides

Members of Consulting Committee

Professor J. Amdahl, Norwegian University of Science and Technology, Norway

Professor M. Papadrakakis, National Technical University of Athens, Greece

Professor M. Samuelides, National Technical University of Athens, Greece

Publication Reference Data
Marinatos, J.N.
Determination of failure criteria and incorporation in FE codes for the simulation of ship's hull in extreme loading conditions
PhD Thesis
National Technical University of Athens, School of Naval Architecture and Marine Engineering, Marine Structures Division
September 2015
Keywords: Equivalent plastic strain; RTCL; BWH; Extreme loading; Material modeling; True stress-strain curve; Rupture criteria in non-linear FE codes; Indentation tests; Mesh size effect; Strain rate effect

Contents

Preface

The thesis has been performed in the Marine Structures Division of the School of Naval Architecture and Marine Engineering department at the National Technical University of Athens during the period from May 2011 to September 2015.

Above all, I would like to thank my supervisor Professor Manolis Samuelides for his help and guidance over the past four years and for the pertinent comments and suggestions during the implementation of the thesis. I thank him for being always present and willing to give me his advice.

I would also like to thank the members of the consulting committee Professor Jørgen Amdahl from the Norwegian University of Science and Technology and Manolis Papadrakakis from the School of Civil Engineering of the National Technical University of Athens for their valuable comments during our meetings that contributed to the improvement of this work.

I am particularly grateful to Dr. Michael Toulios, expertise in Mechanical and Naval Engineering, for the valuable discussions on many theoretical issues and the enormous amount of assistance on solving numerical and programming problems. His contribution and support for the completion of the thesis was of great importance to me.

I would like to thank Professor Nikos Andrianopoulos for the inspiring discussions about the material behaviour and the theory of T-criterion.

I also wish to thank all my colleagues from the Marine Structures Division and in particular Ilias Zilakos for his full support on many issues related with numerical analyses and programming.

Thanks to all undergraduate and postgraduate colleagues that we shared great moments and to Dimitris Kazagas and Stefanos Dallas from the basketball team. I would like to express my gratitude to the following persons: Christos Pollalis and Charalampos Souliotis for helping me in the early stages of the research, Dionisis Grekas, Dimitris Fouflias, Anastassis Charitopoulos, Panagiotis Kontoulis, Kostas Aivalis, Ilias Chatzidouros, Thanasis Markoulis and Haris Ksanthis.

My sincere thanks to Mr. Christodoulos Fragoudakis, Mr. Markos Karampatsis and Mr. Stefanos Foukaridis from the Computer Center of the National Technical University of Athens for their assistance.

Many thanks to Mr. Vassilios Dimoulas from Bureau Veritas for providing me with the drawings of a new built Bulk Carrier used for the full-scale model. I would also wish to thank Mr. Elias Kariambas from the American Bureau of Shipping and Mrs. Kaliopi Karela from Lloyd's Register for their assistance in the search for the drawings of the Bulk Carrier involved in the examined accident and Mrs. Aimilia Alisafaki for her assistance in the search for sister ships.

In addition, I would like to thank my family and friends for the support, understanding and their love.

Last but not least, I thank Sevasti for the support and encouragement during the last three years.

This research has been co-financed by the European Union (European Social Fund-ESF) and Greek national funds through the Operational Program "Education and Lifelong Learning" of the National Strategic Reference Framework (NSRF)-Research Funding Program: Heracleitus II. Investing in knowledge society through the European Social Fund.

The financial support from the Research Funding Program: Heracleitus II is gratefully acknowledged. Many thanks to Mrs. Paty Karagkiozopoulou and Mr. Manolis Tsimas.

...to Eni

Abstract

The object of the thesis is the definition of a numerical procedure for the finite element (FE) simulation of the response of ship structures under accidental loading conditions in a realistic manner. In particular, focus is placed on the investigation of the effect of material modeling, i.e. material curve in combination with a rupture criterion, as well as of the strain-rate effect and the mesh size on the assessment of the strength of the ship structure and on the prediction of the damage patterns that occur during the event. In general, FE simulations of accidents aim either in the prediction of the crashworthiness of a ship structure in terms of load carrying capacity or in terms of energy absorption capacity versus the extent of the damage, or in the prediction of the damage when one or two vessels are involved in a given impact scenario.

In order to define an appropriate modeling technique, twenty three tests that are reported in the literature are simulated. The tests that were selected for the benchmark study are representative of the modes of damage that occur in ship impacts, i.e. bending, stretching, tearing under in-plane loads, buckling, crushing and curling. Further, the selected tests were performed on models having thicknesses from 3 mm to 20 mm and were loaded beyond their maximum load carrying capacity quasi-statically and dynamically-one test.

The true stress-strain curve is determined from uniaxial tensile tests until necking, whereas different representations are investigated for the post-necking region. Three rupture criteria are considered for the simulation of the initiation and propagation of rupture. These are a criterion based on the equivalent true plastic strain (Marinatos and Samuelides 2013a, 2013b and 2015), which is referred as SHEAR due to a critical change in the shape of the element that precedes rupture, the BWH instability criterion (Alsos et al. 2008) and the RTCL damage criterion (Törnqvist 2003). The behaviour of these criteria as well as of other criteria that are reported in the literature is investigated to identify the reasons that they produce different results when applied for the prediction of rupture under plane stress conditions.

Following the benchmark study and the investigation of the parameters that affect the behavior of the criteria, it is recommended to use a criterion based on a critical equivalent true plastic strain, i.e. SHEAR criterion, with a cut-off value of triaxialities equal to -1/3 below which the criterion is not activated in combination with a powerlaw material curve and an element length over thickness ratio between two and four, i.e. $2 \leq l_e/t \leq 4$. The recommendation is appropriate for the simulation of ship impacts using FE codes in association with plane stress elements.

Such a numerical simulation technique may be employed for the investigation of innovative structural configurations of ship structures that may resist impacts and the assessment of the crashworthiness of the structures in the framework of an Accidental Limit State (ALS) analysis that includes the determination of residual strength, stability and oil outflow in damaged condition.

In the present work, the simulation tool has been used to investigate the effect on the extent of damage that occurs on the side of a ship structure when she is struck by a deformable bow. The analysis revealed that the assumption of a rigid bow not only imposes higher loading, in terms of energy, to the ship that is struck by a bow, but it also has a substantial effect on the geometry of the contact area between the colliding ships and consequently on the prediction of the damage that occurs during a collision scenario.

Περίληψη

Στόχος της παρούσας διδακτορικής διατριβής με τίτλο: «Προσδιορισμός κριτηρίων αστοχίας υλικών και εφαρμογή τους σε κώδικα πεπερασμένων στοιχείων για την προσομοίωση απόκρισης της γάστρας πλοίων σε ακραία φορτία», είναι ο καθορισμός μιας αριθμητικής διαδικασίας, για τη ρεαλιστική προσομοίωση της απόκρισης της γάστρας του πλοίου στην περίπτωση ατυχημάτων, όπως σύγκρουσης ή προσάραξης, με τη μέθοδο των πεπερασμένων στοιχείων (ΠΣ). Ιδιαίτερα, η μελέτη εστιάζει στη διερεύνηση της επίδρασης που έχει το μοντέλο του υλικού, δηλαδή η καμπύλη του υλικού σε συνδυασμό με ένα κριτήριο αστοχίας, καθώς και ο ρυθμός παραμόρφωσης και το μήκος του στοιχείου που χρησιμοποιείται για τη διακριτοποίηση του μοντέλου στην εκτίμηση της ικανότητας της κατασκευής να καταπονείται σε φορτία που δέχεται κατά την εμπλοκή της σε ατύχημα και στην πρόβλεψη της μορφής της ζημιάς λόγω των φορτίων αυτών. Γενικά, οι προσομοιώσεις ατυχημάτων πλοίων με τη μέθοδο των ΠΣ, στοχεύουν είτε στον προσδιορισμό της σχέσης δύναμης και απορροφούμενης ενέργειας αφενός και έκτασης της ζημιάς αφετέρου ή στην πρόβλεψη της ζημιάς όταν ένα ή δύο πλοία εμπλέκονται σε ατυχήματα, που αναπτύσσονται κρουστικά φορτία.

Για τον καθορισμό της κατάλληλης τεχνικής μοντελοποίησης, είκοσι τρία πειραματικά μοντέλα τα οποία είναι διαθέσιμα στη βιβλιογραφία προσομοιώνονται. Στα εν λόγω πειράματα, που επιλέχθηκαν για τη συγκριτική ανάλυση, παρατηρούνται οι μορφές παραμόρφωσης που συμβαίνουν στα ατυχήματα των πλοίων, δηλαδή κάμψη, μεμβρανικές τάσεις, σχίσιμο υπό την επιβολή φορτίων στο επίπεδο του εξεταζόμενου στοιχείου, λυγισμός, σύνθλιψη και περιστροφική αναδίπλωση (curling). Επιπλέον, τα πειραματικά μοντέλα διέθεταν πάχη από $3\,mm$ έως $20\,mm$ και είχαν φορτιστεί ψευδο-στατικά ενώ σε μία περίπτωση δυναμικά.

Η καμπύλη πραγματικής τάσης-παραμόρφωσης καθορίζεται από πειράματα μονοαξονικού εφελκυσμού μέχρι το σχηματισμό του λαιμού, ενώ διαφορετικές σχέσεις πραγματικής τάσης-παραμόρφωσης διερευνώνται πέρα από το σημείο αυτό. Για την προσομοίωση της έναρξης και διάδοσης της ρωγμής λαμβάνονται τρία κριτήρια αστοχίας. Αυτά είναι ένα κριτήριο το οποίο βασίζεται στην ισοδύναμη πραγματική πλαστική παραμόρφωση (Marinatos and Samuelides 2013a, 2013b και 2015) και αναφέρεται ως SHEAR λόγω της κρίσιμης αλλαγής της μορφής του στοιχείου πριν τη θραύση, το BWH κριτήριο αστάθειας (Alsos et al. 2008) και το RTCL κριτήριο ζημιάς, (Törnqvist 2003). Η συμπεριφορά αυτών των κριτηρίων, καθώς και άλλων κριτηρίων τα οποία αναφέρονται στη βιβλιογραφία, διερευνάται με στόχο τον προσδιορισμό των αιτίων λόγω των οποίων αυτά παράγουν διαφορετικά αποτελέσματα όταν εφαρμόζονται για την πρόβλεψη της θραύσης σε συνθήκες επίπεδης εντατικής κατάστασης.

Με βάση τη συγκριτική ανάλυση και τη διερεύνηση των παραμέτρων οι οποίες επηρεάζουν τη συμπεριφορά των κριτηρίων, συνιστάται η χρήση ενός κριτηρίου το οποίο βασίζεται σε μια κρίσιμη ισοδύναμη πραγματική πλαστική παραμόρφωση, δηλαδή το κριτήριο SHEAR, το οποίο δεν ενεργοποιείται όταν η τιμή της τριαξονικότητας των τάσεων

είναι ίση ή μικρότερη από -1/3 σε συνδυασμό με μια καμπύλη υλικού εκθετικού τύπου και ένα λόγο μήκους στοιχείου προς πάχος μεταξύ δύο και τέσσερα, ή $2 \leq l_e/t \leq 4$. Η πρόταση αυτή είναι κατάλληλη για την προσομοίωση σύγκρουσης πλοίων με χρήση κωδίκων ΠΣ σε συνεργασία με στοιχεία επίπεδης τάσης.

Η εν λόγω τεχνική αριθμητικής προσομοίωσης, μπορεί να εφαρμοσθεί για τη διερεύνηση καινοτόμων κατασκευαστικών διατάξεων στα πλοία και την εκτίμηση της αντοχής σε σύγκρουση των κατασκευών στο πλαίσιο μιας ανάλυσης Οριακής Κατάστασης Ατυχήματος (ALS) η οποία περιλαμβάνει τον καθορισμό της εναπομείνασας αντοχής, της ευστάθειας και της εκροής πετρελαίου μετά από ατύχημα.

Στην παρούσα εργασία, η τεχνική αριθμητικής προσομοίωσης χρησιμοποιήθηκε για τη διερεύνηση της επίδρασης στην έκταση της ζημιάς που προκαλείται στην πλευρά ενός πλοίου όταν αυτό συγκρουστεί με μια παραμορφώσιμη πλώρη. Η ανάλυση έδειξε, ότι η υπόθεση μιας άκαμπτης πλώρης, όχι μόνο επιβάλλει υψηλότερη φόρτιση, από πλευράς ενέργειας, στο πλοίο που δέχεται το χτύπημα, αλλά έχει επίσης σημαντική επίδραση στη γεωμετρία της επιφάνειας επαφής ανάμεσα στα συγκρουόμενα πλοία και συνεπώς στην πρόβλεψη της ζημιάς που συμβαίνει κατά τη διάρκεια ενός σεναρίου σύγκρουσης.

List of Publications

1. Marinatos, J.N. and Samuelides, M. (2013a). *Material modeling for Finite-Element simulation of ship impacts*. In: The 4th International Conference on Marine Structures (MARSTRUCT) 2013. Espoo, Finland.

2. Marinatos, J.N. and Samuelides, M. (2013b). *Material characterization and implementation of the RTCL, BWH and SHEAR failure criteria to finite element codes for the simulation of impacts on ship structures*. In: The 6th International Conference of Collision and Grounding of Ships (ICCGS) 2013. Trondheim, Norway.

3. Marinatos, J.N. and Samuelides, M. (2015). *Towards a unified methodology for the simulation of rupture in collision and grounding of ships*. Marine Structures, 42, 1-32.

This page is intentionally left blank

List of Symbols and Abbreviations

Roman Symbols

A_f	Coefficient of the third order polynomial
a_p	Material factor (Peschmann 2001)
B_f	Coefficient of the third order polynomial
b	Index (Indicates buckling in the full-scale model)
C	Material parameter (Okazawa et al. 2004)
C_f	Coefficient of the third order polynomial
C_1, C_2, C_3	Material parameters (Lou et al. 2012)
c	Index (indicates collapse of outer shell in the full-scale model)
D	Numerator of the fraction in the definition of D_{RTCL} damage parameter
D_f	Coefficient of the third order polynomial
D_i	Damage parameter (McClintock 1968)
D_{CS}	Material parameter (Cowper and Symonds 1957)
D_{SHEAR}	Damage parameter in the case of SHEAR criterion
D_{RTCL}	Damage parameter in the case of RTCL criterion
D_{BWH}	Damage parameter in the case of BWH criterion
$D_1, D_2, D_3, D_4,\ D_5$	Material constants (Johnson and Cook 1983 and 1985)
d	Constant of the tangent type true stress-strain curve
dt_u	Time step increment
dD	Increment of D
E	Young's modulus
E_{total}	Total energy
E_{pl}	Inelastic strain energy
E_{fr}	Frictional dissipation energy
E_T	Internal or total energy per unit mass
E_p	Inelastic energy per unit mass
e	Natural logarithm
F	Yield function
F_c, F_b	Forces (at outer shell collapse, at upper deck buckling)
f	Triaxiality function
G	Shear modulus
H	Hardening
I_R	Rupture index (Lehmann and Yu 1998)
i	Index
J_2	Second stress invariant of the deviatoric stress tensor
j	Index

K	Strength coefficient
K'	Bulk modulus
k	Index
l_e	Element length
m	Parameter (Lehmann and Yu 1998)
n	Strain-hardening index
n_{CS}	Material parameter (Cowper and Symonds 1957)
$\hat{n}$	Unit vector
n_1, n_2	Components of $\hat{n}$
q	Index
R	Dynamic over static yield stress ratio (Cowper and Symonds 1957)
s_{ij}	Deviatoric true stress tensor
$s_{ij_{tr}}$	Deviatoric trial true stress tensor
T	Stress triaxiality
T^*	Homologous temperature (Johnson and Cook 1983 and 1985)
ΔT	Increment of the total strain energy density
ΔT_{pl}	Increment of the plastic strain energy density
T_D	Dilatational elastic strain energy density
T_V	Distortional elastic strain energy density
t	Initial thickness
t'	Current thickness
t_u	Time at the previous step
U	Displacement
U_p	Displacement in the perpendicular to the struck ship direction
u	Index
v	Loading velocity
w	Weight constant (Ling 1996)
z	Constant of the tangent type true stress-strain curve

Greek symbols

α	$\dot{\sigma}_2/\dot{\sigma}_1$ ratio
β	$\dot{\varepsilon}_2/\dot{\varepsilon}_1$ ratio
δ_{ij}	Kronecker delta
ε_{eng}	Total engineering strain
$\varepsilon_{u_{eng}}$	Total engineering ultimate strain
ε_{fr}	Total engineering fracture strain
ε_{true}	Total true strain
ε_{pl}	True plastic strain
ε_u	True plastic strain at the onset of diffuse necking

ε_{eq}	Equivalent true plastic strain
$d\bar{\varepsilon}^{el}$	Increment of the equivalent true elastic strain
$d\bar{\varepsilon}^{pl}$	Increment of the equivalent true plastic strain
ε_{cr}	Critical equivalent true plastic strain
ε_{ij}^{el}	True elastic strain tensor
ε_{ij}^{pl}	True plastic strain tensor
ε_P	Equivalent fracture strain (Peschmann 2001)
ε_t	Necking strain
ε_g	Uniform strain
ε_f	Fracture strain (Johnson and Cook 1983 and 1985)
ε_1	Major in-plane principal true plastic strain
ε_2	Minor in-plane principal true plastic strain
ε_3	Through thickness true plastic strain
ε_{3cr}	Critical through thickness strain (Zhang et al. 2004)
$\dot{\varepsilon}$	Engineering mid strain-rate
$\dot{\varepsilon}_1$	Major in-plane principal true plastic strain-rate
$\dot{\varepsilon}_2$	Minor in-plane principal true plastic strain-rate
$\dot{\varepsilon}_{eq}$	Equivalent true plastic strain-rate
$\dot{\varepsilon}^*$	Dimensionless plastic strain-rate (Johnson and Cook 1983 and 1985)
ε_R	One-dimensional true rupture strain (Lehmann and Yu 1998)
ε_{vr}	Multi-axial true rupture strain
ε_v	Multi-axial effective true plastic strain
$\bar{\varepsilon}_{f,s}$	Equivalent true fracture strain in pure shear (Lou et al. 2012)
$\bar{\varepsilon}_{f,t}$	Equivalent true fracture strain in uniaxial tension
$\bar{\varepsilon}_{f,p}$	Equivalent true fracture strain in plane strain
$\bar{\varepsilon}_{f,b}$	Equivalent true fracture strain in equal biaxial stretching
Θ	Elastic unit volume change
λ	Lame's constant
ν	Poisson's ratio
ρ	Density
σ_{eng}	Engineering stress
σ_y	Engineering yield stress
$\sigma_{u_{eng}}$	Engineering ultimate stress
σ_u	True stress at the onset of diffuse necking
σ_{eq}	Equivalent true stress
$\sigma_{eq_{tr}}$	Trial equivalent true stress
σ_m	Mean true stress
$\sigma_{m_{tr}}$	Trial mean true stress

σ_{true}	True stress
σ_{y_S}	Equivalent static yield stress
σ_{y_D}	Equivalent dynamic yield stress
σ_{ij}	True stress tensor
$\sigma_{ij_{tr}}$	Trial true stress tensor
σ_1	Major in-plane principal true stress
σ_2	Minor in-plane principal true stress
σ_3	Out of-plane true stress
$\dot{\sigma}_1$	Major in-plane principal true stress-rate
$\dot{\sigma}_2$	Minor in-plane principal true stress-rate
$\sigma_{1_{cr}}$	Critical in-plane principal true stress
σ_{Mises}	Mises stress (ABAQUS 2010)
τ_{max}	Maximum true shear stress
φ	Angle between σ_1 and $\hat{n}$ (Stören and Rice 1975)

Other symbols

.	Dot (indicates time derivative)

Abbreviations

ALS	Accidental Limit State
BD	Both deformable (full-scale simulations)
BWH	Bressan-Williams-Hill instability criterion
C3D8R	Eight-node three-dimensional elements
C3D6	Six-node three-dimensional elements (prism elements)
CPU	Central processing unit
D/H	Double hull
DSS	Double side skin
FE	Finite element
FEM	Finite element method
FLD	Forming limit diagram
FLSD	Forming limit diagram (expressed in terms of stresses)
FFLD	Fracture forming limit diagram
INF	Irradiated nuclear fuels
RB	Rigid bow (full-scale simulations)
RTCL	Rice-Tracey-Cockcroft-Latham damage criterion
S4R	Four-node plane stress reduced integration elements
SSS	Single side skin
VLCC	Very large crude carriers

Chapter 1

Introduction

1.1 Overview

Amongst the types of accidents at sea, ship grounding and collision are of the most hazardous, as both may result in: i) loss of human lives, ii) severe environmental consequences; oil spillage etc. and iii) financial consequences to local communities close to the accident as well as to ship owners due to ship loss and penalties (Simonsen 1997, Törnqvist 2003, Alsos and Amdahl 2007). According to the Baltic Marine Environment Protection Commission report on shipping accidents in the Baltic sea area during the period 2000-2009, groundings and collisions accounted for 45% and 32% of shipping accidents, respectively (HELCOM 2009). The steady increase in the world's merchant fleet on one hand and the size of the ships on the other, due to the increasing demand in the international markets, has also increased the risk of collision and grounding events, in particular where sea-traffic density is high and the sea routes may be narrow (Ringsberg 2010). In addition, operational velocities of new build merchant ships are getting higher and higher, which may lead to excessive loads, i.e. during a collision incident, which could be disastrous.

Through the years many amendments to codes and regulations have been incorporated as a response to numerous disasters at sea. One of the most important legislations to mitigate the consequences of impacts was the Oil Pollution Act 1990 (OPA ’90) (Papanikolaou et al. 2006) that is referred here as one of the most crucial not only in the prevention or reduction of oil pollution, but also in the minimization of the possibility of vessel loss. The collision event between the crude oil tanker Independenţa and the cargo ship Evriali in 1979 (MEPC 58/INF.2 2008) as well as the Exxon Valdez grounding incident in 1989, are representative accidents of single hull vessels which resulted in tens of thousands of tons of oil spill.

According to the EMSA Maritime Accident Review 2010 (EMSA 2010), there have now been no shipping accidents on the scale of the Estonia disaster in the Baltic sea for nearly 20 years and no accidents involving major pollution since the Prestige disaster off Spain over 13 years ago. However, although the severity of accidents at sea has substantially reduced in recent years, as human error remains the major contributing factor in about 60% of shipping accidents, with other research suggesting that this percentage significantly increases in the case of collisions and groundings (HORIZON 2012 referred in Butt et al. 2013), new methodologies and ideas with respect to the design and operation of ships will always be needed, in order to reduce the risk involved with ship impacts.

1.2 Investigation of ship impacts

Within over fifty years of research a continuous effort is made by the research community on one hand to comprehend the various mechanisms, which are directly associated with the complicated phenomena that take place in a collision or grounding event and on the other to propose reasonable and practical solutions to prevent the disastrous consequences with the least cost. To this end, various methods have been developed for the investigation of ship impacts.

1.2.1 External dynamics vs. internal mechanics

In a ship impact analysis, the problem can be decoupled into external dynamics and internal mechanics, as described below:

- External dynamics: Include the ship or ships motion prior, during and after the collision or grounding event, taking into account the pressure of the surrounding fluid

- Internal mechanics: Include the structural response of the participating ship or ships due to impact loads, in conjunction with the material's non-linear response and subsequent failure. During the impact the ship structure experiences mainly membrane, bending, tearing and crushing of structural elements

In case of a collision, the decoupling of the internal mechanics and the external mechanics is achieved using the equations of conservation of momentum and energy. Under the assumption of fully plastic collision, which ends when the contact areas of the ships involved move with the same velocity in the horizontal plane, it is possible to determine the energy that is dissipated in the colliding structures, i.e. the energy that causes plastic deformation and rupture as well as the friction energy, from the initial kinetic energy of the striking ship and the characteristics of the collision incident. These are the displacement of both vessels and their moment of inertia in yaw, the location of the collision, the velocity of the struck vessel and the angle of the velocities of the struck and striking ships. The effect of the surrounding fluid is considered by adding to the mass and the inertia of each one of the struck and striking vessels an additional mass and inertia. Examples of procedures to calculate the energy that is dissipated in the colliding structures from the initial kinetic energy of the striking ship may be found in (Woisin 1987, Hegazy 1980, Minorsky 1959, Pedersen and Zhang 1998). The procedures assume that the colliding vessels move in the horizontal plane, i.e. pitch, roll and heave motions are not considered.

When investigating grounding there are two possibilities: if the ship is still after the grounding, all her kinetic energy is dissipated to deform the structure and friction. However, there are cases when a ship that comes in contact with the sea bed does not stop but continues her motion after losing contact with the sea bed. In this case the energy dissipated is the difference between the initial kinetic energy and the final energy. Under these conditions, the dissipated energy may be calculated a priori, only if it is possible to assume the velocity of ship after the grounding event, which is a rather arbitrary assumption.

It is noted that, the present study deals with the internal mechanics in ship impacts. The methods in internal mechanics for the determination of the energy absorption capacity of ship structures can be classified in: i) empirical-experimental, ii) analytical and iii) numerical.

1.2.2 Empirical-experimental methods

Empirical-experimental methods have been applied extensively during the past decades and constitute a helpful tool, which gives researchers the capability to make a fast evaluation of the ship's absorption capacity, under accidental loading conditions, with trivial computational cost.

The earliest attempt to address ship collisions was the semi-empirical method proposed by Minorsky (1959). According to the method, the energy absorption capacity of ship structures is related with an empirical linear relation with the volume of the damaged material. Further, the energy that is released during a collision for causing structural damage is determined using the principle of momentum and energy conservation, postulating that the two ships behave as one body after the impact. A constant added mass was also included in the methodology calculations, so as to account for the interaction between the vessels and the surrounding water. Ever since, Minorsky's approach was followed by designers and researchers.

Minosky’s empirical relationship was established on the basis of observations of actual ship collisions. Woisin (1976) extended the method of Minorky using the results of large scale tests that were conducted in Germany. Later Woisin introduced an approach to deal with external mechanics, as he established a methodology to determine the energy that is available to cause structural damage in the case of arbitrary collisions geometries and ship’s speeds (Woisin 1987). The approach of Woisin for external mechanics assumed that during the collisions both ships may undergo surge, sway and yaw motions.

The empirical methods yield rough estimates of the energy dissipated for structural deformation in high-energy ship impacts. However, evaluation of the amount of energy absorbed by the colliding vessels prior to rupture is also of great importance, especially in the cases of merchant ships carrying hazardous cargoes. To this end, analytical and numerical methods have been developed.

1.2.3 Analytical methods

Analytical methods are practical and require low computational effort. Their development is based on the a priori assumption of the mode of structural response of the structural elements (see e.g. Amdahl 1983, Reckling 1983, Pedersen and Zhang 1998, Lützen et al. 2000, Hong and Amdahl 2008b and Buldgen et al. 2012, 2013). However, they do not account for the interaction between the structural elements during their structural response. Further, in most cases it is assumed that the material is perfectly plastic and at least in the case of transverse loading their application is limited up to the point of rupture.

At this point, numerical methods come to take over the baton aiming to give more detailed solutions and description of damage.

1.2.4 Numerical methods

The last decade, due to the remarkable evolution in the computer technology, which resulted in high computer performance, i.e. short response time for a given task, fast data compression and decompression, short data transmission time etc., detailed numerical simulations of collision and grounding of ships with non-linear FE codes, have been practicable. Nowadays, solutions may be derived within acceptable central processing unit (CPU) time, between two to seven days with numerical models counting approximately 800,000 elements in the first case and more than 1.5 million elements in the second. At the moment, many reliable finite element method (FEM) packages are available, such as LS DYNA, ABAQUS, etc. which can account for various complicated calculations involving contact between rigid-deformable or deformable-deformable structures, non-linear material behaviour and rupture. Thus, detailed estimation of the contact forces acting on each deformable structure or part of it as well as the structural energy of the participating bodies is achieved. In addition, using non-linear FE codes there is no need to assume deformation modes, which are obtained for the colliding and struck ships as a result of the simulation. This allows the user to gain a better insight regarding the collision or grounding mechanisms. FE analysis may be used to determine the force-penetration or energy-penetration curve of the structures involved in an impact or to simulate an impact with both colliding bodies free to move.

The results of simulations procedures using FE codes have been correlated against experimental results by many researchers (see e.g. Ehlers 2010a, Tautz et al. 2013, Villavicencio et al. 2013, Lehmann and Yu 1998, Peschmann 2001, Servis 2003, Servis and Samuelides 2006, Törnqvist 2003, Alsos et al. 2009 and Lou et al. 2012). Non-linear FE codes have been employed to evaluate the energy absorption capacity of conventional and innovative ship structures, as can be seen for instance in Hung et al. (2010), Ehlers et al. (2010) and more recently in Hogström and Ringsberg (2013) and Schöttelndreyer et al. (2013) as well as for benchmark studies to investigate the behaviour and validity of different rupture criteria (see e.g. Bao and Wierzbicki 2004, Ehlers et al. 2008, Savvas 2009, Hogström 2012 and Marinatos and Samuelides 2013a, 2013b and 2015).

An essential advantage associated with the use of FE codes is the flexibility that is offered, which allows to employ them to address particular aspects of ship impacts, such as the flexibility of both structures, global bending, ballast water and residual strength.

Kitamura (2001) performed ship-ship collision simulations, in order to investigate the effect of the global hull girder horizontal bending when a ship has been struck in her midship region considering a right angle collision as well as the effect of the forward velocity of the struck ship under different angles of collision. Very large crude carriers (VLCC) and container ships were the striking ships and irradiated nuclear fuels (INF) the struck ships. The investigation, in terms of the global hull girder horizontal bending effect in a right angle collision, showed that the determining factor is the form and strength of the colliding bow. He concluded that in general, global hull girder horizontal bending may be limited, because the contact area during a collision is relatively small with respect to the size of the struck ship. Moreover, when the struck ship is free to move with a forward velocity, damage of the side structure is limited as bending of the bulbous bow occurs and a significant amount of the initial kinetic energy is absorbed by friction and yawning motion of the struck ship. In that case, the critical angle of collision is ranging from 60° (from behind) to 150° (head-on).

Endo et al. (2004) conducted ship-ship collision simulations with double hull (D/H) VLCC ship type models, using different angles and velocities of collision and two kinds of stiffening system of bulb, i.e. transverse and longitudinal. The authors verified that the buffer bow design, i.e. blunt shaped bow with transverse stiffening system, is advantageous as damage on the struck ship is minimized, particularly in conjunction with reduced shell thickness of bulb.

Ozguc et al. (2006) made a comparative study, to investigate the integrity of single side (SSS) and double side skin (DSS) Bulk carriers prior to collision damage with different rigid bulbous bow shapes and the residual strength of the damaged ship girder in hogging and sagging conditions. They found, that the absorbed energy when the inner side plate of a DSS Bulk carrier ruptures is 2.2 times more than for the SSS Bulk carrier.

Konter et al. (2004) made a detailed study, in an attempt to interpret the disagreement between the experimental and numerical results, regarding a series of full-scale collision experiments performed by TNO on Y-type structures (Wevers and Vredeveldt 1999). They concluded that, overestimation of the amount of damage in the simulations occurred, when sloshing effects in the partially filled ballast tanks of the experimental models were disregarded. Numerical results in Konter et al. (2004) analysis were also verified a few years later by Tabri et al. (2009a), who presented a theoretical model for the prediction of the absorbed energy in ship-ship collisions, taking also into account the sloshing effect.

1.3 Scope of the thesis

1.3.1 Motivation

Although non-linear FE codes offer flexibility, the results are highly dependent on the selection of the input parameters, i.e. material curve, rupture criterion, discretization, time increment in case of dynamic analysis as well as the experience of the user. One essential parameter, that influences the assessment of the determination of the crashworthiness of a ship structure involved in an impact and the extent of the damage, is the modeling of the material behaviour. This includes the definition of a true stress-logarithmic strain relation (true stress-strain curve) until rupture and an appropriate rupture criterion to simulate the initiation and propagation of rupture within the structure.

Many attempts towards this direction have been made, that is to introduce numerical methods in order to obtain numerically stable and realistic results when dealing with failure and rupture of the material (see e.g. Törnqvist 2003, Alsos et al. 2009, Hogström 2012 and Kõrgesaar 2015). However, benchmark studies in ship-ship collision simulations with FE codes using various rupture criteria and numerical techniques (see e.g. Ehlers et al. 2008, Hogström 2012), show that there is a great scatter in the results and that the material model has a strong effect on them. Thus, there is still a need for the definition of a numerical method that would lead in a realistic description of the material behaviour up to the final stage of rupture and produce objective and reliable results.

1.3.2 Object of the thesis

The object of the thesis is the definition of a numerical procedure to simulate the response of ship structures under accidental loading conditions, which suffer various different modes of failure, namely membrane, bending, tearing and crushing, in a realistic manner.

In particular focus is placed in the investigation of the effect of material modeling, i.e. material curve and rupture criterion as well as mesh size and strain-rate effect on the strength of the ship structure, the energy absorption capacity of the structure and the modes of deformation that occur during the event. Such a numerical simulation technique may be employed for the i) investigation of innovative structural configurations of ship structures that may resist impacts and ii) assessment of the crashworthiness of the structures in the framework of an Accidental Limit State (ALS) analysis, that includes the determination of residual strength, stability and oil outflow in damaged condition.

In the present work, the simulation tool has been used to investigate the effect of the simulation of the flexibility of a bow on the damage of a side structure during a collision incident.

1.3.3 Methodology

A series of eight sets of small to medium scale indentation tests, performed by various research groups in six different countries, are simulated. The tests were selected, so as to include the various modes of damage that have been identified in actual damages of marine structures subjected to impact loads. The models, which represent structural units of a ship structure, have a thickness that varies between 3 mm to 20 mm and were subjected to quasi-static and dynamic transverse and in-plane loading conditions.

The true stress-strain curve is determined from uniaxial tensile tests until necking, whereas different representations have been tested for the post-necking region. Three rupture criteria are considered for the simulation of the initiation and propagation of rupture. These are a criterion based on the equivalent plastic strain (Marinatos and Samuelides 2013a, 2013b and 2015), which is referred as SHEAR due to a critical change in the shape of the element that precedes rupture, the BWH instability criterion (Alsos et al. 2008) and the RTCL damage criterion (Törnqvist 2003).

The simulations were performed using the Abaqus/Explicit FE code and the rupture criteria were implemented into VUMAT subroutine (ABAQUS 2010), which interacts with the explicit FE code and refers to an isotropic hardening material that follows the J_2 flow theory assuming plane stress conditions. The programming steps for the development of VUMAT subroutine are presented in Appendix C.

The modeling investigation includes the a) definition of the appropriate material stress-strain curve, b) modeling of rupture, c) determination of the mesh parameters and d) estimation of strain-rate effect in dynamic collisions. The effect of the modeling parameters on the simulation results is investigated in the aforementioned tests, by comparing the experimental force and absorbed energy vs. penetration curves with those that are derived from the numerical analysis. Representations of the deformation patterns, as observed during the tests and as predicted numerically, are also compared. A procedure to determine the relevant material parameters, taking into account the mesh sensitivity, is further identified. Finally, the numerical method is applied in a real ship-ship collision case between a Tankship and a Bulk carrier.

1.3.4 Layout of the thesis

The thesis consists of the following chapters:

Chapter 2 compiles the various tests, which have been conducted during two decades by different research groups and summarizes the experiments that have been investigated in the present work as well as the material properties. The powerlaw parameters for each material component as found in the present work are also presented.

Chapter 3 discusses procedures that have been suggested to determine the true stress-strain curves prior and beyond the initiation of the neck, in a uniaxial tensile test. An analysis for the definition of the true stress-strain relation and the determination of the appropriate true stress-strain curve until fracture, taking also into account the relevant mesh size, is also presented.

Chapter 4 investigates the behaviour of the various failure criteria that have been proposed and implemented in FE codes for the simulation of rupture initiation and propagation as well as the various modeling techniques. The uncertainties with respect to the various parameters which are included in numerical analyses are illustrated and discussed. Application of the selected criteria in the present FE analyses with shell-plane stress elements is further discussed and a comparative study with the various criteria under plane stress conditions is demonstrated. Finally, patterns on how the variables of the material and rupture criteria are calibrated as well as how the critical strain in the cases of SHEAR and RTCL rupture criteria is set to take into account the mesh size sensitivity, are presented.

Chapter 5 presents the numerical results of the benchmark study. The effect of the modeling parameters on the simulation results is assessed and discussed through a comparative study, including comparisons of the numerical and the experimental force and absorbed energy vs. penetration curves as well as of the representations of the deformable structures as observed during the tests and as predicted numerically.

Chapter 6 presents the full-scale ship-ship collision models, regarding the various collision scenarios and the form of the participating structures, i.e. collision angles, rigid or deformable forms, respectively. Numerical results with respect to the contact force and absorbed energy as well as the deformation patterns of the ships, are shown in each case and discussed. Comparisons between the various collision scenarios are also presented. The simulations focus on the effect of a deformable bow.

Chapter 7 reports the conclusions of the work and suggests aspects that need further investigation.

1.3.5 Assumptions

In the present study the following assumptions were adopted:

- Plane stress conditions, as the thickness of the structural components is significantly smaller than the other dimensions, i.e. less than 1/10 and the ship may be considered a thin walled structure. This is in accordance with the formulation of shell elements in FE codes

- Adopting an isotropic hardening material that follows the J_2 flow theory and assuming that loading is monotonically increased and reloading in the opposite direction in the case of unloading is limited and within the elastic region

Chapter 2

Experimental Database

2.1 Overview

During the last decades various research groups in many countries performed indentation tests, in order to investigate the crashworthiness of ship structural elements or structural assemblies. Based on the loading conditions during the test, they can be classified in two categories:

- quasi-static indentation tests
- dynamic collision tests

The participating bodies, which come into contact during the tests, are models of double bottom and side structure assemblies, stringer decks and plates with or without stiffeners. The model, that is considered to be the struck, is loaded transversely or in-plane, either quasi-statically or dynamically by rigid or deformable indenters, which indenters represent ship bows or the sea bed. Some of these experiments are presented in the following.

Amdahl and Kavlie (1992) conducted a series of mid-scale indentation experiments, where scaled down double bottom structures were penetrated quasi-statically by a rigid truncated cone. A similar study is also reported in Wang et al. (2000). In this case the structural damage was investigated for different indenter geometries. The indenters were modeled as cones with a spherical nose. The shape variation was enforced by varying the nose radius and cone spreading angle.

ISSC (2003) presents two series of collision tests (ASIS 1993), which had been conducted in Japan. During the tests, a stringer deck with attached plating was loaded in its plane, quasi-statically and dynamically, by a rigid bow shape indenter. The test components represented part of the side of a double hull vessel. In the case of the dynamic loading test, the rigid indenter was dropped successively on the deformable structure from $4.8\,m$ above the initial position of the outer hull, until the penetration depth reached one meter.

DNV (1993) and Astrup (1994) present a set of four experiments, concerning the cutting of pairs of parallel stiffened and unstiffened plates by a rigid wedge. The thicknesses of the specimens were $15\,mm$ and $20\,mm$, which are close to those used in the shipbuilding industry. A couple of years later Paik and Tak (1995) conducted tearing tests using four plates with different stiffener configurations. The specimens were loaded quasi-statically in their plane by a rigid sharp wedge.

Wevers and Vredeveldt (1999) reported full-scale collision experiments with two inland vessels, which had been conducted in the Netherlands by TNO. Two different structural configurations were tested, i.e. the Y-type and X-type configuration. In the case of the Y-type structure the ballast tanks of the ships were partially filled with water.

Paik et al. (1999), performed mid-scale indentation experiments using double skinned structural models. A total of six double skinned structural models, namely four mild steel and two aluminum alloy models, were tested in quasi-static loading condition, varying plate thickness and initial impact location of the cone shape indenter, namely between webs and on webs.

Mid-scale indentation experiments were also carried out by Alsos and Amdahl (2009), in order to investigate the response of stiffened plates under transverse loading. Five test components with different stiffener configurations were penetrated quasi-statically by a rigid cone shape indenter.

Liu et al. (2012) conducted small scale drop weight impact tests on rectangular plates, in order to study the influence of the impact velocity and the diameter of the indenter on the plastic behaviour and fracture of the plates.

More recently Gong et al. (2013), Villavicencio et al. (2013) and Tautz et al. (2013) conducted indentation experiments on ship structural components. Specifically, in the case of Gong et al. (2013) experiments, two stiffened plates with the same configuration were quasi-statically forced in the transverse direction by a rigid indenter, in the first case on the plate, while in the second case on the stiffeners. Villavicencio et al. (2013) reported small-scale tanker side panels which were punched quasi-statically at the mid-span by a rigid knife and flat edge indenter. In the experiments of Tautz et al. (2013), a bulbous bow in rigid form in one case and with a deformable part on the other, was driven quasi-statically against a model of ship side structure considering a right angle collision.

Although such tests are very time-consuming and expensive, provide researchers with valuable experimental data, which then can be used for the verification of predictions that are obtained from theoretical, either numerical or analytical procedures.

2.2 Simulated tests

Twenty three different panel indentation experiments are simulated during the present work. These are:

i. Quasi-static transverse loading of an un-stiffened plate (US Plate) and a plate with one and two flat bar stiffeners, i.e. 1-FB and 2-FB respectively (Alsos and Amdahl 2009)

ii. Quasi-static transverse loading of four double skinned structural models, where the impact location of the cone shape indenter on the outer skin plating was varied between webs and on webs, ST-3-BW, ST-3-OW, ST-4-BW and ST-4-OW (Paik et al. 1999)

iii. Quasi-static in-plane loading by a rigid sharp wedge of four plates with different configurations, i.e. an un-stiffened plate (US), a plate with two longitudinal stiffeners (LS), a plate with two transverse stiffeners (TS) and a plate with two longitudinal and transverse stiffeners (OS) (Paik and Tak 1995)

iv. Quasi-static and dynamic in-plane loading of a stringer deck with attached plating, as part of a double hull referred to as COLLISION STATIC and COLLISION DYNAMIC models (ASIS 1993 reported in ISSC 2003)

v. Quasi-static transverse loading of two stiffened plates with the same configuration, where the rigid indenter was forced in the first case on the plate, while in the second case on the stiffeners, referred to as OUTER SHELL and INNER SHELL models (Gong et al. 2013)

vi. Small-scale tanker side panels, punched quasi-statically at the mid-span by a rigid knife and flat edge indenter, referred to as KNIFE SPECIMEN and FLAT SPECIMEN (Villavicencio 2012 and Villavicencio et al. 2013)

vii. A bulbous bow in rigid form in one case and with a deformable part on the other, driven quasi-statically against a model of ship side structure considering a right angle collision, referred to as the CE-1 and CE-2 models, respectively (Tautz et al. 2013 and Fricke et al. 2014)

viii. Quasi-static in-plane loading of pairs of un-stiffened and stiffened plates by a rigid wedge, reported as P1-15, P2-15 and S1-20, S2-20 models, respectively (DNV 1993)

In all of the examined experiments, except in the case of the CE-2 model (see Tautz et al. 2013 and Fricke et al. 2014), a rigid indenter was driven towards or dropped on different small and mid-scaled structures, which constitute parts of a ship. The configuration of each test, the dimensions of the test components, the form of the rigid indenters and the stress-strain engineering curves for each material are presented in Appendix A. The material properties and thickness of each component are summarized in Table 2.1. Note that, all dimensions are in (mm). For a more detailed description of the tests see the related references, which are included in Table 2.1 and Appendix A. In Table 2.1, E is the Young's modulus of each material, σ_y and $\sigma_{u_{eng}}$ the engineering yield and ultimate stresses respectively, $\varepsilon_{u_{eng}}$, ε_{fr} and $\dot{\varepsilon}$ the engineering ultimate and fracture strains and mid strain-rate respectively, while K and n the material parameters, which are derived according to the procedure described in section 3.2 of the next chapter.

It is also noted that, Table 2.1 includes material data with respect to experiments that were not modelled in the present work. However, it was considered appropriate this data to be included, in order the experimental data base to be more complete. The tests that were not simulated are listed below:

1. Quasi-static transverse loading of a plate with one and two HP stiffeners respectively (Alsos and Amdahl 2009)

2. Quasi-static transverse loading of mid-scale double bottom structures by a rigid truncated cone (Amdahl and Kavlie 1992)

3. Quasi-static transverse loading of mid-scale double bottom structures by rigid indenters with different geometries, i.e. various nose radius and cone spreading angles (Wang et al. 2000)

4. Small scale drop weight impact tests on rectangular plates (Liu et al. 2012)

It is noted that, the above tests 1. are similar to the simulated tests in i. and the OUTER SHELL model in v., while the above tests 2. and 3. are similar to the simulated tests in ii. Moreover, in the tests of Liu et al. (2012) the thicknesses were rather small (see Table 2.1).

Table 2.1. Experimental data base. Mechanical properties of steels used in the experiments and powerlaw parameters

	Component		$\dot{\varepsilon}$ (sec^{-1})	Thickness (mm)	E (GPa)	σ_y (MPa)		σ_{ueng} (MPa)		$\varepsilon_{u_{eng}}$		ε_{fr}		K (MPa)		n	
Alsos and Amdahl (2009)	Plate US, 1-FB & 2-FB		$\dot{\varepsilon} \cong 0$	5	210	285		416		0.275		0.35		740		0.24	
	Plate 1-HP		$\dot{\varepsilon} \cong 0$	5	210	340		442		0.23		0.327		750		0.2	
	Plate 2-HP		$\dot{\varepsilon} \cong 0$	5	210	260		367		0.25		0.365		640		0.22	
	FB Stiffeners		$\dot{\varepsilon} \cong 0$	6	210	340		442		0.255		0.35		760		0.225	
	HP Stiffeners		$\dot{\varepsilon} \cong 0$	6	210	390		495		0.201		0.29		830		0.18	
Paik et al. (1999)	Plates, Webs		$\dot{\varepsilon} \cong 0$	2.8	197.7	245.3		337.8		0.25		0.461		590		0.221	
	Plates, Webs		$\dot{\varepsilon} \cong 0$	3.95	199.7	319.8		412.6		0.23		0.36		702		0.205	
Paik and Tak (1995)	Plates, Stiffeners		$\dot{\varepsilon} \cong 0$	7.03-7.57	210	330.8		416.7		0.175		0.374		656		0.159	
ASIS (1993) reported in ISSC (2003)	Static - Dynamic models Side Shell : $t = 10\ mm$ Transverse Web : $t = 8\ mm$ Transverse Web Stif. : $t = 7\ mm$ Stringer Deck : $t = 7\ mm$ Stringer Deck Stif. : $t = 7\ mm$		$\dot{\varepsilon} \cong 0$	7	207.2	322		448.3		0.329		0.433		851		0.282	
				8	211.9	330.1		453		0.29		0.427		827		0.252	
				10	212.8	303.1		433.6		0.297		0.454		797		0.257	
			$\dot{\varepsilon} \cong 1.0$	7	207.2	493.9		491.5		0.189		0.401		790		0.17	
				8	211.9	491.5		498.8		0.191		0.425		804		0.172	
				10	212.8	453.7		482.7		0.176		0.432		761		0.159	
			$\dot{\varepsilon} \cong 7.6$	7	207.2	540		512.1		0.159		0.398		786		0.145	
				8	211.9	562.6		514.5		0.14		0.413		763		0.128	
				10	212.8	508.7		505.2		0.146		0.452		758		0.134	
			$\dot{\varepsilon} \cong 88.4$	7	207.2	694.6		561.6		0.173		0.447		880		0.156	
				8	211.9	686.7		573.4		0.144		0.419		856		0.131	
				10	212.8	662.2		547		0.188		0.474		877		0.169	
						M1	M2	M1	M2	M1	M2	M1	M2	M1	M2	M1	M2
Amdahl and Kavlie (1992)	Models M1 & M2	Plates	$\dot{\varepsilon} \cong 0$	4	210	321.3	321	451.4	441.2	0.208	0.187	0.349	0.368	746	707	0.186	0.169
		Floors/Girders	$\dot{\varepsilon} \cong 0$	3	210	331.4	343.1	481.2	476.3	0.209	0.156	0.3	0.288	796	727	0.187	0.143
		Stiffeners	$\dot{\varepsilon} \cong 0$	3	210	331.2	279.2	435.7	428.2	0.24	0.227	0.343	0.4	751	726	0.213	0.202
Wang et al. (2000)	Plates, Webs		$\dot{\varepsilon} \cong 0$	2.3	210	276.6		-		-		-		-		-	
Liu et al. (2012)	Plates		$\dot{\varepsilon} \cong 0$	1.4	206	228		364		0.18		0.23		577		0.163	
Gong et al. (2013)	Plate		$\dot{\varepsilon} \cong 0$	3.6	210	312		467		0.153		0.225		700		0.14	
	Stiffener		$\dot{\varepsilon} \cong 0$	4.4	210	255.5		396.5		0.173		0.244		630		0.157	
Villavicencio (2012) and Villavicencio et al. (2013)	Plate		$\dot{\varepsilon} \cong 0$	3	206	200		296		0.167		0.22		460		0.153	
	Stiffener		$\dot{\varepsilon} \cong 0$	5	206	250		369		0.166		0.24		572		0.151	
Tautz et al. (2013) and Fricke et al. (2014)	Shell		$\dot{\varepsilon} \cong 0$	4	204	329.5		454.1		0.189		0.28		730		0.17	
	Web Frame		$\dot{\varepsilon} \cong 0$	5	196.5	328		461		0.165		0.293		714		0.15	
	Longitudinal Stiffener		$\dot{\varepsilon} \cong 0$	7	213.1	319.3		487.3		0.172		0.256		763		0.156	
DNV (1993)	Models P1-15 & P2-15		$\dot{\varepsilon} \cong 0$	15	208.5	417		544		0.163		0.3		839		0.148	
	Models S1-20 & S2-20		$\dot{\varepsilon} \cong 0$	20	198.3	393		526		0.159		0.317		807		0.145	

This page is intentionally left blank

Chapter 3

Material Characterization

3.1 Overview

The FE code requires the introduction of a true stress-strain curve in the elastic and plastic strain region. This curve represents the relation between true stresses and strains in a multi-axial stress state and is usually calculated on the basis of the applied force and displacement measurements obtained during uniaxial tensile tests, i.e. the engineering stress-strain curve. The true stress-strain curve incorporates the localized damage that occurs during tension and captures the stress field generated in the neck, which depends on the thickness of the specimen. However, such a procedure implies that the axial stress field in the cross-section is uniaxial, which is not the case in the neck region of a specimen. The multi-axial stress field in the neck region may be observed in the results from FE simulations of tensile tests (see e.g. Ehlers and Vastra 2009). Further, the engineering stress-strain curve and consequently the true stress-strain curve depend on the gauge length. The effect of this dependency on the result of the simulation of the response of a structure is not significant, when the response under consideration is limited to small plastic strains, i.e. for mild steel the strains in the region of the yield plateau, but it becomes important, when the simulation involves the regions of the material curve beyond the point of necking, i.e. the point of ultimate load in a uniaxial tensile test. Beyond that point, uniformity is violated and plastic instabilities prevail until the final stage of fracture. Thus, it is important for the user to supply the finite element code with a true stress-strain curve that corresponds to the actual behaviour of the material in large plastic strains. A number of researchers have suggested alternative methodologies for the calculation of the true stress-strain relation in the post-necking region from standard tensile experiments, either by using empirical correction factors, Bridgman (1952), or through an iterative FE-based procedure by changing the true stress-strain relation, used as input for the simulation, until compliance with the corresponding experiment is achieved (see e.g. Zhang 1995, Ling 1996, Zhang et al. 1999 and Isselin et al. 2006). Further, benchmark studies were performed to investigate how the structural response of a loaded structure depends on the procedure that was followed to determine the true stress-strain curve. Ehlers and Vastra (2009) and Hogström et al. (2009) investigated the dependency of the stress-strain material curves from the gauge length.

Ehlers and Vastra (2009), investigated if the material model, i.e. material curve and rupture criterion, employed in a FE simulation, needs to take into account the mesh size. The authors performed benchmark tests using two material models: one which incorporated a material power law and a mesh independent failure strain according to ASM Handbook and the other, introduced by the authors, which used a mesh dependent true stress-strain relationship. The true strain was measured on a reference length, which varied from $0.88\,mm$ to $4.4\,mm$ and the true stress was calculated using the average of the actual cross-sectional areas of the specimen along the reference length. The rupture criterion was defined as the maximum effective plastic strain, being assumed to be equal with the axial maximum strain, which was measured during the tensile tests using, as described above, different reference lengths and consequently being mesh dependent. The curves were used to simulate tensile tests and the authors concluded that, the mesh dependent true equivalent stress-strain curve predicted more accurately the engineering stress-strain curve for seven different mesh sizes between $0.88\,mm$ to $4.4\,mm$. Rupture, i.e. the last point of the engineering stress-strain curve, was also more accurately predicted with the mesh dependent curve and in particular with mesh sizes less or equal to $2\,mm$.

Hogström et al. (2009) defined true stress-strain curves for three materials, NVA mild steel, Domex 355 high strength steel and NV5083 aluminum, from measurements obtained from tensile tests on $4\,mm$ thick specimens. From the figures of the publication, it can be observed that the steel curves show considerable dependency on the gauge length, which varies from $6\,mm$ to $78\,mm$, whereas the aluminum curve shows a relatively low dependency on the value of ultimate strain for gauge lengths varying from $6\,mm$ to $42\,mm$. The authors applied a piecewise curve of mild steel for a FE simulation of the tensile tests on models with mesh size varying from $2\,mm$ to $8\,mm$. The results showed no dependency from the mesh size up to a strain of 22%, which had been defined by the authors as the onset of damage. In Ehlers (2010a) the author concluded that, when simulating punching of $4.12\,mm$ thick plates, the fracture and the plate thinning are captured accurately when the true stress-strain relationship used is determined on the basis of a gauge length corresponding to the element size. However, the force-displacement curves obtained from the simulation of the punching tests, show relatively low sensitivity to the various true stress-strain curves. Further, in Ehlers (2010b and 2010c) the author compared the effect of the above mentioned material models, when used to simulate the structural response of a hull struck by a bow. He found that the energy absorption capacity was much more sensitive to the mesh size, when using the material model with the power law constitutive equation, rather than when using the material model presented in Ehlers and Vastra (2009). However, it has not been investigated if the relatively better performance is to be attributed to the mesh dependency of the constitutive equation or the rupture criterion (Samuelides 2009). The issue is addressed by Ehlers (2010c) and it remains open to investigation how to define the appropriate true stress-strain curve in case of relatively large mesh size, i.e. $l_e \geq 50\,mm$, commonly used in ship impact simulations.

ISSC Committee V.III (2003) defined a true stress-strain curve of mild steel with and without including the necking effect, although it is not described how the curve which includes necking is defined. It is understood that the curve, which does not account for necking, is taken to follow the power law with the constants being calculated on the basis of the measurements up to the point of maximum load. The curve that includes necking shows a considerable decrease of the true stresses after the point of maximum load. The resulted curves were used in a FE simulation of tensile tests and it was found that, the curve including necking effects gave considerable better results than the curve which did not include them. However, when the material models were used for the simulation of response of more complicated specimens, the results were influenced to a lesser extent from these models.

Following Okazawa et al. (2004) there are two sources that soften the behaviour of a structure during tension: one is attributed to the material, i.e. to development of micro-voids, temperature rise and shear band formation and is incorporated in the constitutive equation and the other is related to the global tangent stiffness matrix. Okazawa et al. (2004) performed FE simulations of tensile tests employing LS-DYNA and using Belytschko-Lin-Tsay plate elements, which may have constant thickness or incorporate changes in thickness. The relationship between true stress and true plastic strain was determined on the basis of the direct measurements of the axial and one transverse displacement during uniaxial tensile tests. The other transverse displacement was taken equal to the one measured, since the cross-section of the specimen was square. The axial displacement measurements were made by an optical system, which monitored the displacement of points spaced 1 mm apart. The side of the square cross-section was 10 mm. From the measurements the authors defined the material parameters C and n of the relationship:

$$\sigma_{eq} = \sigma_y\left(1 + C\varepsilon_{eq}\right)^n \tag{3.1}$$

where σ_{eq} is the equivalent true stress, ε_{eq} the equivalent true plastic strain, and σ_y the yield stress. For the Japanese Industrial Standard SS400 steel with Young's Modulus $E = 194\ GPa$ and Poisson's ratio $\nu = 0.278$, it was found that $\sigma_y = 262\ MPa$, $C = 74.3$ and $n = 0.274$. The paper does not clarify how the constants were calculated and if the measurements were taken until breaking of the specimen or up to maximum load. From the results of the simulations it can be concluded that, the selection of the elements with the option to change the thickness makes it possible to capture necking and the subsequent decrease of the applied load. The drop of the stress after necking shows a dependency on the element size, which size varied from 6 mm to less than 1 mm.

Zhang et al. (2004) suggested a powerlaw type curve for modeling the true stress-strain relationship:

$$\sigma_{eq} = K{\varepsilon_{eq}}^n \tag{3.2}$$

where $n = ln\,(1 + \varepsilon_{u_{eng}})$ and $K = \sigma_{u_{eng}} \left(\frac{e}{n}\right)^n$, $\sigma_{u_{eng}}$ being the ultimate engineering stress and $\varepsilon_{u_{eng}}$ the maximum engineering uniform strain, related to the ultimate tensile stress $\sigma_{u_{eng}}$ and e the natural logarithm. For shipbuilding steel with $\sigma_{u_{eng}}$ less than 355 MPa, the author suggested that if $\varepsilon_{u_{eng}}$ is not known, the following relationship may be used:

$$\varepsilon_{u_{eng}} = \frac{1}{0.24 + 0.01395\sigma_{u_{eng}}} \tag{3.3}$$

Using the above, the true stress-strain curve for mild steel with $\sigma_{u_{eng}} = 355\ MPa$ is:

$$\sigma_{eq} = 575{\varepsilon_{eq}}^{0.176} \tag{3.4}$$

Villavicencio and Soares (2011) defined a true stress-strain relationship using the suggestion of Zhang et al. (2004) for the region beyond ultimate load and a power law curve, obtained from the measurements of the engineering values for the pre-necking region. Both the curve of Zhang and the combined curve were used to simulate a tensile test of a 4 mm thick specimen with 5 mm and 2 mm shell elements. The results showed that, the combined curve simulated more accurately the response of the specimen, in terms of the engineering stress-strain curves, although the differences are not considered significant. Beyond necking, an influence of the mesh on the numerically obtained engineering stress-strain curve was observed.

In the present work, the true stress-strain relation beyond necking is determined between two limit curves, i.e. between the tangent to the stress-strain curve at the point of necking and a power law curve that is defined beyond the same point.

3.2 True stress-strain relation

Up to the point of neck initiation, which is assumed to occur at maximum load or ultimate engineering stress in a uniaxial tensile test, the true stress-logarithmic (true) strain curves, σ_{true}-ε_{true} are derived by simply transforming the engineering stress-strain curves adopting the volume incompressibility concept. This leads to the following two familiar relationships:

$$\begin{aligned} \sigma_{true} &= \sigma_{eng}(1 + \varepsilon_{eng}) \\ \varepsilon_{true} &= ln(1 + \varepsilon_{eng}) \end{aligned} \tag{3.5}$$

where σ_{eng} and ε_{eng} indicate the engineering values of stress and total strain as occurred from a uniaxial tensile test. True plastic strains ε_{pl} are calculated by subtracting the true elastic strains from total true strains, that is:

$$\varepsilon_{pl} = \varepsilon_{true} - \frac{\sigma_{true}}{E} \tag{3.6}$$

where E the Young's modulus of each material sample.

Beyond the point of necking there are three alternatives for the extrapolation of the curve up to fracture: the experimental, the powerlaw and the tangent type as illustrated in Figure 3.1 (see also Marinatos and Samuelides 2013b).

The experimental type has the following form:

$$\sigma_{eq} = \sigma_u \ \ for \ \ \varepsilon_{eq} \geq \varepsilon_u \tag{3.7}$$

where σ_u and ε_u are the true values of stress and plastic strain at the point the neck is initiated and can be calculated by (3.5) and (3.6). The FE code assumes that the curve follows equation (3.7) beyond the last point that the user inputs, i.e. if the state of stress and strain in an element lies beyond the extreme point of the true stress-strain curve that has been provided as input, then the program assumes that the true stress-strain curve beyond that point remains parallel to the axis of equivalent plastic strain.

The powerlaw type has the form:

$$\sigma_{eq} = K\ {\varepsilon_{eq}}^n \quad for \ \ \varepsilon_{eq} \geq \varepsilon_u \tag{3.8}$$

The parameters K and n are the material parameters, namely the strength coefficient and the strain-hardening index. At the onset of necking, i.e. $(\varepsilon_u, \sigma_u)$, in a uniaxial tension test following Considère's (1885) approach it is:

$$\sigma_{eq} = \sigma_u \quad \text{and} \quad \frac{d\sigma_{eq}}{d\varepsilon_{eq}} = \sigma_u \tag{3.9}$$

Thus, parameters K and n can be determined easily as

$$n = \varepsilon_u \quad \text{and} \quad K = \frac{\sigma_u}{{\varepsilon_u}^{\varepsilon_u}} \tag{3.10}$$

Following equation (3.10) the powerlaw type becomes:

$$\sigma_{eq} = \left(\frac{\sigma_u}{{\varepsilon_u}^{\varepsilon_u}}\right) {\varepsilon_{eq}}^{\varepsilon_u} \quad for \ \ \varepsilon_{eq} \geq \varepsilon_u \tag{3.11}$$

For the tangent type, it is assumed that the true curve beyond the point of necking is linear and tangent to it at point $(\varepsilon_u, \sigma_u)$. Hence, it will have the following form:

$$\sigma_{eq} = z\varepsilon_{eq} + d \quad for \ \ \varepsilon_{eq} \geq \varepsilon_u \tag{3.12}$$

where the coefficients z and d of the linear expression (3.12), can be determined according to (3.9) which will give $z = \sigma_u$ and $d = \sigma_u(1 - \varepsilon_u)$.

Finally tangent type true curve takes the form:

$$\sigma_{eq} = \sigma_u(1 - \varepsilon_u + \varepsilon_{eq}) \quad for \;\; \varepsilon_{eq} \geq \varepsilon_u \tag{3.13}$$

Ling (1996) proposed a general type for σ_{eq} after the point of necking, by introducing an unknown weight constant w which varies between 0 and 1. This weight constant combines relations (3.11) and (3.13) and has the following form:

$$\sigma_{eq} = \sigma_u \left[w\left(1 - \varepsilon_u + \varepsilon_{eq}\right) + (1 - w)\left(\frac{\varepsilon_{eq}}{\varepsilon_u}\right)^{\varepsilon_u} \right] \tag{3.14}$$

Zero value for w leads to a powerlaw type curve, while w equal to one leads to a tangent type curve. For intermediate values of w, true curves between the powerlaw and tangent type are derived. Thus, powerlaw type curve represents the lower bound and tangent type the upper bound of the curves obtained by relationship (3.14).

It is noted that, the experimental type true stress-strain representation has not been considered in the simulations of the present work, because they exhibit an unrealistic material behaviour, as it has been concluded in Marinatos and Samuelides (2013b).

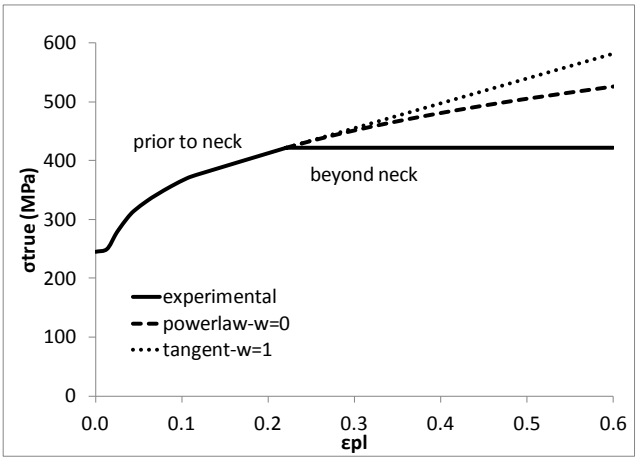

Figure 3.1. Experimental, powerlaw and tangent type true stress-strain curves beyond necking

It is also noted that, in all cases of the examined tests simulated in the present work, the material used is steel and it is assumed to have isotropic plastic properties, following the plane stress J_2 flow theory during the modeling process. The engineering stress-strain curves for the various materials were obtained by tensile testing of flat specimens and are presented in Appendix A with the related references.

3.3 Uniaxial simulations

3.3.1 Definition of the appropriate stress-strain relation

Definition of the appropriate true stress-strain curve beyond the point of necking, that is the one that yields the best reproduction of the experimental stress-strain curve, was achieved through uniaxial simulations without fracture by following an iterative procedure (Ling 1996). In the present work it was further considered the relevant mesh size. It is noted that, regardless of the element size and curve type used for the uniaxial simulations up to maximum load, i.e. prior to the neck, coincidence of the numerical results is achieved (see also Hogström et al. 2009 and Marinatos and Samuelides 2013b). The uniaxial simulations were performed with the Abaqus/Implicit FE code for materials that the uniaxial tensile tests had been performed quasi-statically, i.e. $\dot{\varepsilon} \cong 0\ sec^{-1}$ and with the Abaqus/Explicit FE code for materials that the uniaxial tensile tests had been performed with $\dot{\varepsilon} > 0\ sec^{-1}$ according to ASIS (1993) reported in ISSC (2003) (see Table 2.1, chapter 2). In the latter simulations the FE code was supplied with true strain-rate dependent material curves. The four-node reduced integration quadrilateral Belytschko-Lin-Tsay shell elements, i.e. S4R with five section or integration points through the thickness, were chosen for the meshing of the models (see Figure 3.2 and ABAQUS 2010). All specimens have rectangular cross-sections. Several different mesh sizes were used to study the mesh dependence. The aspect ratio of the elements was kept as close as possible to 1:1 at the beginning of the simulation. Note that high aspect ratios, namely over 4, were in general avoided in the numerical simulations, at least close to the point of interest, because this would have affected the accuracy of the results (ABAQUS 2010).

It has been observed that, in most cases of the uniaxial simulations, the use of a true stress-strain relation which exhibited high hardening, i.e. $w > 0.8$, close to the tangent type true stress-strain curve, beyond the point of necking, led to better reproduction of the experimental stress-strain curve for ratios $l_e/t < 1$, while the use of a true stress-strain relation which exhibited lower hardening, i.e. $w < 0.4$, close to the powerlaw type true stress-strain curve, led to a better reproduction of the experimental stress-strain curve for ratios $l_e/t > 1$ (see Figure 3.2). This trend is in line with the experiments presented in Ehlers and Vastra (2009). In Ehlers and Vastra (2009) the experimental true stress-strain curves were determined using different gauge lengths. The optical measurements produced true material curves which exhibited lower hardening in the case where the corresponding gauge length was bigger, than in the case that it was smaller and thus closer to the local neck.

The above trend is explained as follows. The area of the specimen section inside the neck is smaller and as a result higher true Mises stresses are developed for the same load. Equivalent true plastic strains are also higher inside the neck. Fine meshes, i.e. $l_e/t < 1$, can reproduce the formation of the neck and capture these strains, as the elements are as close as possible to the point the neck is formed (see Figure 3.3). On the other hand, a course mesh, i.e. $l_e/t > 1$, leads to large elements that stretch mostly in the loading direction and cannot reproduce correctly the reduction of the width of the specimen inside the necking zone (see Figure 3.3). Consequently, lower true Mises stresses are developed for the same load with

respect to the ones in a fine meshed model. Moreover, although the relative displacement between the two nodes of an element in a coarse mesh is higher with respect to the one of an element in a fine mesh, the element length is much larger. Therefore, equivalent true plastic strains are lower. Hence, usually true stress-strain curves with high hardening, i.e. $w > 0.8$, are included in the simulations for fine meshed models, i.e. $l_e/t < 1$ and with lower hardening, i.e. $w < 0.4$, in the simulations for coarse meshed models, i.e. $l_e/t > 1$. It is noted that, ratios $l_e/t < 1$ were not used in the simulations of the benchmark study in chapter 5 and the full-scale simulations (see also Villavicencio 2012).

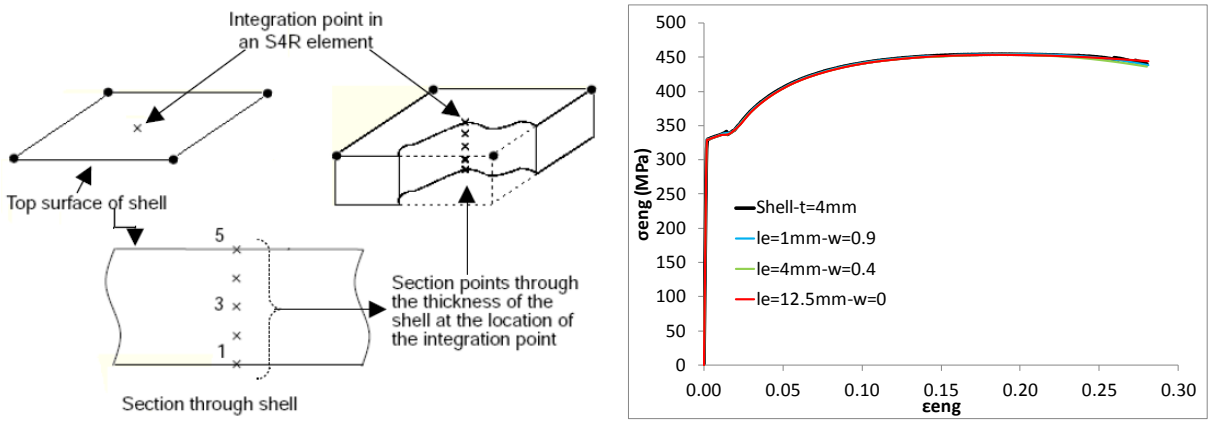

Figure 3.2. The S4R element with five through thickness integration points (on the left) and reproduction of the uniaxial tests for the shell component of the CE-1 model with $l_e = 1$, 4 and 12.5 mm, using true stress-strain curves with $w = 0.9$, 0.4 and 0 (on the right)

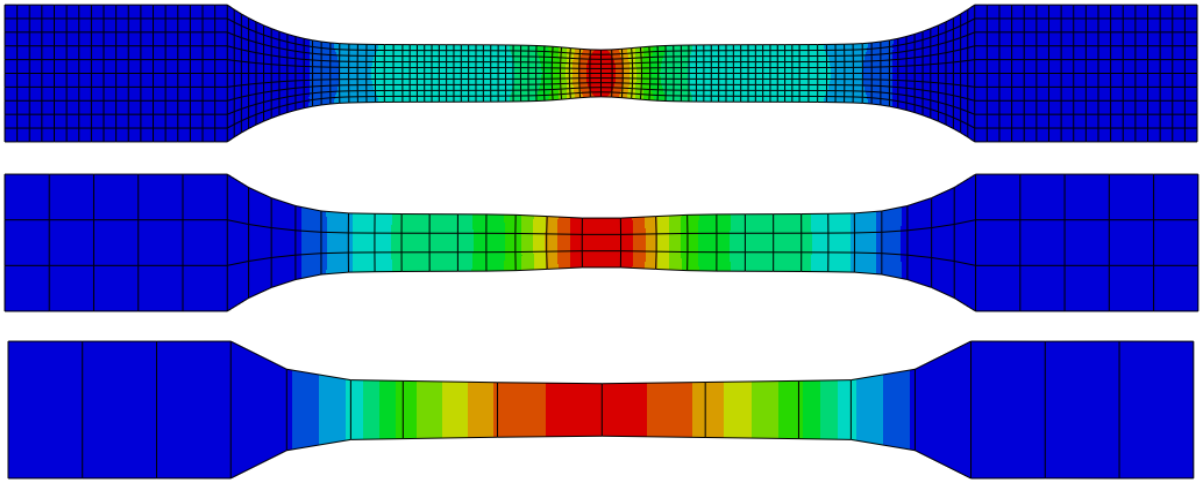

Figure 3.3. Uniaxial simulations. Example shell CE-1 model, $t = 4\,mm$, $l_e = 1$, 4 and 12.5 mm mesh sizes displayed $l_e/t = 0.25$, 1 and 3.125

3.3.2 Strain-rate effect

As already mentioned in the previous sub-section, uniaxial simulations in the cases of materials that the uniaxial tensile tests had been carried out with $\dot{\varepsilon} > 0\ sec^{-1}$ were performed using Abaqus/Explicit FE code, in order to account for strain-rate effects. The original form of Cowper and Symonds (1957) empirical expression is available in Abaqus/Explicit with the following form (ABAQUS 2010):

$$\dot{\varepsilon}_{eq} = D_{CS}(R-1)^{n_{cs}} \tag{3.15}$$

where $\dot{\varepsilon}_{eq}$ is the equivalent true plastic strain-rate, R the ratio of the equivalent yield stress at non zero strain-rate or dynamic yield stress to the respective equivalent static yield stress, i.e. $\frac{\sigma_{y_D}}{\sigma_{y_S}}$ and D_{CS}, n_{CS} are material parameters.

Cowper and Symonds (1957) found that, the values of the aforementioned parameters for a reasonable estimation of initial yielding in mild steels are $D_{CS} = 40.4\ sec^{-1}$ and $n_{CS} = 5$. However, application of these values of the material parameters beyond the point of initial yielding, would exhibit relatively high stresses. Therefore, the material parameters should be calibrated appropriately in order to capture the post yield material behaviour. An example is shown in Figure 3.4.

Figure 3.4 illustrates comparisons between experimental results and results from uniaxial simulations using the expression in equation (3.15) with $n_{CS} = 5$ and three different values for parameter D_{CS} and numerical results where all the powerlaw type true strain-rate dependent material curves were given as input (see also Figure 5.23, chapter 5). The simulation refers to a uniaxial tensile test of the material used in the experiments of ASIS (1993) reported in ISSC (2003), that has a thickness of 7 mm and has been loaded at its ends with a speed equal to approximately 380 mm/sec, which corresponds to a mid strain-rate equal to $\dot{\varepsilon} \cong 7.6\ sec^{-1}$ for a 50 mm gauge length (see also Appendix A). Note that, in the simulations with the Cowper-Symonds expression the powerlaw type true stress-strain curve of the static tensile test was given as input (see also Figure 5.23, chapter 5). The time of the simulation was defined according to the mid strain-rate of the experiment and the gauge length of the specimen. The values 2560 sec^{-1} and 3200 sec^{-1} with respect to parameter D_{CS} were selected, the former according to the ISSC (2003) report and the latter according to the proposed value for high tensile steels (see also Villavicencio 2012).

From Figure 3.4 it is obvious that, the best reproduction of the experiment is achieved in the case where all the powerlaw type true strain-rate dependent material curves were given directly as input to the FE code. Simulations using Cowper-Symonds expression with $D_{CS} = 40.4\ sec^{-1}$ give a good estimation of the initial yield strength but, as discussed previously, highly overestimate the strength of the material beyond that point. Numerical results with $D_{CS} = 2560$ and $3200\ sec^{-1}$ are almost identical. Contrary to the results in the case with $D_{CS} = 40.4\ sec^{-1}$, the initial yield strength of the material is underestimated. Although the reproduced stress-strain engineering curves are closer to the experiment in

terms of the case with $D_{CS} = 40.4\, sec^{-1}$, they also predict a material that exhibits high hardening.

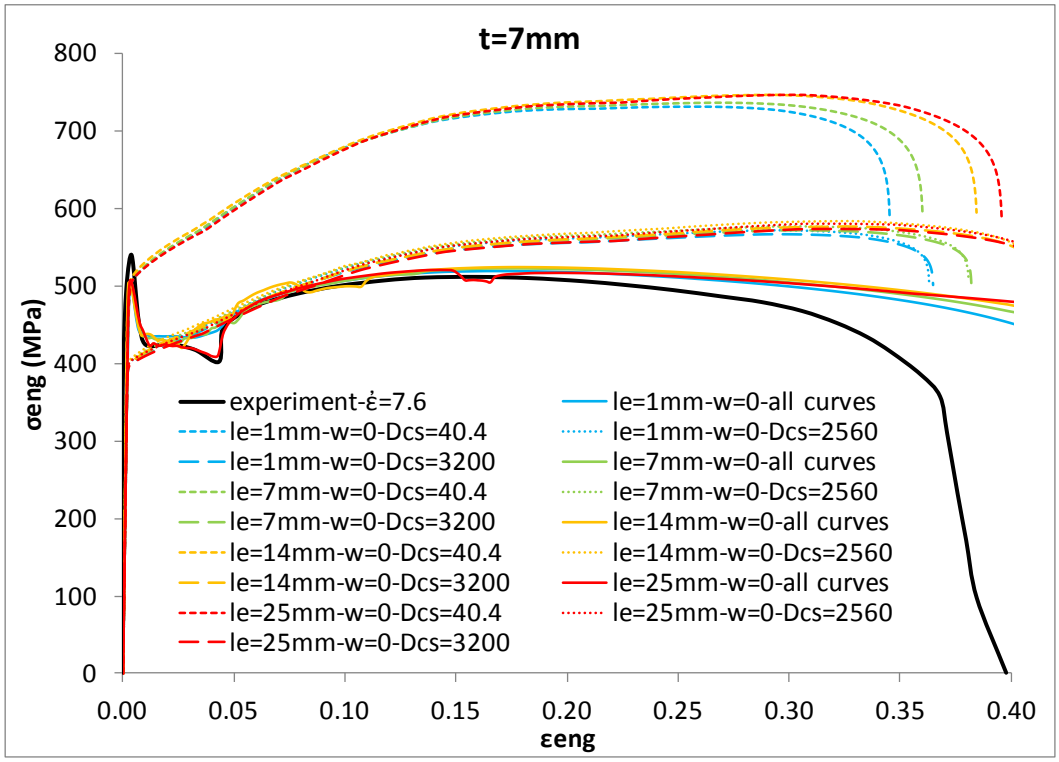

Figure 3.4. Reproduction of the uniaxial tests with $\dot{\varepsilon} \cong 7.6\, sec^{-1}$ for the 7 mm thick material using Cowper-Symonds formula with $D_{cs} = 40.4$, 2560 and 3200 sec^{-1}, $n_{cs} = 5$ and all powerlaw type true strain-rate dependent material curves for $l_e = 1$, 7, 14 and 25 mm

Chapter 4

Failure Criteria

4.1 Instability and rupture criteria

4.1.1 Overview

In sheet metal forming processes as well as in crashworthiness analyses, correct prediction of initiation and propagation of rupture is of great importance. Hence, researchers have proposed various failure criteria, aiming to the interpretation of the different failure mechanisms that are encountered within the different states of loading of a material.

Failure criteria may be classified in two main categories: i) instability criteria and ii) fracture or rupture criteria. Instability criteria account for necking instability, while rupture criteria account for fracture. Usually, instability criteria assume that fracture of the material occurs just after the formation of a local neck. However, this assumption leads to an earlier initiation of rupture. Although the earlier initiation of rupture is considered as conservative, it is noted that, this is not always the case when simulating the impact of two deformable bodies. In such a case the results are conservative for the body that is subjected first to damage but non-conservative for the other body involved in the impact. A basic assumption regarding the various criteria is that, during the loading process the loading path as well as plastic deformation are proportional, i.e. linear loading paths, which is more or less the case up to initiation of necking, i.e. point of maximum load in the case of a uniaxial tensile test. However, when an integral is included in their definition the criteria account for localized, non-linear loading paths, although there is not always theoretical evidence that it is applicable in these cases. Thus, it could be said that, integral-form criteria are more general, as they may capture the possible non-linear behaviour of the material as the deformation proceeds, considering monotonically increasing loading states; reverse loading is limited and within the elastic region.

According to most of the rupture criteria that account for shear damage or void growth, the initiation of rupture depends on the state of stress involved. One parameter to describe the state of stress is the triaxiality T, that is defined as the ratio of the mean or hydrostatic stress to the effective or von Mises equivalent stress, i.e. $T = \sigma_m/\sigma_{eq}$. The mean stress is linked to dilatation and thus is responsible for the change in volume of a solid element as it deforms. The effective stress is directly related to octahedral shearing stress, which in turn is related to distortional strain energy to change the shape of a solid element as it deforms. In other words, it could be stated that stress triaxiality is the ratio of volume change to shape change (Jeong et al. 2008).

Knowledge of triaxiality during a loading process provides the engineer with important information with respect to the stress state encountered. Close to zero and negative values of triaxialities correspond to shear and compression stress states, while positive values of triaxialities to tension stress states. It is noted that, for triaxialities equal and below -1/3, rupture does not take place in the case of ductile materials, according to observations from related experiments (see e.g. Bao and Wierzbicki 2005).

Rupture criteria could be also characterized as i) strain-based criteria, whereby rupture takes place when the deformed material reaches a critical strain value, ii) stress-based criteria, whereby rupture takes place in a critical state of stress and iii) energy-based criteria, which relate the occurrence of rupture when the energy stored during stressing the material or stored within the material volume reaches a critical value. However in the case the loading path is assumed linear up to fracture, strain-based criteria may be transformed to stress-based and vice versa.

The majority of the rupture criteria determine fracture at some critical plastic strain. Keeler and Backofen (1964) introduced the forming limit diagram or FLD criterion, which is a useful concept to determine the amount of deformation that a material can withstand prior to the onset of necking, accounting for different loading processes, i.e. between compression and tension. During these loading processes, the ratio between the strain-rates of the minor to the major in-plain principal true strains is assumed constant, i.e. $\beta = \dot{\varepsilon}_2/\dot{\varepsilon}_1 = \text{constant}$, linear loading path. FLDs include the major and minor in-plane principal true strains at the initiation of the neck, while the fracture forming limit diagrams or FFLD's, illustrate the major and minor in-plane principal true strains at fracture (Törnqvist 2003).

Strain-based rupture criteria may be also expressed in terms of stresses, under the assumption of monotonic loading in the plastic region. Arrieux et al. (1982) presented for the first time stress-based FLDs or FLSDs. Many years later, extensive studies were carried out by Stoughton (2000), Stoughton (2001), Stoughton and Zhu (2004) and Wu et al. (2005) for the derivation of FLSDs. These diagrams include the major and minor in-plane principal true stresses at the initiation of the neck. Contrary to FLDs, FLSDs show small dependence on the strain path, whereby FLSD criterion depends only on the current state of stress.

A useful approach for the determination of rupture has also proved to be the use of a critical strain energy level. Practically, this implies that rupture will take place when the elastic energy stored in a solid element becomes greater than a critical value which constitutes a material property (Andrianopoulos and Theocaris 1985).

Instability and rupture criteria are discussed in the following two sub-sections. Note that, plane stress conditions are considered in the theory of instability criteria.

4.1.2 Instability criteria

Swift (1952) postulated that a diffuse neck, i.e. thinning of the sheet during a sheet metal forming process over a large area of the sheet, is formed when the load reaches a maximum along both principal directions in the plane of the sheet. Thus, two constraints arise from this assumption:

$$\dot{\sigma}_1 = \dot{\varepsilon}_1 \sigma_1 \quad \text{and} \quad \dot{\sigma}_2 = \dot{\varepsilon}_2 \sigma_2 \tag{4.1}$$

where σ_1, σ_2, $\dot{\sigma}_1$ and $\dot{\sigma}_2$ are the major and minor in-plane principal true stresses and their stress rates, respectively. Using a Von Mises yield function and a powerlaw of the form $\sigma_{eq} = K\,{\varepsilon_{eq}}^n$, the following relation for the true equivalent plastic strain at diffuse necking is derived, see Stoughton and Zhu (2004). The range is $-1 < \beta \leq 1$:

$$\varepsilon_{eq} = \frac{4n(1-\alpha+\alpha^2)^{\frac{3}{2}}}{4-3\alpha-3\alpha^2+4\alpha^3} \tag{4.2}$$

where α is the ratio between the minor and major in-plane principal true stresses.

Hill (1952) assumed that instability occurs, when a local neck is initiated under tension, i.e. when the force per unit width acting on a sheet in the direction of the major principal direction reaches a maximum. This leads to the maximum tension condition, which is only valid for $\beta > -1$ and has the following form:

$$\dot{\sigma}_1 = (\dot{\varepsilon}_1 + \dot{\varepsilon}_2)\sigma_1 \quad \text{or} \quad \frac{d\sigma_1}{d\varepsilon_1} = (1+\beta)\sigma_1 \tag{4.3}$$

With a powerlaw of the form $\sigma_1 = K\,{\varepsilon_1}^n$, the above expression gives the major strain at instability:

$$\varepsilon_1 = \frac{n}{1+\beta} \tag{4.4}$$

Hill's instability criterion yields rational results, which are in good agreement with experiments in the range of $-1 < \beta \leq 0$. It is noted that, the Swift (1952) and Hill (1952) criteria are based on the assumption of a proportional process, i.e. constant ratio of minor over major strain.

Stören and Rice (1975) stated that responsible for the onset of localized necking in thin sheets under biaxial stretching is the development of a vertex on the yield locus. They derived

analytical solutions for the determination of the major in-plane principal true plastic strain ε_1 at local neck, considering negative and positive values of β, that is in the range of $-1 < \beta \leq 1$, in two cases:

i) For $-1 < \beta \leq 0$ (Stören-Rice 1975a):

$$\varepsilon_1 = \frac{n}{\left[\frac{(1-n)}{2} + \sqrt{\frac{(1+n)^2}{4} - \beta\frac{n}{(1+\beta)^2}}\right](1+\beta)} \tag{4.5}$$

and $\varphi = arctan\left(\sqrt{-\beta}\right)$

assuming that the local neck forms at an angle φ with respect to the direction of σ_1 and that the strain increments in the direction of the neck are zero.

ii) For $-1 \leq \beta \leq 1$ (Stören-Rice 1975b):

$$\varepsilon_1 = \frac{3\beta^2 + n(2+\beta)^2}{2(2+\beta)(1+\beta+\beta^2)} \tag{4.6}$$

and $\varphi = 0$

assuming that the local neck forms along the direction of the minor in-plane principal true plastic strain ε_2, i.e. $n_2 = 0$, the second component of the unit vector $\hat{n}$, where the latter is perpendicular to the direction of the local neck.

Bressan and Williams (1983) proposed a critical shear stress criterion for the prediction of local necking in a sheet under biaxial stretching condition. They postulated that, the shear instability will initiate in an inclined direction through the thickness of a sheet, when the local shear stress reaches a critical value. This critical value is considered a material property. Alsos et al. (2008) combined Hill's (1952) criterion which yields good results in the range of $-1 < \beta \leq 0$ and Bressan and Williams (1983) criterion which accounts for $0 \leq \beta \leq 1$ and introduced BWH failure criterion, which is based on a critical membrane stress level, that is reached when the material becomes instable and loses its capacity to carry loads (see sub-section 4.2.5).

4.1.3 Rupture criteria

McClintock (1968) proposed a failure criterion for the description of damage of a material due to void growth. In a simplified version the criterion takes the following simple form:

$$D_i = \int \left(\frac{\sigma_m}{\sigma_{eq}}\right) d\bar{\varepsilon}^{pl} \tag{4.7}$$

where D_i is the damage parameter and $d\bar{\varepsilon}^{pl}$ an increment of the equivalent true plastic strain. When D_i becomes equal to the critical strain, void coalescence occurs and the material ruptures.

Rice and Tracey (1969) introduced a failure criterion, which is consistent in predicting rupture in the case of the tensile tests due to void growth. On the other hand, Cockcroft and Latham (1968) proposed a criterion which yielded reasonable results under shear damage. Törnqvist (2003) combined the aforementioned criteria and proposed a strain based criterion which accounts for the whole range of stress triaxiality, the so called RTCL damage criterion (see sub-section 4.2.4).

Johnson and Cook (1983) introduced a fracture model which is dependent on the strain, strain-rate, temperature and pressure. Fracture strain is calculated by the following expression:

$$\varepsilon_f = \left[D_1 + D_2 exp\left(D_3 \frac{\sigma_m}{\sigma_{eq}}\right)\right][1 + D_4 ln\dot{\varepsilon}^*][1 + D_5 T^*]$$

and (4.8)

$$T^* = \frac{T' - T_{ROOM}}{T_{MELT-}T_{ROOM}}$$

where D_1 - D_5 are material constants, $\dot{\varepsilon}^* = \dot{\varepsilon}/\dot{\varepsilon}_0$ the dimensionless plastic strain-rate with $\dot{\varepsilon}_0 = 1.0\ sec^{-1}$ and T^* the homologous temperature (see Johnson and Cook 1983 and 1985).

Andrianopoulos and Theocaris (1985) proposed the T-criterion, which correlates the reversible elastic energy density storage process with both brittle and ductile rupture. A dual limit to the elastic strain energy that is stored within the material is defined. The one is determined by the capacity of the material to store elastic strain energy density due to volume change, i.e. the dilatational elastic strain energy density T_D and the other by the capacity of the material to store elastic strain energy due to change in shape, i.e. the distortional elastic strain energy density T_V. In the case that the material has a linear elastic behaviour, the aforementioned elastic strain energy densities are given by the following expressions:

$$T_D = \int \sigma_{eq} d\bar{\varepsilon}^{el} = \frac{1}{6G}{\sigma_{eq}}^2$$

and (4.9)

$$T_V = \int \sigma_m d\Theta = \frac{1}{2K'}{\sigma_m}^2 = \frac{1}{2}K'\Theta^2$$

where $d\bar{\varepsilon}^{el}$ an increment of the equivalent true elastic strain, Θ the elastic unit volume change and G, K' the shear and bulk modulus of the material, respectively. The critical values of these energies are independent of the applied loads and the geometry of the material, but are dependent on the strain-rate and temperature. Currently, T-criterion is used to predict the initiation of pre-existent macroscopic cracks as well as in the calculation of FLDs for metal forming processes (Andrianopoulos et al. 1996).

Lehmann and Yu (1998) based on studies within the framework of continuum damage mechanics, proposed the rupture index or I_R criterion. The only parameter for the calibration of rupture index criterion is the one-dimensional true rupture strain from a uniaxial tensile test ε_R. They expressed the multi-axial true rupture strain ε_{vr} as a function of ε_R by introducing a stress triaxiality function of the following form:

$$f\left(\frac{\sigma_m}{\sigma_{eq}}\right) = \frac{2}{3}(1+\nu) + 3(1-2\nu)\left(\frac{\sigma_m}{\sigma_{eq}}\right)^2 \tag{4.10}$$

where ν the Poisson's ratio. Thus:

$$\varepsilon_{vr} = \varepsilon_R f^{-m}\left(\frac{\sigma_m}{\sigma_{eq}}\right) \tag{4.11}$$

and $m = 2n + 1$

Finally the rupture index criterion takes the form:

$$I_R = \varepsilon_v f^m\left(\frac{\sigma_m}{\sigma_{eq}}\right) \tag{4.12}$$

where ε_v the multi-axial effective true plastic strain. The criterion is satisfied when ε_v becomes greater or equal to ε_{vr}, i.e. $I_R \geq \varepsilon_R$.

Peschmann (2001) proposed an equivalent fracture strain criterion, where the critical value of strain depends on the thickness t of the plate and is obtained by the following relation:

$$\varepsilon_P = \varepsilon_g + \mathrm{a}_p \frac{t}{l_e} \tag{4.13}$$

where ε_g is the uniform strain, a_p a factor depending on the necking strain and the length of the neck and l_e the element length. The various values of ε_g and a_p with respect to the thickness, are summarized in Table 4.1.

Table 4.1. Values of the Peschmann criterion parameters for different thicknesses

$t\ (mm)$	ε_g	a_p
5	0.1	0.8
12.5-20	0.08	0.65

Zhang et al. (2004) introduced a strain criterion, which postulates that damage is initiated at a critical through thickness strain. The critical through thickness strain is calculated from the following relation:

$$\varepsilon_{3_{cr}} = \varepsilon_g + \varepsilon_t \frac{t}{l_e} \tag{4.14}$$

where ε_g is the uniform strain and ε_t the necking strain. The various values of ε_g and ε_t with respect to the element type, are summarized in Table 4.2.

Table 4.2. Values of the Zhang criterion parameters for different element types

Element type	ε_g	ε_t
Shell	0.056	0.54
Beam	0.079	0.76

Peschmann (2001) and Zhang et al. (2004) criteria, is recommended to be used with element length over thickness ratios over five in numerical analyses with shell elements.

Ehlers and Vastra (2009) after conducting tensile tests using an optical measuring system, which measured the local displacements at the surface of the specimen and calculated local strain on the basis of a discrete amount of pixel recordings until failure, proposed a strain criterion which is defined by the maximum allowable effective plastic strain that is dependent on the element size.

More recently Lou et al. (2012) formulated a ductile fracture criterion, which accounts for the various mechanisms of damage, that is nucleation, growth and shear coalescence of voids, through three different parameters C_1, C_2 and C_3, by simply multiplying three damage accumulating models. The criterion has the following expression, in the case of non-proportional loading:

$$\frac{1}{C_3}\int\left(\frac{2\tau_{max}}{\sigma_{eq}}\right)^{C_1}\left(\frac{\langle 1+3T\rangle}{2}\right)^{C_2} d\bar{\varepsilon}^{pl} = D$$
$$\text{and} \quad \langle 1+3T\rangle = \begin{cases} 0 & for \quad x<0 \\ x & for \quad x\geq 0 \end{cases} \tag{4.15}$$

where τ_{max} is the maximum shear stress, while C_1, C_2 and C_3 parameters are assumed to be constant. These parameters can be calibrated through experiments, i.e. uniaxial tensile test, plane strain test, pure shear test and equal biaxial tensile test, by determining the corresponding critical strains in each case. Actually, three experiments suffice for the calibration of the parameters.

In the case where the loading path is assumed to be linear the above expression is reduced to:

$$\left(\frac{2\tau_{max}}{\sigma_{eq}}\right)^{C_1}\left(\frac{\langle 1+3T\rangle}{2}\right)^{C_2}\varepsilon_{eq} = C_3 \tag{4.16}$$

Based on the above expression, the following relationships are derived for different loading processes (see also Table 4.3 in section 4.3):

i) Pure shear

$$\left(\frac{2}{\sqrt{\overline{3}}}\right)^{C_1}\left(\frac{1}{2}\right)^{C_2}\bar{\varepsilon}_{f,s} = C_3 \tag{4.17}$$

ii) Uniaxial tension

$$\bar{\varepsilon}_{f,t} = C_3 \tag{4.18}$$

iii) Plane strain

$$\left(\frac{2}{\sqrt{\overline{3}}}\right)^{C_1}\left(\frac{1+\sqrt{3}}{2}\right)^{C_2}\bar{\varepsilon}_{f,p}=C_3 \tag{4.19}$$

iv) Equal biaxial stretching

$$\left(\frac{3}{2}\right)^{C_2}\bar{\varepsilon}_{f,b}=C_3 \tag{4.20}$$

where $\bar{\varepsilon}_{f,s}$, $\bar{\varepsilon}_{f,t}$, $\bar{\varepsilon}_{f,p}$ and $\bar{\varepsilon}_{f,b}$ the critical equivalent plastic strains for each loading process. By dividing (4.19) with (4.17) results to the expression for the derivation of C_2:

$$C_2=\frac{log\left(\bar{\varepsilon}_{f,s}\right)-log\left(\bar{\varepsilon}_{f,p}\right)}{log\left(1+\sqrt{3}\right)} \tag{4.21}$$

and finally

$$C_1=\frac{log(C_3)-log\left[\left(\frac{1+\sqrt{3}}{2}\right)^{C_2}\bar{\varepsilon}_{f,p}\right]}{log\left(\frac{2}{\sqrt{\overline{3}}}\right)} \tag{4.22}$$

or

$$C_1=\frac{log(C_3)-log\left[\left(\frac{1}{2}\right)^{C_2}\bar{\varepsilon}_{f,s}\right]}{log\left(\frac{2}{\sqrt{\overline{3}}}\right)}$$

In the simulation of impacts on large marine structures using non-linear FE codes, the structures are mostly modeled with shell plane stress elements and the criteria are incorporated to their formulation. It should be therefore considered that, the numerical simulation does not capture the triaxial state of stress that may actual occur and is further included in the theory of many criteria. However, plane stress elements allow for the variation of the in-plane stresses as well as for the thickening or thinning of the element in compression and tension stress states, through the definition of an appropriate number of through thickness integration points.

4.2 Modeling of rupture

4.2.1 Rupture criteria and modeling techniques in non-linear FE codes

Most of the rupture criteria referred in the previous section have been used in FE codes. The procedure, that is used to deal with material rupture in FE analyses, is to remove the element, which models the part of the structure, where rupture occurs. This technique although is not the only possible method to deal with rupture; an alternative could be to simulate loss of material integrity by removing the attachment between nodes of adjacent elements. However, the former method is preferred by almost all researchers performing simulations of collisions and groundings with finite elements.

The simpler rupture criteria that have been used in FE codes are based on a damage parameter, which is an integral along the strain path of the element (see e.g. Lehmann and Peschmann 2002 and Simonsen and Törnqvist 2004). The most common of such a criterion is based on a maximum allowable plastic strain, either the plastic component of the Mises strain (Lehmann and Peschmann 2002) or the thru thickness plastic strain (Zhang et al. 2004). However, the reliability of the criterion depends on the mode of deformation of the structure under consideration, i.e. the criterion has inconsistent performance. This is understandable, because the criteria have been calibrated on the basis of measurements obtained from particular tests, usually uniaxial tensile tests. This issue is addressed by Bao and Wierzbicki (2004), who investigated the performance of nine damage criteria, when applied to predict the rupture that occurred during two sets of uniaxial compression tests and three tests of uniaxial tension tests. The comparison of the test results versus the prediction, obtained by the various criteria, revealed that the general Rice and Tracey (1969) and the hydrostatic stress criteria were consistent in predicting rupture in the case of the tensile tests and the Cockcroft and Latham (1968) criterion in the case of compression. Thus, it seems that a unique criterion, at least to our present understanding, is not adequate to predict rupture during all modes of structural response that occur in ship-ship collisions and it is more appropriate to use a set of criteria (see e.g. Törnqvist 2003 and Alsos et al. 2008). Servis and Samuelides (2006) have also incorporated the T-criterion in Abaqus/Explicit, for the simulation of the various failure modes in ship-ship collisions.

A further distinction that has been used in the treatment of rupture, concerns the initiation of rupture in the weld lines. This failure mode, which has been observed in collision tests, has been simulated by inserting particular elements to simulate the welds and by incorporating a rupture criterion that is based on a critical stress value (see e.g. Lehmann and Peschmann 2002, Huatao and Röhr 2004 and Alsos et al. 2009).

All criteria are sensitive to mesh size. In particular criteria that are based on plastic strains are rather more sensitive, because plastic strains increase relatively faster as a collision progresses and the distribution of plastic stains largely depends on the size of the element. Criteria that use as control parameters stress fields (Alsos et al. 2008) or the elastic strain energy (Servis and Samuelides 2006), although they are relatively less sensitive to mesh size, they too exhibit a certain sensitivity. A widely applied remedy to this fundamental problem,

is to define the critical values of control parameters as a function of the size of the element (see e.g. Kitamura 1997, Peschmann 2001, Zhang et al. 2004, Alsos et al. 2009, Ehlers and Vastra 2009, Hogström et al. 2009 and Marinatos and Samuelides 2013a, 2013b and 2015).

A further challenge related to the use of the above criteria is the definition of the parameters that are associated with them, i.e. the specific values which when they are reached, rupture allegedly occurs and the element is removed. Various combinations of experiments and numerical simulations have been proposed for their determination. As far as the removal of element is concerned, there are various options that the user may select. In the case of a shell element with more than one integration points through the thickness, the element may be removed when the criterion is met in all points or in the mid-point. For example material 123 of LS DYNA, allows the user to select the number of through thickness points which should meet the criterion to remove the element. When the user selects to consider only the mid-point, bending strains are ignored in the initiation of rupture, i.e. it is assumed that rupture occurs as a result solely of the axial forces that are developed in the cross-section. In the case of solid elements, the element is removed when the criterion is met in the single integration point and bending strain field is taken into account via the number of elements through the thickness of the plate. Yuen and Nurick (2005) have used eight-node brick (C3D8R) and six-node prism (C3D6) elements of LS-DYNA to simulate the response of small plates under transverse blast load.

FE codes provide the user with the option to apply a damage evolution law, in order to account for the material degradation beyond necking initiation and up to the fracture point. Once damage is initiated, the material stiffness is degraded progressively according to the specified damage evolution response. Hogström (2012) and more recently Kõrgesaar (2015) applied the damage evolution concept in FE codes, so as to investigate the effect of softening of the material in the results. In Hogström and Ringsberg (2012) the authors concluded that, a mesh size dependent equivalent plastic strain criterion in combination with a damage evolution law is appropriate in ship collision analyses. They also added that, FLD and FLSD criteria could be also used but without taking into account the post necking behaviour, i.e. without the use of a damage evolution law. In Kõrgesaar and Romanoff (2014), the authors simulated the US Plate and 1-FB tests referred in Alsos and Amdahl (2009). They applied on one hand a fracture criterion, in which formulation the effect of the stress triaxiality, mesh size as well as softening of the material was taken into account and on the other a mesh dependent equivalent plastic strain criterion or shear criterion. They employed Lou et al. (2012) concept for the calibration of the parameters C_1, C_2 and C_3 and defined the critical equivalent plastic strain for different stress states. The results were compared with the respective results from the numerical analysis referred in Alsos et al. (2009), i.e. with BWH and RTCL criteria, using however coarser meshes. The authors found that, results with the proposed fracture criterion tend to converge between different meshes in the range of $1 \leq l_e/t \leq 8$, contrary to the cases of RTCL and shear criteria. However, they concluded that softening has a rather small effect in the results, compared to analyses where the latter is excluded and that shear criterion yields also good correlation with the experiments using a fine mesh, i.e. l_e/t close to 1.

4.2.2 Benchmark studies

The effect of the various parameters and the uncertainties, which arise from the FE simulations of ship-ship impacts, have been also investigated by many researchers the last years, in order to determine the reliability of the numerical results. Ehlers et al. (2008) presented a study on the effect of the mesh size and modeling of material rupture on the results of simulations of large scale collision tests, using LS-DYNA. The authors used for the simulations the four-node Belytschko-Lin-Tsay element with five integration points through the thickness. To the author's knowledge, this is one of the few systematic convergence studies using large scale models, as there are publications which present FE simulations of structural response of large size structures under extreme loading conditions, which lack adequate evidence to support the selection of mesh. In general, results obtained with models made with 25 mm elements, were closer to the test results rather than with models made with 50 mm and 100 mm elements. However, the load penetration curves do not show a similar consistent trend in all three cases that were analyzed, i.e. the proximity of these curves to the experimental curve varies with the penetration and in some cases it is not obvious which criteria should be used for the determination of the best correlation. For one of the tests, where the side structure modeled a conventional double hull, the authors presented a comparison of the experimental force-penetration curve and i) the respective curves as obtained from simulations with three models, all having a mesh of 25 mm and three different rupture models, ii) the curve obtained from Peschmann (2001), who included the effect of the supports of the side structure to the hull of the struck vessel and iii) a force-penetration curve that was obtained using the model of the structure from Peschmann (2001) with the model of rupture based on the RTCL criterion (Törnqvist 2003). The comparison highlights the difficulties associated with the definition of an appropriate modeling technique. Further the authors showed that the propagation of fracture depends highly on the material failure criterion, even in the case of the densest model that employed the 25 mm elements.

Hogström and Ringsberg (2012) studied the effect of the uncertainty in the material model and the parameters and concluded that they affect significantly the assessment of the survivability of a ship involved in a collision. The authors simulated the response of a model of a double hull structure, loaded transversely by a rigid intender. Eighteen simulations were performed, using six material rupture criteria and three sets of material properties. The best performance was obtained with a rupture criterion based on Mises strain and with the values of material parameters being equal to the average values obtained from tensile tests minus two standard deviations. When the same eighteen material models were used to investigate a collision, the results showed a large scatter and the damaged area of the side structure varied from 3.8 m^2 to 69.1 m^2. However, it is noted that the material model that gave the best results when simulating the test, gave the largest damaged area, i.e. 69.1 m^2, in the collision investigation. This observation illustrates the need for further investigation of the uncertainties that are involved in the investigation of contact accidents.

An extensive study, with respect to the effect of the material model, mesh size and strain-rate in ship-ship collision FE analysis, has been also performed by Marinatos and Samuelides (2013a, 2013b) and more recently by Marinatos and Samuelides (2015). The work reported in these papers is included in the present thesis.

In the present work three rupture criteria were selected for the modeling of rupture. The critical equivalent plastic strain criterion or SHEAR criterion (Marinatos and Samuelides 2013a, 2013b and 2015), the RTCL damage criterion (Törnqvist 2003) and the BWH instability criterion (Alsos et al. 2008). Rupture is determined under different conditions according to the selected criteria. SHEAR and RTCL criteria, both determine rupture at a critical equivalent plastic strain, which is taken equal to the fracture strain of a uniaxial tensile test, but SHEAR criterion does not take into account the dependence of this critical strain on the stress triaxiality. On the other hand BWH criterion determines rupture at a critical stress, depending only on the current state of stress and is therefore independent of the strain path. Thus, the different mechanisms with respect to the different criteria, that lead to rupture of the material under various loading conditions, are investigated. A brief description of the criteria and their modeling parameters is given in the following.

4.2.3 SHEAR criterion

Critical equivalent plastic strain criterion or SHEAR criterion, is one of the first used rupture criteria in finite element simulations. It is widely used due to its simple form that makes it convenient for simulations with finite elements. According to it, rupture is determined at some critical equivalent plastic strain. However, SHEAR criterion neglects the state of stress in the definition of the threshold value for rupture. As a result, it shows constant ductility for all variations of stress triaxialities and may even yield fracture in pure compression, contrary to experimental evidence (see e.g. Bao and Wierzbicki 2005). In the present analysis it has been assumed that the SHEAR criterion is not activated for triaxialities below -1/3, i.e. for states of stress dominated by compression. The formulation of SHEAR criterion is presented in relation (4.23).

$$D_{SHEAR} = \frac{\int d\bar{\varepsilon}^{pl}}{\varepsilon_{cr}} \tag{4.23}$$

where $d\bar{\varepsilon}^{pl}$ is an increment of the true equivalent plastic strain, ε_{cr} is the critical equivalent true plastic strain and D_{SHEAR} the damage parameter. The element is removed from the mesh when $D_{SHEAR} \geq 1$ in all of the through thickness integration points of the element.

4.2.4 RTCL criterion

RTCL criterion is a strain based criterion and it constitutes a combination of the Rice and Tracey (1969) and Cockcroft and Latham (1968) damage criteria. It has the following expression (Törnqvist 2003):

$$D_{RTCL} = \frac{\int f\left(\frac{\sigma_m}{\sigma_{eq}}\right)_{RTCL} d\bar{\varepsilon}^{pl}}{\varepsilon_{cr}} \tag{4.24}$$

where

$$f\left(\frac{\sigma_m}{\sigma_{eq}}\right)_{RTCL} = \begin{cases} 0 & \frac{\sigma_m}{\sigma_{eq}} \le -\frac{1}{3} \quad \text{(cut-off value)} \\ 2\dfrac{1+\frac{\sigma_m}{\sigma_{eq}}\sqrt{12-27\left(\frac{\sigma_m}{\sigma_{eq}}\right)^2}}{3\frac{\sigma_m}{\sigma_{eq}}+\sqrt{12-27\left(\frac{\sigma_m}{\sigma_{eq}}\right)^2}} & -\frac{1}{3} < \frac{\sigma_m}{\sigma_{eq}} < \frac{1}{3} \quad \text{(Cockcroft-Latham)} \\ \frac{1}{1.65} exp\left(\frac{3\sigma_m}{2\sigma_{eq}}\right) & \frac{\sigma_m}{\sigma_{eq}} \ge \frac{1}{3} \quad \text{(Rice-Tracey)} \end{cases} \tag{4.25}$$

The element is removed from the mesh when $D_{RTCL} \geq 1$ in all of the through-thickness integration points of the element. For a more detailed presentation of the RTCL criterion see Törnqvist (2003).

In Figure 4.1, one may observe that f is a monotonically increasing function of stress triaxiality, which for triaxialities between -1/3 and 1/3, i.e. uniaxial compression, pure shear and uniaxial tension processes follows the Cockcroft-Latham expression, while for triaxialities over 1/3, i.e. uniaxial tension, plane strain and equal biaxial stretching processes, the Rice-Tracey expression. Its range is [0,+∞). For shell elements, the maximum value of triaxiality which corresponds to $\beta = 1$, i.e. equal biaxial stretching with $\sigma_1 = \sigma_2$ the major and minor in-plane principal true stresses, equals 2/3 (see also section 4.3).

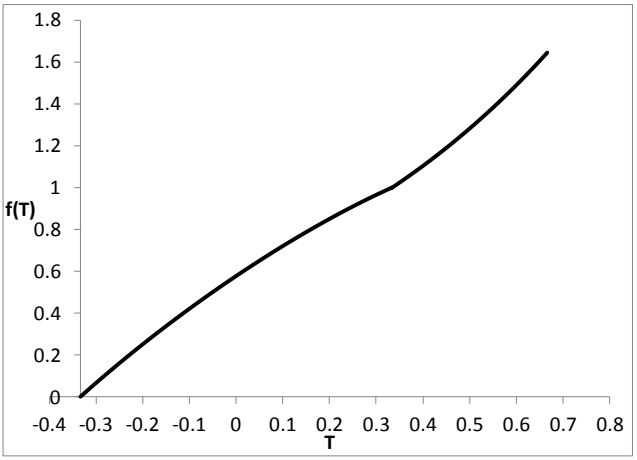

Figure 4.1. Function $f(T)$

4.2.5 BWH criterion

BWH criterion is a stress based criterion and it constitutes a combination of the local necking analysis presented by Hill (1952) with the Bressan and Williams (1983) shear stress criterion (Alsos et al. 2008). It has the following expression:

$$D_{BWH} = \frac{\sigma_1}{\sigma_{1_{cr}}} \tag{4.26}$$

where σ_1 is the major in-plane principal true stress in a plane stress state and $\sigma_{1_{cr}}$ the critical in-plane principal true stress according to the following relation (Alsos et al. 2008):

$$\sigma_{1_{cr}} = \begin{cases} \dfrac{2K}{\sqrt{3}} \dfrac{1+\frac{1}{2}\beta}{\sqrt{\beta^2+\beta+1}} \left(\dfrac{2n}{\sqrt{3}} \dfrac{\sqrt{\beta^2+\beta+1}}{1+\beta} \right)^n & -1 < \beta \leq 0 \quad \text{(Hill)} \\ \dfrac{2K}{\sqrt{3}} \dfrac{\left(\frac{2}{\sqrt{3}}n\right)^n}{\sqrt{1-\left(\frac{\beta}{2+\beta}\right)^2}} & \beta \geq 0 \quad \text{(Bressan – Williams)} \end{cases} \tag{4.27}$$

Here β is the ratio between the strain-rates of the minor and major in-plane principal true strains and K, n are the material parameters, namely the strength coefficient and the strain-hardening index, respectively.

The element is removed from the mesh when $D_{BWH} \geq 1$ at the integration point in the middle layer of the element, i.e. when the major in-plane principal true membrane stress reaches a critical value (see also Figure 3.2, chapter 3). For a more detailed presentation of the BWH criterion see Alsos et al. (2008).

The variation of $\sigma_{1_{cr}}/\sigma_u$ for different values of n, where σ_u the true value of the stress at maximum load under uniaxial loading condition with respect to β, is shown in Figure 4.2.

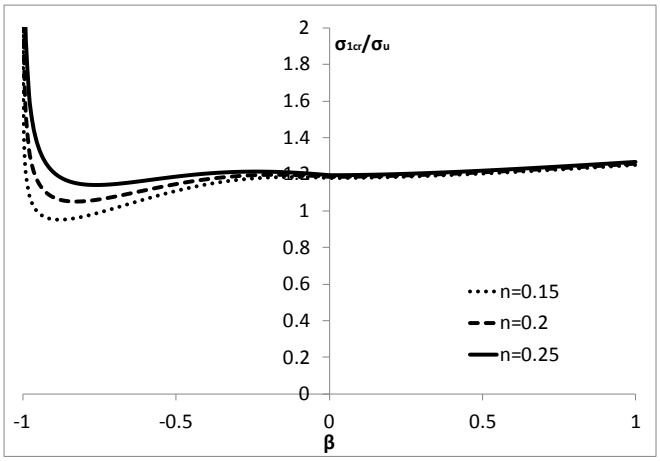

Figure 4.2. Illustration of $\sigma_{1_{cr}}/\sigma_u$ for a steel with $n = 0.15$, 0.2 and 0.25 as a function of β

For $\beta \leq 0$, i.e. plane strain, uniaxial tension, pure shear and uniaxial compression processes, the critical stress is derived by the Hill expression, while for positive values of β, i.e. plane strain and equal biaxial stretching processes, by the Bressan-Williams formula. It is noted that, equation (4.27) does not predict any limit stress for $\beta \leq$ -1, namely for $\beta =$ -1, that is a pure shear state and -2 $< \beta <$ -1, that is a state between pure shear and uniaxial compression, because $\sigma_{1_{cr}}$ cannot be defined according to (4.27) for negative values of the parenthesis. This is reasonable, as according to Hill's (1952) analysis, in the range -2 $\leq \beta \leq$ -1, tension will never reach a maximum and as a result a local neck will not be formed.

4.3 Investigation of uncertainties

The present sub-section investigates the behaviour of the various rupture criteria, which have been referred in the previous two sections, considering plane stress conditions and different loading states, i.e. between uniaxial compression and biaxial tension. The investigation is performed by comparing the FLDs and FLSDs as well as the variation of the true equivalent plastic strain ε_{eq} and the major in-plane principal true stress σ_1 versus β. The Johnson and Cook (1983) criterion as well as the T-criterion (Andrianopoulos and Theocaris 1985) are excluded from the present analysis, due to the uncertainties in the calibration of the relevant material constants within their formulation.

The properties of the material, which has been selected for the comparative study, are included in the first row of Table 2.1, chapter 2. The powerlaw parameters of the selected material are $K = 740\,MPa$ and $n = 0.24$. Also, the critical equivalent true plastic strain in uniaxial tension, i.e. $\varepsilon_{cr} = 0.361$ was selected for an element length over thickness ratio $l_e/t = 2$. This critical value was derived from uniaxial simulations, using a powerlaw type true stress-strain curve beyond necking of the form $\sigma_{eq} = K\,{\varepsilon_{eq}}^n$ and is included in Table 5.1, chapter 5.

Parameter β in a plane stress state, is connected to the ratio between the minor σ_2 and major σ_1 in-plane principal true stresses α and stress triaxiality T, by the following two relations:

$$\beta = \frac{2\alpha - 1}{2 - \alpha} \tag{4.28}$$

and

$$T = \frac{1}{\sqrt{3}} \frac{\beta + 1}{\sqrt{\beta^2 + \beta + 1}} \qquad for \quad \beta \leq 1 \tag{4.29}$$

The variation of T with respect to β under plane stress conditions in the range -2 $< \beta \leq 1$ is presented in Figure 4.3.

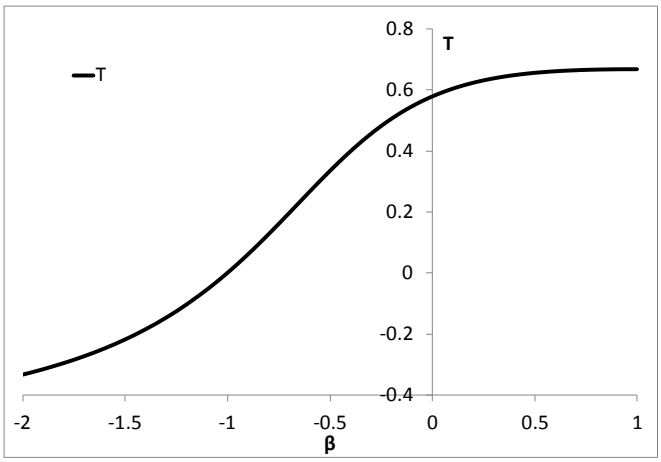

Figure 4.3. Illustration of T as a function of β under plane stress conditions

The major in-plane principal true stress and strain components, under plane stress conditions, are given by the following relations (see also Marciniak et al. 2002):

$$\sigma_1 = \frac{\sigma_{eq}}{\sqrt{1-\alpha+\alpha^2}} \tag{4.30}$$

and

$$\varepsilon_1 = \frac{\varepsilon_{eq}}{\sqrt{\frac{4}{3}(1+\beta+\beta^2)}} \tag{4.31}$$

Moreover, due to the volume constancy in plasticity, i.e. $\varepsilon_1 + \varepsilon_2 + \varepsilon_3 = 0$, the through thickness true plastic strain is given by the following expression:

$$\varepsilon_3 = ln\frac{t'}{t} = -(1+\beta)\varepsilon_1 \tag{4.32}$$

where t', t the current and initial thicknesses, respectively.

The maximum shear stress is defined in the general triaxial state as:

$$\tau_{max} = max\left\{\left|\frac{\sigma_1-\sigma_2}{2}\right|, \left|\frac{\sigma_2-\sigma_3}{2}\right|, \left|\frac{\sigma_3-\sigma_1}{2}\right|\right\} \tag{4.33}$$

which for $\sigma_3 = 0$, is reduced to the following expresion:

$$\tau_{max} = max\left\{\left|\frac{\sigma_1-\sigma_2}{2}\right|, \left|\frac{\sigma_2}{2}\right|, \left|\frac{-\sigma_1}{2}\right|\right\} \tag{4.34}$$

or

$$\tau_{max} = max\left\{\left|\sigma_1\frac{(1-\alpha)}{2}\right|, \left|\sigma_1\frac{\alpha}{2}\right|, \left|\sigma_1\frac{(-1)}{2}\right|\right\} \tag{4.35}$$

Finally by substituting (4.30) to (4.35) it yields:

$$\tau_{max} = max\left\{\left|\sigma_{eq}\frac{(1-\alpha)}{2\sqrt{1-\alpha+\alpha^2}}\right|, \left|\sigma_{eq}\frac{\alpha}{2\sqrt{1-\alpha+\alpha^2}}\right|, \left|\sigma_{eq}\frac{(-1)}{2\sqrt{1-\alpha+\alpha^2}}\right|\right\} \tag{4.36}$$

Following the precedent analysis, Figures 4.4 and 4.5 illustrate the forming limit curves of the various criteria in the strain and stress fields as well as variables σ_1 and ε_{eq} versus β. In the case of Lou et al. (2012) criterion, the determination of the critical equivalent true plastic strains in pure shear and plane strain loading processes, i.e. $\bar{\varepsilon}_{f,s}$ and $\bar{\varepsilon}_{f,p}$, were calculated as follows. For β = -1 the critical equivalent true plastic strain in pure shear $\bar{\varepsilon}_{f,s}$ was determined as the average value of the respective strains according to the SHEAR, RTCL, Rupture Index and Peschmann (2001) criteria. The Swift (1952), McClintock (1968), Stören-Rice (1975a), Zhang et al. (2004) and BWH criteria were not considered, because they do not define any value for β = -1. In addition, the Stören-Rice (1975b) criterion was not considered in the determination of $\bar{\varepsilon}_{f,s}$, as it yields fairly different results compared to the rest criteria (see Figures 4.4b and 4.5a). Similarly, for $\beta = 0$ the critical equivalent true plastic strain in plain strain $\bar{\varepsilon}_{f,p}$ was determined as the average value of the respective strains according to the Swift (1952), Stören-Rice (1975b), Rupture Index, RTCL and BWH criteria. The aforementioned criteria converge towards the same value (see Figure 4.5). The determination of the parameters deserves further investigation. Hence, the critical equivalent true plastic strains in pure shear and plane strain loading processes were taken equal to $\bar{\varepsilon}_{f,s} = 0.462$ and $\bar{\varepsilon}_{f,p} = 0.267$, respectively. Finally, according to relations (4.21) and (4.22) from sub-section 4.1.3, the calibrated parameters are $C_1 = 0.935$ and $C_2 = 0.545$. Parameter C_3 was taken equal to ε_{cr} in uniaxial tension, i.e. $C_3 = 0.361$ (see also Table 5.1, chapter 5).

Significant differences between the various criteria are noticed in the strain field (see Figures 4.4a and 4.5b). The equivalent plastic strain at fracture reaches a minimum between uniaxial and plane strain loading processes in the case of the Swift (1952) criterion, which is based on diffuse necking and close to plain strain loading process, in the cases of the Stören-Rice (1975a,b) and BWH criteria, which account for local necking initiation and then is increasing. On the contrary, excluding the SHEAR and Peschmann (2001) criteria, in the cases of the rest criteria, which account for fracture beyond local necking, the equivalent plastic strain at fracture follows a downward trend, moving from uniaxial compression to equal biaxial stretching loading processes. This behaviour is also in line with experimental observations (see e.g. Bao and Wierzbicki 2004) and is interpreted by the growth and coalescence of voids inside the material close to fracture, which leads in a quick drop of the fracture strain value.

Moreover, it is observed that the Swift (1952), McClintock (1968), BWH and Zhang et al. (2004) criteria are constrained in the range of $-1 < \beta \leq 1$ and the Stören-Rice (1975a,b) criteria in the range of $-1 \leq \beta \leq 1$, that is between pure shear and equal biaxial stretching. This is reasonable, as a diffuse neck according to Swift (1952) and a local neck according to Hill (1952) and Stören and Rice (1975a,b), will not form between pure shear and uniaxial compression loading processes. Also, in the cases of the McClintock (1968) and Zhang et al. (2004) criteria, with respect to the former void growth is not possible and considering the latter the through thickness strain vanishes under shear conditions. Interesting is the fact that the Stören-Rice (1975b) criterion in the case where $n_2 = 0$, that is when the local neck forms

along the direction of the minor in-plane principal true plastic strain ε_2, shows an almost identical to the BWH criterion behaviour especially in the range of $0 \leq \beta \leq 1$. In addition, the Stören-Rice (1975b) criterion determines a limit stress in a pure shear loading process, i.e. $\beta = -1$ (see Figure 4.5a).

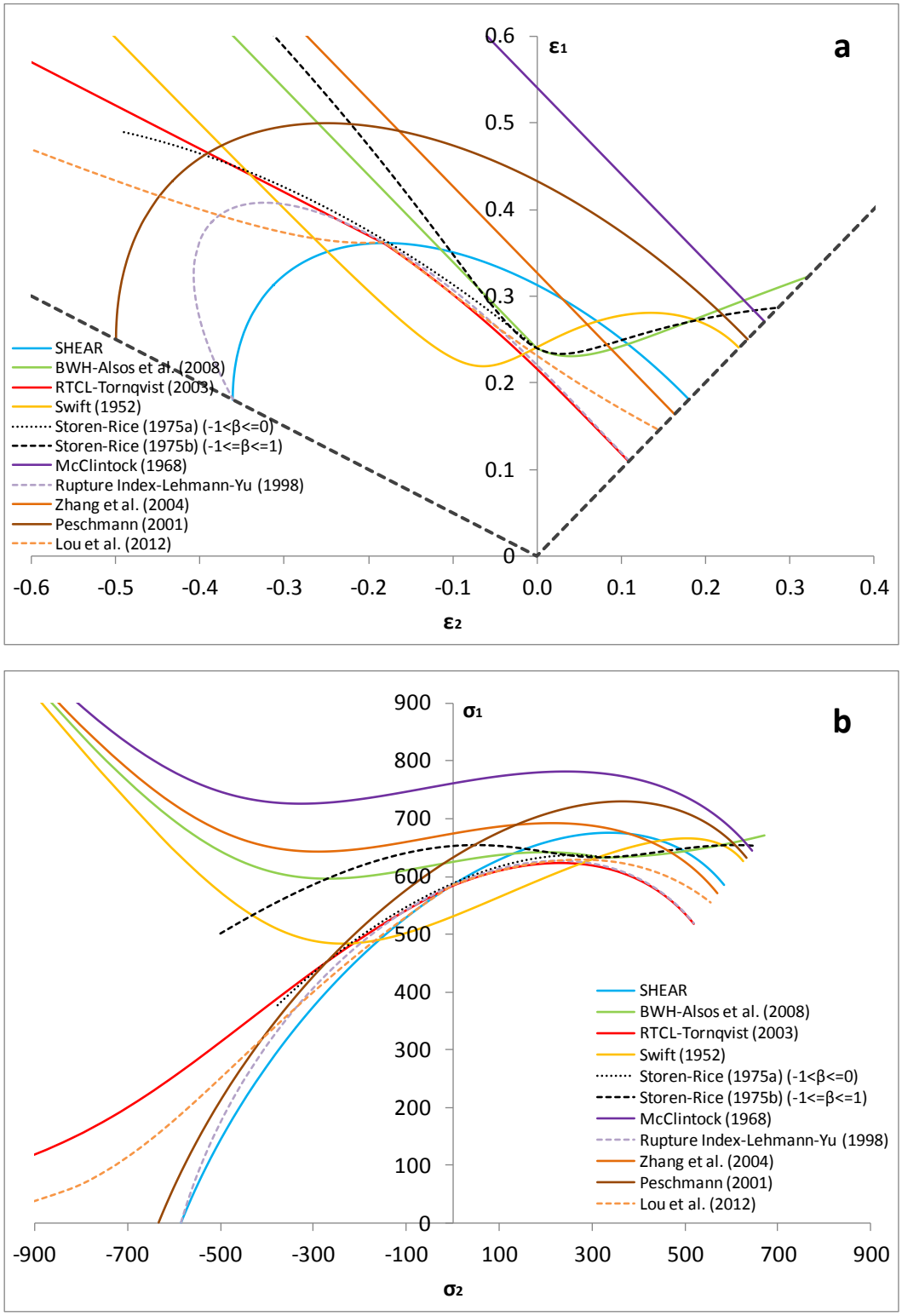

Figure 4.4. Forming limit curves in the strain (a) and stress fields (b)

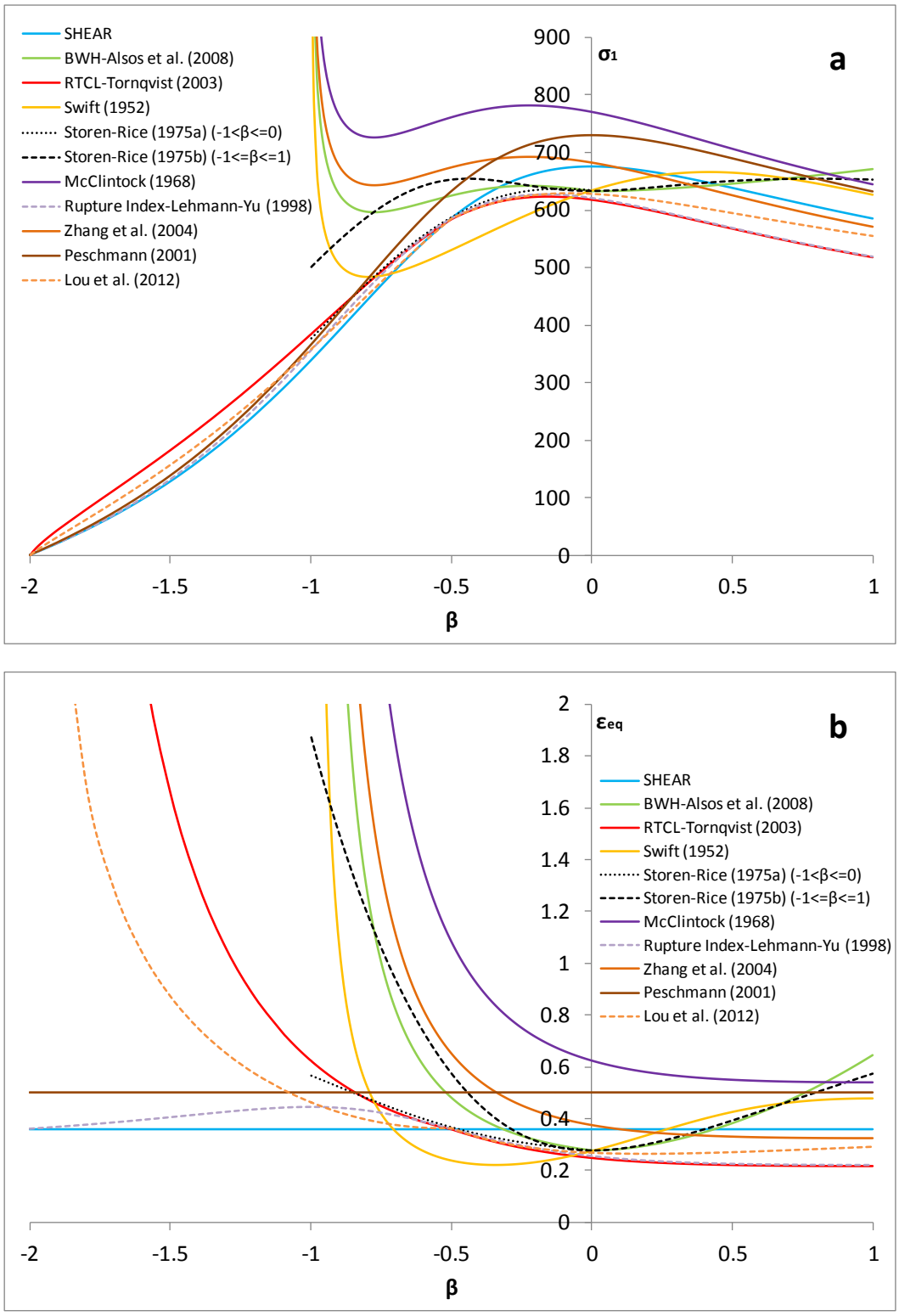

Figure 4.5. Limit stress σ_1 (c) and limit strain ε_{eq} (d) variables as functions of β

Table 4.3 summarizes the relation between the various stress and strain variables and parameters for each loading state, under plane stress conditions.

Table 4.3. Relation between the various stress and strain variables and parameters under plane stress conditions

	Stress and strain variables and parameters										
Loading states	α	β	T	ε_1	ε_2	ε_3	σ_1	σ_2	σ_{eq}	ε_{eq}	τ_{max}
Uniaxial compression	$-\infty$	-2	$-\frac{1}{3}$	$-\frac{\varepsilon_2}{2}, \varepsilon_3$	$-2\varepsilon_1, -2\varepsilon_3$	ε_1	0	$-\sigma_{eq}$	$-\sigma_2$	$2\varepsilon_1 , -\varepsilon_2$	$\frac{\sigma_{eq}}{2}$
Pure shear	-1	-1	0	$-\varepsilon_2$	$-\varepsilon_1$	0	$-\sigma_2 , \frac{\sigma_{eq}}{\sqrt{3}}$	$-\sigma_1 , -\frac{\sigma_{eq}}{\sqrt{3}}$	$\sqrt{3}\sigma_1 , -\sqrt{3}\sigma_2$	$\frac{2}{\sqrt{3}}\varepsilon_1, -\frac{2}{\sqrt{3}}\varepsilon_2$	$\frac{\sigma_{eq}}{\sqrt{3}}$
Uniaxial tension	0	$-\frac{1}{2}$	$\frac{1}{3}$	$-2\varepsilon_2 , -2\varepsilon_3$	$-\frac{\varepsilon_1}{2}, \varepsilon_3$	$-\frac{\varepsilon_1}{2}, \varepsilon_2$	σ_{eq}	0	σ_1	$\varepsilon_1, -2\varepsilon_2$	$\frac{\sigma_{eq}}{2}$
Plane strain	$\frac{1}{2}$	0	$\frac{1}{\sqrt{3}}$	$-\varepsilon_3$	0	$-\varepsilon_1$	$2\sigma_2 , \frac{2\sigma_{eq}}{\sqrt{3}}$	$\frac{\sigma_1}{2} , \frac{\sigma_{eq}}{\sqrt{3}}$	$\frac{\sqrt{3}}{2}\sigma_1 , \sqrt{3}\sigma_2$	$\frac{2}{\sqrt{3}}\varepsilon_1$	$\frac{\sigma_{eq}}{\sqrt{3}}$
Equal biaxial stretching	1	1	$\frac{2}{3}$	$\varepsilon_2 , -\frac{\varepsilon_3}{2}$	$\varepsilon_1 , -\frac{\varepsilon_3}{2}$	$-2\varepsilon_1 , -2\varepsilon_2$	σ_2 , σ_{eq}	σ_1 , σ_{eq}	σ_1 , σ_2	$2\varepsilon_1 , 2\varepsilon_2$	$\frac{\sigma_{eq}}{2}$

4.4 Element size sensitivity and calibration of BWH, RTCL and SHEAR criteria

The RTCL and SHEAR rupture criteria are related to a critical equivalent plastic strain, which is determined from uniaxial tensile tests. This critical value is sensitive to the changes of the l_e/t ratio. In the present analysis the mesh sensitivity of ε_{cr} was taken into account by the following formula (Marinatos and Samuelides 2013a, 2013b and 2015):

$$\varepsilon_{cr} = A_f \left(log \frac{l_e}{t} \right)^3 + B_f \left(log \frac{l_e}{t} \right)^2 + C_f \left(log \frac{l_e}{t} \right) + D_f \tag{4.37}$$

where ε_{cr} the critical equivalent true plastic strain, t the thickness of the element, l_e the element length and parameters A_f - D_f the coefficients that were determined independently for each material. The values of parameters A_f - D_f were given as input to VUMAT subroutine (ABAQUS 2010). Note that, application of equation (4.37) is limited for element length over thickness ratios below 20, i.e. $l_e/t < 20$ (see also Figure 4.6).

BWH damage criterion due to its formulation exhibits lesser mesh sensitivity, as the material parameters K and n included in the equations are assumed to be independent of the element size, in particular up to the point of ultimate load in a uniaxial tensile test, where a uniform behaviour is considered regardless of the element length. The derivation of K and n material parameters has already been described in section 3.2 of chapter 3.

Simulations of the uniaxial tensile tests with different mesh sizes were performed for the calibration of the RTCL and SHEAR rupture criteria. Finite element models were made to simulate the tensile tests. One end of the model of the simulated specimen was totally fixed, while at the opposite end a controlled displacement was applied. The displacement of two nodes, one at the left and the other at the right end of the gauge length was monitored during the simulation. When the relative displacement of the selected nodes reached the value obtained at the experimental point of fracture (see Table 2.1, chapter 2), the maximum value of the equivalent plastic strain was detected at the mid-section of the specimen and identified as the critical equivalent plastic strain.

The preceding procedure was followed in all of the examined materials. A maximum of eight values for ε_{cr} were selected for different l_e/t ratios and then suitable values for the parameters A_f - D_f of relation (4.37) were determined to obtain the best polynomial fit through the simulated points. The scaling of ε_{cr} according to the ratio l_e/t, using the proposed formula for each material, is illustrated in Figure 4.6 with respect to uniaxial simulations for different meshes. The coefficients A_f to D_f vary between -1.5 and 1.5 and were calibrated with the least square method, in order the third order polynomial to interpolate the value of ε_{cr} between the minimum and maximum values of length to thickness ratio, which have been used for their determination. It is noted that, the RTCL and SHEAR rupture criteria were not calibrated in the case of the drop weight test, i.e. COLLISION DYNAMIC model (ASIS 1993 reported in ISSC 2003) as strain-rate effect was neglected in rupture modeling. However, uniaxial simulations using various strain-rates were performed, so as to determine the appropriate true stress-strain curve beyond necking (see section 3.3) for element length over thickness ratios $l_e/t > 1$, which were used in the simulations of the

drop weight test. It was found that, for element length over thickness ratios $l_e/t > 1$, powerlaw type true stress-strain curves yielded the best reproduction of the experimental engineering curves for the various strain-rates, as indicated in Table 5.1, chapter 5. The powerlaw true strain-rate dependent material curves are illustrated in Figure 5.23, chapter 5.

A detailed description with respect to the calibration of SHEAR and RTCL rupture criteria is presented in Appendix B.

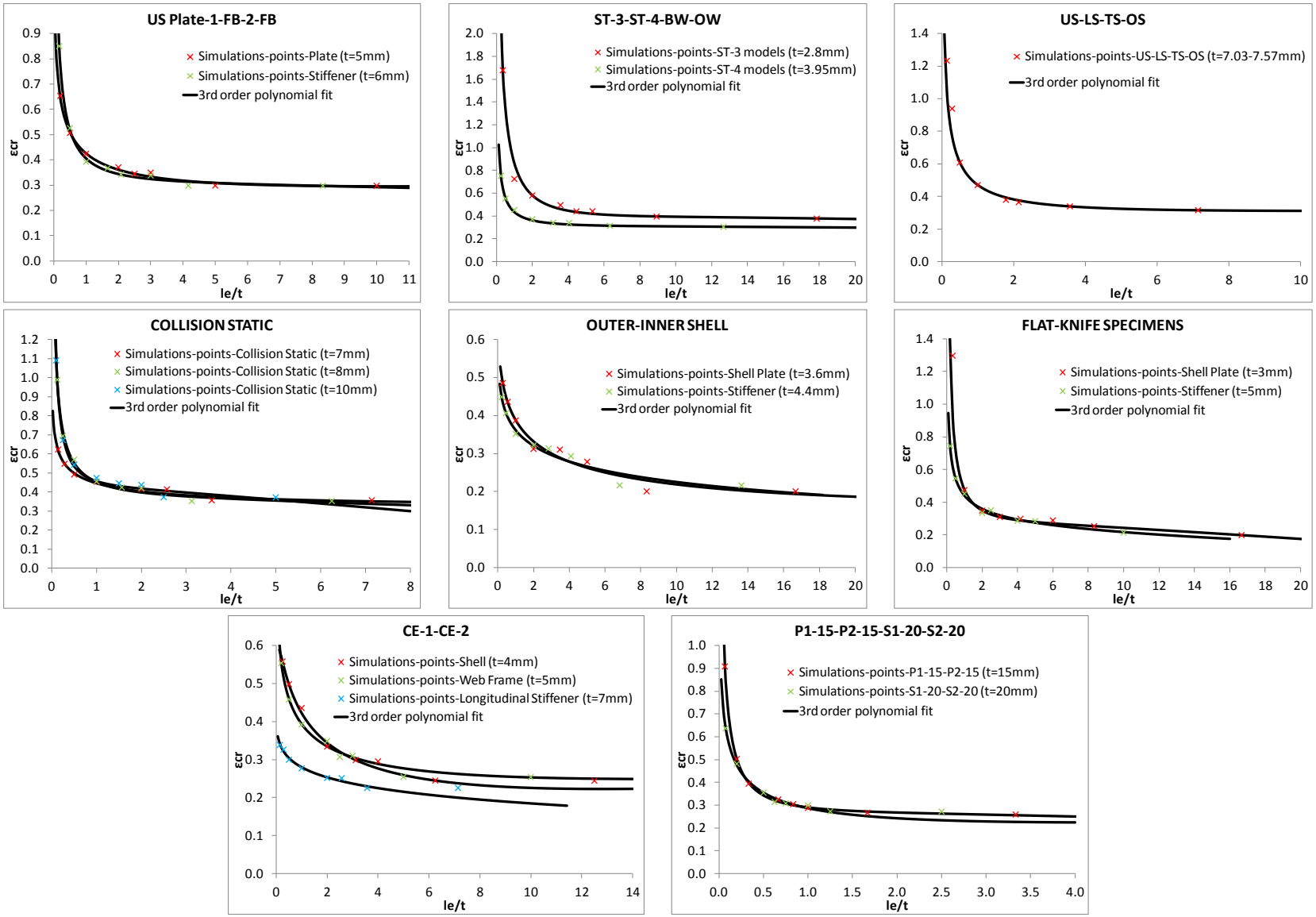

Figure 4.6. Equivalent plastic failure strains for different element sizes (uniaxial simulations)

This page is intentionally left blank

Chapter 5

Numerical Analysis

5.1 Numerical modeling

The simulations were performed using the Abaqus/Explicit FE code with the four-node reduced integration quadrilateral Belytschko-Lin-Tsay shell elements, i.e. S4R with five integration points through the thickness (see Figure 3.2 and ABAQUS 2010). Contact between the rigid or deformable indenters and the structural configurations, was handled with the general contact algorithm provided within the Abaqus/Explicit FE code, which accounts for contact between different surfaces as well as interactions with self of the participating geometries. A static friction coefficient equal to 0.3 was assumed and used in all simulations, based on the work of Törnqvist (2003), Ehlers et al. (2008), Alsos et al. (2009), Hogström et al. (2010) and Hogström and Ringsberg (2012). In the cases of the CE-1 and CE-2 models, the coefficient was taken equal to 0.23, following Tautz et al. (2013), see Table 5.1. For all quasi-static tests, the loading velocity of the indenter was taken equal to $3\,m/sec$ (see also Samuelides et al. 2007). This choice was twofold, namely: i) minimize inertial effects, i.e. the kinetic energy of the deforming material should not exceed a small fraction (typically 5% to 10%) of its internal energy throughout most of the process (ABAQUS 2010) and ii) derive solutions within reasonable CPU time. It was found that the kinetic energy did not exceed 1% of the internal energy during the simulations of the benchmark study. In the case of the drop weight test, i.e. COLLISION DYNAMIC model, an initial velocity equal to the actual velocity of the indenter, i.e. $9.7\,m/sec$, was used (see ASIS 1993 reported in ISSC 2003). The selected boundary conditions represent the actual boundary conditions of the tests (see Appendix A).

The true stress-strain curve used in the simulations was obtained up to the ultimate load from the engineering curve and beyond necking according to equation (3.14) Ling (1996). The value of w was selected independently for each element size, so as to give the closest reproduction of the engineering experimental stress-strain curve in uniaxial tension tests. In most cases of the examined materials for ratios $l_e/t > 1$, the value of w which gave the best reproduction was equal to zero, which corresponds to the powerlaw curve (see Figure 3.1 and Table 5.1). Values of w not equal to zero were used in the cases of the materials that correspond to the plate and stiffener components of the OUTER-INNER SHELL models, the stiffener component in the case of the FLAT-KNIFE SPECIMENS models and the web frame component in the case of the CE-1 model (see Table 5.1). The welds were modeled in the cases of the plate with one flat bar and two flat bar stiffeners, respectively, i.e. 1-FB and 2-FB models, as described in Alsos and Amdahl (2009) (see also Table 5.1). Data was not available in the rest experiments and modeling of welds was not applied.

Modeling of rupture initiation and propagation was achieved using three rupture criteria, i.e. SHEAR (Marinatos and Samuelides 2013a, 2013b and 2015), RTCL (Törnqvist 2003) and BWH (Alsos et al. 2008). The criteria were implemented into VUMAT subroutine (see also Appendix C and ABAQUS 2010), which interacts with the explicit FE code and refers to an isotropic hardening material that follows the J_2 flow theory assuming plane stress conditions.

In Abaqus/Explicit by default, element deletion is achieved when a rupture criterion is satisfied in all of the through thickness integration points of a shell element. There are no alternatives for the user and as a result an element will not be removed from the mesh in any other case; for example by selecting a specific through thickness integration point, or a number of through thickness integration points other than the total number. However, BWH criterion is satisfied when the major in-plane principal true membrane stress reaches a critical value, which implies that bending is neglected. Hence, the criterion should be activated when this critical stress is reached only in the middle layer of a shell element, regardless of the magnitude of the stress concerned in the rest through thickness integration points. Therefore, in the case of BWH criterion, VUMAT subroutine was further developed in order the element to be removed from the mesh when the criterion was satisfied in the middle layer of a shell element. In order to achieve this, data had to be written for every through thickness integration point of all shell elements in the model at each time step and saved until the next time step. Then the state variable, which controls element deletion, would be activated only when the condition of the criterion was reached at the through thickness integration point of the middle layer of a shell. Unfortunately, this procedure could be applied only if the simulations were performed using no more than one CPU, which introduced limitations concerning the size of the models and meshes used in the simulations in contrast to the rest criteria. BWH rupture criterion was applied in the cases of the US Plate, 1-FB, 2-FB, ST-3, ST-4, US, LS, TS, OS, COLLISION STATIC, OUTER-INNER SHELL, FLAT-KNIFE SPECIMENS, P1-15, P2-15 and S1-20, S2-20 models. It is also noted that, RTCL and SHEAR rupture criteria were used in its scaled forms, i.e. RTCLS, SHEARS (Marinatos and Samuelides 2013a, 2013b and 2015). The modeling parameters for each simulated model are summarized in Table 5.1.

Strain-rate effect was investigated in the case of the COLLISION DYNAMIC model, without including modeling of rupture. Simulations using RTCLS and SHEARS rupture criteria were also performed in this case, however without including strain-rate effect on the material curve (see also Samuelides 2015 and Marinatos and Samuelides 2015). Hence, the critical values of equivalent plastic strain remained the same as in the case of the COLLISION STATIC model (see Table 5.1).

Table 5.1. Simulated models and modeling parameters

	Simulated models																	
Modeling parameters	US Plate-1-FB-2-FB Alsos and Amdahl (2009)						ST-3 models Paik et al. (1999)			ST-4 models Paik et al. (1999)			US-LS-TS-OS Paik and Tak (1995)					
	Components						Components			Components			Components					
	Plates US, 1-FB & 2-FB $t = 5\,mm$			FB Stiffener $t = 6\,mm$			Plates, Webs $t = 2.8\,mm$			Plates, Webs $t = 3.95\,mm$			Plates $t = 7.03\text{-}7.4\,mm$			Stiffeners $t = 7.13\text{-}7.57\,mm$		
$l_e\ (mm)$	5	10	18	5	10	18	5.6	12.5	25	7.9	12.5	25	8	16	30	8	16	30
l_e/t	1.0	2.0	3.6	0.83	1.67	3.0	2.0	4.46	8.93	2.0	3.16	6.33	1.08-1.14	2.16-2.28	4.05-4.27	1.06-1.12	2.11-2.24	3.96-4.21
ε_{cr}	0.425	0.361	0.322	0.43	0.357	0.324	0.58	0.433	0.395	0.362	0.335	0.315	0.45-0.458	0.37-0.375	0.33-0.333	0.452-0.461	0.371-0.377	0.331-0.334
w	0	0	0	0	0	0	0	0	0	0	0	0	0	0	0	0	0	0
Loading velocity $v\ (m/sec)$	3.0																	
Contact	Application of the general contact algorithm in Abaqus/Explicit																	
Static friction coefficient	0.3																	
Welds	Weld seams rows of 6 mm wide elements On the plate side thickness increase: 2 mm On the stiffener side thickness increase: 4 mm						Not applied											

continued on next page

continued from previous page

Modeling parameters	Simulated models																	
	COLLISION STATIC ASIS (1993) reported in ISSC (2003)						COLLISION DYNAMIC ASIS (1993) reported in ISSC (2003)						P1-15-P2-15 models DNV (1993)			S1-20-S2-20 models DNV (1993)		
	Components						Components						Components			Components		
	Transv. Web Stif. Str. Deck Str. Deck Stif. $t = 7\ mm$		Transv. Web $t = 8\ mm$		Side Shell $t = 10\ mm$		Transv. Web Stif. Str. Deck Str. Deck Stif. $t = 7\ mm$		Transv. Web $t = 8\ mm$		Side Shell $t = 10\ mm$		Plates $t = 15\ mm$			Plates $t = 20\ mm$		
$l_e\ (mm)$	12.5	25	12.5	25	12.5	25	12.5	25	12.5	25	12.5	25	15	30	45	20	40	60
l_e/t	1.8	3.57	1.56	3.125	1.25	2.5	1.8	3.57	1.56	3.125	1.25	2.5	1.0	2.0	3.0	1.0	2.0	3.0
ε_{cr}	0.409	0.375	0.413	0.375	0.443	0.408	0.409	0.375	0.413	0.375	0.443	0.408	0.291	0.269	0.259	0.286	0.242	0.228
w	0	0	0	0	0	0	0	0	0	0	0	0	0	0	0	0	0	0
Loading or initial velocity $v\ (m/sec)$	3.0						9.7						3.0					
Contact	Application of the general contact algorithm in Abaqus/Explicit																	
Static friction coefficient	0.3																	
Welds	Not applied																	

Modeling parameters	Simulated models													
	OUTER-INNER SHELL Gong et al. (2013)				FLAT-KNIFE SPECIMENS Villavicencio (2012) and Villavicencio et al. (2013)				CE-1-CE-2 Tautz et al. (2013) and Fricke et al. (2014)					
	Components				Components				Components					
	Plates $t = 3.6\ mm$		Stiffeners $t = 4.4\ mm$		Plates $t = 3\ mm$		Stiffeners $t = 5\ mm$		Shell $t = 4\ mm$		Web Frame $t = 5\ mm$		Long. Stif. $t = 7\ mm$	
$l_e\ (mm)$	8	16	8	16	8	16	8	16	12.5	25	12.5	25	12.5	25
l_e/t	2.22	4.44	1.82	3.64	2.67	5.33	1.6	3.2	3.125	6.25	2.5	5	1.79	3.57
ε_{cr}	0.323	0.27	0.326	0.285	0.319	0.276	0.383	0.313	0.299	0.245	0.319	0.277	0.258	0.23
w	0.7	0.2	0.7	0.2	0	0	0.2	0	0	0	0.2	0	0	0
Loading velocity $v\ (m/sec)$	3.0													
Contact	Application of the general contact algorithm in Abaqus/Explicit													
Static friction coefficient	0.3								0.23					
Welds	Not applied													

5.2 Numerical results and discussion

The following paragraphs present and discuss in detail the results of the numerical simulations in terms of force-penetration curves and absorbed energy-penetration curves as well as the failure modes for different element lengths. Contours of the damage variable are also presented. The experimental force and absorbed energy-penetration curves are compared with the corresponding curves obtained from the FE simulations for various meshes. The patterns of deformation of the specimens as observed during the tests are also compared with those predicted from the FE simulations. The comparison is performed for the cases where pictures of the deformed specimens were available in the literature. In the cases of the ST-4-BW, ST-4-OW, US, LS, TS, OS and COLLISION STATIC models, pictures of the deformed specimens were not available. The best results, regarding the correlation with the experiments, i.e. experimental force and absorbed energy-penetration curves and deformation patterns, are identified in each case. Note that, in some cases results with more than one rupture criterion were in good correlation with the experiments and were designated as best. The differences between the numerical and experimental results using the various criteria and mesh sizes are also quantified, by comparing the force peaks and troughs as well as the energy absorbed by the structures in each case. The results of the latter analysis are presented in Appendix D.

5.2.1 US Plate, 1-FB and 2-FB models-(Alsos and Amdahl 2009)

Figure 5.1 refers to the US Plate model and illustrates comparisons of the experimental force-penetration and absorbed energy-penetration curves with the corresponding numerical curves for three mesh sizes, in the cases of the RTCLS and SHEARS criteria and two mesh sizes in the case of BWH criterion. The material behaviour beyond necking is represented by the powerlaw curve. Moreover, Figure 5.2 presents a comparison of the damage as predicted using the three criteria and different meshes with the corresponding picture of the experiment (Alsos and Amdahl 2009). According to the experimental observations in Alsos and Amdahl (2009), rupture of the plate took place at a certain load under biaxial stretching that followed extended thinning in a large area of the sheet. Numerical analyses with all rupture criteria and meshes show the same trend, namely the numerical curves follow closely the experimental force-penetration curve, but differ at the prediction of rupture initiation. The difference between RTCLS, SHEARS and BWH rupture criteria is obvious. As already mentioned in sub-section 4.2.5, BWH predicts local instability, which is initiated prior to fracture and applies to membrane stresses and strains. Thus, BWH tends to predict rupture at a rather earlier stage. Furthermore, due to the biaxial loading of the plate, high stress triaxialities, i.e. $T > 1/\sqrt{3}$, are developed early in the simulation and the stress triaxiality function in the majority of the loading steps is over one, i.e. $f(T) > 1$ (see Figure 4.1, chapter 4 and Figure 5.59 in section 5.3). As a result the critical equivalent plastic strain is reached sooner and RTCLS criterion tends to predict initiation of rupture at an earlier stage. The best reproduction of the experimental curve is achieved in the case of SHEARS criterion using a fine mesh, although underestimation of the experimental force-penetration point is also evident here.

A similar behaviour, with respect to the various criteria and meshes, is also observed in the case of the 1-FB model. Results in the case of SHEARS criterion and a fine mesh are in good agreement with the experimental force and energy-penetration curves (see Figure 5.3). It is noted that, all criteria predict rupture on the plate far from the intersection with the stiffener, while according to Alsos and Amdahl (2009), rupture was observed on the plate next to the weld toe (see Figure 5.4). In the case of the 2-FB model, BWH and SHEARS criteria yield very good correlation with the experimental force and energy-penetration curves for a coarse mesh. Satisfactory prediction of the residual strength, i.e. strength beyond rupture initiation as well as representation of rupture is achieved by all rupture criteria (see Figures 5.5 and 5.6).

One may observe that mesh size seems to have a much less effect on BWH criterion. In fracture analyses with finite elements the numerical solution is sensitive to the mesh size. As BWH criterion is activated before the final stage of fracture, mesh size effect is not as significant as it is with the other criteria. However, when the mesh size is too fine high stresses are developed, especially in the vicinity of geometric constraints, i.e. boundary conditions, intersections between plates and stiffeners, etc., where localized phenomena are dominant and as a result rupture is predicted to occur at an earlier stage. This for instance is observed in the case of the 2-FB model (see Figure 5.5). Table 5.2 summarizes the best results for each simulated model (see also Appendix D).

Table 5.2. Numerical results for each simulated model and rupture criterion

	Rupture Criteria		
Simulated Models	SHEARS	RTCLS	BWH
US Plate	Not good correlation between different meshes Underestimation of resistance in all cases Best results for $l_e = 5\ mm$ or $l_e/t = 1$ (*), (**)	Not good correlation between different meshes Underestimation of resistance in all cases Best results for $l_e = 5\ mm$ or $l_e/t = 1$ (**)	Good correlation between different meshes Underestimation of resistance in all cases Best results for $l_e = 18\ mm$ or $l_e/t = 3.6$
1-FB	Good correlation between meshes with $l_e/t > 1$ Underestimation of resistance for meshes with $l_e/t > 1$ Best results for $l_e = 5\ mm$ or $l_e/t = 1$ (*)	Good correlation between meshes with $l_e/t > 1$ Underestimation of resistance in all cases Best results for $l_e = 5\ mm$ or $l_e/t = 1$	Good correlation between different meshes Underestimation of resistance in all cases Best results for $l_e = 18\ mm$ or $l_e/t = 3.6$
2-FB	Good correlation between meshes with $l_e/t < 3$ Underestimation of resistance for meshes with $l_e/t < 3$ Best results for $l_e = 18\ mm$ or $l_e/t = 3.6$ (**)	Good correlation between meshes with $l_e/t < 3$ Underestimation of resistance in all cases Best results for $l_e = 18\ mm$ or $l_e/t = 3.6$ (**)	Not good correlation between different meshes Underestimation of resistance for a meshes with $l_e/t < 3$ Best results for $l_e = 18\ mm$ or $l_e/t = 3.6$ (*), (**)

(*): best correlation with experimental force and energy-penetration curves, (**): best representation of rupture

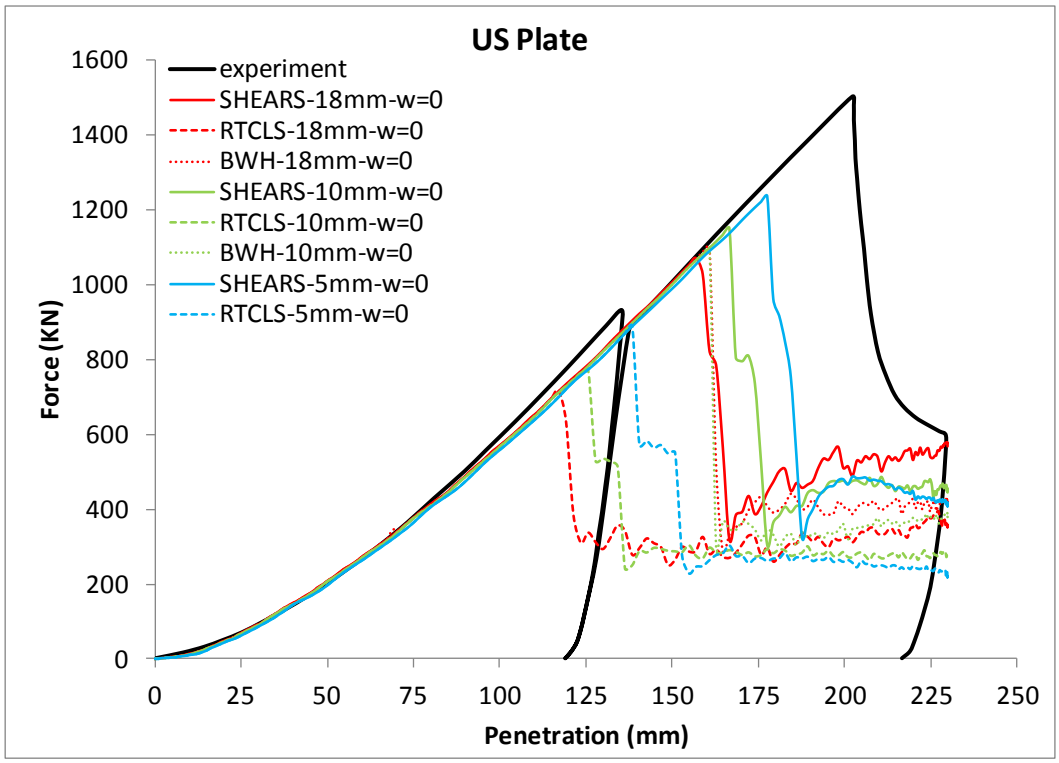

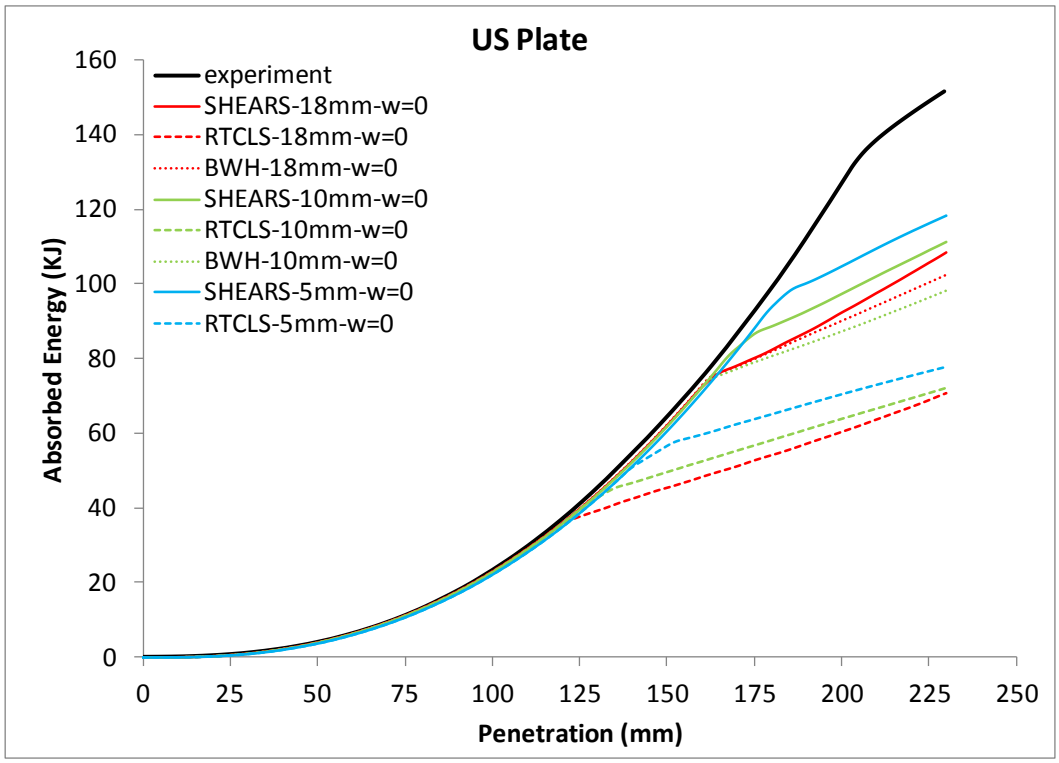

Figure 5.1. US Plate model. Force and absorbed energy-penetration curves.
Prediction of rupture according to SHEARS, RTCLS and BWH rupture criteria in combination with the powerlaw type material curve

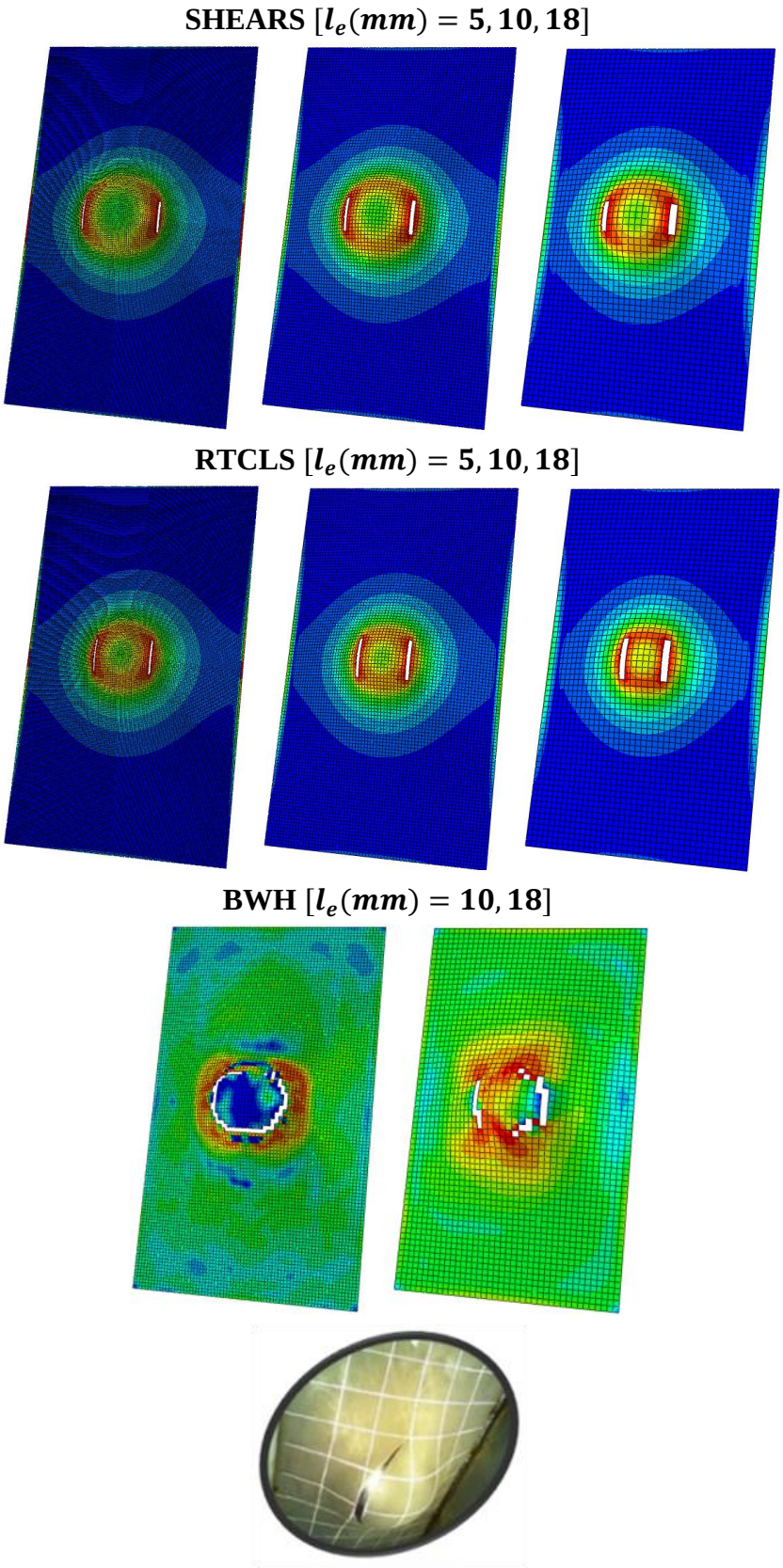

Figure 5.2. US-Plate model. Representation of damage according to SHEARS, RTCLS and BWH rupture criteria (Alsos and Amdahl 2009)

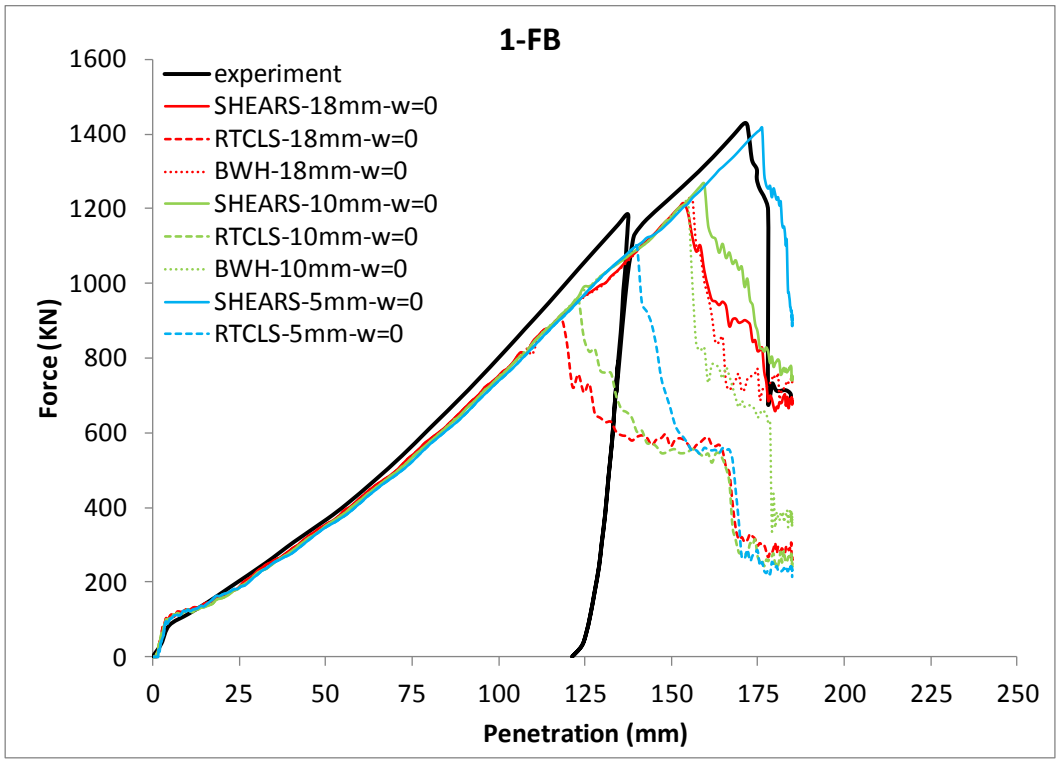

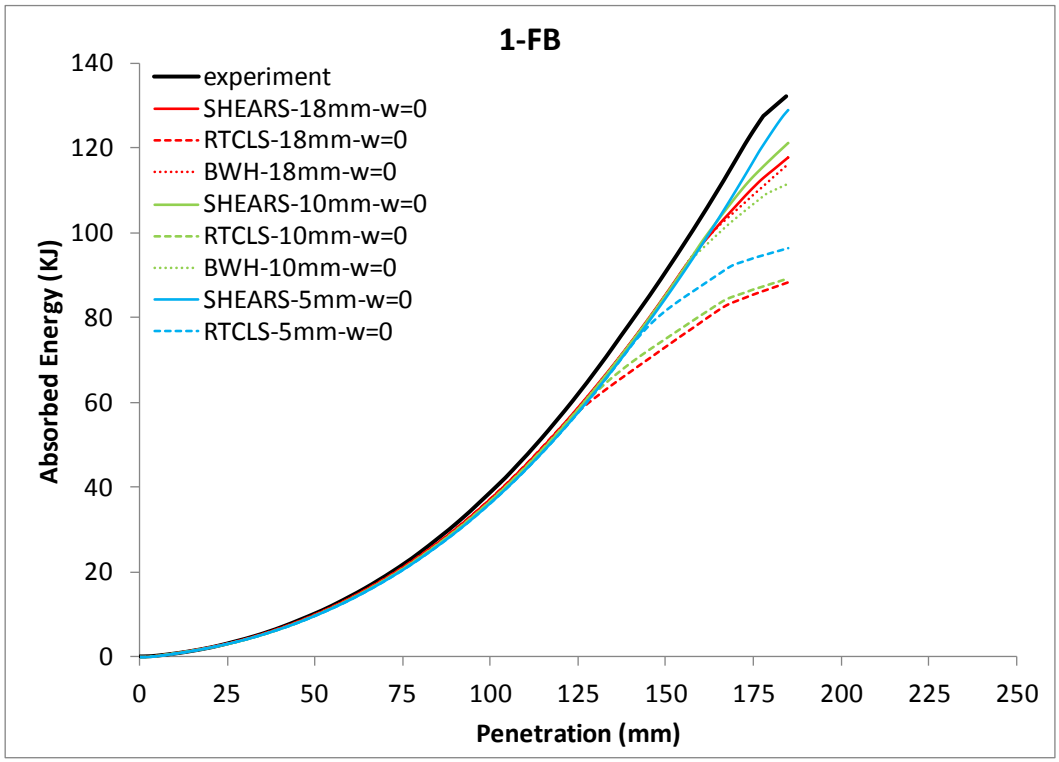

Figure 5.3. 1-FB model. Force and absorbed energy-penetration curves.
Prediction of rupture according to SHEARS, RTCLS and BWH rupture criteria in combination with the powerlaw type material curve

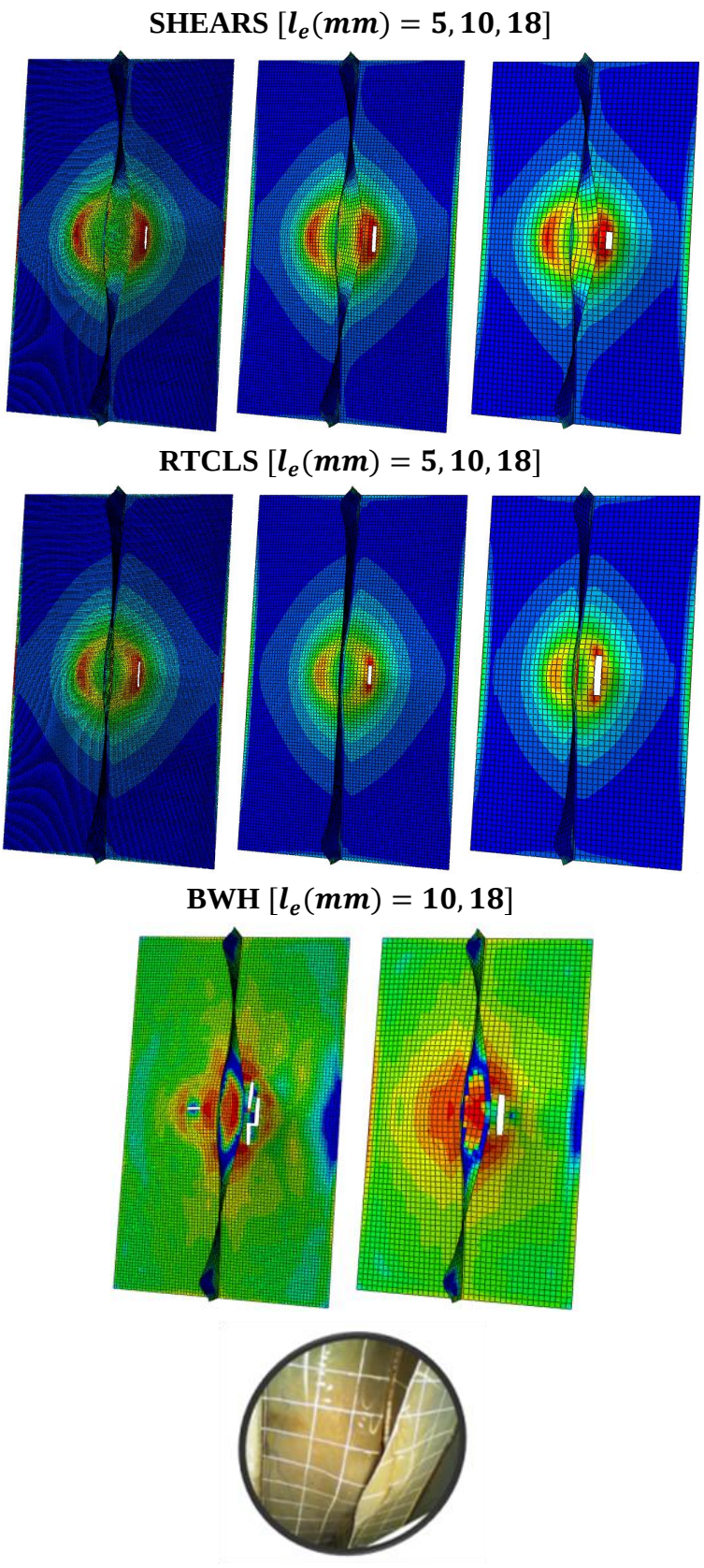

Figure 5.4. 1-FB model. Representation of damage according to SHEARS, RTCLS and BWH rupture criteria (Alsos and Amdahl 2009)

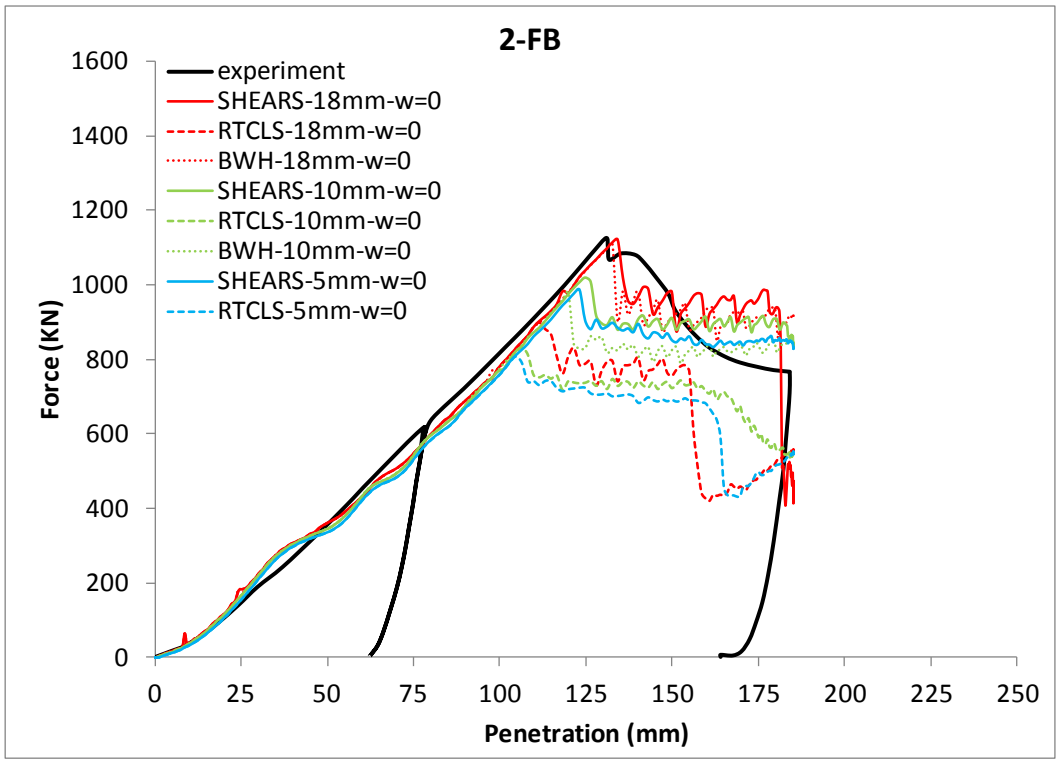

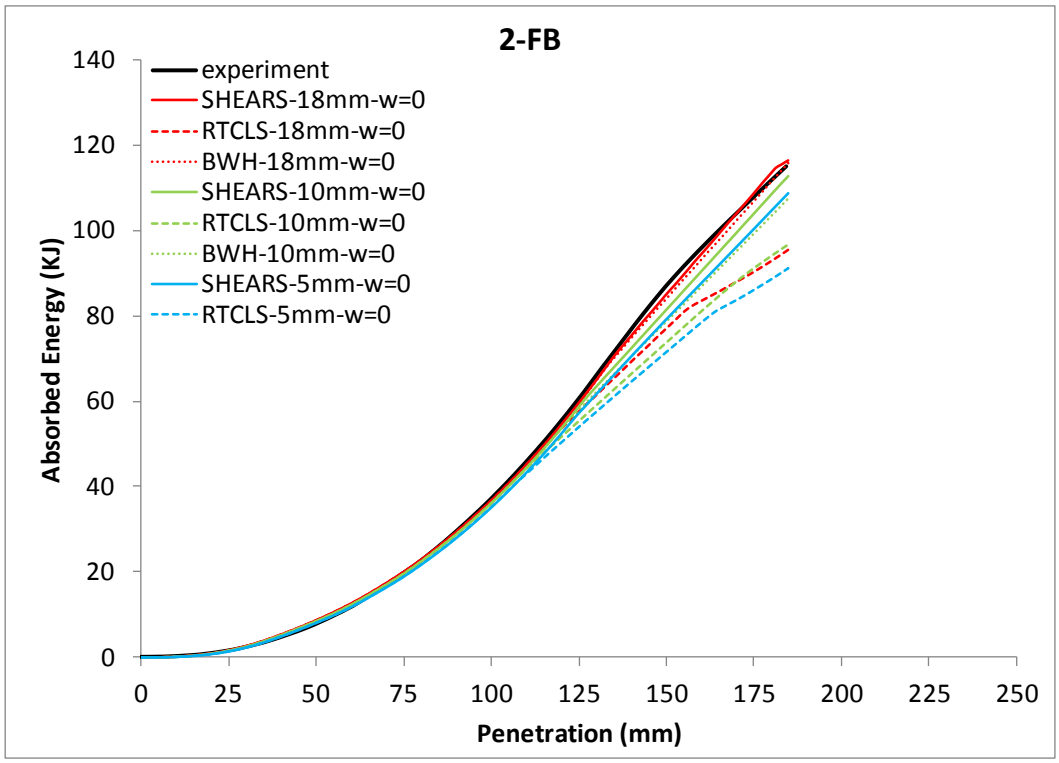

Figure 5.5. 2-FB model. Force and absorbed energy-penetration curves.
Prediction of rupture according to SHEARS, RTCLS and BWH rupture criteria in combination with the powerlaw type material curve

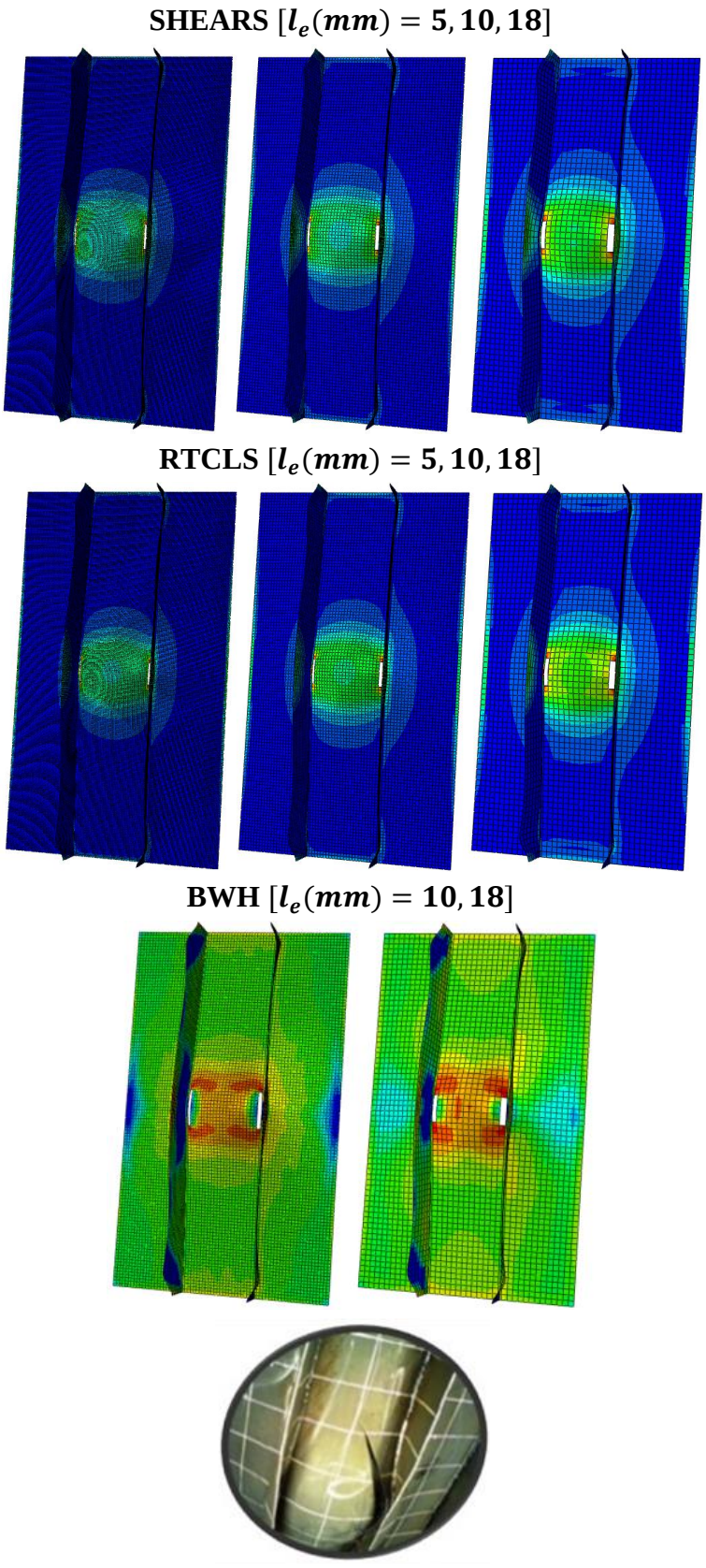

Figure 5.6. 2-FB model. Representation of damage according to SHEARS, RTCLS and BWH rupture criteria (Alsos and Amdahl 2009)

5.2.2 ST-3-BW, ST-3-OW, ST-4-BW and ST-4-OW models-(Paik et al. 1999)

Figures 5.7, 5.9, 5.11 and 5.13 refer to the ST-3-BW, ST-3-OW, ST-4-BW and ST-4-OW models and illustrate comparisons of the experimental force-penetration and absorbed energy-penetration curves with the corresponding numerical curves for three mesh sizes, in the cases of the RTCLS and SHEARS criteria and one mesh size in the case of BWH criterion. The material behaviour beyond necking is represented by the powerlaw curve. Furthermore, Figures 5.8, 5.10, 5.12 and 5.14, illustrate the representation of damage with respect to the three criteria for different meshes. Comparisons with the corresponding pictures of the experiments (Paik et al. 1999) are also included in Figures 5.8 and 5.10.

From Figures 5.7, 5.9, 5.11 and 5.13, one may observe that all criteria show a similar behaviour and numerical results tend to converge for finer meshes, i.e. $l_e/t < 5$. In the cases of the ST-3-BW and ST-4-BW models, SHEARS and RTCLS criteria yield close results for all different mesh sizes, while in the cases of the ST-3-OW and ST-4-OW models convergence between the two criteria is achieved for a fine mesh, i.e. $l_e/t = 2$. Results obtained using BWH criterion and a coarse mesh, i.e. $l_e/t > 6$, are close to the results of the rest criteria for the respective mesh size in all cases.

In the cases of the ST-3-BW and ST-4-BW models, all criteria capture fairly well the first part of the experimental curve, i.e. at approximately 180 mm penetration, where according to Paik et al. (1999), due to the fixed boundary conditions, membrane tension effects reach a maximum, as the indenter pushes the adjacent webs towards the outside, the outer skin plating starts to buckle and the force drops (see Figures 5.7 and 5.11). After that point, divergence from the experimental curve and overestimation of the structure's resistance is observed, especially for coarser meshes. Simulations with finer meshes correlate better with the last part of the experimental curves, i.e. beyond 300 mm penetration (see Figures 5.7 and 5.11). From Figure 5.8 it is obvious that the finer the mesh the less stiff the behaviour of the structure. This is depicted through the buckling of the side webs, which is not the case in the experiment. Best representation of the deformation pattern and rupture is achieved by SHEARS criterion using a coarse mesh. Similarly to the precedent models, in the cases of the ST-3-OW and ST-4-OW models, good correlation with the experimental force and energy-penetration curves is achieved for finer meshes (see Figures 5.9 and 5.13). Best representation of the deformation pattern is achieved by SHEARS criterion using a 12.5 mm mesh (see Figure 5.10). Table 5.3 summarizes the best results for each simulated model (see also Appendix D).

Table 5.3. Numerical results for each simulated model and rupture criterion

	Rupture Criteria		
Simulated Models	SHEARS	RTCLS	BWH
ST-3-BW	Good correlation between different meshes and with experimental results for $l_e/t < 5$ Best results for $l_e = 5.6, 12.5\ mm$ or $2 \leq l_e/t \leq 4.5$ (*), (**) for $l_e = 25\ mm$	Good correlation between different meshes and with experimental results for $l_e/t < 5$ Best results for $l_e = 5.6, 12.5\ mm$ or $2 \leq l_e/t \leq 4.5$ (*)	Good correlation with experimental results up to 180 mm penetration depth and overestimation of resistance beyond that point $l_e/t > 6$
ST-3-OW	Good correlation between different meshes and with experimental results for $l_e/t < 5$ Best results for $l_e = 5.6, 12.5\ mm$ or $2 \leq l_e/t \leq 4.5$ (*), (**) for $l_e = 12.5\ mm$	Good correlation between different meshes and with experimental results for $l_e/t < 5$ Best results for $l_e = 5.6, 12.5\ mm$ or $2 \leq l_e/t \leq 4.5$	Overestimation of resistance, especially in the first 100 mm and the last 150 mm of penetration $l_e/t > 6$
ST-4-BW	Good correlation between different meshes and with experimental results for $l_e/t < 4$ Best results for $l_e = 7.9, 12.5\ mm$ or $2 \leq l_e/t \leq 3.2$ (*)	Good correlation between different meshes and with experimental results for $l_e/t < 4$ Best results for $l_e = 7.9, 12.5\ mm$ or $2 \leq l_e/t \leq 3.2$ (*)	Good correlation with experimental results up to 180 mm penetration depth and overestimation of resistance beyond that point $l_e/t > 6$
ST-4-OW	Good correlation between different meshes and with experimental results Best results for $l_e = 7.9, 12.5\ mm$ or $2 \leq l_e/t \leq 3.2$ (*)	Good correlation between different meshes and with experimental results for $l_e/t < 4$ Best results for $l_e = 7.9, 12.5\ mm$ or $2 \leq l_e/t \leq 3.2$ (*)	Overestimation of resistance, especially in the first 100 mm and the last 100 mm of penetration $l_e/t > 6$

(*): best correlation with experimental force and energy-penetration curves, (**): best representation of rupture

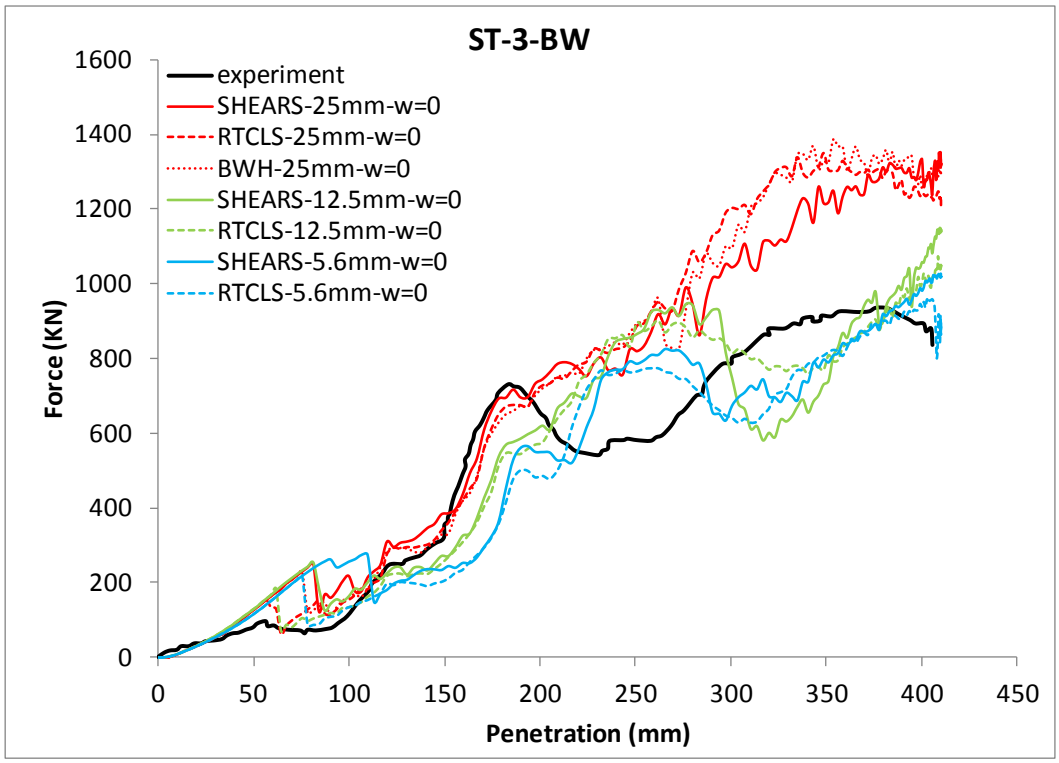

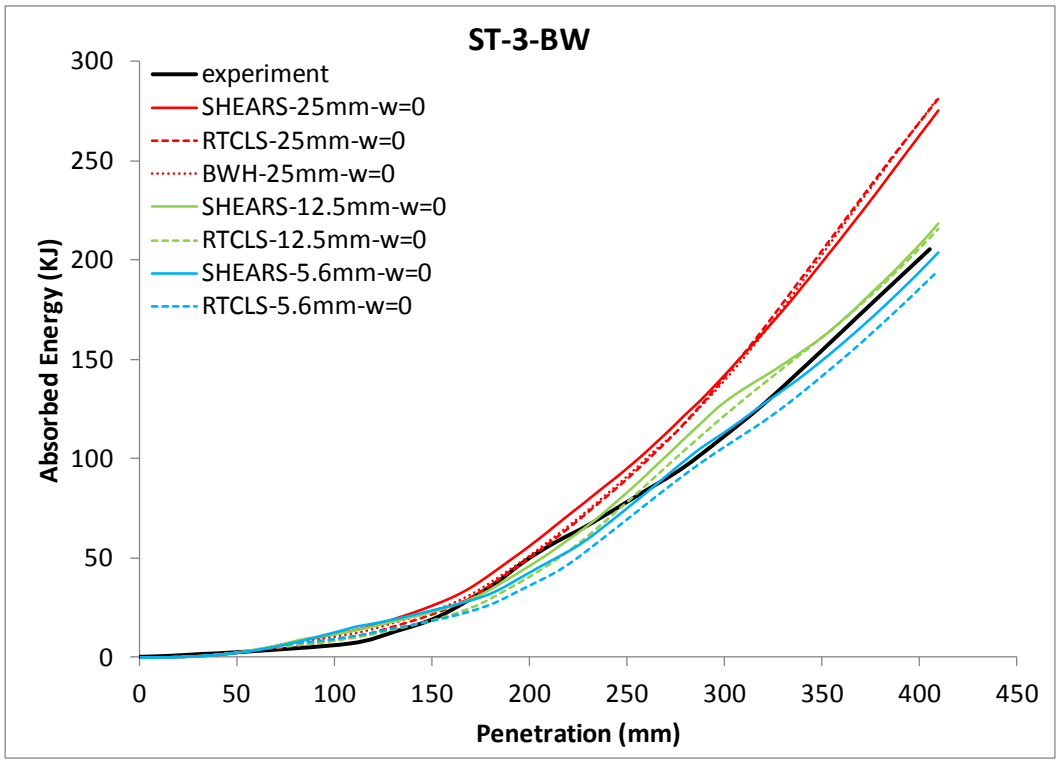

Figure 5.7. ST-3-BW model. Force and absorbed energy-penetration curves.
Prediction of rupture according to SHEARS, RTCLS and BWH rupture criteria in combination with the powerlaw type material curve

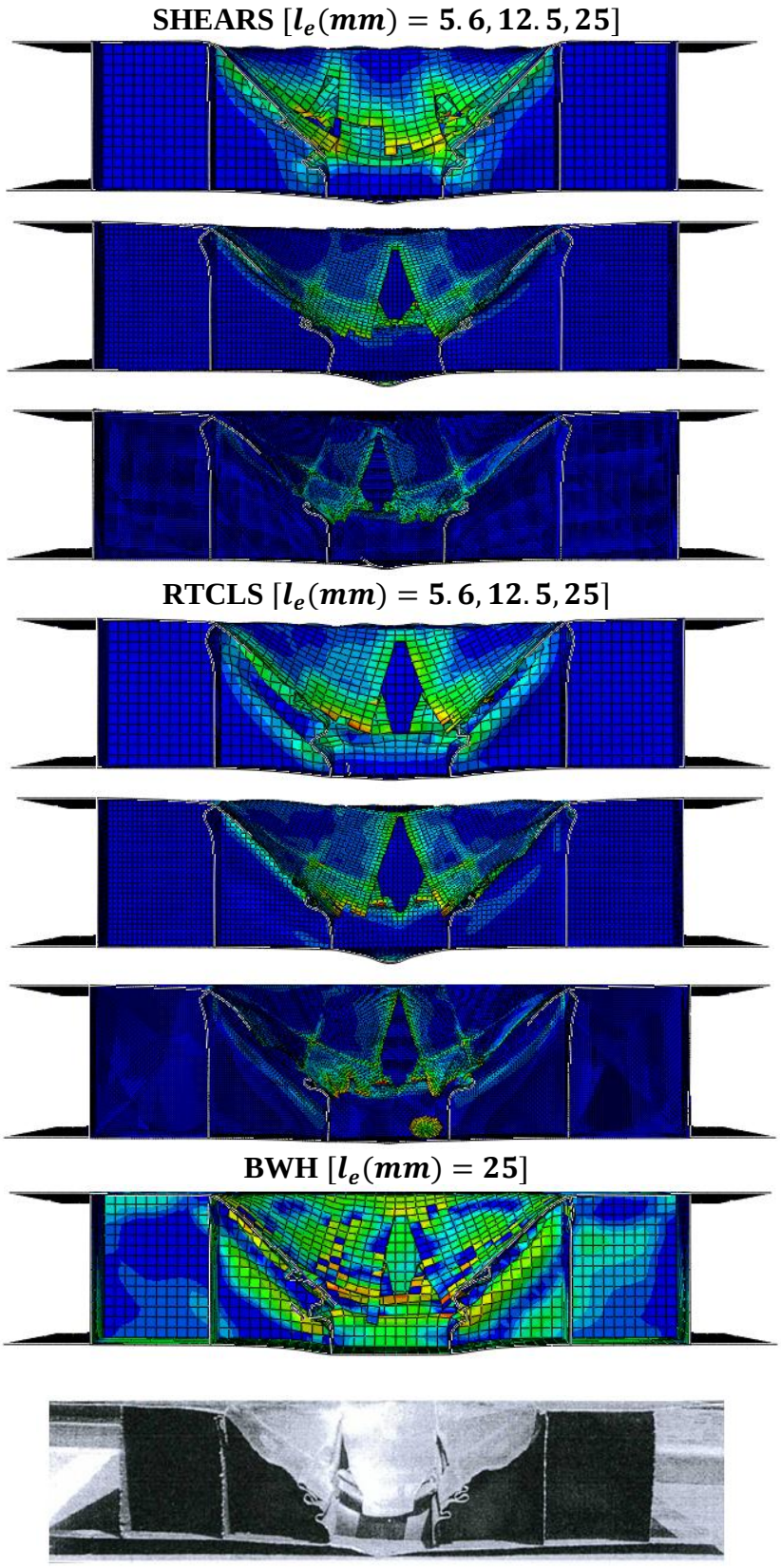

Figure 5.8. ST-3-BW model. Representation of damage according to SHEARS, RTCLS and BWH rupture criteria (Paik et al. 1999)

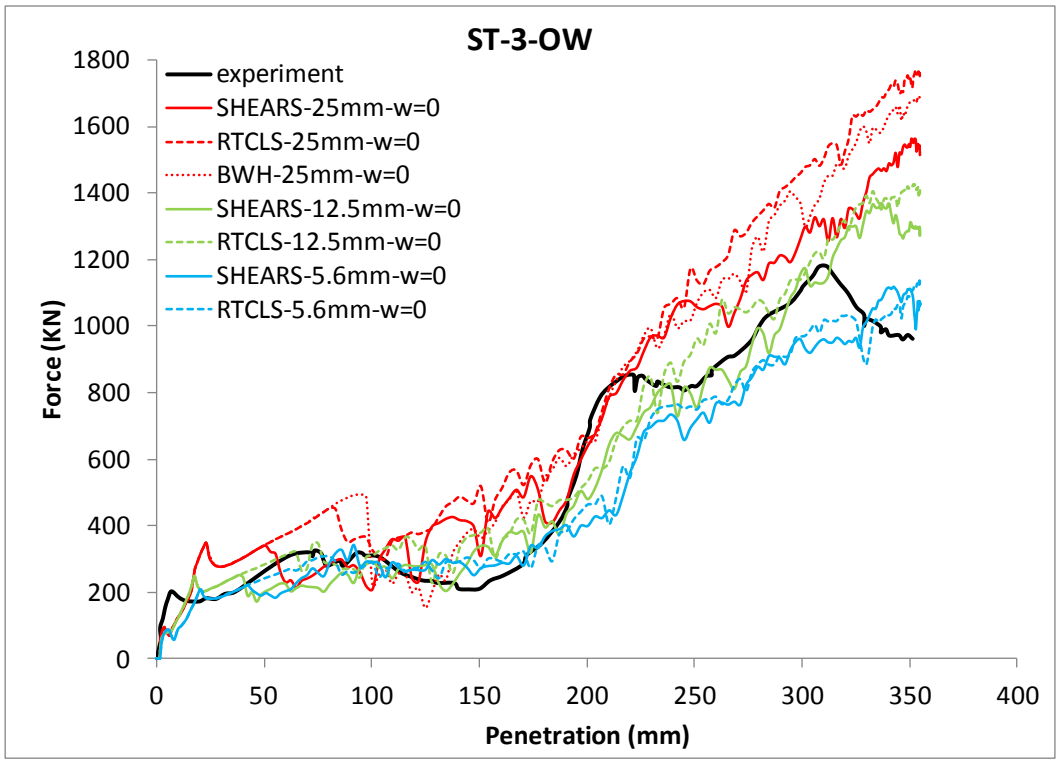

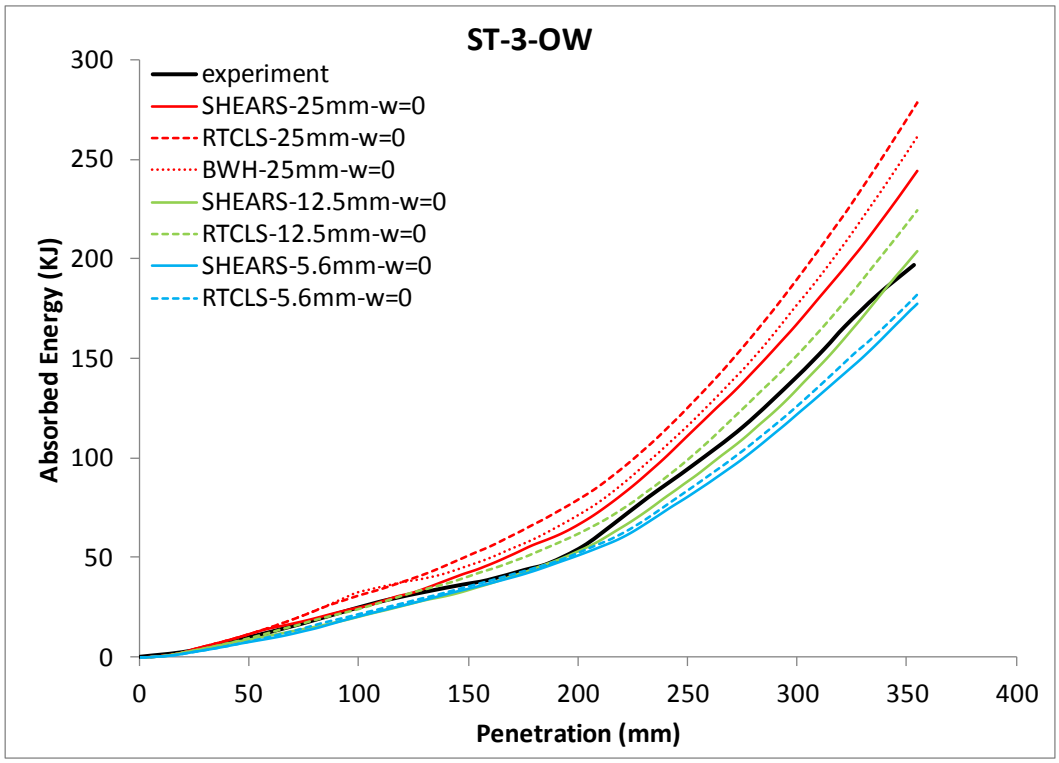

Figure 5.9. ST-3-OW model. Force and absorbed energy-penetration curves.
Prediction of rupture according to SHEARS, RTCLS and BWH rupture criteria in combination with the powerlaw type material curve

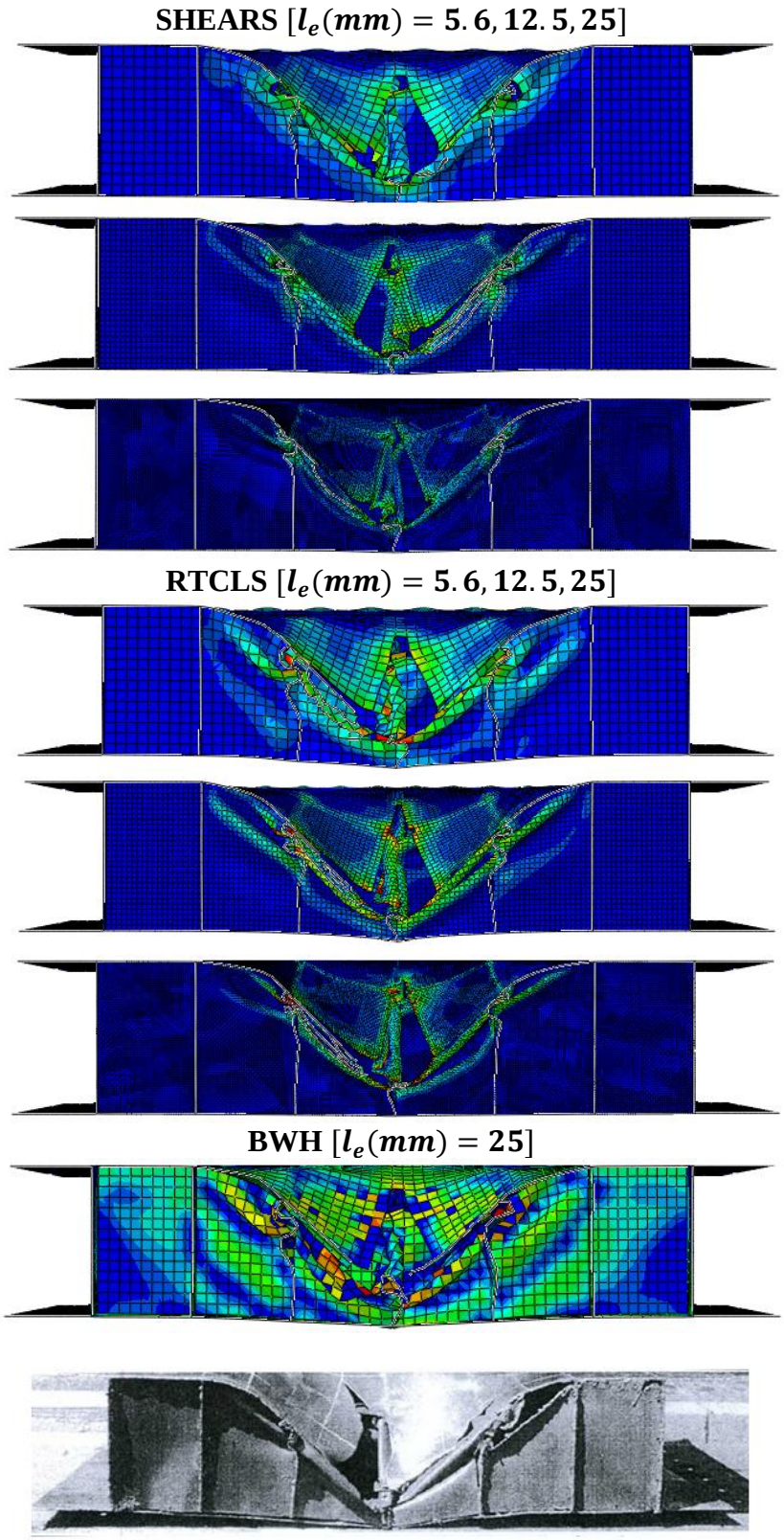

Figure 5.10. ST-3-OW model. Representation of damage according to SHEARS, RTCLS and BWH rupture criteria (Paik et al. 1999)

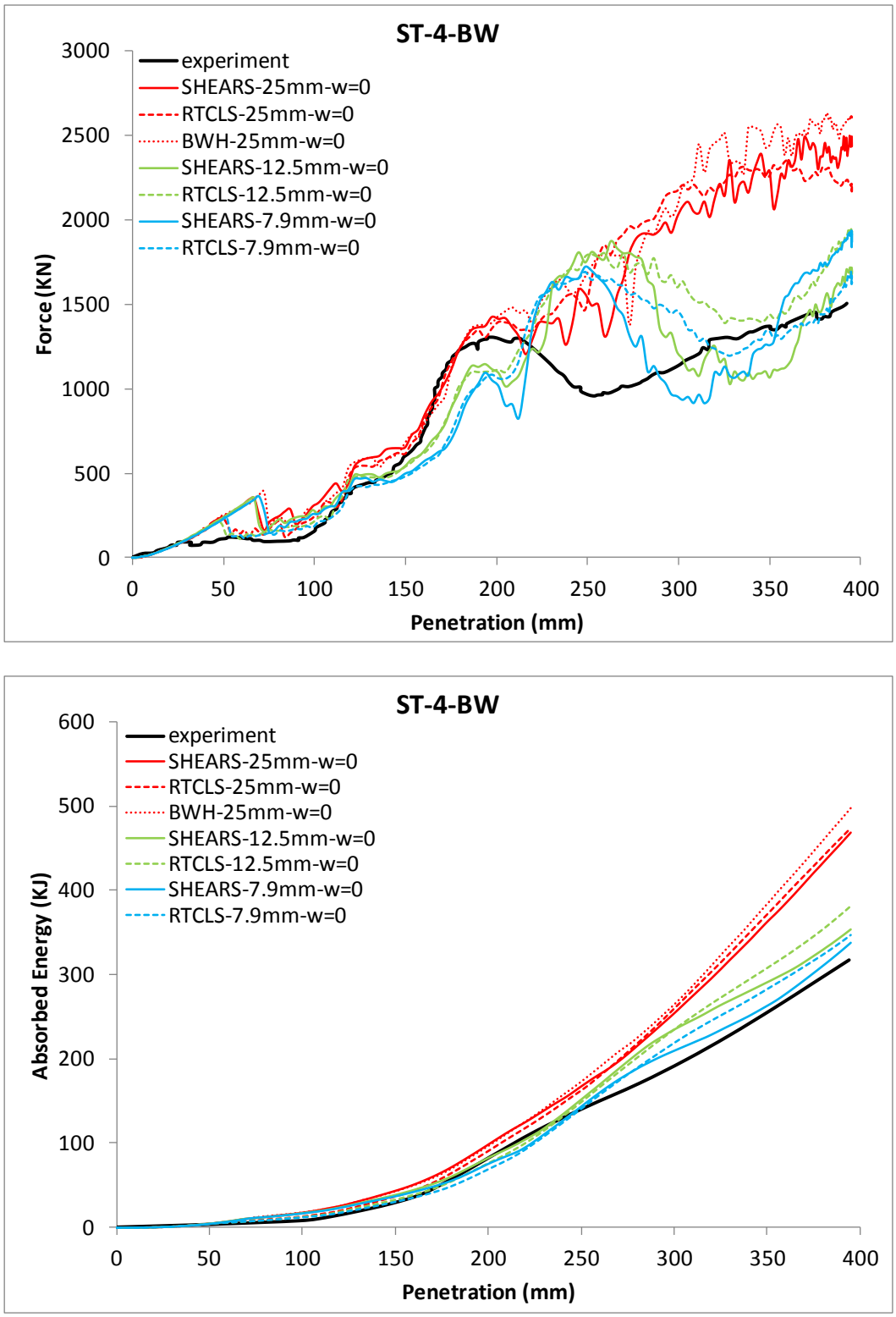

Figure 5.11. ST-4-BW model. Force and absorbed energy-penetration curves.
Prediction of rupture according to SHEARS, RTCLS and BWH rupture criteria in combination with the powerlaw type material curve

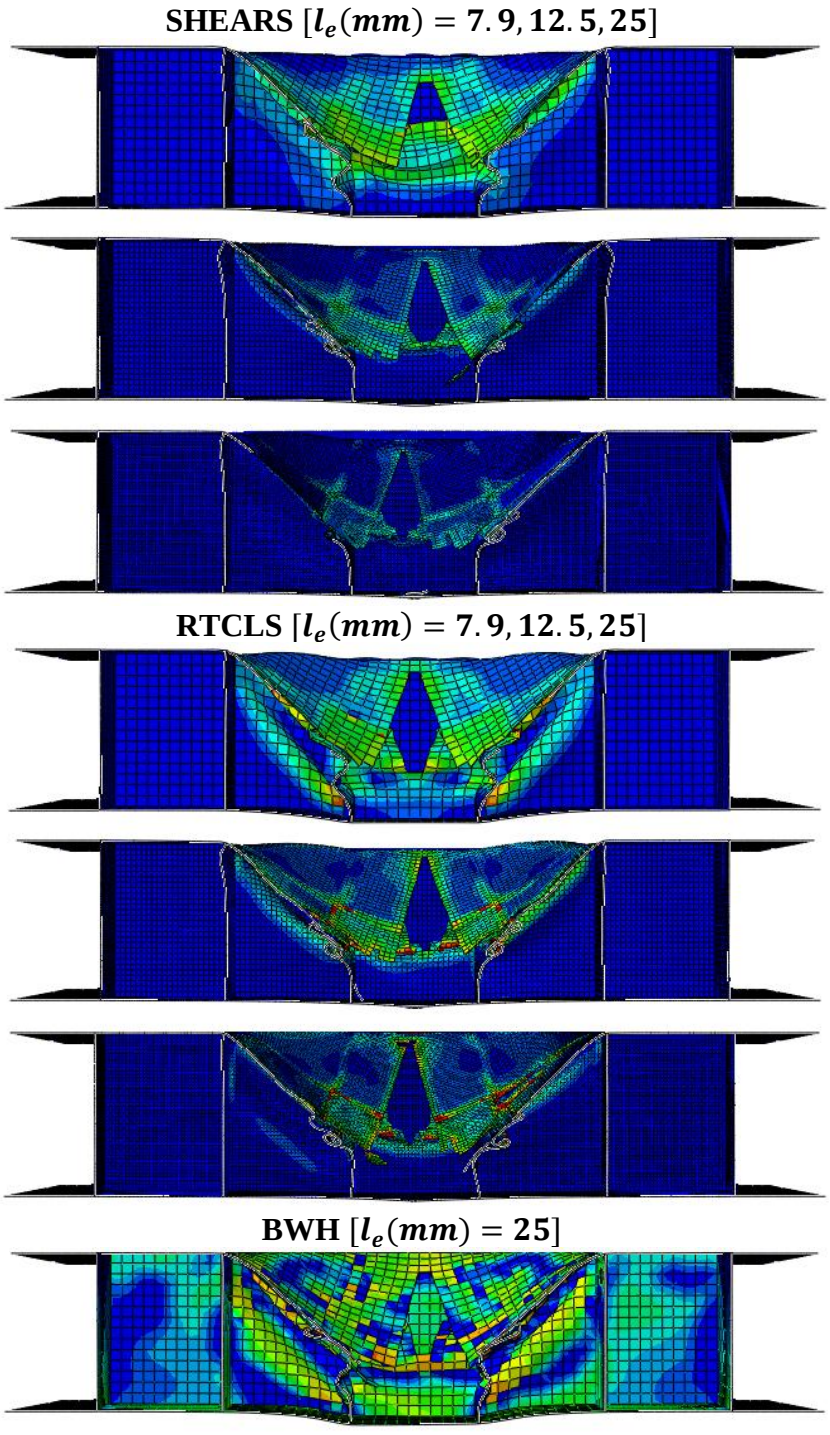

Figure 5.12. ST-4-BW model. Representation of damage according to SHEARS, RTCLS and BWH rupture criteria

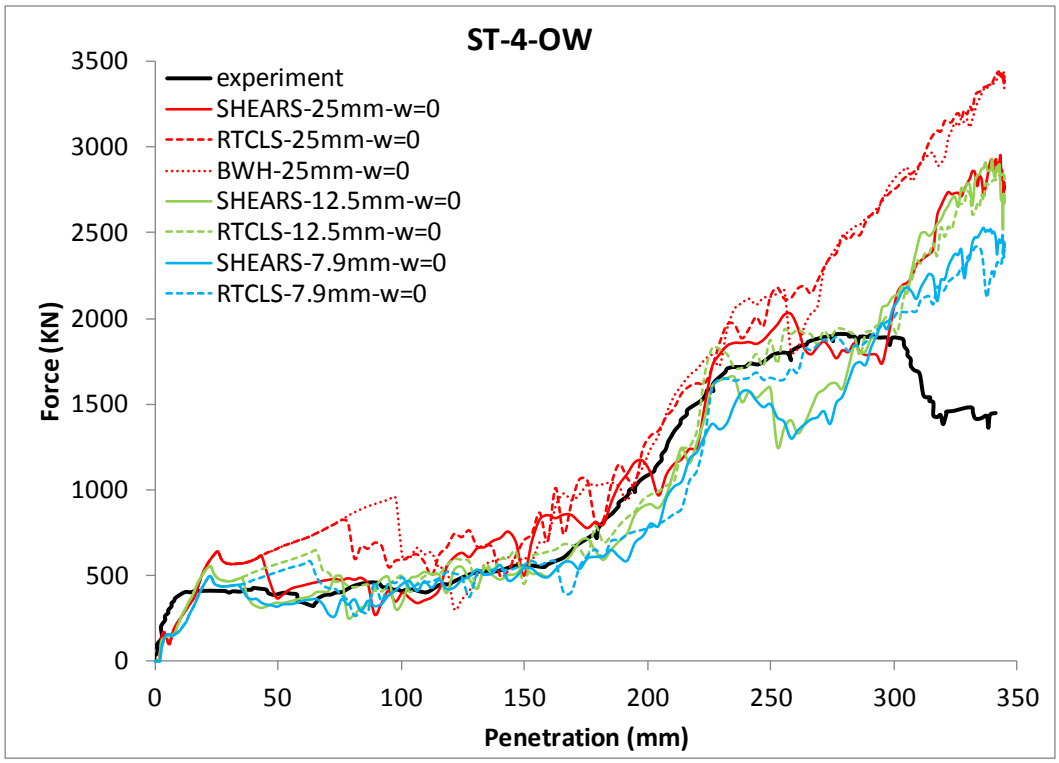

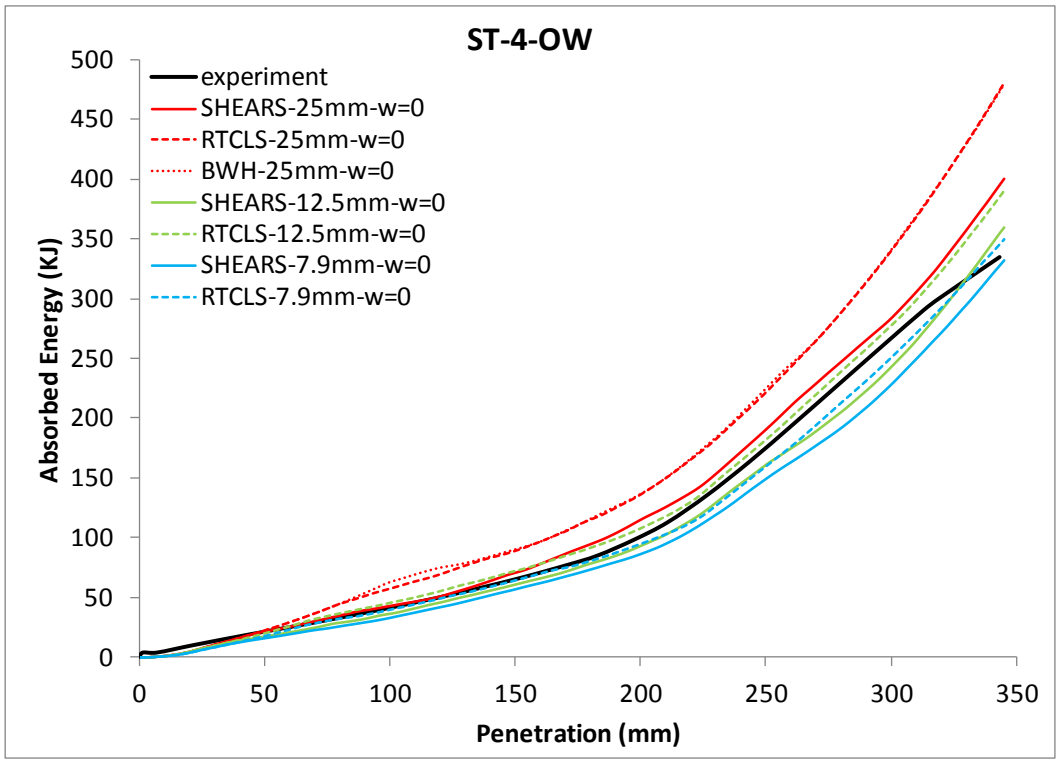

Figure 5.13. ST-4-OW model. Force and absorbed energy-penetration curves.
Prediction of rupture according to SHEARS, RTCLS and BWH rupture criteria in combination with the powerlaw type material curve

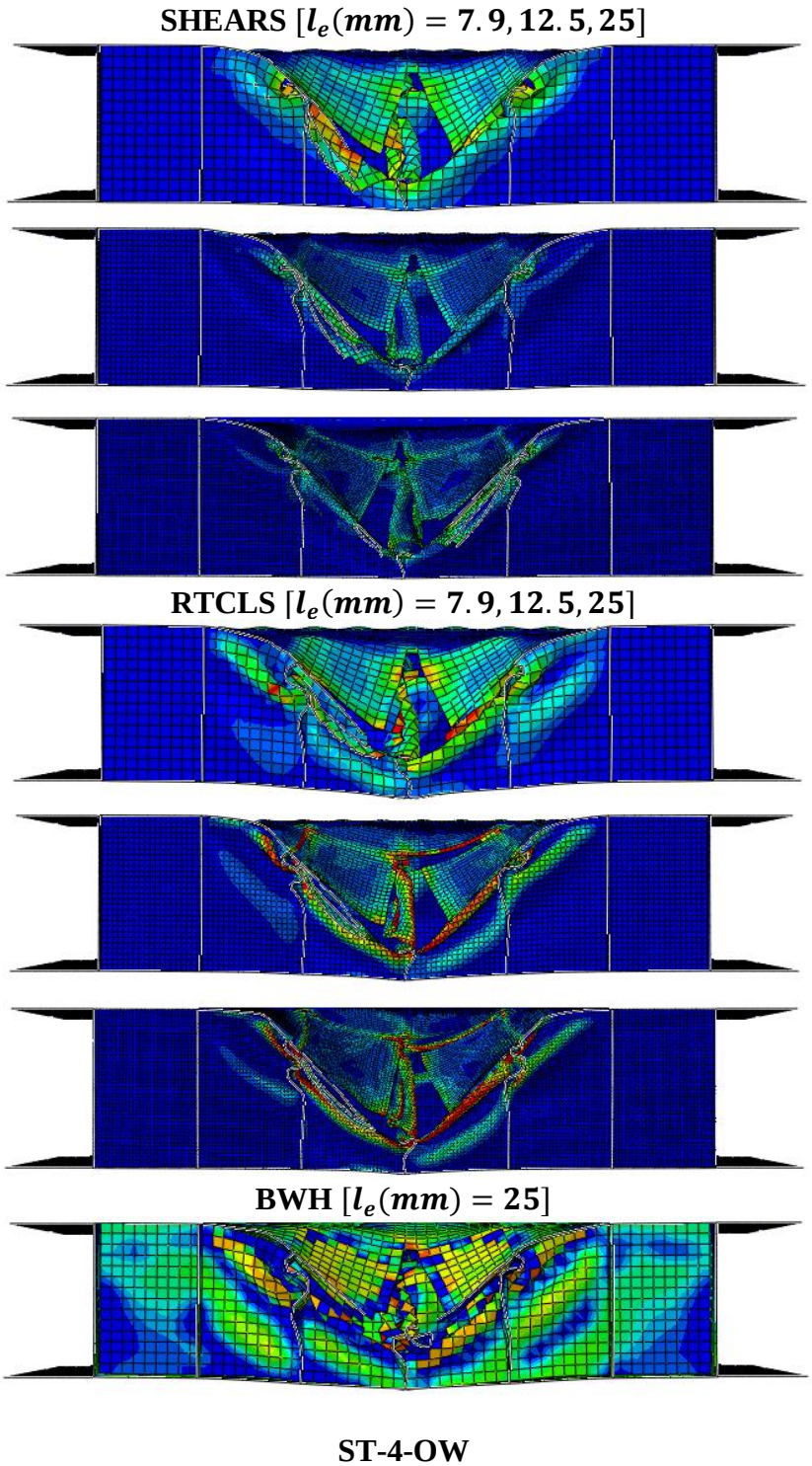

Figure 5.14. ST-4-OW model. Representation of damage according to SHEARS, RTCLS and BWH rupture criteria

5.2.3 US, LS, TS and OS models-(Paik and Tak 1995)

Figures 5.15, 5.17, 5.19 and 5.21 refer to the US, LS, TS and OS models and illustrate comparisons of the experimental force-penetration and absorbed energy-penetration curves with the corresponding numerical curves according to SHEARS, RTCLS and BWH rupture criteria for three mesh sizes. The material behaviour beyond necking is represented by the powerlaw curve. Moreover, Figures 5.16, 5.18, 5.20 and 5.22, illustrate the representation of damage with respect to the three criteria for different meshes.

The basic characteristic of the simulations of the cutting tests simulations is the sharp variations in the force-penetration curves (see Figures 5.15, 5.17, 5.19 and 5.21 and Figures 5.41, 5.45, 5.49 and 5.54 of sub-section 5.2.8). The formation of these sharp variations is attributed to the loading and unloading of the elements adjacent to the contact area, which is very intense during the cutting process and to substantial changes in the contact area between the plate and the indenter that follow the deletion of an element. For finer meshes, i.e. $l_e/t \cong 1$, it is obvious that the sharp peaks and troughs are reduced. In the latter case a better correlation with the experimental force and absorbed energy-penetration curves is achieved with all rupture criteria. In particular, according to Figures 5.19 and 5.21, RTCLS criterion using a fine mesh, shows good correspondence with the experimental curves in the cases of the TS and OS models. SHEARS and BWH criteria yield also good results in all cases of the cutting tests using a fine mesh (see Figures 5.15, 5.17, 5.19 and 5.21). However, the three criteria predict different deformation patterns. As the paper Paik and Tak (1995) does not include pictures of the deformed specimens, the deformation patterns obtained from the simulations were examined against the descriptions given in Paik and Tak (1995).

In the case of the US model, cutting and curling of the plate was observed during the loading process and a stable contact of the plate flaps with the wedge face occurred from about 150 mm penetration up to the end of the test. This description is in accordance with the results in the cases of SHEARS and BWH criteria (see Figure 5.16).

In the case of the LS model, curling of the plate precedes buckling of the longitudinal stiffeners. This trend is also captured by SHEARS and BWH criteria (see Figure 5.18). In the case of the TS model, curling of the plate was observed in the beginning of the loading process and the concertina tearing mode around 125 mm and up to 155 mm penetration. Thereafter, a rapid rise of the loading force due to contact of the wedge tip with the transverse stiffener took place and finally cutting of the latter. In Figure 5.20, it seems that the precedent behaviour is reproduced satisfactorily by all rupture criteria, especially when using a fine mesh.

In the case of the OS model, a combination of the damage phenomena which were observed in the previous cases was evident. The sequence was as follows (Paik and Tak 1995): i) cut and curling of the plate, ii) contact of the curled part of plate with the longitudinal stiffeners, iii) contact of the plate flaps with the wedge face, iv) large out of plane bending of the longitudinal stiffeners, v) contact of the wedge tip with the transverse stiffener, vi) cut of the transverse stiffener and vii) contact of the flaps with the wedge face leading to a new rise in the loading force. All the aforementioned steps during the loading

process seem to have been captured by all rupture criteria with relatively fine meshes, i.e. $l_e/t < 3$ (see Figure 5.22).

During the loading process of cutting of the plates, stress triaxialities in the range of $-1/3 < T < 0$ or $-2 < \beta < -1$, i.e. triaxialities corresponding to modes between uniaxial compression and pure shear processes, are mainly developed. In the case of RTCLS rupture criterion the stress triaxiality function within this range of stress triaxialities is way below one, i.e. $f(T) < 1$ (see Figure 4.1, chapter 4 and Figure 5.60 in section 5.3). As a result the critical equivalent plastic strain is reached at a later stage and RTCLS criterion tends to overestimate the stiffness of the structure. This trend is obvious in the present cases (see Figures 5.15-5.20). It is noted that, in both cases of the scaled forms of RTCL and SHEAR rupture criteria the damage parameters D_{SHEAR} and D_{RTCL}, in equations (4.23) and (4.24) respectively, do not increase for triaxialities which are below -1/3, i.e. cut-off value, although equivalent plastic strains may be developed (see Figure 4.1, chapter 4 and Figure 5.60 in section 5.3). Table 5.4 summarizes the best results for each simulated model (see also Appendix D).

Table 5.4. Numerical results for each simulated model and rupture criterion

	Rupture Criteria		
Simulated Models	SHEARS	RTCLS	BWH
US	Not good correlation between different meshes Best results for $l_e = 8\ mm$ or $l_e/t = 1.1$ (*), (**)	Not good correlation between different meshes and with experimental results	Not good correlation between different meshes Best results for $l_e = 8\ mm$ or $l_e/t = 1.1$
LS	Good correlation between different meshes and with experimental results for $l_e/t < 3$ Best results for $l_e = 8, 16\ mm$ or $1.1 \le l_e/t \le 2.3$ (*), (**) for $l_e = 16\ mm$	Not good correlation between different meshes and with experimental results	Good correlation between different meshes and with experimental results for $l_e/t < 3$ Best results for $l_e = 8, 16\ mm$ or $1.1 \le l_e/t \le 2.3$ (*), (**) for $l_e = 16\ mm$
TS	Not good correlation between different meshes Best results for $l_e = 8\ mm$ or $l_e/t = 1.1$ (*), (**)	Not good correlation between different meshes Best results for $l_e = 8\ mm$ or $l_e/t = 1.1$	Good correlation between different meshes for $l_e/t < 3$ Best results for $l_e = 8, 16\ mm$ or $1.1 \le l_e/t \le 2.3$ (**) for $l_e = 8\ mm$
OS	Good correlation between different meshes for $l_e/t < 3$ Best results for $l_e = 8, 16\ mm$ or $1.1 \le l_e/t \le 2.3$ (*), (**) for $l_e = 16\ mm$	Good correlation between different meshes for $l_e/t < 3$ Best results for $l_e = 8, 16\ mm$ or $1.1 \le l_e/t \le 2.3$ (*), (**) for $l_e = 16\ mm$	Good correlation between different meshes for $l_e/t < 3$ Best results for $l_e = 8, 16\ mm$ or $1.1 \le l_e/t \le 2.3$ (*), (**) for $l_e = 16\ mm$

(*): best correlation with experimental force and energy-penetration curves, (**): best representation of rupture

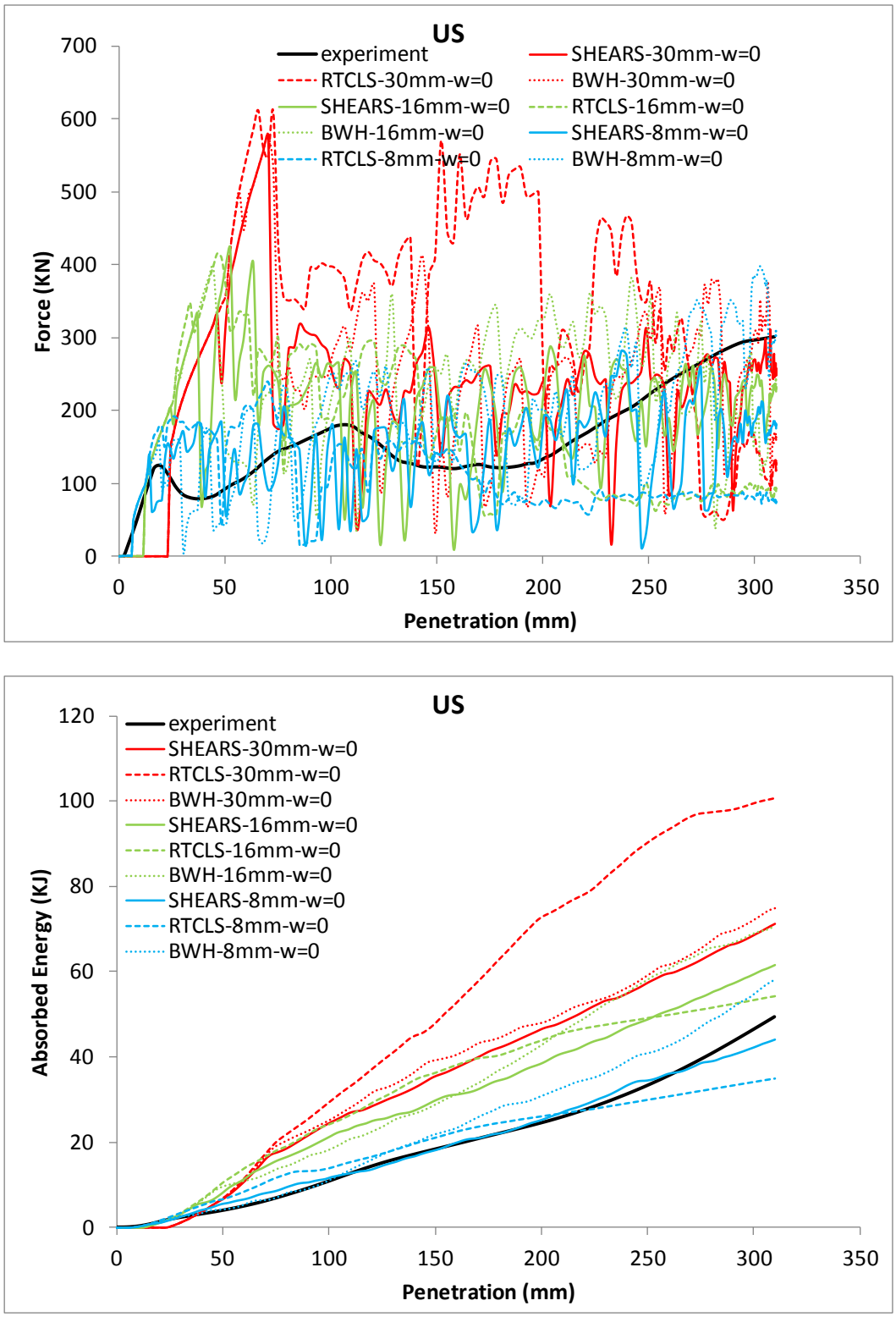

Figure 5.15. US model. Force and absorbed energy-penetration curves.
Prediction of rupture according to SHEARS, RTCLS and BWH rupture criteria in combination with the powerlaw type material curve

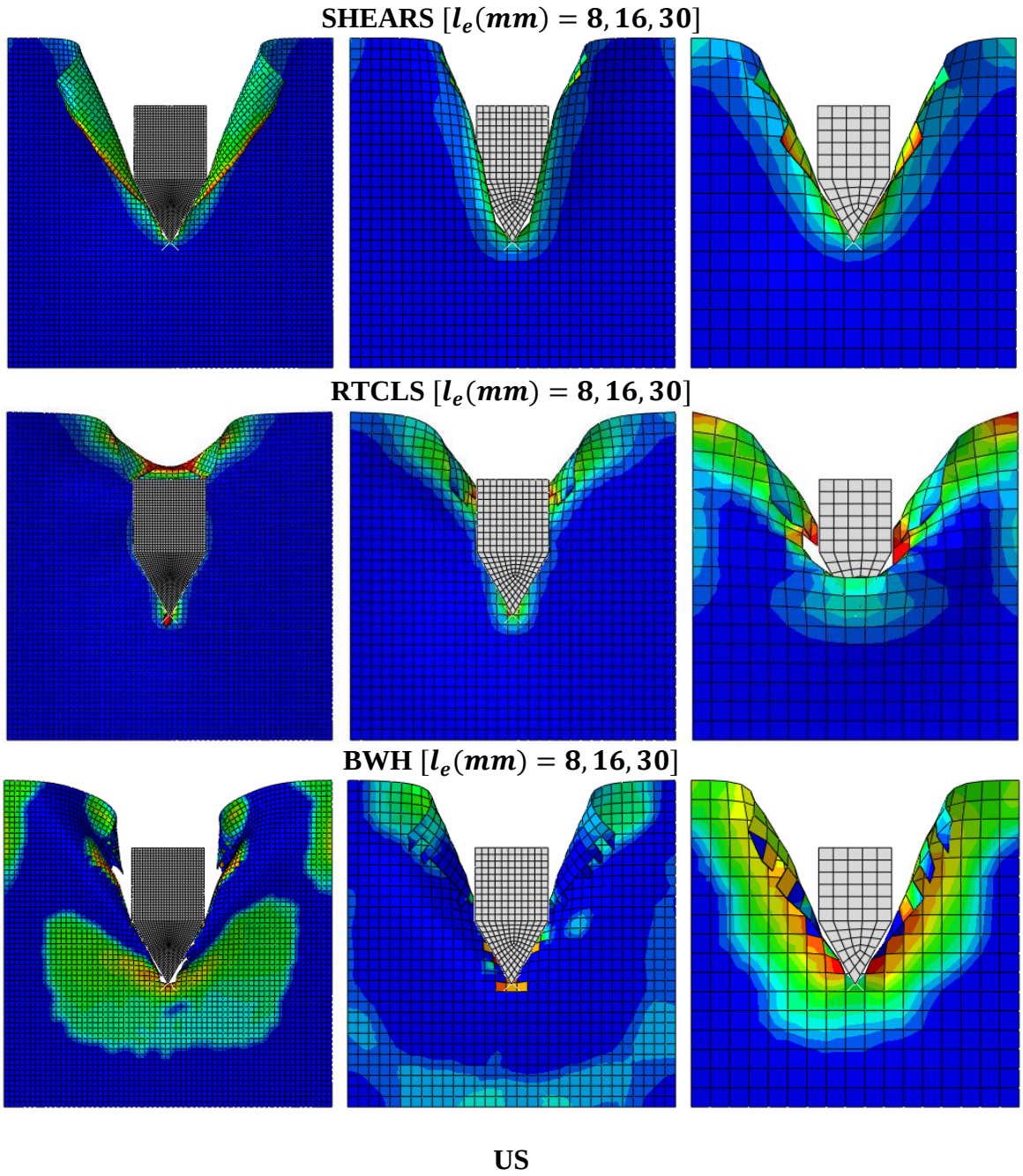

Figure 5.16. US model. Representation of damage according to SHEARS, RTCLS and BWH rupture criteria

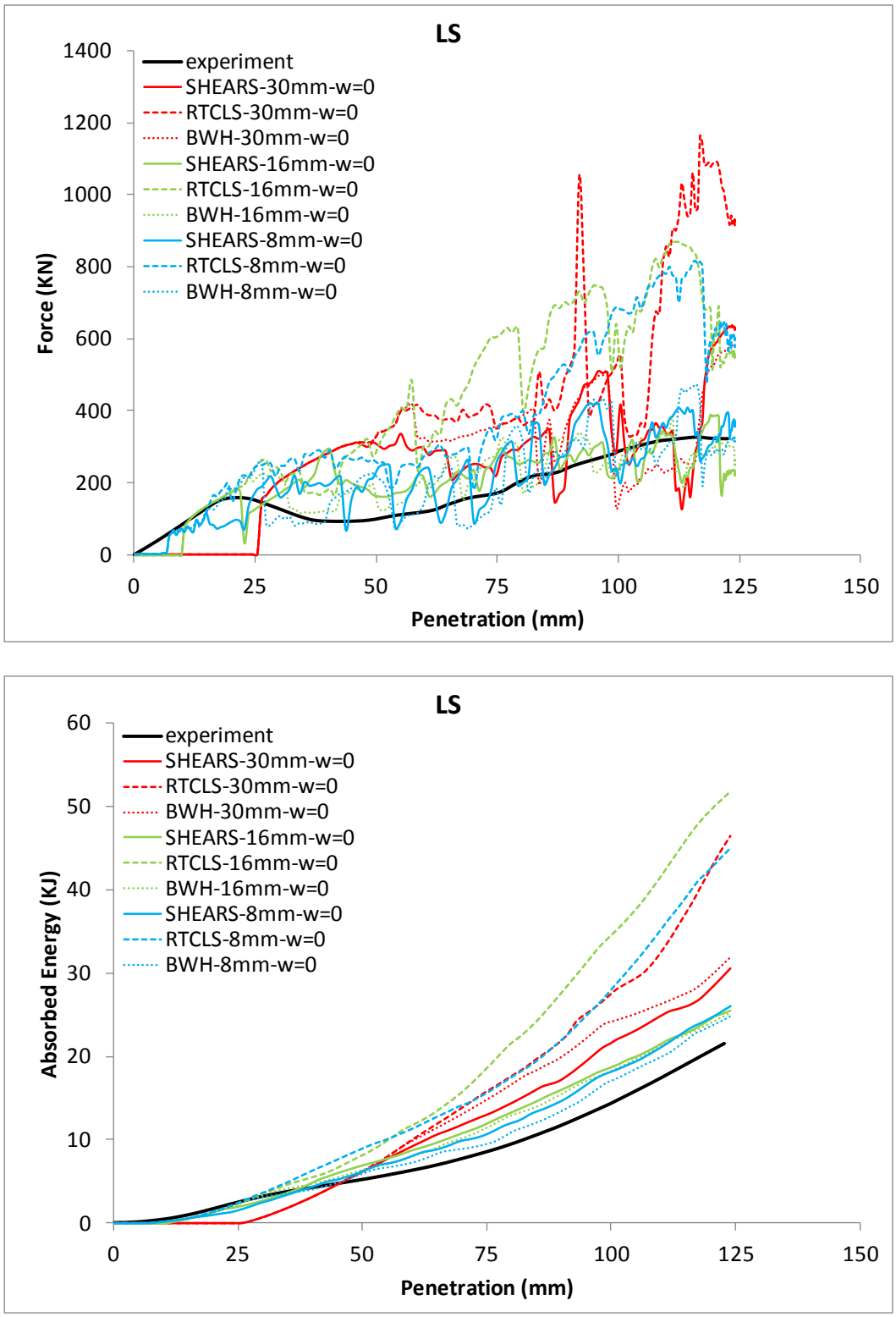

Figure 5.17. LS model. Force and absorbed energy-penetration curves.
Prediction of rupture according to SHEARS, RTCLS and BWH rupture criteria in combination with the powerlaw type material curve

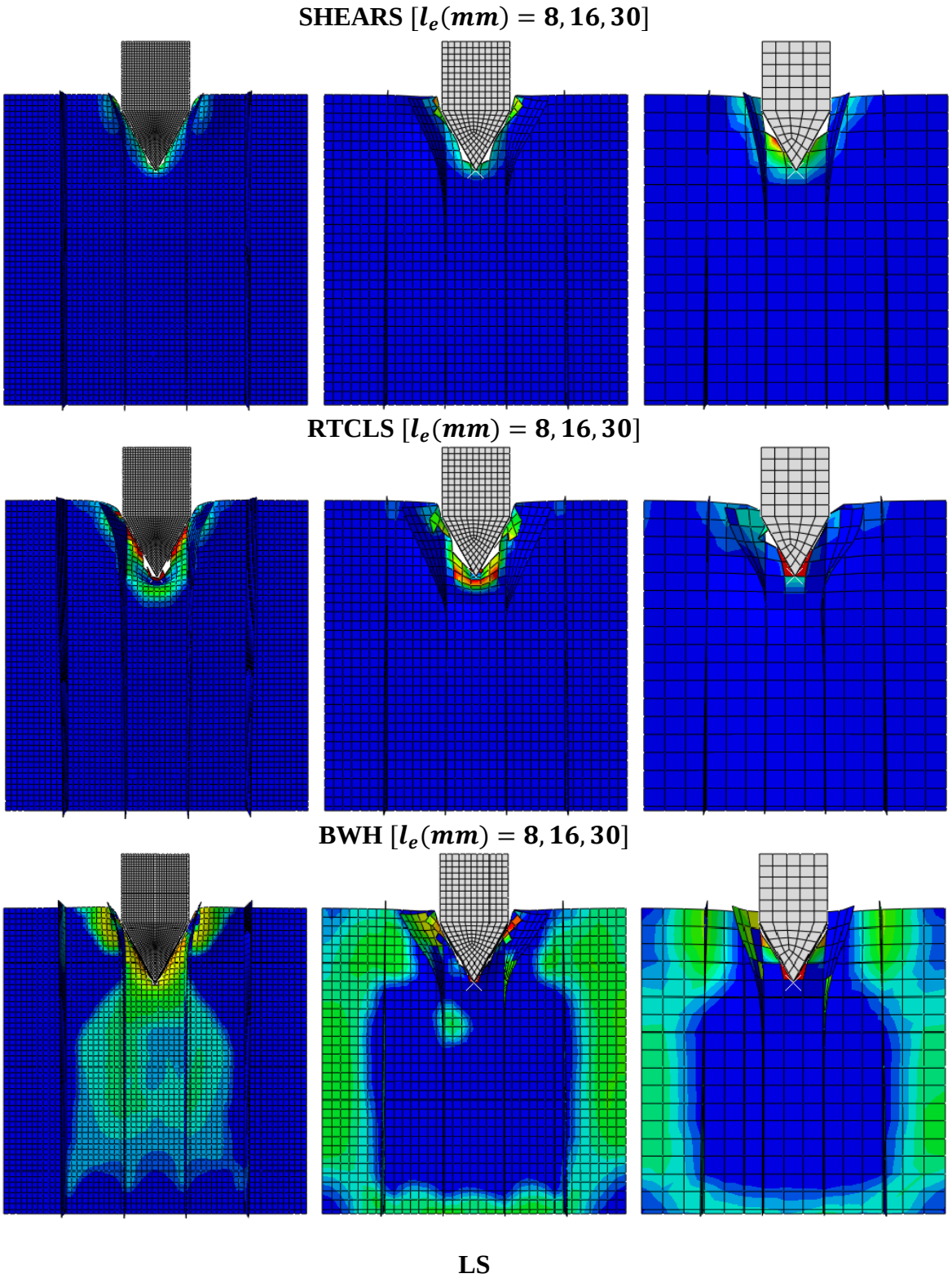

Figure 5.18. LS model. Representation of damage according to SHEARS, RTCLS and BWH rupture criteria

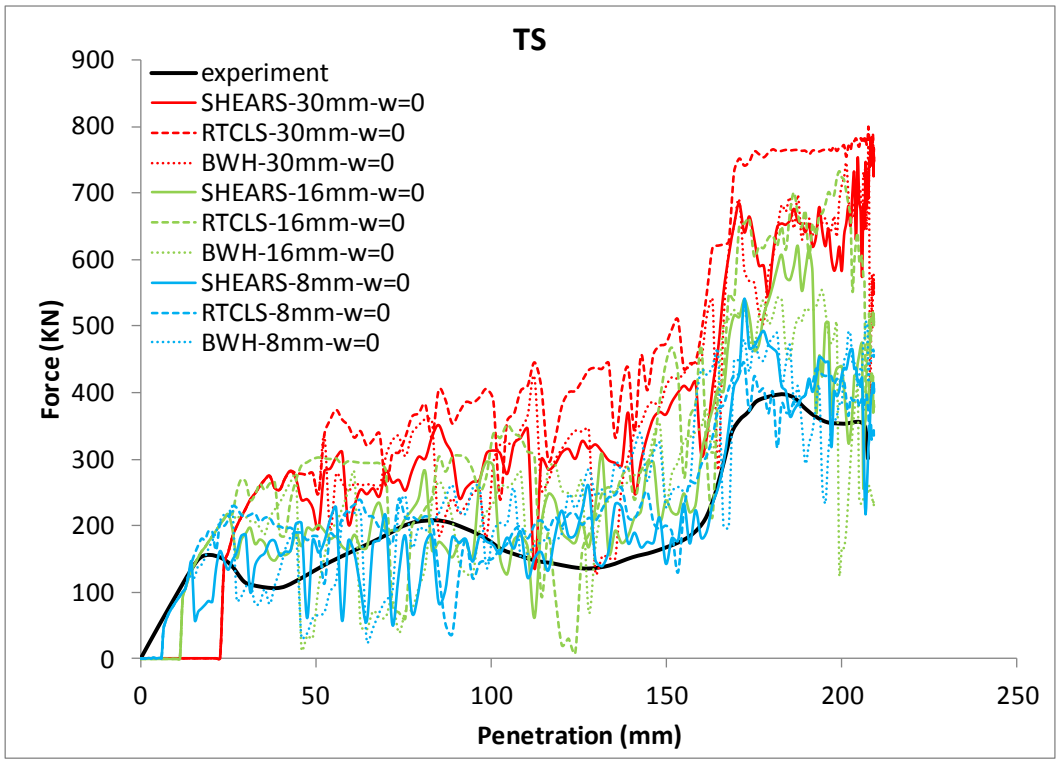

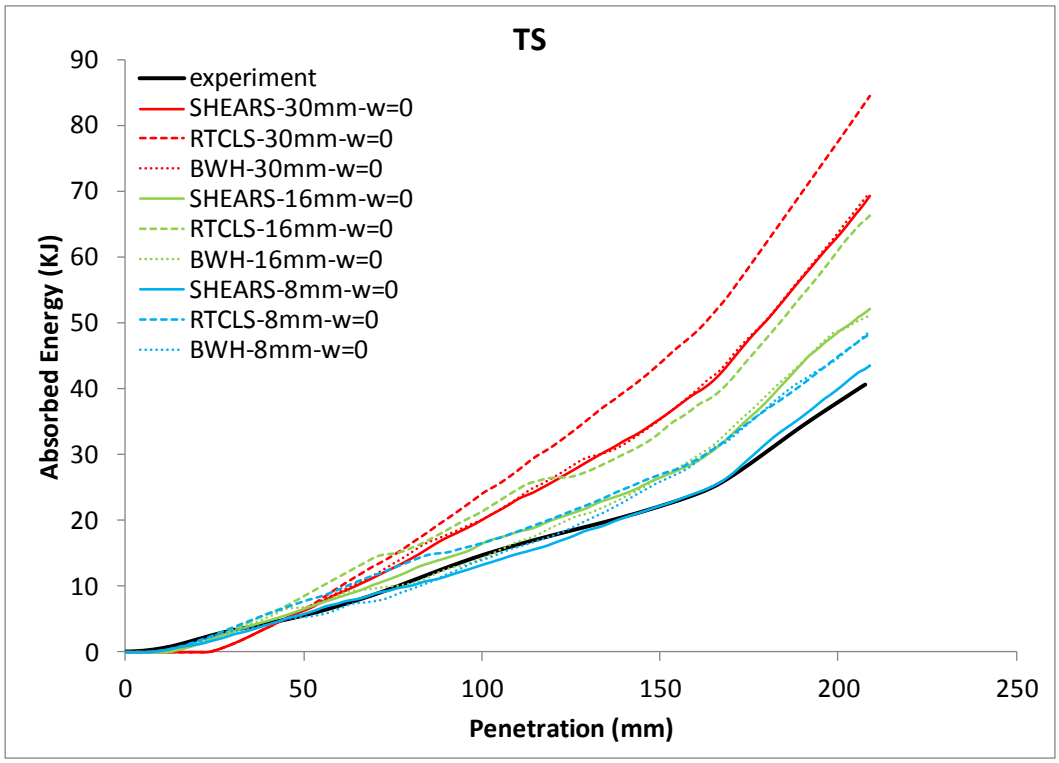

Figure 5.19. TS model. Force and absorbed energy-penetration curves.
Prediction of rupture according to SHEARS, RTCLS and BWH rupture criteria in combination with the powerlaw type material curve

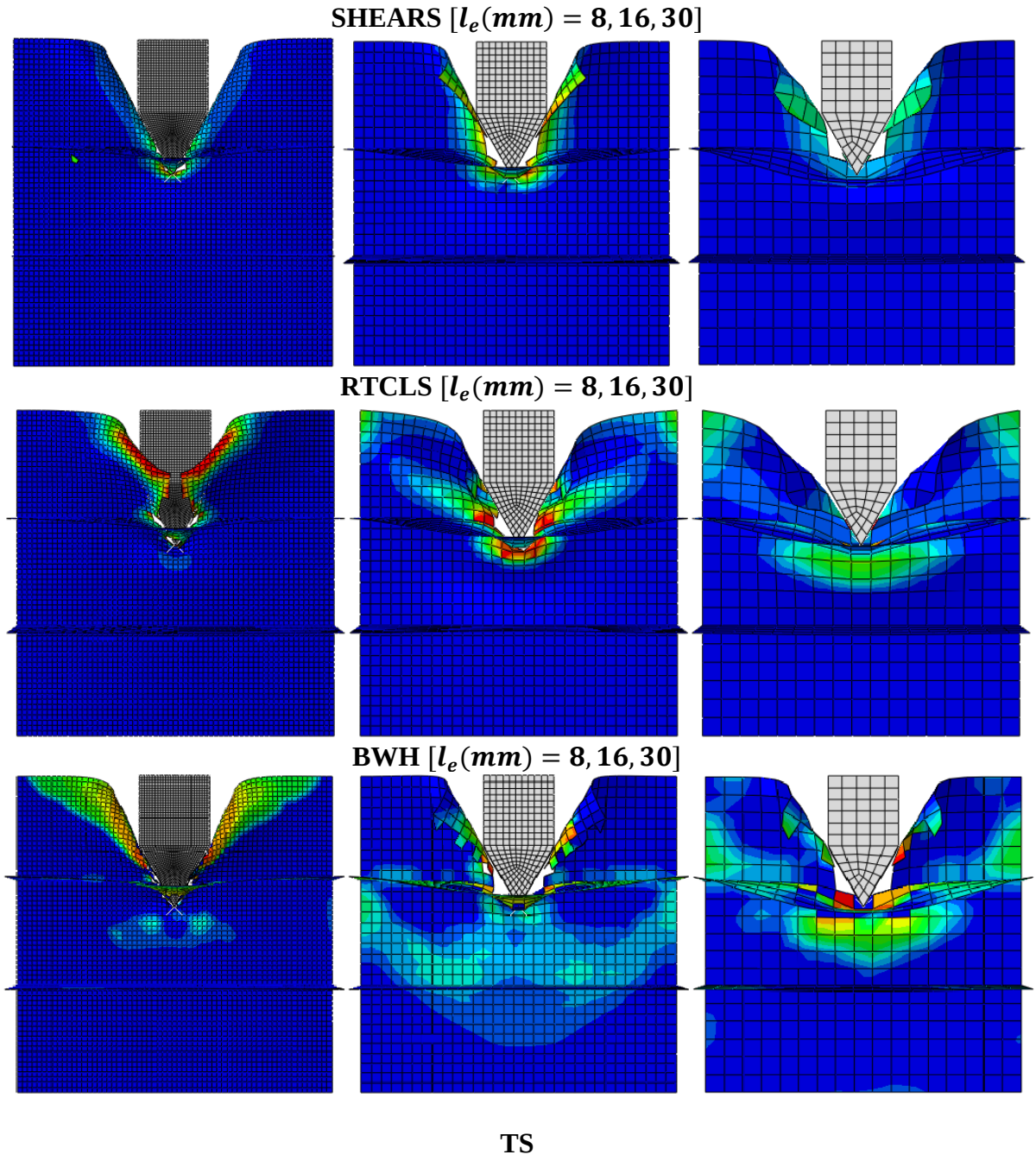

Figure 5.20. TS model. Representation of damage according to SHEARS, RTCLS and BWH rupture criteria

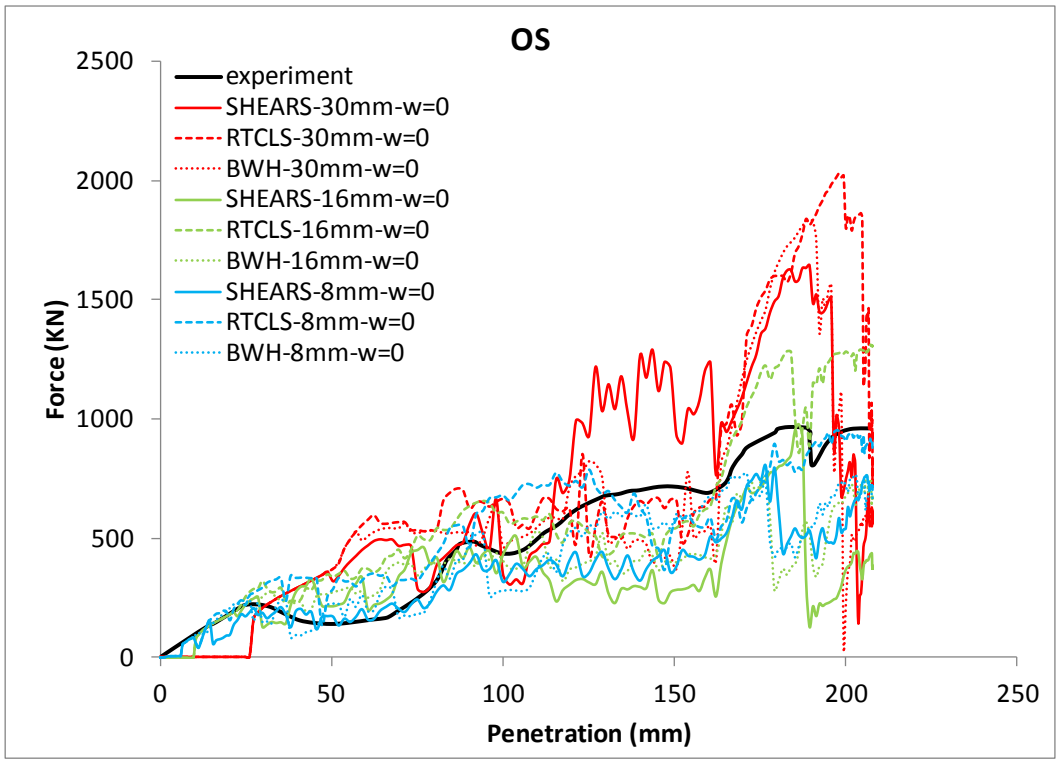

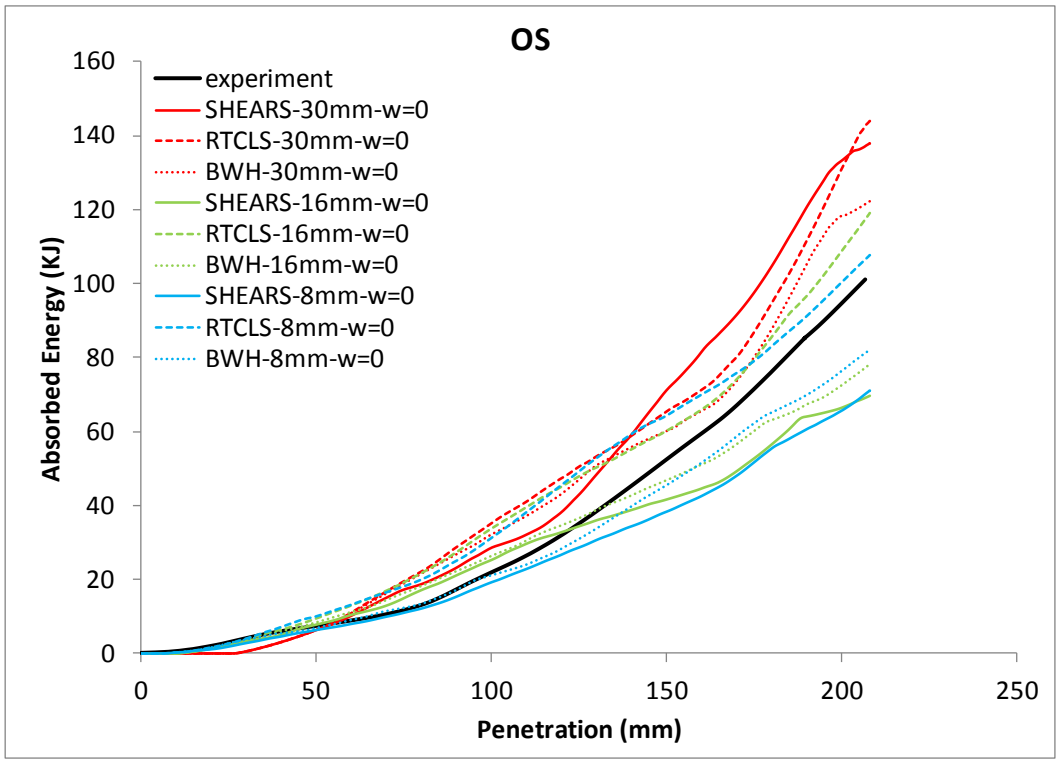

Figure 5.21. OS model. Force and absorbed energy-penetration curves.
Prediction of rupture according to SHEARS, RTCLS and BWH rupture criteria in combination with the powerlaw type material curve

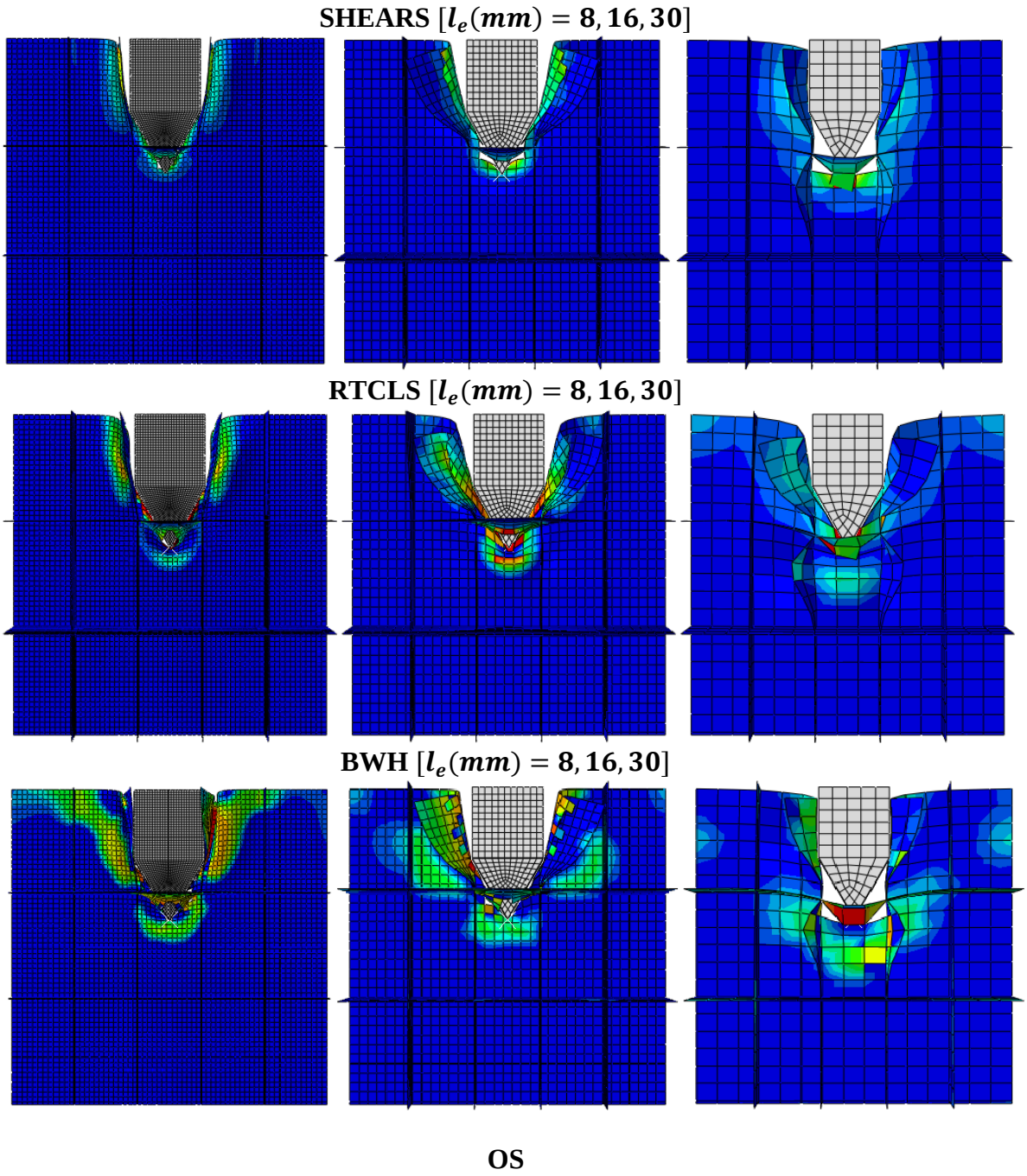

Figure 5.22. OS model. Representation of damage according to SHEARS, RTCLS and BWH rupture criteria

5.2.4 COLLISION STATIC and COLLISION DYNAMIC models-(ASIS 1993 reported in ISSC 2003)

Figure 5.24 refers to the COLLISION STATIC model and illustrates comparisons of the experimental force-penetration and absorbed energy-penetration curves with the corresponding numerical curves for two mesh sizes, in the cases of SHEARS and RTCLS criteria and one mesh size in the case of BWH criterion. The material behaviour beyond necking is represented by the powerlaw curve. Moreover, Figure 5.25 illustrates the representation of damage with respect to the three criteria for different meshes.

According to Figures 5.24 and 5.25 it is obvious that the three criteria yield considerably different results. In particular, SHEARS criterion predicts rupture of the stringer deck and stringer deck stiffeners at the joint with the right web using a coarse mesh, i.e. $l_e/t \cong 3$ as well as rupture of the side shell at the same point using a fine mesh, i.e. $l_e/t \cong 1.5$ (see Figure 5.25). RTCLS criterion shows consistency and predicts in both cases rupture of the side shell, stringer deck and stringer deck stiffeners at the joint with the webs and rupture along the joint with the webs, while BWH criterion is not activated under such loading conditions using a coarse mesh (see Figure 5.25). Due to lack of pictures of the experimental deformation patterns, comparison was realized in terms of the correspondence between numerical and experimental force and absorbed energy-penetration curves. Thus, from Figure 5.24 one may observe that numerical results in the case of RTCLS criterion are in good agreement with the experimental results and the numerical force-penetration curves follow the trend of the experiment, especially in the case of a coarse mesh. However, in both cases RTCLS criterion underestimates the resistance capacity of the structure approximately beyond $600\ mm$ penetration. SHEARS criterion yields also good results using a fine mesh, although overestimation of the structure's stiffness in the majority of the loading steps is evident.

In the case of the drop weight test, i.e. COLLISION DYNAMIC model, with impact speed almost equal to $10\ m/sec$ or $19.4\ knots$, the material was modeled in three different ways: a) without including strain-rate effects and modeling of rupture, b) including strain-rate effects on the true stress-strain curves without including modeling of rupture and c) without including strain-rate effects but including modeling of rupture using SHEARS and RTCLS rupture criteria. It is noted that, in the numerical simulations of the COLLISION DYNAMIC model, all four drops as occurred in the experiment were performed, taking into account the change in the initial velocity due to the change of the height the indenter was positioned above the structure after the end of each drop (see Figures 5.26 and 5.27). Figure 5.26 illustrates comparisons of the experimental force-penetration and absorbed energy-penetration curves with the corresponding numerical curves for two mesh sizes in the cases of material models a) and b), while Figure 5.27 in the case of material model c). The material behaviour beyond necking is represented by the powerlaw curve. Figure 5.28 illustrates the representation of damage with respect to the selected criteria for two different meshes.

Considering material models a) and b), the structure shows a much stiffer behaviour than in the experiment when the effect of strain-rate is included on the true stress-strain curve of the material (see Figure 5.26). Figure 5.23 compares the true strain-rate dependent material curves and the true material curve of the quasi-static uniaxial tension test for each material (see also Appendix A). It is observed that, the higher the strain-rate the stiffer the material, prior and beyond necking. It is noted that, ultimate stress in Figure 5.23 is the true stress at the point of ultimate load of the engineering stress-strain curve, i.e. σ_u. A reason for such a stiffer behaviour could be that, in case the material behaviour at various strain-rates is determined by tensile tests, where the rate of strain is controlled by monitoring the rate over the gauge length, the strain-rate at the neck is usually higher. Hence, the parts of the true stress-strain curves at and beyond necking may correspond to higher strain-rates than the mid strain-rates used in the experiments. However, further research is needed before concluding if strain-rate effect is essential in the numerical analyses of ship impacts.

Figures 5.27 and 5.28 present the results of material model c). From Figure 5.28, it is observed that in both cases RTCLS criterion predicts rupture of the stringer deck along the joint with the webs, which has not been observed in the test. SHEARS criterion shows a good representation of the deformation pattern as well as good correlation with the experimental curves especially in the case of a fine mesh, where the penetration depth at the end of the fourth drop is captured satisfactorily (see Figure 5.27). Table 5.5 summarizes the best results for each simulated model (see also Appendix D).

Table 5.5. Numerical results for each simulated model and rupture criterion

<table>
<tr><td rowspan="2"></td><td colspan="2">Rupture Criteria</td></tr>
<tr><td>Simulated Models</td><td>SHEARS</td><td>RTCLS</td></tr>
<tr><td>COLLISION STATIC</td><td>Not good correlation between different meshes
Best results for
$l_e = 12.5\,mm$ or
$l_e/t \cong 1.5$</td><td>Good correlation between different meshes
Best results for
$l_e = 25\,mm$ or
$l_e/t \cong 3$(*)</td></tr>
<tr><td>COLLISION DYNAMIC

Without strain-rate effect</td><td>Good correlation between different meshes and with experimental results
Best results for
$l_e = 12.5\,mm$ or
$l_e/t \cong 1.5$
(*), (**)</td><td>Not good correlation between different meshes and with experimental results</td></tr>
<tr><td rowspan="2"></td><td colspan="2">No damage</td></tr>
<tr><td>With strain-rate effect</td><td>Without strain-rate effect</td></tr>
<tr><td>COLLISION DYNAMIC</td><td>Good correlation between different meshes
Best results for
$l_e = 12.5\,mm$ or
$l_e/t \cong 1.5$</td><td>Good correlation between different meshes and with experimental results
Best results for
$l_e = 25\,mm$ or
$l_e/t \cong 3$</td></tr>
</table>

(*): best correlation with experimental force and energy-penetration curves, (**): best representation of rupture

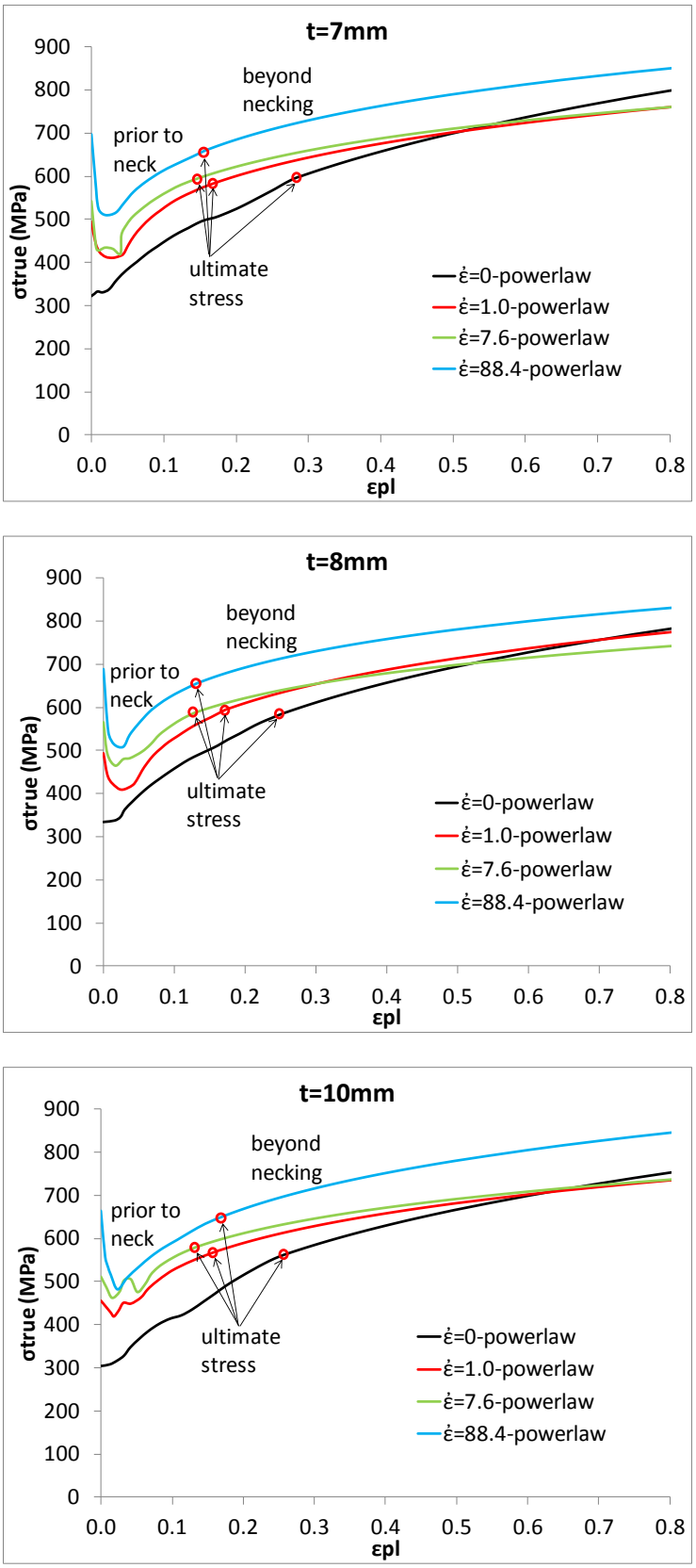

Figure 5.23. Stress-strain relation for various strain-rates in the case of the drop weight test

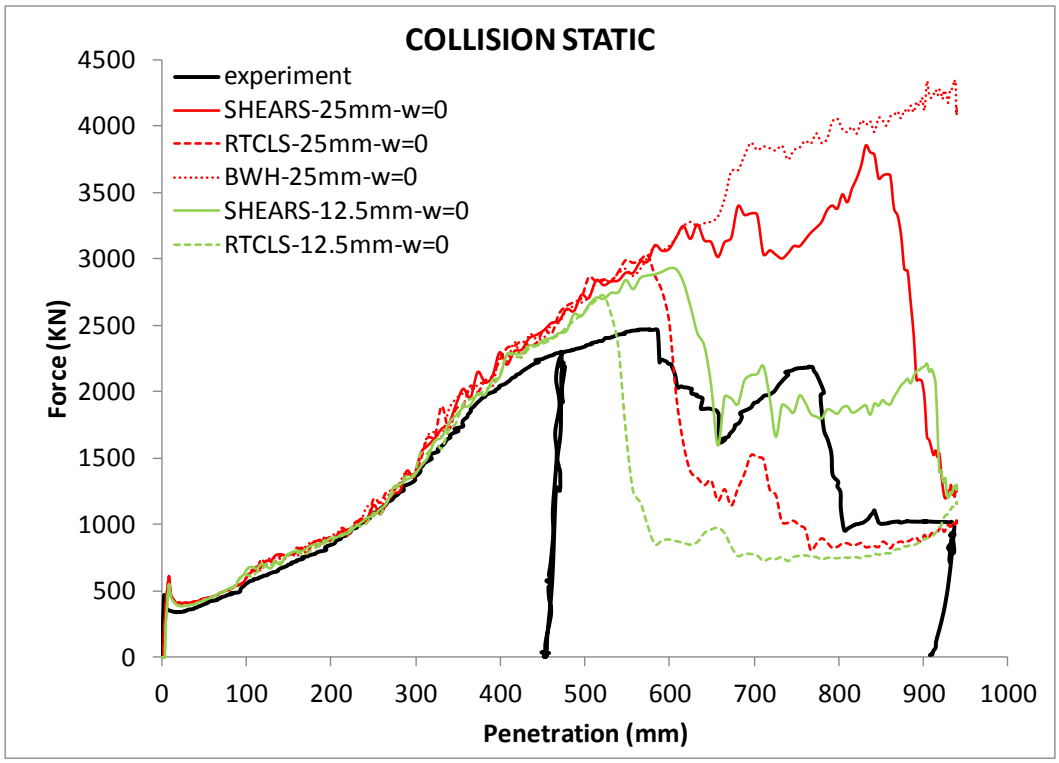

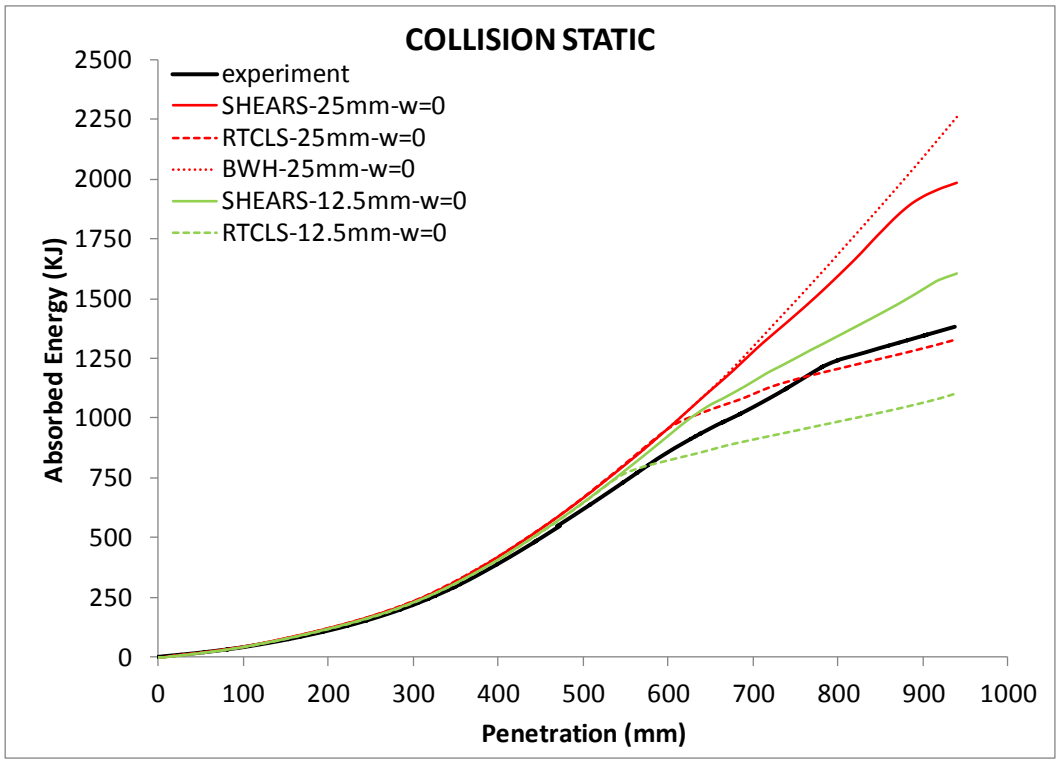

Figure 5.24. COLLISION STATIC model. Force and absorbed energy-penetration curves. Prediction of rupture according to SHEARS, RTCLS and BWH rupture criteria in combination with the powerlaw type material curve

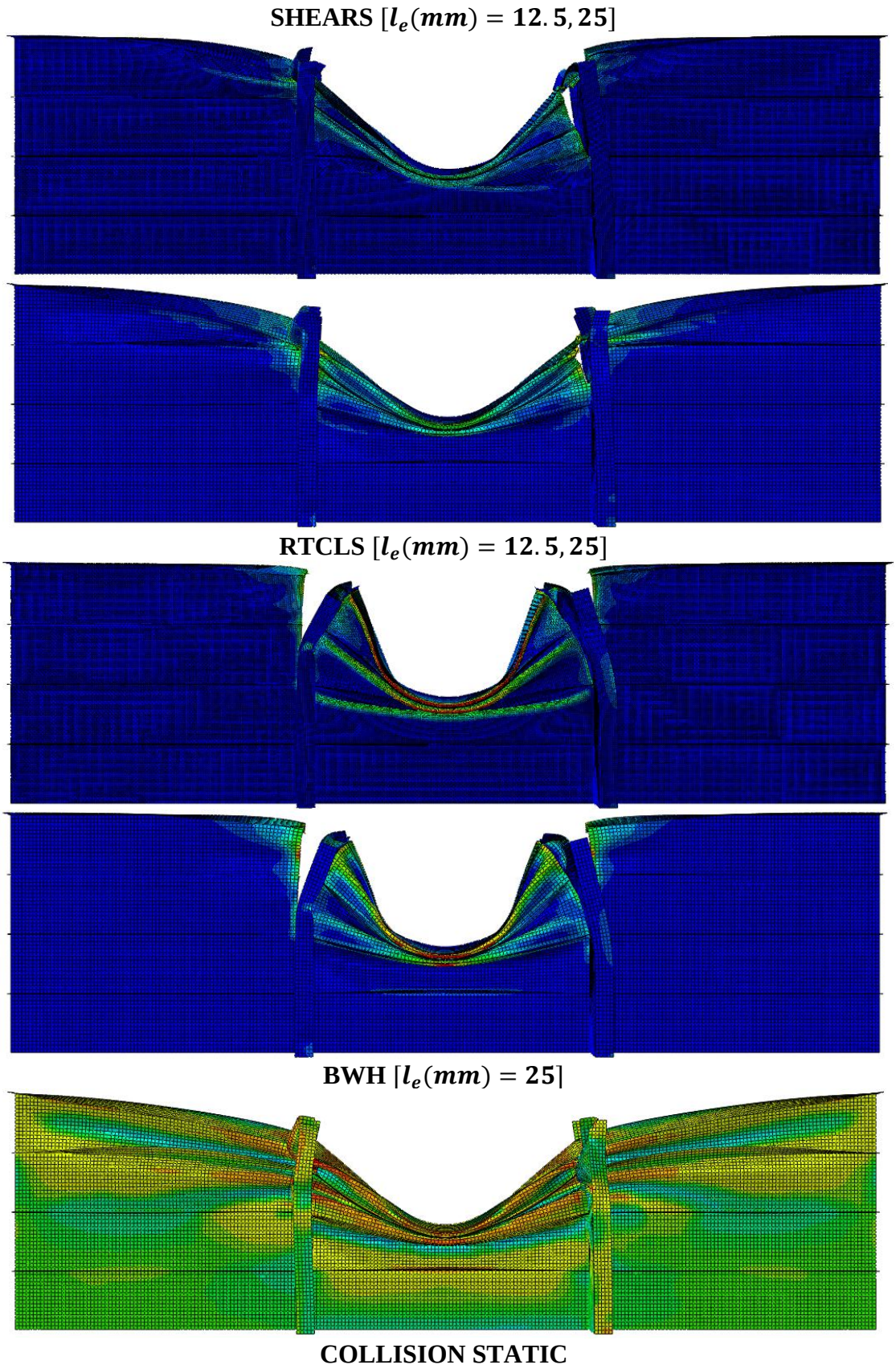

Figure 5.25. COLLISION STATIC model. Representation of damage according to SHEARS, RTCLS and BWH rupture criteria

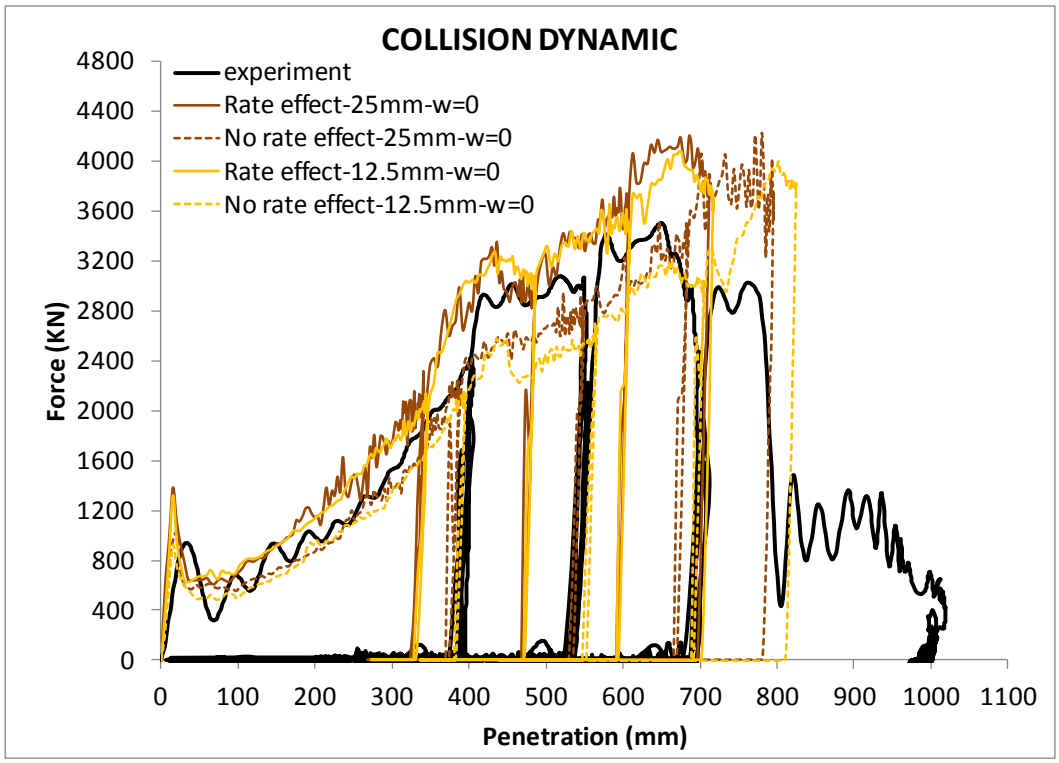

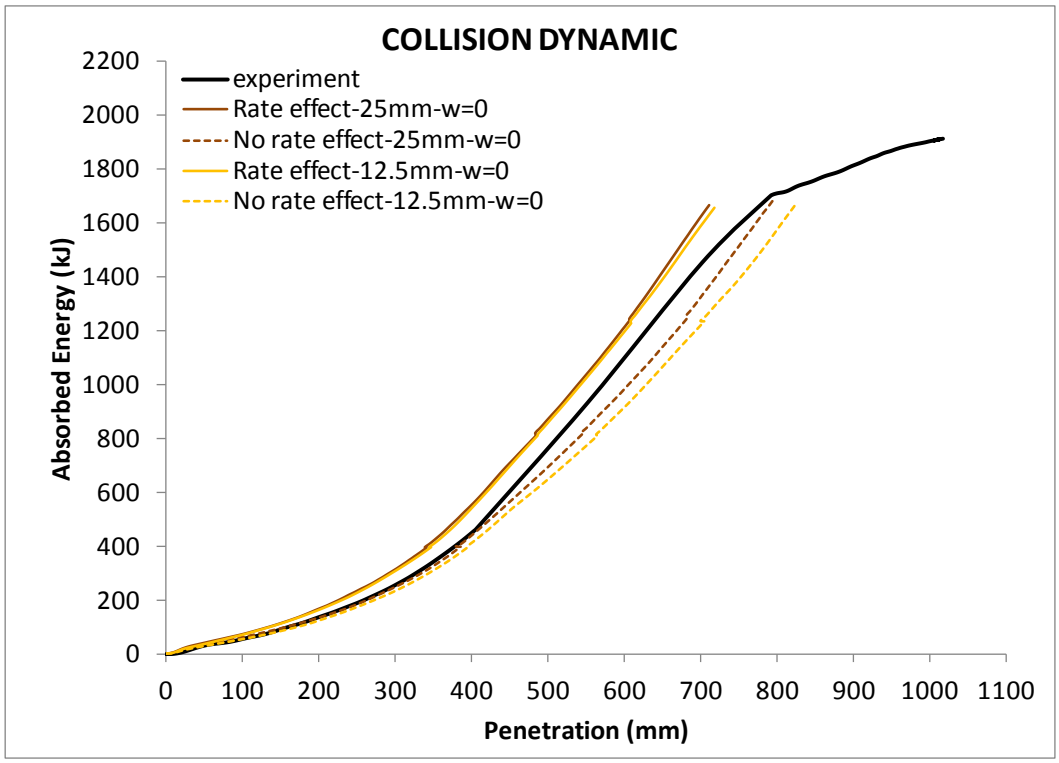

Figure 5.26. COLLISION DYNAMIC model. Force and absorbed energy-penetration curves. Comparison between results with and without strain-rate effect and no damage in combination with the powerlaw type material curve

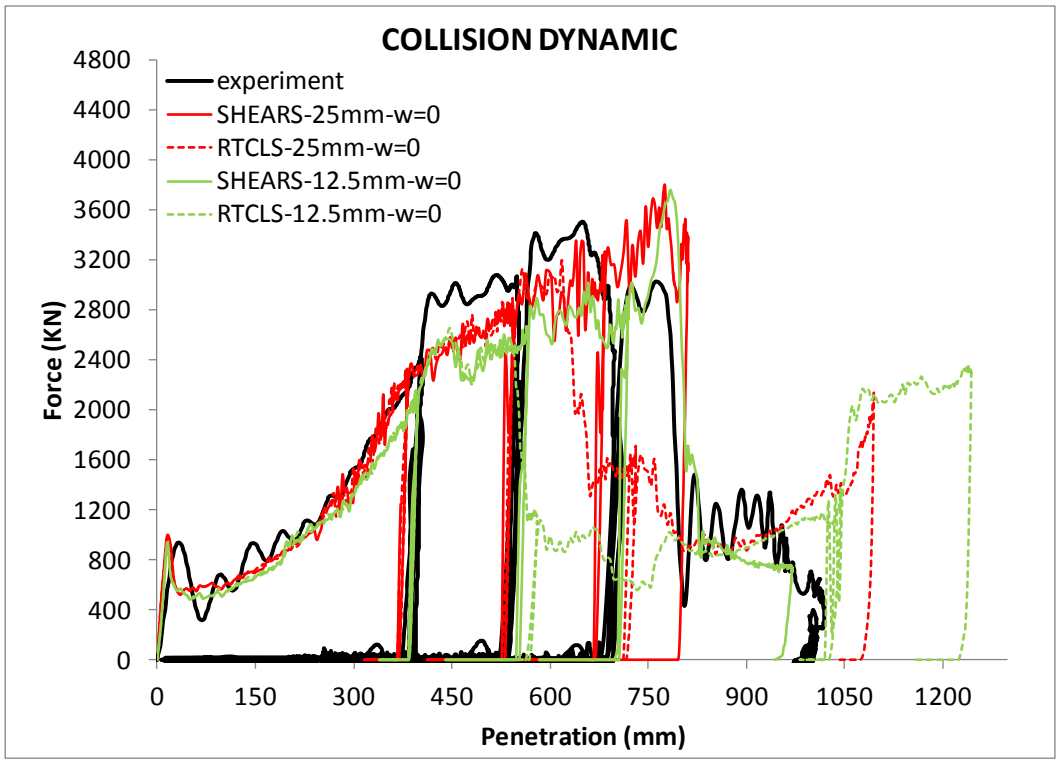

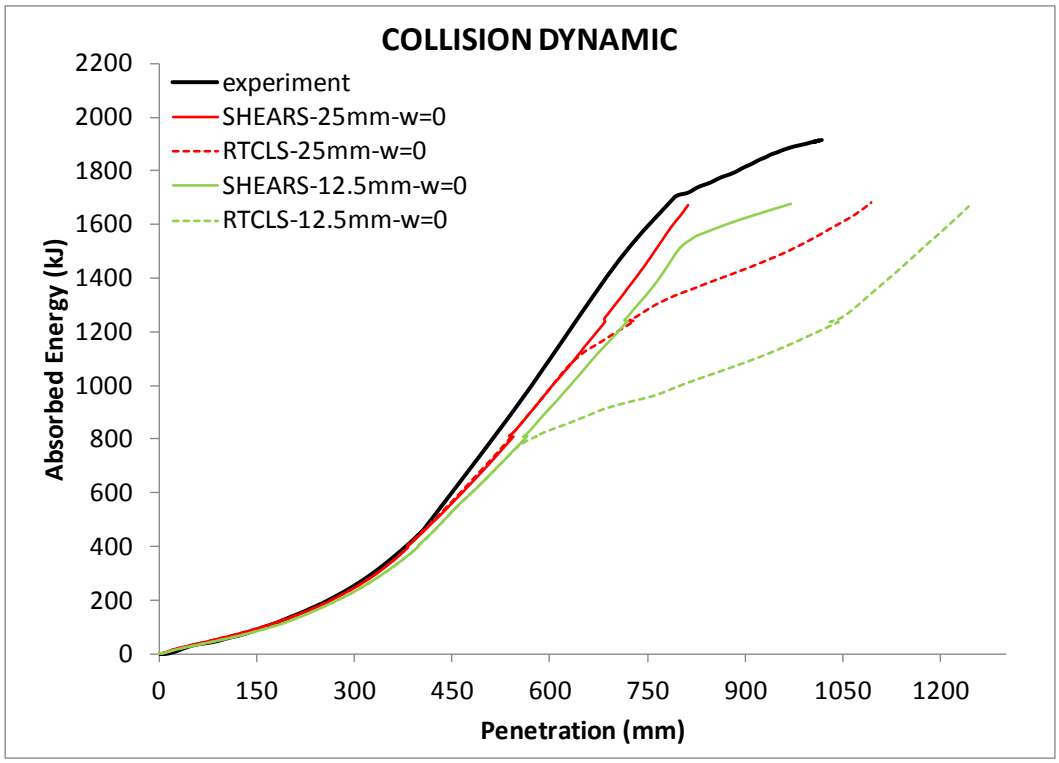

Figure 5.27. COLLISION DYNAMIC model. Force and absorbed energy-penetration curves. Prediction of rupture according to SHEARS and RTCLS rupture criteria without strain-rate effect in combination with the powerlaw type material curve

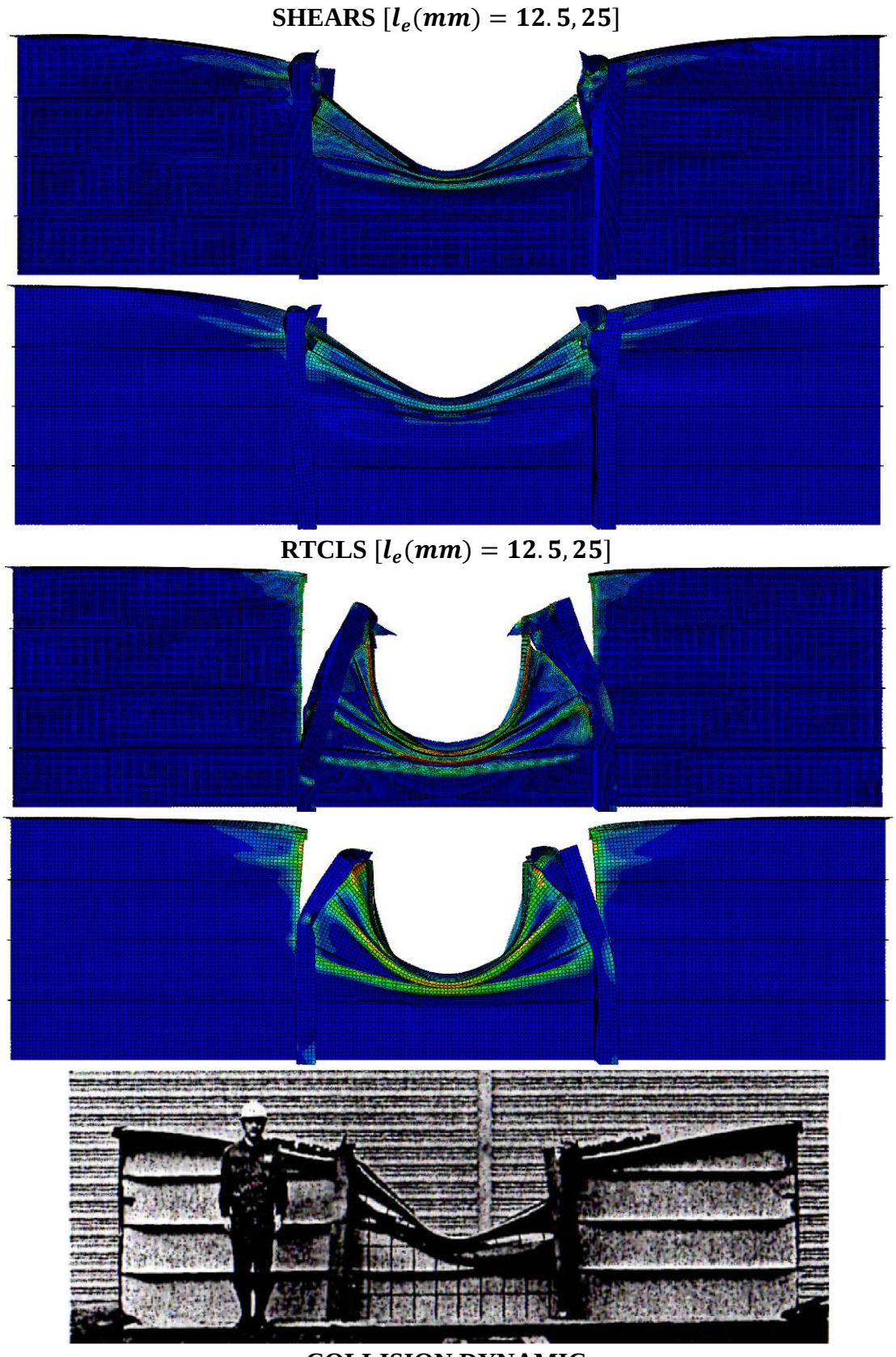

Figure 5.28. COLLISION DYNAMIC model. Representation of damage according to SHEARS and RTCLS rupture criteria (ASIS 1993 reported in ISSC 2003)

5.2.5 OUTER SHELL and INNER SHELL models-(Gong et al. 2013)

Figures 5.29 and 5.31 refer to the OUTER SHELL and INNER SHELL models and show comparisons of the experimental force-penetration and absorbed energy-penetration curves with the corresponding numerical curves according to SHEARS, RTCLS and BWH rupture criteria for two mesh sizes. The material behaviour beyond necking is represented by true stress-strain curves with $w = 0.2$ and 0.7. Also, Figures 5.30 and 5.32 present comparisons of the damage as predicted using the three criteria and different meshes, with the corresponding pictures of the experiments (Gong et al. 2013).

The case of the OUTER SHELL model is similar to the case of the 2-FB model, which has already been discussed in sub-section 5.2.1. In both cases of the experiments, stiffened plates were loaded transversely by rigid bulbous shape indenters, which position was in the middle of the plates and between a pair of stiffeners. The two tests differ in terms of the thicknesses and dimensions of the structural components as well as of the number of the stiffeners and the shape of the indenter. According to the experimental observations, referred in Gong et al. (2013), rupture initially occurred at the stiffener welding seam at a certain load and then fracture propagated on the plate, in the region between the stiffeners, forming an ellipsoidal crack (see also Figure 5.30). All rupture criteria using a fine mesh, i.e. $l_e/t \cong 2$, capture the initiation of rupture that is just next to the joints of the stiffeners with the plate (see Figure 5.30). RTCLS criterion predicts the formation of the ellipsoidal crack using a coarse mesh, i.e. $l_e/t \cong 4$. This is also evident in Figure 5.29, where the numerical curve follows the trend of the experimental force-penetration curve beyond rupture initiation. However, in that case initiation of rupture is not captured properly; rupture initiates away from the stiffener joint (see Figure 5.30). In Figure 5.29, it is obvious that RTCLS criterion in both cases and BWH criterion using a fine mesh underestimate the load capacity of the configuration, while SHEARS and BWH criteria overestimate the load capacity of the configuration using a coarse mesh. Best correlation with the experimental point of rupture initiation is achieved with SHEARS criterion and a fine mesh.

In the case of the INNER SHELL model, following Gong et al. (2013), rupture initially occurred at the ends of the two middle stiffeners and subsequently in the middle of the long edge of the plate close to its boundary. Fracture at the ends of the two middle stiffeners is captured by all rupture criteria using a fine mesh (see Figure 5.32). However, RTCLS criterion in both cases predicts rupture on the plate, under the indenter next to the stiffeners joint, that has not been observed in the test which results in an abrupt drop of the loading force (see Figures 5.31 and 5.32). None of the rupture criteria captures fracture in the middle of the long edge of the plate at the end of the test. Table 5.6 summarizes the best results for each simulated model (see also Appendix D).

Table 5.6. Numerical results for each simulated model and rupture criterion

	Rupture Criteria		
Simulated Models	SHEARS	RTCLS	BWH
OUTER SHELL	Not good correlation between different meshes Best results for $l_e = 8\,mm$ or $l_e/t \cong 2$ (*), (**)	Good correlation between different meshes Best results for $l_e = 16\,mm$ or $l_e/t \cong 4$ (*), (**)	Not good correlation between different meshes Best results for $l_e = 8\,mm$ or $l_e/t \cong 2$ (**)
INNER SHELL	Good correlation between different meshes Best results for $l_e = 8\,mm$ or $l_e/t \cong 2$ (*), (**)	Good correlation between different meshes Not good correlation with experimental results	Good correlation between different meshes Best results for $l_e = 8\,mm$ or $l_e/t \cong 2$ (*), (**)

(*): best correlation with experimental force and energy-penetration curves, (**): best representation of rupture

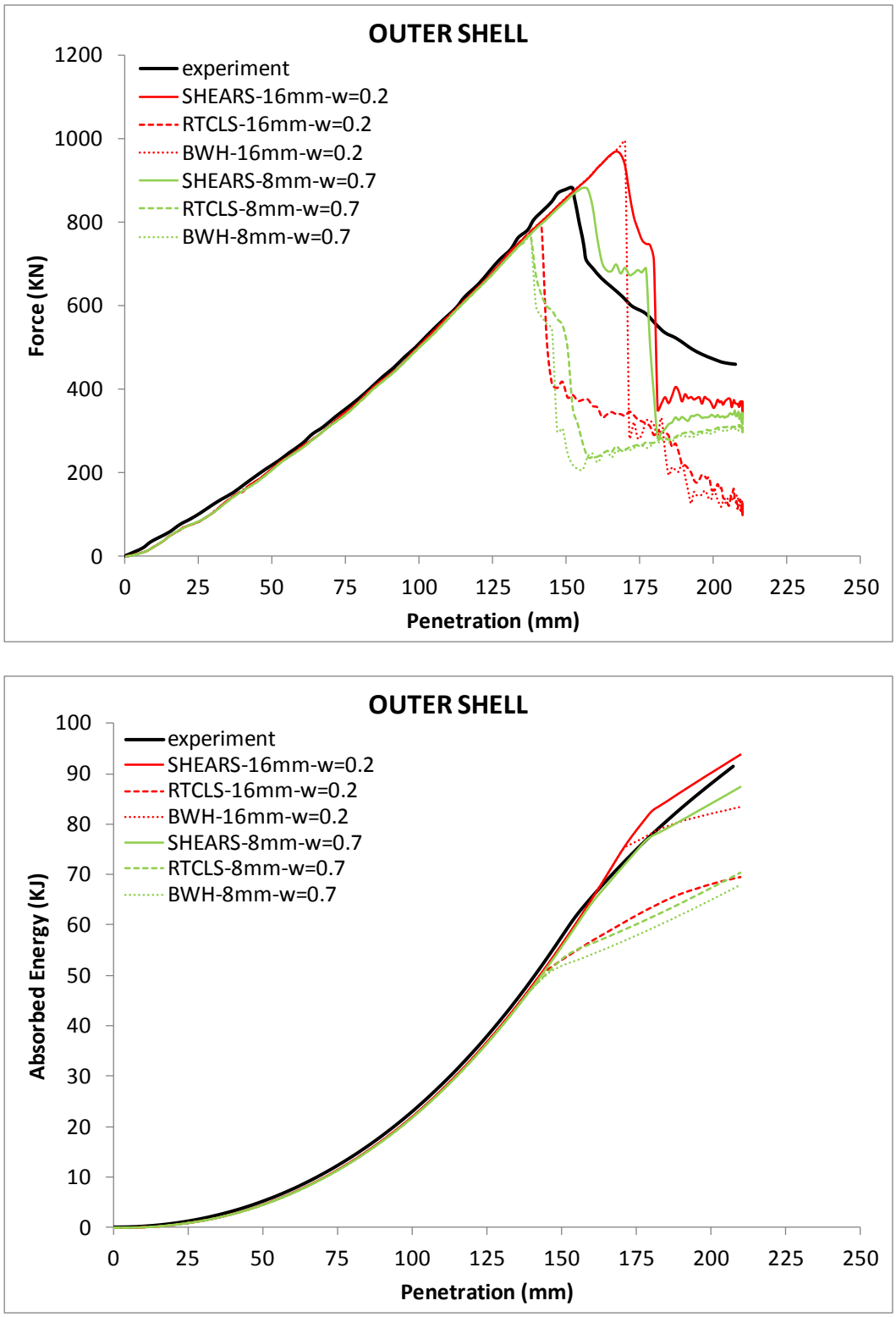

Figure 5.29. OUTER SHELL model. Force and absorbed energy-penetration curves. Prediction of rupture according to SHEARS, RTCLS and BWH rupture criteria in combination with true stress-strain curves with $w = 0.2$ and 0.7

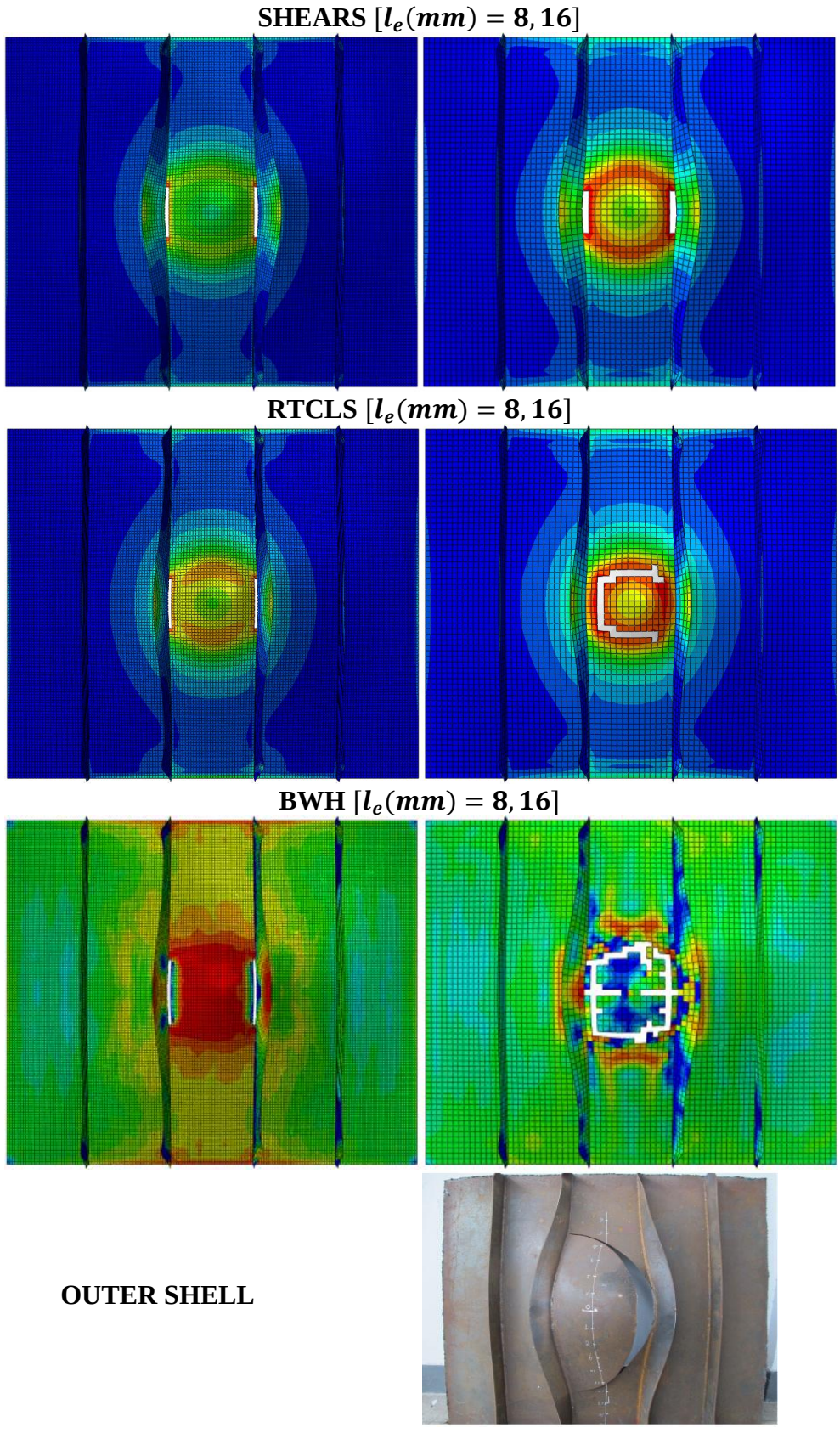

Figure 5.30. OUTER SHELL model. Representation of damage according to SHEARS, RTCLS and BWH rupture criteria (Gong et al. 2013)

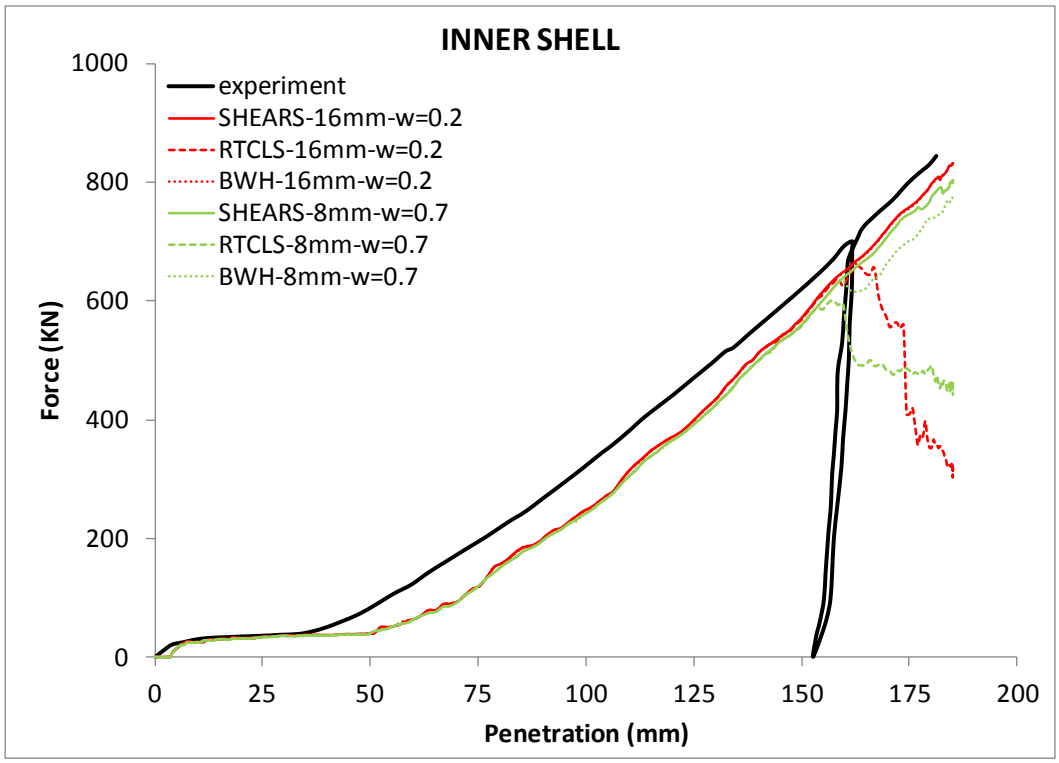

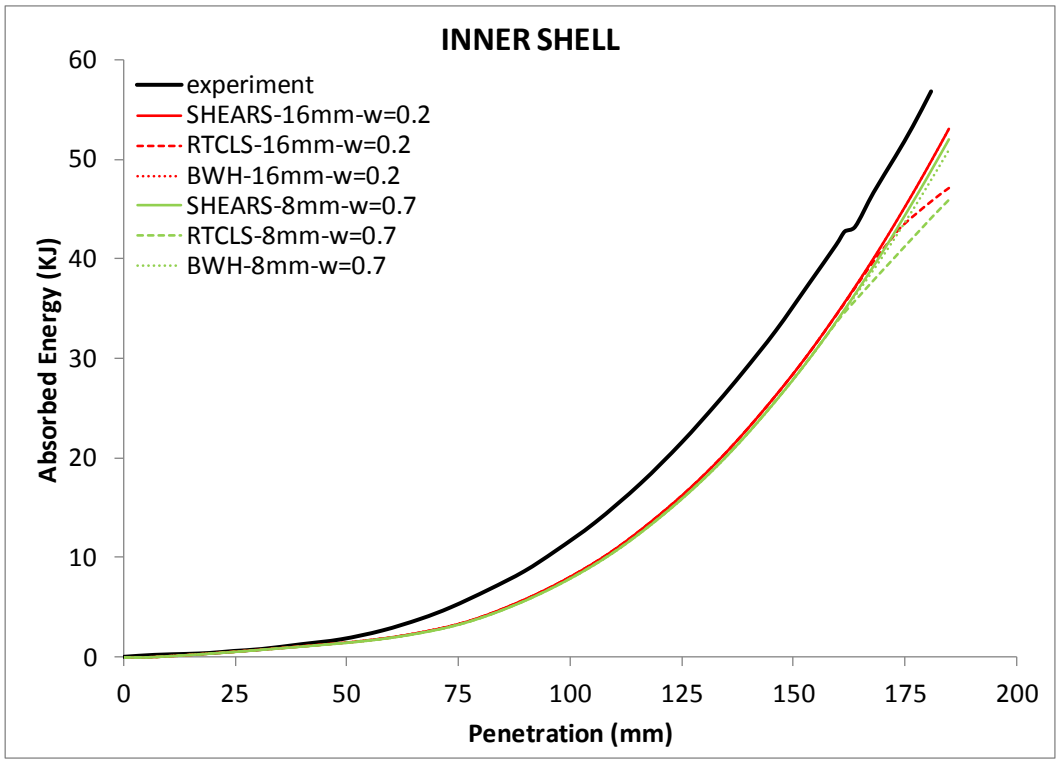

Figure 5.31. INNER SHELL model. Force and absorbed energy-penetration curves.
Prediction of rupture according to SHEARS, RTCLS and BWH rupture criteria in combination with true stress-strain curves with $w = 0.2$ and 0.7

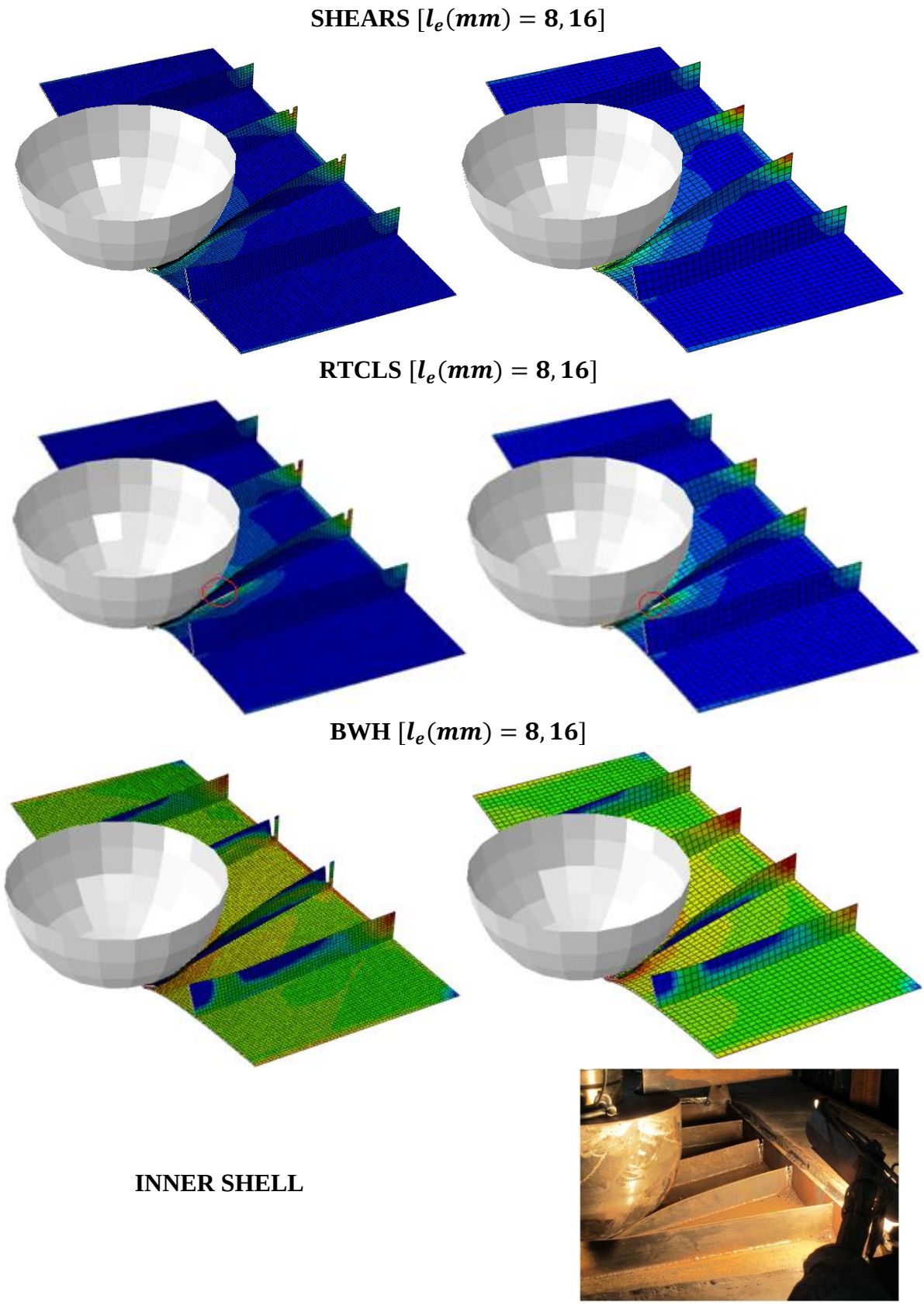

Figure 5.32. INNER SHELL model. Representation of damage according to SHEARS, RTCLS and BWH rupture criteria (Gong et al. 2013)

5.2.6 FLAT SPECIMEN and KNIFE SPECIMEN models-(Villavicencio 2012 and Villavicencio et al. 2013)

Figures 5.33 and 5.35 refer to the FLAT SPECIMEN and KNIFE SPECIMEN models and illustrate comparisons of the experimental force-penetration and absorbed energy-penetration curves with the corresponding numerical curves according to SHEARS, RTCLS and BWH rupture criteria for two mesh sizes. The material behaviour beyond necking is represented by true stress-strain curves with $w = 0$ and 0.2. Moreover, Figures 5.34 and 5.36 present comparisons of the damage as predicted using the three criteria and different meshes, with the corresponding pictures of the experiments (Villavicencio 2012 and Villavicencio et al. 2013).

According to the experimental observations, referred in Villavicencio (2012) and Villavicencio et al. (2013), in the case of the FLAT SPECIMEN model, rupture of the plate initially occurred under the short edges of the indenter at a penetration depth approximately $60\,mm$. This is shown by the drop in the force in Figure 5.33. Then the crack propagated diagonally and towards the stiffeners joint (see Figure 5.34). RTCLS and SHEARS criteria in both cases predict correctly the initiation and propagation of the crack, while RTCLS criterion also captures the first drop in the force using a coarse mesh, i.e. $l_e/t \cong 4$ (see Figures 5.33 and 5.34). Numerical results in the case of BWH criterion are also in good agreement with the experimental observations up to the initiation of rupture. However, beyond that point in both cases BWH criterion underestimates the structure's strength, as it predicts rupture of the plate and stiffener in the middle of the structure, which is more extensive in the case of a fine mesh, i.e. $l_e/t \cong 2$ (see Figures 5.33 and 5.34).

Similarly to the FLAT SPECIMEN model case, initiation of rupture in the case of the KNIFE SPECIMEN model occurred on the plate at the ends of the indenter and then the crack propagated on the plate along the sharp edge of the indenter (see Figure 5.36). The initiation of rupture is captured fairly well by all rupture criteria using different meshes. Propagation of rupture is not predicted in the cases of RTCLS and SHEARS criteria and tripping of the middle stiffener takes place, which has not been observed in the test (see Figure 5.36). BWH criterion predicts correctly rupture propagation using a fine mesh, but also fracture of the middle stiffener and thus underestimates the structure's stiffness (see Figures 5.35 and 5.36). Table 5.7 summarizes the best results for each simulated model (see also Appendix D).

Table 5.7. Numerical results for each simulated model and rupture criterion

	Rupture Criteria		
Simulated Models	SHEARS	RTCLS	BWH
FLAT SPECIMEN	Good correlation between different meshes Best results for $l_e = 16\ mm$ or $l_e/t \cong 4$ (*), (**)	Good correlation between different meshes Best results for $l_e = 16\ mm$ or $l_e/t \cong 4$ (*), (**)	Not good correlation between different meshes Best results for $l_e = 16\ mm$ or $l_e/t \cong 4$ (*)
KNIFE SPECIMEN	Good correlation between different meshes Best results for $l_e = 8\ mm$ or $l_e/t \cong 2$ (*)	Good correlation between different meshes Best results for $l_e = 16\ mm$ or $l_e/t \cong 4$ (*)	Not good correlation between different meshes Best results for $l_e = 16\ mm$ or $l_e/t \cong 4$ (**) for $l_e = 8\ mm$

(*): best correlation with experimental force and energy-penetration curves, (**): best representation of rupture

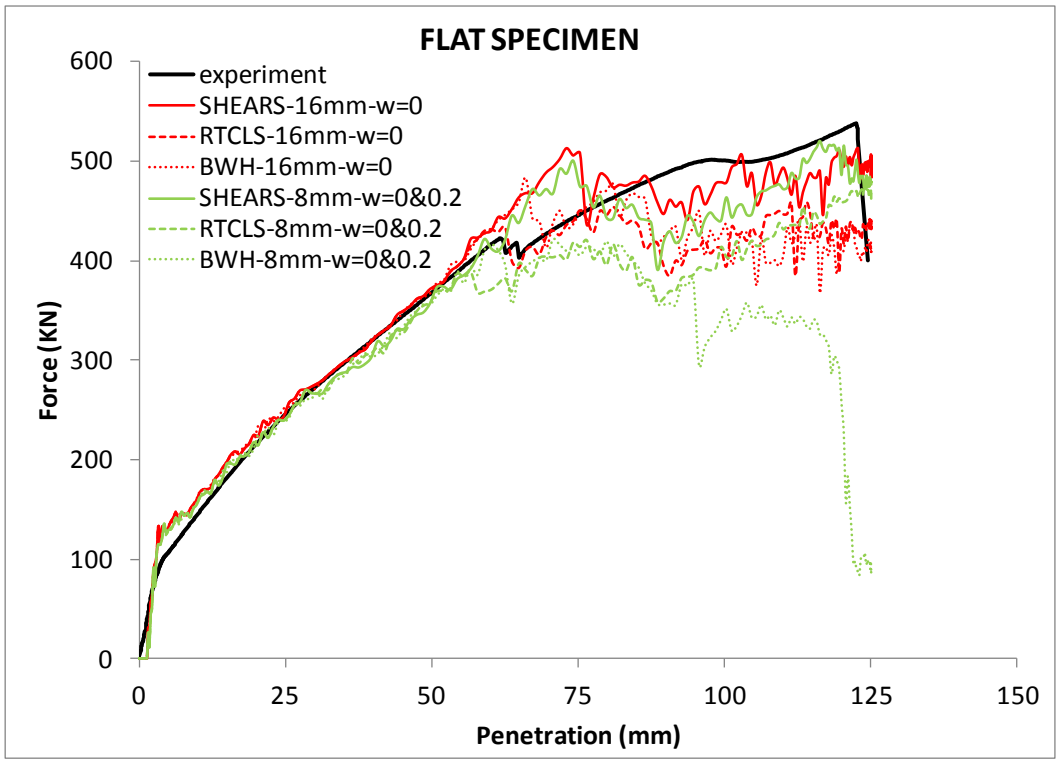

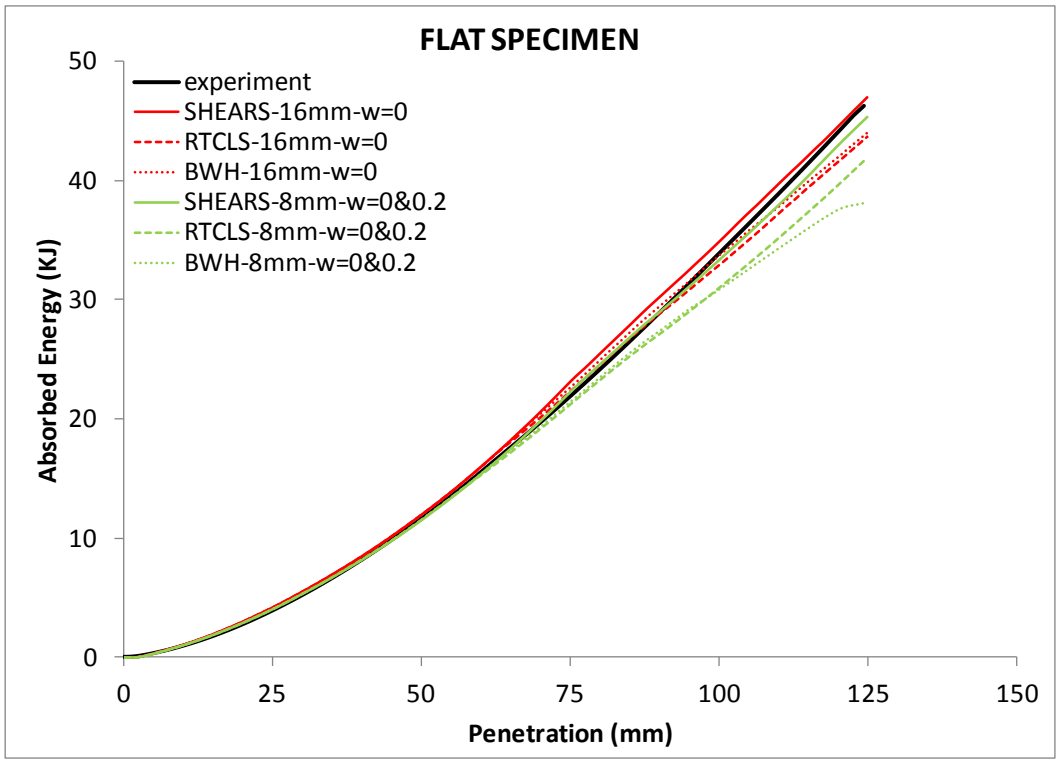

Figure 5.33. FLAT SPECIMEN model. Force and absorbed energy-penetration curves. Prediction of rupture according to SHEARS, RTCLS and BWH rupture criteria in combination with true stress-strain curves with $w = 0$ and 0.2

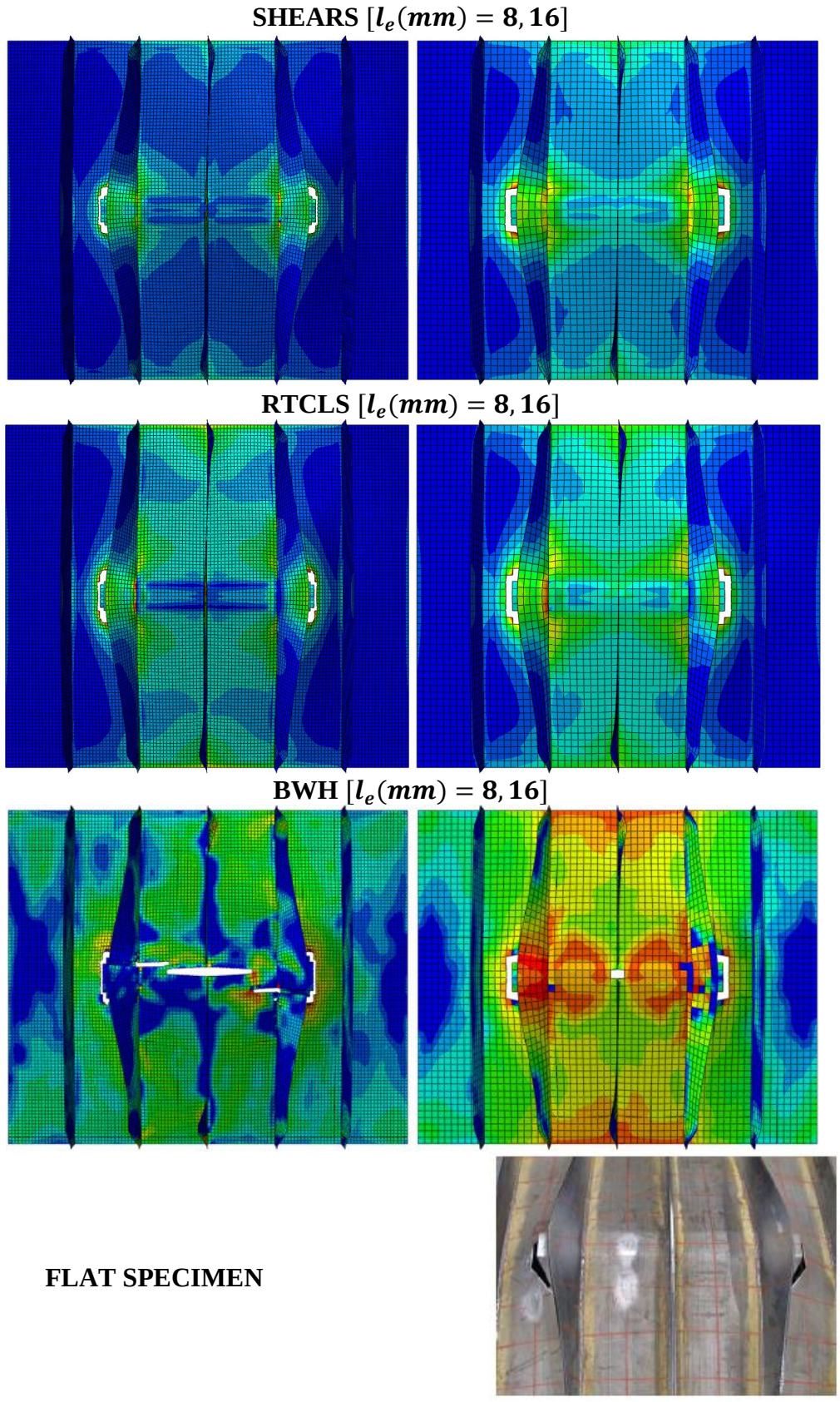

Figure 5.34. FLAT SPECIMEN model. Representation of damage according to SHEARS, RTCLS and BWH rupture criteria (Villavicencio 2012 and Villavicencio et al. 2013)

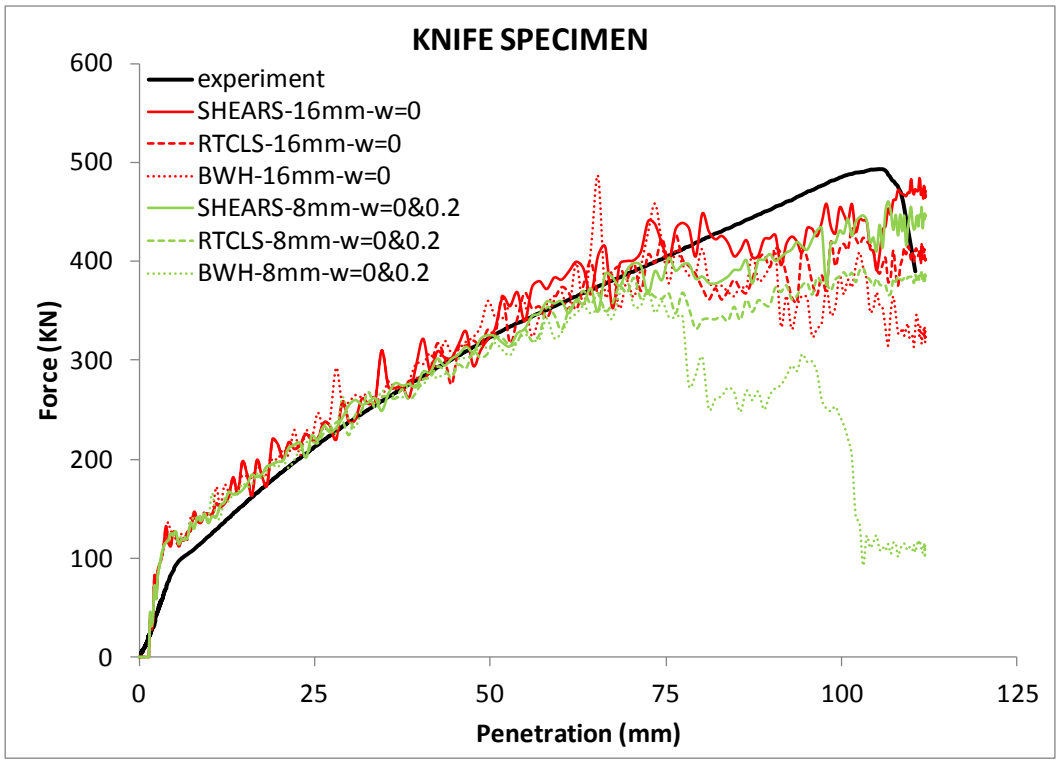

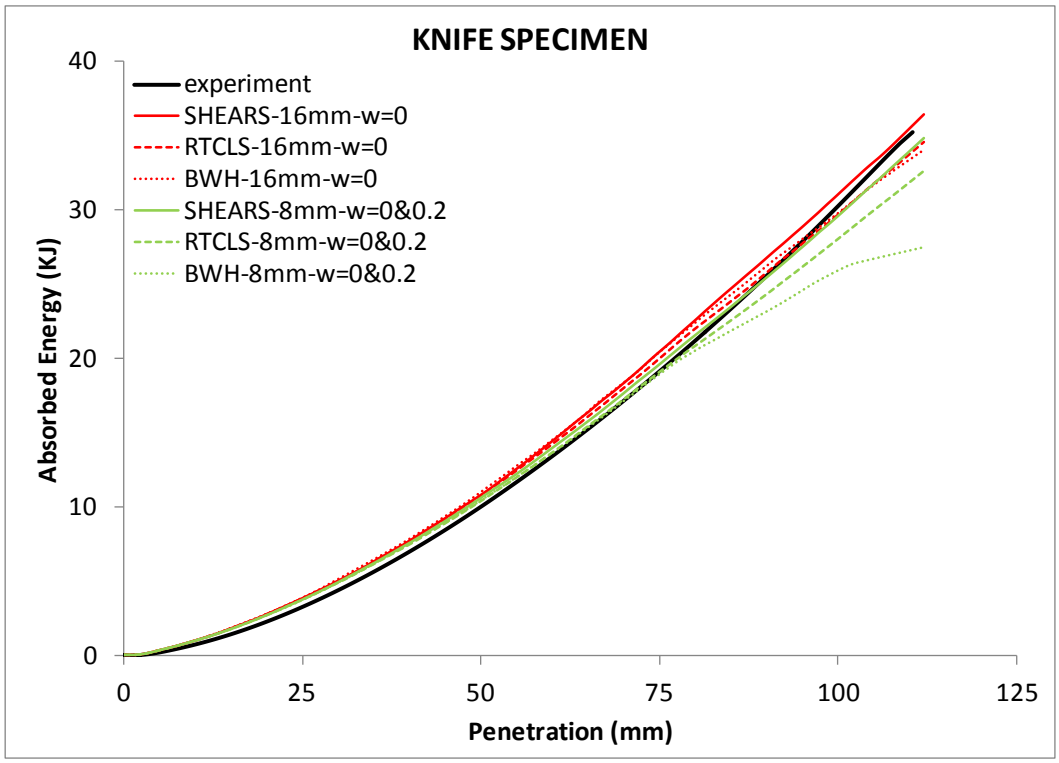

Figure 5.35. KNIFE SPECIMEN model. Force and absorbed energy-penetration curves. Prediction of rupture according to SHEARS, RTCLS and BWH rupture criteria in combination with true stress-strain curves with $w = 0$ and 0.2

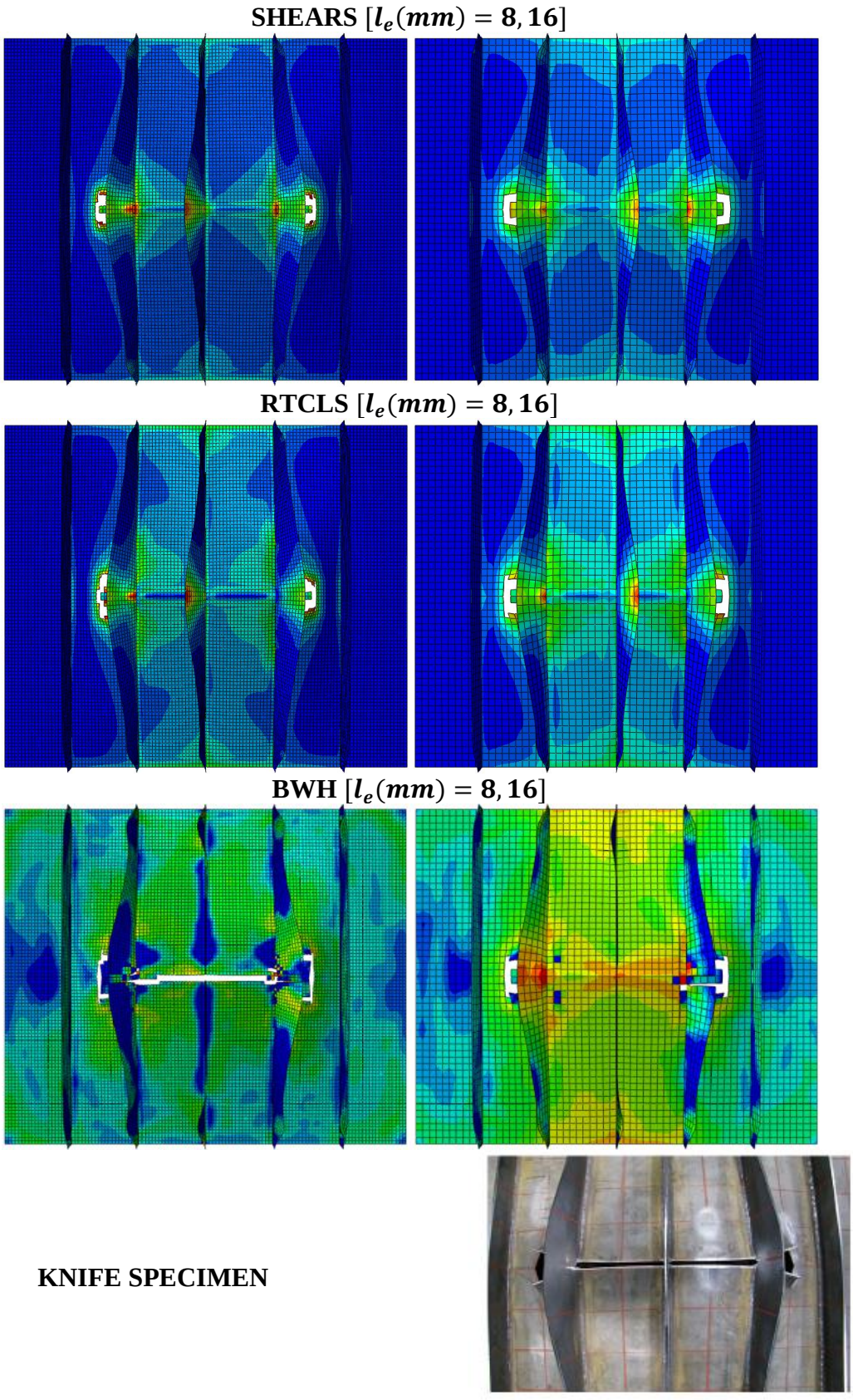

Figure 5.36. KNIFE SPECIMEN model. Representation of damage according to SHEARS, RTCLS and BWH rupture criteria (Villavicencio 2012 and Villavicencio et al. 2013)

5.2.7 CE-1 and CE-2 models-(Tautz et al. 2013 and Fricke et al. 2014)

Figures 5.37 and 5.39 refer to the CE-1 and CE-2 models and illustrate comparisons of the experimental force-penetration and absorbed energy-penetration curves with the corresponding numerical curves according to SHEARS and RTCLS rupture criteria for two mesh sizes. The material behaviour beyond necking is represented by true stress-strain curves with $w = 0$ and 0.2. Also, Figures 5.38 and 5.40 present comparisons of the damage as predicted using the two criteria and different meshes, with the corresponding pictures of the experiments (Tautz et al. 2013 and Fricke et al. 2014). Table 5.8 summarizes the observations during the experiments of the CE-1 and CE-2 models, according to Tautz et al (2013).

Table 5.8. Experimental observations for each test

		Experimental Models	
	Observations	CE-1	CE-2
(i)	Rupture of outer shell	At approximately 60 mm penetration depth	At approximately 480 mm penetration depth
(ii)	Collapse of outer shell stiffeners	At approximately 330, 410 and 430 mm penetration depths	At approximately 530 and 560 mm penetration depths
(iii)	Contact of bulbous bow indenter with inner hull	At approximately 900 mm penetration depth	-
(iv)	Contact of deformed parts of outer shell with longitudinal stiffeners of inner shell	-	At approximately 800 and 1000 mm penetration depths
(v)	Rupture of inner shell	At approximately 1020 mm penetration depth	At approximately 1200 mm penetration depth
(vi)	Collapse of inner shell stiffeners	At approximately 1170 and 1250 mm penetration depths	At approximately 1440 mm penetration depth

According to Figure 5.37, one may observe that in the case of the CE-1 model numerical results with both criteria are in good agreement with the experimental force and absorbed energy-penetration curves and the simulation follows the trend of the experimental force with respect to the peaks and troughs. The force-penetration curve in the case of RTCLS criterion captures fairly well the first peak, which is related to (ii) as well as the phenomena in (iii) and (v) as described in Table 5.8, especially when a coarse mesh is used, i.e. $l_e/t \cong 4.7$. However, RTCLS criterion underestimates the stiffness of the structure beyond 1000 mm penetration, which is more obvious when a fine mesh is used, i.e. $l_e/t \cong 2.3$ (see Figure 5.37). SHEARS criterion tends to overestimate the stiffness of the structure during the simulation, but it gives a good estimate of the absorbed energy the moment the inner shell ruptures, using a fine mesh (see Figure 5.37 and (v) in Table 5.8).

In the case of the CE-2 model, a similar to the CE-1 model case behaviour is observed. It is worth noticing that the force peaks in the first part of the test up to 550 mm penetration, i.e. (i) and (ii) in Table 5.8, are perfectly predicted by RTCLS criterion, especially when a coarse mesh is used, i.e. $l_e/t \cong 5.3$. Also here, both criteria predict correctly the absorbed energy the moment the inner shell ruptures; RTCLS criterion using a coarse mesh and SHEARS criterion using a fine mesh (see Figure 5.39 and (v) in Table 5.8). Table 5.9 summarizes the best results for each simulated model (see also Appendix D).

Table 5.9. Numerical results for each simulated model and rupture criterion

	Rupture Criteria	
Simulated Models	SHEARS	RTCLS
CE-1	Good correlation between different meshes Best results for $l_e = 12.5\ mm$ or $l_e/t \cong 2.3$ (*)	Good correlation between different meshes Best results for $l_e = 25\ mm$ or $l_e/t \cong 4.7$ (*)
CE-2	Good correlation between different meshes Best results for $l_e = 12.5\ mm$ or $l_e/t \cong 2.6$ (*)	Good correlation between different meshes Best results for $l_e = 25\ mm$ or $l_e/t \cong 5.3$ (*), (**)

(*): best correlation with experimental force and energy-penetration curves, (**): best representation of rupture

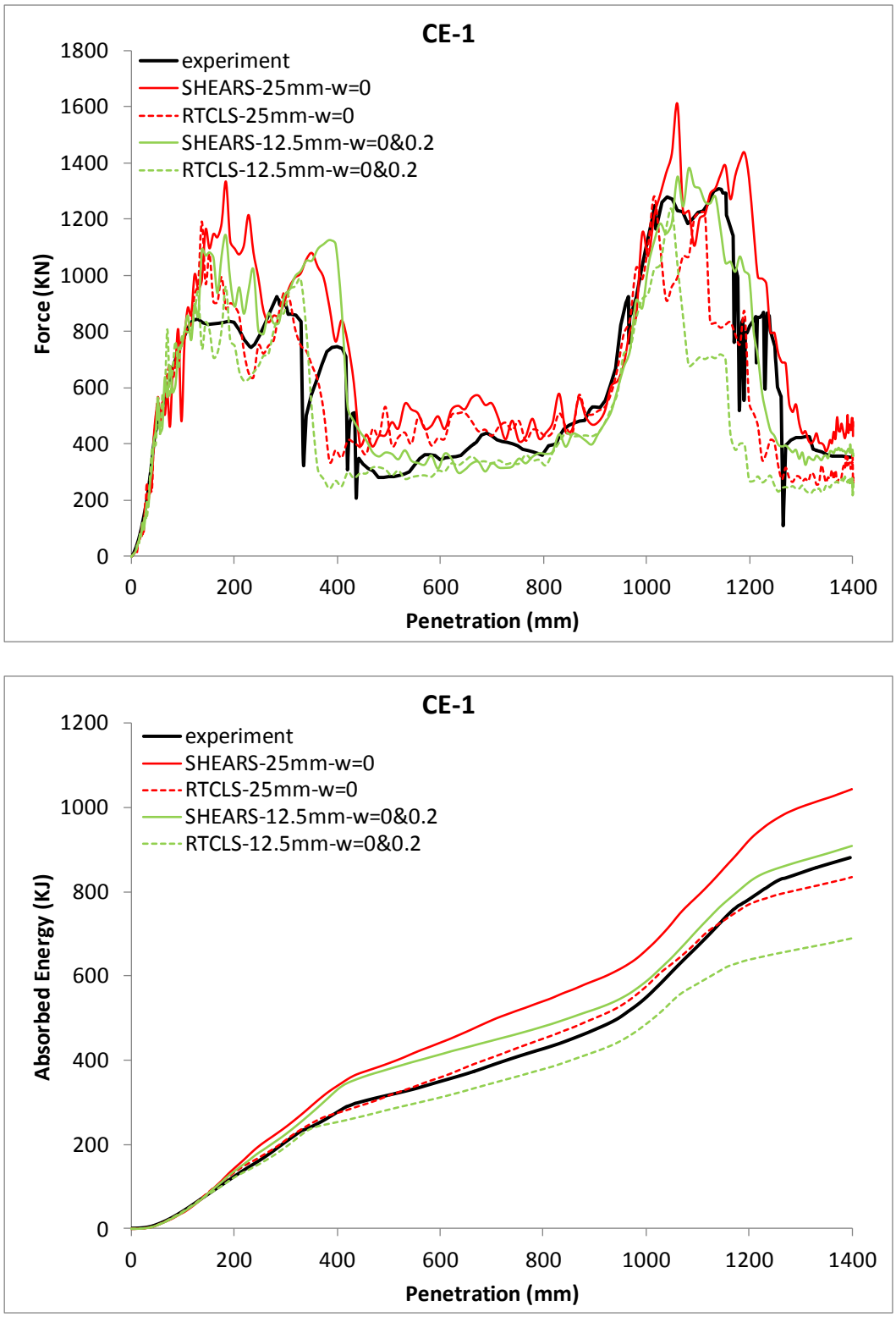

Figure 5.37. CE-1 model. Force and absorbed energy-penetration curves.
Prediction of rupture according to SHEARS and RTCLS rupture criteria in combination with true stress-strain curves with $w = 0$ and 0.2

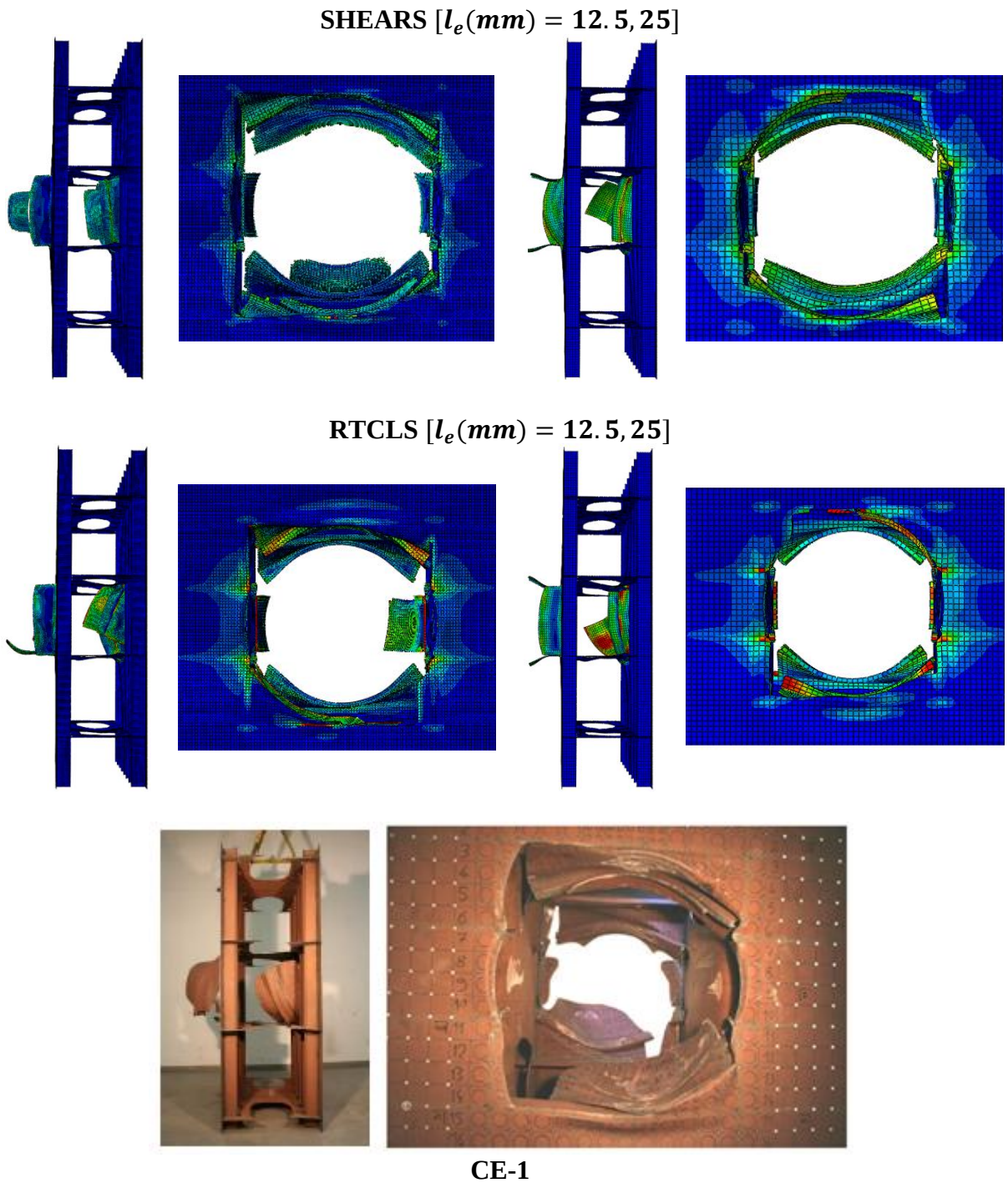

Figure 5.38. CE-1 model. Representation of damage according to SHEARS and RTCLS rupture criteria (Tautz et al. 2013 and Fricke et al. 2014)

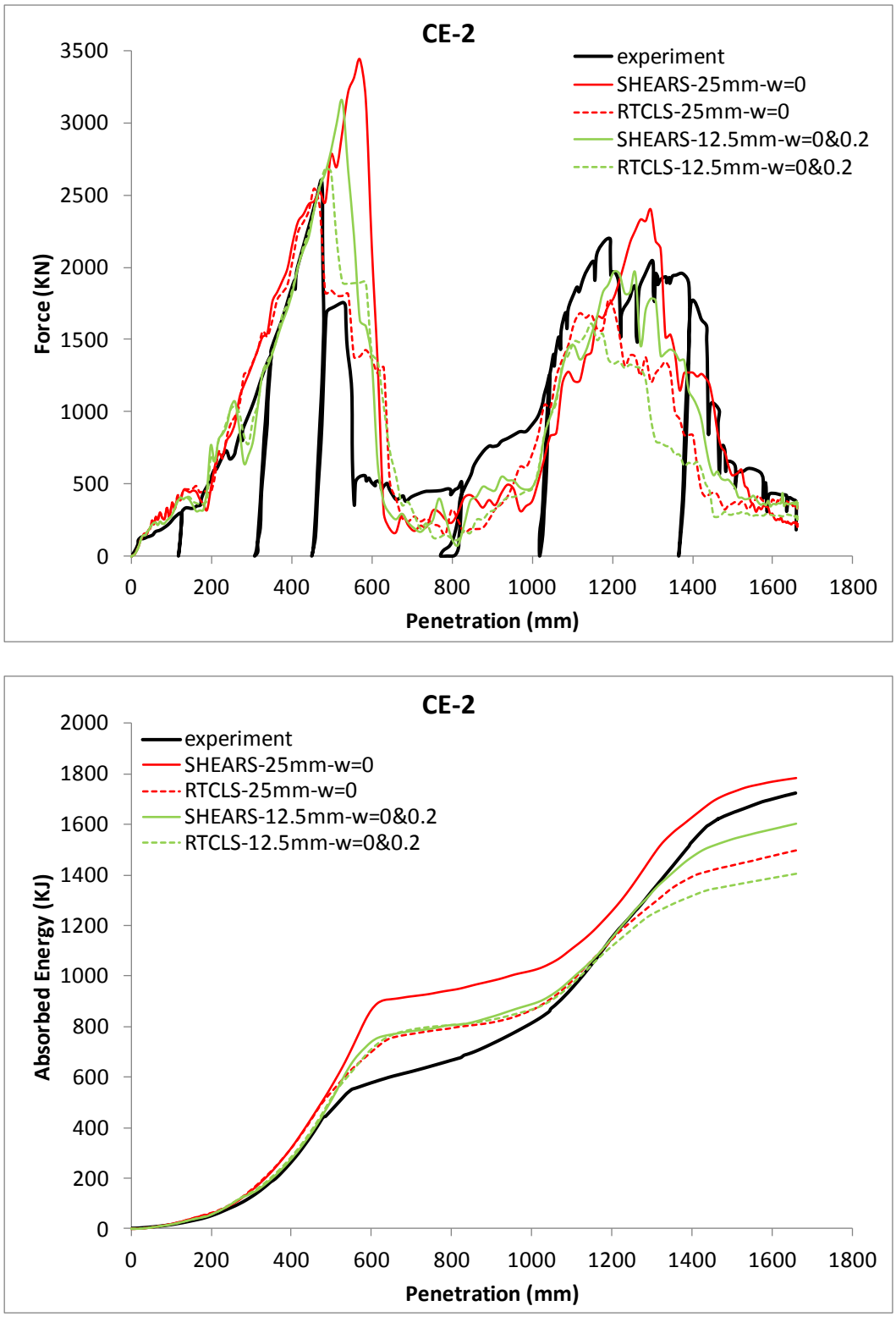

Figure 5.39. CE-2 model. Force and absorbed energy-penetration curves.
Prediction of rupture according to SHEARS and RTCLS rupture criteria in combination with true stress-strain curves with $w = 0$ and 0.2

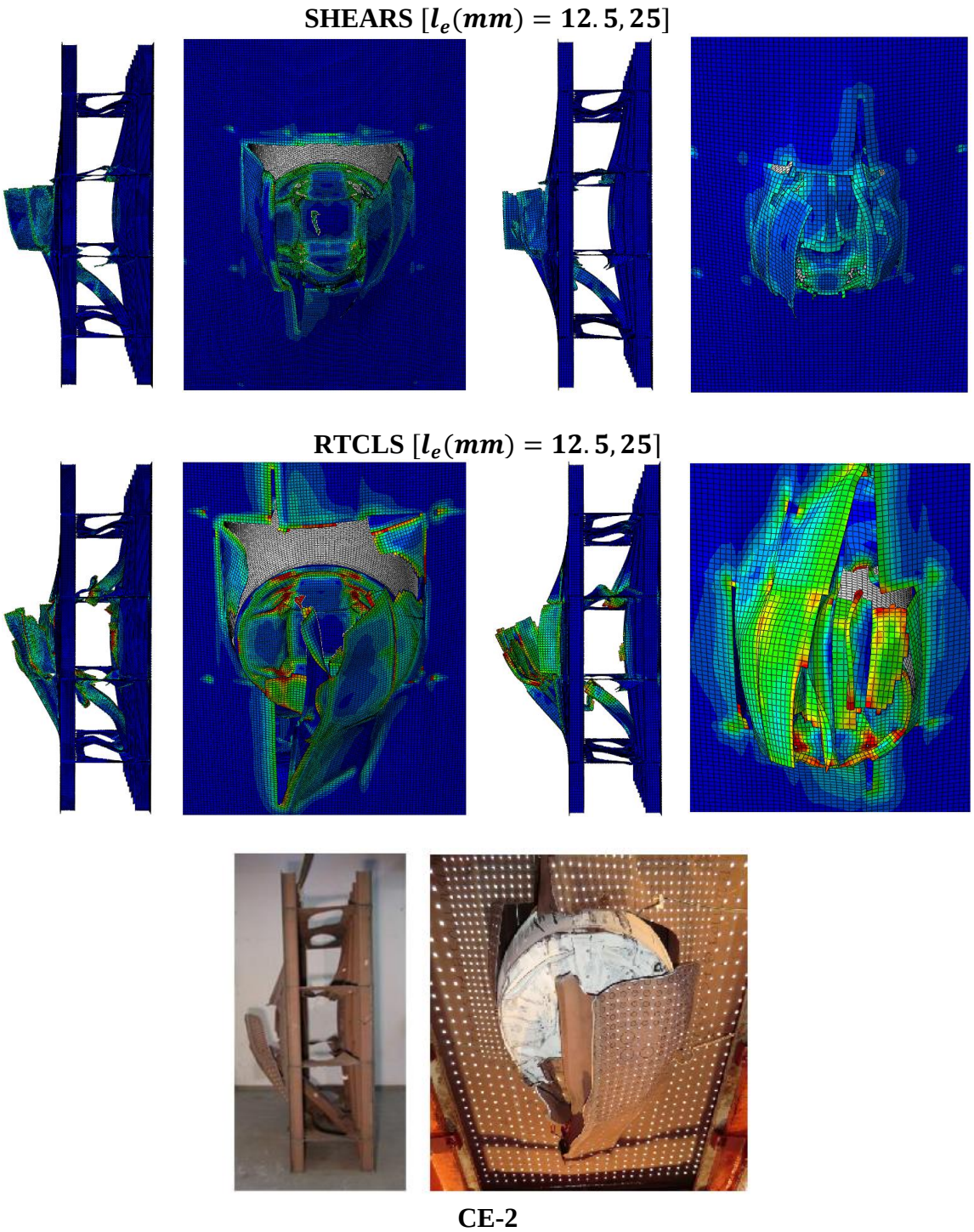

Figure 5.40. CE-2 model. Representation of damage according to SHEARS and RTCLS rupture criteria (Tautz et al. 2013 and Fricke et al. 2014)

5.2.8 P1-15, P2-15, S1-20 and S2-20 models-(DNV 1993)

Figures 5.41, 5.45, 5.49 and 5.54 refer to the P1-15, P2-15, S1-20 and S2-20 models and illustrate comparisons of the experimental force-penetration and absorbed energy-penetration curves with the corresponding numerical curves for three mesh sizes, in the cases of the RTCLS and SHEARS criteria and two mesh sizes in the case of BWH criterion. The material behaviour beyond necking is represented by the powerlaw curve. Moreover, Figures 5.42-5.44, 5.46-5.48, 5.50-5.53 and 5.55-5.57, show comparisons of the damage as predicted using the three criteria and different meshes with the corresponding pictures of the experiments (DNV 1993). A similar numerical analysis has already been described and discussed in sub-section 5.2.3 (Paik and Tak 1995). However, in the present case the thicknesses of the plates are very close to the actual thicknesses of the plates used in the shipbuilding industry. Furthermore, pictures of the deformation patterns during and at the end of the experimental process were available, which contributed in the derivation of more comprehensive conclusions throughout the comparative study between the numerical and the experimental observations.

According to Figures 5.41, 5.45, 5.49 and 5.54, it is obvious that the finer the mesh the less the sharp variations in the force-penetration curves and the better the correlation with the experimental force and absorbed energy-penetration curves. In Figures D.21-D.24 in Appendix D, are also presented the numerical force-penetration curves of the P1-15, P2-15, S1-20 and S2-20 models simulations for each mesh, using the moving average technique with a period equal to ten force values. The selected period for the application of the method was deemed appropriate, in order to minimize the sharp force peaks and troughs without losing the trend of each curve at the same time. This way it was easier to assess the correlation between the numerical and experimental results.

In the cases of the P1-15 and P2-15 models following DNV (1993) report, during the cutting process a global bulge of the plates in front of the wedge, accompanied by cutting and curling of the material, was observed (see Figures 5.44 and 5.48). SHEARS criterion captures the cutting and curling of the plates in both cases of the P1-15 and P2-15 models, whilst the global bulge is only predicted in the case of the P2-15 model using a coarse mesh, i.e. $l_e/t = 3$ (see Figures 5.42 and 5.46). A similar behaviour is shown in the case of BWH criterion, regarding the cutting and curling patterns, while the global bulge of the plates is predicted with a 30 mm mesh, i.e. $l_e/t = 2$ (see Figures 5.44 and 5.48). RTCLS criterion in both cases of the P1-15 and P2-15 models, overestimates the stiffness of the plates for coarser meshes, i.e. $2 \leq l_e/t \leq 3$. However, when fine meshes are used, i.e. $l_e/t = 1$, RTCLS criterion captures fairly well the cutting and curling of the plates as well as the global bulge in front of the wedge (see Figures 5.43 and 5.47).

In the first phase of the experiment, in the case of the S1-20 model, the behaviour was similar to the P1-15 and P2-15 models following DNV (1993) report. The parts of the plates, on the left and on the right of the wedge, started to bend initially in one direction and then the bending was reversed. After the second peak in the experimental force-penetration curve the

specimen was cut smoothly and the material formed a steady curl, up to a penetration depth approximately 1100 mm, when the test was stopped in order to reposition the crosshead. Upon restarting the experiment, the material started to bend in the opposite direction and tearing of the plates was observed at each side of the wedge, i.e. the concertina mode, for a few millimetres of penetration, until the last phase of the experiment, concerning the part of the curve beyond the third force peak, where the tearing mode changed back to a cutting mode. From Figure D.23 in Appendix D, one may observe that the first phase of the experiment, i.e. up to the second peak, is captured by RTCLS and BWH criteria, using coarser meshes, i.e. $2 \leq l_e/t \leq 3$ and SHEARS criterion using a coarse mesh, i.e. $l_e/t = 3$. As the simulation progresses, SHEARS criterion predicts a steady cutting mode and curling of the material, especially for ratios $1 \leq l_e/t \leq 2$, BWH criterion shows mixed cutting and tearing modes, while in the case of RTCLS criterion the concertina mode is evident almost from the beginning of the simulation (see Figures 5.50-5.52). These different patterns are also obvious in Figure 5.53 and indicate the different trends in the force-penetration curves in Figure 5.49 and more clearly in Figure D.23 of Appendix D.

According to DNV (1993) report in the case of the S2-20 model, beyond the initial phase of the experiment, i.e. up to the second peak, the specimen behaved in a rather different manner. Piling up of the material in front of the wedge and tearing of the upper plate along the joint with the stiffeners and the lower plate closer to the indenter's tip, up to a penetration depth approximately 800 mm, was observed. After this point, tearing of the plates stopped and the tearing mode changed back to a cutting mode. However, numerical results in the case of the S2-20 model are almost identical to the previous model (see Figures 5.49-5.57 and Figures D.23 and D.24 in Appendix D). Repeatability during the experiments is not always achieved, especially when the conditions are different, i.e. intermediate ceasing of the S1-20 test. Table 5.10 summarizes the best results for each simulated model (see also Appendix D).

Table 5.10. Numerical results for each simulated model and rupture criterion

	Rupture Criteria		
Simulated Models	SHEARS	RTCLS	BWH
P1-15	Not good correlation between different meshes Best results for $l_e = 15\ mm$ or $l_e/t = 1$ (*)	Not good correlation between different meshes and with experimental results for $2 \leq l_e/t \leq 3$ Best results for $l_e = 15\ mm$ or $l_e/t = 1$ (*), (**)	Good correlation between different meshes Best results for $l_e = 30\ mm$ or $l_e/t = 2$ (*)
P2-15	Not good correlation between different meshes Best results for $l_e = 15\ mm$ or $l_e/t = 1$ (*)	Not good correlation between different meshes and with experimental results for $2 \leq l_e/t \leq 3$ Best results for $l_e = 15\ mm$ or $l_e/t = 1$ (*), (**)	Good correlation between different meshes Best results for $l_e = 30\ mm$ or $l_e/t = 2$ (*)
S1-20	Good correlation between different meshes Best results for $l_e = 60\ mm$ or $l_e/t = 3$ (**)	Not good correlation with experimental results	Good correlation between different meshes Best results for $l_e = 40\ mm$ or $l_e/t = 2$ (*), (**)
S2-20	Good correlation between different meshes Best results for $l_e = 60\ mm$ or $l_e/t = 3$ (**)	Not good correlation with experimental results	Good correlation between different meshes Best results for $l_e = 40\ mm$ or $l_e/t = 2$ (*), (**)

(*): best correlation with experimental force and energy-penetration curves, (**): best representation of rupture

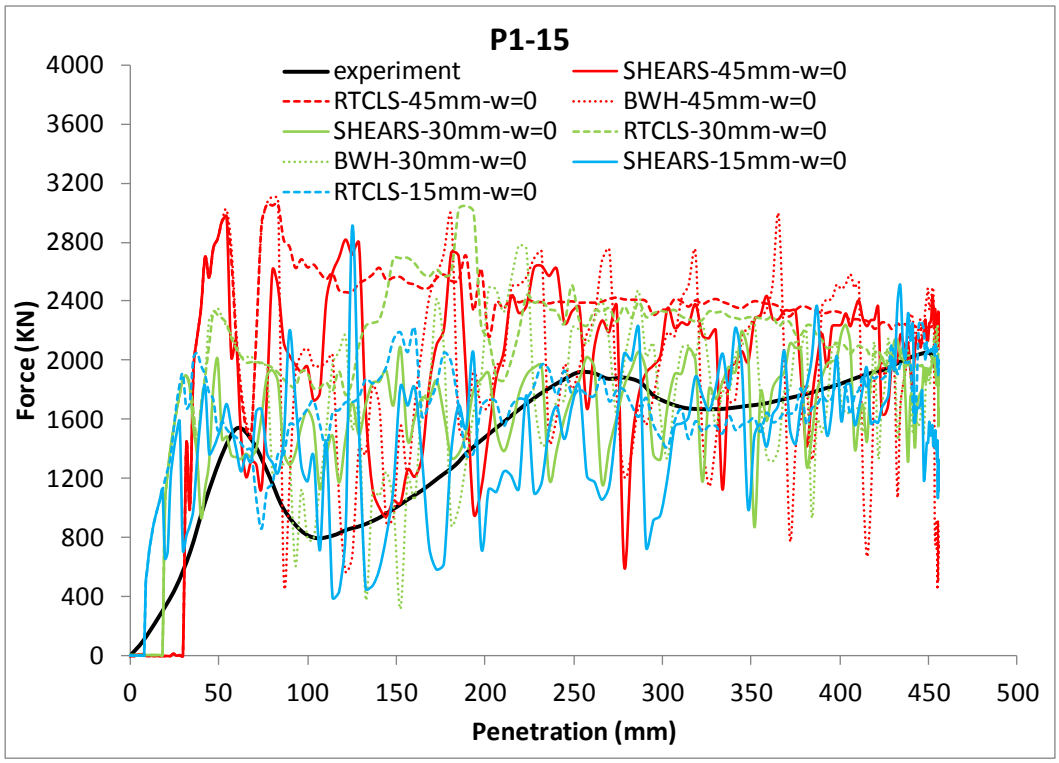

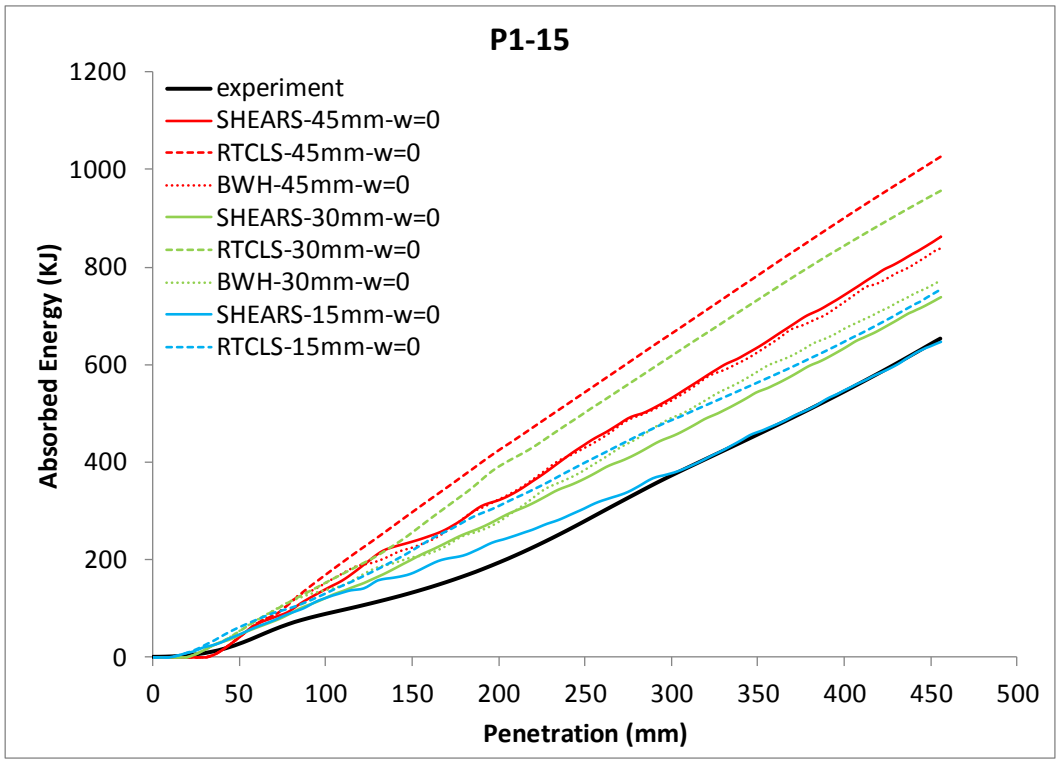

Figure 5.41. P1-15 model. Force and absorbed energy-penetration curves.
Prediction of rupture according to SHEARS, RTCLS and BWH rupture criteria in combination with the powerlaw type material curve

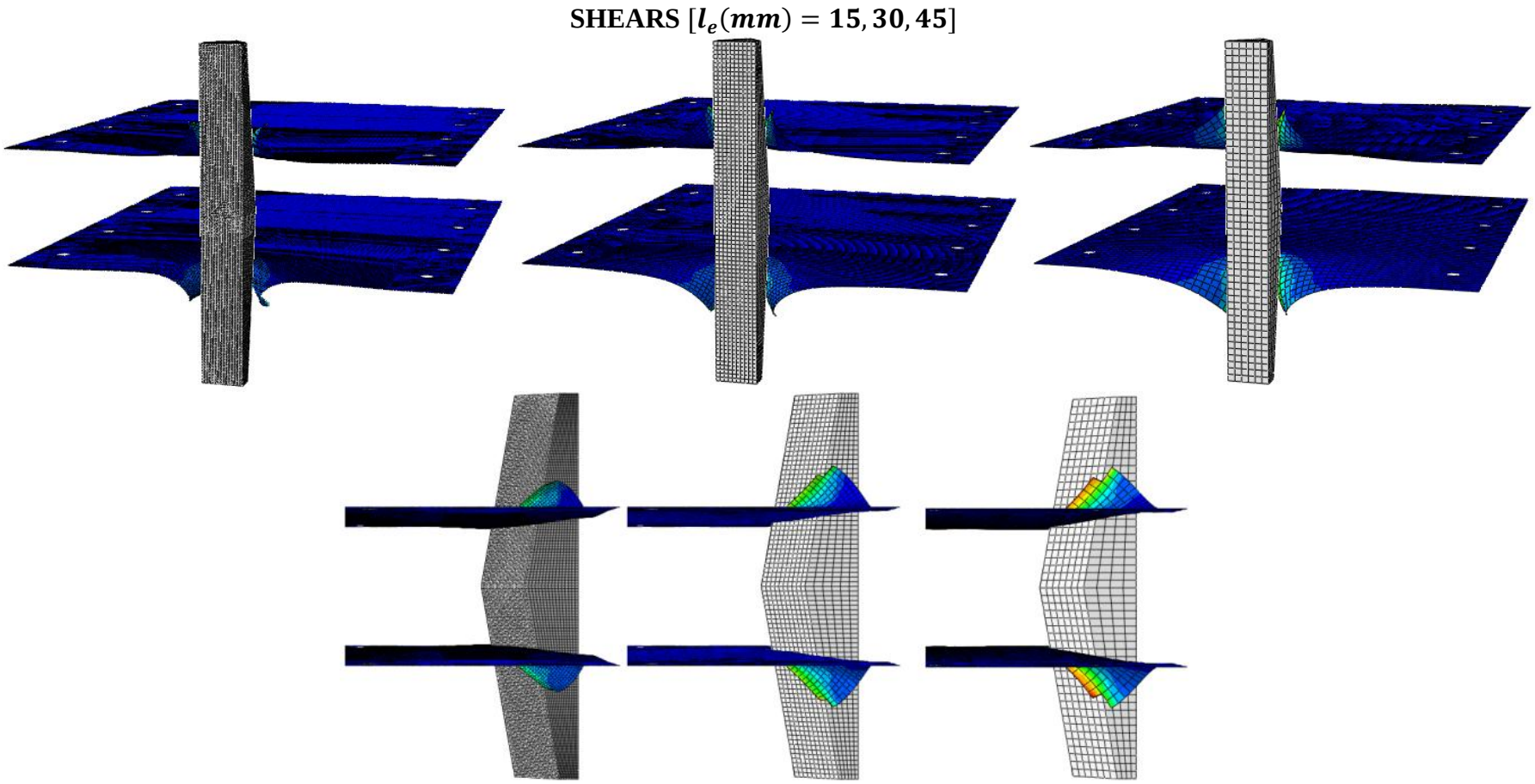

Figure 5.42. P1-15 model. Representation of damage according to SHEARS rupture criterion

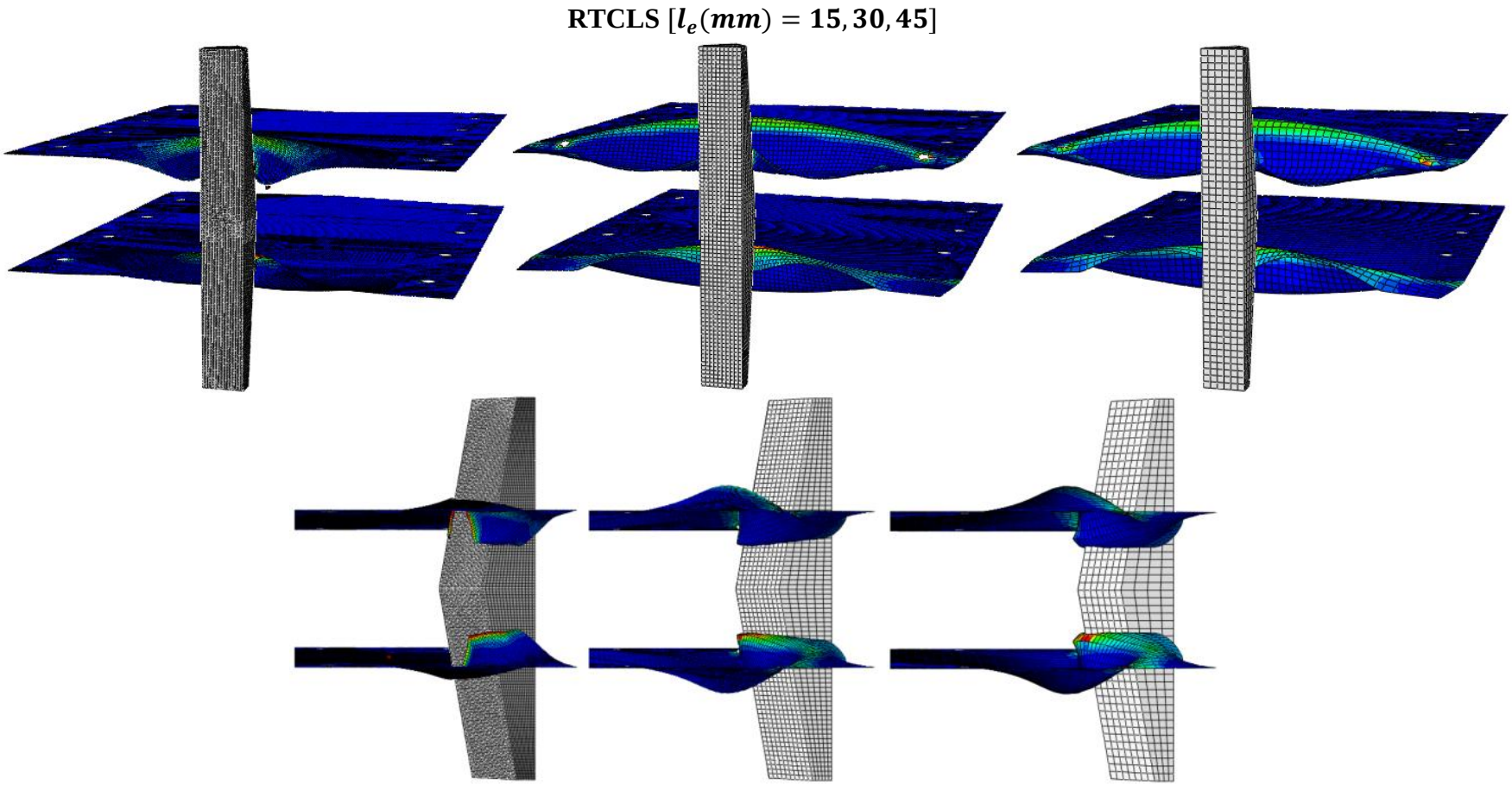

Figure 5.43. P1-15 model. Representation of damage according to RTCLS rupture criterion

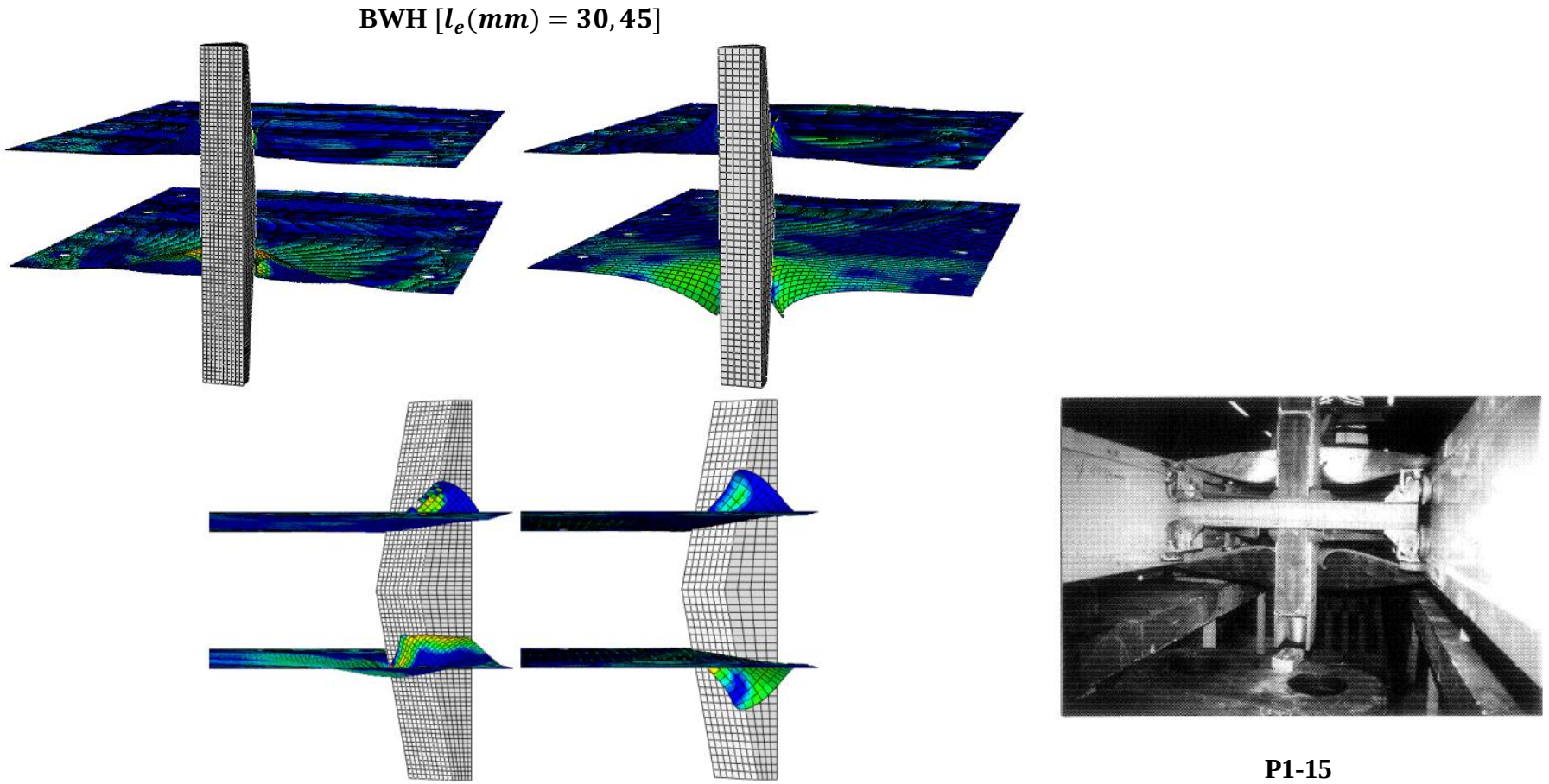

Figure 5.44. P1-15 model. Representation of damage according to BWH rupture criterion (DNV 1993)

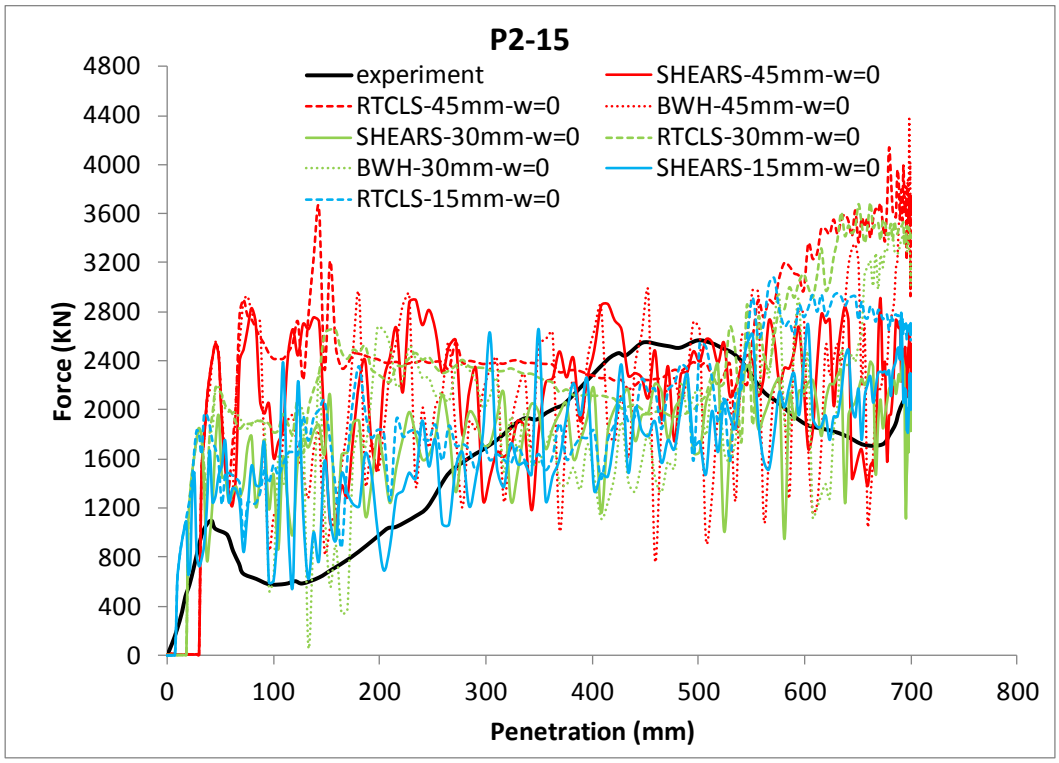

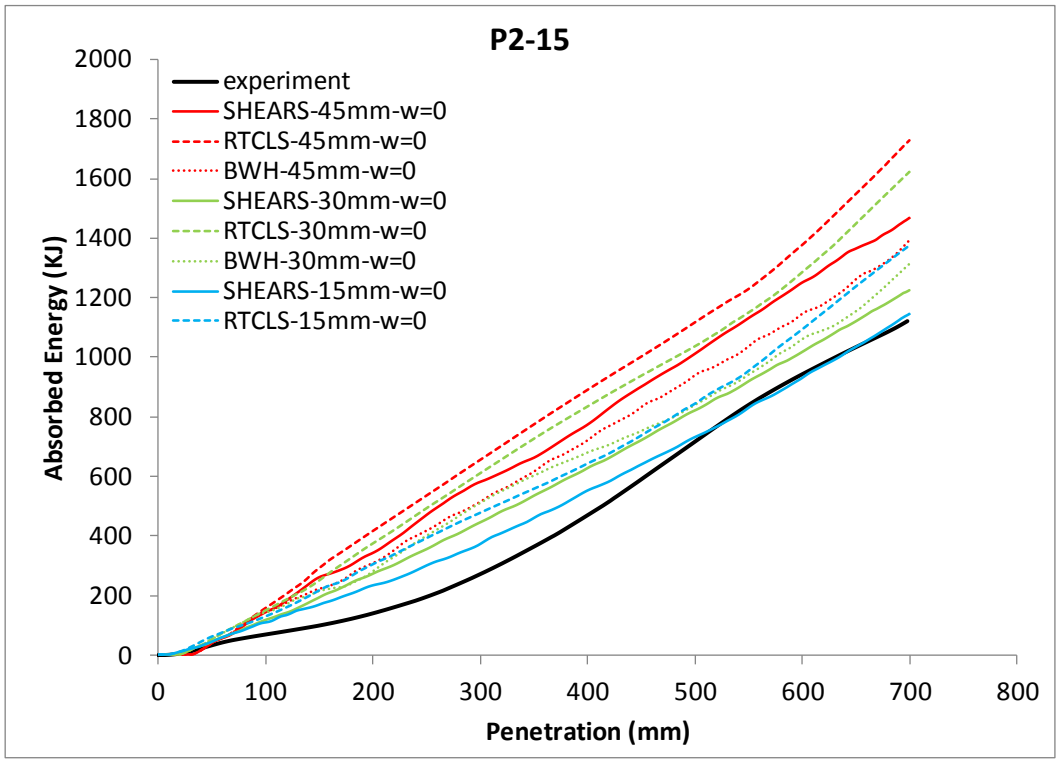

Figure 5.45. P2-15 model. Force and absorbed energy-penetration curves.
Prediction of rupture according to SHEARS, RTCLS and BWH rupture criteria in combination with the powerlaw type material curve

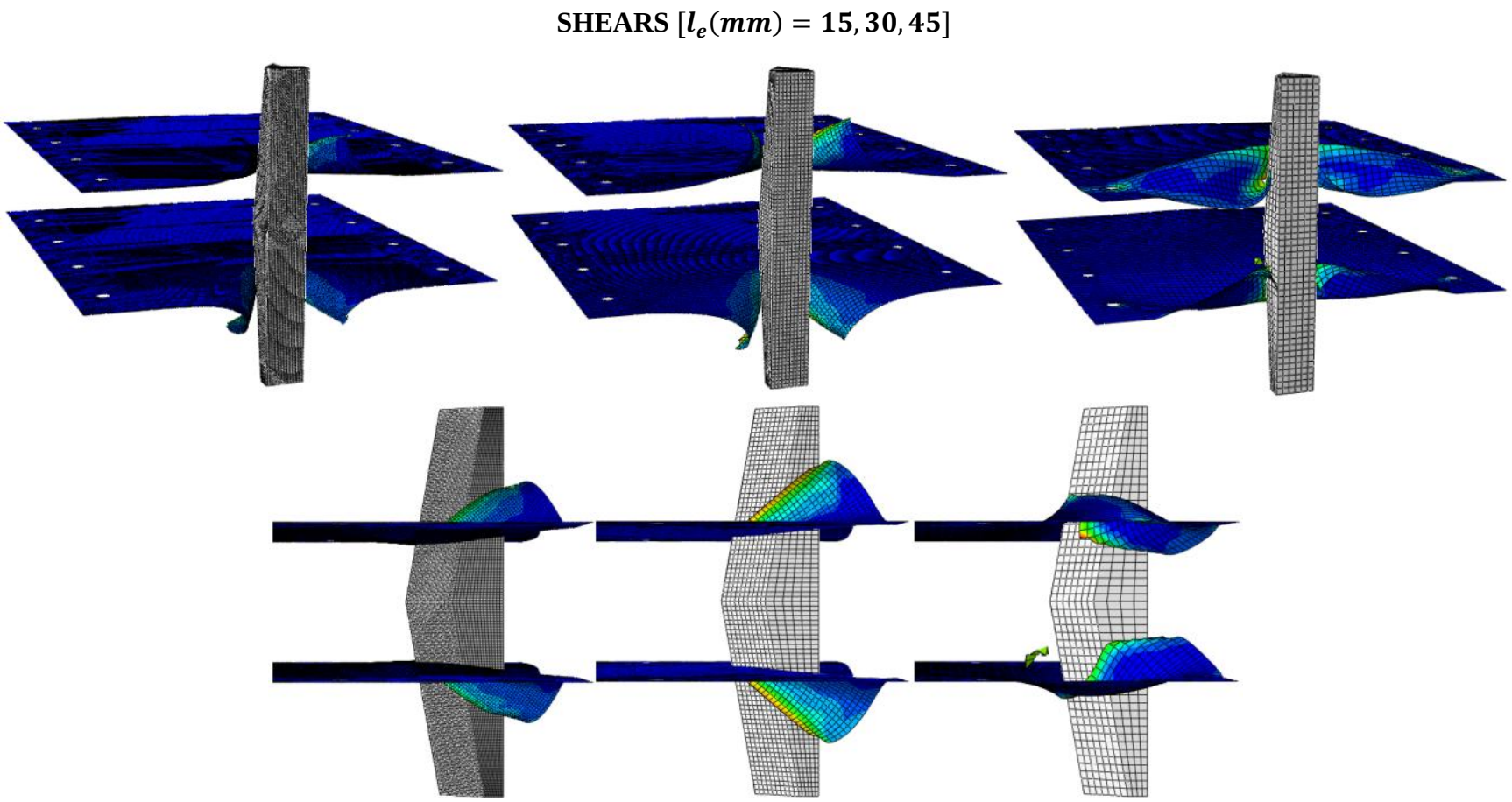

Figure 5.46. P2-15 model. Representation of damage according to SHEARS rupture criterion

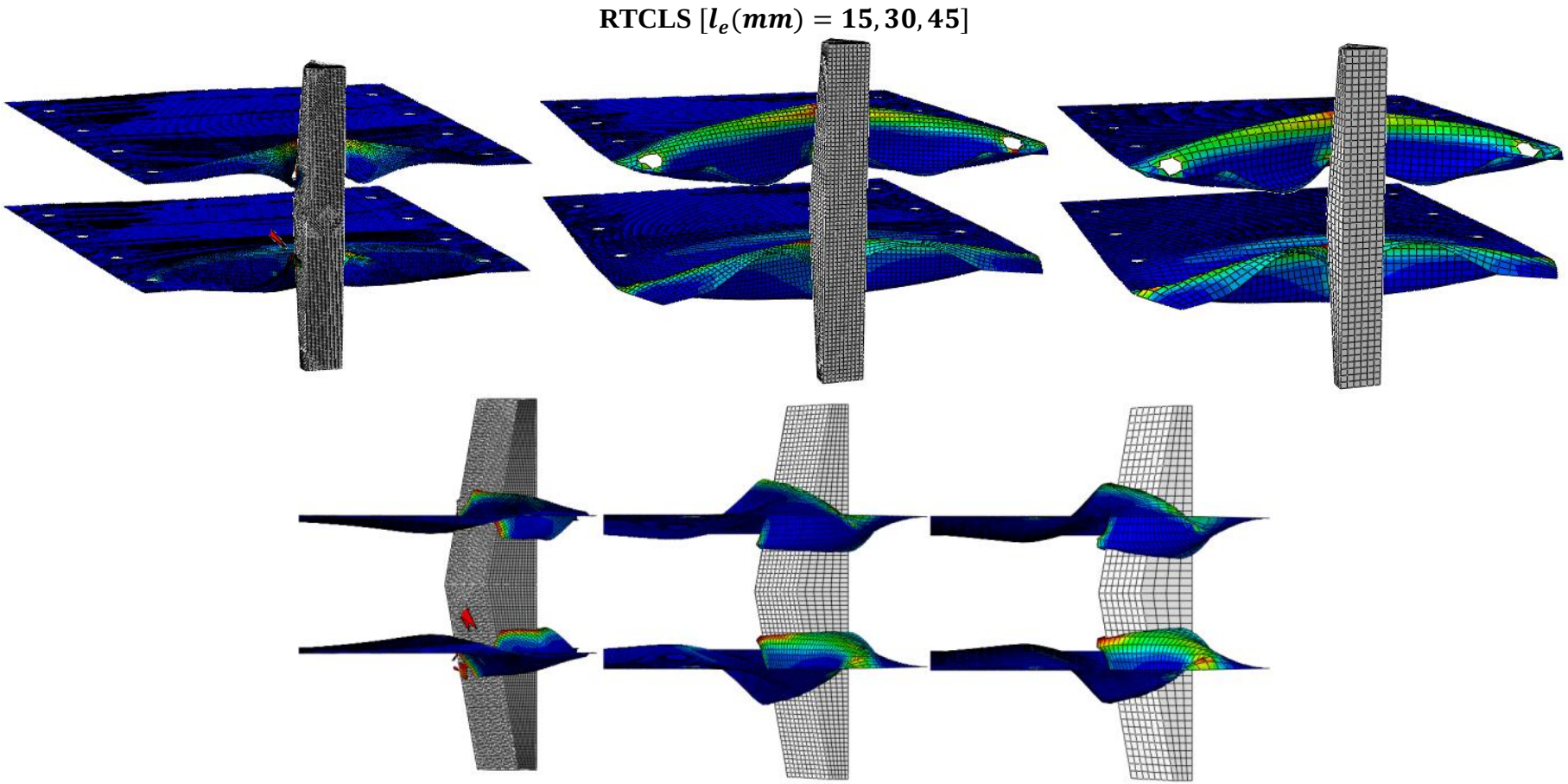

Figure 5.47. P2-15 model. Representation of damage according to RTCLS rupture criterion

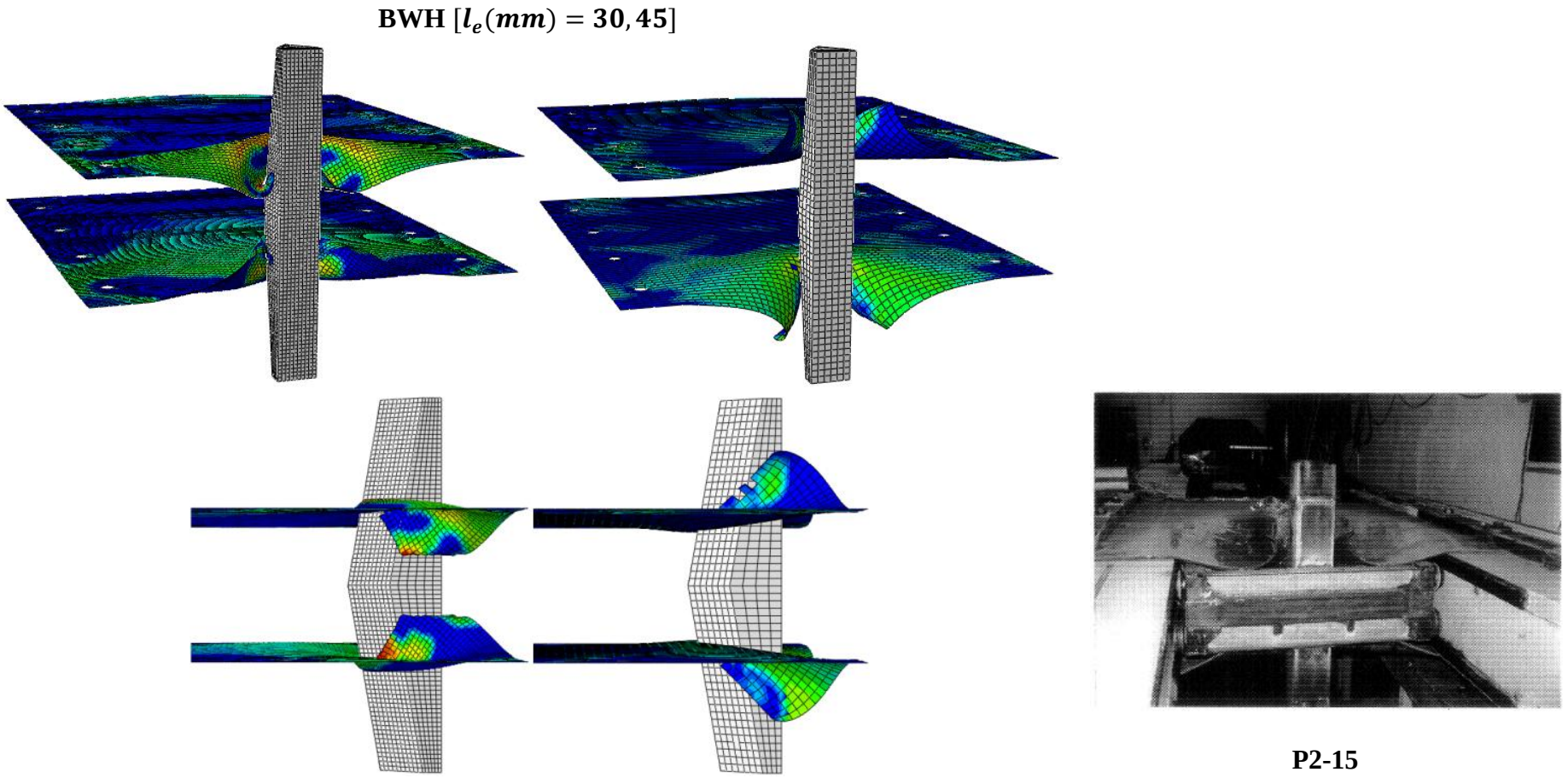

Figure 5.48. P2-15 model. Representation of damage according to BWH rupture criterion (DNV 1993)

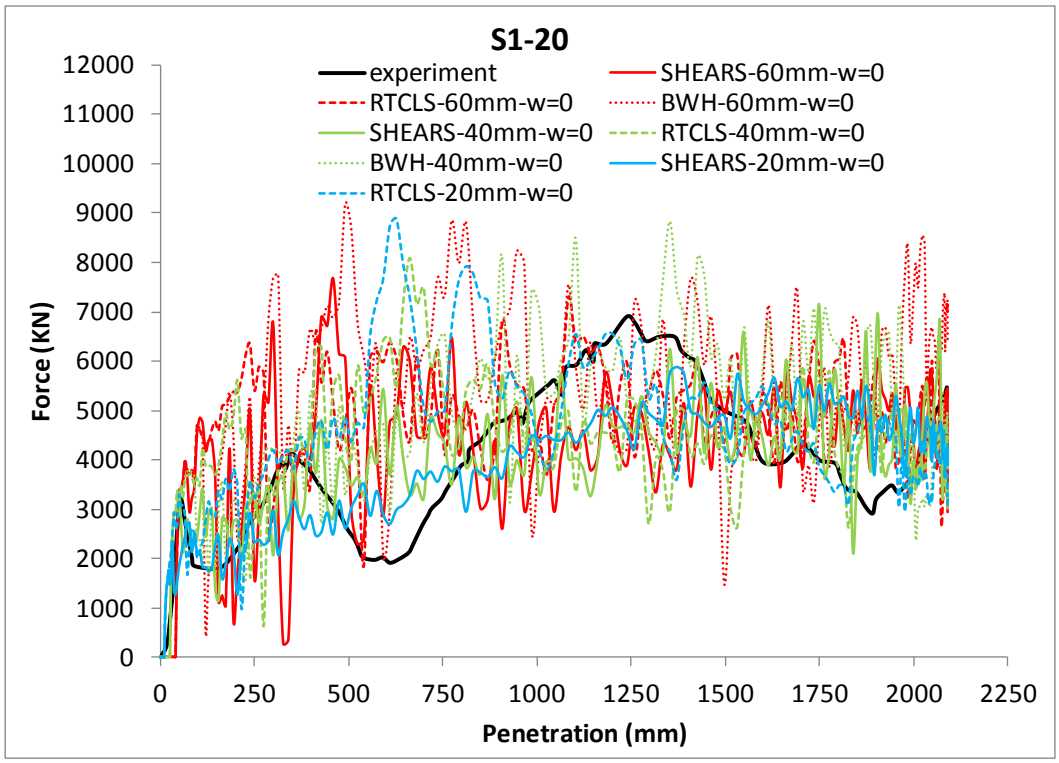

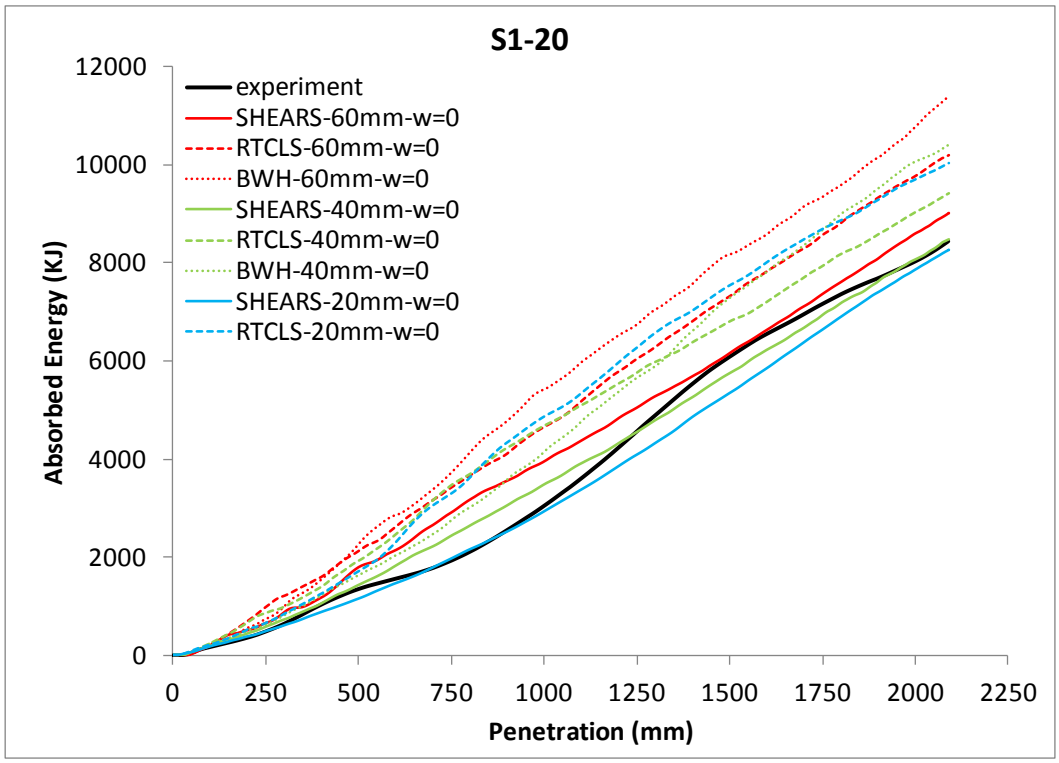

Figure 5.49. S1-20 model. Force and absorbed energy-penetration curves.
Prediction of rupture according to SHEARS, RTCLS and BWH rupture criteria in combination with the powerlaw type material curve

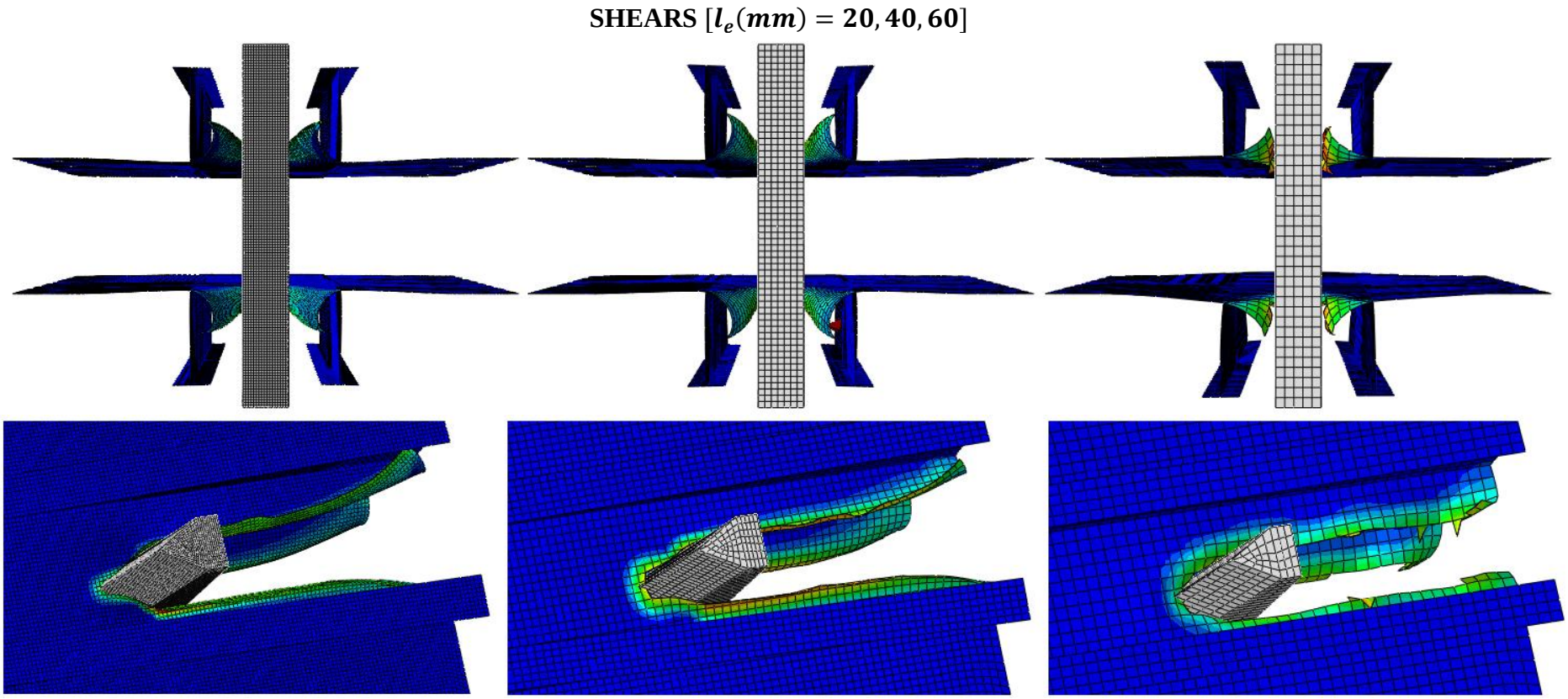

Figure 5.50. S1-20 model. Representation of damage according to SHEARS rupture criterion

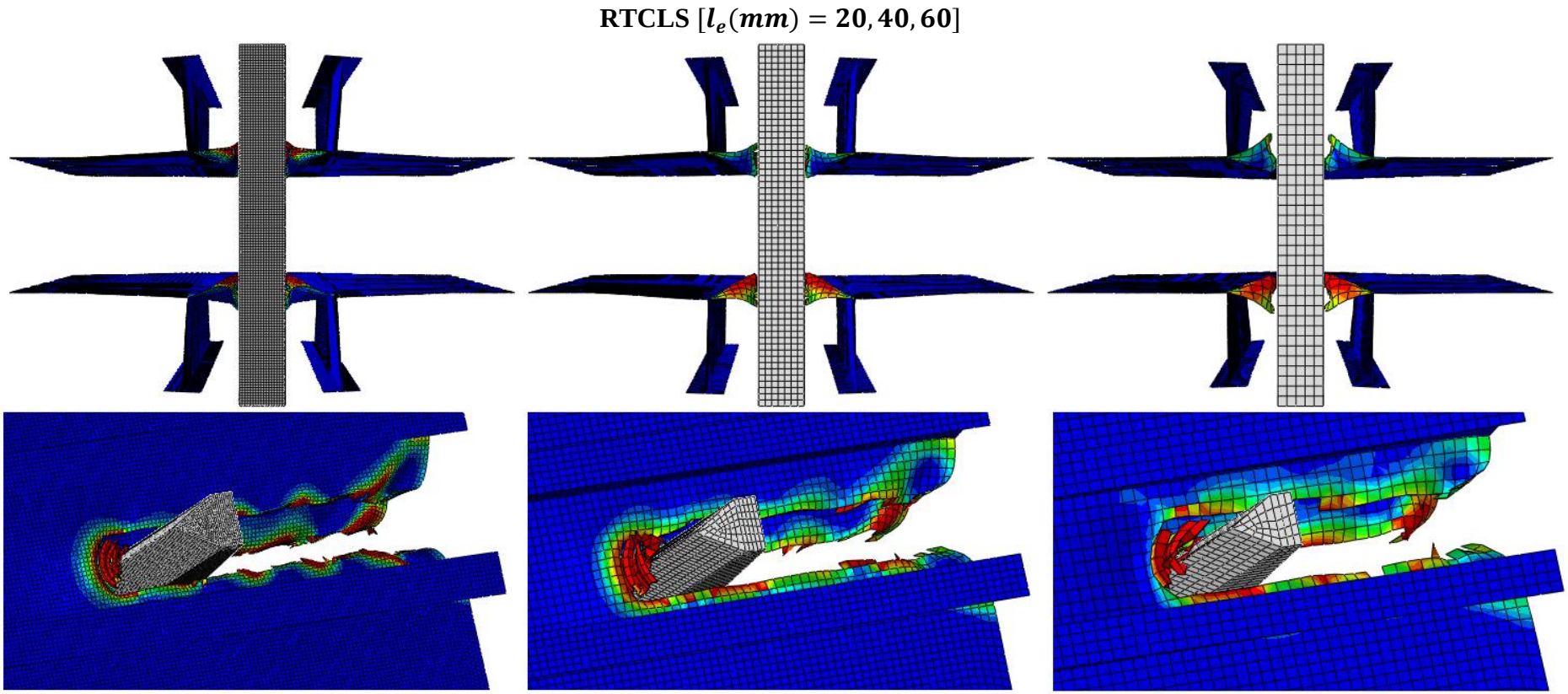

Figure 5.51. S1-20 model. Representation of damage according to RTCLS rupture criterion

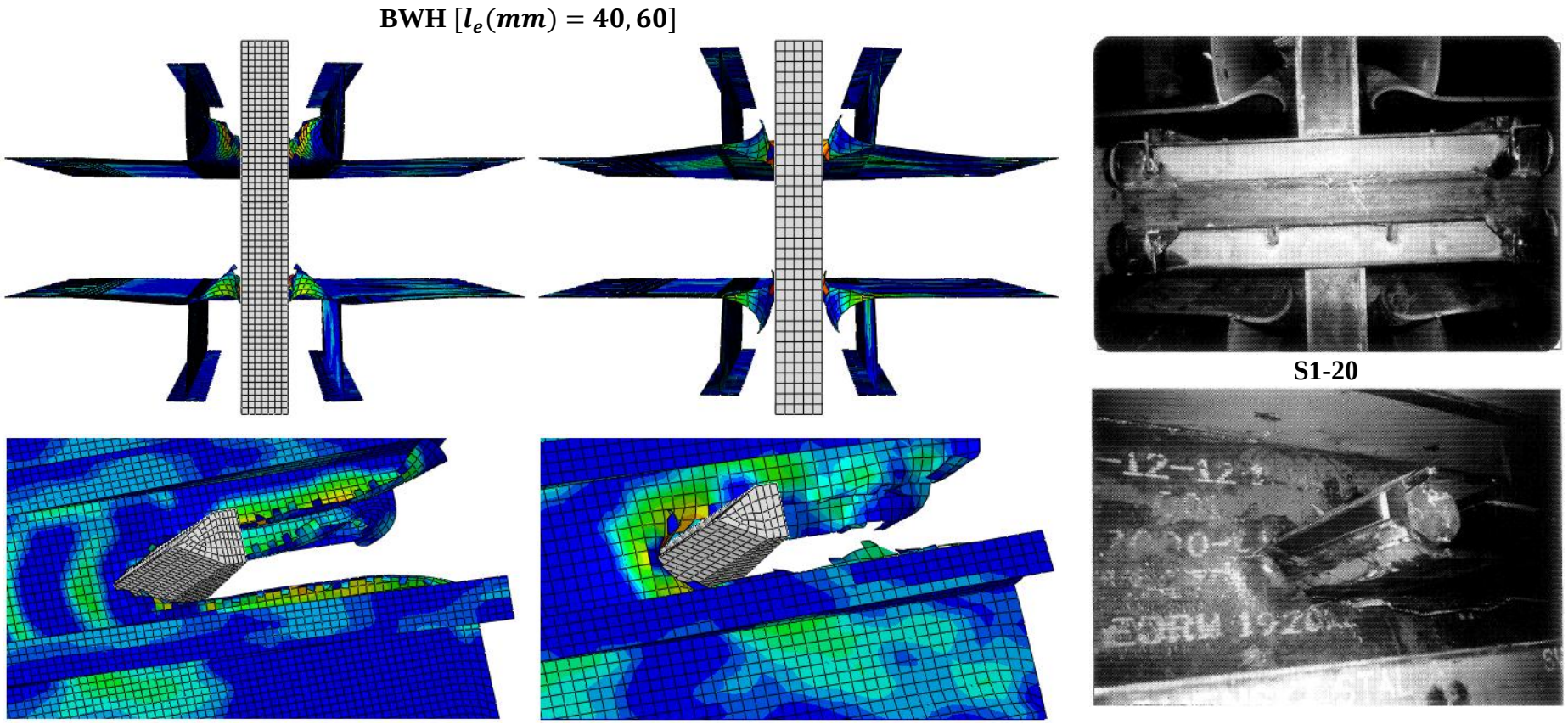

Figure 5.52. S1-20 model. Representation of damage according to BWH rupture criterion (DNV 1993)

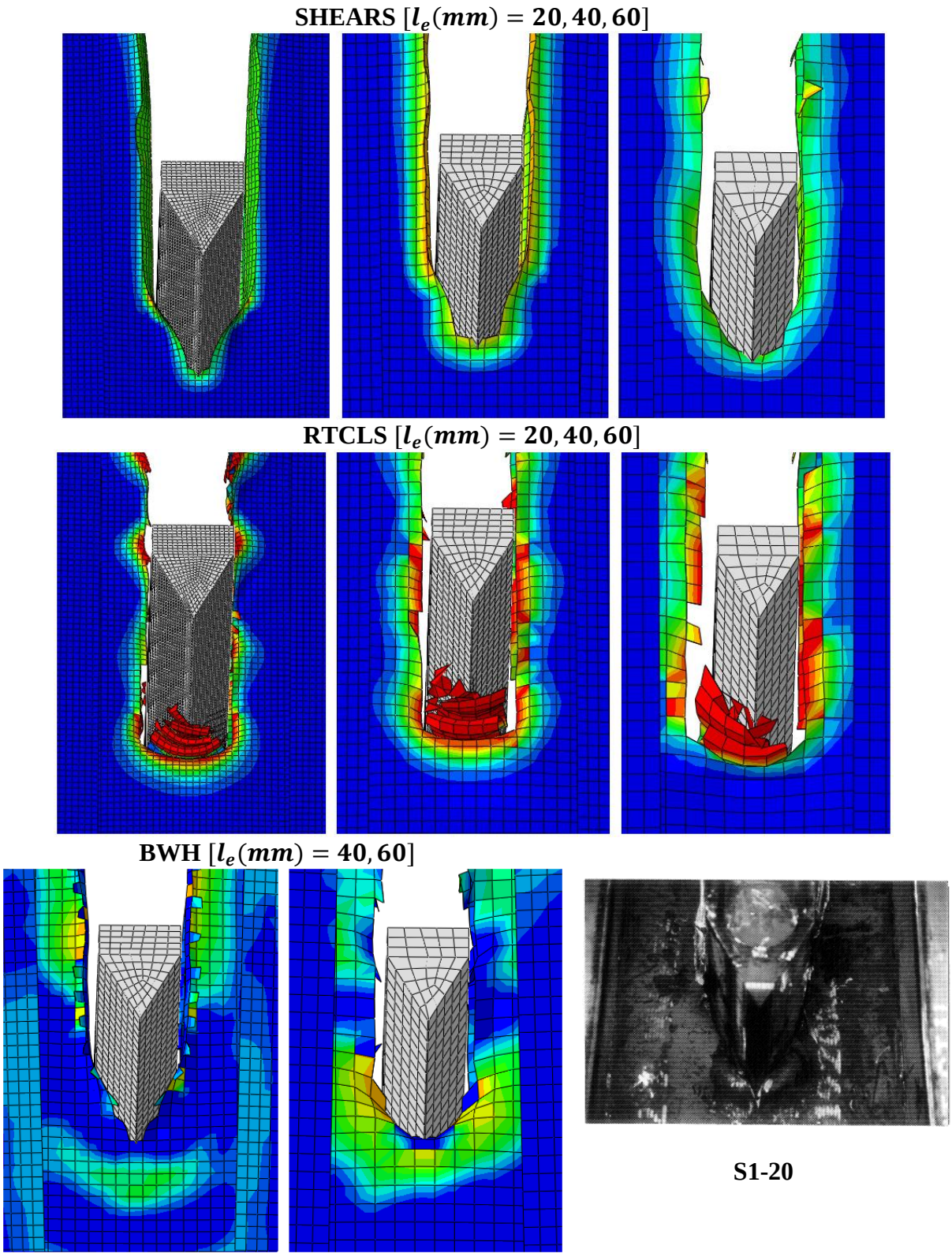

Figure 5.53. S1-20 model. Representation of damage according to SHEARS, RTCLS and BWH rupture criteria (DNV 1993)

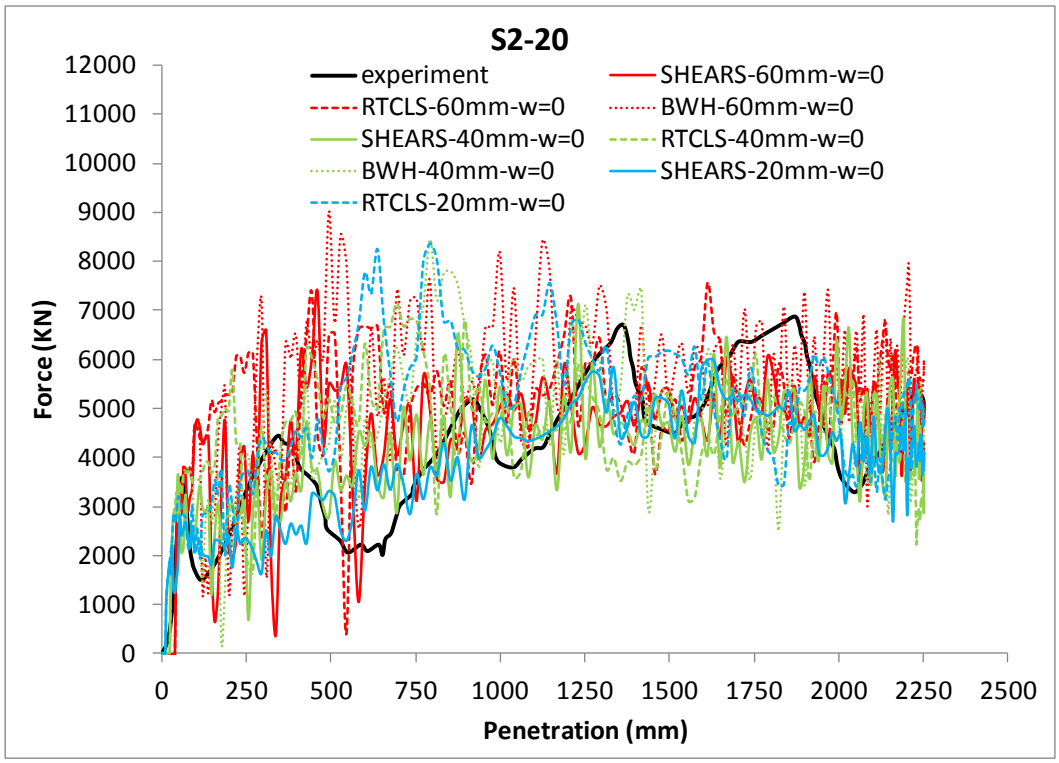

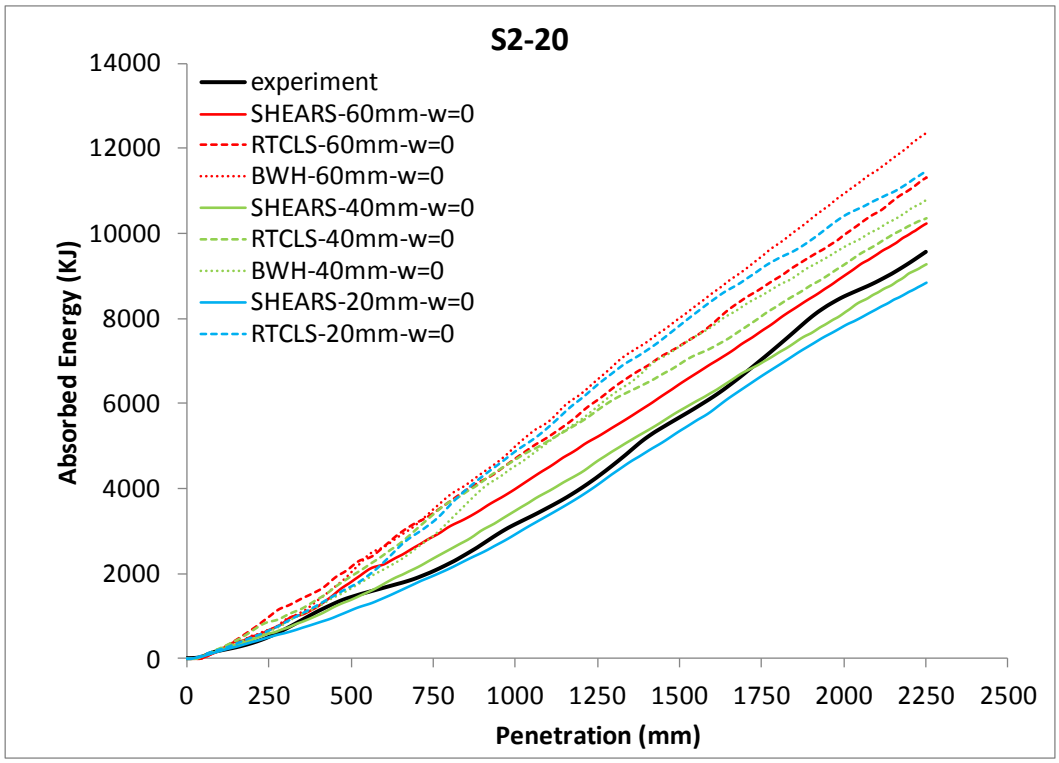

Figure 5.54. S2-20 model. Force and absorbed energy-penetration curves.
Prediction of rupture according to SHEARS, RTCLS and BWH rupture criteria in combination with the powerlaw type material curve

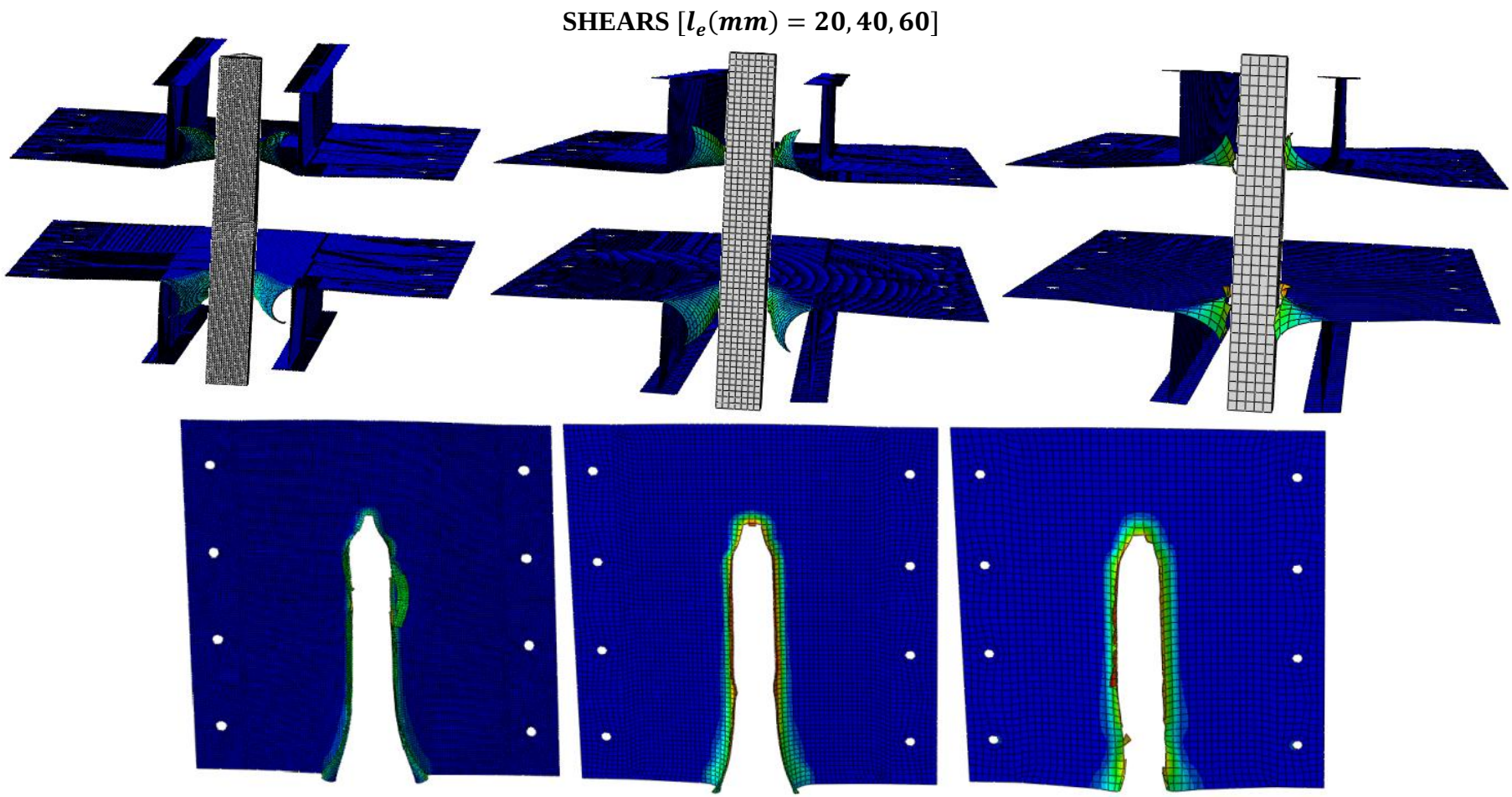

Figure 5.55. S2-20 model. Representation of damage according to SHEARS rupture criterion

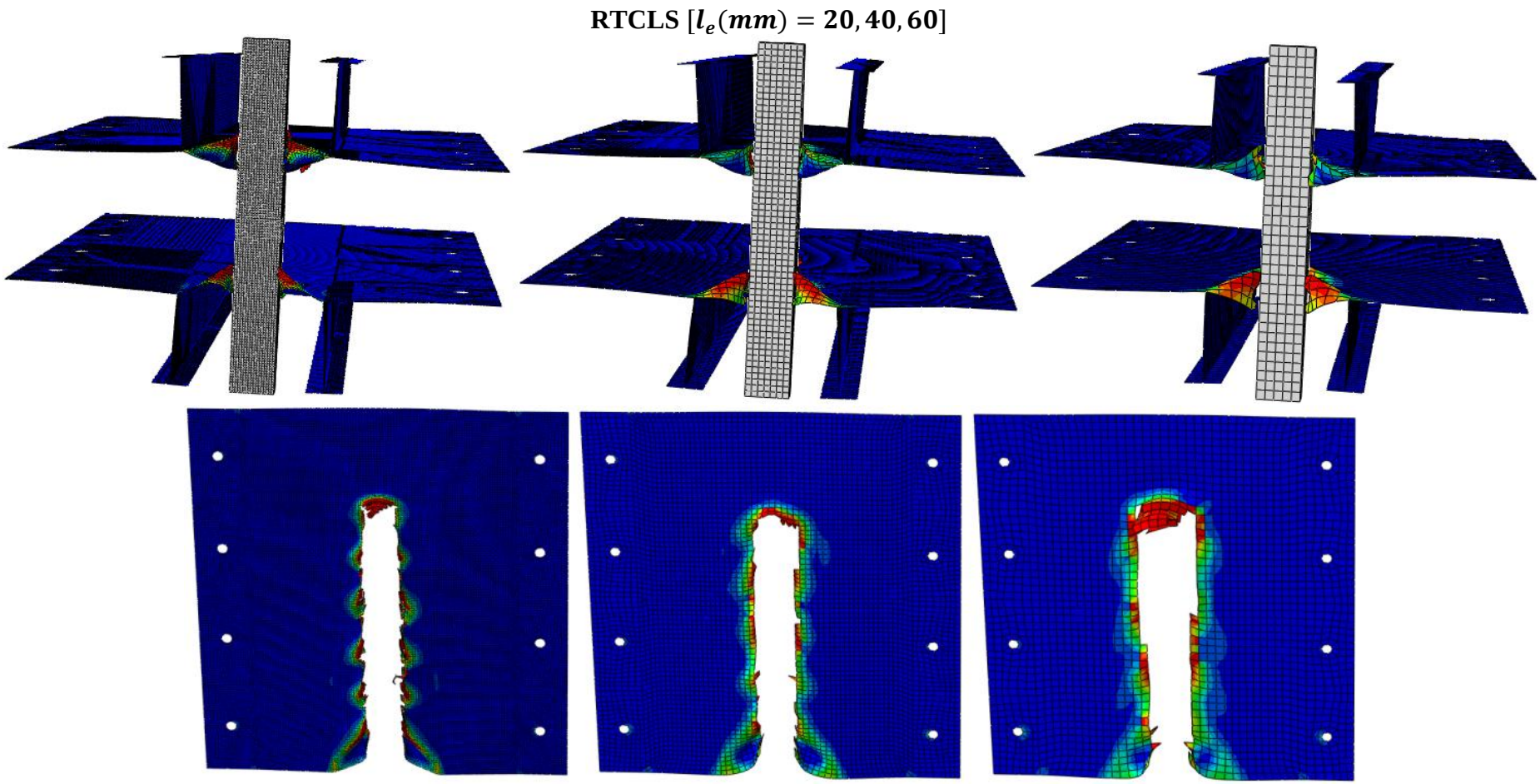

Figure 5.56. S2-20 model. Representation of damage according to RTCLS rupture criterion

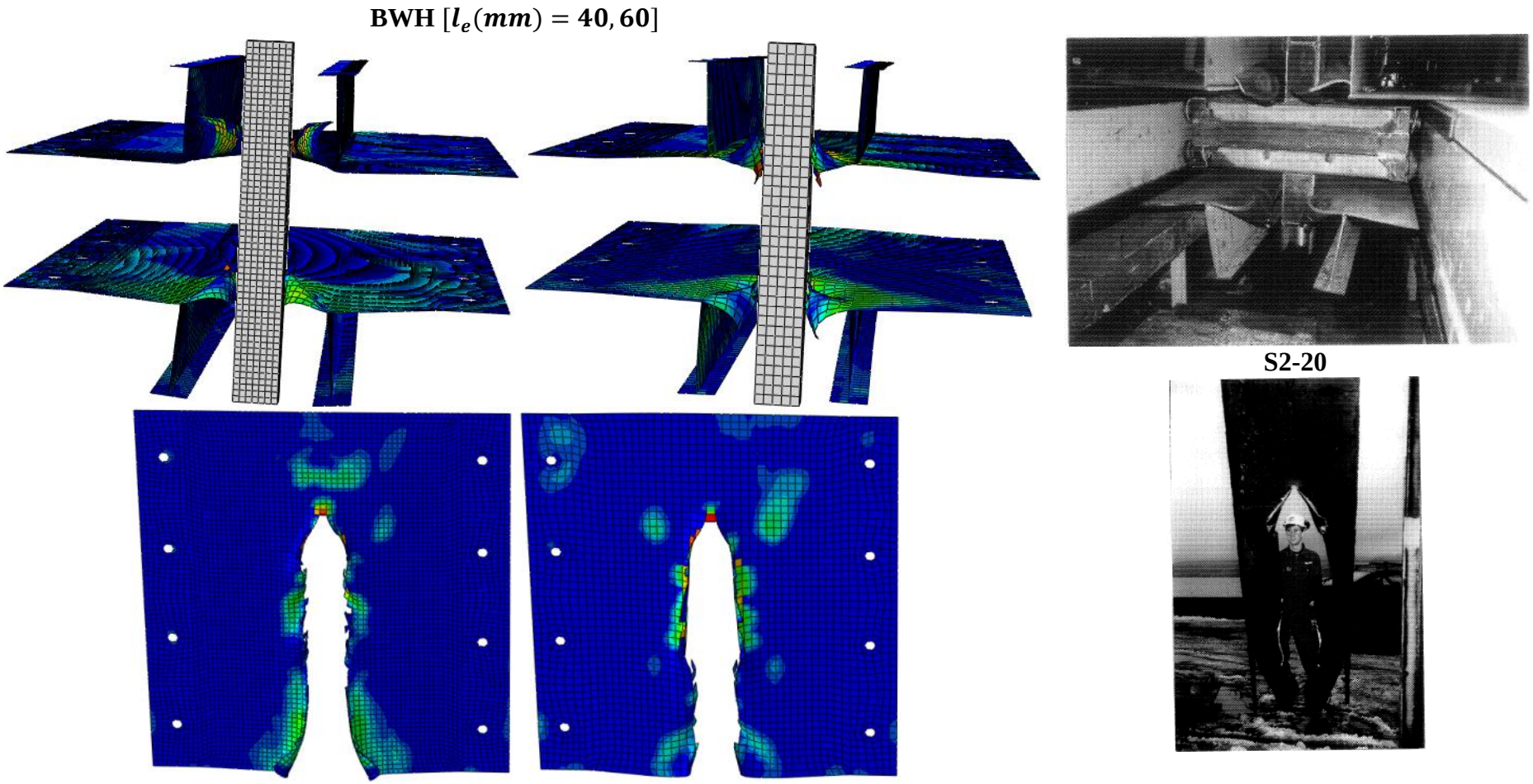

Figure 5.57. S2-20 model. Representation of damage according to BWH rupture criterion (DNV 1993)

5.3 Discussion

The comparison of the force vs. penetration curves as well as of the energy vs. penetration curves, obtained from the numerical simulations with FE models with different mesh sizes, illustrates that in the majority of the examined cases in section 5.2, the finer the mesh used in the simulations the lower the resultant force and as a consequence the absorbed energy at the same penetration depth. Thus, in most cases the models were less stiff for ratios l_e/t below 2. This behaviour was observed irrespective of the rupture criterion that has been used. However, the opposite trend was observed in the cases of the tests of punching the un-stiffened plate and the plate with one flat bar stiffener, i.e. US Plate and 1-FB models (see Figures 5.1 and 5.3), when the scaled form of the RTCL and SHEAR rupture criteria, designated as RTCLS and SHEARS, were incorporated in the simulations. A similar behaviour is also depicted in the results presented in Alsos et al. (2009) for the US Plate and 1-FB models. However, in all simulations of the punching of plates, stiffened and un-stiffened (see Figures 5.1, 5.3 and 5.5), the numerically obtained force penetration curves follow closely the respective experimental curves, until the rupture criterion that is used triggers the removal of an element. For this reason, it is assumed that this trend of the results when using the SHEARS and RTCLS criteria, as derived in the present analysis and in Alsos et al. (2009), i.e. stiffer structure for finer element size, may be attributed to the scaling of the SHEAR and RTCL criteria, i.e. the relationship of the critical value vs. mesh size. Moreover, according to the experimental observations referred in Alsos and Amdahl (2009) in the case of the US Plate model, extensive thinning up to 50% over the plate's surface was the dominant characteristic. This implies that due to the absence of geometrical constraints, the strains were uniformly developed over a large area of the plate before rupture occurred. However, local necking in terms of additional sheet thinning was detected along the fracture path, but according to the authors it could be assumed that rupture occurred almost at the same time with local necking.

Following the previous discussion, in analyses where local phenomena are not dominant and the strain field is rather uniform, it has been observed that scaling of the critical strain has a strong effect on the results. This is obvious in the simulations of the US Plate model using the scaled forms of SHEAR and RTCL rupture criteria, where extended scatter is evident on the results between analyses with different meshes (see Figure 5.1). On the other hand, in analyses where local phenomena exist due to geometrical constraints, as for example in the case of the 2-FB model, better convergence between the results with different meshes is achieved when the critical strain is scaled (see Figure 5.5). Figure 5.58 shows the differences in the behaviour of the scaling law in the cases of the US Plate and 2-FB models using SHEARS criterion, i.e. RTCLS criterion yields similar results. Figure 5.58 illustrates plots of the equivalent true plastic strain versus penetration, in each of the two cases, considering simulations with a fine and a coarse mesh, i.e. $l_e/t = 1$ and $l_e/t = 3.6$ respectively. Elements

at adjacent locations between the simulations with a fine and a coarse mesh were selected in each case, at points where the strains are maximized. Note that, in the case of the 2-FB model, the strains are maximized close to the stiffeners joints where rupture occurs. The diagrams also include the scaling of the critical strain for the material of the plate component with thickness $5\,mm$. The values of the critical strain for the element length over thickness ratios used in the simulations with respect to a fine and coarse mesh are indicated in each case. In Figure 5.58b, it is obvious that the strains are developed rapidly when a fine mesh is used in the case of the 2-FB model. This behaviour is reasonable as due to the geometrical constraints, high strain concentrations are developed in the vicinity of the stiffeners joints. Small elements capture these strains and rupture occurs at an earlier stage. However, in Figure 5.58a, regarding the case of the US Plate model, differences in terms of strains prior to rupture are not significant between analyses with a fine and a coarse mesh and the strains seem to develop in both cases uniformly up to the point the element is deleted from the mesh. In addition, the structure shows a stiffer behaviour when a fine mesh is used. This is attributed to the fact that stress concentrations are not developed on the surface of the plate and scaling of the critical strain leads to the opposite trend. Note that, the scaling of the critical strain accounts for local phenomena, which in the case of the US Plate model are not dominant. However, in actual ship impacts local phenomena are rather dominant due to complicated geometries and an appropriate value of the critical strain should be selected for the relevant mesh size, i.e. application of a scaling law.

On the contrary, better convergence was observed between the results of analyses with different meshes using BWH criterion in the case of the US Plate model (see Figure 5.1). This is explained by the fact that in the case of the US Plate model rupture initiates immediately after local necking, which is in line with BWH criterion's concept. In addition, no geometrical constraints, such as stiffeners, exist and as a result no stress concentrations are developed, that would provoke activation of BWH criterion in an early stage with a finer mesh. However, in the case of the 2-FB model where local phenomena are dominant, convergence is not achieved and BWH criterion underestimates the resistance of the structure when a fine mesh is used (see Figure 5.5). It is noted that, in the case of the 1-FB model a similar behaviour to the US Plate model is evident in the numerical results (see Figures 5.1 and 5.3), although according to the experimental fracture observations referred in Alsos and Amdahl (2009) fracture was localized on the plate next to the weld toe of the stiffener. This is explained by the fact, already discussed in sub-section 5.2.1, that all rupture criteria contrary to the experimental observations predicted initiation of rupture on the plate far from the stiffener joint and not locally (see Figure 5.4).

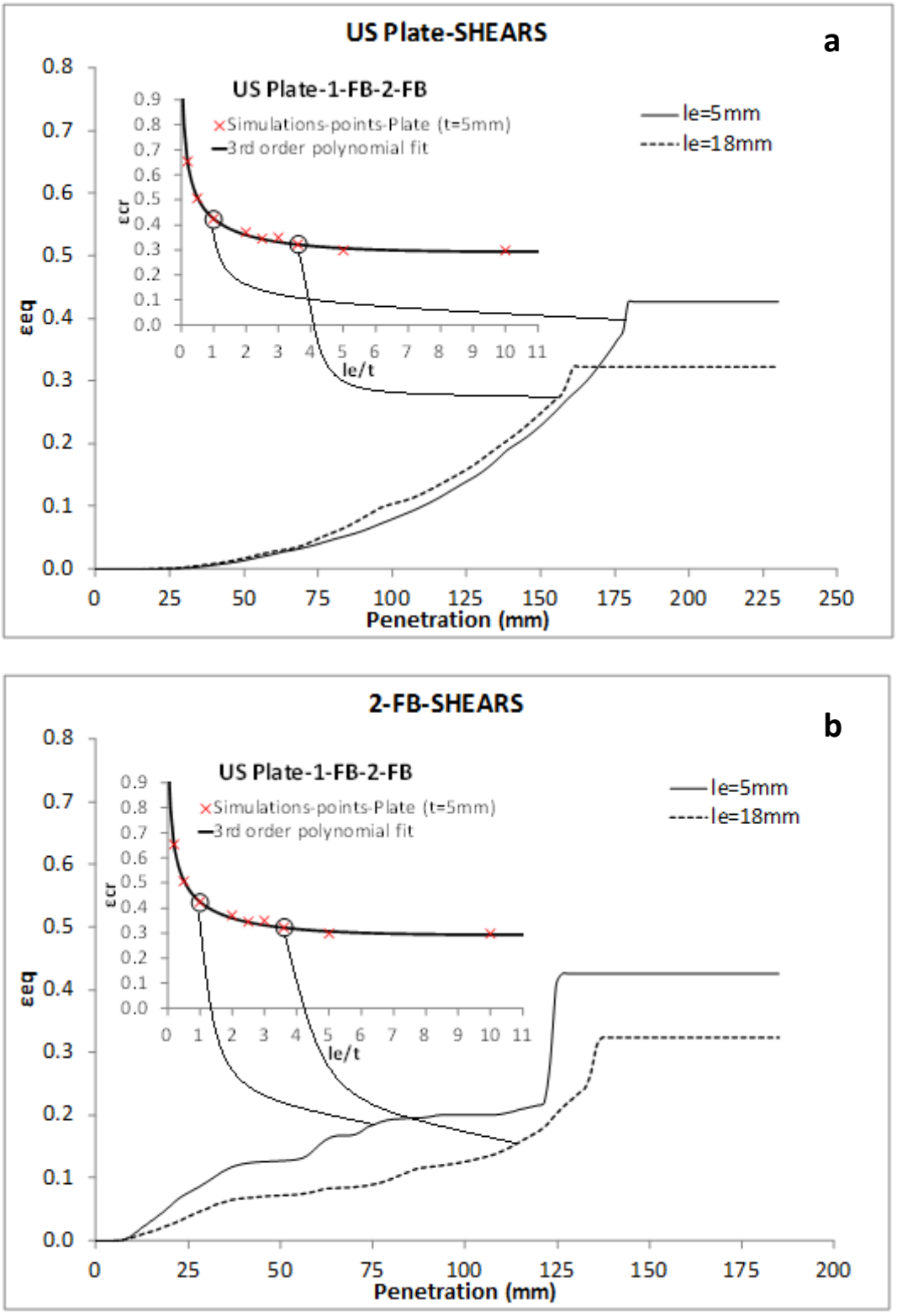

Figure 5.58. The effect of scaling of the critical strain in cases where the strain field is rather uniform (a) or local phenomena are dominant (b)

SHEARS rupture criterion shows a rather consistent behaviour, as it predicts relatively well the force vs. penetration curves and the energy vs. penetration curves in the majority of the examined models for a ratio l_e/t between 2 and 3 and in some cases for ratios l_e/t close to 1 and 4 (see Tables 5.2-5.7, 5.9 and 5.10). Similarly using SHEARS criterion, the representation of the deformation patterns is also predicted well for the respective ratios, i.e. $1 \leq l_e/t \leq 4$. RTCLS and BWH rupture criteria, yield also in some cases good results, better than SHEARS criterion, but the representation of the failure modes are rather different with respect to the experiments in many cases. In the cases of the COLLISION DYNAMIC model, in Figure 5.28 and INNER SHELL model, in Figure 5.32, RTCLS predicts rupture of the stringer deck along the joint with the webs and rupture of the plate respectively, which has not been observed in the tests. BWH underestimates the load carrying capacity of the structure in the cases of the FLAT and KNIFE SPECIMEN models and a fine mesh (see Figures 5.33-5.36). Moreover, in the case of the US Plate and OUTER SHELL models, in Figures 5.2 and 5.30, the representation of rupture initiation according to BWH criterion is different to the experimental observation. For the latter models as well as for the 1-FB and 2-FB models cases, RTCLS underpredicts the initiation of rupture (see Figures 5.1, 5.3, 5.5 and 5.29). Finally, in the cases of the cutting tests and particularly models US, LS, S1-20 and S2-20, RTCLS criterion predicts different deformation patterns with respect to the experimental observations (see Figures 5.16, 5.18, 5.51, 5.53 and 5.56).

For more complex structural configurations as in the cases of the experiments in Paik et al. (1999), where many deformation patterns arise simultaneously; in particular membrane, bending, folding and crushing, a significant variation of the magnitude of triaxialities is observed in the vicinity of these regions. Therefore, for example deletion of an element at a structural component may be due to a biaxial stretching loading state, while at the same time deletion of an element at a structural component next to it, due to a pure shear loading state. Thus, it is observed that the differences in the force penetration curves using different criteria, when multiple failure patterns are present, are relatively smaller than in the case where a failure pattern dominates.

The comparison between the numerical predictions and the experimental observations is complicated, because it is not sufficient to compare single values, for example peak loads, but the comparison should cover the trend of relations such as force vs. penetration curves. Further, the comparison of the damage patterns may only be performed in a descriptive manner. It is also observed that convergence is not achieved equally well in all cases. However in the majority of the simulated tests, results tend to be closer with each other for ratios $2 \leq l_e/t \leq 3$ and in some cases for ratios $1 \leq l_e/t \leq 2$.

In order to understand in a more comprehensive manner and interpret the numerical results regarding the various criteria, two of the examined models, i.e. the US Plate and TS model, respectively, were further analyzed. The specific tests were selected, as they represent different loading conditions.

In the case of the US Plate model, the dominant loading state is biaxial stretching, with triaxialities mainly over $1/\sqrt{3}$, while in the case of the TS model, the dominant loading states are between pure shear and uniaxial compression, i.e. triaxialities below zero. In Figures 5.59 and 5.60, the behaviour of the scaled forms of SHEAR and RTCL rupture criteria and BWH rupture criterion are compared in each of the two cases, considering the true stress-strain relation and variation of T, $f(T)$, ε_{eq}, β, D_{SHEAR} and D variables versus penetration. The comparison is effected for the through thickness integration or section point at the mid-plane of a shell element, i.e. section point 3 in Figure 3.2 of chapter 3, up to its deletion. It is noted that, the selected elements which through thickness integration point is examined are the same for the three criteria, in each of the two cases. Results in the case of the US Plate model correspond to a mesh 10 mm, that is an element length over thickness ratio equal to 2, while in the case of the TS model to a mesh 8 mm, that is an element length over thickness ratio about 1.1 (see Table 5.1). D is the numerator of the fraction $\int f\left(\frac{\sigma_m}{\sigma_{eq}}\right)_{RTCL} d\bar{\varepsilon}^{pl}/\varepsilon_{cr}$ in the case of RTCL rupture criterion and ε_{eq} the equivalent true plastic strain during the analysis. The first three diagrams of each case include the critical equivalent true plastic strain, i.e. $\varepsilon_{cr} = 0.361$ and $\varepsilon_{cr} = 0.456$ for the US Plate and TS models respectively (see Table 5.1), the critical in plane true stress $\sigma_{1_{cr}}$ and the major in-plane true stress σ_1. The reference to the stresses is in relation with the BWH criterion. Furthermore, Figures 5.59 and 5.60 include the ultimate stress point beyond which the neck initiates, i.e. $(\varepsilon_u, \sigma_u)$, the true material curve given as input to the program as well as the σ_{Mises} curve, which is the numerically reproduced true material curve up to deletion of the through thickness integration point. The sharp variations of the σ_{Mises} curve in the case of the TS model, is attributed to the loading and unloading of the elements adjacent to the contact area and to the changes in the contact area between the plate and the indenter following the deletion of elements. This is not observed in the case of the US Plate model.

According to Figures 5.59 and 5.60, one may observe that in both cases of the US Plate and TS models, SHEARS rupture criterion is activated exactly at the point where the equivalent true plastic strain during the analysis becomes equal to the critical equivalent true plastic strain. RTCL rupture criterion tends to underpredict rupture, when during the loading process triaxialities are mainly over $1/\sqrt{3}$ or $\beta > 0$, as is the case for the US Plate model. In these cases, function f of the integral $\int f\left(\frac{\sigma_m}{\sigma_{eq}}\right)_{RTCL} d\bar{\varepsilon}^{pl}$, is $f \geq 1$ in the majority of the loading steps (see also Figure 4.1, chapter 4). As a result the critical equivalent plastic strain is reached sooner. The opposite behaviour is observed for triaxialities that are mainly below zero or $\beta <$ -1 and as a result RTCL tends to overpredict rupture, as is the case for the TS model. As already mentioned in sub-section 5.2.3, in both cases of the RTCL and SHEAR rupture criteria the damage parameters D_{SHEAR} and D_{RTCL}, in equations (4.23) and (4.24) respectively, do not increase for triaxialities which are below -1/3; cut-off value, although equivalent plastic strains may be developed.

BWH is a stress based criterion, based on local necking, which in the case of a tensile test appears after the maximum load. It has been observed that in loading processes, where the dominant triaxialities are over $1/\sqrt{3}$, i.e. US Plate, when the BWH criterion is activated, the equivalent true plastic strains are lower than the critical equivalent true plastic strain values of the other criteria. This behaviour is also encountered in analyses with fine meshes, due to high stress concentrations at structural intersections and changes in geometry. On the contrary, BWH criterion is not activated for triaxialities equal and below zero, namely between pure shear and uniaxial compression loading states (see also sub-section 4.2.5 and equation (4.27)). At this range of β values, formation of a local neck is not possible. This trend is illustrated in the case of the TS model in Figure 5.60.

The different behaviour of SHEAR, RTCL and BWH rupture criteria, considering the cases of the US Plate and TS models, is also investigated following the concept of section 4.3 of chapter 4. Figures 5.61 and 5.62 show the relation between the limit stress and limit strain variables respectively with parameter β. The diagrams in Figures 5.61 and 5.62 include also the failure criteria discussed in section 4.3 for comparison. The points that correspond to the values of triaxialities, which were dominant during the analyses, are indicated in each of the two cases. In the case of the US Plate model, triaxialities during loading and close to fracture were approximately equal to 0.643, namely in the range of $0 \leq \beta \leq 1$, i.e. between plane strain, uniaxial tension and equal biaxial stretching loading states (see also Figure 5.59). In particular for $T \cong 0.643$ the parameter $\beta \cong 0.36$. As one may observe in Figure 5.61, BWH and RTCL criteria for $\beta \cong 0.36$ predict lower values for the limit stress and strain respectively than SHEAR criterion and are activated sooner. This is in line with the results shown in the example in Figure 5.59. On the other hand, in the case of the TS model triaxialities are mostly below zero, namely $\beta <$ -1, i.e. between pure shear and uniaxial compression loading states (see also Figure 5.59). At this range of triaxialities BWH criterion does not define a limit stress and RTCL criterion gives a significantly higher limit strain than SHEAR criterion (see Figure 5.62). As a result according to BWH and RTCL criteria rupture is delayed (see also Figure 5.60).

In the present work the damage evolution concept was not adopted in the simulations. This choice is justified by the following observations and conclusions, also in terms of the work of other researchers. In the cases of SHEAR and RTCL rupture criteria, following the discussion in sections 3.3 and 4.4, i.e. chapters 3 and 4 respectively, the critical equivalent plastic strain was determined at fracture taking into consideration both the true stress-strain relation and the mesh size. In other words, the two criteria were calibrated for different mesh sizes in combination with the true stress-strain curves, which yielded the best reproduction of the experimental curves from uniaxial tests up to the point of fracture. Therefore, due to the numerical method, which was applied for the calibration of SHEAR and RTCL rupture criteria, inclusion of a damage evolution law was not considered necessary, i.e. damage evolution is activated at necking initiation prior to fracture. Moreover, as already mentioned in section 5.1, in Abaqus/Explicit the element is removed from the mesh when the criterion is satisfied in all of the through thickness integration points or material points (see Figure 3.2,

chapter 3). When the criterion is activated in a layer, i.e. material point, Abaqus/Explicit passes zero stresses and strain increments at the specific point in the next time step of the simulation. Thus, the capability of the element to carry loads and the resistance capacity of the structure is gradually reduced.

The difference between the applied method and the damage evolution law concept is that the stiffness of the element is not altered during the loading process in the former case. Furthermore, according to the conclusions in Kõrgesaar and Romanoff (2014), softening seem not to have a significant effect in the modeling of rupture using the specific criteria at least in the cases of the experiments in Alsos and Amdahl (2009). Instead, instability criteria as is the case of BWH criterion, it would be more appropriate to be used in combination with a damage evolution law. The work in Kõrgesaar and Romanoff (2014) showed that convergence between different meshes is better compared to the results in the present work for the specific cases of the US Plate and 1-FB models. However, there is not yet a widely established method for the calibration of the damage or softening parameters used in analyses with damage evolution. In addition, the concept for the definition of the material model in the present analysis is simple and in the majority of the examined cases consistency with the experiments is achieved, based solely on the experimental data from uniaxial tensile tests.

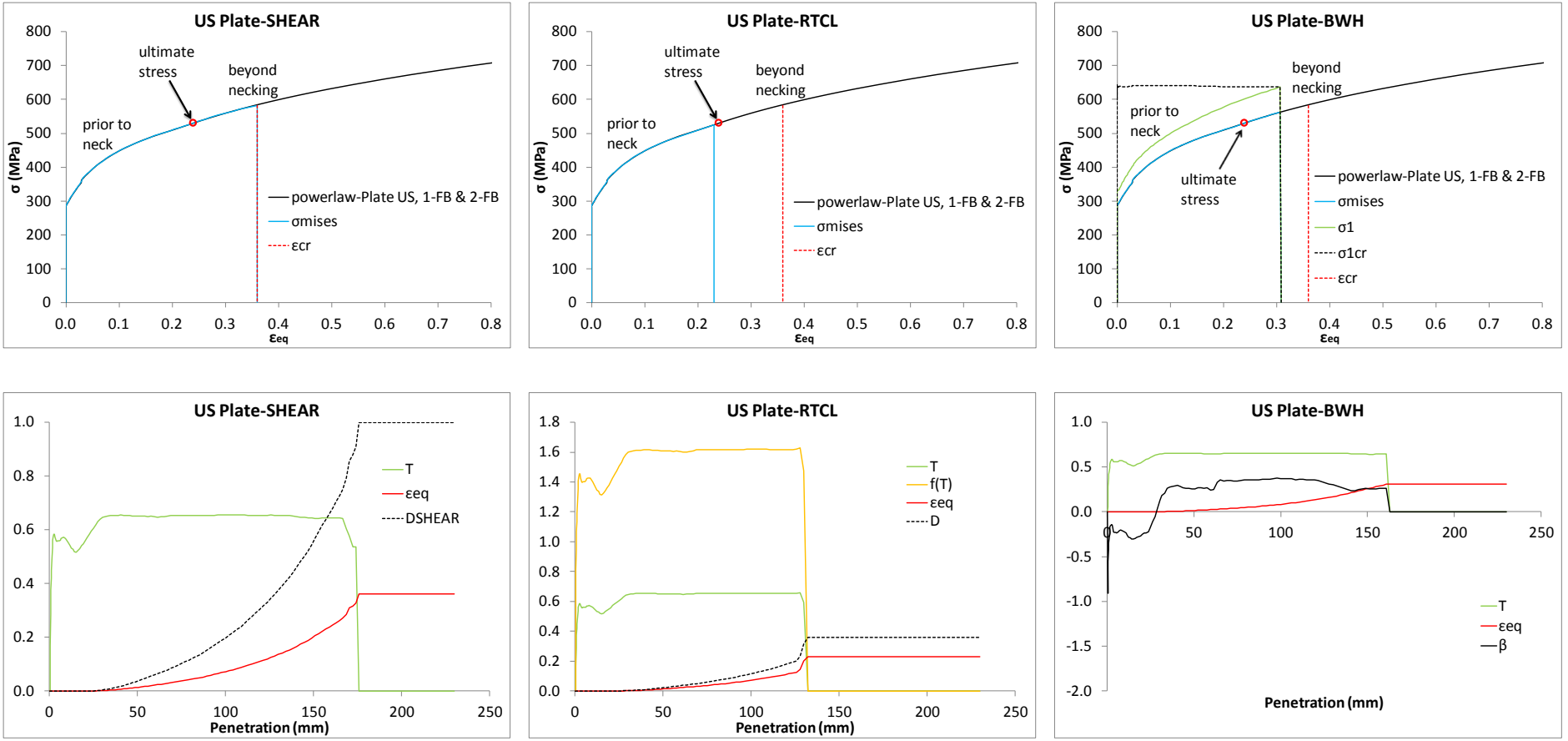

Figure 5.59. Stress-strain relation for the through thickness integration point at the mid-plane of a shell element up to its deletion and T, $f(T)$, ε_{eq}, β, D_{SHEAR} and D versus penetration depth in the case of the US Plate model with the scaled forms of SHEAR and RTCL rupture criteria and BWH rupture criterion

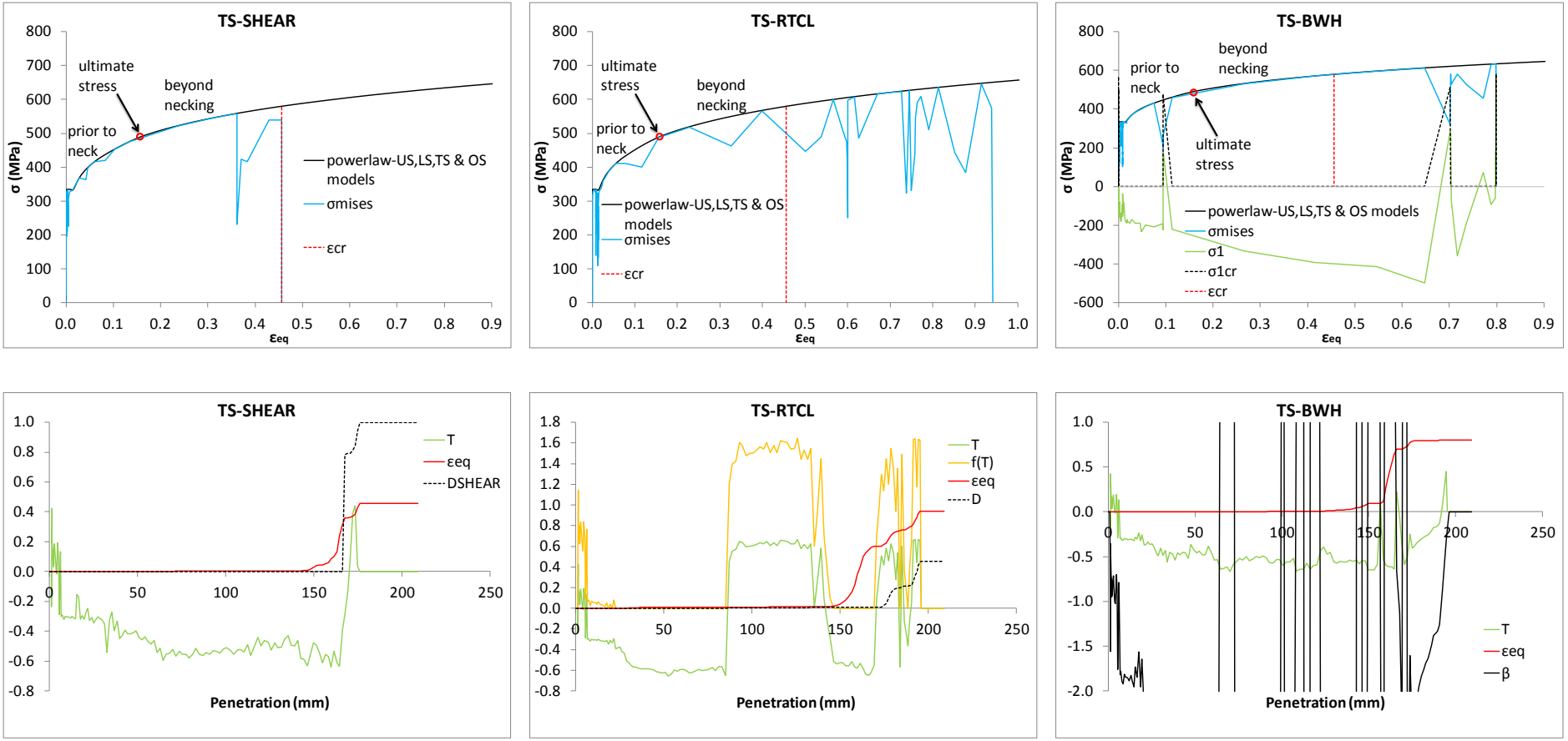

Figure 5.60. Stress-strain relation for the through thickness integration point at the mid-plane of a shell element up to its deletion and T, $f(T)$, ε_{eq}, β, D_{SHEAR} and D versus penetration depth in the case of the TS model with the scaled forms of SHEAR and RTCL rupture criteria and BWH rupture criterion

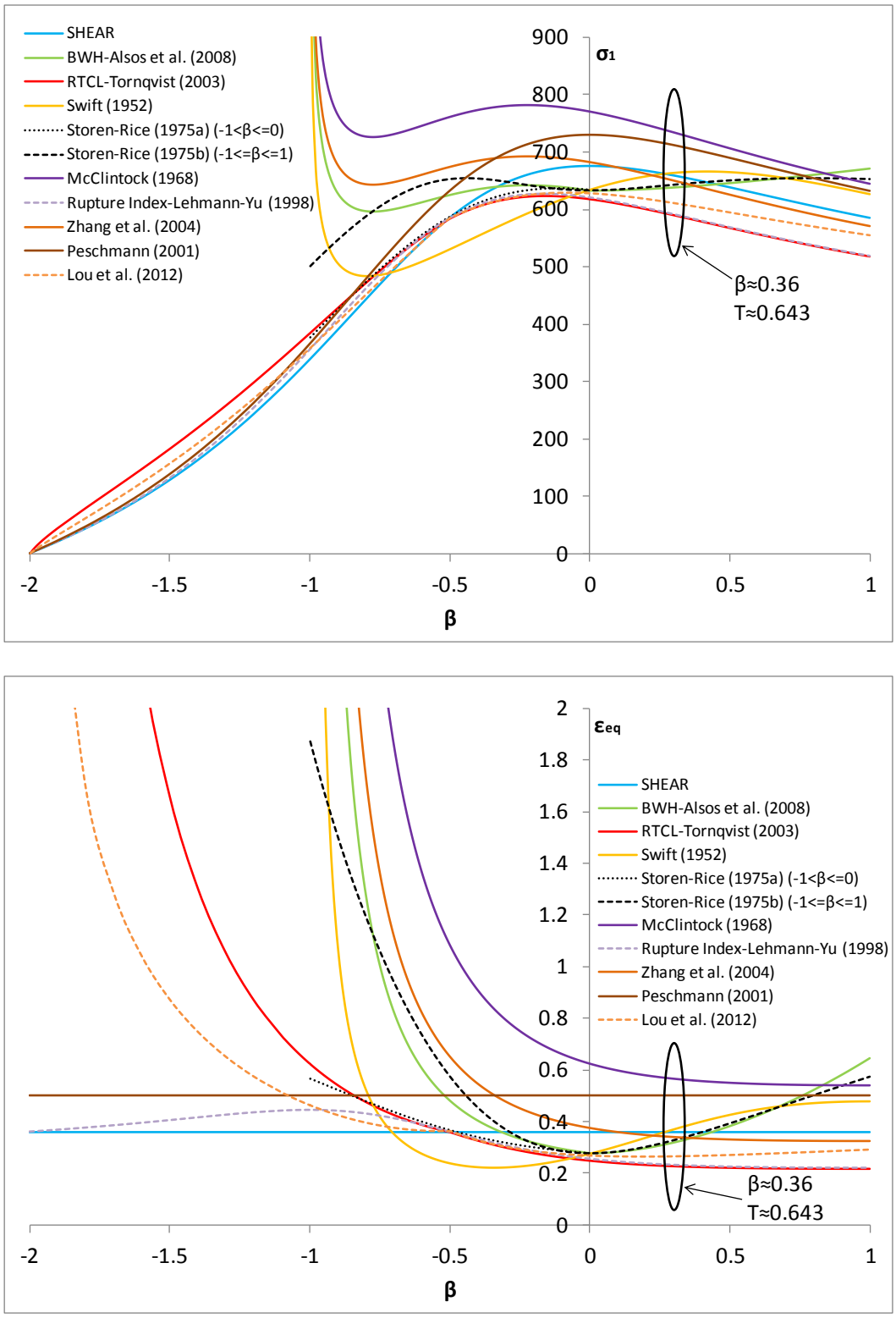

Figure 5.61. Limit stress σ_1 and limit strain ε_{eq} variables as functions of β in the case of the US Plate model

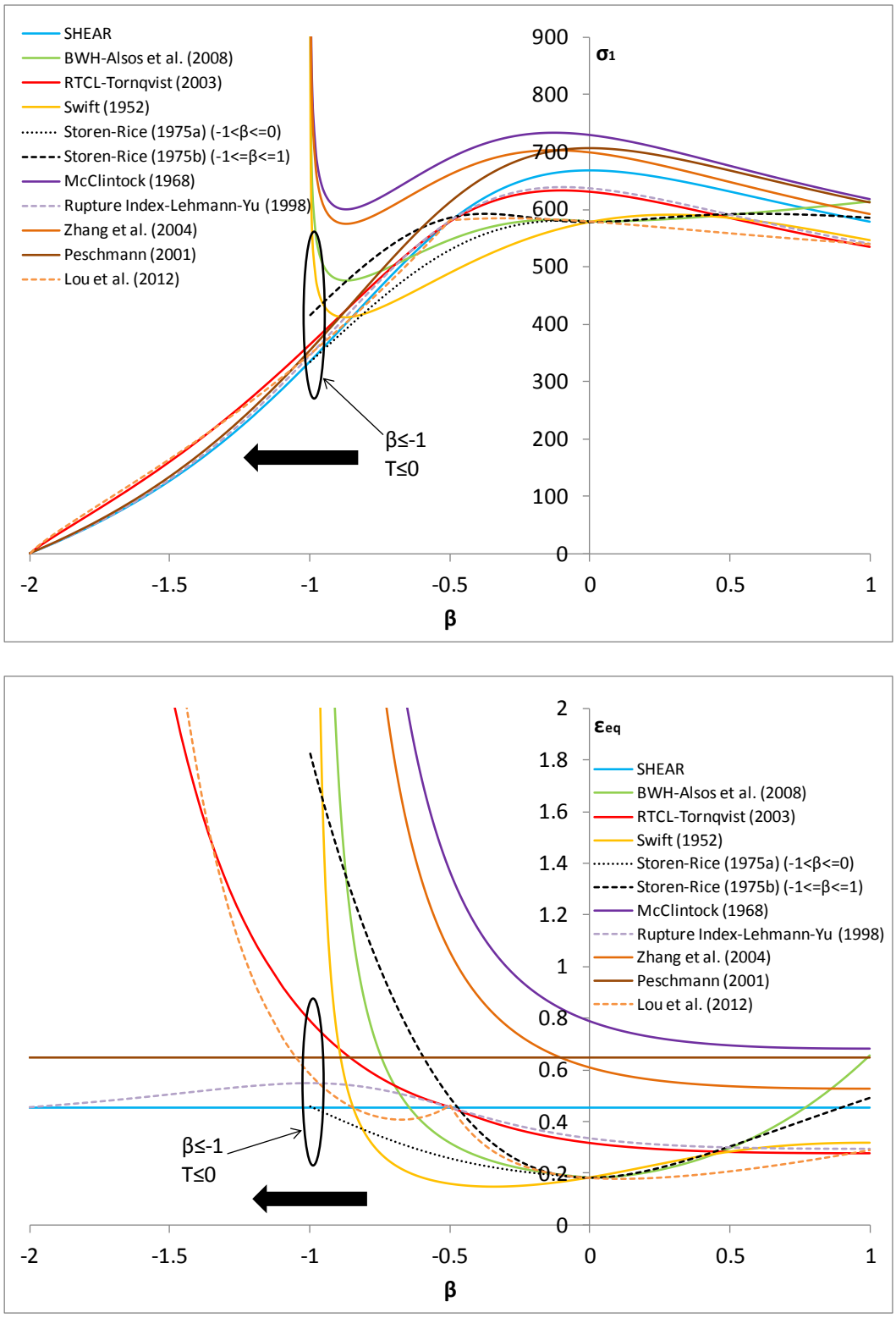

Figure 5.62. Limit stress σ_1 and limit strain ε_{eq} variables as functions of β in the case of the TS model

Chapter 6

Full-Scale Simulations

6.1 Full-scale model

This chapter presents the simulation of a full-scale ship-ship collision. The struck ship is considered to be a sister ship of the Tankship BALTIC CARRIER, which was struck by the Bulk Carrier TERN in the Baltic Sea on 29 March 2001 (see also AbuBakar et al. 2010). The striking ship is a new built Bulk Carrier having similar particulars as TERN. However, as the striking ship considered is built rather recently, the structure of the bow may differ significantly. The general particulars of the striking ship involved in the actual collision, i.e. TERN, and the ships used for the full scale collision simulation, are summarized in Table 6.1 (see also DIMA 2001 and The Republic of the Marshall Islands 2002). During the incident in the Baltic Sea, the Bulk Carrier collided at the center of the last oil cargo tank, i.e. adjacent to the engine room, with an angle approximately equal to 50°, i.e. moving towards the stern of the Tankship (see Figure 6.1). The striking ship came into contact below her upper deck with the upper deck of the struck ship, while the bow of the former collided in the area over the double bottom location of the latter.

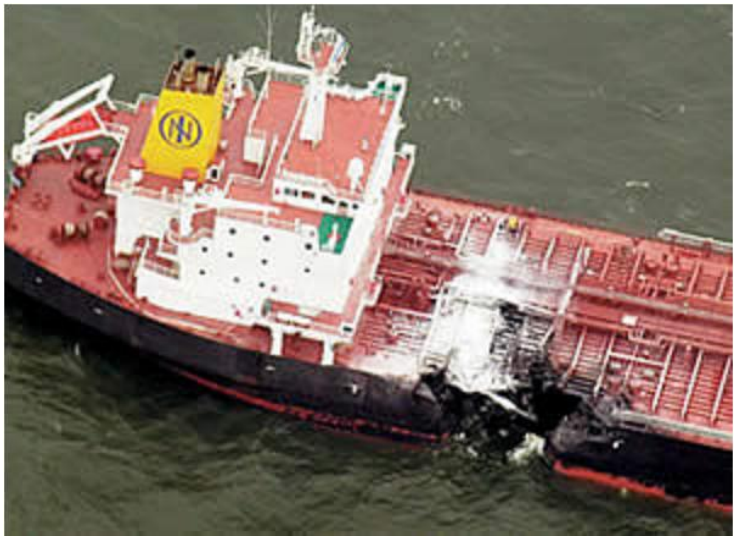

Figure 6.1. Top view showing the damaged side of the Tankship
From: http://wwz.cedre.fr/en/Our-resources/Spills/Spills/Baltic-Carrier-Tern

Table 6.1. General particulars of the ships

	SHIPS		
GENERAL PARTICULARS	PRODUCT CARRIER for the modeling	BULK CARRIER TERN	BULK CARRIER for the modeling
$L_{OA}(m)$	175	174.96	176. 2
$L_{BP}(m)$	-	-	168
$B(m)$	27.34	26	26.05
$D(m)$	16. 7	15. 5	14
$T(m)$	10. 85	11. 15	9.92
$DWT(tons)$	37000	34365	30000
Year of built	2000	1973	2010

Different collision scenarios were examined and the ships were defined as rigid or deformable structures. Specifically, for two different collision angles, namely 50° and 90° and the use of the scaled forms of SHEAR and RTCL rupture criteria, simulations were performed where:

i. the bow was defined as rigid body
ii. the bow was defined as deformable structure and the side of the Tankship as rigid body
iii. the bow was defined as deformable structure, which was forced towards a rigid wall
iv. both ships were defined as deformable structures

The aim was to apply the numerical method that has been adopted in the previous analyses in a full-scale ship-ship collision simulation, in order to i) estimate the crashworthiness of the ship structures under different loading conditions, ii) investigate the effect of a deformable bow and iii) assess the energy absorbed by the participating bodies in each case.

The bow of the Bulk Carrier up to the fore watertight transverse bulkhead as well as two cargo tanks of the Tankship were modeled in detail, in order to achieve a reasonable ship length for the application of the boundary conditions for the struck ship. Both ships were modeled in the design environment of ABAQUS, i.e. ABAQUS CAE. However, the hull of the bow was designed in Rhinoceros and then imported as a separate part in ABAQUS CAE. The pictures on the top of Figure 6.2 illustrate the geometries of both ships. The part of the bow construction defined as rigid, is also included in the pictures on the right of Figure 6.2. The rigid part of the bow was modeled and included in the simulations, in order sufficient length of the striking ship to be available, in case it came in contact with the side parts of the struck ship during the simulation at certain penetration depths.

Two steels were used for the full-scale simulations, i.e. Grade 'A' mild steel of minimum yield stress 235 MPa and Grade 'AH' high tensile steel of minimum yield stress 315 MPa and the powerlaw type true stress-strain curve beyond necking initiation. For the definition of the material curves the material properties of two steels were selected from the experimental data base included in Table 2.1, chapter 2. The choice of the steels was made in terms of the thickness that is to be close to the thicknesses used in the shipbuilding industry, i.e. $t \geq 10\ mm$, as well as of the yield stress.

Thus, the steel in the case of the STATIC-DYNAMIC models (ASIS 1993 reported in ISSC 2003), with thickness $t = 10\,mm$ and a yield stress equal to 303.1 MPa was selected to represent the Grade 'A' mild steel and the steel in the case of the S1-20 and S2-20 models (DNV 1993), with thickness $t = 20\,mm$ and a yield stress equal to 393 MPa was selected to represent the Grade 'AH' high tensile steel (see Table 2.1, chapter 2 and Appendix A). The scaling of ε_{cr} according to the ratio l_e/t for the selected steels is illustrated in Figure 4.6, chapter 4.

The parts of the ships close to the impact location were finely meshed, i.e. $l_e \cong 50\,mm$ or $2 \leq l_e/t \leq 4$, while far from the impact location coarse meshes, i.e. $l_e > 500\,mm$ were used (see pictures on the bottom of Figure 6.2). It is noted that, the mesh between fine and coarse meshes was gradually changed and the parts with different meshes were tied together with the tie constraint, using the node to surface formulation in Abaqus/Explicit. According to this formulation, the shared nodes between master and slave surfaces are eliminated from the master surface (ABAQUS 2010). Thus, the surfaces with the coarser meshes should be chosen as master surfaces for best accuracy. Note that, ties between surfaces with the same mesh density are also possible. Hence, a smooth transition between the different meshes was achieved, avoiding the formation of poor elements, for example elements with $l_e/t > 10$ and without losing connectivity. The tie constraint was also used to join different parts in the bow model, where the surfaces were free form and more complex, for example between frames, decks and buttocks with hull. However, appropriate partitions in the participated surfaces should have been made, in order to enable tie seams to be created, i.e. generation of nodes and retain surface connectivity (see Figure 6.3).

The edges of the Tankship were considered fixed throughout the simulations. The maximum stresses far from the impact location and close to the fixed boundaries were detected at the upper deck of the struck ship and were below 180 MPa, i.e. well within the elastic region. The rigid part of the bow of the Bulk Carrier, which was coupled with the fore watertight bulkhead, i.e. no relative motion between the two parts, was restricted to move in one direction at a constant speed equal to $6\,m/sec$, in order to derive solutions within reasonable CPU time, avoiding excessive inertial effects at the same time (see also Törnqvist 2003 and Samuelides et al. 2007). A static friction coefficient equal to 0.3 was assumed and used in the full-scale simulations (see e.g. Törnqvist 2003, Ehlers et al. 2008, Alsos et al. 2009, Hogström et al. 2010 and Hogström and Ringsberg 2012).

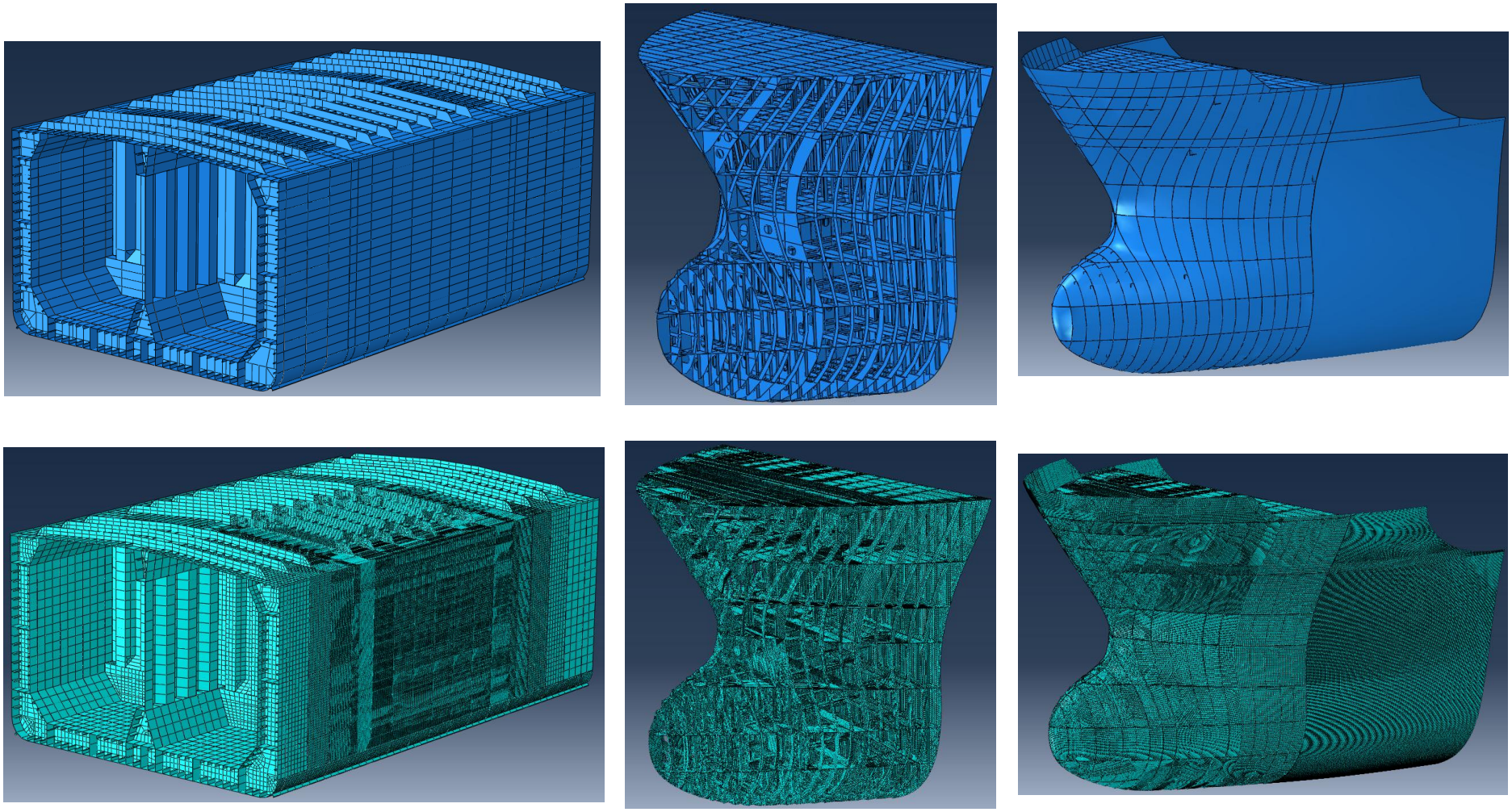

Figure 6.2. Ship geometries (top) and meshed models (bottom)

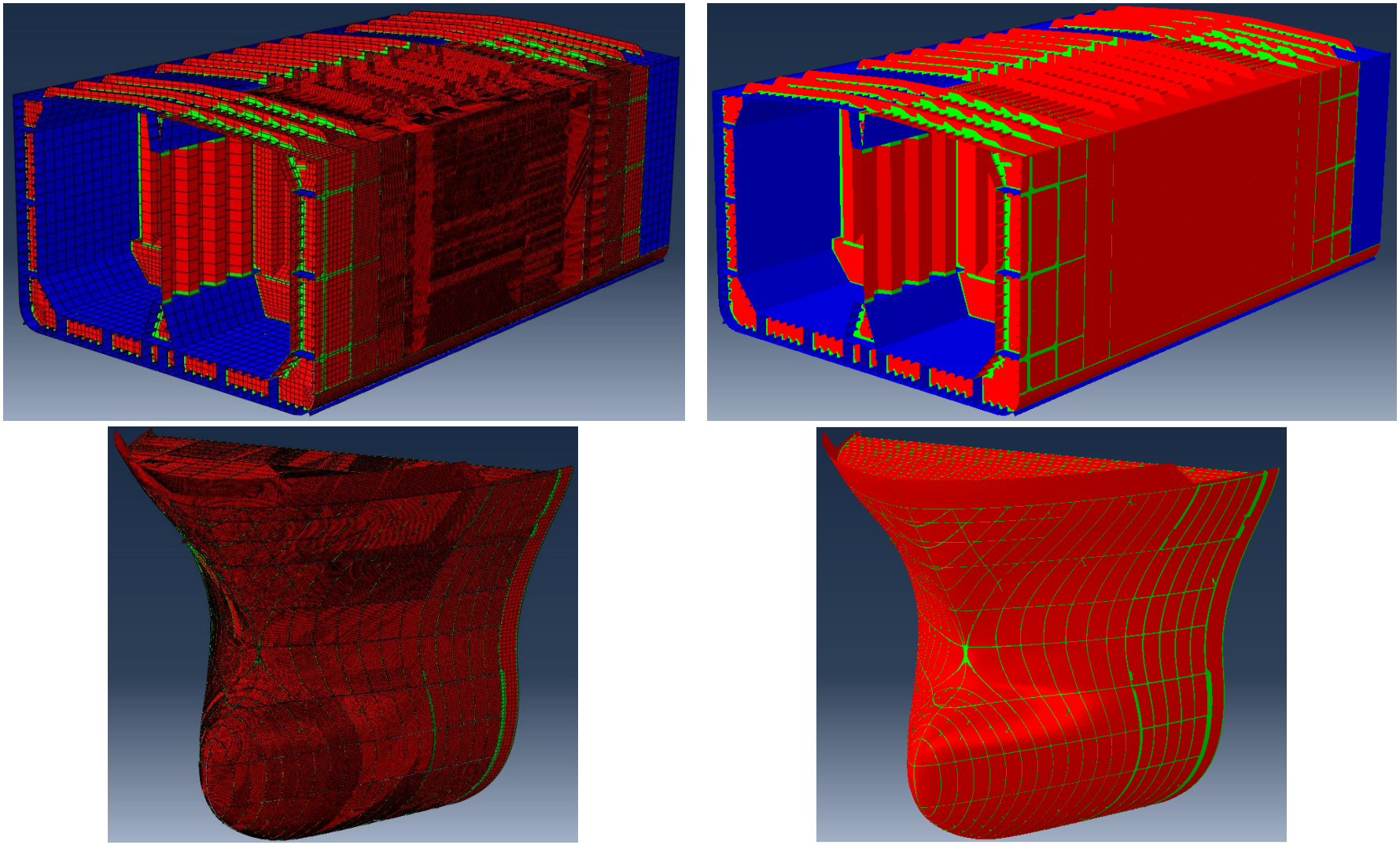

Figure 6.3. Tie seams. Green lines indicate the tied nodes between different surfaces

6.2 Angle of collision 90°

6.2.1 Rigid bow on deformable Tanker side

Figure 6.4 illustrates the force-displacement and energy-displacement curves according to SHEARS and RTCLS rupture criteria in combination with the powerlaw type material curve. Also, Figures 6.5 and 6.6 present the damaged side shell of the Tankship after $8\,m$ of displacement of the rigid bow as predicted by the two criteria.

In Figure 6.4, E_{pl} and E_{fr} are the inelastic strain and frictional dissipation energies respectively and E_{total} the sum of these energies, i.e. the absorbed energy by the Tankship. The relevant forces were derived by differentiating the corresponding energies along the displacement of the rigid bow. The diagrams of Figure 6.4 indicate the points of total force-displacement and total energy-displacement, which correspond to the instants when rupture initiated in the outer shell, inner shell and upper deck of the Tankship respectively, according to SHEARS and RTCLS rupture criteria. Table 6.2 also, summarizes the total force, total energy and displacement values at the aforementioned points and compares the results in each case.

It is observed that, RTCLS criterion predicts rupture of the outer and inner shell of the Tankship at an earlier stage than SHEARS criterion. However, rupture of the upper deck according to RTCLS criterion initiates after almost $2\,m$ of further displacement, contrary to SHEARS criterion's predictions (see Figure 6.4 and Table 6.2). The shape of the bulb is rather similar to the shape of most of the indenters used in the indentation tests (see also Appendix A). Therefore, as already shown in section 5.3 of chapter 5 considering the case of the US Plate model, high stress triaxialities are developed over the contact area between the bow and the side shell, i.e. $T > 1/\sqrt{3}$, so that RTCLS criterion is activated sooner. On the other hand, the shape of the stem, which comes into contact with the upper deck of the Tankship, is similar to the shape of a wedge. According to the analysis presented in section 5.3 and the results in the cases of the cutting tests (see sub-sections 5.2.3 and 5.2.8, chapter 5), it has been found that for triaxialities below zero, where shearing is dominant, RTCLS criterion tends to overestimate the initiation of tearing of the plates. As a result, RTCLS criterion predicts tearing of the upper deck at a later stage. This difference is also obvious in the force-displacement and energy-displacement diagrams in Figure 6.4, between 5-7 m of displacement. An amount of energy almost 48% greater than in the case of SHEARS criterion is absorbed by the Tankship structure, before tearing of the upper deck (see Table 6.2). It is noted that, in both cases, the rigid stem of the Bulk Carrier comes into contact with the upper deck of the Tankship at approximately $3\,m$ of displacement. From Figures 6.5 and 6.6 one may observe that prediction of the deformation pattern of the damaged side of the struck ship at the end of the simulation, with respect to the two criteria, is quite the same. However, tearing of the upper deck is more extensive in the case of SHEARS criterion.

Table 6.2. Rigid bow-Angle of collision 90°. Comparison of numerical values of force, energy and displacement for each rupture criterion at damage points

	SHEARS			RTCLS		
Outer shell rupture initiation (force peak)	$F_1(MN)$	$E_1(MJ)$	$U_1(m)$	$F_1(MN)$	$E_1(MJ)$	$U_1(m)$
	27.7	13.3	1.053	18.6	6.3	0.707
	$F_1(MN)$ differ.		$E_1(MJ)$ differ.		$U_1(m)$ differ.	
	38.9%		71.9%		39.4%	
Inner shell rupture initiation	$F_2(MN)$	$E_2(MJ)$	$U_2(m)$	$F_2(MN)$	$E_2(MJ)$	$U_2(m)$
	25.6	44.4	2.820	17.1	25.5	2.268
	$F_2(MN)$ differ.		$E_2(MJ)$ differ.		$U_2(m)$ differ.	
	40.1%		54.1%		21.7%	
Upper deck rupture initiation	$F_3(MN)$	$E_3(MJ)$	$U_3(m)$	$F_3(MN)$	$E_3(MJ)$	$U_3(m)$
	45.5	126.1	5.321	46.6	205.4	7.332
	$F_3(MN)$ differ.		$E_3(MJ)$ differ.		$U_3(m)$ differ.	
	-2.3%		-47.8%		-31.8%	

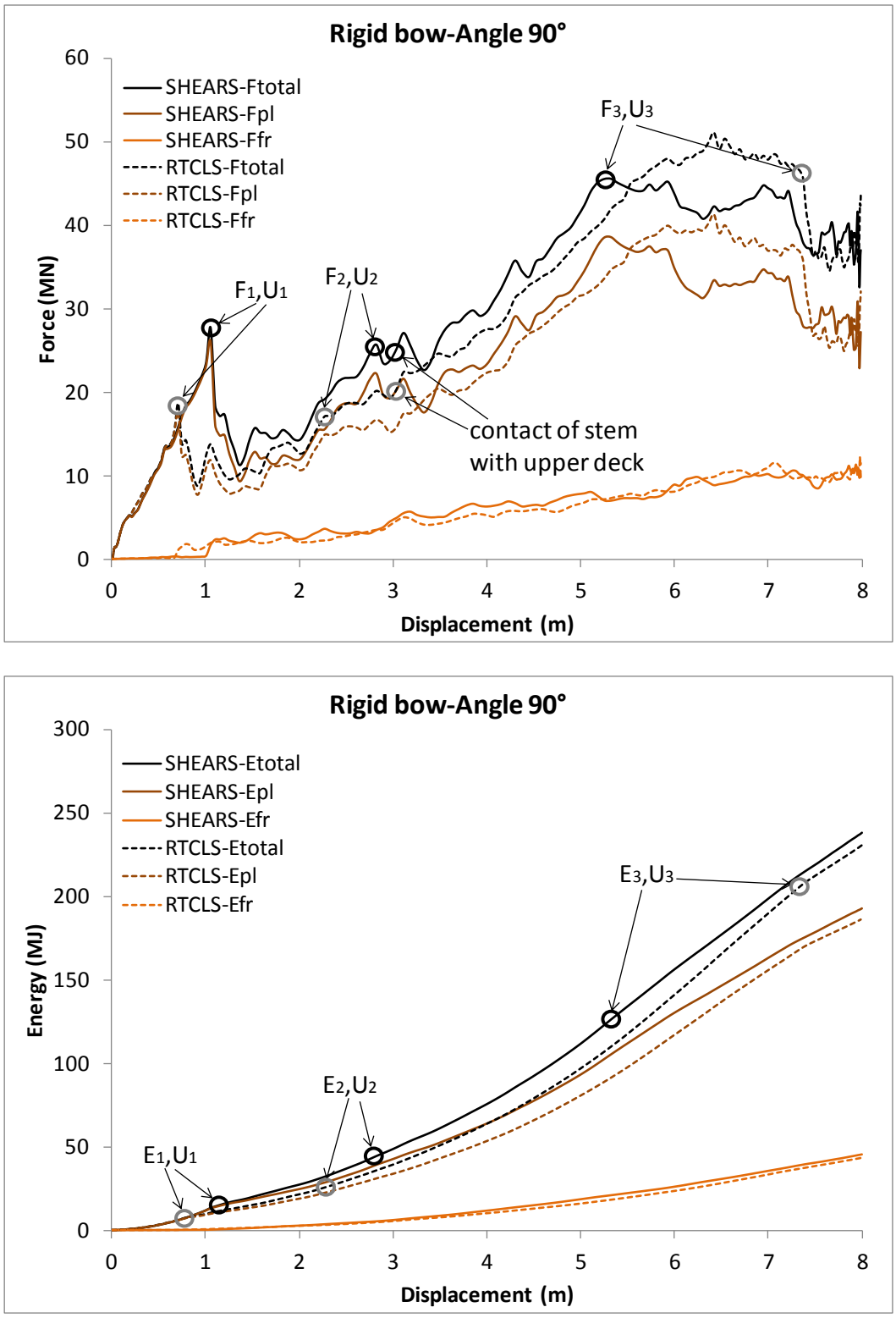

Figure 6.4. Rigid bow-Angle of collision 90°. Force and energy-displacement curves. Prediction of rupture according to SHEARS and RTCLS rupture criteria in combination with the powerlaw type material curve. E_{pl}: inelastic strain energy, E_{fr}: frictional dissipation energy, $E_{total} = E_{pl} + E_{fr}$ (similarly with the forces) (black circle: SHEARS criterion, grey circle: RTCLS criterion)

SHEARS

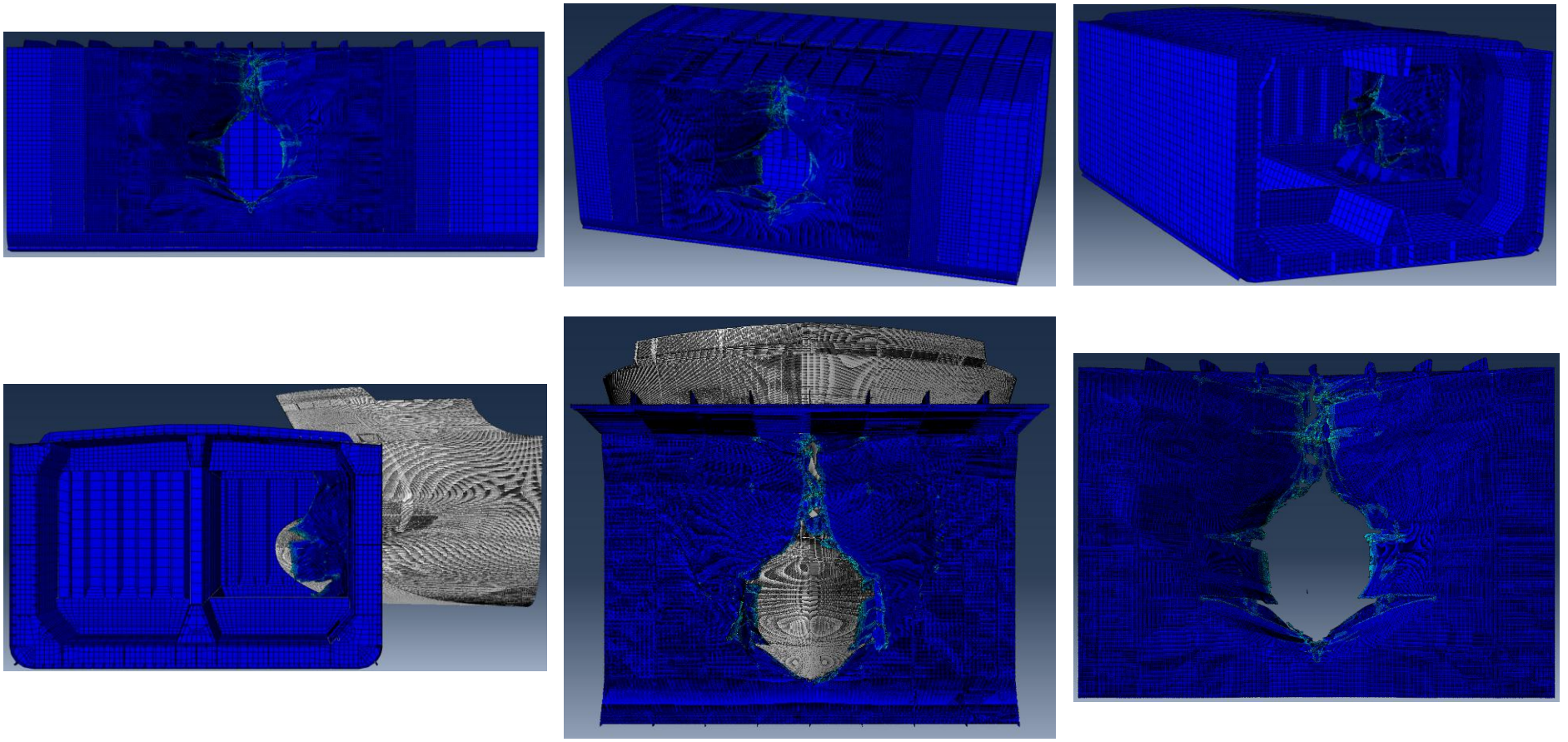

Figure 6.5. Rigid bow-Angle of collision 90°. Representation of damage according to SHEARS rupture criterion

RTCLS

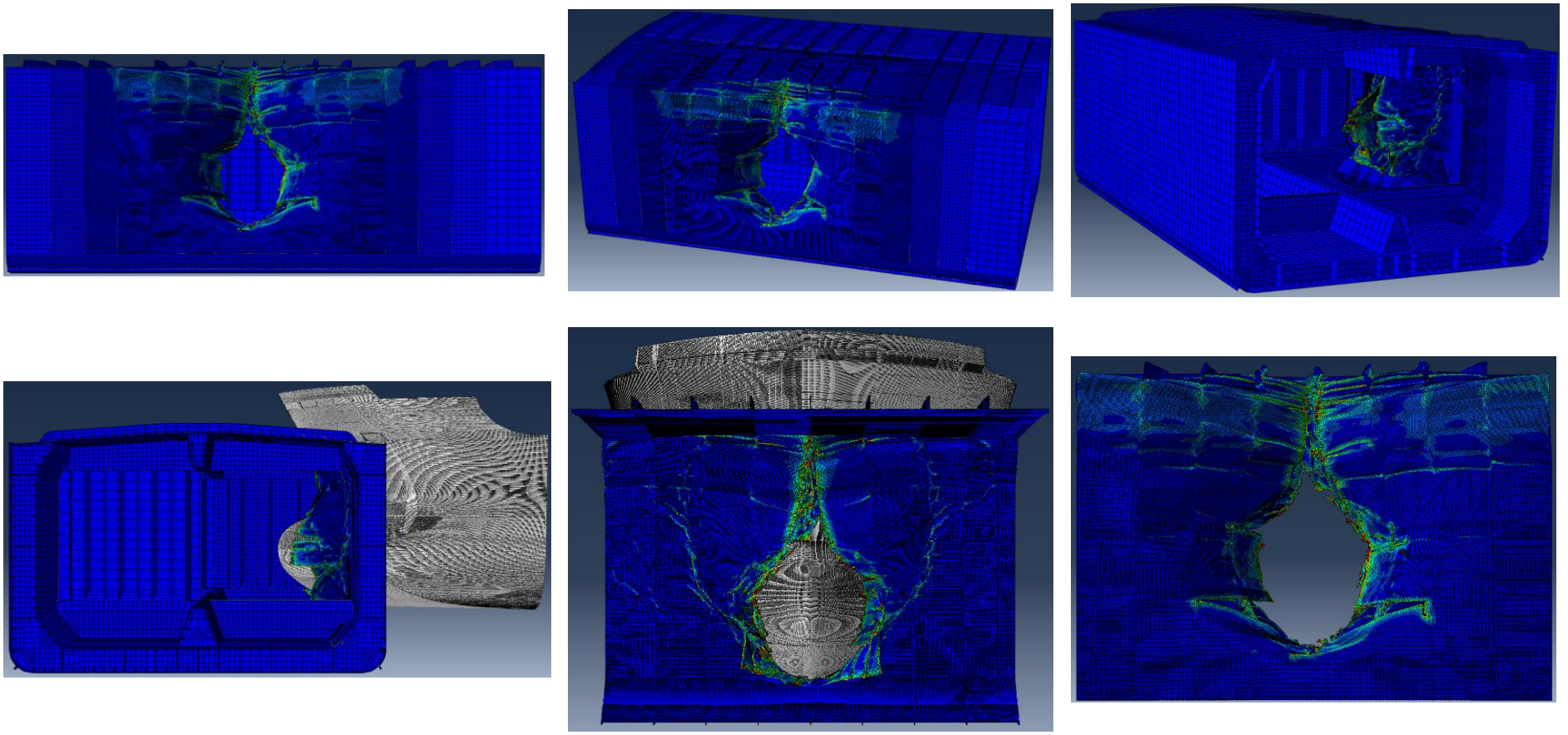

Figure 6.6. Rigid bow-Angle of collision 90°. Representation of damage according to RTCLS rupture criterion

6.2.2 Deformable bow on rigid Tanker side

Figure 6.7 illustrates the force-displacement and energy-displacement curves according to SHEARS and RTCLS rupture criteria in combination with the powerlaw type material curve. Moreover, Figure 6.8 presents the deformation pattern of the bow after 8 m of displacement of the rigid part of the bow towards the rigid Tanker side as predicted by the two criteria.

Following the analysis in sub-section 6.2.1 in Figure 6.7, E_{pl}-Bulb and E_{pl}-Stem are the inelastic strain energies with respect to the bulb and the stem sections of the Bulk Carrier. $E_{pl_{total}}$ is the sum of these energies and E_{total} the sum of $E_{pl_{total}}$ and frictional dissipation energy, i.e. E_{fr}. Note that, the bulb section is considered as the part of the Bulk Carrier up to the fourth deck and the upper structure is related to the stem section (see Figure 6.2). Sets of the aforementioned sections were created, in order to estimate the inelastic or structural energy absorbed by the corresponding structural components. Herein, the relevant forces are also obtained by differentiating the corresponding energies along the displacement of the rigid part of the bow.

According to Figure 6.7, it is observed that results with respect to the two criteria are very close. In addition, both criteria predict the same deformation pattern of the striking ship (see Figure 6.8). In Figure 6.7, the fluctuations of the total force approximately every 600 mm of displacement, i.e. the distance between the frames of the bow, is due to the crushing, i.e. buckling and folding, of the structure between the corresponding frames (see also Figure 6.8). In particular, this happens at the points where the force drops and troughs are formed. Up to the end of the simulations almost thirteen frames were crushed. However, the consistency of these variations in the total force-displacement curve is slightly changed between 3-5 m of displacement, namely just after the stem came into contact with the upper deck of the Tankship. Moreover, at approximately 4.6 m of displacement where the total force reaches a peak, the stem due to the geometry of the rigid Tanker side started to bend. Interesting is the fact, that even after almost 4 m of further displacement, i.e. from the time the stem initiated to bend, tearing of the stem did not occur. In addition, no rupture in the rest part of the bow occurred. This behaviour may be explained by the fact that, the stiffening system of the bow construction is transverse with no longitudinal stiffeners, which is one of the characteristics of the so called buffer bow design (see also Kitamura 2000 and Endo et al. 2004). Therefore, the bow construction may withstand significant deformation, through the buckling and folding mechanisms, without being breached.

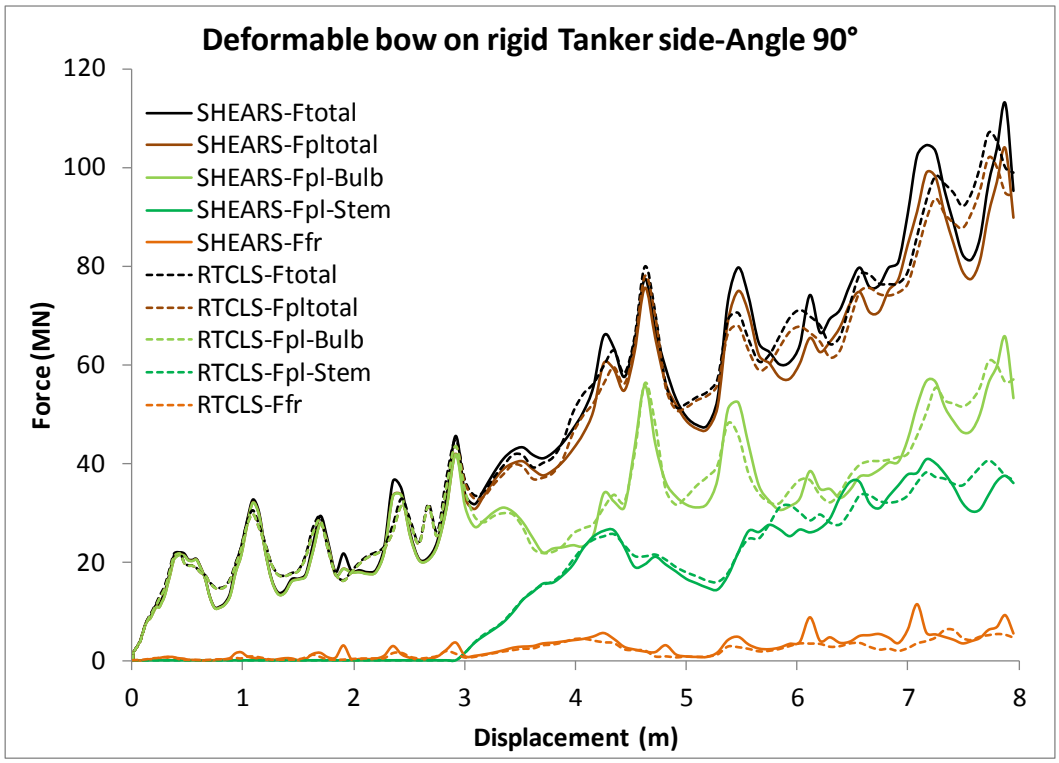

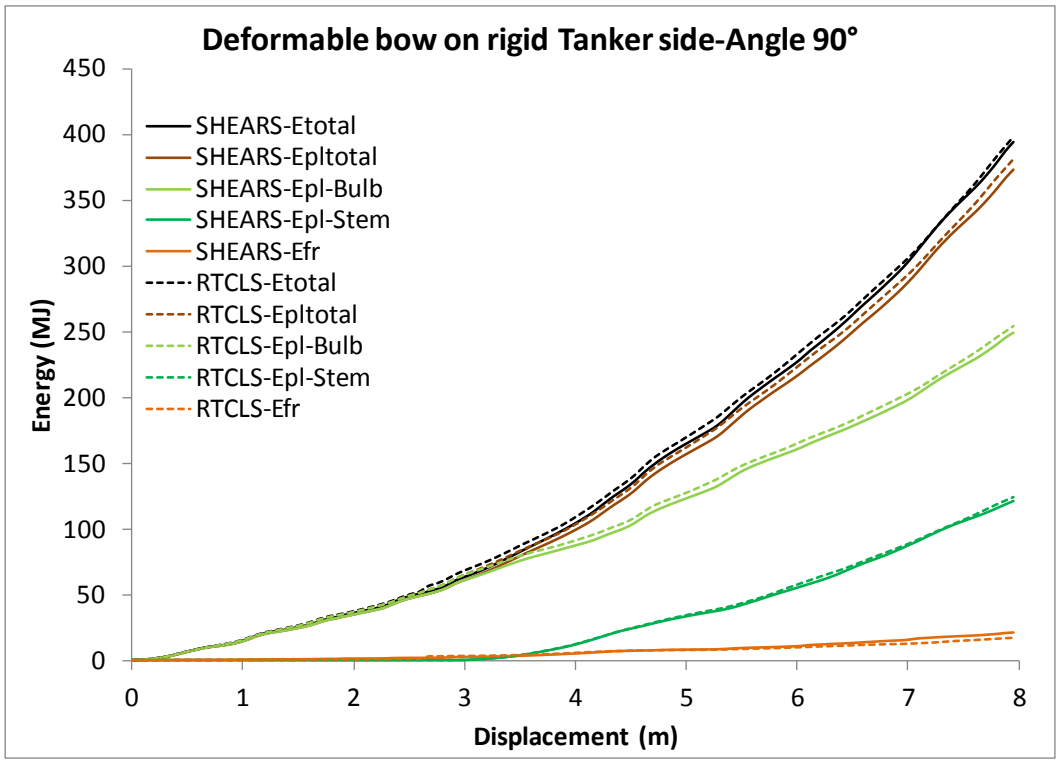

Figure 6.7. Deformable bow on rigid Tanker side-Angle of collision 90°. Force and energy-displacement curves. Prediction of rupture according to SHEARS and RTCLS rupture criteria in combination with the powerlaw type material curve. E_{pl}: inelastic strain energy, E_{fr}: frictional dissipation energy, $E_{pl_{total}} = E_{pl}$-Bulb + E_{pl}-Stem, $E_{total} = E_{pl_{total}} + E_{fr}$ (similarly with the forces)

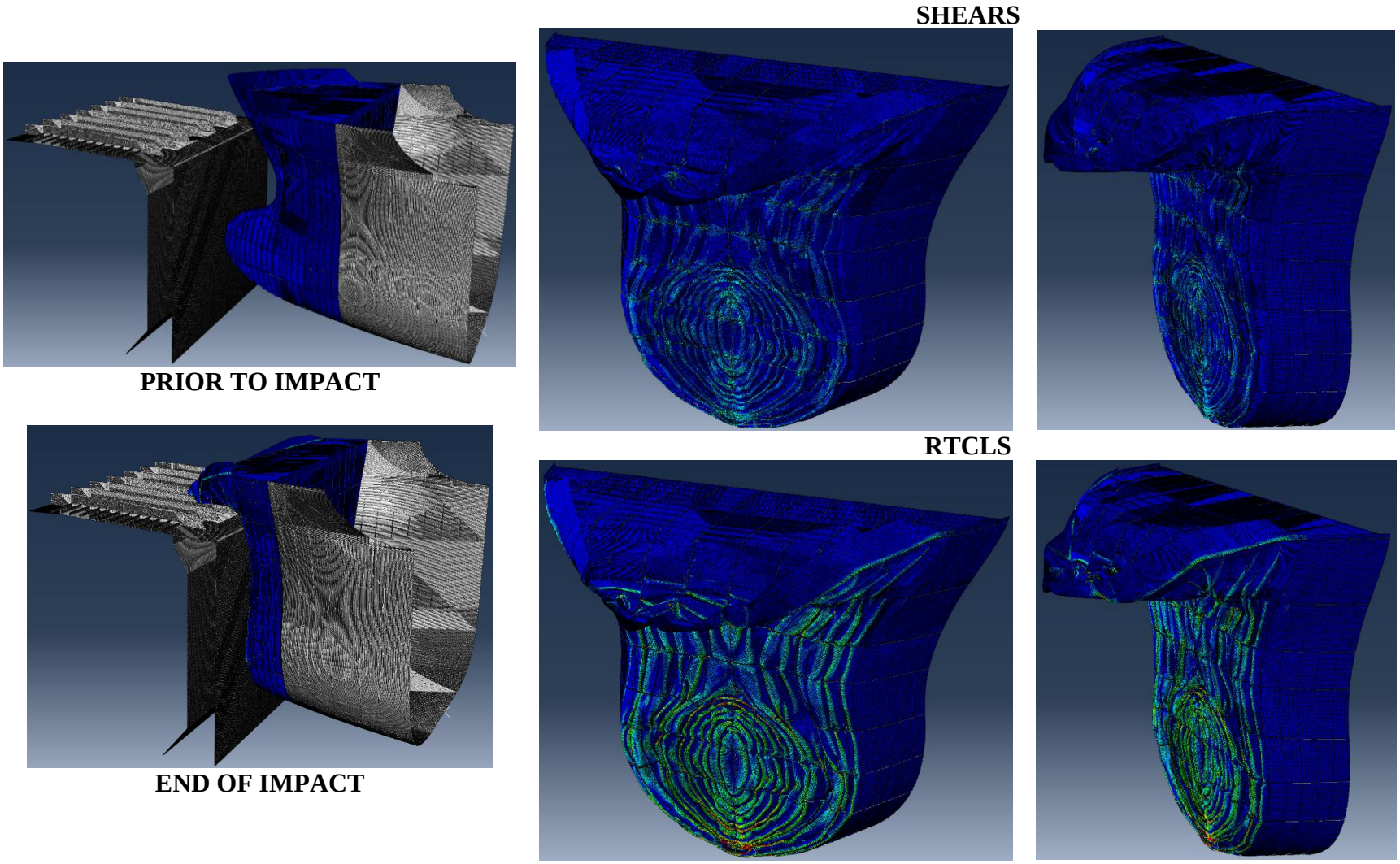

Figure 6.8. Deformable bow on rigid Tanker side-Angle of collision 90°. Representation of damage according to SHEARS and RTCLS rupture criteria

6.2.3 Deformable bow on rigid wall

Figure 6.9 illustrates the force-displacement and energy-displacement curves according to SHEARS and RTCLS rupture criteria in combination with the powerlaw type material curve. Furthermore, Figure 6.10 presents the deformation pattern of the bow after approximately $5\,m$ of displacement of the rigid part of the Bulk Carrier towards the rigid wall as predicted by the two criteria.

The only difference in this collision scenario, with respect to the one analyzed before, is that herein the total area of the bow structure takes part in the impact. Both the bulb and stem sections come into contact with the rigid wall, almost at the beginning of the simulation and finally are crushed. Contrary to the case of the rigid Tanker side, the amount of the energy absorbed by each of the two sections of the bow is comparable (see Figures 6.7 and 6.9). Also in this case, SHEARS and RTCLS criteria yield close results with respect to the force and energy-displacement curves as well as the representation of the deformation pattern (see Figures 6.9 and 6.10).

Once again rupture did not occur in the bow structure. Instead, extensive buckling and folding of the structural components, i.e. decks, frames, buttocks and outer shell is observed and the deformed structure obtains the concertina form (see Figure 6.10).

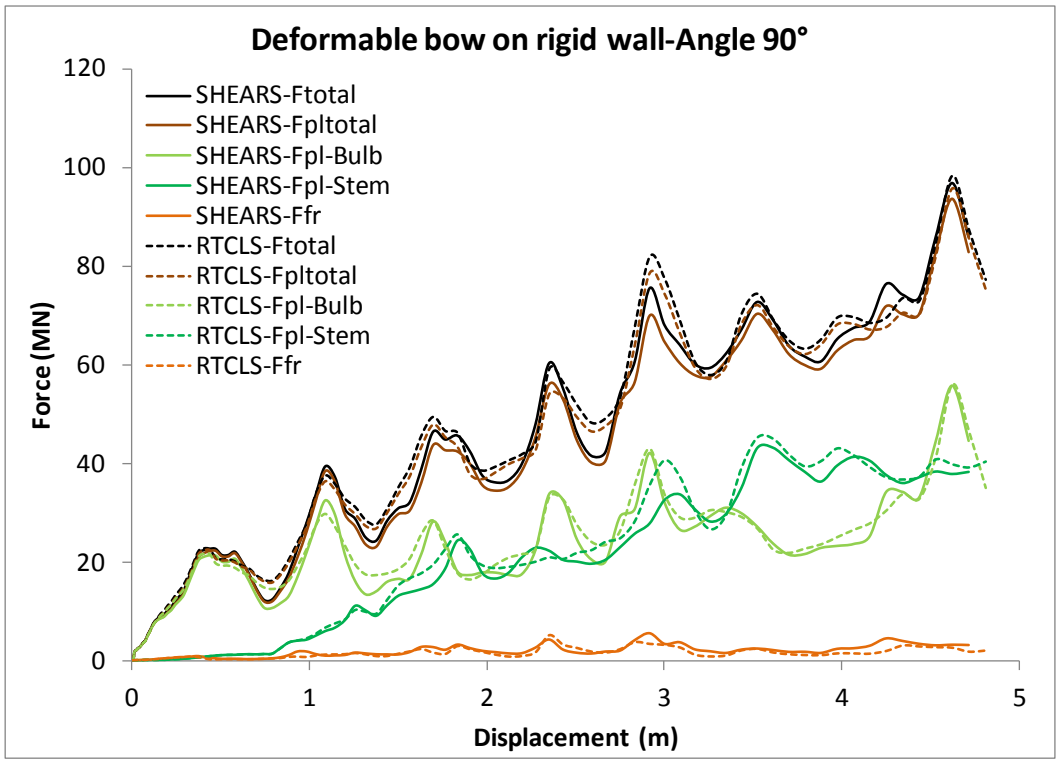

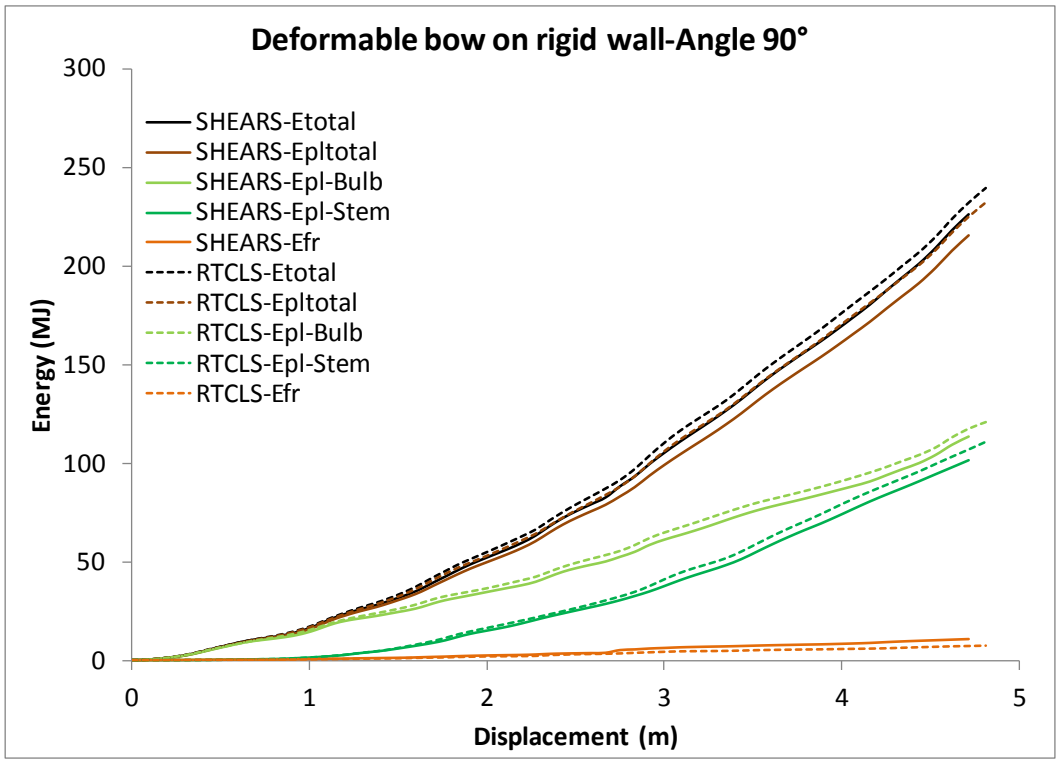

Figure 6.9. Deformable bow on rigid wall-Angle of collision 90°. Force and energy-displacement curves. Prediction of rupture according to SHEARS and RTCLS rupture criteria in combination with the powerlaw type material curve. E_{pl}: inelastic strain energy, E_{fr}: frictional dissipation energy, $E_{pl_{total}} = E_{pl}$-Bulb + E_{pl}-Stem, $E_{total} = E_{pl_{total}} + E_{fr}$ (similarly with the forces)

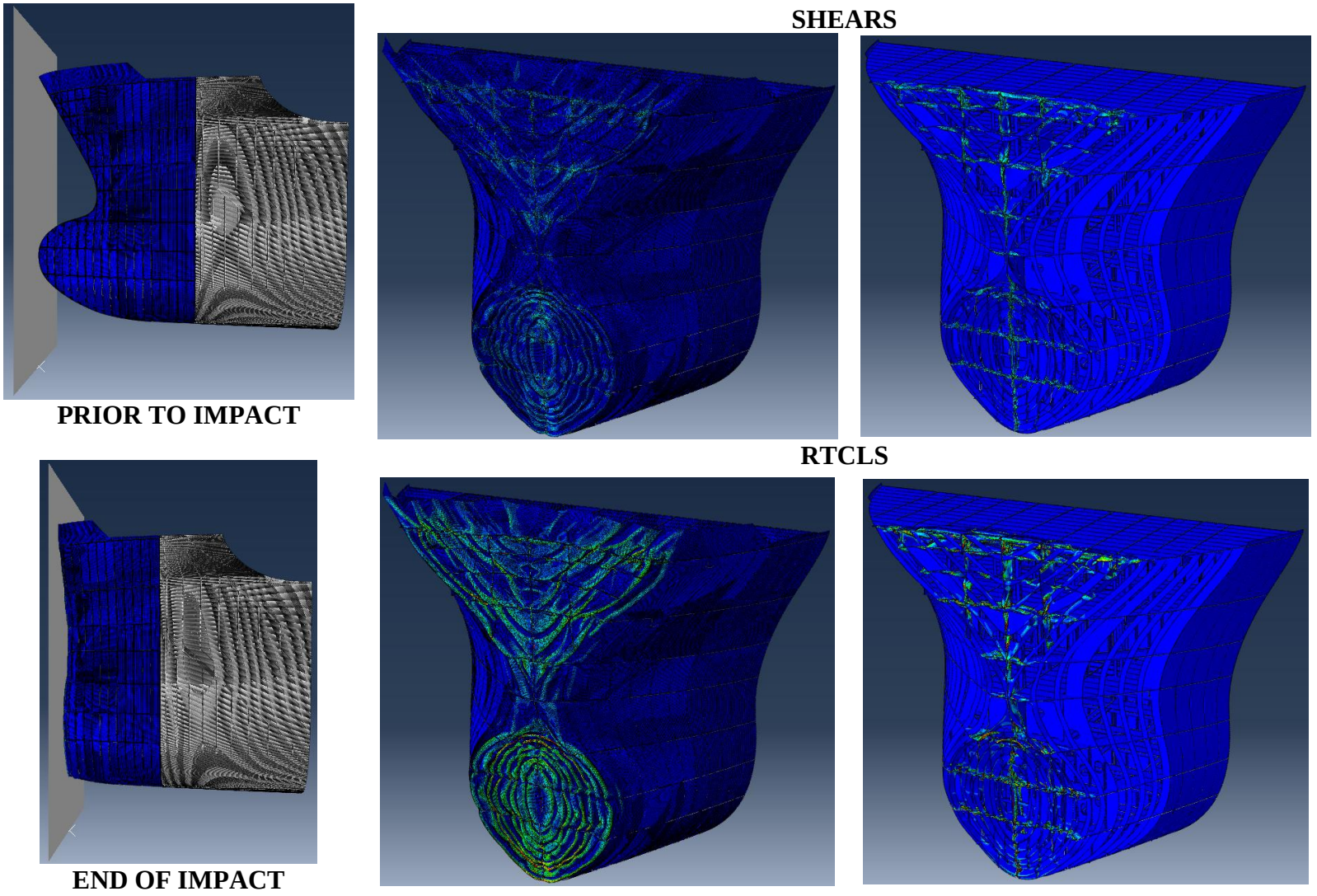

Figure 6.10. Deformable bow on rigid wall-Angle of collision 90°. Representation of damage according to SHEARS and RTCLS rupture criteria

6.2.4 Both ships as deformable structures

Figure 6.11 illustrates the force-displacement and energy-displacement curves according to SHEARS and RTCLS rupture criteria in combination with the powerlaw type material curve. Also, Figures 6.12 and 6.13 present the deformation patterns of both ships as predicted by the two criteria after $8\,m$ of displacement of the rigid part of the bow, i.e. total displacement.

Similarly to the previous collision scenarios, in Figure 6.11 E_{total} is the sum of $E_{pl_{total}}$ and E_{fr}, where $E_{pl_{total}}$ is the inelastic or structural energy of both ships, i.e. the energy dissipated for the plastic deformation of the structures and E_{fr} the frictional dissipation energy during the impact. Also here, the relevant forces were derived by differentiating the corresponding energies along the total displacement that is the displacement of the rigid part of the bow. The total force-displacement and total energy-displacement points depicted in the diagrams of Figure 6.11, in the order of appearance are related with: i) outer shell rupture initiation, ii) outer shell collapse, i.e. the force reaches a peak (F_c), iii) inner shell rupture initiation and iv) upper deck rupture initiation with respect to the Tankship. Table 6.3 summarizes in detail the total force, total energy and displacement values at the aforementioned points and results are compared between the two criteria.

According to the data in Table 6.3, one may observe that RTCLS criterion predicts outer and inner shell rupture of the struck ship at an earlier stage compared to SHEARS. In particular, RTCLS criterion predicts rupture initiation and collapse of the outer shell of the Tankship at almost $600\,mm$ and $900\,mm$ of total displacement respectively, that is approximately $450\,mm$ and $1\,m$ of total displacement respectively sooner compared to SHEARS criterion's predictions (see also sub-section 6.2.1). In addition, inner shell rupture occurs at about $1.8\,m$ of total displacement later with respect to SHEARS criterion. In both cases, the stem of the Bulk Carrier comes into contact with the upper deck of the Tankship at approximately $3\,m$ of total displacement, accompanied by a steep rise in force (see Figure 6.11). At that time according to RTCLS criterion, rupture of the inner shell has already initiated. Rupture initiation at the upper deck in the case of RTCLS criterion is predicted at almost $1.7\,m$ of total displacement later than SHEARS criterion (see also sub-section 6.2.1).

From Figures 6.12 and 6.13, it is obvious that SHEARS criterion predicts a rather different deformation pattern for the bulb of the bow from RTCLS criterion. Specifically, in the case of SHEARS criterion the bulb crushes and folds along a distance almost equal to two frames, i.e. $1200\,mm$, while in the case of RTCLS criterion the bulb is not severely affected and crushing is limited to approximately $300\,mm$. This is attributed to the earlier rupture of the outer shell of the struck ship compared to the case of SHEARS criterion. Therefore, a considerable amount of energy is absorbed by the bulb in the case of SHEARS criterion prior to inner shell rupture, which also explains the significant differences in the predictions between the two criteria. Furthermore, according to SHEARS criterion the stem is slightly affected, after almost $5\,m$ of total displacement, i.e. from the time it first came into contact with the upper deck of the Tankship. The deformation of the stem is more intense when RTCLS criterion is used (see Figures 6.12 and 6.13).

Table 6.3. Both ships deformable-Angle of collision 90°. Comparison of numerical values of force, energy and total displacement for each rupture criterion at damage points

	SHEARS			RTCLS		
Outer shell rupture initiation	$F_1(MN)$	$E_1(MJ)$	$U_1(m)$	$F_1(MN)$	$E_1(MJ)$	$U_1(m)$
	20.0	11.6	1.035	12.3	4.0	0.579
	$F_1(MN)$ differ.		$E_1(MJ)$ differ.		$U_1(m)$ differ.	
	47.6%		97.4%		56.5%	
Outer shell collapse (force peak)	$F_c(MN)$	$E_c(MJ)$	$U_c(m)$	$F_c(MN)$	$E_c(MJ)$	$U_c(m)$
	27.1	29.2	1.835	17.8	8.5	0.883
	$F_c(MN)$ differ.		$E_c(MJ)$ differ.		$U_c(m)$ differ.	
	41.5%		109.5%		70.0%	
Inner shell rupture initiation	$F_2(MN)$	$E_2(MJ)$	$U_2(m)$	$F_2(MN)$	$E_2(MJ)$	$U_2(m)$
	46.2	101.8	4.253	18.5	29.2	2.509
	$F_2(MN)$		$E_2(MJ)$		$U_2(m)$	
	85.6%		110.9%		51.6%	
Upper deck rupture initiation	$F_3(MN)$	$E_3(MJ)$	$U_3(m)$	$F_3(MN)$	$E_3(MJ)$	$U_3(m)$
	42.5	140.2	5.187	50.1	182.6	6.912
	$F_3(MN)$ differ.		$E_3(MJ)$ differ.		$U_3(m)$ differ.	
	-16.4%		-26.3%		-28.5%	

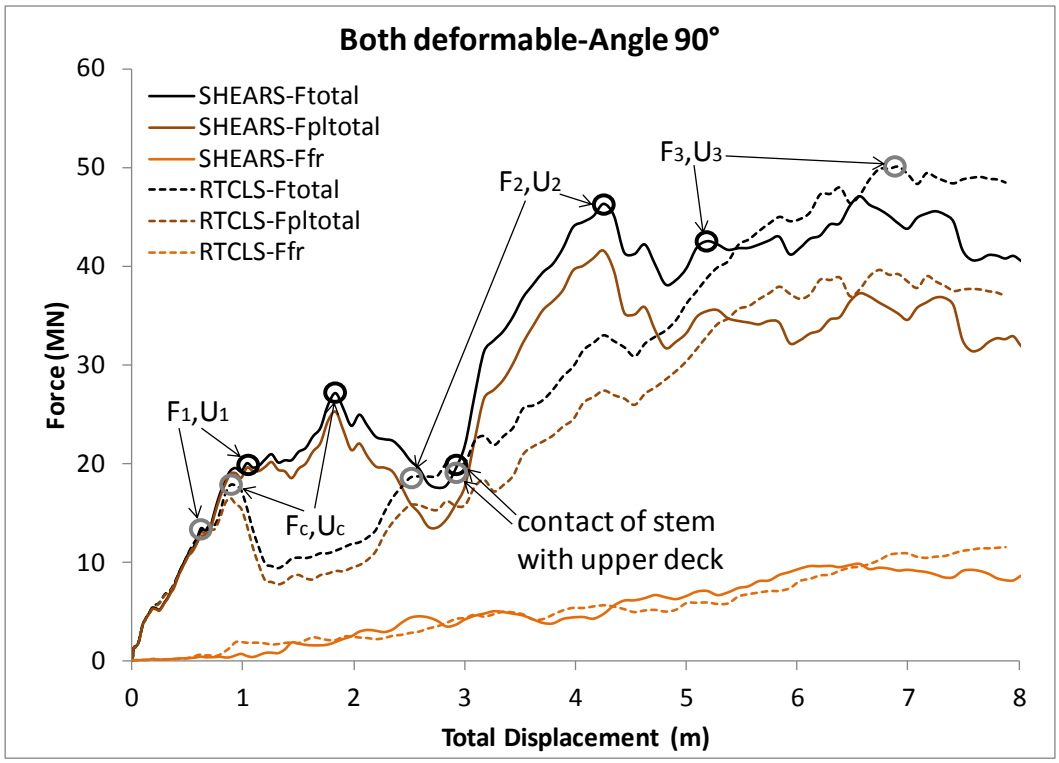

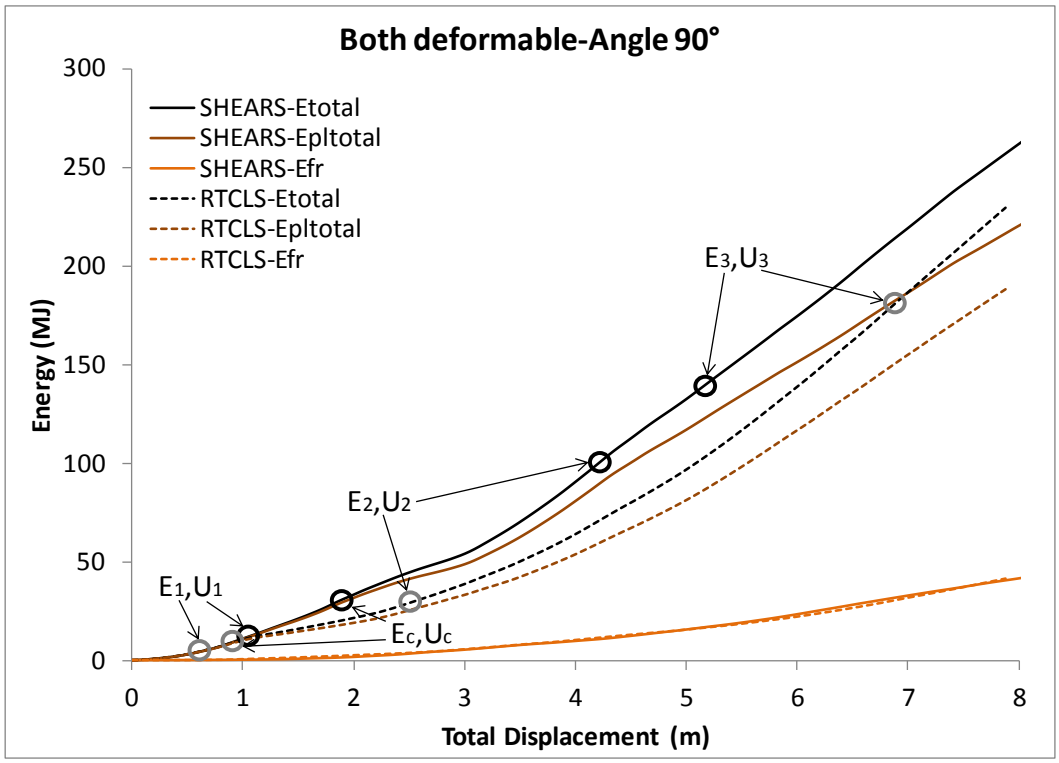

Figure 6.11. Both ships deformable -Angle of collision 90°. Force and energy-displacement curves. Prediction of rupture according to SHEARS and RTCLS rupture criteria in combination with the powerlaw type material curve. $E_{pl_{total}}$: inelastic strain energy, E_{fr}: frictional dissipation energy, $E_{total} = E_{pl_{total}} + E_{fr}$ (similarly with the forces) (black circle: SHEARS criterion, grey circle: RTCLS criterion)

SHEARS

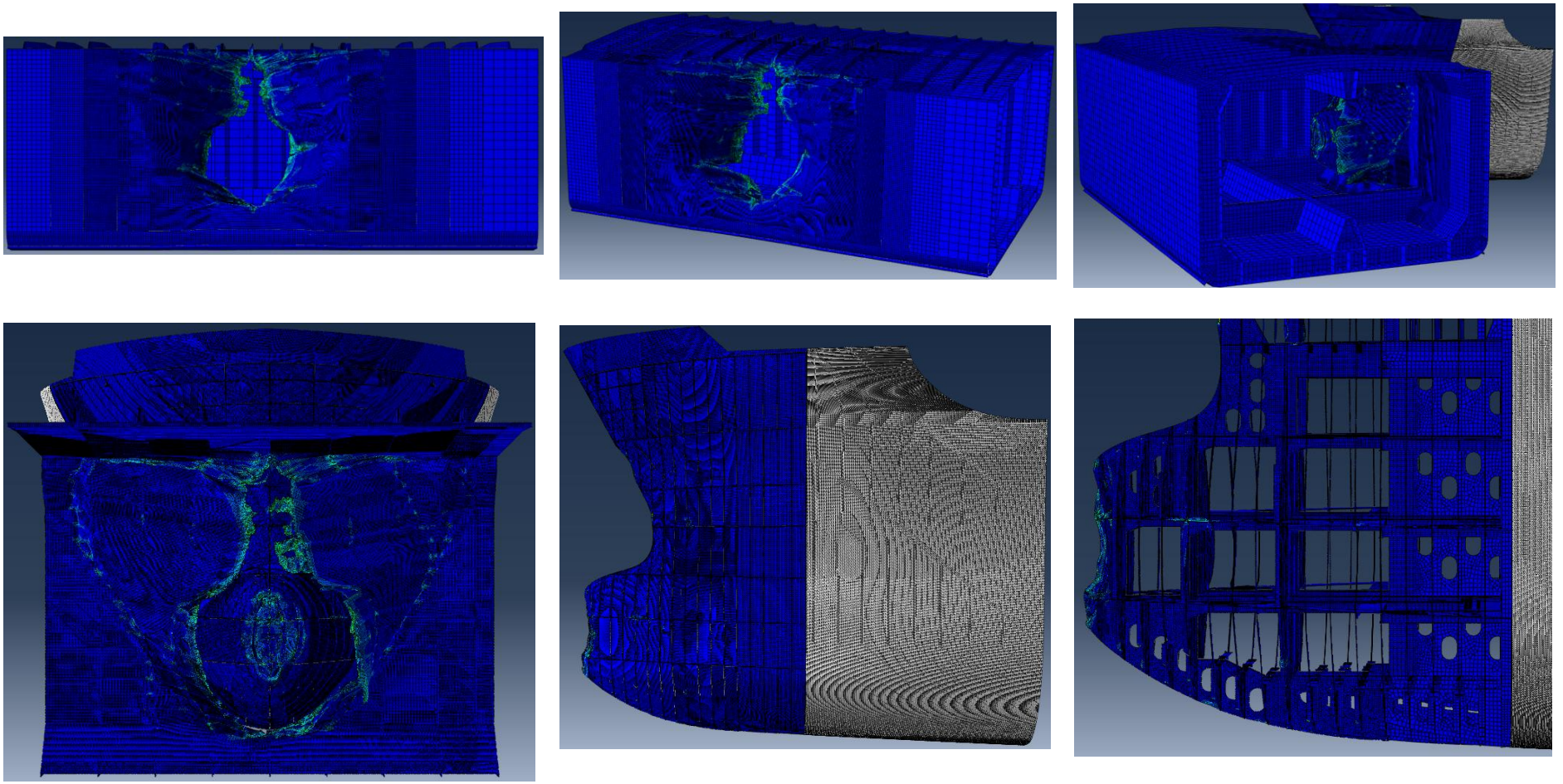

Figure 6.12. Both ships deformable-Angle of collision 90°. Representation of damage according to SHEARS rupture criterion

RTCLS

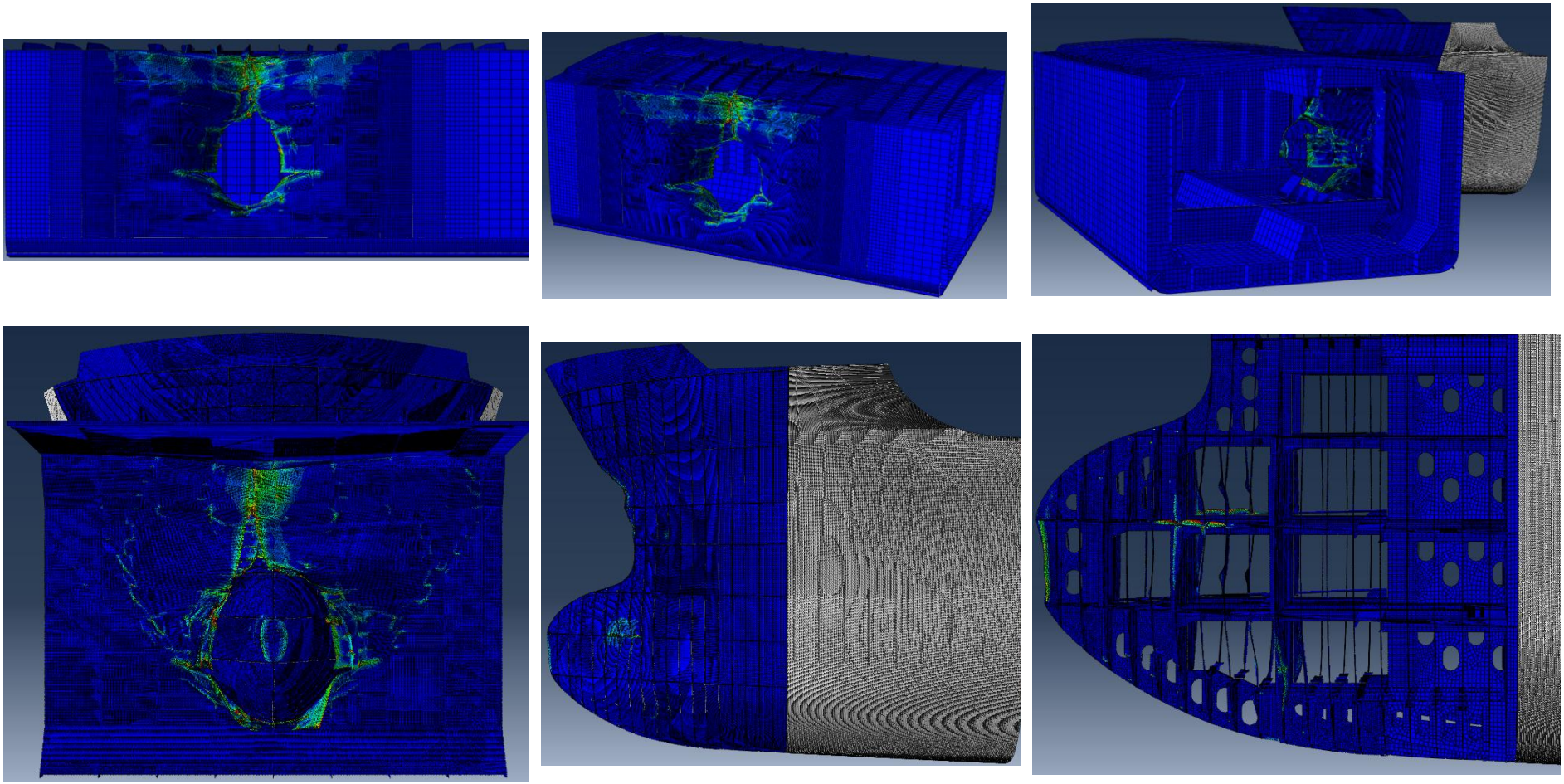

Figure 6.13. Both ships deformable -Angle of collision 90°. Representation of damage according to RTCLS rupture criterion

6.3 Angle of collision 50°

6.3.1 Rigid bow on deformable Tanker side

Figure 6.14 illustrates the force-displacement and energy-displacement curves according to SHEARS and RTCLS rupture criteria in combination with the powerlaw type material curve. Also, Figures 6.15 and 6.16 present the damaged side shell of the Tankship after 10 m of displacement of the rigid bow as predicted by the two criteria. It is noted that, in all cases of collision scenarios included in section 6.3 where the angle of collision is 50°, the force and energy quantities were derived in the direction of the striking ship, which is one of the three global directions in ABAQUS environment. The aim of the present simulation is to investigate the dependency of the structural energy versus penetration relationship from the loading angle, i.e. the angle of attack of the striking ship with respect to the longitudinal direction of the struck ship.

Following the same concept as in the analyses in the previous section, the total force-displacement and total energy-displacement points, which are related to the initiation of rupture at the inner shell, outer shell and upper deck respectively of the Tankship, are shown in Figure 6.14. The respective values are summarized in Table 6.4. RTCLS criterion, shows a similar behaviour to the one described in sub-section 6.2.1, i.e. the case with a rigid bow and a collision angle equal to 90° and predicts rupture of the outer shell sooner than SHEARS criterion and of the upper deck of the Tankship at a later stage. However, in the present collision scenario the two criteria yield closer results. Moreover, both criteria predict rupture of the inner shell at the same displacement, exhibiting also almost equal forces and absorbed energy (see Figure 6.14 and Table 6.4).

At approximately 2.6 m of displacement, the stem of the rigid bow comes into contact with the upper deck and the side of the Tankship and as the simulation progresses the contact area between the two ships becomes greater. This is also proved by the steep increase in the forces in Figure 6.14. Although rupture of inner shell occurs virtually at 4.3 m of displacement, the forces keep on increasing up to 6.3 m of displacement where they reach a maximum. Beyond that point, extensive buckling and finally, after a few millimeters of further displacement, tearing of the upper deck occurs (see Figures 6.15 and 6.16). However, the tanker side seems to withstand further loading, as a rather small drop in the force is observed while it remains almost constant up to the end of the simulation. In addition, in the case of RTCLS criterion the force starts to rise again after 8 m of displacement (see Figure 6.14). Due to the relative position of the two ships, i.e. 50° angle of collision, a larger proportion of the surfaces of the two vessels comes into contact and plastic strains are developed in a large area. This phenomenon is also evident in the deformation pattern of the Tankship side as predicted by the two rupture criteria and is presented in Figures 6.15 and 6.16. Representation of damage is very similar in both cases.

Table 6.4. Rigid bow-Angle of collision 50°. Comparison of numerical values of force, energy and displacement for each rupture criterion at damage points

	SHEARS			RTCLS		
Outer shell rupture initiation (force peak)	$F_1(MN)$	$E_1(MJ)$	$U_1(m)$	$F_1(MN)$	$E_1(MJ)$	$U_1(m)$
	29.2	21.7	1.565	22.7	13.0	1.200
	$F_1(MN)$ differ.		$E_1(MJ)$ differ.		$U_1(m)$ differ.	
	24.9%		50.3%		26.4%	
Inner shell rupture initiation	$F_2(MN)$	$E_2(MJ)$	$U_2(m)$	$F_2(MN)$	$E_2(MJ)$	$U_2(m)$
	59.9	120.8	4.253	57.9	116.1	4.253
	$F_2(MN)$ differ.		$E_2(MJ)$ differ.		$U_2(m)$ differ.	
	3.4%		4.0%		0.0%	
Upper deck rupture initiation	$F_3(MN)$	$E_3(MJ)$	$U_3(m)$	$F_3(MN)$	$E_3(MJ)$	$U_3(m)$
	61.3	331.4	7.491	62.5	346.4	8.095
	$F_3(MN)$ differ.		$E_3(MJ)$ differ.		$U_3(m)$ differ.	
	-1.9%		-4.4%		-7.7%	

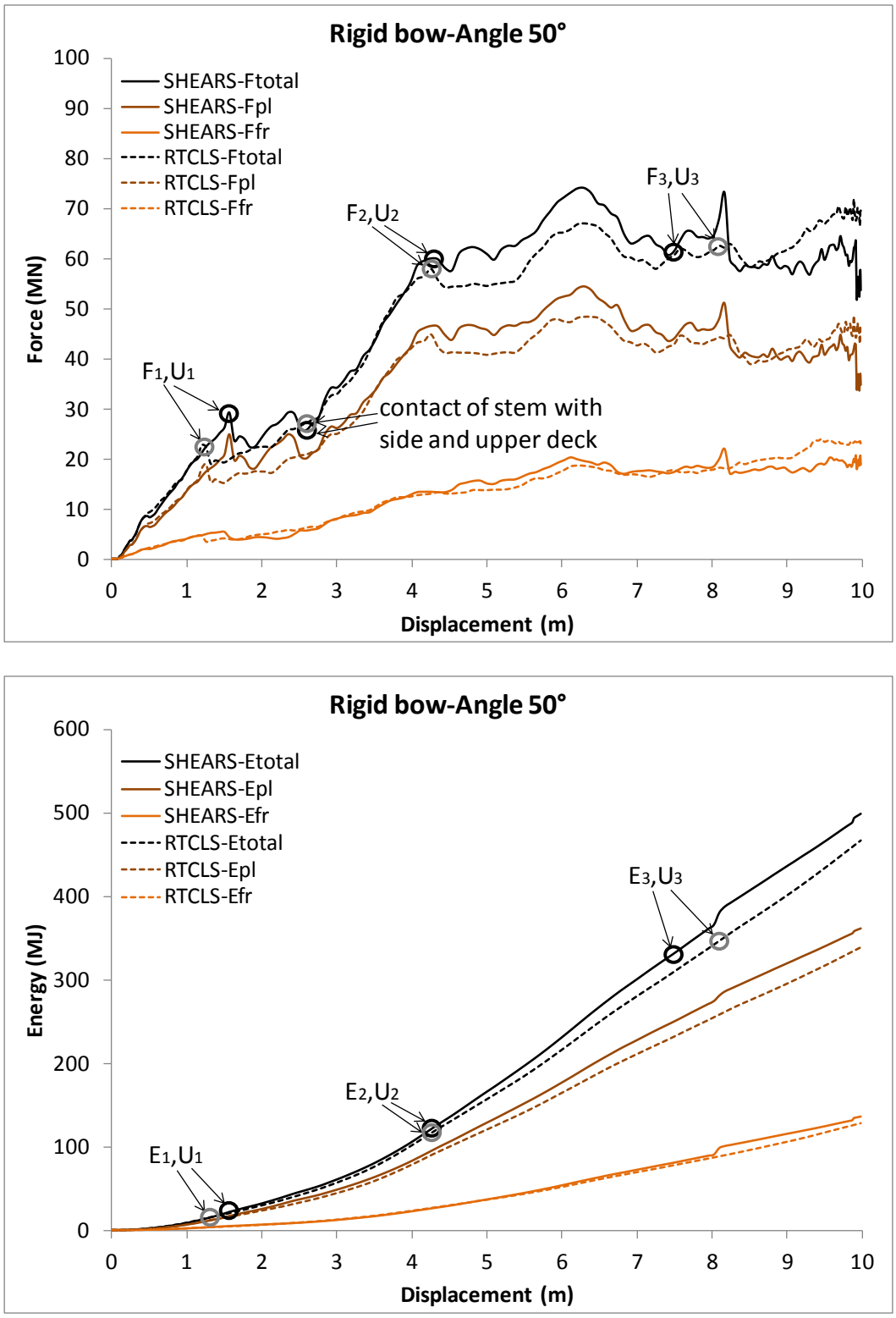

Figure 6.14. Rigid bow-Angle of collision 50°. Force and energy-displacement curves. Prediction of rupture according to SHEARS and RTCLS rupture criteria in combination with the powerlaw type material curve. E_{pl}: inelastic strain energy, E_{fr}: frictional dissipation energy, $E_{total} = E_{pl} + E_{fr}$ (similarly with the forces) (black circle: SHEARS criterion, grey circle: RTCLS criterion)

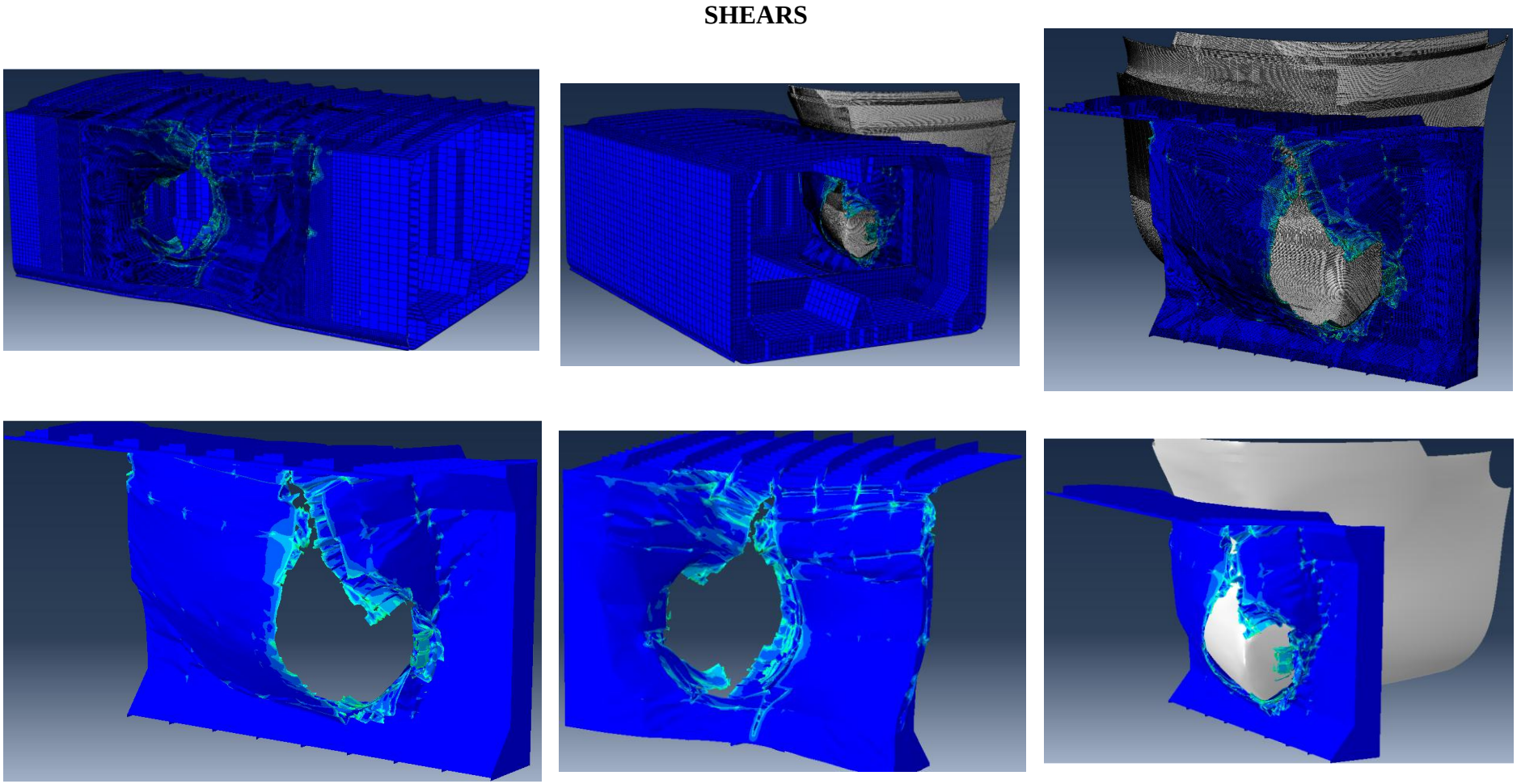

Figure 6.15. Rigid bow-Angle of collision 50°. Representation of damage according to SHEARS rupture criterion

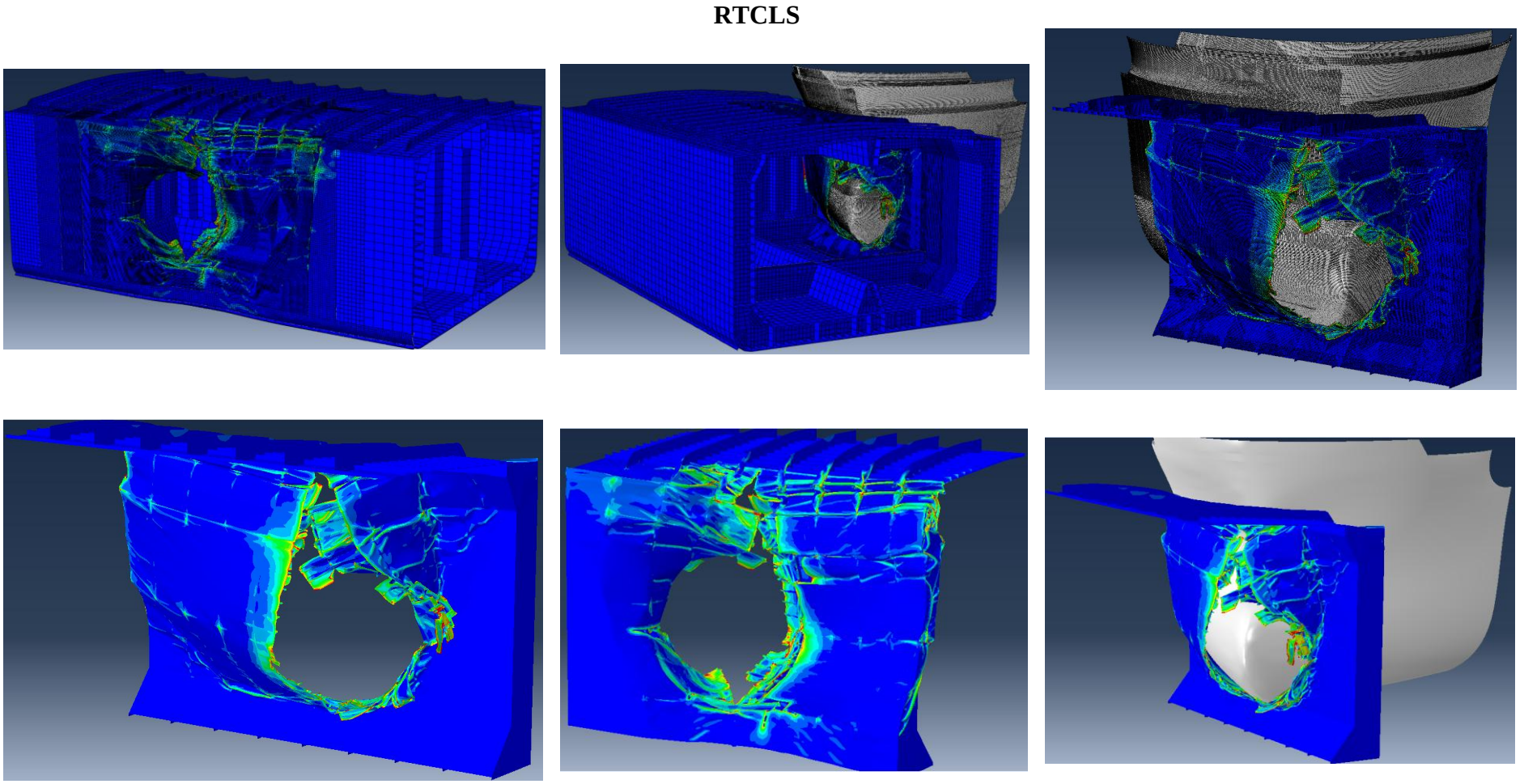

Figure 6.16. Rigid bow-Angle of collision 50°. Representation of damage according to RTCLS rupture criterion

6.3.2 Deformable bow on rigid Tanker side

Figure 6.17 illustrates the force-displacement and energy-displacement curves according to SHEARS and RTCLS rupture criteria in combination with the powerlaw type material curve. Furthermore, Figure 6.18 presents the deformation pattern of the bow after $4\,m$ of displacement of the rigid part of the bow towards the rigid Tanker side as predicted by the two criteria. It is noted that, in the collision scenarios of this and the next sub-section, where the bow is driven towards the rigid Tanker side and a rigid wall with a 50° angle of collision, the displacement is limited to $4\,m$ due to the restrictions in the boundary conditions, i.e. for further displacement the rigid part of the bow would come into contact with the rigid Tanker side or rigid wall, respectively. The aim of the collision scenarios in sub-sections 6.3.2 and 6.3.3 is to calculate the stiffness of the bow in different directions.

From Figures 6.17 and 6.18, one may observe that results according to the two criteria are almost identical with respect to the force and energy-displacement curves as well as the prediction of the deformation pattern of the deformable bow. At approximately $1.3\,m$ of displacement, the front part of the bulb section that is up to the third frame, initiates to buckle and bend, which results in the slight decrease of the forces for about $400\,mm$ of displacement, as can be seen in Figure 6.17. As the simulation progresses, the surface of the bulb section which comes into contact with the rigid Tanker side and consequently the force are increased. In addition, at almost $2.6\,m$ of displacement the stem section of the bow comes into contact with the rigid Tanker side. This is also depicted in Figure 6.17 with the increase of the dark green curve, which is related to the force with respect to the stem section, i.e. F_{pl}-Stem. Beyond that point and up to the end of the simulation the forces as well as the corresponding energies, except in the case of the bulb section, steadily increase. In the bulb location, due to the excessive buckling and bending of the structural components, including almost 10 frames, 3 decks and the central buttock, the force with respect to the bulb section, i.e. F_{pl}-Bulb in Figure 6.17 drops. The latter force starts to increase again after $600\,mm$ of further displacement, as the back part of the bulb section, which was intact up to this point, comes into contact with the rigid Tanker side. Thus, the resistance of the bulb section increases again (see Figures 6.17 and 6.18).

In Figure 6.18 it is observed that, almost the entire surface of the right or starboard side of the hull up to the fore watertight bulkhead comes into contact with the rigid Tanker side. However, the most part of the total energy is absorbed by the bulb section, which is excessively deformed, due to the relative position of the two bodies, i.e. the bow and the rigid Tanker side (see Figures 6.17 and 6.18). Moreover, no rupture in the bulb and stem sections of the deformable bow was detected (see also sub-section 6.2.2 and Figure 6.18).

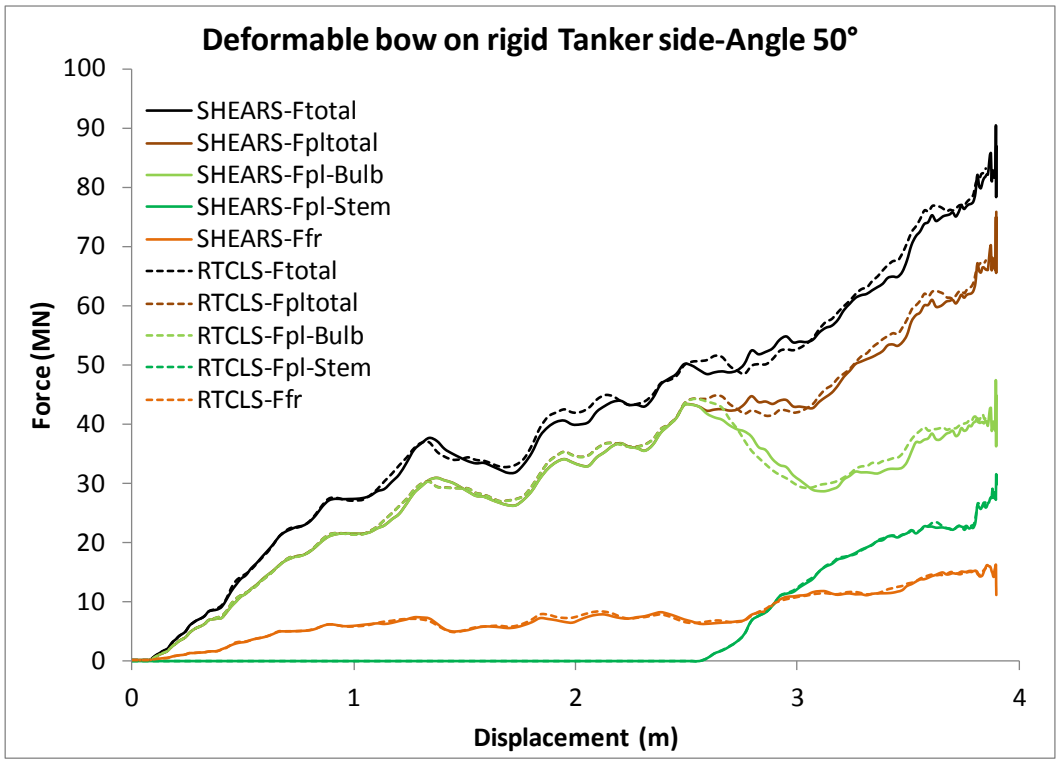

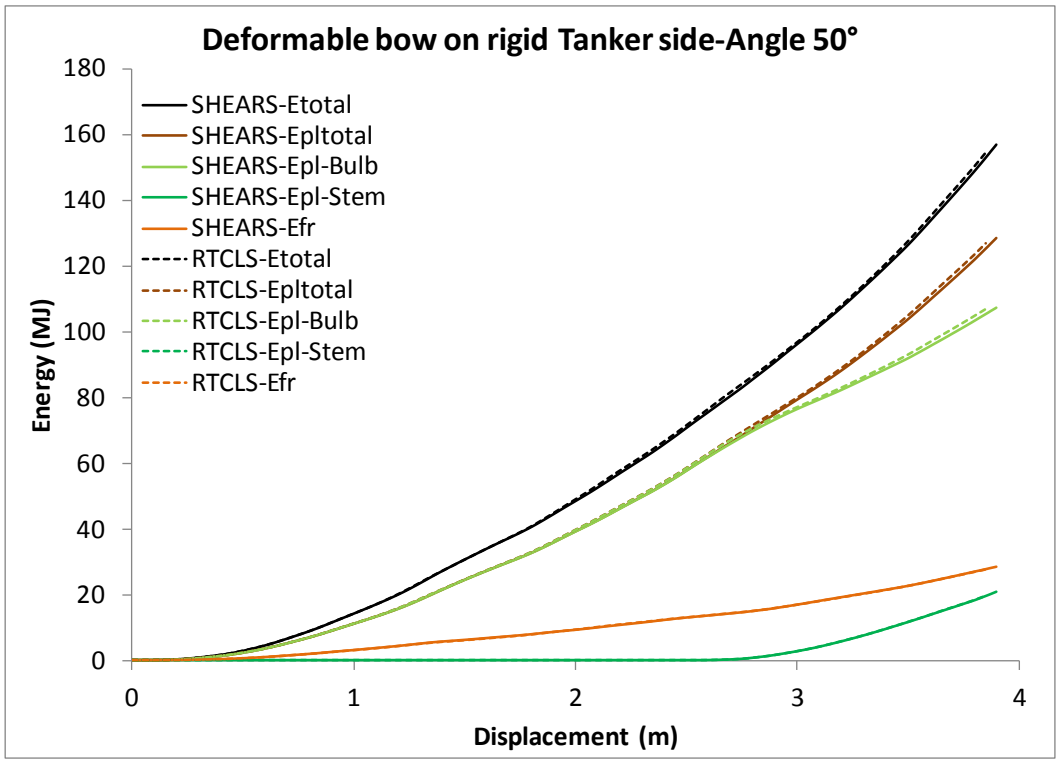

Figure 6.17. Deformable bow on rigid Tanker side-Angle of collision 50°. Force and energy-displacement curves. Prediction of rupture according to SHEARS and RTCLS rupture criteria in combination with the powerlaw type material curve. E_{pl}: inelastic strain energy, E_{fr}: frictional dissipation energy, $E_{pl_{total}} = E_{pl}$-Bulb + E_{pl}-Stem, $E_{total} = E_{pl_{total}} + E_{fr}$ (similarly with the forces)

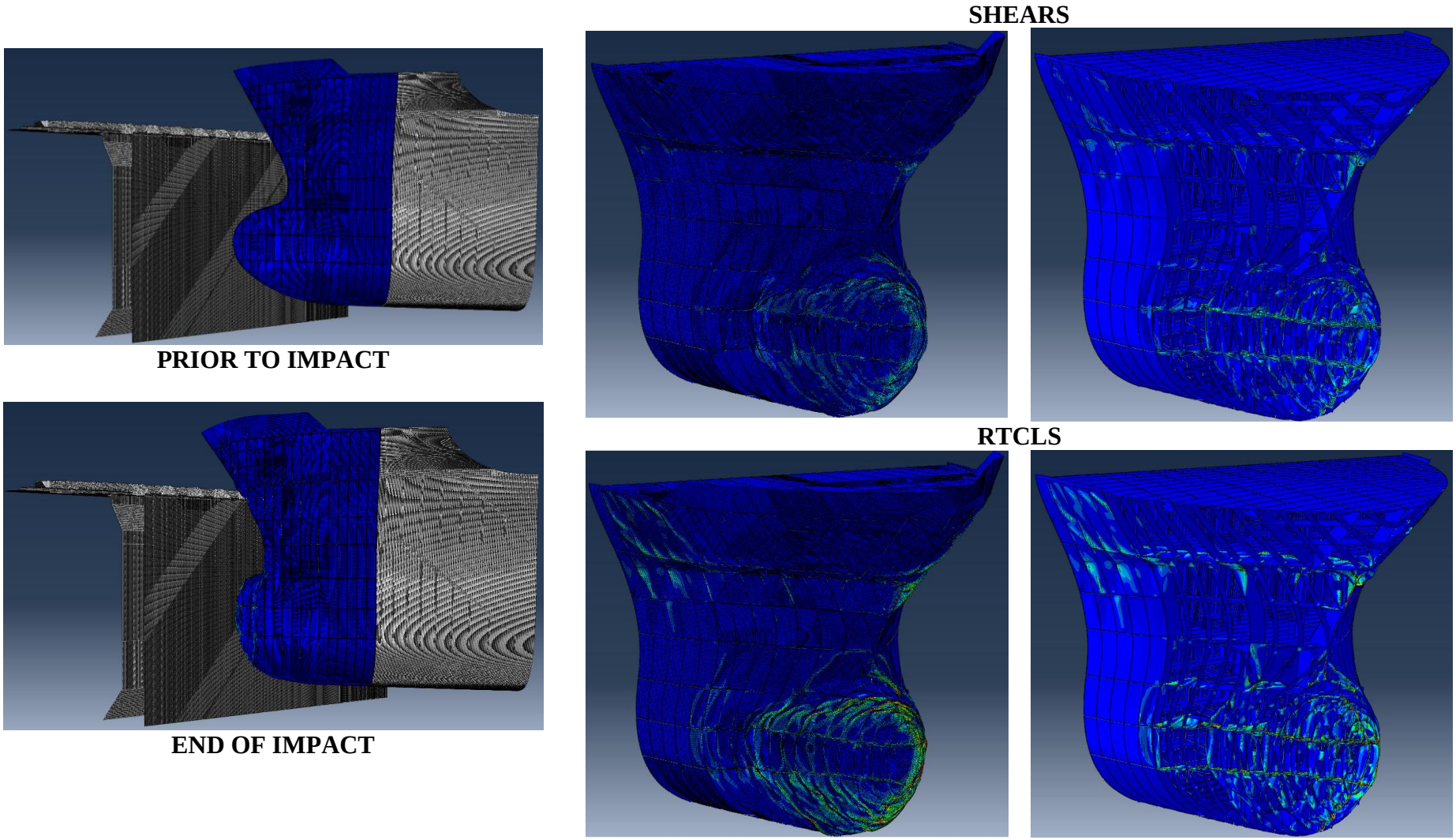

Figure 6.18. Deformable bow on rigid Tanker side-Angle of collision 50°. Representation of damage according to SHEARS and RTCLS rupture criteria

6.3.3 Deformable bow on rigid wall

Figure 6.19 illustrates the force-displacement and energy-displacement curves according to SHEARS and RTCLS rupture criteria in combination with the powerlaw type material curve. In addition, Figure 6.20 presents the deformation pattern of the deformable bow after 4 m of displacement of its rigid part towards the rigid wall, as predicted by the two criteria.

Also in this case, SHEARS and RTCLS rupture criteria yield close results with respect to the force and energy-displacement curves as well as the representation of the deformation pattern of the bow (see Figures 6.19 and 6.20). In this collision scenario contrary to the previous case, the stem section of the deformable bow comes into contact with the rigid wall at an earlier stage. This is due to the differences in the geometry of the upper and lower part of the bow, i.e. above the sixth deck of the bow the frames are more open curved (see Figures 6.2 and 6.3), which make it possible in a 50° angle collision scenario. In addition, the stem section is affected more by the impact than the bow section and a greater amount of energy is absorbed for the deformation of the former (see Figures 6.19 and 6.20).

No sooner than after almost 1.8 m of initial displacement, the bulb section of the bow came into contact with the rigid wall and the force with respect to the bulb section, i.e. F_{pl}-Bulb in Figure 6.19, increased. In general the forces follow an upward route up to the end of the simulation, except in the case of F_{pl}-Bulb, where the force slightly drops at approximately 3 m of displacement (see Figure 6.19). The drop in the latter force is related to the bending and buckling of the front part of the bulb section (see Figure 6.20). However, the resistance of the bulb section increases again after 400 mm of further displacement, as the contact surface between the two bodies, i.e. the bow and the rigid wall, becomes greater (see Figure 6.19). No rupture in the bulb and stem sections of the deformable bow was detected (see Figure 6.20).

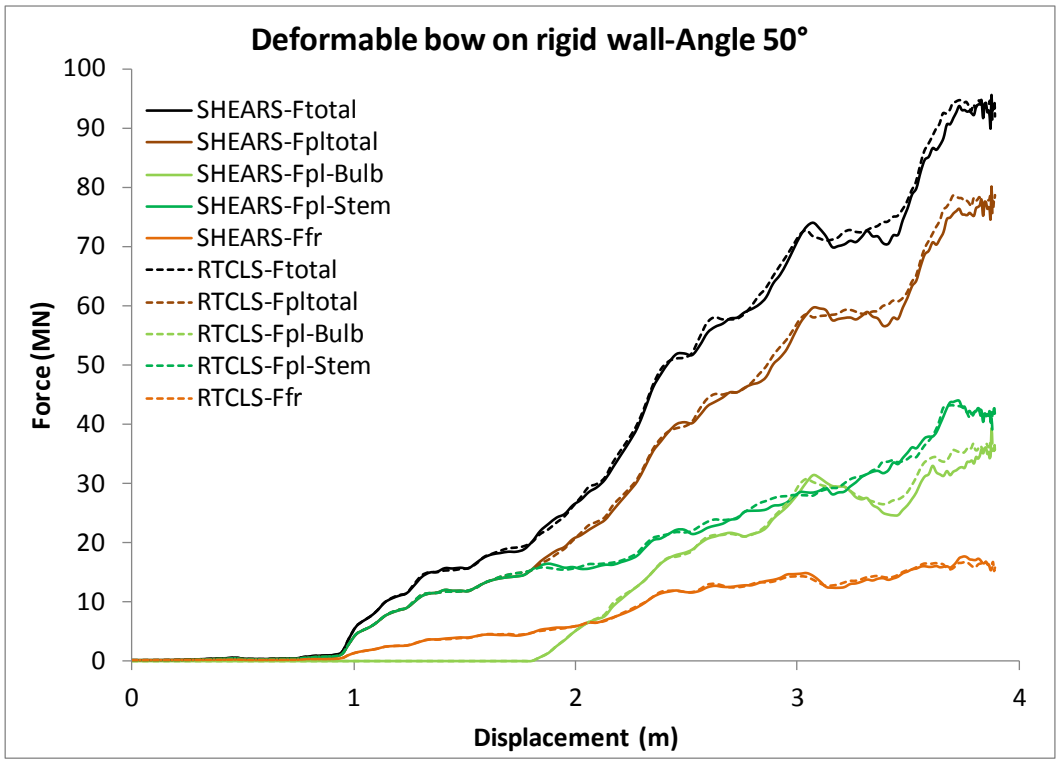

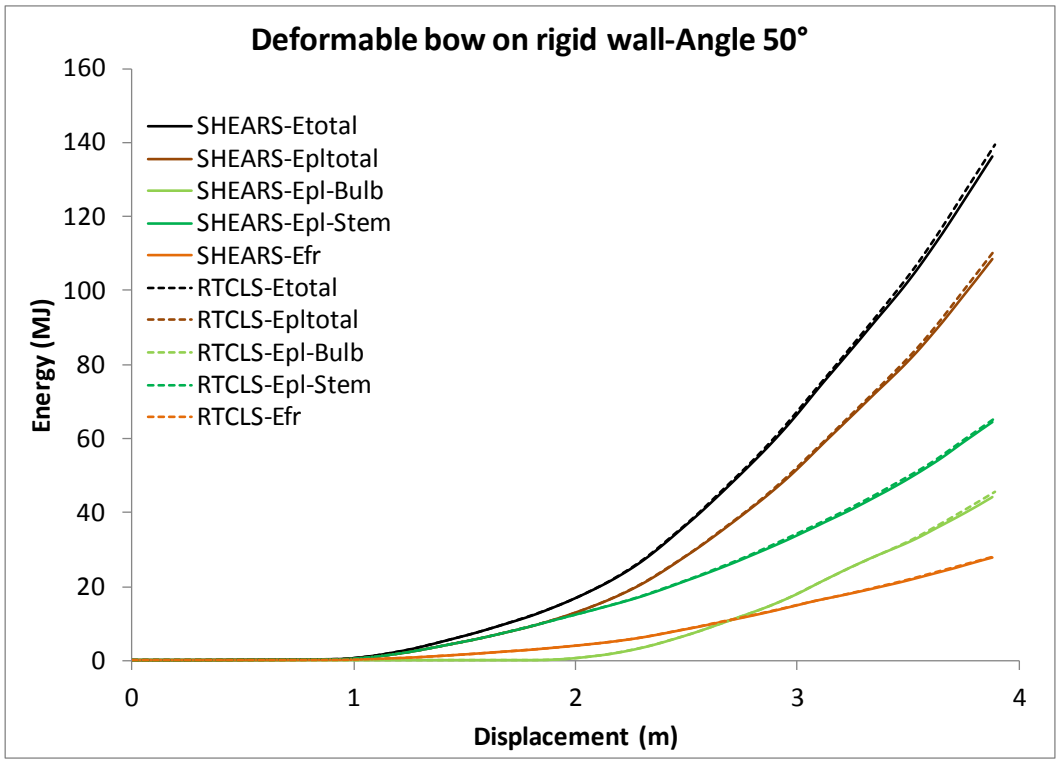

Figure 6.19. Deformable bow on rigid wall-Angle of collision 50°. Force and energy-displacement curves. Prediction of rupture according to SHEARS and RTCLS rupture criteria in combination with the powerlaw type material curve. E_{pl}: inelastic strain energy, E_{fr}: frictional dissipation energy, $E_{pl_{total}} = E_{pl}$-Bulb + E_{pl}-Stem, $E_{total} = E_{pl_{total}} + E_{fr}$ (similarly with the forces)

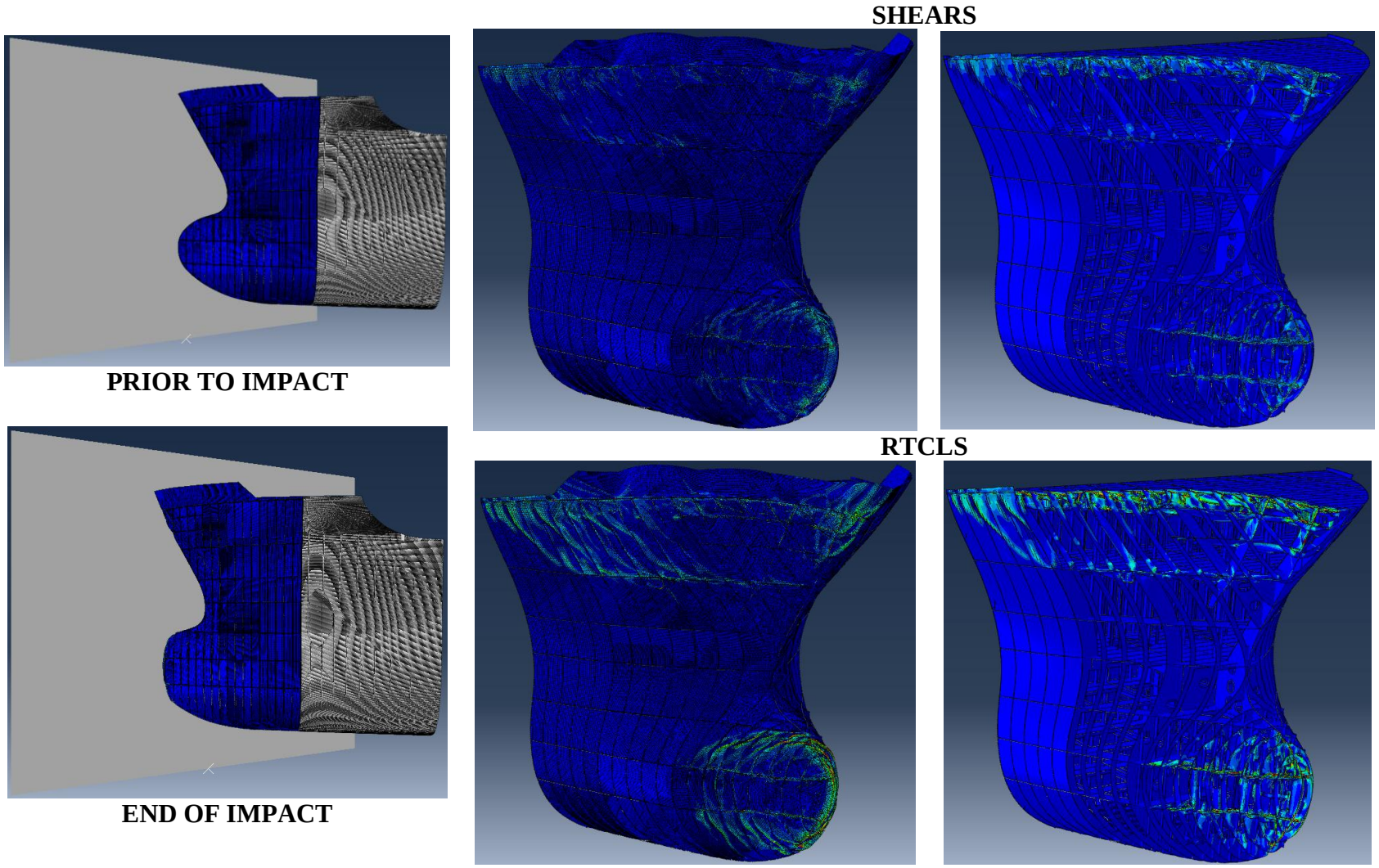

Figure 6.20. Deformable bow on rigid wall-Angle of collision 50°. Representation of damage according to SHEARS and RTCLS rupture criteria

6.3.4 Both ships as deformable structures

Figure 6.21 illustrates the force-displacement and energy-displacement curves according to SHEARS and RTCLS rupture criteria in combination with the powerlaw type material curve. It is noted that, the total displacement is considered in Figure 6.21, i.e. the displacement of the rigid part of the bow, during the simulation. Also, Figures 6.22 and 6.23 present the deformation patterns of both ships as predicted by the two criteria, after almost 7 m of total displacement.

The total force-displacement and total energy-displacement points depicted in the diagrams of Figure 6.21, in the order of appearance are related to: i) outer shell rupture initiation, ii) outer shell collapse, i.e. the force reaches a peak (F_c), iii) inner shell rupture initiation, iv) upper deck buckling, i.e. (F_b), with respect to the Tankship. Furthermore, Table 6.5 summarizes the total force, total energy and displacement values at the aforementioned points and compares the results between the two criteria. Based on the data included in Table 6.5 as well as in Figures 6.21, 6.22 and 6.23, it is observed that predictions with respect to SHEARS and RTCLS rupture criteria are considerably different.

According to SHEARS criterion, rupture of the outer shell initiates at almost 1 m of total displacement later compared to RTCLS criterion's predictions. In addition, collapse of outer shell as well as inner shell rupture is not predicted by SHEARS criterion. On the other hand, RTCLS criterion predicts breaching of the outer shell of the Tankship at almost 2 m of total displacement, accompanied by a gradual drop in the forces (see Figure 6.21). In both cases at approximately 2.6 m of total displacement the stem comes into contact with the side and the upper deck of the Tankship and as the simulation progresses the contact area between the two ships becomes greater. This is also shown by the steep increase in the forces in Figure 6.21. Rupture of the inner shell occurs at almost 4.3 m of total displacement according to RTCLS criterion and finally after virtually 1.5 m of further total displacement, the two criteria predict buckling of the upper deck of the Tankship (see Table 6.5). However, in both cases no rupture of the upper deck occurs up to the end of the simulation.

Figures 6.22 and 6.23, manifest that the bulb in the case of SHEARS criterion is excessively deformed during the impact contrary to the predictions of RTCLS criterion (see also sub-section 6.2.4). In particular, according to SHEARS criterion extensive bending and buckling in the location of the bulb is observed, while in the case of RTCLS criterion only the area close to the bulb tip is affected. Due to the considerable amount of energy that is absorbed by the bulb, outer shell rupture of the Tankship is delayed in the case of SHEARS criterion. In both cases the stem, even after almost 4.5 m of total displacement, i.e. from the time it first came into contact with the upper deck of the Tankship, is slightly affected (see Figures 6.22 and 6.23).

Table 6.5. Both ships deformable-Angle of collision 50°. Comparison of numerical values of force, energy and total displacement for each rupture criterion at damage points

	SHEARS			RTCLS		
Outer shell rupture initiation	$F_1(MN)$	$E_1(MJ)$	$U_1(m)$	$F_1(MN)$	$E_1(MJ)$	$U_1(m)$
	31.5	36.6	2.199	17.8	10.2	1.143
	$F_1(MN)$ differ.		$E_1(MJ)$ differ.		$U_1(m)$ differ.	
	55.6%		112.5%		63.1%	
Outer shell collapse (force peak)	$F_c(MN)$	$E_c(MJ)$	$U_c(m)$	$F_c(MN)$	$E_c(MJ)$	$U_c(m)$
	Not predicted			27.7	30.0	1.977
	$F_c(MN)$		$E_c(MJ)$		$U_c(m)$	
	-		-		-	
Inner shell rupture initiation	$F_2(MN)$	$E_2(MJ)$	$U_2(m)$	$F_2(MN)$	$E_2(MJ)$	$U_2(m)$
	Not predicted			63.4	112.7	4.253
	$F_2(MN)$ differ.		$E_2(MJ)$ differ.		$U_2(m)$ differ.	
	-		-		-	
Upper deck buckling	$F_b(MN)$	$E_b(MJ)$	$U_b(m)$	$F_b(MN)$	$E_b(MJ)$	$U_b(m)$
	95.9	250.5	5.747	69.1	216.8	5.839
	$F_b(MN)$		$E_b(MJ)$		$U_b(m)$	
	32.5%		14.4%		-1.6%	

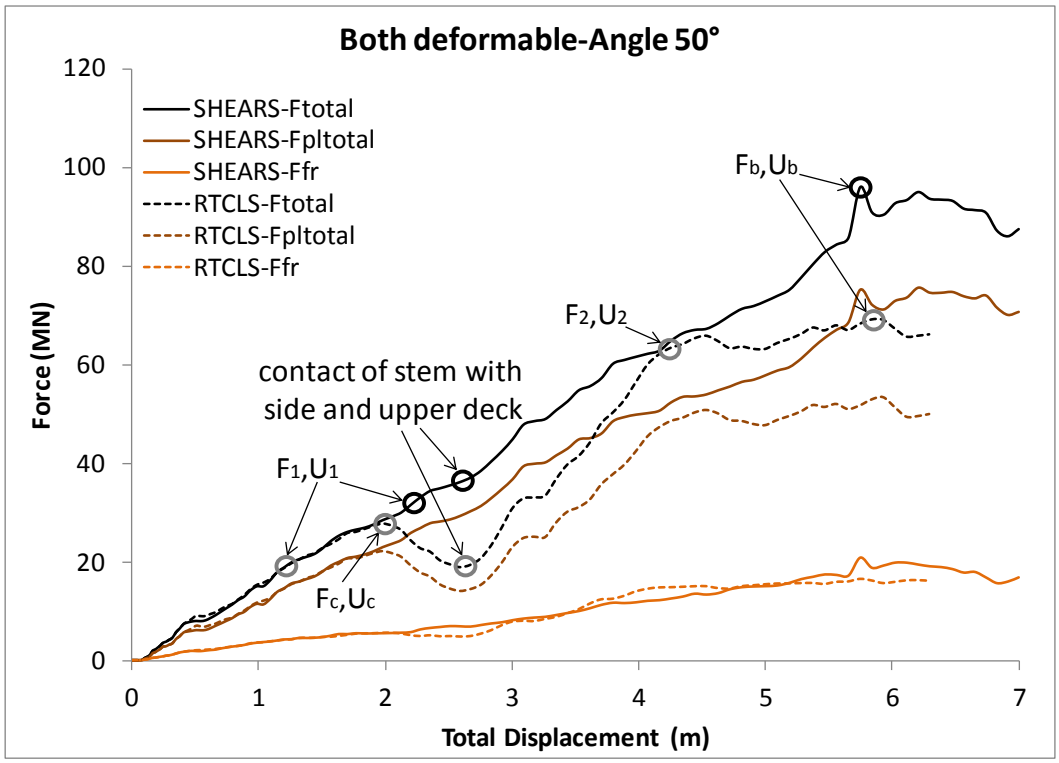

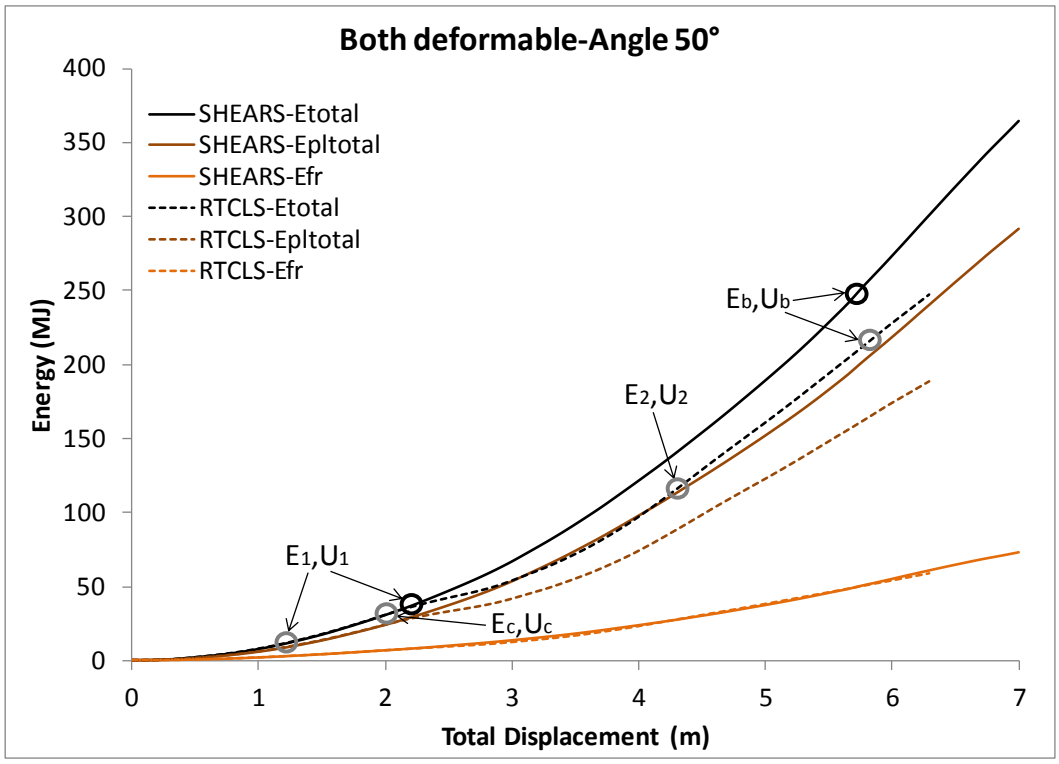

Figure 6.21. Both ships deformable -Angle of collision 50°. Force and energy-displacement curves. Prediction of rupture according to SHEARS and RTCLS rupture criteria in combination with the powerlaw type material curve. $E_{pl_{total}}$: inelastic strain energy, E_{fr}: frictional dissipation energy, $E_{total} = E_{pl_{total}} + E_{fr}$ (similarly with the forces) (black circle: SHEARS criterion, grey circle: RTCLS criterion)

SHEARS

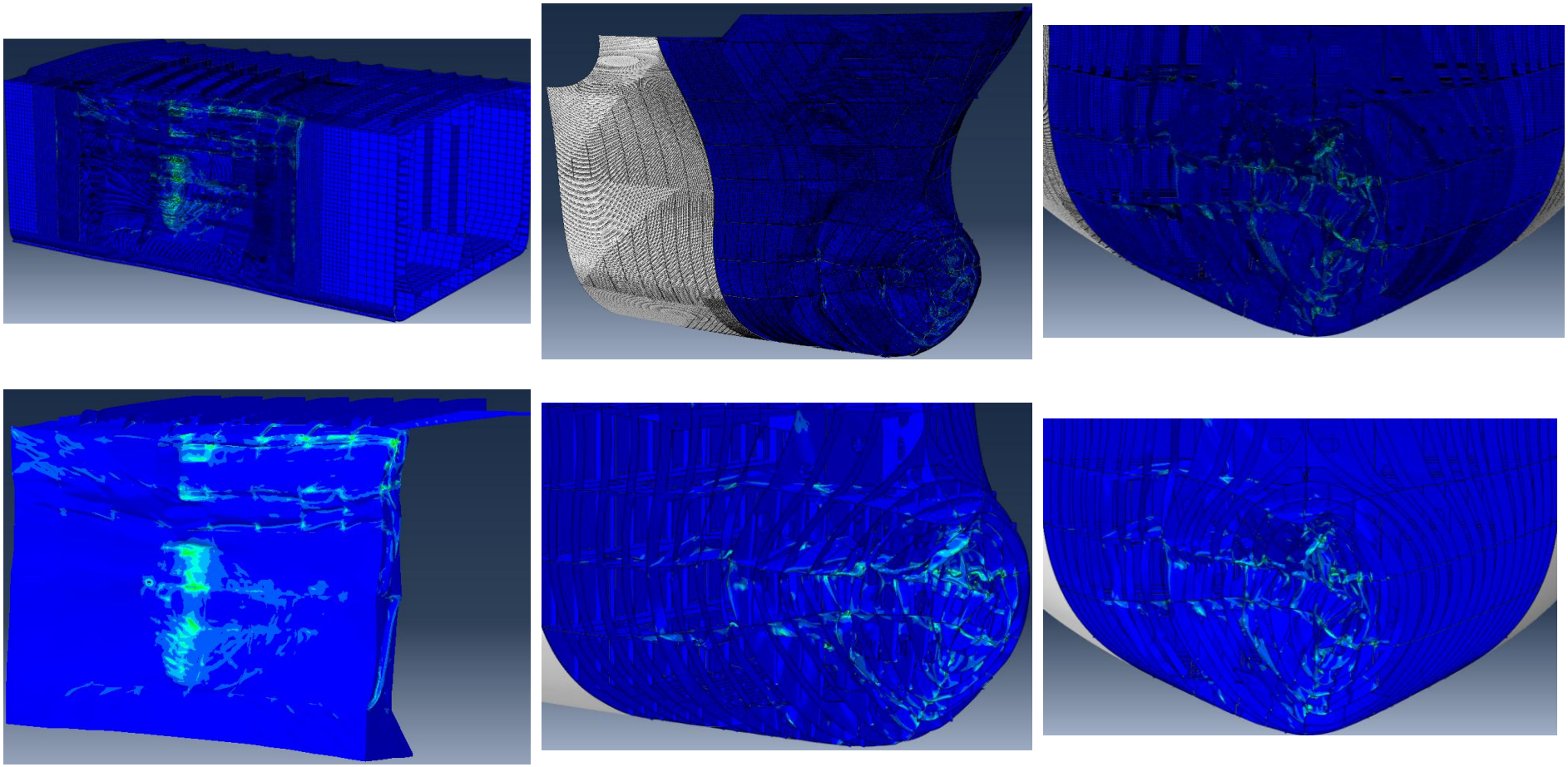

Figure 6.22. Both ships deformable-Angle of collision 50°. Representation of damage according to SHEARS rupture criterion

RTCLS

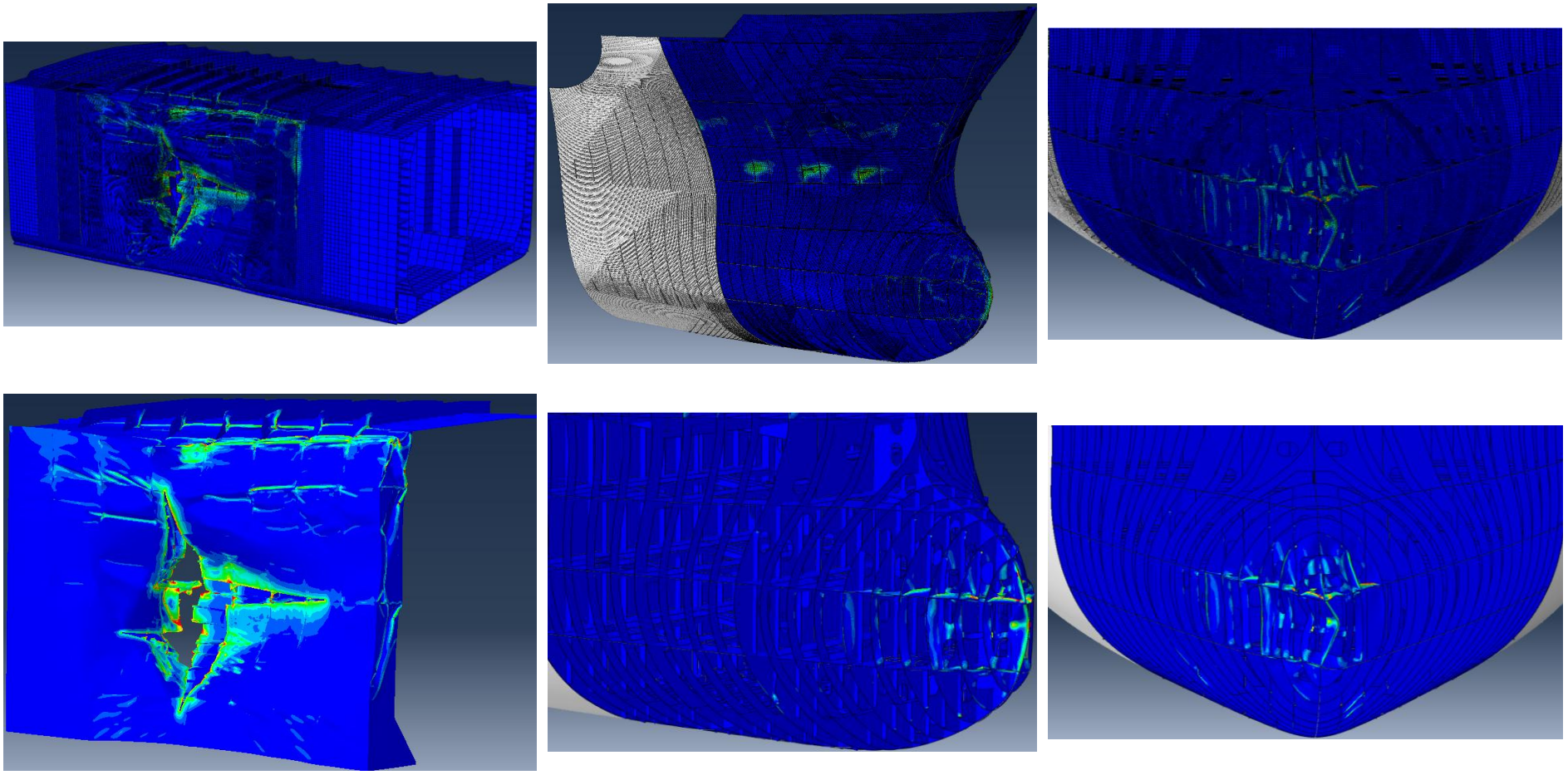

Figure 6.23. Both ships deformable -Angle of collision 50°. Representation of damage according to RTCLS rupture criterion

6.4 Comparative study

In the present section a comparative study takes place, based on the numerical analysis in the two previous sections. In particular, comparisons of the numerical results in terms of the force and energy-displacement curves with respect to different collision scenarios are performed.

Figures 6.24-6.32 illustrate the force and energy-displacement curves, according to SHEARS and RTCLS rupture criteria in combination with the powerlaw type true stress-strain curve considering different collision scenarios. The following comparisons are performed: a) between the results of the simulations of the rigid bow and both deformable structures (RB and BD respectively) regarding the collision scenarios with angles of collision 90° and 50° respectively, b) between the results of the RB and c) of the BD simulations, with angles of collision 90° and 50° (RB90, RB50, BD90, BD50 respectively). In addition, Figures 6.24-6.32 depict the force-displacement and energy-displacement points, which are related to the instants that specific damage occurred. Furthermore, the numerical values of force, energy and displacement at the aforementioned points are summarized in Tables 6.6-6.9 and the differences are quantified. Note that, Tables 6.6-6.9 include two comparisons: 1) the first comparison is in terms of the results between the two rupture criteria for each collision scenario and 2) the second with respect to the results between the different collision scenarios for each rupture criterion. Figure 6.33 shows pictures of both ships taken after the accident.

According to the comparison in a), the black curves in Figures 6.24, 6.26, 6.27 and 6.29 correspond to the RB simulation, while the red curves to the BD simulation. In particular, Figures 6.24 and 6.27 show the force-displacement and energy-displacement curves versus the displacement of a node selected at the tip of the rigid or deformable bulb, while Figures 6.26 and 6.29 show the respective curves versus the total displacement, i.e. the displacement of the rigid part of the bow. In addition, Figures 6.25 and 6.28 illustrate energy-bulb tip displacement curves, considering the collision scenarios with angles of collision 90° and 50° respectively, according to the predictions of both criteria. Figures 6.25 and 6.28 include the total energy, the frictional dissipation energy and the energies absorbed by the deformable structures, i.e. the side of the struck ship and the bulb and stem of the striking ship. The points in Figures 6.24-6.29 in the order of appearance are related with: i) outer shell collapse, ii) inner shell rupture and iii) upper deck rupture of the struck ship. It is noted that, in the case of the RB simulations the points that are related to outer shell collapse coincide with initiation of outer shell rupture. Further, the extent of damage at initiation of outer shell rupture in the RB simulations corresponds to the damage that is observed in the BD simulations at outer shell collapse.

As one may observe in Figures 6.24 and 6.26, in terms of the 90° angle collision scenario, the red curve with respect to RTCLS criterion follows fairly well the respective black curve. On the contrary, in the case of SHEARS criterion the two curves show a very different behaviour, especially in the range of 2-5 m of bulb tip displacement in Figure 6.24. This is explained by the fact that at approximately 3 m of total displacement, i.e. 2 m of bulb tip displacement in the BD case according to SHEARS and 2.7 m according to RTCLS criterion,

the stem of the Bulk Carrier comes into contact with the upper deck of the Tankship (see also section 6.2.4). Note that, contact of the stem with the upper deck at $3\,m$ is also observed in the RB simulation. However, in the RB simulation for both criteria as well as in the case of the BD simulation with RTCLS criterion, contact of the stem with the upper deck follows the inner shell rupture (see Figures 6.24, 6.26 and Table 6.6). Moreover, the bulb of the bow in the BD simulation using SHEARS criterion is far more deformed than in the case of RTCLS criterion (see Figures 6.12 and 6.13). This is also evident in Figure 6.25, by comparing the energy dissipated for the deformation of the bulb based on the predictions of both criteria. In Figure 6.26 is clearly shown that outer shell collapse, i.e. force peaks, in the case of the BD simulation according to SHEARS criterion, occurs at almost $800\,mm$ of total displacement later than in the case of the RB simulation, due to the crushing of the bulb. Therefore, in the BD collision scenario using SHEARS criterion, on one hand outer shell collapse is delayed and on the other the stem of the striking ship comes into contact with the upper deck of the struck ship before inner shell rupture occurs. As a result, a significant increase in the energy absorbed by the two ships is observed before rupture of the inner shell of the struck ship (see Figures 6.24 and 6.26). The deformation of the bulb is also responsible for the difference in the absorbed energies at outer shell collapse between the RB and DB simulations using SHEARS criterion (see Figure 6.24 and Table 6.6). Following the previous discussion, eventually the upper deck ruptures at an earlier stage in the BD simulation with respect to the RB simulation according to both criteria (see Figure 6.24). However, at that point RB and BD simulations yield close predictions in terms of the amount of the energy that is absorbed by the deformable structures (see Table 6.6). The trend is the same irrespective of the criteria. It is noted that, almost the same amount of energy is dissipated by friction also with respect to results by both rupture criteria (see Figures 6.4, 6.11 and 6.25).

In the case of the 50° angle collision scenario, it is also observed that a small amount of energy is dissipated for the deformation of the bulb according to RTCLS criterion's predictions, i.e. the criterion is activated sooner at the side of the struck ship (see Figures 6.23 and 6.28). On the contrary, according to SHEARS criterion's predictions a significant amount of energy is absorbed by the bulb which buckles and bends (see Figures 6.22 and 6.28). Figures 6.27 and 6.28 illustrate the differences between the RB and BD simulations using the two criteria in terms of the force and the dissipated energies versus the displacement of the bulb tip (see also Table 6.7). It is obvious that RB and BD simulations with RTCLS criterion yield close results. However, results between the RB and BD simulations with SHEARS criterion are fairly different. This is due to the following reasons considering the BD simulation: 1) bending and buckling of the bulb without inner shell rupture of the struck ship and limited outer shell rupture, i.e. a small crack initiates at the outer shell of the struck ship and as a result a great amount of energy is dissipated by friction throughout the simulation (see also Figures 6.22 and 6.28) and 2) contact of the stem of the striking ship with the side and upper deck of the struck ship almost $1\,m$ earlier than in the RB simulation, i.e. at $1.7\,m$ of bulb tip displacement that corresponds to $2.6\,m$ of total displacement.

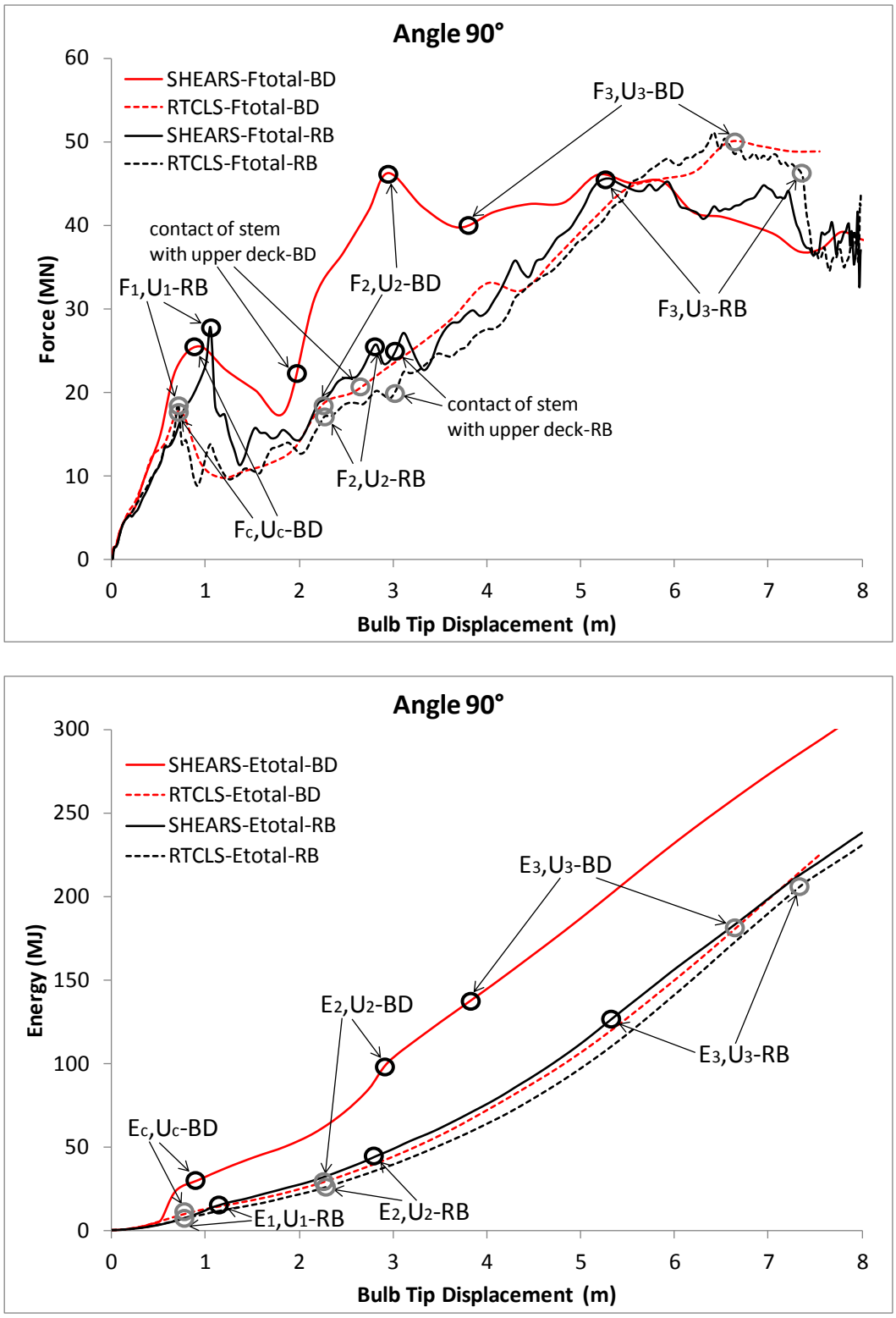

Figure 6.24. Angle of collision 90°. Force and energy-displacement curves.
Comparison between the rigid bow (RB) and both deformable (BD) simulations according to SHEARS and RTCLS rupture criteria in combination with the powerlaw type material curve
(black circle: SHEARS criterion, grey circle: RTCLS criterion)

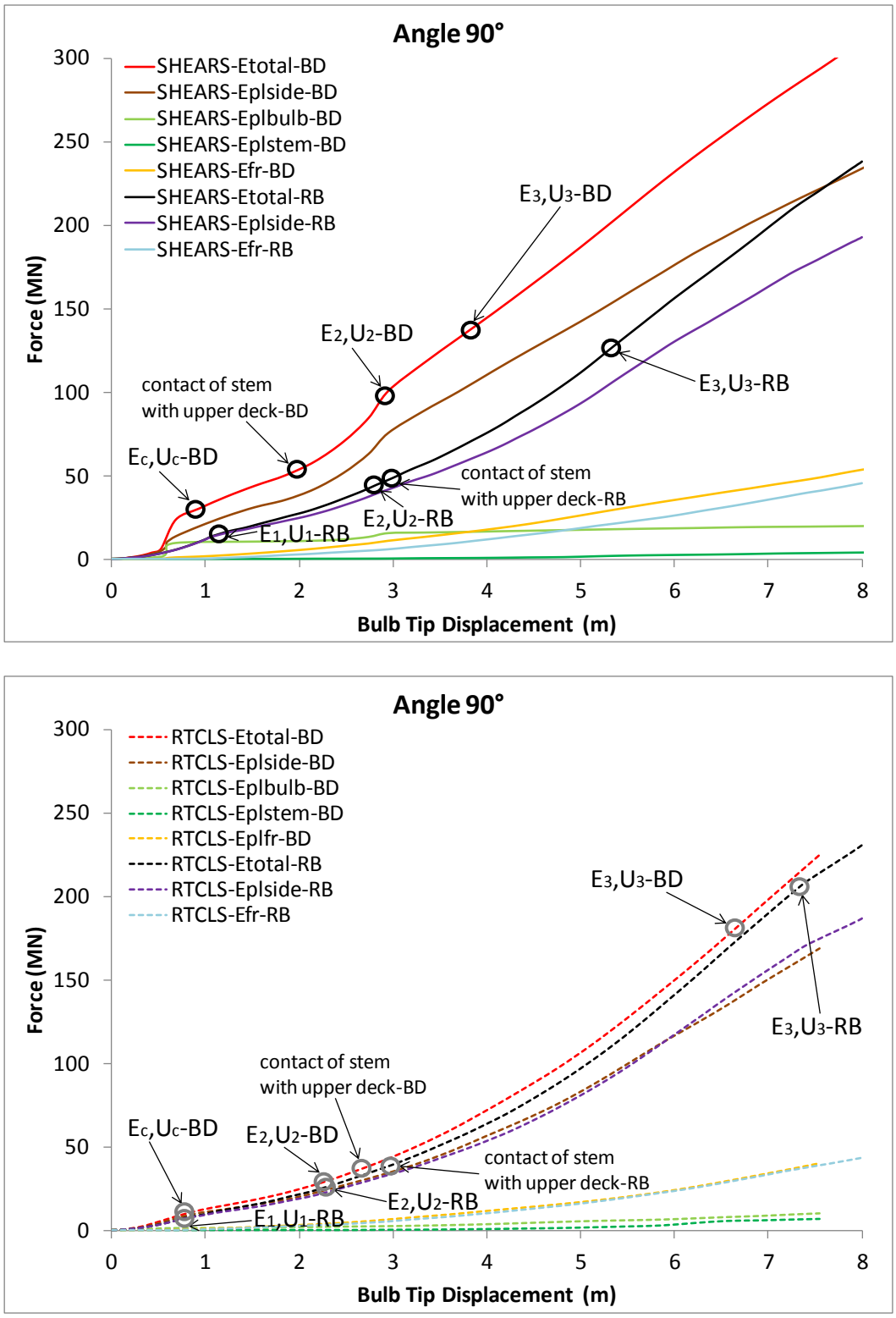

Figure 6.25. Angle of collision 90°. Energy-displacement curves
Comparison between the rigid bow (RB) and both deformable (BD) simulations according to SHEARS and RTCLS rupture criteria in combination with the powerlaw type material curve

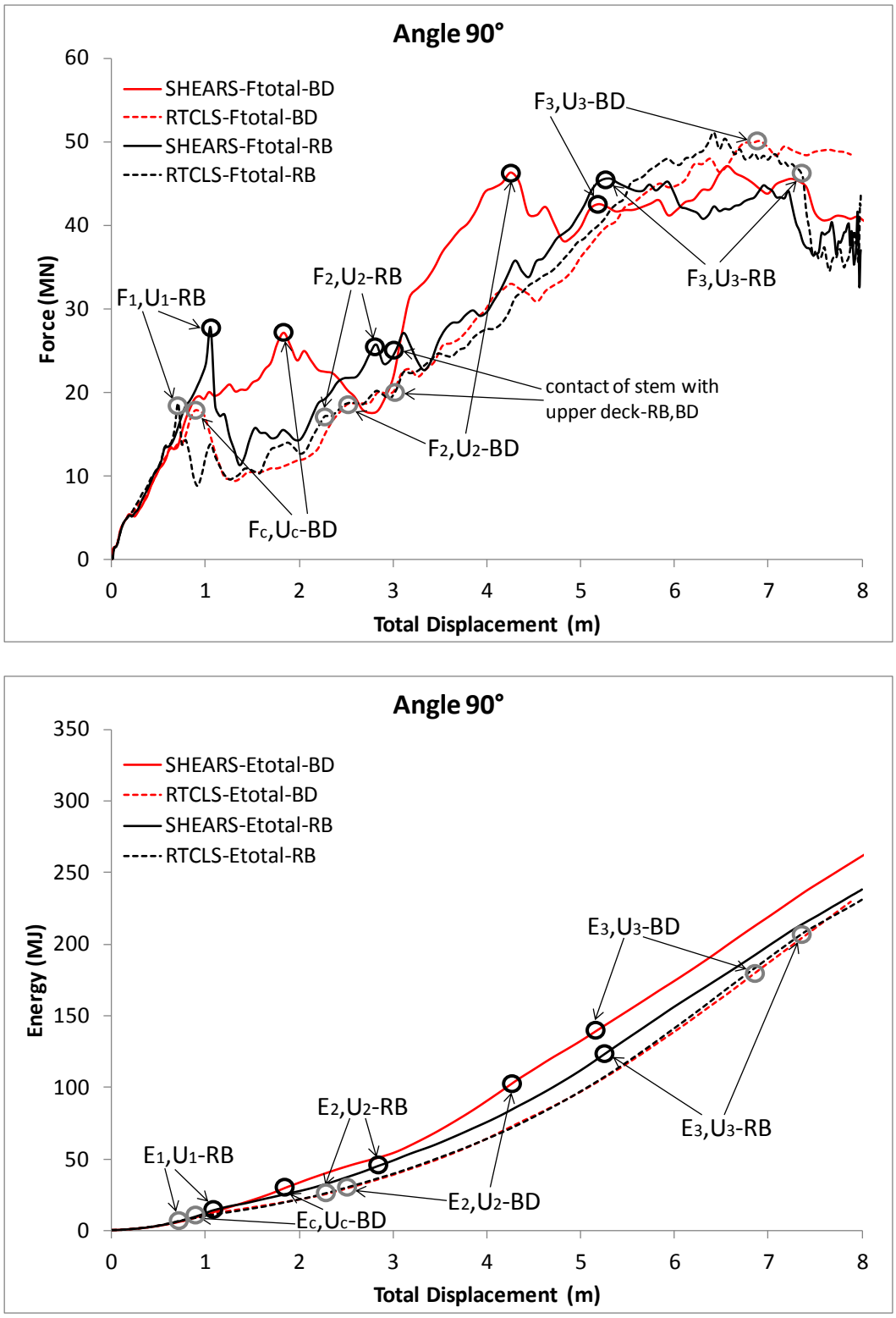

Figure 6.26. Angle of collision 90°. Force and energy-displacement curves
Comparison between the rigid bow (RB) and both deformable (BD) simulations according to SHEARS and RTCLS rupture criteria in combination with the powerlaw type material curve
(black circle: SHEARS criterion, grey circle: RTCLS criterion)

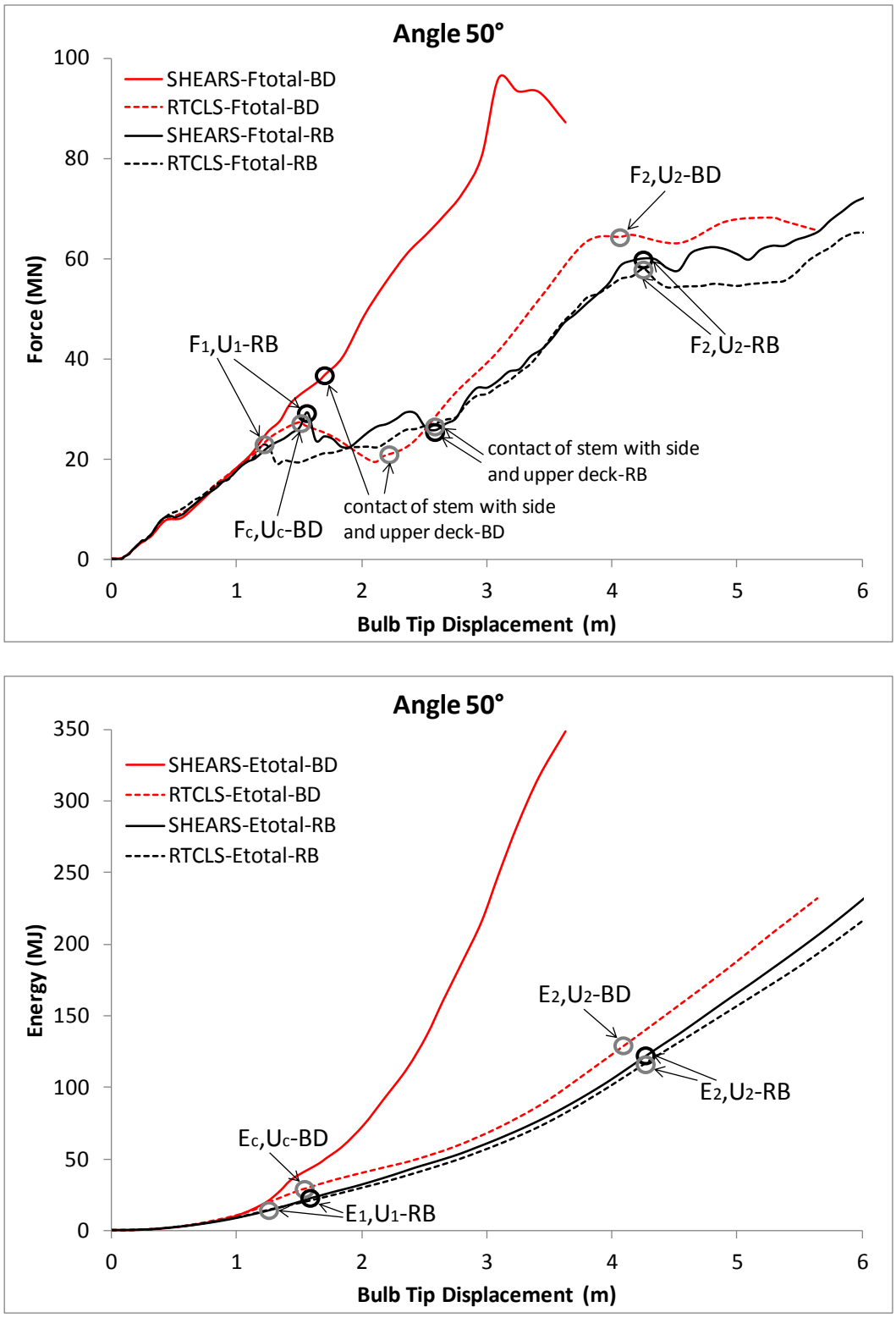

Figure 6.27. Angle of collision 50°. Force and energy-displacement curves.
Comparison between the rigid bow (RB) and both deformable (BD) simulations according to SHEARS and RTCLS rupture criteria in combination with the powerlaw type material curve
(black circle: SHEARS criterion, grey circle: RTCLS criterion)

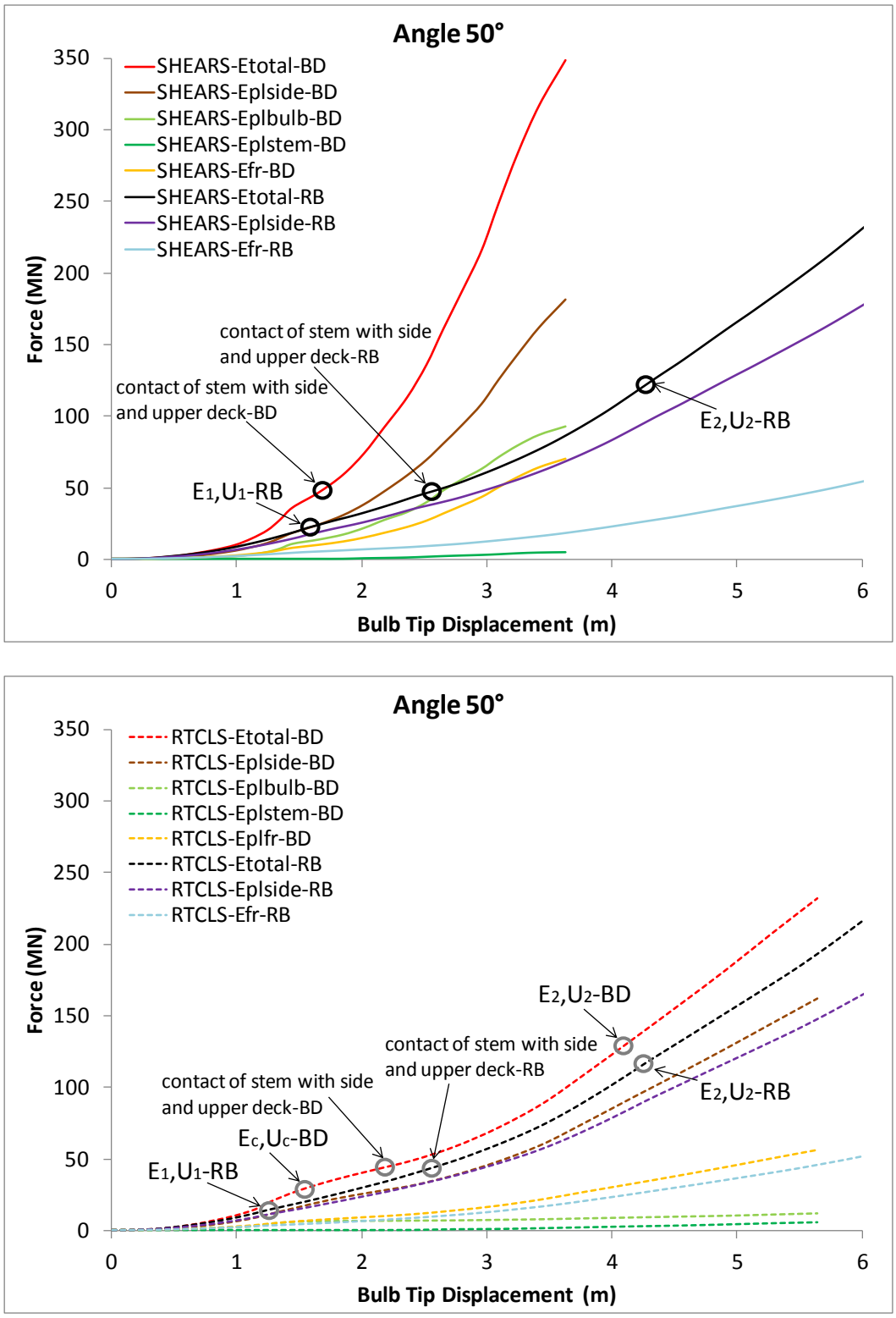

Figure 6.28. Angle of collision 50°. Energy-displacement curves
Comparison between the rigid bow (RB) and both deformable (BD) simulations according to SHEARS and RTCLS rupture criteria in combination with the powerlaw type material curve

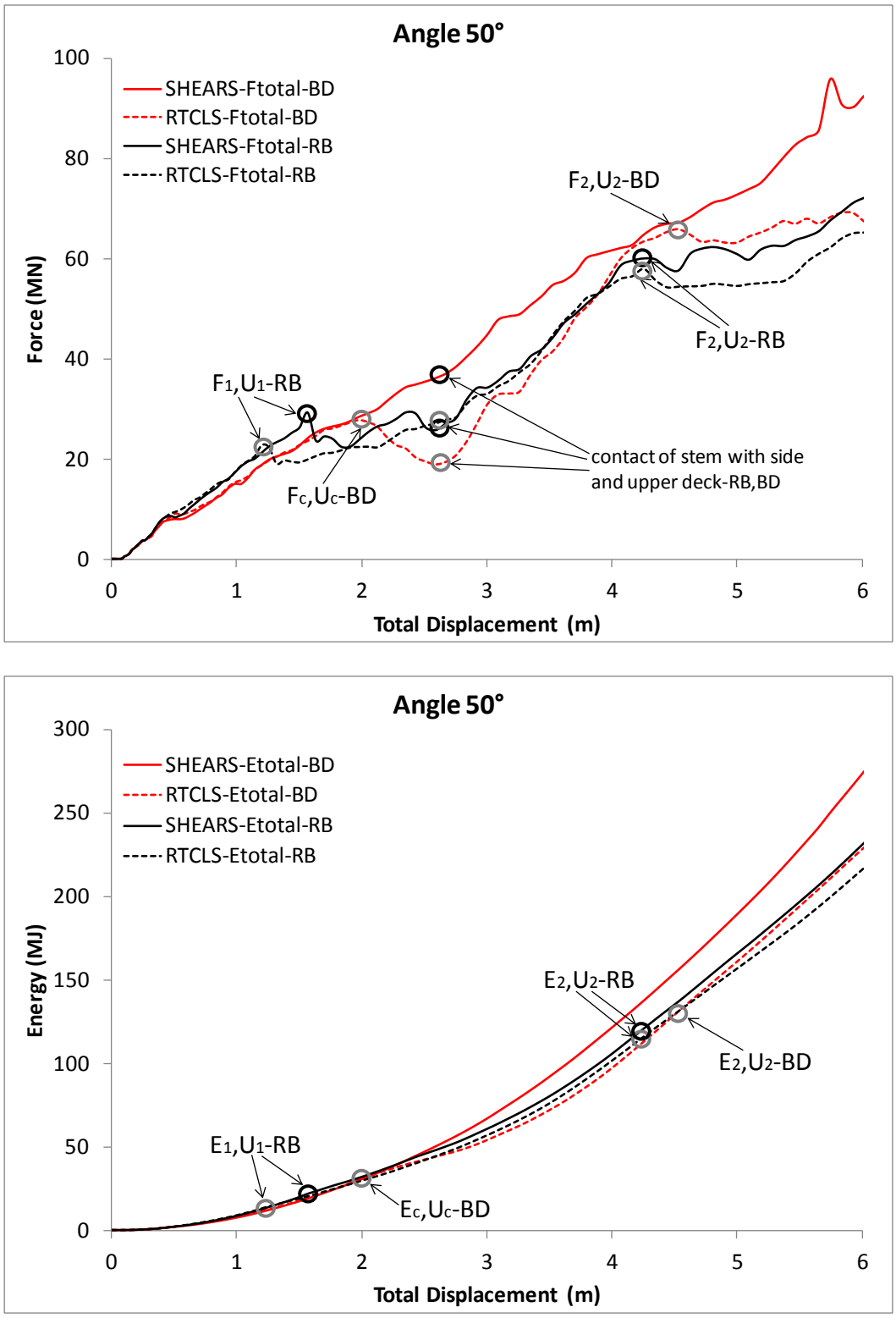

Figure 6.29. Angle of collision 50°. Force and energy-displacement curves
Comparison between the rigid bow (RB) and both deformable (BD) simulations according to SHEARS and RTCLS rupture criteria in combination with the powerlaw type material curve
(black circle: SHEARS criterion, grey circle: RTCLS criterion)

Moving on, according to the comparisons in b) and c), the inelastic strain energy or structural energy, which was dissipated during the RB and BD simulations with angles of collision 50° and 90° respectively as well as the corresponding force, are plotted versus the displacement which is perpendicular to the direction of the struck ship (see Figures 6.30-6.32). As frictional dissipation is greater in the RB50 and BD50 simulations than the RB90 and BD90 simulations (see Figures 6.4 and 6.14 and Figures 6.11 and 6.21), friction in both cases was not included in the comparative study, in order to investigate the differences only in terms of plastic dissipation. The force-displacement and energy-displacement points depicted in Figure 6.30, i.e. comparison b), are related with: i) outer shell rupture, ii) inner shell rupture and iii) upper deck rupture initiation of the struck ship, while the respective points in Figure 6.31, i.e. comparison c), are related with: i) outer shell rupture initiation, ii) outer shell collapse, i.e. the force reaches a peak (F_c) and iii) inner shell rupture initiation of the struck ship. Tables 6.8 and 6.9 summarize and compare the numerical values of force, energy and bulb tip displacement at the aforementioned points in each case. It is noted that, the notations U_i-50°, 90° in Figures 6.30 and 6.31 and U_{p_i} in Tables 6.8 and 6.9 for $i = 1$, 2, c and 3, are related to the bulb tip displacement as derived from the RB50 and BD50 simulations respectively, expressed in the perpendicular to the struck ship direction, i.e. multiplied by $sin50°$. Similarly, the notation U_i-50°, 90° in Figure 6.32, is related to the total displacement expressed in the perpendicular to the struck ship direction, i.e. BD50 simulation.

From Figures 6.30-6.32 and the quantified numerical data in Tables 6.8 and 6.9, it is obvious that the RB90 and BD90 simulations yield more conservative results with respect to the RB50 and BD50 simulations using both rupture criteria. This implies that damage, i.e. outer shell rupture etc., in the latter cases is predicted to occur at larger bulb tip displacements. In addition, the energy absorbed for structural plastic deformation at the damage points is significantly higher (see Tables 6.8 and 6.9). An interpretation to the previous observations is that, in the RB90 and BD90 simulations the stem of the Bulk Carrier comes into contact with the upper deck of the Tankship at $3\,m$ of total displacement, while the respective total displacement in the RB50 and BD50 simulations is $2.6\,m$, i.e. approximately $2\,m$ in the perpendicular to the struck ship direction U_p, that is almost $1\,m$ of total displacement sooner (see also sub-sections 6.2.1, 6.2.4, 6.3.1 and 6.3.4). This is also shown in Figures 6.30 and 6.32, where the forces start to increase after $2\,m$ of total displacement in the perpendicular to the struck ship direction. Consequently, as contact of the upper deck of the Tankship with the stem of the bow occurs at an earlier stage in the RB50 and BD50 simulations, the resistance of the structures is also increased sooner and thus damage, especially beyond $2\,m$ of total displacement, takes place at higher energies. It is noted that, solely in the case of the RB90 simulation using RTCLS criterion, rupture of the upper deck occurred at a greater displacement than in the respective case of the RB50 simulation (see sub-section 6.2.1). However, the corresponding inelastic strain energy at that point was almost 42% higher than in the RB90 simulation (see Table 6.8).

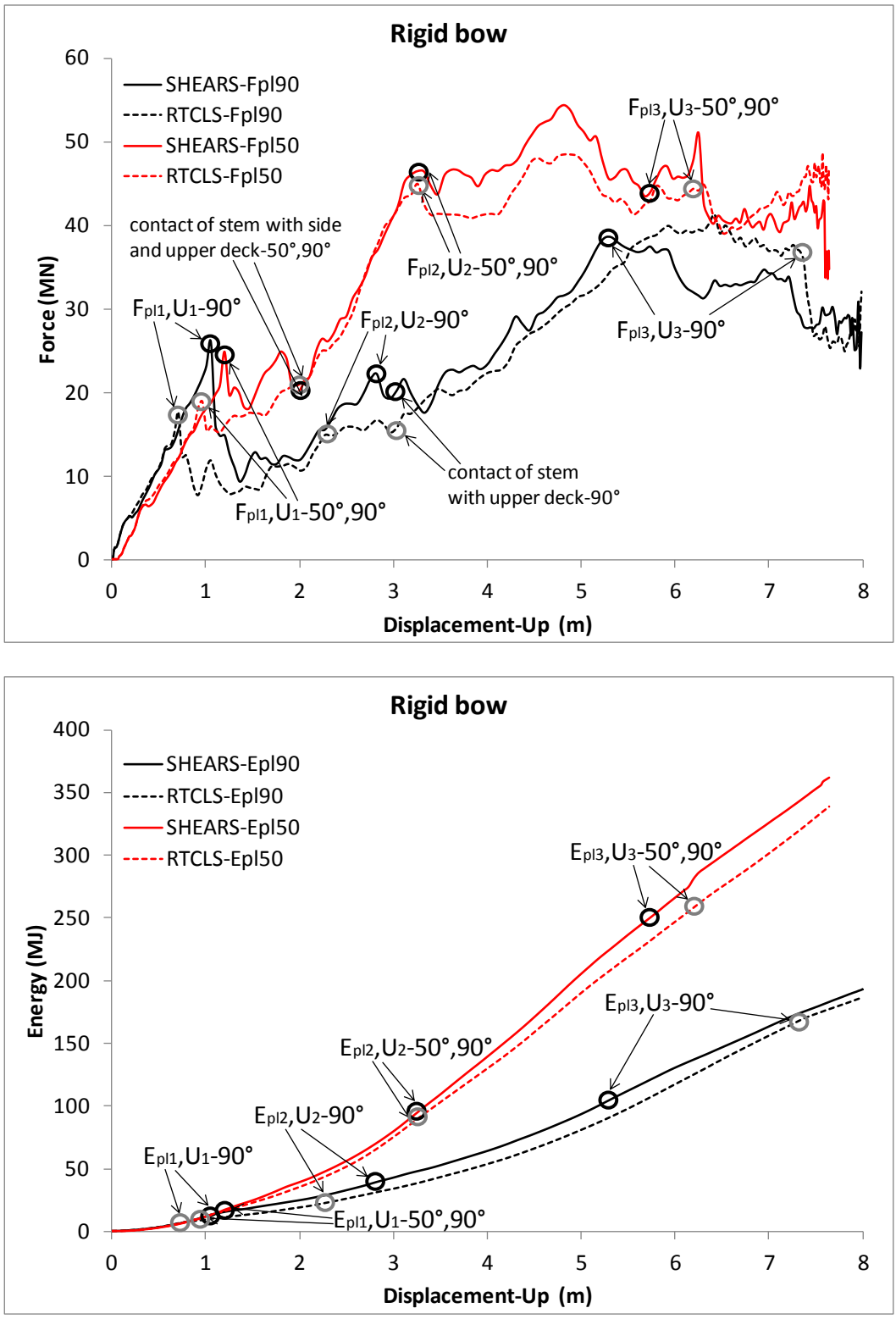

Figure 6.30. Rigid bow. Force and energy-displacement curves. Comparison between the two simulations with angles of collision 50° and 90° according to SHEARS and RTCLS rupture criteria in combination with the powerlaw type material curve. $E_{pl_{90°}}$, $E_{pl_{50°}}$: inelastic strain energies with respect to the 90° and 50°angle of collision simulations as functions of the displacement in the perpendicular to the struck ship direction (U_p) (similarly with the forces) (black circle: SHEARS criterion, grey circle: RTCLS criterion)

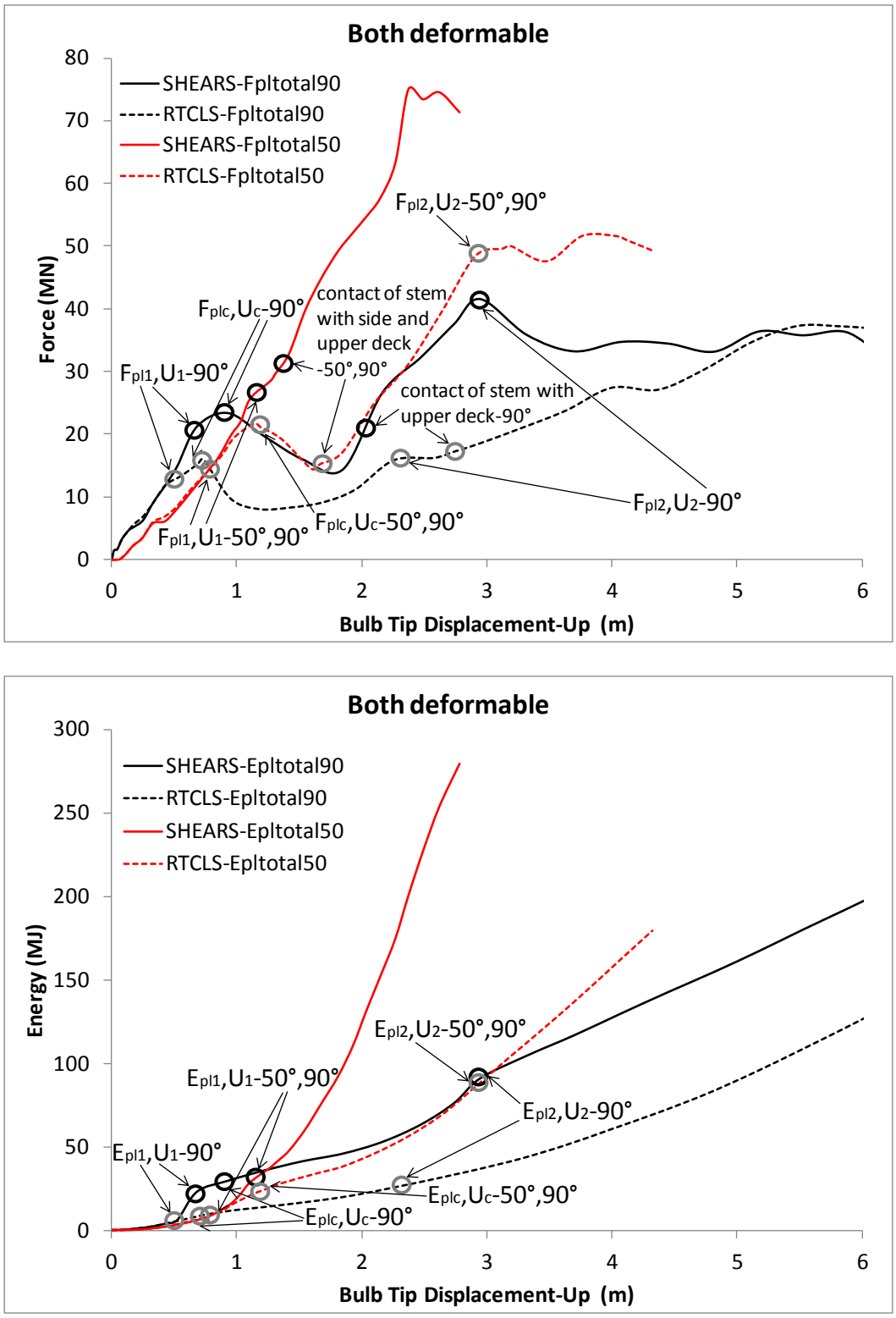

Figure 6.31. Both deformable. Force and energy-displacement curves. Comparison between the two simulations with angles of collision 50° and 90° according to SHEARS and RTCLS rupture criteria in combination with the powerlaw type material curve. $E_{pl_{total_{90°}}}$, $E_{pl_{total_{50°}}}$: total inelastic strain energies with respect to the 90° and 50°angle of collision simulations as functions of the bulb tip displacement in the perpendicular to the struck ship direction (U_p) (similarly with the forces) (black circle: SHEARS criterion, grey circle: RTCLS criterion)

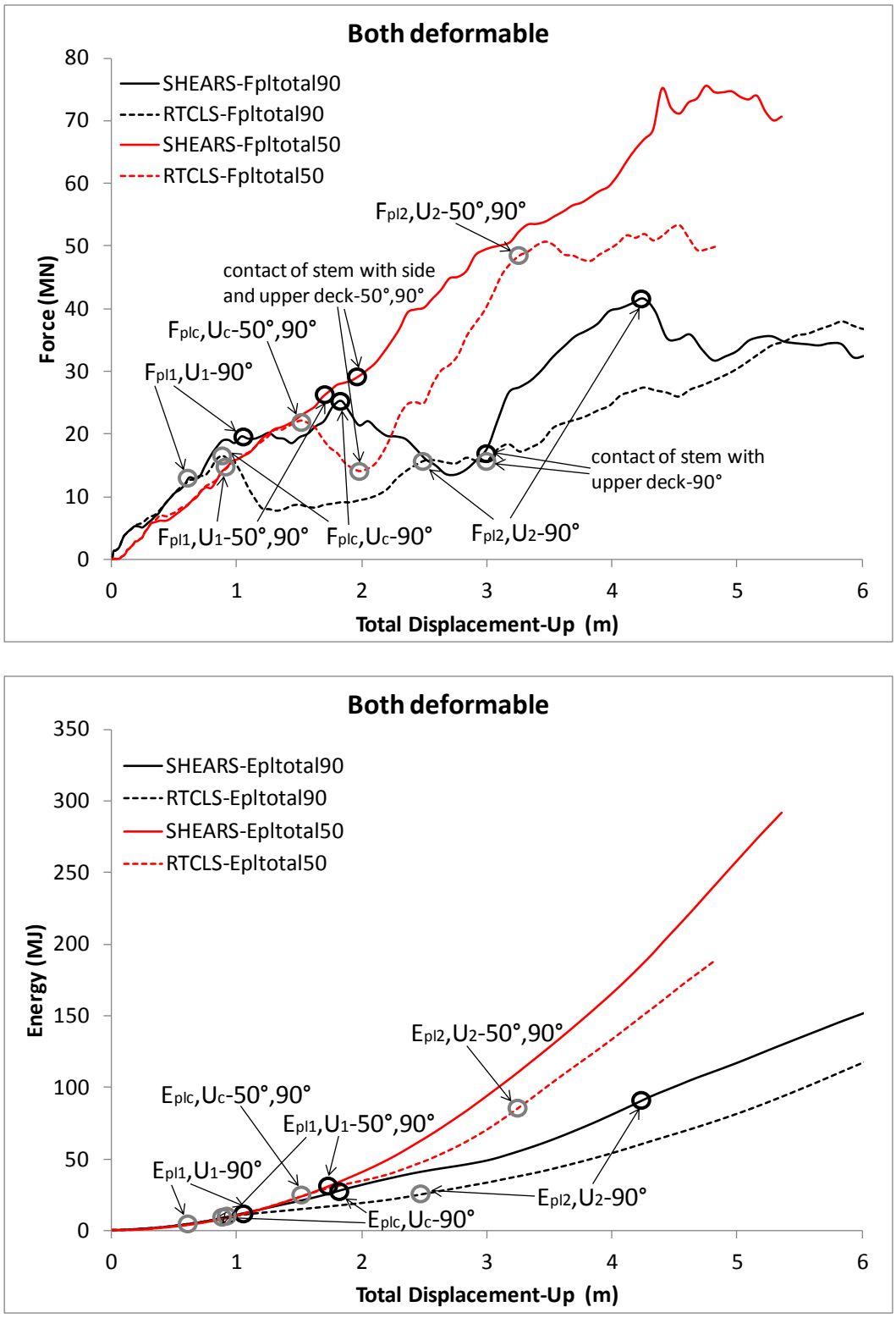

Figure 6.32. Both deformable. Force and energy-displacement curves. Comparison between the two simulations with angles of collision 50° and 90° according to SHEARS and RTCLS rupture criteria in combination with the powerlaw type material curve. $E_{pl_{total_{90°}}}$, $E_{pl_{total_{50°}}}$: total inelastic strain energies with respect to the 90° and 50°angle of collision simulations as functions of the total displacement in the perpendicular to the struck ship direction (U_p) (similarly with the forces) (black circle: SHEARS criterion, grey circle: RTCLS criterion)

From the comparative study it is observed that, the RB and BD simulations yield close results when using RTCLS criterion, which predicts rupture of the side of the struck ship at a rather early stage. Due to this, a rather small amount of energy is absorbed for the plastic deformation of the bulb of the striking ship in the case of the BD simulations and as a result the bulb behaves more or less as a rigid body. However, a completely different behaviour is observed in the corresponding case with SHEARS criterion, whereby the deformable bulb of the striking ship is significantly deformed, before the rupture and consequently the decrease in the stiffness of the side shell. Thus, the structural energy versus penetration curves that are obtained by the RB and BD simulations when using SHEARS criterion, are considerably different.

According to the results from the benchmark study in chapter 5, in the majority of the examined cases, where the structures were loaded transversely by rigid indenters with a rather similar shape to the shape of the bulb in the full-scale analyses, biaxial straining was dominant, i.e. triaxialities mainly over $1/\sqrt{3}$ or $\beta > 0$ and RTCLS criterion predicted rupture sooner than occurred in the experiments. Nevertheless, in one simulation, that is in the case of the CE-2 model, where the rigid indenter had a deformable cap, RTCLS criterion captured well the first peak in the experimental force-penetration curve, while SHEARS criterion overestimated the strength of the struck model. Thus, from the examination of all simulations of the tests it is observed that, where the impacted plating was loaded transversely, with the exception of the CE-2 model, SHEARS tends to produce results that are closer to the experimental observations.

As far as the behaviour of the SHEARS and RTCLS criteria in the simulation of the CE-2 model, further investigation led to the following observation: rupture on the outer shell initiated at the points where the rigid part of the indenter came into contact with the side shell, which were located under the perimeter of the rigid ring. This was observed in the simulations with either SHEARS or RTCLS criterion. In addition, both criteria predicted similar deformation patterns for the deformable cap. This pattern of damage differs from the damage that was predicted by SHEARS and RTCLS criteria in the simulation of an actual collision, where the crack that was initiated on the side of the struck ship, propagated vertically in front of the bulb tip of the striking ship. However, in the actual collision simulation SHEARS and RTCLS criteria predicted different deformation patterns for the bulb. The differences between the damage patterns, with respect to the simulations of the CE-2 and the full-scale models, are mainly due to the different structural configurations of the deformable cap and the actual bulb. The geometry of the deformable cap is rather simple, i.e. a thin curved unstiffened shell. On the other hand, the geometry of the actual bulb is more complex and consists of stringers, i.e. decks, frames and buttocks. Further, a close examination of the simulation results revealed that, the triaxialities on the side of the struck structure, in the case of CE-2 model, were mainly in the range of $0 < T < 1/\sqrt{3}$, whereas the triaxialities, in the case of the full-scale model on the side of the struck ship, were over $1/\sqrt{3}$, which are rather close to the triaxialities that were observed in the simulations of the tests on transversely loaded plates. As already discussed in section 5.3, RTCLS criterion yields rather different predictions compared to the experimental observations for triaxialities over $1/\sqrt{3}$

and below zero. Therefore, as the triaxialities monitored in the case of the actual collision simulation are greater than $1/\sqrt{3}$, for which the SHEARS criterion produced good results, and the damage pattern of the side shell in the full scale simulation differs considerably from the damage pattern of CE-2 model, it is concluded that SHEARS criterion produces predictions that represent better the results of actual collisions.

PRODUCT CARRIER-BALTIC **BULK CARRIER-TERN**

Figure 6.33. The damaged side of the Tankship (on the left) and the ruptured bow of the Bulk Carrier (on the right) after the accident (The Republic of the Marshall Islands 2002)

Table 6.6. Angle of collision 90°. Comparison between the rigid bow (RB) and both deformable (BD) simulations. Numerical values of force, energy and bulb tip displacement for each rupture criterion at damage points

	Simulation											
	Rigid bow						Both deformable					
	SHEARS			RTCLS			SHEARS			RTCLS		
Outer shell rupture (force peaks)	$F_1(MN)$	$E_1(MJ)$	$U_1(m)$	$F_1(MN)$	$E_1(MJ)$	$U_1(m)$	$F_c(MN)$	$E_c(MJ)$	$U_c(m)$	$F_c(MN)$	$E_c(MJ)$	$U_c(m)$
	27.7	13.3	1.053	18.6	6.3	0.707	24.8	28.4	0.865	16.7	8.2	0.688
	$F_1(MN)$ differ.		$E_1(MJ)$ differ.		$U_1(m)$ differ.		$F_c(MN)$ differ.		$E_c(MJ)$ differ.		$U_c(m)$ differ.	
	38.9%		71.9%		39.4%		39.2%		110.4%		22.8%	
	SHEARS (RB-BD) differ.						RTCLS (RB-BD) differ.					
	$F_{1,c}(MN)$ differ.		$E_{1,c}(MJ)$ differ.		$U_{1,c}(m)$ differ.		$F_{1,c}(MN)$ differ.		$E_{1,c}(MJ)$ differ.		$U_{1,c}(m)$ differ.	
	11.0%		-72.6%		19.6%		11.3%		-26.9%		2.7%	
	Simulation											
	Rigid bow						Both deformable					
	SHEARS			RTCLS			SHEARS			RTCLS		
Inner shell rupture initiation	$F_2(MN)$	$E_2(MJ)$	$U_2(m)$	$F_2(MN)$	$E_2(MJ)$	$U_2(m)$	$F_2(MN)$	$E_2(MJ)$	$U_2(m)$	$F_2(MN)$	$E_2(MJ)$	$U_2(m)$
	25.6	44.4	2.820	17.1	25.5	2.268	46.2	100.6	2.946	18.5	28.6	2.252
	$F_2(MN)$ differ.		$E_2(MJ)$ differ.		$U_2(m)$ differ.		$F_2(MN)$ differ.		$E_2(MJ)$ differ.		$U_2(m)$ differ.	
	40.1%		54.1%		21.7%		85.6%		111.3%		26.7%	
	SHEARS (RB-BD) differ.						RTCLS (RB-BD) differ.					
	$F_2(MN)$ differ.		$E_2(MJ)$ differ.		$U_2(m)$ differ.		$F_2(MN)$ differ.		$E_2(MJ)$ differ.		$U_2(m)$ differ.	
	-57.3%		-77.6%		-4.4%		-8.2%		-11.7%		0.7%	
	Simulation											
	Rigid bow						Both deformable					
	SHEARS			RTCLS			SHEARS			RTCLS		
Upper deck rupture initiation	$F_3(MN)$	$E_3(MJ)$	$U_3(m)$	$F_3(MN)$	$E_3(MJ)$	$U_3(m)$	$F_3(MN)$	$E_3(MJ)$	$U_3(m)$	$F_3(MN)$	$E_3(MJ)$	$U_3(m)$
	45.5	126.1	5.321	46.6	205.4	7.332	40.6	140.0	3.885	49.7	181.0	6.660
	$F_3(MN)$ differ.		$E_3(MJ)$ differ.		$U_3(m)$ differ.		$F_3(MN)$ differ.		$E_3(MJ)$ differ.		$U_3(m)$ differ.	
	-2.3%		-47.8%		-31.8%		-20.1%		-25.6%		-52.6%	
	SHEARS (RB-BD) differ.						RTCLS (RB-BD) differ.					
	$F_3(MN)$ differ.		$E_3(MJ)$ differ.		$U_3(m)$ differ.		$F_3(MN)$ differ.		$E_3(MJ)$ differ.		$U_3(m)$ differ.	
	11.3%		-10.4%		31.2%		-6.5%		12.6%		9.6%	

Table 6.7. Angle of collision 50°. Comparison between the rigid bow (RB) and both deformable (BD) simulations. Numerical values of force, energy and bulb tip displacement for each rupture criterion at damage points

	Simulation											
	Rigid bow						Both deformable					
	SHEARS			RTCLS			SHEARS			RTCLS		
Outer shell rupture (force peaks)	$F_1(MN)$	$E_1(MJ)$	$U_1(m)$	$F_1(MN)$	$E_1(MJ)$	$U_1(m)$	$F_c(MN)$	$E_c(MJ)$	$U_c(m)$	$F_c(MN)$	$E_c(MJ)$	$U_c(m)$
	29.2	21.7	1.565	22.7	13.0	1.200	Not predicted			26.5	29.3	1.556
	$F_1(MN)$ differ.		$E_1(MJ)$ differ.		$U_1(m)$ differ.		$F_c(MN)$ differ.		$E_c(MJ)$ differ.		$U_c(m)$ differ.	
	24.9%		50.3%		26.4%		-		-		-	
	SHEARS (RB-BD) differ.						RTCLS (RB-BD) differ.					
	$F_{1,c}(MN)$ differ.		$E_{1,c}(MJ)$ differ.		$U_{1,c}(m)$ differ.		$F_{1,c}(MN)$ differ.		$E_{1,c}(MJ)$ differ.		$U_{1,c}(m)$ differ.	
	-		-		-		-15.4%		-76.8%		-25.9%	
	Simulation											
	Rigid bow						Both deformable					
	SHEARS			RTCLS			SHEARS			RTCLS		
Inner shell rupture (force peaks)	$F_2(MN)$	$E_2(MJ)$	$U_2(m)$	$F_2(MN)$	$E_2(MJ)$	$U_2(m)$	$F_2(MN)$	$E_2(MJ)$	$U_2(m)$	$F_2(MN)$	$E_2(MJ)$	$U_2(m)$
	59.9	120.8	4.253	59.7	116.1	4.253	Not predicted			64.4	127.5	4.074
	$F_2(MN)$ differ.		$E_2(MJ)$ differ.		$U_2(m)$ differ.		$F_2(MN)$ differ.		$E_2(MJ)$ differ.		$U_2(m)$ differ.	
	3.4%		4.0%		0.0%		-		-		-	
	SHEARS (RB-BD) differ.						RTCLS (RB-BD) differ.					
	$F_2(MN)$ differ.		$E_2(MJ)$ differ.		$U_2(m)$ differ.		$F_2(MN)$ differ.		$E_2(MJ)$ differ.		$U_2(m)$ differ.	
	-		-		-		-10.7%		-9.4%		4.3%	

Table 6.8. Rigid bow. Comparison between the two simulations with angles of collision 50° and 90°. Numerical values of force, inelastic energy and displacement in the direction perpendicular to the struck ship (U_p) for each rupture criterion at damage points

	Angle of collision													
	50°								90°					
	SHEARS				RTCLS				SHEARS			RTCLS		
Outer shell rupture initiation (force peaks)	$F_{pl_1}(MN)$	$E_{pl_1}(MJ)$	$U_1(m)$	$U_{p_1}(m)$	$F_{pl_1}(MN)$	$E_{pl_1}(MJ)$	$U_1(m)$	$U_{p_1}(m)$	$F_{pl_1}(MN)$	$E_{pl_1}(MJ)$	$U_1(m)$	$F_{pl_1}(MN)$	$E_{pl_1}(MJ)$	$U_1(m)$
	24.9	16.9	1.565	1.199	18.2	10.0	1.200	0.919	26.0	13.0	1.053	17.6	6.2	0.707
	$F_{pl_1}(MN)$ differ.		$E_{pl_1}(MJ)$ differ.			$U_1(m)$ differ.			$F_{pl_1}(MN)$ differ.		$E_{pl_1}(MJ)$ differ.		$U_1(m)$ differ.	
	31.1%		51.4%			26.4%			38.6%		71.6%		39.4%	
	SHEARS (50°-90°) differ.								RTCLS (50°-90°) differ.					
	$F_{pl_1}(MN)$ differ.		$E_{pl_1}(MJ)$ differ.			U_{p_1} with U_1 (m) differ.			$F_{pl_1}(MN)$ differ.		$E_{pl_1}(MJ)$ differ.		U_{p_1} with U_1 (m) differ.	
	-4.4%		25.9%			13.0%			3.3%		47.5%		26.1%	
	Angle of collision													
	50°								90°					
	SHEARS				RTCLS				SHEARS			RTCLS		
Inner shell rupture initiation	$F_{pl_2}(MN)$	$E_{pl_2}(MJ)$	$U_2(m)$	$U_{p_2}(m)$	$F_{pl_2}(MN)$	$E_{pl_2}(MJ)$	$U_2(m)$	$U_{p_2}(m)$	$F_{pl_2}(MN)$	$E_{pl_2}(MJ)$	$U_2(m)$	$F_{pl_2}(MN)$	$E_{pl_2}(MJ)$	$U_2(m)$
	46.5	94.8	4.253	3.258	44.9	89.7	4.253	3.258	22.2	39.1	2.820	14.9	22.3	2.268
	$F_{pl_2}(MN)$ differ.		$E_{pl_2}(MJ)$ differ.			$U_2(m)$ differ.			$F_{pl_2}(MN)$ differ.		$E_{pl_2}(MJ)$ differ.		$U_2(m)$ differ.	
	3.5%		5.6%			0.0%			39.5%		54.7%		21.7%	
	SHEARS (50°-90°) differ.								RTCLS (50°-90°) differ.					
	$F_{pl_2}(MN)$ differ.		$E_{pl_2}(MJ)$ differ.			U_{p_2} with U_2 (m) differ.			$F_{pl_2}(MN)$ differ.		$E_{pl_2}(MJ)$ differ.		U_{p_2} with U_2 (m) differ.	
	70.8%		83.1%			14.4%			100.5%		120.2%		35.8%	
	Angle of collision													
	50°								90°					
	SHEARS				RTCLS				SHEARS			RTCLS		
Upper deck rupture initiation	$F_{pl_3}(MN)$	$E_{pl_3}(MJ)$	$U_3(m)$	$U_{p_3}(m)$	$F_{pl_3}(MN)$	$E_{pl_3}(MJ)$	$U_3(m)$	$U_{p_3}(m)$	$F_{pl_3}(MN)$	$E_{pl_3}(MJ)$	$U_3(m)$	$F_{pl_3}(MN)$	$E_{pl_3}(MJ)$	$U_3(m)$
	44.0	250.1	7.491	5.738	44.3	258.1	8.095	6.201	38.6	105.3	5.321	36.8	168.3	7.332
	$F_{pl_3}(MN)$ differ.		$E_{pl_3}(MJ)$ differ.			$U_3(m)$ differ.			$F_{pl_3}(MN)$ differ.		$E_{pl_3}(MJ)$ differ.		$U_3(m)$ differ.	
	-0.8%		-3.1%			-7.7%			4.6%		-46.1%		-31.8%	
	SHEARS (50°-90°) differ.								RTCLS (50°-90°) differ.					
	$F_{pl_3}(MN)$ differ.		$E_{pl_3}(MJ)$ differ.			U_{p_3} with U_3 (m) differ.			$F_{pl_3}(MN)$ differ.		$E_{pl_3}(MJ)$ differ.		U_{p_3} with U_3 (m) differ.	
	13.1%		81.5%			7.5%			18.5%		42.1%		-16.7%	

Table 6.9. Both deformable. Comparison between the two simulations with angles of collision 50° and 90°. Numerical values of force, inelastic energy and bulb tip displacement in the direction perpendicular to the struck ship (U_p) for each rupture criterion at damage points

	Angle of collision													
	50°								90°					
	SHEARS				RTCLS				SHEARS			RTCLS		
Outer shell rupture initiation	$F_{pl_1}(MN)$	$E_{pl_1}(MJ)$	$U_1(m)$	$U_{p_1}(m)$	$F_{pl_1}(MN)$	$E_{pl_1}(MJ)$	$U_1(m)$	$U_{p_1}(m)$	$F_{pl_1}(MN)$	$E_{pl_1}(MJ)$	$U_1(m)$	$F_{pl_1}(MN)$	$E_{pl_1}(MJ)$	$U_1(m)$
	25.8	28.8	1.446	1.108	13.8	7.8	0.978	0.749	19.1	11.4	0.576	11.8	3.9	0.430
	$F_{pl_1}(MN)$ differ.		$E_{pl_1}(MJ)$ differ.			$U_1(m)$ differ.			$F_{pl_1}(MN)$ differ.		$E_{pl_1}(MJ)$ differ.		$U_1(m)$ differ.	
	60.7%		114.7%			38.6%			47.0%		97.3%		29.0%	
	SHEARS (50°-90°) differ.								RTCLS (50°-90°) differ.					
	$F_{pl_1}(MN)$ differ.		$E_{pl_1}(MJ)$ differ.			U_{p_1} with U_1 (m) differ.			$F_{pl_1}(MN)$ differ.		$E_{pl_1}(MJ)$ differ.		U_{p_1} with U_1 (m) differ.	
	29.9%		86.8%			63.1%			15.3%		66.2%		54.1%	
	Angle of collision													
	50°								90°					
	SHEARS				RTCLS				SHEARS			RTCLS		
Outer shell collapse (force peaks)	$F_{pl_c}(MN)$	$E_{pl_c}(MJ)$	$U_c(m)$	$U_{p_c}(m)$	$F_{pl_c}(MN)$	$E_{pl_c}(MJ)$	$U_c(m)$	$U_{p_c}(m)$	$F_{pl_c}(MN)$	$E_{pl_c}(MJ)$	$U_c(m)$	$F_{pl_c}(MN)$	$E_{pl_c}(MJ)$	$U_c(m)$
	Not predicted				21.1	23.4	1.556	1.192	22.8	27.9	0.865	15.2	8.2	0.688
	$F_{pl_c}(MN)$ differ.		$E_{pl_c}(MJ)$ differ.			$U_c(m)$ differ.			$F_{pl_c}(MN)$ differ.		$E_{pl_c}(MJ)$ differ.		$U_c(m)$ differ.	
	-		-			-			39.9%		108.7%		22.8%	
	SHEARS (50°-90°) differ.								RTCLS (50°-90°) differ.					
	$F_{pl_c}(MN)$ differ.		$E_{pl_c}(MJ)$ differ.			U_{p_c} with U_c (m) differ.			$F_{pl_c}(MN)$ differ.		$E_{pl_c}(MJ)$ differ.		U_{p_c} with U_c (m) differ.	
	-		-			-			32.6%		95.8%		53.7%	
	Angle of collision													
	50°								90°					
	SHEARS				RTCLS				SHEARS			RTCLS		
Inner shell rupture initiation	$F_{pl_2}(MN)$	$E_{pl_2}(MJ)$	$U_2(m)$	$U_{p_2}(m)$	$F_{pl_2}(MN)$	$E_{pl_2}(MJ)$	$U_2(m)$	$U_{p_2}(m)$	$F_{pl_2}(MN)$	$E_{pl_2}(MJ)$	$U_2(m)$	$F_{pl_2}(MN)$	$E_{pl_2}(MJ)$	$U_2(m)$
	Not predicted				48.5	85.8	3.793	2.905	41.5	91.0	2.946	15.7	25.5	2.252
	$F_{pl_2}(MN)$ differ.		$E_{pl_2}(MJ)$ differ.			$U_2(m)$ differ.			$F_{pl_2}(MN)$ differ.		$E_{pl_2}(MJ)$ differ.		$U_2(m)$ differ.	
	-		-			-			90.1%		112.5%		26.7%	
	SHEARS (50°-90°) differ.								RTCLS (50°-90°) differ.					
	$F_{pl_2}(MN)$ differ.		$E_{pl_2}(MJ)$ differ.			U_{p_2} with U_2 (m) differ.			$F_{pl_2}(MN)$ differ.		$E_{pl_2}(MJ)$ differ.		U_{p_2} with U_2 (m) differ.	
	-		-			-			101.9%		108.4%		25.3%	

This page is intentionally left blank

Chapter 7

Concluding Remarks and Proposals for Future Research

7.1 Overview of the work

In the present investigation twenty two indentation tests and a drop weight test have been modeled using Abaqus/Explicit FE code, in order to study the behaviour of thin walled structures made of steel, which represent parts of a ship structure, under extreme loading conditions. Such loadings that may arise in the case of impacts involving ship structures for example collisions and groundings, cause different modes of failure, i.e. membrane, bending, tearing and crushing.

The scope of this study was to find a procedure for the simulation of ship impacts, which would lead in a realistic description of the material behaviour up to the final stage of rupture and produce reliable results. To this end, focus was placed on the determination of an effective material model, namely a suitable combination of a true stress-strain curve and a rupture criterion, taking also into account the mesh size effect. In addition, strain-rate effect has been investigated in the case of the drop weight test, where the strains were developed with relatively high rates.

The true stress-strain curve until necking was determined from uniaxial tensile tests, whereas the appropriate true stress-strain curve beyond necking was selected to be between a powerlaw and a tangent type material curve, i.e. tangent to the point of maximum load of the engineering stress-strain curve. Uniaxial simulations of tensile tests were performed in each case using different mesh sizes.

Three rupture criteria were programmed into VUMAT subroutine (ABAQUS 2010) to account for rupture, namely the critical equivalent plastic strain criterion or SHEAR criterion (Marinatos and Samuelides 2013a, 2013b and 2015), the BWH instability criterion (Alsos et al. 2008) and the RTCL damage criterion (Törnqvist 2003). SHEAR rupture criterion was defined not to be activated for triaxialities below -1/3. Further, the behaviour of the failure criteria that have been implemented in FE codes as well as other criteria for the prediction of rupture initiation and propagation, were investigated. Also, a procedure for the definition of the critical equivalent plastic strain as a function of the ratio l_e/t has been proposed and applied in the analysis. The numerical results of the benchmark study were compared with the experimental force-penetration, energy-penetration curves as well as with the damaged forms of the experimental models using different mesh sizes.

Based on the benchmark study investigation, the simulation procedure that has been defined was also applied in an actual ship-ship collision, in order to assess the behaviour of a deformable bow. Four full-scale collision scenarios were examined considering two angles of collision, namely 90° and 50°. The ships were modeled as rigid or deformable bodies and in the most realistic collision scenario both ships were defined as deformable structures. The simulations were based on the real ship-ship collision accident between the Tankship BALTIC CARRIER and the Bulk Carrier TERN that took place in the Baltic Sea on 29 March 2001. The prediction of the deformation patterns and the assessment of the structural energy dissipated during different collision scenarios, was achieved through the application of the scaled forms of RTCL and SHEAR rupture criteria, where the rupture strain depends on the element length, in combination with the powerlaw type true stress-strain curve.

7.2 Conclusions

The conclusions from the present work are summarized in the following:

- Material curve

  - Beyond the point of necking the powerlaw type true stress-strain curve, i.e. $w = 0$, is the best choice for element length over thickness ratios greater than one, i.e. $l_e/t > 1$, in most cases

  - True stress-strain-rate dependent material curves yield the best reproduction of the experimental stress-strain rate dependent engineering curves and should be used to account for strain-rate dependency

- Failure criteria

  - Instability criteria show a very different behaviour compared to rupture criteria in the strain field considering the various loading states

  - Differences between the various criteria are rather minimized in the stress field especially in the range of $\beta \geq 0$

  - The Swift (1952) instability criterion yields more conservative results with respect to the rest criteria in the range of $-1 < \beta < 0$

  - The Stören-Rice (1975b) criterion yields almost identical predictions with the BWH criterion especially in the range of $0 \leq \beta \leq 1$, while it further determines a limit stress in a pure shear loading process, i.e. $\beta = -1$

- The reference to criteria that are independent from the stress/strain state is misleading. It is noted that, a criterion using constant equivalent strain, i.e. SHEAR and Peschmann (2001) criteria, may be expressed in terms of principal strain or stress which depends on the stress/strain state

- The Peschmann (2001), SHEAR, RTCL, Lou et al. (2012) and Rupture Index criteria, show a similar behaviour considering the various loading states

- Simulation technique

- The finer the mesh the lower the resultant force and as a consequence the absorbed energy at the same penetration depth in the majority of the simulations due to local phenomena, i.e. geometrical constraints that lead to strain and stress concentrations, which are captured by small elements; rupture occurs at an earlier stage

- In analyses where the strain field is uniform and local phenomena are not dominant, scaling of the critical strain results in extended scatter when using different meshes, i.e. the case of the US Plate model. However, in actual ship impacts local phenomena are rather dominant due to complicated geometries and an appropriate value of the critical strain should be selected for the relevant mesh size, i.e. application of a scaling law

- Convergence between different meshes is observed in the majority of the simulations for element length over thickness ratios between two and three, i.e. $2 \leq l_e/t \leq 3$ and in some cases between one and two, i.e. $1 \leq l_e/t \leq 2$

- Triaxialities during the loading process and up to rupture in most of the examined cases were over 1/3 or $\beta >$ -1/2. Significant variations of the magnitude of triaxialities were observed in the case of the tearing tests and in models with a more complex geometry

- RTCL criterion predicts rupture at an earlier stage when compared with experimental results in the cases where the structures are loaded transversely and biaxial straining is dominant, i.e. triaxialities are mainly over $1/\sqrt{3}$ or $\beta > 0$. The opposite trend is observed when compared with experimental results of cutting tests, i.e. triaxialities are mainly below zero or $\beta <$ -1

- When a material curve that is obtained from a tensile test is associated with the mid strain-rate applicable to the ends of the specimen during the test, the effect of strain-rate on material behaviour is overestimated. This is because the so defined mid strain-rate is lower than the true strain-rate inside the neck

- Element length over thickness ratios up to 4 yield realistic representation of the deformation patterns especially in more complex structures

- Realistic simulation of the indentation tests and consistency in terms of the representation of the deformation patterns and the estimation of the absorbed energy is achieved with

  - the scaled form of SHEAR rupture criterion, i.e. the criterion based on maximum equivalent plastic strain, with a cut-off value of triaxialities equal to -1/3 below which the criterion is not activated, whereby the threshold value of strain depends on the element length over thickness ratio

  - a true stress-strain curve that is appropriate for the relevant element length; in most cases a powerlaw type material curve is the best choice for element length over thickness ratios greater than one, i.e. $l_e/t > 1$

  - an element length over thickness ratio between two and four, i.e. $2 \leq l_e/t \leq 4$ in most of the examined cases

- Actual impacts between deformable bodies

- RTCLS criterion is activated sooner than SHEARS criterion and predicts outer and inner shell rupture of the struck ship at an earlier stage, i.e. triaxialities over $1/\sqrt{3}$, yielding also lower force and absorbed energy values at the specific points

- Tearing of the upper deck of the struck ship is predicted at a later stage using RTCLS criterion, i.e. triaxialities below zero

- The bulb in the cases where both ships are deformable is not significantly deformed during the impact according to RTCLS predictions, due to the earlier rupture of the side of the struck ship

- RTCLS and SHEARS criteria predict similar deformation patterns and force and energy-displacement curves in the case of the collision scenario with a rigid bow and collision angle 50°

- Rupture of the stem or the bulb of the striking ship is not predicted by RTCLS and SHEARS criteria in the cases where the deformable bow is driven towards the rigid Tanker side and rigid wall. As a result both criteria predict similar deformation patterns and force and energy-displacement curves

- Damage occurs at an earlier stage accompanied also with lower plastic dissipation energies according to simulations with collision angle 90° compared to the respective simulations with collision angle 50°

- In the cases of collision scenarios with collision angle 90° the bulb of the striking ship is crushed, i.e. concertina form, while in the cases of collision scenarios with collision angle 50° bending and buckling of the bulb is observed

- The bending and buckling of the bulb in the 50° collision scenario, where both ships are deformable, leads to limited outer shell rupture of the side of the struck ship according to SHEARS criterion's predictions

- The extent of damage on the struck ship is highly dependent on the relative position of the ships as it is found from the analyses with different collision angles. It is noted that, in the cases of collision scenarios with collision angle 50°, where the bow of the striking ship is considered rigid, the extent of damage on the side of the struck ship is greater than in the respective cases of collision scenarios with collision angle 90°

- Frictional dissipation is greater in analyses with collision angle 50°, especially in the case of the collision scenario where both ships are deformable using SHEARS criterion. In this case rupture of the side of the struck ship is limited and bending of the bulb results in an increased contact area during the impact

7.3 Research achievements

In the following are listed the achievements of the present work:

- Definition of the appropriate material relation, i.e. true stress-strain curve, and rupture criterion that should be used in non linear FE simulations with plane stress elements, taking also into account the mesh size effect as well as strain-rate effect

- Establishing of an experimental data base of tests simulating the modes of deformation that mostly occur in ship impacts, which tests can be used for the verification of the numerical simulation techniques

- Definition of a procedure to determine the critical equivalent plastic strain as a function of the element length over thickness ratio

- Determination of modeling parameters for the simulation of the response of ship structures under accidental loading conditions

- Explanation of the behaviour of various failure criteria under plane stress conditions
- Explanation of the behaviour of scaling law in rupture criteria under different strain patterns
- Developing VUMAT subroutine in order to incorporate three rupture criteria in Abaqus/Explicit
- Investigation of the effect of a deformable bow when the bow and the stem is in contact with the side structure in collision simulations

7.4 Proposals for future research

The section discusses the issues that have been emerged from the present work and should be investigated in the future.

1. The present investigation showed that the criterion based on a critical equivalent true plastic strain, i.e. SHEARS criterion, with a cut-off value of triaxialities equal to -1/3 below which the criterion is not activated, whereby the threshold value of strain depends on the material curve and the element length over thickness ratio, simulates the tests in a realistic manner. Though, in this form of SHEARS criterion, the critical equivalent true plastic strain is independent from the stress/strain state encountered during the loading of a structure. On the other hand, the ductile fracture criterion proposed by Lou et al. (2012), is a critical equivalent true plastic strain criterion that accounts for the various fracture mechanisms associated with nucleation, growth and shear coalescence of voids, which may arise within the material volume during loading, by introducing three material parameters (see sub-section 4.1.3, chapter 4). However, a practical and reliable method for the calibration of these parameters, taking also into consideration the mesh size is not yet established and needs further investigation.

2. The proposed formula for the scaling of the critical equivalent true plastic strain accounts for local phenomena and it seems that it overestimates the effect of the element size when the strain is rather uniform over a large area. Thus, it is suggested to investigate if the scaling law should take into account the uniformity of strain pattern and consequently if needed to suggest a scaling law that includes this factor.

3. RTCL criterion yields good results for stress triaxialities in the range of $0 < T < 1/\sqrt{3}$, or $-1 < \beta < 0$. However, as already discussed in section 5.3 of chapter 5, beyond this range it yields rather different results from the experimental observations. This different behaviour may be attributed to the values of the stress triaxiality function $f(T)$ that is multiplied with the increments of the equivalent true plastic strain. Thus, further investigation is needed to define appropriate expressions of function $f(T)$ outside the above range of stress triaxialities.

4. From the full-scale analyses it is evident that the relative position of the striking and struck ship has a strong effect on the results, because it influences the contact area between the two ships, in particular in a realistic simulation with both bodies being deformable. Further, it was shown that the direction of the loading has an effect on the energy that is needed to cause damage at a specific penetration depth, i.e. the dimension of the damage that is normal to the direction of the length of the struck ship. Further investigation is needed, in order to identify the collision scenarios that should be defined for the assessment of the structural crashworthiness of a ship.

5. The ABAQUS and VUMAT interaction should be investigated and eventually further development of the VUMAT subroutine is needed, so that it will be possible a) to use it in association with BWH criterion in a parallel-process environment and b) to include the effect of the strain-rate on rupture, when providing as input a bundle of true stress-strain curves with a strain-rate dependency.

6. In order to improve and validate simulation techniques, it is essential to reproduce damage patterns that occur in actual ship impacts. Unfortunately, accidents still happen and it is suggested to inspect damaged structures, so as to obtain data that may be used in a benchmark study for the verification of the proposed methodology.

This page is intentionally left blank

References

ABAQUS 6.10-2. Documentation, 2010.

AbuBakar, A., Dow, R., Tigkas, I.G., Samuelides, M.S. and Spyrou, K.J. (2010). *Investigation of an actual collision incident between a Tanker and a Bulk Carrier*. In: The 11th International Symposium on Practical Design of Ships and Other Floating Structures (PRADS) 2004. Rio de Janeiro, Brazil.

Alsos, H.S. and Amdahl, J. (2007). *On the resistance of tanker bottom structures during stranding*. Marine Structures 20(4): 218-237.

Alsos, H.S., Hopperstad, O.S., Törnqvist, R. and Amdahl, J. (2008). *Analytical and numerical analysis of local necking using a stress based instability criterion*. International Journal of Solids and Structures 45(7-8): 2042-2055.

Alsos, H.S. and Amdahl, J. (2009). *On the resistance to penetration of stiffened plates, part I: experiments*. International Journal of Impact Engineering 36(6): 799-807.

Alsos, H.S., Amdahl, J. and Hopperstad, O.S. (2009). *On the resistance to penetration of stiffened plates, part II: numerical analysis*. International Journal of Impact Engineering 36(7): 875-887.

Amdahl J. (1983). *Energy absorption in ship-platform impacts.* Department of Marine Technology. Trondheim, Norway. The University of Trondheim. Doctoral Thesis. Report No. UR-83-34.

Amdahl, J. and Kavlie, D. (1992). *Experimental and numerical simulation of double hull stranding*. DNV-MIT workshop on: mechanics of ship collision and grounding.

Andrianopoulos N.P. and Theocaris, P.S. (1985). *The Griffith-Orowan fracture theory revisited: The T-Criterion*. Int. J. Mech. Sci. Vol.27, No. 11/12, pp. 793-80.

Andrianopoulos, N.P., Dodd, B., Kourouklis, S.K. and Limin, L. (1996). *Forming-limit diagrams for Al 2124 and Al−Li 8090 through fracture mechanics and perturbation analysis*. Journal of Materials Processing Technology, 275-282.

ArcelorMittal (2009). *High strength steels*. From http://fce.arcelormittal.com/repository/Automotive_Product%20offer/HighStrengthSteels.pdf

Arrieux, R., Bedrin, C. and Boivin, M. (1982). *Determination of an intrinsic forming limit stress diagram for isotropic metal sheets*. In: Proceedings of the 12th Biennial Congress IDDRG, pp. 61-71.

ASIS. (1993). *The Conference on "Prediction Methodology of Tanker Structural Failure & Consequential Oil Spill"*. Association of Structural Improvement of Shipbuilding Industry of Japan.

ASTM. (2004). International, Designation: E 8M-04. *Standard Test Methods for Tension Testing of Metallic Materials* [Metric], United States.

Astrup, O. (1994). *Cutting of thick plates by a wedge - an experimental study*. MIT-Industry Joint Program on Tanker Safety, Report No. 27, Department of Ocean Engineering, MIT, USA.

Bao, Y. and Wierzbicki, T. (2004). *A comparative study on various ductile crack formation criteria*. Transactions of the ASME;126: 314-24.

Bao, Y. and Wierzbicki, T. (2004). *On fracture locus in the equivalent strain and stress triaxiality space*. International Journal of Mechanical Sciences;46: 81–98.

Bao, Y. and Wierzbicki, T. (2005). *On the cut-off value of negative triaxiality for fracture*. Engineering Fracture Mechanics;72: 1049-69.

Bressan, J.D. and Williams, J.A. (1983). *The use of a shear instability criterion to predict local necking in sheet metal deformation*. International Journal of Mechanical Science 25, 155–168.

Bridgman, P.W. (1952). *Studies in large flow and fracture*. New York: McGraw-Hill.

Buldgen, L., Le Sourne, H., Besnard, N. and Rigo, P. (2012). *Extension of the super-element method to the analysis of oblique collision between two ships*. Marine Structures 29: 22-57.

Buldgen, L., Le Sourne, H. and Rigo, P. (2013). *A simplified analytical method for estimating the crushing resistance of an inclined ship side*. Marine Structures 33: 265-296.

Butt, N., Johnson, D., Pike, K., Pryce-Roberts, N. and Vigar, N. (2013). *15 Years of Shipping Accidents: A review for WWF*. Southampton Solent University.

Cockcroft, M.G. and Latham, D.J. (1968). *Ductility and the workability of metals*, J. Inst. Metals 96, 33-39.

Considère, A. (1885). *Ann. des Ponts et Chaussées*, 9: 574.

Cowper, G.R. and Symonds, P.S. (1957). *Strain hardening and strain-rate effects in the impact loading of cantilever beams*. Brown University Division of Applied Mathematics Report No. 28, September 1957.

DIMA (2001). *Collision on 29 March 2001 between the Tanker BALTIC CARRIER, registered on Marshall Island and the Bulk Carrier TERN, registered on Cyprus*. Danish Maritime Authority, Ministry of Trade and Industry. Division for Investigation of Marine Accidents, Casualty Report, 18 July 2001.

DNV. (1993). Report 93-2080. *Cutting of thick plates by a wedge - an experimental study*. Norway.

Ehlers, S., Broekhuijsen, J., Alsos, H. S., Biehl, F. and Tabri, K. (2008). *Simulating the collision response of ship side structures: a failure criteria benchmark study*. International Shipbuilding Progress 55(1-2): 127-144.

Ehlers, S. and Varsta, P. (2009). *Stress and strain relations for non-linear finite element simulations*. Thin-Walled Structures 47(11): 1203-1217.

Ehlers, S., Tabri, K., Romanoff, J. and Varsta, P. (2010). *Numerical and Experimental Investigation on the Collision Resistance of the X-core Structure*. Journal of Ships and Offshore Structures, Special Issue on Collision and Grounding: 1-9.

Ehlers, S. (2010a). *Strain and stress relation until fracture for finite element simulations of a thin circular plate*. Thin-Walled Structures 48, 1-8.

Ehlers, S. (2010b). *A material relation for numerical ship collision analysis*. In Proceedings of 5th International Conference on Collision and Grounding of Ships, Helsinki, Finland.

Ehlers, S. (2010c). *The influence of the material relation on the accuracy of collision simulations*. Marine Structures 23;462-474.

EMSA. (2010). *Maritime Accident Review 2010.* European Maritime Safety Agency.

Endo, H., Yamada, Y. and Kawano, H. (2004). *Verification on the effectiveness of buffer bow structure through FEM simulation*. In: The 3rd International Conference of Collision and Grounding of Ships (ICCGS) 2004. Tokyo, Japan.

Fricke, W., Schöttelndreyer, M. and Tautz, I. (2014). *Validierung von Kollisionsberechnungen durch Großversuche an Konstruktionsvarianten von Seitenhüllen*. Technische Universität Hamburg-Harburg, ELKOS 03SX284B.

Gong, A.Y.F., Liu, J.X., Xiao, B.S.M. and Wang, N. (2013). *The analysis and comparison of double side skin crashworthiness*. In: The 6th International Conference of Collision and Grounding of Ships (ICCGS) 2013. Trondheim, Norway.

Hegazy, E.H. (1980). *A method for estimating the energy absorbed by ship structures during collisions*. University of Newcastle upon Tyne.

HELSINKI COMMISSION. (2009). *Report on shipping accidents in Baltic Sea area during 2009*. Baltic Marine Environment Protection Commission.

Hill, R. (1952). *On discontinuous plastic states with special reference to localized necking in thin sheets*. Journal of the Mechanics and Physics of Solids 1, 19-30.

Hogström, P., Ringsberg, J.W. and Johnson, E. (2009). *An experimental and numerical study of the effects of length scale and strain state on the necking and fracture behaviours in sheet metals*. International Journal of Impact Engineering 36(10-11): 1194-1203.

Hogström, P., Ringsberg, J.W. and Johnson, E. (2010). *Analysis of a struck ship with damage opening - influence from model and material properties uncertainties*. In Proceedings of 29th Conference on Ocean, Offshore and Arctic Engineering (OMAE 2010), Shanghai, China, June 6-11.

Hogström, P. and Ringsberg, J. (2012). *An extensive study of a ship's survivability after collision - A parameter study of material characteristics, non-linear FEA and damage stability analyses*. Marine Structures 27:1-28.

Hogström, P. (2012). *RoPax Ship Collision-a Methodology for Survivability Analysis*. Department of Shipping and Marine Technology. Gothenburg, Sweden. Chalmers University of Technology. Doctoral Thesis.

Hogström, P. and Ringsberg, J. (2013). *Assessment of the crashworthiness of a selection of innovative ship structures*. Ocean Engineering 59(1):58-72.

Hong, L. and Amdahl, J. (2008b). *Plastic mechanism analysis of the resistance of ship longitudinal girders in grounding and collision*. Ships and Offshore Structures, 3(3):159-171.

HORIZON. (2012). *Project Horizon-A wake-up call*. Research report 2012. Part EU funded Project No. FP7 234000

Huatao, J. and Röhr, U. (2004). *Investigation of the Rupture Failure of Welding Lines*. In: The 3rd International Conference of Collision and Grounding of Ships (ICCGS) 2004. Izu, Japan.

Hung, C.F., Wu, K.P. and Huang, Y.T. (2010). *The strength characteristics of different types of double hull structures in collision*. In: The 5th International Conference of Collision and Grounding of Ships (ICCGS) 2010. Espoo, Finland.

ISSC Committee V.III. (2003). *Collision and Grounding*. In Proceedings of the 15th International Ship and Offshore Structures Congress, San Diego, USA, edited by Mansour, A.E. and Ertekin, R.C.

Isselin, J., Lost, A., Golel, J., Najjar, D. and Bigerelle, M. (2006). *Assessment of the constitutive law by inverse methodology: small punch test and hardness*. Journal of Nuclear Materials 352(1–3): 97-106.

Jeong, D.Y., Yu, H., Gordon, J.E. and Tang, Y.H. (2008). *Finite element analysis of unnotched charpy impact tests*. In: The Materials Science and Technology Conference and Exhibition, 2008.

Johnson, G.R. and Cook, W.H. (1983). *A constitutive model and data for metals subjected to large strains, high strain-rates and high temperatures*. In: The 7th International symposium on ballistics. The Hague; pp. 541-7.

Johnson, G.R. and Cook, W.H. (1985). *Fracture characteristics of three metals subjected to various strains, strain-rates, temperatures and pressures*. Engineering Fracture Mechanics; 21: 31-48.

Keeler, S.P. and Backhofen, W.A. (1964). *Plastic instability and fracture in sheet stretched over rigid punches*. ASM Transactions Quarterly 56, 25-48.

Kitamura, O. (1997). *Comparative Study on Collision Resistance of Side Structure*. Marine Technology 34, 293-308.

Kitamura, O. (2000). *Buffer bow design for the improved safety of ships*. Proceedings of the SSC/SNAME/ASNE Symposium 2000 ‘‘Ship Structures for the New Millennium’’, Arlington.

Kitamura, O. (2001). *FEM Approach to the Simulation of Collision and Grounding Damage*. In: The 2nd International Conference on Collision and Grounding of Ships (ICCGS) 2001. Copenhagen, Denmark.

Konter, A. Broekhuijsen, J. and Vredeveldt, A. (2004). *A quantitative assessment of the factors contributing to the accuracy of ship collision predictions with the finite element method*. In: Proceedings of the 3rd International Conference on Collision and Grounding of Ships (ICCGS) 2004. Tokyo, Japan.

Kõrgesaar, M. and Romanoff, J. (2014). *Influence of mesh size, stress triaxiality and damage induced softening on ductile fracture of large-scale shell structures*. Marine Structures, 38, 1-17.

Kõrgesaar, M. (2015). *Modeling ductile fracture in ship structures with shell elements*. Department of Applied Mechanics. Helsinki, Finland. Aalto University. Doctoral Thesis.

Lehmann, E. and Yu, X. (1998). *On Ductile Rupture Criteria for Structural Tear in the Case of Ship Collision and Grounding*. Practical Design of Ships and Mobile Units, PRADS. Elsevier Science B.V.

Lehmann, E. and Peschmann, J. (2002). *Energy absorption by the steel structure of ships in the event of collisions*. Marine Structures 15(4-5): 403-428.

Ling, Z. (1996). *Uniaxial true stress-strain after necking*. AMP Journal of Technology;5: 37-48.

Liu, B., Villavicencio, R. and Soares, C.G. (2012). *Experimental and numerical plastic response and failure of laterally impacted rectangular plates*. In: Proceedings of the 31st International Conference on Ocean, Offshore and Arctic Engineering (OMAE 2012), Rio de Janeiro, Brazil, June 10-15.

Lou, Y.S., Huh, H., Lim, S. and Pack, K. (2012). *New ductile fracture criterion for prediction of fracture forming limit diagrams of sheet metals*. International Journal of Solids and Structures 49, 3605-3615.

Lützen, M., Simonsen, B.C. and Pedersen, P.T. (2000). *Rapid prediction of damage to struck and striking vessels in a collision event*. In: Proceedings of Ship Structure Symposium 2000, Washington D.C., USA.

Marciniak, Z., Duncan, J.L. and Hu, S.J. (2002). *Mechanics of sheet metal forming*. Oxford, U.K. Butterworth-Heinemann.

Marinatos, J.N. and Samuelides, M. (2013a). *Material modeling for Finite-Element simulation of ship impacts*. In: The 4th International Conference on Marine Structures (MARSTRUCT) 2013. Espoo, Finland.

Marinatos, J.N. and Samuelides, M. (2013b). *Material characterization and implementation of the RTCL, BWH and SHEAR failure criteria to finite element codes for the simulation of impacts on ship structures*. In: The 6th International Conference of Collision and Grounding of Ships (ICCGS) 2013. Trondheim, Norway.

Marinatos, J.N. and Samuelides, M. (2015). *Towards a unified methodology for the simulation of rupture in collision and grounding of ships*. Marine Structures, 42, 1-32.

McClintock, F.A. (1968). *A Criterion of Ductile Fracture By the Growth of Holes*. ASME Journal of Applied Mechanics, 35, pp. 363-371.

MEPC 58/INF.2 (2008). *"FSA-crude oil tankers, Details of the Formal Safety Assessment"*. Submitted by Denmark, IMO London, 4 July 2008.

Minorsky, V.U. (1959). *An analysis of ship collisions with reference to protection of nuclear power plants*. Journal of Ship Research 3: 1-4.

Okazawa, S., Fujikubo, M. and Hiroi, S. (2004). *Static and dynamic necking analysis of steel plates in tension.* In: Proceedings of the 3rd International Conference on Collision and Grounding of Ships (ICCGS) 2004. Tokyo, Japan.

Ozguc, O., Das, P.K. and Barltrop, N.(2006). *A comparative study on the structural integrity of single and double side skin bulk carriers under collision damage*. Marine Structures, 18 (7-8): 511-547.

Paik, J.K. and Tak, L.K. (1995). *Cutting tests for a stiffened plate by a wedge*. In Proceedings of the International Conference on Technologies for Marine Environment Preservation;Vol.1, Tokyo, Japan.

Paik, J.K., Chung, J.Y., Choe, I.H., Thayamballi, A.K., Pedersen, P.T. and Wang, G. (1999). *On rational design of double hull tanker structures against collision*. In: The Society of Naval Architects and Marine Engineers;Vol. 107: 323-363.

Papanikolaou, A., Eliopoulou, E. and Mikelis, N. (2006) *Impact of hull design on tanker pollution*. In: Proceedings of 9th International Marine Design Conference (IMDC 2006), May 16-19 2006, Ann Arbor, Michigan.

Pedersen, P.T. and Zhang, S. (1998). *On Impact mechanics in ship collisions*. Marine Structures 11, 429-449.

Peschmann, J. (2001). *Energy absorption computations of ship steel structures under collision and grounding* (translated from German language). Hamburg, Germany. Technical University of Hamburg. Doctoral Thesis.

Reckling, K.A. (1983). *Mechanics of minor ship collisions*. International Journal of Impact Engineering. 1:281–299.

Rice, J. and Tracey, D. (1969). *On the ductile enlargement of voids in triaxial stress fields*. Journal of the Mechanics and Physics of Solids 17, 201-217.

Ringsberg, J.W. (2010). *Characteristics of material, ship side structure response and ship survivability in ship collisions*. Ships and Offshore Structures, Vol. 5, No. 1, 51-66.

Samuelides, M. S., Voudouris, G., Toulios, M., Amdahl, J. and Dow, R. (2007). *Simulation of the behavior of double bottoms subjected to grounding actions*. In: The 4th International Conference of Collision and Grounding of Ships (ICCGS) 2007. Hamburg, Germany.

Samuelides, M.S. (2009). *Design against collision: Fifty years of research*. In: Proceedings of 10th International Marine Design Conference (IMDC) 2009, Trondheim, Norway.

Samuelides, M.S. (2015). *Recent advances and future trends in structural crashworthiness of ship structures subjected to impact loads*. Ships and Offshore Structures, Vol. 0, No. 0, 1-10.

Savvas, D.N. (2009). *Criteria to predict damage of structures made of ductile materials in various stress states and application in finite element codes*. School of Naval Architecture and Marine Engineering. Athens, Greece. National Technical University of Athens. Post Graduate Thesis.

Servis, D. (2003). *Structural response and material failure in ship impacts*. School of Naval Architecture and Marine Engineering. Athens, Greece. National Technical University of Athens. Doctoral Thesis.

Servis, D. and Samuelides, M. (2006). *Implementation of the T-failure criterion in finite element methodologies*. Computers and Structures 84, 196-214.

Schöttelndreyer M., Tautz I., Fricke W. and Lehmann E. (2013). *Side Structure filled with multicellular glass hollow spheres in a quasi-static collision test*. In: Proceedings of 6th International Conference on Collision and Grounding of Ships (ICCGS) 2013. Trondheim, Norway.

Simonsen, B.C. (1997). *Mechanics of ship grounding*. Department of Naval Architecture and Offshore Engineering. Lyngby, Denmark. Technical University of Denmark. Doctoral Thesis.

Simonsen, B.C. and Törnqvist, R. (2004). *Experimental and numerical modelling of ductile crack propagation in large-scale shell structures*. Marine Structures 17, 1-27.

Stören, S. and Rice, J.R. (1975). *Localized necking in thin sheets*. Journal of the Mechanics and Physics of Solids 23, 421.

Stoughton, T.B. (2000). *A general forming limit criterion for sheet metal forming*. International Journal of Mechanical Science 42, 1-27.

Stoughton, T.B. (2001). *Stress-based forming limits in sheet metal forming*. Journal of Engineering Materials and Science 123, 417-422.

Stoughton, T.B. and Zhu, X. (2004). *Review of theoretical models of the strain-based FLD and their relevance to the stress-based FLD.* International Journal of Plasticity 20(8-9): 1463-1486.

Swift, H.W. (1952). Journal of the Mechanics and Physics of Solids 1, 1-18.

Tabri, K., Broekhuijsen, J., Matusiak, J. and Varsta, P. (2009a). *Analytical modelling of ship collision based on full-scale experiments*. Marine Structures 22(1): 42-61.

Tautz, I., Schöttelndreyer, M., Lehmann, E. and Fricke, W. (2013). *Collision tests with rigid and deformable bulbous bows driven against double hull side structures*. In: The 6th International Conference of Collision and Grounding of Ships (ICCGS) 2013. Trondheim, Norway.

The Republic of the Marshall Islands (2002). *Report of Investigation in the Matter of the Collision between the Tankship BALTIC CARRIER (O.N. 1430) and the Bulk Carrier TERN in the Baltic Sea on 29 March* 2001. Decision of the Maritime Administrator, 20 May 2002.

Törnqvist, R. (2003). *Design of crashworty ship strucures*. Department of Naval Architecture and Offshore Engineering. Lyngby, Denmark. Technical University of Denmark. Doctoral Thesis.

Villavicencio, R. and Soares, C.G. (2011). *Numerical prediction of impact loads in rectangular plates*. In: Proceedings of Advances in Marine Structures (MARSTRUCT) 2001. Hamburg, Germany edited by Guedes Soares and Fricke.

Villavicencio, R. (2012). *Response of ship structural components to impact loading*. IST. Lisbon, Portugal. Technical University of Lisbon. Doctoral Thesis.

Villavicencio, R., Liu, B. and Soares, C.G. (2013). *Response of a tanker side panel punched by a knife edge indenter*. In: The 6th International Conference of Collision and Grounding of Ships (ICCGS) 2013. Trondheim, Norway.

Wang, G., Arita, K. and Liu, D. (2000). *Behaviour of a double hull in a variety of stranding or collision scenarios*. Marine Structures; 13:147-87.

Wevers, L.J. and Vredeveldt, A.W. (1999). *Full scale ship collision experiments 1998*, TNO. Report 98-CMC-R1725. The Netherlands: Delft;. p. 260

Whirley, R.G., Hallquist, J.O. and Goudreau, G.L. (1989). *An assessment of numerical algorithms for plane stress and shell elastoplasticity on supercomputers*. Methods Development Group, L-122, Lawrence Livermore National Laboratory, PO Box 808, Livermore, CA 94550, USA.

Woisin, G. (1976). *Die Kollisionsversuche der GKSS (The Collision Tests of the GKSS)*. Jahrbuch der Schiffbautechnischen Gesellschaft, Berlin, Heidelberg, New York, Vol. 17, pp.465–487.

Woisin, G. (1987). *Instantaneous loss of energy with unsymmetric ship collisions*. In: Proceedings of PRADS 1987, Trondheim.

Wu, P.D., Graf, McEwen, S.R., Lloyd, D.J., Jain, M. and Neale, K.W. (2005). *On forming limit stress diagram analysis*. International Journal of Solids and Structures 42, 2225-2241.

Zhang, K.S. (1995). *Fracture prediction and necking analysis*. Engineering Fracture Mechanics;52(3): 575-82.

Zhang, Z.L., Hauge, M., Ødegard, J. and Thaulow, C. (1999). *Determining material true stress-strain curve from tensile specimens with rectangular cross-section*. International Journal of Solids and Structures;36(23): 3497–516.

Zhang, Z.L., Egge, E.D. and Brunhs, H. (2004). *Approval Procedure Concept for Alternative Arrangements*. In: The 3rd International Conference on Collision and Grounding of Ships (ICCGS) 2004. Tokyo, Japan.

Appendix A

Experimental Data

The annex summarizes the configurations of each test, the dimensions of the test components, the form of the rigid or deformable indenters and the stress-strain engineering curves for each material used in the examined experiments.

A.1 US Plate, 1-FB and 2-FB models-(Alsos and Amdahl 2009)

Figure A.1 illustrates the plate, stiffeners and frame configuration as well as the stress-strain engineering curves for the plate and the stiffener. The dimensions of each component are included in the schematic view of the test set-up. The plate is welded to a strong frame, while the stiffeners are welded to the plate and the stiffener ends are fixed to the frame. The plate and the flat bar stiffeners are made from mild steel (S235JR EN10025).

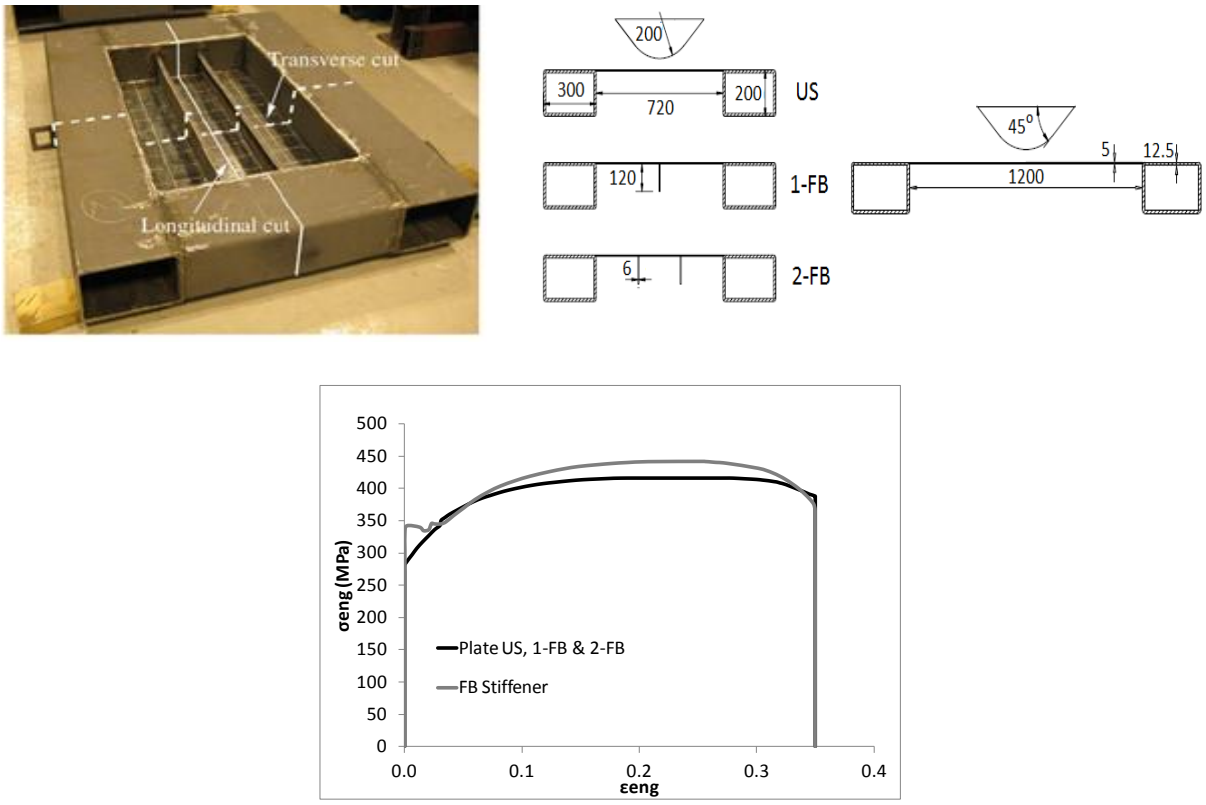

Figure A.1. The test set-up and schematic view of each component (upper) and stress-strain engineering curves for the plates and the FB stiffeners (lower)

A.2 ST-3-BW, ST-3-OW, ST-4-BW and ST-4-OW models-(Paik et al. 1999)

Figure A.2 illustrates a schematic view of the rigid indenter and its position between and on webs, respectively. The boundaries of the test models are considered to be fixed. The location of the indenter is at the center of the test structure. The double bottom models are made from mild steel and are composed of outer-inner skin plating and longitudinal-transverse webs. Figure A.3 shows a more detailed description of the models. The depth between the outer-inner skin plating in each case is 350 mm. The thicknesses of the structural components are 2.8 mm and 3.95 mm for the cases of the ST-3 and ST-4 models, respectively. The stress-strain engineering curves for each material are illustrated in Figure A.4.

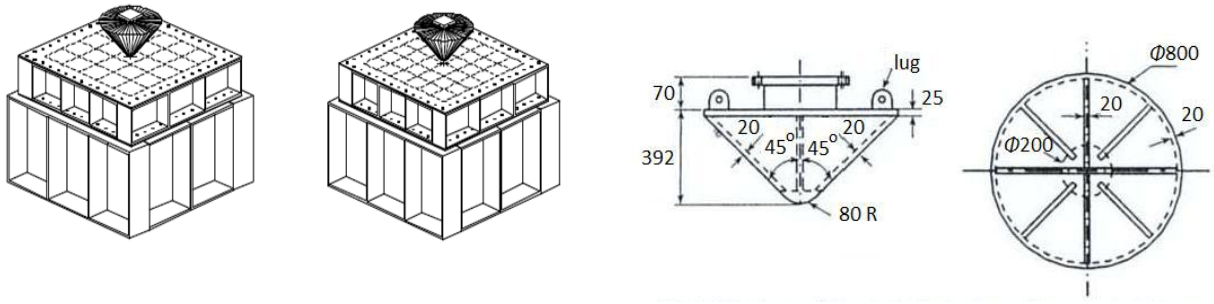

Figure A.2. Schematic view of the test set-up for initial colliding ‘between webs’ and ‘on webs’ (on the left) and the rigid indenter (on the right)

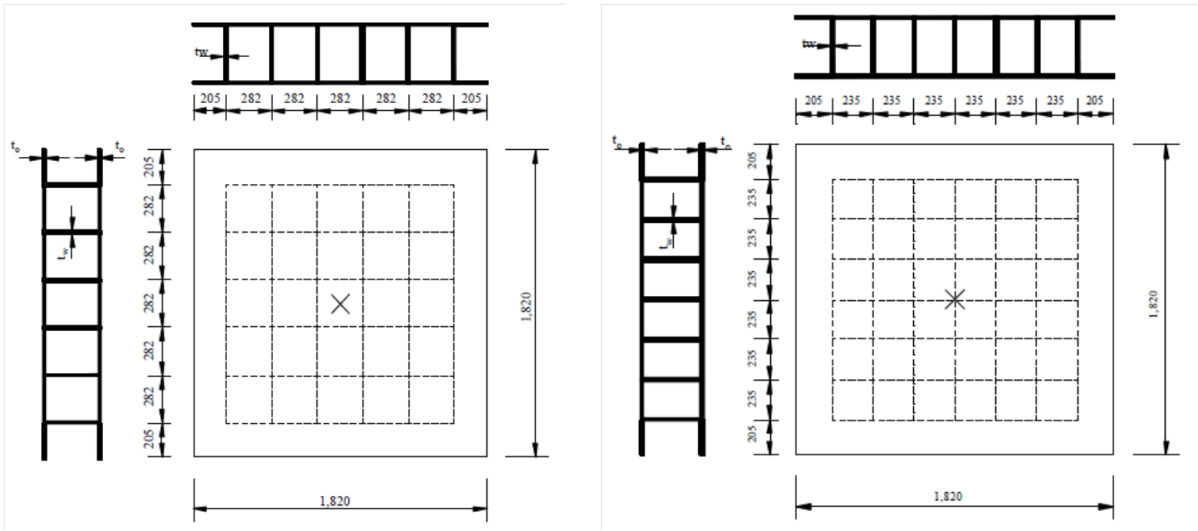

Figure A.3. Details of the ST-3-BW and ST-4-BW models (on the left) and of the ST-3-OW and ST-4-OW models (on the right)

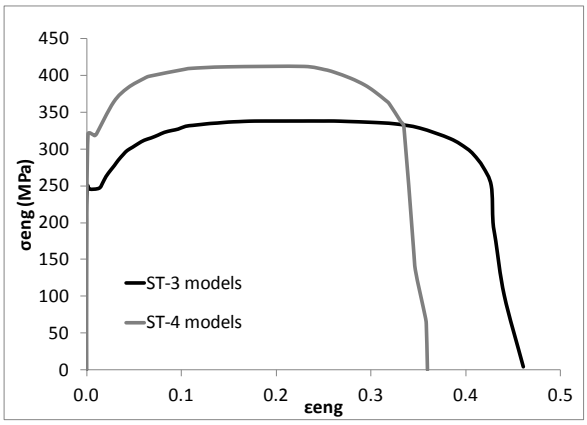

Figure A.4. Stress-strain engineering curves for the ST-3 and ST-4 models

A.3 US, LS, TS and OS models-(Paik and Tak 1995)

Figure A.5 illustrates the schematic view of the test set-up, representing the stiffened plate with two longitudinal and transverse stiffeners and the rigid wedge. Table A.1 summarizes the dimensions of each component shown in Figure A.5. The angle and breadth of the wedge are 60° and 110 mm, respectively. The edges of the plate and the transverse stiffeners are considered fixed, except at the side that faces the rigid sharp wedge.

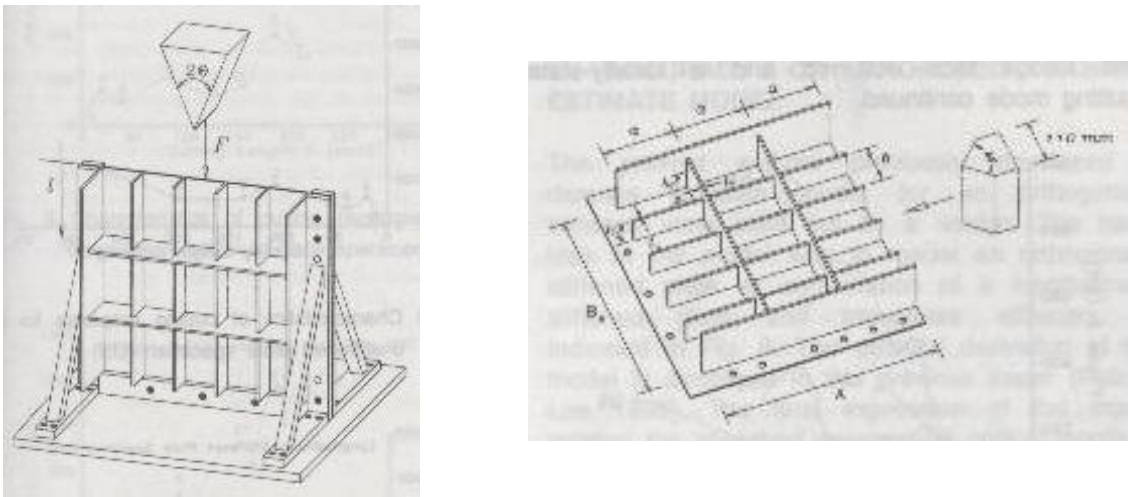

Figure A.5. Schematic view of the test set-up (on the left) and geometry of the orthogonally stiffened plate and rigid sharp wedge (on the right)

Table A.1. Details of the test specimens (mm)

Specimen	A	B_s	t	t_L	h_L	t_T	h_T	a	b
US	499.0	502.5	7.03	-	-	-	-	-	-
LS	502.5	499.0	7.05	7.34	71.53	-	-	-	97.6
TS	504.0	502.5	7.30	-	-	7.57	104.0	166.5	-
OS	500.0	499.5	7.40	7.13	69.55	7.17	105.8	165.2	100.3

A.4 COLLISION STATIC and COLLISION DYNAMIC models-(ASIS 1993 reported in ISSC 2003)

Figure A.6 shows the schematic views of the double hull model and the bow. The test model is scaled down with a factor of about 1:2. The left and right ends of the model are welded to very rigid support structures and the bottom plate is fixed to the test bed with bolts and nuts. The details of the double hull model are presented in Figure A.8.

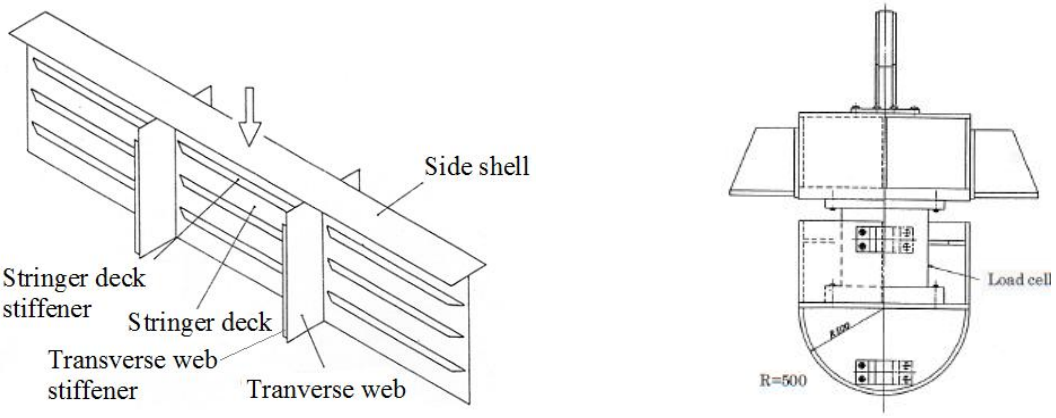

Figure A.6. Schematic view of the double hull (on the left) and bow (on the right)

In the dynamic test the rigid bow shape indenter with a dummy weight and a load cell, having an overall weight about 8.4 $tons$, was freely fallen from 4.8 m above the initial position of the outer hull. The colliding velocity was approximately 9.7 m/sec. Free fall loadings were repeated until the penetration of the bow reached at about 900 mm. To account for the strain-rate effect, uniaxial tensile tests were conducted with loading velocities varying between 0.05-5 m/sec. For specimens with a 50 mm gauge length, this implies strain-rate values between 1-100 sec^{-1}. Figure A.7 shows the test specimen used in the static and dynamic tensile tests. The stress-strain relationships measured in the static and dynamic tests for three material thicknesses are shown in Figure A.9. Note that, the strain-rate values are mid engineering values.

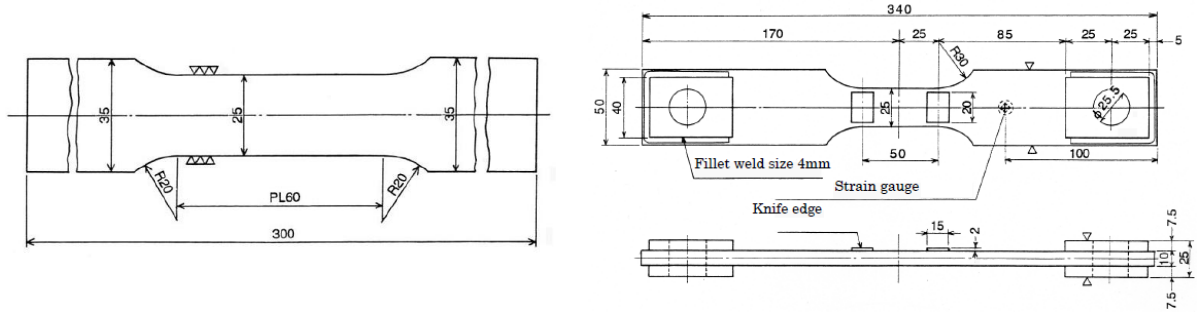

Figure A.7. Test specimen of static tensile (on the left) and dynamic test (on the right)

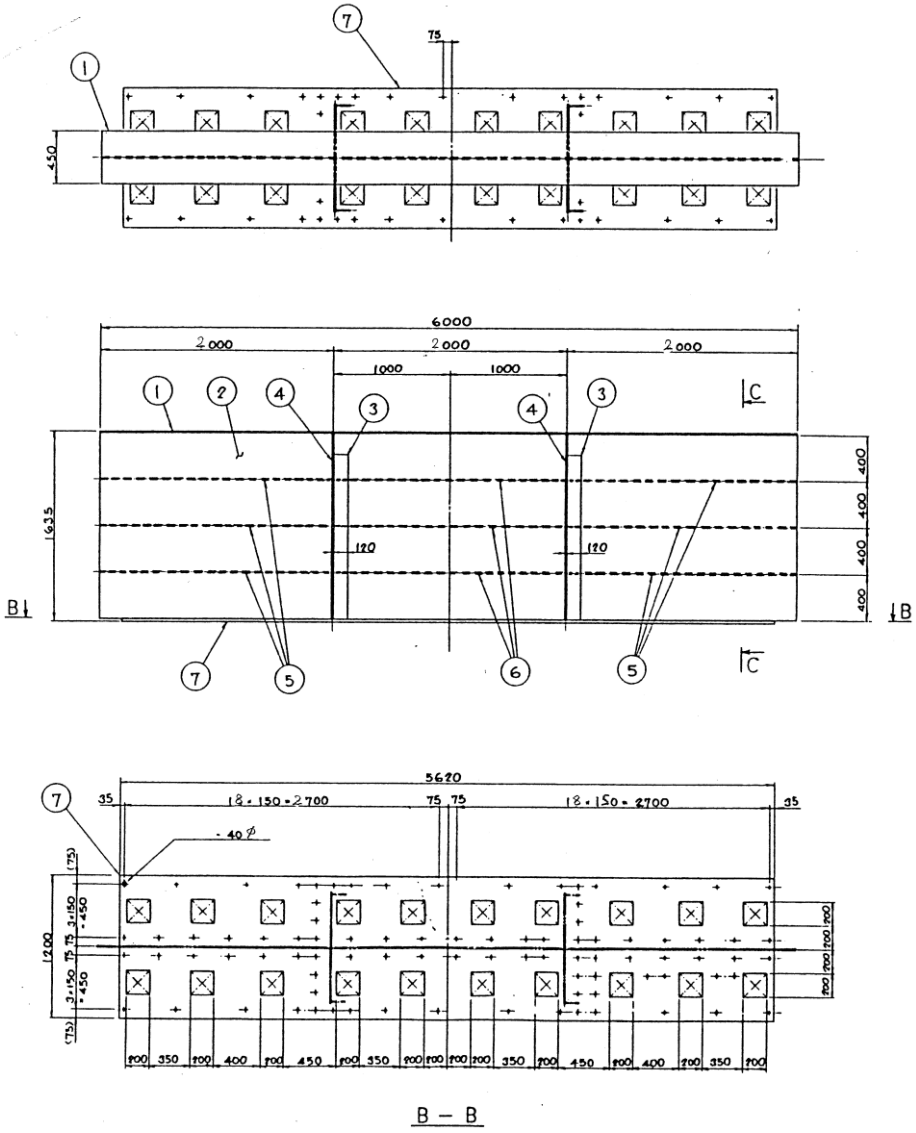

Plate	thickness	Plate size
(7)	25 *mm*	1200×5620
(6)	7 *mm*	100×1992
(5)	7 *mm*	100×1996
(4)	8 *mm*	461.5×1600
(3)	7 *mm*	120×1422
(2)	7 *mm*	1600×6000
(1)	10 *mm*	450×6000

Figure A.8. Double hull model

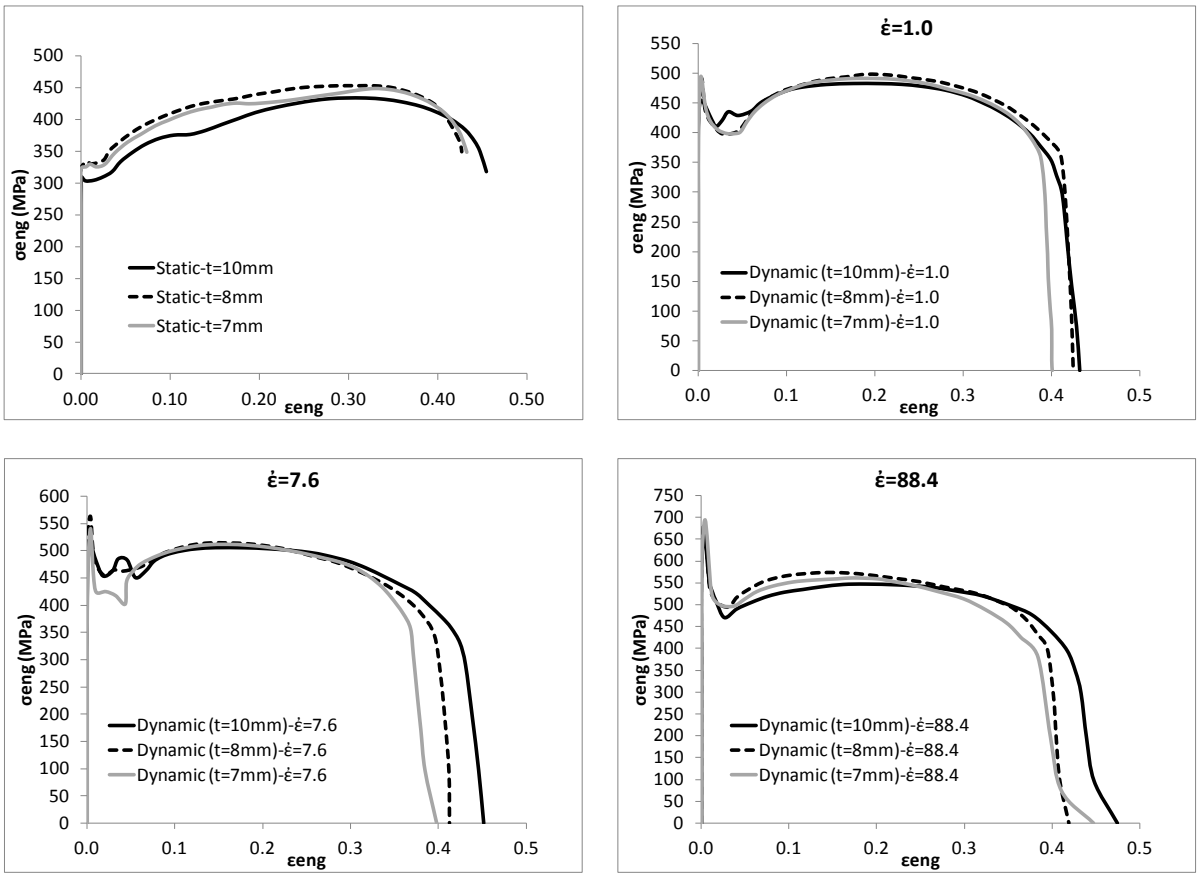

Figure A.9. Stress-strain engineering curves for the Collision Static and Dynamic tests

A.5 OUTER SHELL and INNER SHELL models-(Gong et al. 2013)

Figure A.10 illustrates the schematic views of the outer and inner shell structure models. Model boundaries are welded to a strong frame. Figure A.11 presents the test specimen and the engineering stress-strain curves of the plate and stiffeners, respectively.

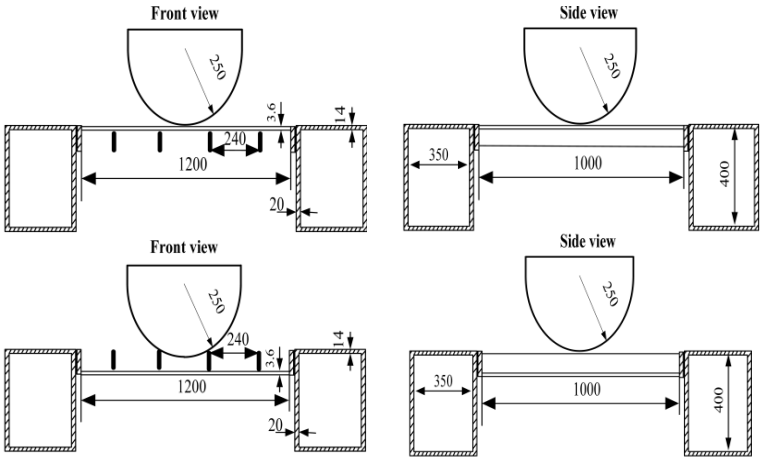

Figure A.10. Schematic view of the outer (upper) and inner (lower) shell structure models

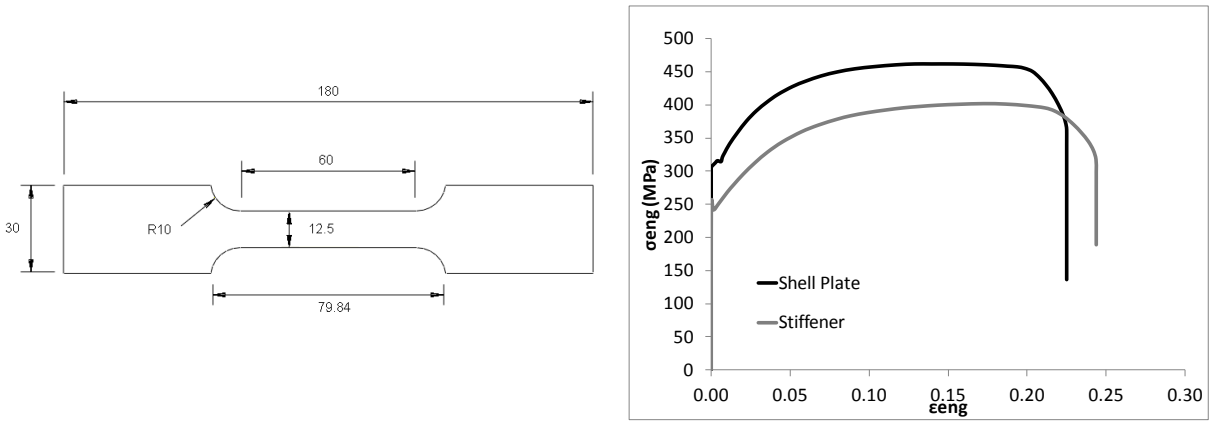

Figure A.11. Test specimen (on the left) and stress-strain engineering curves (on the right) for the shell plate and stiffener components

A.6 FLAT SPECIMEN and KNIFE SPECIMEN models-(Villavicencio 2012 and Villavicencio et al. 2013)

Figure A.12 shows the schematic views of the specimen and the indenters with the knife and flat edges. Model boundaries are welded to a strong frame. Figure A.13 illustrates the test specimen and the engineering stress-strain curves of the plate and stiffener components.

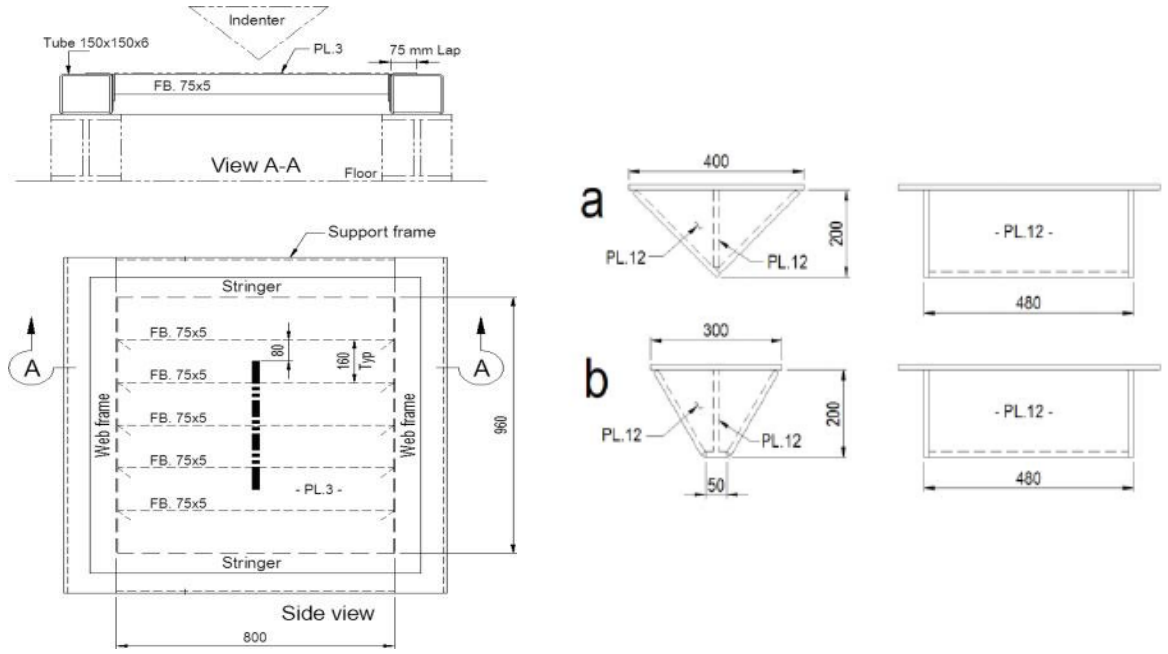

Figure A.12. Geometry of the side panel specimen (on the left) and the (a) knife and (b) flat edge indenters (on the right)

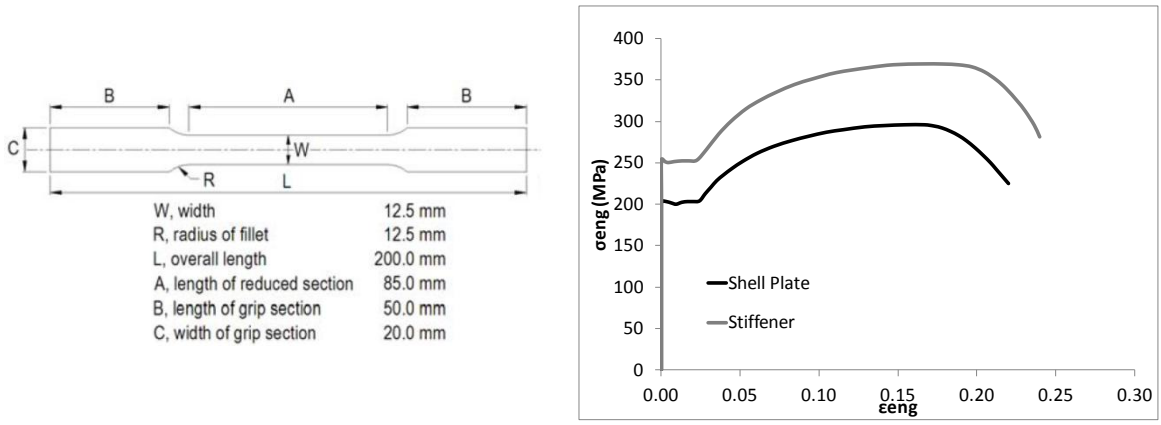

Figure A.13. Test specimen (on the left) and stress-strain engineering curves (on the right) for the shell plate and stiffener components

A.7 CE-1 and CE-2 models-(Tautz et al. 2013 and Fricke et al. 2014)

Figure A.14 shows the test rig of TUHH, Institute for Ship Structural Design and Analysis and the top view of the side structure. The test model is scaled down with a factor of about 1:3. The test rig is mounted on two longitudinal girders. The model area is welded within a massive supporting frame that represents the boundary conditions of the surrounding structure.

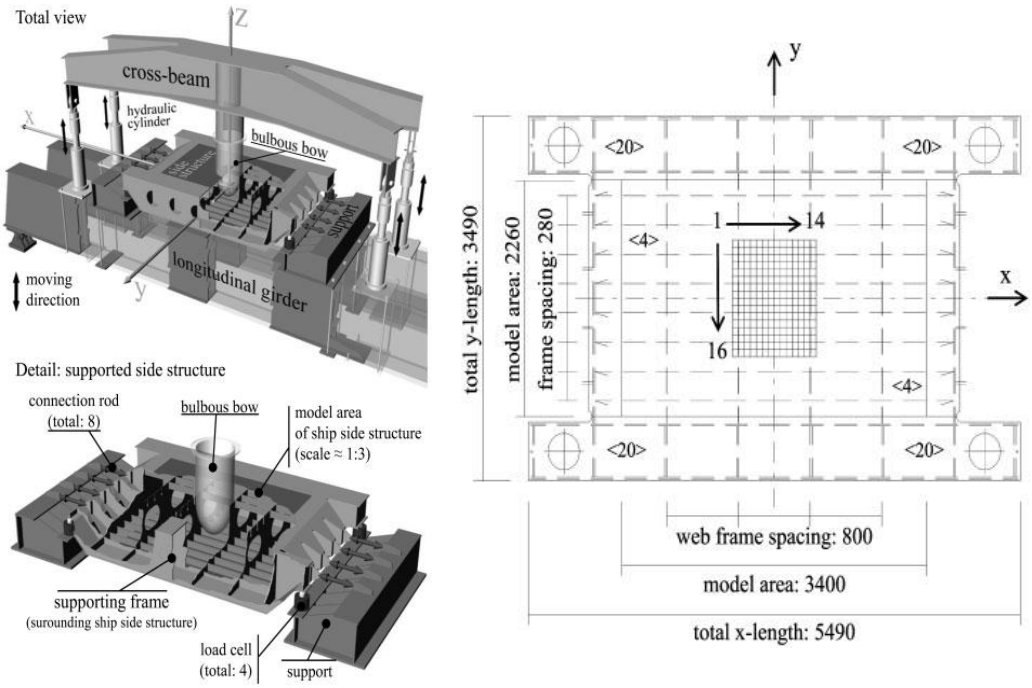

Figure A.14. Collision test rig-total and detailed view (on the left) and top view on side structure (on the right)

Figure A.15 presents the geometries of the rigid and deformable bulbous bows. It is noted that, in the case of the deformable bulbous bow a sheet metal cap 3 *mm* thick is attached to the rigid part of the indenter. The test specimens and the engineering stress-strain curves for each component are illustrated in Figure A.16.

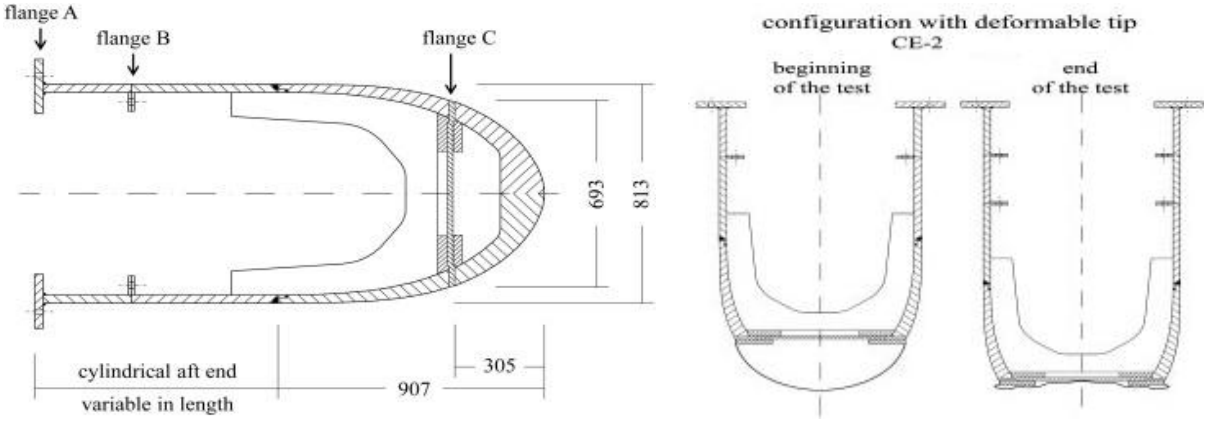

Figure A.15. The rigid bulbous bow (on the left) and the bulbous bow with deformable tip (on the right)

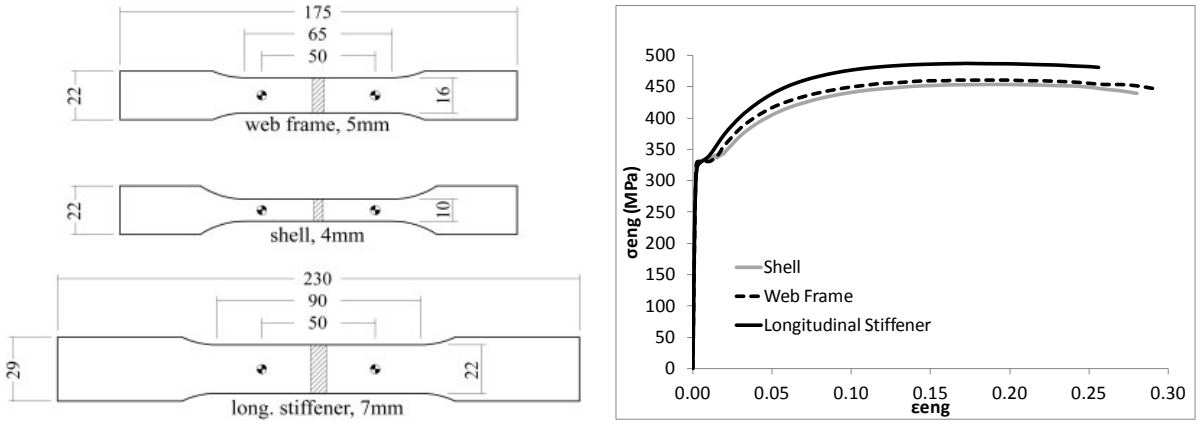

Figure A.16. Stress-strain engineering curves for the shell, web frame and longitudinal stiffener

A.8 P1-15, P2-15, S1-20 and S2-20 models-(DNV 1993)

Figure A.17 illustrates the schematic views of the experimental set-up, the test specimens, i.e. the un-stiffened and stiffened plates and the rigid wedge. The specimen material is a standard ship steel (NVE36). The specimens are fixed to a strong frame by eight high tension bolts of 80 mm diameter. The wedge is welded to a base, which again is fitted to guides between the test rig frame.

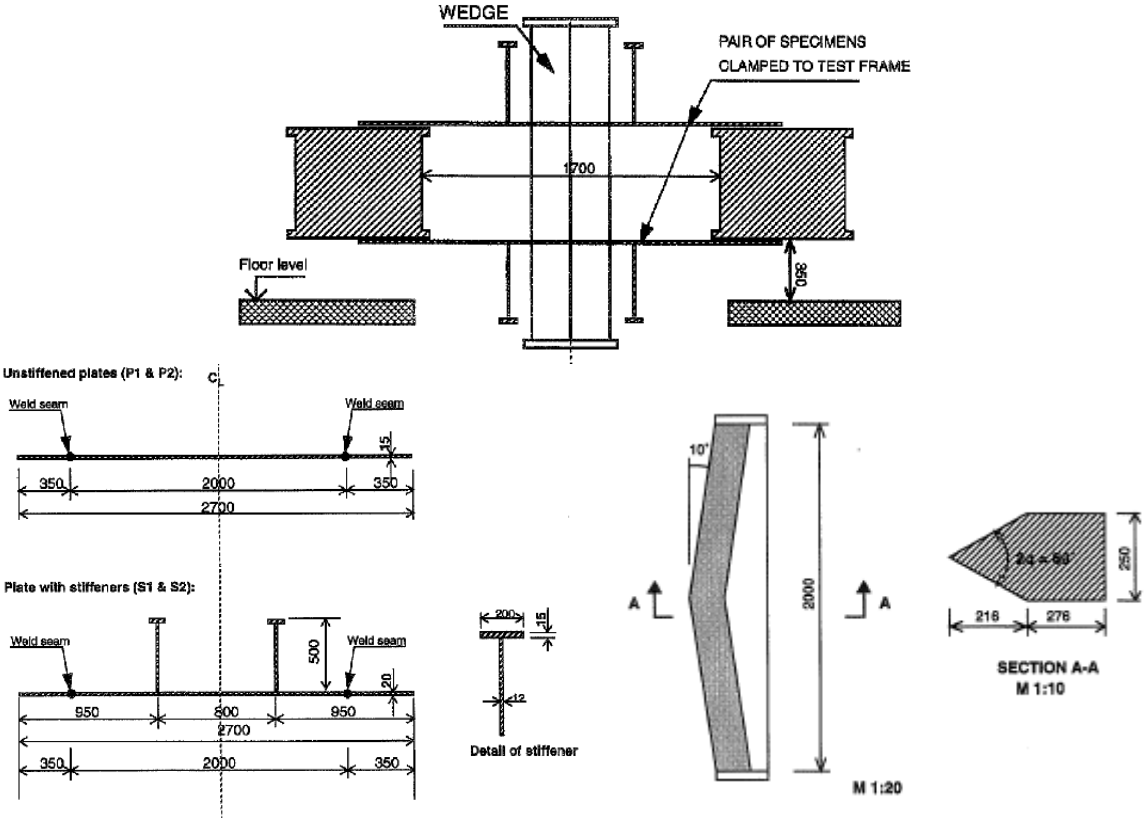

Figure A.17. Experimental set-up (upper), specimen configuration (lower on the left) and schematic view of the wedge (lower on the right)

It is noted that, the stress-strain engineering curves in the preceding figures are in digitized form except in the case of the shell, web frame and longitudinal stiffener components of the CE-1 and CE-2 models, which were provided by the author in Tautz et al. (2013).

In the cases of Paik and Tak (1995) and DNV (1993) experiments, the stress-strain engineering curves were not available. Alternatively, stress-strain engineering curves were selected according to ArcelorMittal (2009), based on the mechanical properties of the materials included in the relevant experiments (see Table 2.1, chapter 2). Moreover, due to lack of the geometries of the flat specimens used in the uniaxial tension tests in the cases of Alsos and Amdahl (2009), Paik et al. (1999), Paik and Tak (1995) and DNV (1993) experiments, test specimens with dimensions as derived according to the ASTM (2004) standard were used in the corresponding uniaxial simulations.

Finally, in the case of the CE-2 model (Tautz et al. 2013 and Fricke et al. 2014), the material of the shell component, but with thickness 3 *mm*, was also used for the modeling of the deformable part of the bulbous bow indenter, as the actual stress-strain engineering curve was not available.

Appendix B

Calibration of SHEAR and RTCL Criteria

In the present analysis SHEAR and RTCL rupture criteria were calibrated through uniaxial simulations by calculating the value of the integral $\int f\left(\frac{\sigma_m}{\sigma_{eq}}\right) d\bar{\varepsilon}^{pl} = D$ up to the experimental point of fracture. For the calculation of the integral in the case of SHEAR criterion function $f\left(\frac{\sigma_m}{\sigma_{eq}}\right)$ of the integral was taken equal to one, that is for triaxialities 1/3, (see also Figure 4.1, chapter 4). The actual value of $f\left(\frac{\sigma_m}{\sigma_{eq}}\right)$ at the integration point should be taken for the calculation of the critical strain to be used with RTCL criterion. However, it has been found that in the case of uniaxial tests the triaxialities are close to 1/3, so that the values of $f\left(\frac{\sigma_m}{\sigma_{eq}}\right)$ are approximately 1 and the use of the actual value does not alter significantly the results. This is portrayed in the following diagrams of Figure B.1 for three of the examined materials, i.e. the shell component with thickness 4 mm (see Tautz et al. 2013 and Fricke et al. 2014) and the components in ASIS (1993) reported in ISSC (2003), with thicknesses 7 mm and 10 mm, respectively using various l_e/t ratios (see also Table 2.1, chapter 2). The diagrams include the variation:

i. of triaxiality $T = \frac{\sigma_m}{\sigma_{eq}}$
ii. of function $f(T)$
iii. of the integral $\int f\left(\frac{\sigma_m}{\sigma_{eq}}\right) d\bar{\varepsilon}^{pl} = D$
iv. of the equivalent true plastic strain ε_{eq} and
v. of the increments dD, $d\bar{\varepsilon}^{pl}$, i.e. defined as $d\varepsilon_{eq}$ in the diagrams of Figure B.1, of the integral D and equivalent true plastic strain, respectively

as the uniaxial simulation progresses. As can be seen, in each case the values of the two variables D and ε_{eq} up to the point the critical displacement is reached are very close. The critical displacement is defined by the engineering fracture strain (see Table 2.1, chapter 2) and the gauge length which is equal to 50 mm. In all of the materials used in the simulations this is the case for ratios $l_e/t \geq 1$, which were used in the simulations of the small to mid-scale models.

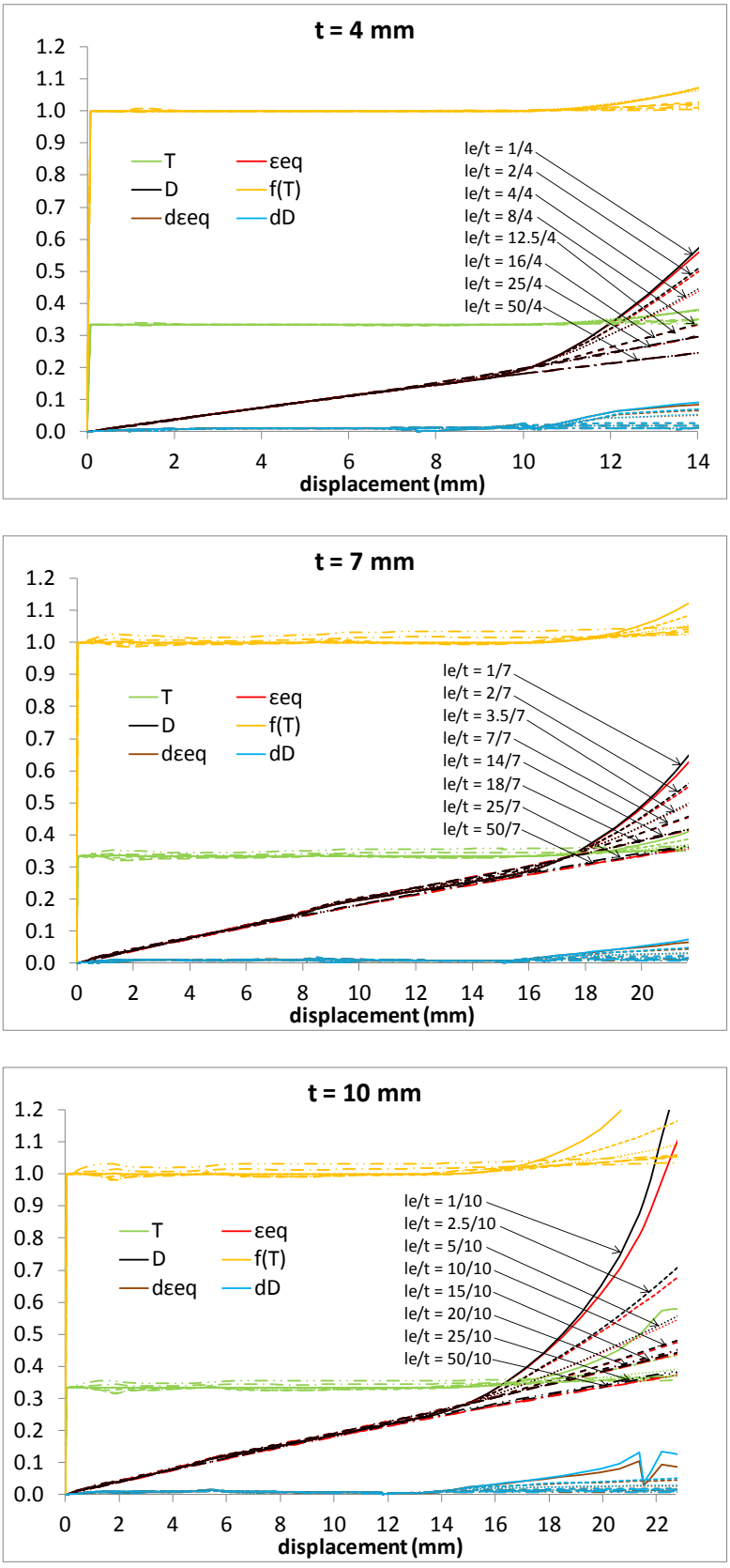

Figure B.1. Variation of T, $f(T)$, ε_{eq}, D, $d\bar{\varepsilon}^{pl}$ and dD variables as the uniaxial simulation progresses for three materials and various l_e/t ratios

Appendix C

VUMAT Subroutine

A brief description of the programming steps for the development of VUMAT subroutine (ABAQUS 2010) is given in the following. VUMAT interacts with the Abaqus/Explicit FE code and refers to an isotropic hardening material that follows the J_2 flow theory assuming plane stress conditions. The program applies the iterative radial return plasticity algorithm presented in Whirley et al. (1989), in order to achieve plane stress conditions, i.e. $\sigma_{33} = 0$.

C.1 Interaction with Abaqus/Explicit

ABAQUS calls VUMAT for a number of through thickness integration points or material points at each time step of the numerical analysis. In Abaqus/Explicit the time step depends on the length of the smallest element in the mesh and is usually in the order of magnitude of $10^{-6} sec$. In ABAQUS 6.10-2, the maximum number of material points called at a time step is 136. For example, assume the model is discretized with the four-node reduced integration quadrilateral Belytschko-Lin-Tsay shell elements, i.e. S4R with one integration point and five integration points through the thickness and the total number of elements or material points in a layer of the shells is 585. Thus, at a specific time step the model is separated into five blocks of material points, where the first four consist of 136 material points each and the last one consists of 41 material points, i.e. $4 \times 136 + 41 = 585$. Hence, VUMAT is called five times for each one of the five blocks of material points to perform calculations for each one of the five layers, i.e. through thickness material points of the shell, that is 25 times for a time step. This procedure is repeated in a new time step until the total time of the simulation is reached.

The number of the through thickness integration points is defined at the section properties of the shell and the thickness integration rule used in the present work is according to Simpson, i.e. through thickness points of layers 1 and 2 are placed exactly on the upper and lower surfaces of the shell. Note that, VUMAT first performs calculations successively at the material points of the outer layers and finally at the material points of the mid layer of the shells.

C.2 Programming steps

1. Initial stage

- Step time = 0

The stress tensor for an isotropic material is given by the following relation:

$$\sigma_{ij} = 2G\varepsilon_{ij}^{el} + \lambda\Theta\delta_{ij} \tag{C.1}$$

where i, j are indices that vary between 1 and 3, $G = \frac{E}{2(1+\nu)}$ the shear modulus, E the Young's modulus, ν the Poisson's ratio, Θ the elastic unit volume change or the trace of the elastic strain tensor, i.e. $\varepsilon_{11}^{el} + \varepsilon_{22}^{el} + \varepsilon_{33}^{el}$, $\lambda = \frac{E\nu}{(1+\nu)(1-2\nu)}$ Lame's constant and δ_{ij} the Kronecker delta, i.e. $\delta_{ij} = \begin{cases} 0, & i \neq j \\ 1, & i = j \end{cases}$

Substituting $i, j = 3$ in relation (C.1), an increment of the elastic through thickness strain is determined by the following expression:

$$\Delta\varepsilon_{33}^{el} = -\frac{1}{2G+\lambda}\left[-{\sigma_{33}}^{(t_u)} + \lambda\left(\Delta\varepsilon_{11}^{el} + \Delta\varepsilon_{22}^{el}\right)\right] \tag{C.2}$$

where the superscript t_u refers to the previous time step. The stresses with respect to the current time step are derived by the following relation:

$${\sigma_{ij}}^{(t_u+dt_u)} = {\sigma_{ij}}^{(t_u)} + 2G\Delta\varepsilon_{ij}^{el} + \lambda\Delta\Theta\delta_{ij} \tag{C.3}$$

At step time zero it is ${\sigma_{ij}}^{(t_u)} = 0$, while $\Delta\varepsilon_{11}^{el} = \Delta\varepsilon_{22}^{el}$ = -0.001 and $\Delta\varepsilon_{12}^{el} = 0.001$. Note that, in the present analysis the true stress and strain components are considered.

2. Evaluation of the yield function

- Step time > 0

At the beginning of this stage all the stress and strain components are set equal to zero. Then, the trial stresses at the current time step are evaluated by the following expression:

$${\sigma_{ij}}_{tr}^{(t_u+dt_u)} = {\sigma_{ij}}^{(t_u)} + 2G\Delta\varepsilon_{ij}^{el} + \lambda\Delta\Theta\delta_{ij} \tag{C.4}$$

Moreover, the deviatoric trial stresses are given by

$${s_{ij}}_{tr}^{(t_u+dt_u)} = {\sigma_{ij}}_{tr}^{(t_u+dt_u)} - \frac{{\sigma_{kk}}_{tr}^{(t_u+dt_u)}}{3}\delta_{ij} \tag{C.5}$$

where k is an index that varies between 1 and 3 and ${\sigma_m}_{tr}^{(t_u+dt_u)} = \frac{{\sigma_{kk}}_{tr}^{(t_u+dt_u)}}{3}$ the trial mean hydrostatic pressure.

The trial von Mises or equivalent stress is determined by the deviatoric trial stresses as follows:

$$\sigma_{eq}{}_{tr}^{(t_u+dt_u)} = \sqrt{\frac{3}{2} s_{ij}{}_{tr}^{(t_u+dt_u)} s_{ij}{}_{tr}^{(t_u+dt_u)}} \tag{C.6}$$

Finally the yield function F is evaluated, that is:

$$F = \sigma_{eq}{}_{tr}^{(t_u+dt_u)} - \sigma_y \tag{C.7}$$

where σ_y is the yield stress of the material. According to equation (C.7), it is checked if the material behaviour is elastic or if plastic strains have started to develop through yielding. Note that, σ_y is altered during the analysis after the initial yielding of the material and follows the path of the material curve given as input by the user. The yield convention is:

$$If \begin{cases} F \leq 0 & elastic\ or\ neutral\ step \\ F > 0 & plastic\ step \end{cases} \tag{C.8}$$

3. Plane stress conditions-Setting $\sigma_{33} = 0$

If the step is elastic according to the yield convention in relation (C.8), then $\sigma_{33}{}^{(t_u+dt_u)}$ is set equal to zero and the current stresses are determined by relations (C.4)-(C.6). However, if the step is plastic the secant iteration method is applied, in order to determine the increment of the through thickness strain $\Delta\varepsilon_{33}$, which would result in $\sigma_{33}{}^{(t_u+dt_u)} \cong 0$. Thus, σ_{33} is defined as a function of $\Delta\varepsilon_{33}$, i.e. $\sigma_{33}(\Delta\varepsilon_{33})$ and two starting values for $\Delta\varepsilon_{33}$ are given in order the secant iteration method to initiate. The first value is determined by assuming a purely elastic behaviour and $\Delta\varepsilon_{33}{}^{(q-1)}$ is calculated by relation (C.2), while $\sigma_{33}{}^{(q-1)} = 0$. The second value is determined by assuming a fully plastic behaviour, i.e. $\Delta\varepsilon_{11} + \Delta\varepsilon_{22} + \Delta\varepsilon_{33}{}^{(q)} = 0$, that is $\Delta\varepsilon_{33}{}^{(q)} = -(\Delta\varepsilon_{11} + \Delta\varepsilon_{22})$. In the case where $\Delta\varepsilon_{11} = -\Delta\varepsilon_{22}$ and $\sigma_{33}{}^{(t_u)} = 0$, two identical values for $\Delta\varepsilon_{33}$ are yielded and secant iteration fails (see relation (C.2)). To avoid this scenario, it is sufficient to set one of the two strain increments equal to the half of the other, i.e. $\Delta\varepsilon_{11} = 0.5\Delta\varepsilon_{22}$. According to the secant iteration method it is:

$$\sigma_{33}{}^{(q+1)} = \sigma_{33}{}^{(q)} + \frac{\sigma_{33}{}^{(q)} - \sigma_{33}{}^{(q-1)}}{\Delta\varepsilon_{33}{}^{(q)} - \Delta\varepsilon_{33}{}^{(q-1)}} \left(\Delta\varepsilon_{33}{}^{(q+1)} - \Delta\varepsilon_{33}{}^{(q)}\right) \tag{C.9}$$

where q is an index that varies between 1 and 10 and $\sigma_{33}{}^{(q+1)}$ is the through thickness stress at the $q+1$ iteration, where it is set equal to zero. The stresses in terms of the strain increment $\Delta\varepsilon_{33}{}^{(q)}$ are calculated from relations (C.4)-(C.6), while the increment of the equivalent plastic strain $\Delta\bar{\varepsilon}^{pl(q)}$ it can be shown that is determined by the following relationship (see the theory guide in ABAQUS 2010):

$$\Delta\bar{\varepsilon}^{pl(q)} = \frac{\sigma_{eq}{}_{tr}^{(q)} - \sigma_y}{3G + H} \quad and \ H = \frac{d\sigma_{eq}}{d\bar{\varepsilon}^{pl}} \tag{C.10}$$

Also ${\sigma_{33}}^{(q)}$, that is the new stress with respect to $\Delta\bar{\varepsilon}^{pl(q)}$ and ${\Delta\varepsilon_{33}}^{(q)}$ is defined as:

$${\sigma_{33}}^{(q)} = {\sigma_{33}}_{tr}^{(q)} - \frac{3G\Delta\bar{\varepsilon}^{pl(q)}}{{\sigma_{eq}}_{tr}^{(q)}} {s_{33}}_{tr}^{(q)} \tag{C.11}$$

Therefore, substituting (C.11) in (C.9) and solving for ${\Delta\varepsilon_{33}}^{(q+1)}$ by setting ${\sigma_{33}}^{(q+1)} = 0$ it yields:

$${\Delta\varepsilon_{33}}^{(q+1)} = {\Delta\varepsilon_{33}}^{(q)} - \frac{{\sigma_{33}}^{(q)}}{{\sigma_{33}}^{(q)} - {\sigma_{33}}^{(q-1)} + tol}\left({\Delta\varepsilon_{33}}^{(q)} - {\Delta\varepsilon_{33}}^{(q-1)}\right) \tag{C.12}$$

where tol is a specified tolerance in the order of magnitude of 10^{-8}, in order to avoid the denominator of the fraction in the above relationship to take a zero value. The method is checked for convergence with the expression below:

$$\frac{\left|{\Delta\varepsilon_{33}}^{(q+1)} - {\Delta\varepsilon_{33}}^{(q)}\right|}{\left|{\Delta\varepsilon_{33}}^{(q+1)}\right|} < tol \tag{C.13}$$

If the convention in relation (C.13) is not satisfied, then the values of $\Delta\varepsilon_{33}$ and σ_{33} of the current iteration are set as initial values, i.e. ${\Delta\varepsilon_{33}}^{(q-1)} = {\Delta\varepsilon_{33}}^{(q)}$, ${\Delta\varepsilon_{33}}^{(q)} = {\Delta\varepsilon_{33}}^{(q+1)}$ and ${\sigma_{33}}^{(q-1)} = {\sigma_{33}}^{(q)}$ and a new iteration is performed. When the convention is fulfilled, the iterations stop, the through thickness stress ${\sigma_{33}}^{(t_u+dt_u)}$ becomes zero and the values of ${\Delta\varepsilon_{33}}^{(q+1)}$ and $\Delta\bar{\varepsilon}^{pl(q)}$ are accepted as the correct. Note that, a maximum number of iterations may be defined, in order to avoid a great number of iterations, which would unnecessarily increase the computational cost. In the present work the maximum number of iterations was set equal to 10. According to the flow rule the increments of the plastic strain components could be also determined by the following relationship:

$$\Delta\varepsilon_{ij}^{pl} = \frac{3}{2}\frac{\Delta\bar{\varepsilon}^{pl(q)}}{{\sigma_{eq}}_{tr}^{(q)}} {s_{ij}}_{tr}^{(q)} \tag{C.14}$$

The stresses of the current time step are determined by the expression:

$${\sigma_{ij}}^{(t_u+dt_u)} = {\sigma_{ij}}_{tr}^{(q)} - \frac{3G\Delta\bar{\varepsilon}^{pl(q)}}{{\sigma_{eq}}_{tr}^{(q)}} {s_{ij}}_{tr}^{(q)} \tag{C.15}$$

It is noted that, the trial subscripts included within the relations of step 3 are referred to the secant iteration procedure. The von Mises stress and the hydrostatic pressure of the current time step i.e. ${\sigma_{eq}}^{(t_u+dt_u)}$ and ${\sigma_m}^{(t_u+dt_u)}$ respectively, are determined by the new stresses in relation (C.15). Therefore, the stress triaxiality of the current time step is equal to the ratio $\frac{{\sigma_m}^{(t_u+dt_u)}}{{\sigma_{eq}}^{(t_u+dt_u)}}$

4. Energies

The internal or total energy E_T and the inelastic energy E_P per unit mass are derived by the following relationships:

$$E_T{}^{(t_u+dt_u)} = E_T{}^{(t_u)} + \frac{\Delta T}{\rho}$$

and

$$\Delta T = \frac{1}{2}\Big[\big[\sigma_{11}{}^{(t_u)} + \sigma_{11}{}^{(t_u+dt_u)}\big]\Delta\varepsilon_{11} + \big[\sigma_{22}{}^{(t_u)} + \sigma_{22}{}^{(t_u+dt_u)}\big]\Delta\varepsilon_{22} + 2\big[\sigma_{12}{}^{(t_u)} + \sigma_{12}{}^{(t_u+dt_u)}\big]\Delta\varepsilon_{12}\Big] \tag{C.16}$$

$$E_P{}^{(t_u+dt_u)} = E_P{}^{(t_u)} + \frac{\Delta T_P}{\rho}$$

and

$$\Delta T_{pl} = \frac{1}{2}\big[\sigma_{eq}{}^{(t_u)} + \sigma_{eq}{}^{(t_u+dt_u)}\big]\Delta\bar{\varepsilon}^{pl} \tag{C.17}$$

where ΔT, ΔT_{pl} are increments of the total strain and plastic strain energy densities respectively and ρ the density of the material.

This page is intentionally left blank

Appendix D

Quantification of Differences

The annex quantifies the differences between the numerical and experimental results of the benchmark study, by comparing the force peaks and troughs as well as the energy absorbed by the structures in each case. Figures D.1-D.24 illustrate comparisons of the numerical force and absorbed energy-penetration curves, according to the predictions of SHEARS, RTCLS and BWH rupture criteria for each mesh size, with the respective curves from the experiments. The force-penetration diagrams in Figures D.1-D.20 include the points where the force reaches a peak or a trough, as found from the numerical analyses and the experiment. The energy at the specific points is also indicated in the relevant diagrams. Tables D.1-D.20 summarize the numerical force, energy and displacement values at the aforementioned points and compare with the corresponding experimental values in each case. The best results are highlighted.

D.1 US Plate, 1-FB and 2-FB models-(Alsos and Amdahl 2009)

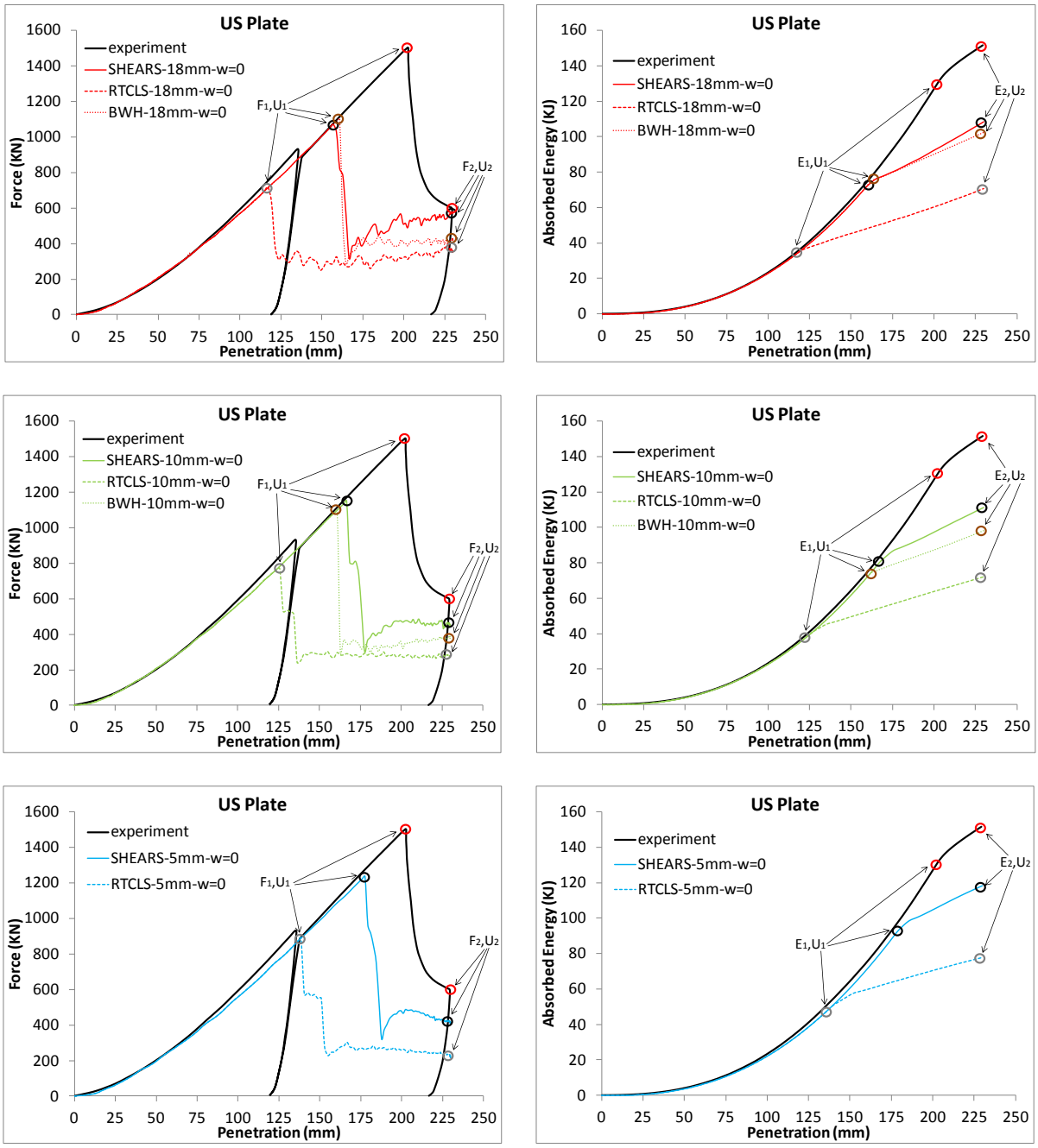

Figure D.1. US Plate model. Force and absorbed energy-penetration curves.
Definition of force peaks and troughs for each element size and rupture criterion and comparison with the corresponding experimental values
(red circle: experiment, black circle: SHEARS, grey circle: RTCLS, brown circle: BWH)

Table D.1. US Plate model. Numerical values of force, energy and penetration depth for each element size and rupture criterion at the selected peaks and troughs and comparison with the corresponding experimental values

SHEARS																	
l_e (mm)																	
5						10						18					
l_e/t = 1						l_e/t = 2						l_e/t = 3.6					
$F_1(KN)$	differ.	$E_1(KJ)$	differ.	$U_1(mm)$	differ.	$F_1(KN)$	differ.	$E_1(KJ)$	differ.	$U_1(mm)$	differ.	$F_1(KN)$	differ.	$E_1(KJ)$	differ.	$U_1(mm)$	differ.
1235.4	-19.5%	91.3	-34.9%	177.7	-12.9%	1151.9	-26.4%	79.7	-48.0%	166.7	-19.2%	1070.3	-33.6%	69.4	-60.8%	156.9	-25.2%
RTCLS																	
l_e (mm)																	
5						10						18					
l_e/t = 1						l_e/t = 2						l_e/t = 3.6					
$F_1(KN)$	differ.	$E_1(KJ)$	differ.	$U_1(mm)$	differ.	$F_1(KN)$	differ.	$E_1(KJ)$	differ.	$U_1(mm)$	differ.	$F_1(KN)$	differ.	$E_1(KJ)$	differ.	$U_1(mm)$	differ.
887.8	-51.4%	49.8	-89.2%	138.5	-37.4%	769.7	-64.5%	40.1	-105.7%	125.8	-46.6%	717.5	-70.7%	33.9	-117.2%	117.2	-53.3%
BWH																	
l_e (mm)																	
5						10						18					
l_e/t = 1						l_e/t = 2						l_e/t = 3.6					
$F_1(KN)$	differ.	$E_1(KJ)$	differ.	$U_1(mm)$	differ.	$F_1(KN)$	differ.	$E_1(KJ)$	differ.	$U_1(mm)$	differ.	$F_1(KN)$	differ.	$E_1(KJ)$	differ.	$U_1(mm)$	differ.
-	-	-	-	-	-	1099.1	-31.0%	73.2	-55.9%	160.9	-22.7%	1103.1	-30.6%	73.7	-55.3%	160.9	-22.7%
US Plate																	
Experiment																	
$F_1(KN)$						$E_1(KJ)$						$U_1(mm)$					
1502.0						130.0						202.2					

continued on next page

continued from previous page

SHEARS																	
l_e (mm)																	
5						10						18					
l_e/t = 1						l_e/t = 2						l_e/t = 3.6					
$F_2(KN)$	differ.	$E_2(KJ)$	differ.	$U_2(mm)$	differ.	$F_2(KN)$	differ.	$E_2(KJ)$	differ.	$U_2(mm)$	differ.	$F_2(KN)$	differ.	$E_2(KJ)$	differ.	$U_2(mm)$	differ.
423.3	-33.8%	118.1	-24.7%	229.4	0.0%	464.4	-24.7%	111.0	-30.8%	229.4	0.0%	576.6	-3.2%	108.2	-33.3%	229.4	0.0%
RTCLS																	
l_e (mm)																	
5						10						18					
l_e/t = 1						l_e/t = 2						l_e/t = 3.6					
$F_2(KN)$	differ.	$E_2(KJ)$	differ.	$U_2(mm)$	differ.	$F_2(KN)$	differ.	$E_2(KJ)$	differ.	$U_2(mm)$	differ.	$F_2(KN)$	differ.	$E_2(KJ)$	differ.	$U_2(mm)$	differ.
233.9	-87.2%	77.7	-64.3%	229.4	0.0%	282.3	-71.4%	71.8	-71.3%	229.4	0.0%	355.6	-50.4%	70.6	-72.8%	229.4	0.0%
BWH																	
l_e (mm)																	
5						10						18					
l_e/t = 1						l_e/t = 2						l_e/t = 3.6					
$F_2(KN)$	differ.	$E_2(KJ)$	differ.	$U_2(mm)$	differ.	$F_2(KN)$	differ.	$E_2(KJ)$	differ.	$U_2(mm)$	differ.	$F_2(KN)$	differ.	$E_2(KJ)$	differ.	$U_2(mm)$	differ.
-	-	-	-	-	-	387.1	-42.4%	97.8	-43.0%	229.4	0.0%	426.5	-33.1%	102.0	-39.0%	229.4	0.0%
US Plate																	
Experiment																	
$F_2(KN)$						$E_2(KJ)$						$U_2(mm)$					
595.4						151.4						229.4					

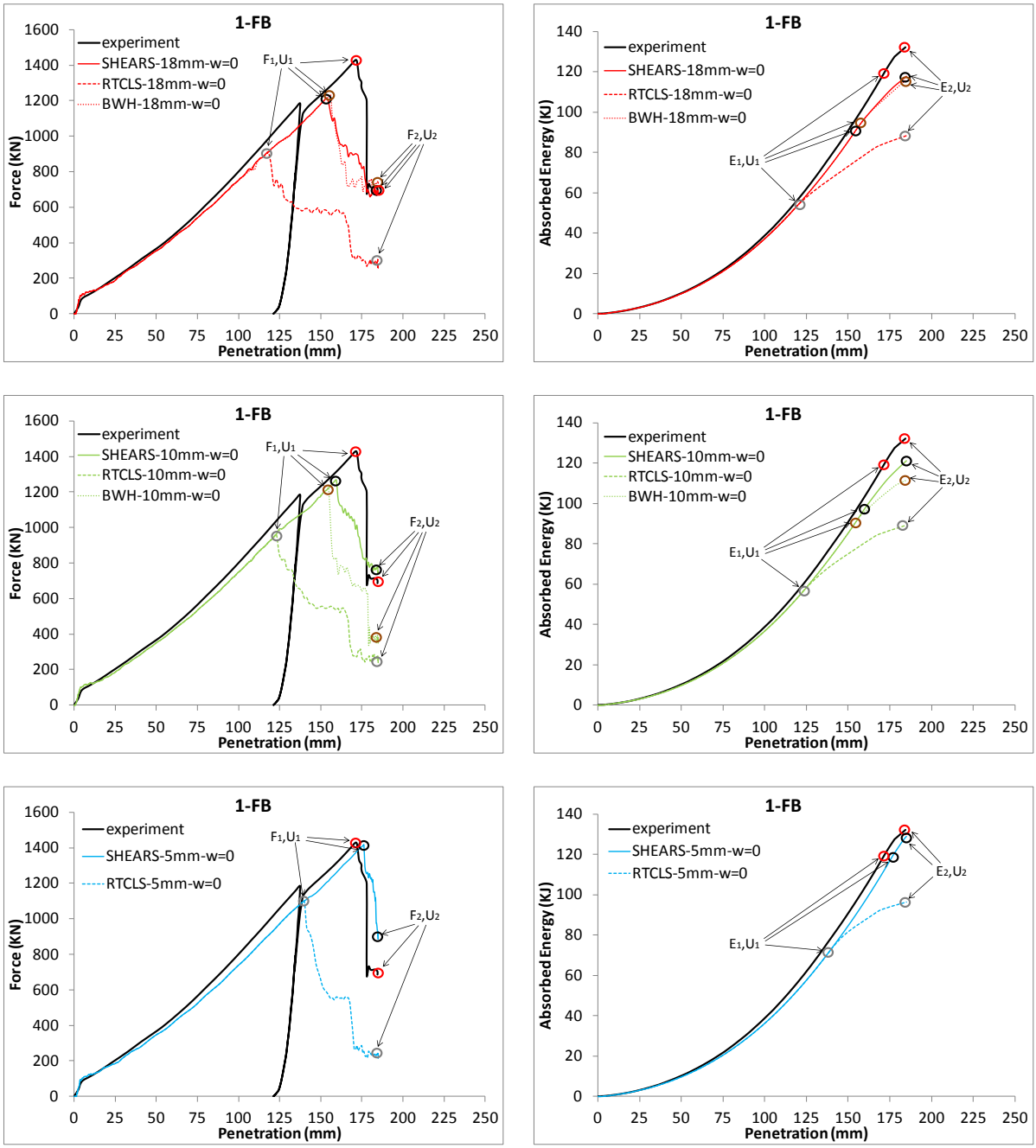

Figure D.2. 1-FB model. Force and absorbed energy-penetration curves.
Definition of force peaks and troughs for each element size and rupture criterion and comparison with the corresponding experimental values
(red circle: experiment, black circle: SHEARS, grey circle: RTCLS, brown circle: BWH)

Table D.2. 1-FB model. Numerical values of force, energy and penetration depth for each element size and rupture criterion at the selected peaks and troughs and comparison with the corresponding experimental values

SHEARS																	
l_e (mm)																	
5						10						18					
l_e/t = 1						l_e/t = 2						l_e/t = 3.6					
$F_1(KN)$	differ.	$E_1(KJ)$	differ.	$U_1(mm)$	differ.	$F_1(KN)$	differ.	$E_1(KJ)$	differ.	$U_1(mm)$	differ.	$F_1(KN)$	differ.	$E_1(KJ)$	differ.	$U_1(mm)$	differ.
1417.0	-0.9%	118.6	-0.4%	176.3	2.8%	1267.2	-12.0%	96.9	-20.5%	159.5	-7.1%	1213.8	-16.3%	89.8	-28.1%	153.6	-10.9%
RTCLS																	
l_e (mm)																	
5						10						18					
l_e/t = 1						l_e/t = 2						l_e/t = 3.6					
$F_1(KN)$	differ.	$E_1(KJ)$	differ.	$U_1(mm)$	differ.	$F_1(KN)$	differ.	$E_1(KJ)$	differ.	$U_1(mm)$	differ.	$F_1(KN)$	differ.	$E_1(KJ)$	differ.	$U_1(mm)$	differ.
1100.8	-26.0%	73.3	-47.6%	140.0	-20.1%	961.3	-39.1%	56.5	-71.3%	123.1	-32.8%	908.8	-44.5%	52.4	-77.8%	118.1	-36.8%
BWH																	
l_e (mm)																	
5						10						18					
l_e/t = 1						l_e/t = 2						l_e/t = 3.6					
$F_1(KN)$	differ.	$E_1(KJ)$	differ.	$U_1(mm)$	differ.	$F_1(KN)$	differ.	$E_1(KJ)$	differ.	$U_1(mm)$	differ.	$F_1(KN)$	differ.	$E_1(KJ)$	differ.	$U_1(mm)$	differ.
-	-	-	-	-	-	1222.7	-15.6%	91.1	-26.7%	154.8	-10.1%	1235.5	-14.5%	92.7	-24.9%	156.0	-9.3%
1-FB																	
Experiment																	
$F_1(KN)$						$E_1(KJ)$						$U_1(mm)$					
1429.2						119.1						171.3					

continued on next page

continued from previous page

SHEARS																	
l_e (mm)																	
5						10						18					
l_e/t = 1						l_e/t = 2						l_e/t = 3.6					
$F_2(KN)$	differ.	$E_2(KJ)$	differ.	$U_2(mm)$	differ.	$F_2(KN)$	differ.	$E_2(KJ)$	differ.	$U_2(mm)$	differ.	$F_2(KN)$	differ.	$E_2(KJ)$	differ.	$U_2(mm)$	differ.
937.4	31.1%	128.4	-2.9%	184.4	0.0%	776.9	12.6%	120.8	-9.0%	184.4	0.0%	690.7	0.8%	117.4	-11.8%	184.4	0.0%
RTCLS																	
l_e (mm)																	
5						10						18					
l_e/t = 1						l_e/t = 2						l_e/t = 3.6					
$F_2(KN)$	differ.	$E_2(KJ)$	differ.	$U_2(mm)$	differ.	$F_2(KN)$	differ.	$E_2(KJ)$	differ.	$U_2(mm)$	differ.	$F_2(KN)$	differ.	$E_2(KJ)$	differ.	$U_2(mm)$	differ.
245.3	-94.5%	96.3	-31.4%	184.4	0.0%	268.7	-87.3%	89.0	-39.0%	184.4	0.0%	294.0	-79.9%	88.0	-40.1%	184.4	0.0%
BWH																	
l_e (mm)																	
5						10						18					
l_e/t = 1						l_e/t = 2						l_e/t = 3.6					
$F_2(KN)$	differ.	$E_2(KJ)$	differ.	$U_2(mm)$	differ.	$F_2(KN)$	differ.	$E_2(KJ)$	differ.	$U_2(mm)$	differ.	$F_2(KN)$	differ.	$E_2(KJ)$	differ.	$U_2(mm)$	differ.
-	-	-	-	-	-	392.0	-54.4%	111.2	-17.2%	184.4	0.0%	740.4	7.8%	115.8	-13.2%	184.4	0.0%
1-FB																	
Experiment																	
$F_2(KN)$						$E_2(KJ)$						$U_2(mm)$					
685.1						132.1						184.4					

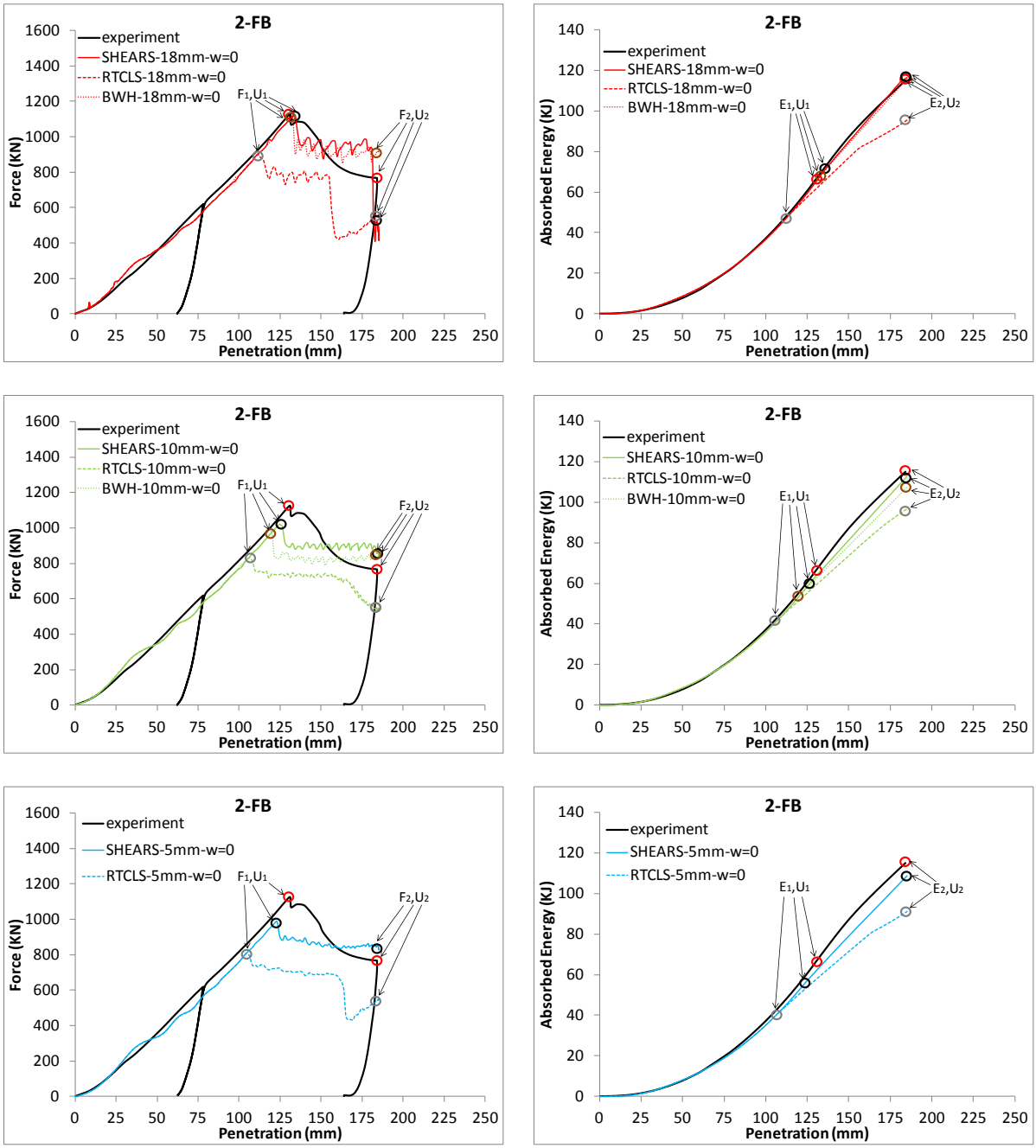

Figure D.3. 2-FB model. Force and absorbed energy-penetration curves.
Definition of force peaks and troughs for each element size and rupture criterion and comparison with the corresponding experimental values
(red circle: experiment, black circle: SHEARS, grey circle: RTCLS, brown circle: BWH)

Table D.3. 2-FB model. Numerical values of force, energy and penetration depth for each element size and rupture criterion at the selected peaks and troughs and comparison with the corresponding experimental values

SHEARS																	
l_e (mm)																	
5						10						18					
l_e/t = 1						l_e/t = 2						l_e/t = 3.6					
$F_1(KN)$	differ.	$E_1(KJ)$	differ.	$U_1(mm)$	differ.	$F_1(KN)$	differ.	$E_1(KJ)$	differ.	$U_1(mm)$	differ.	$F_1(KN)$	differ.	$E_1(KJ)$	differ.	$U_1(mm)$	differ.
986.7	-13.1%	55.3	-19.2%	123.1	-6.2%	1021.4	-9.7%	58.3	-14.0%	124.7	-4.9%	1121.7	-0.3%	69.3	3.3%	134.1	2.4%
RTCLS																	
l_e (mm)																	
5						10						18					
l_e/t = 1						l_e/t = 2						l_e/t = 3.6					
$F_1(KN)$	differ.	$E_1(KJ)$	differ.	$U_1(mm)$	differ.	$F_1(KN)$	differ.	$E_1(KJ)$	differ.	$U_1(mm)$	differ.	$F_1(KN)$	differ.	$E_1(KJ)$	differ.	$U_1(mm)$	differ.
809.1	-32.7%	38.7	-53.6%	104.6	-22.4%	832.2	-29.9%	41.2	-47.8%	106.3	-20.8%	898.7	-22.4%	46.3	-36.7%	111.4	-16.1%
BWH																	
l_e (mm)																	
5						10						18					
l_e/t = 1						l_e/t = 2						l_e/t = 3.6					
$F_1(KN)$	differ.	$E_1(KJ)$	differ.	$U_1(mm)$	differ.	$F_1(KN)$	differ.	$E_1(KJ)$	differ.	$U_1(mm)$	differ.	$F_1(KN)$	differ.	$E_1(KJ)$	differ.	$U_1(mm)$	differ.
-	-	-	-	-	-	977.9	-14.0%	53.4	-22.7%	119.8	-8.9%	1113.5	-1.0%	67.6	0.8%	132.6	1.2%
2-FB																	
Experiment																	
$F_1(KN)$						$E_1(KJ)$						$U_1(mm)$					
1124.9						67.1						131.0					

continued on next page

continued from previous page

SHEARS																	
l_e (mm)																	
5						10						18					
l_e/t = 1						l_e/t = 2						l_e/t = 3.6					
$F_2(KN)$	differ.	$E_2(KJ)$	differ.	$U_2(mm)$	differ.	$F_2(KN)$	differ.	$E_2(KJ)$	differ.	$U_2(mm)$	differ.	$F_2(KN)$	differ.	$E_2(KJ)$	differ.	$U_2(mm)$	differ.
848.7	15.1%	108.2	-6.2%	184.3	0.0%	864.9	17.0%	112.1	-2.6%	184.3	0.0%	486.2	-40.1%	116.0	0.8%	184.3	0.0%
RTCLS																	
l_e (mm)																	
5						10						18					
l_e/t = 1						l_e/t = 2						l_e/t = 3.6					
$F_2(KN)$	differ.	$E_2(KJ)$	differ.	$U_2(mm)$	differ.	$F_2(KN)$	differ.	$E_2(KJ)$	differ.	$U_2(mm)$	differ.	$F_2(KN)$	differ.	$E_2(KJ)$	differ.	$U_2(mm)$	differ.
542.6	-29.4%	90.6	-23.8%	184.3	0.0%	539.7	-29.9%	96.3	-17.7%	184.3	0.0%	551.0	-27.9%	94.9	-19.2%	184.3	0.0%
BWH																	
l_e (mm)																	
5						10						18					
l_e/t = 1						l_e/t = 2						l_e/t = 3.6					
$F_2(KN)$	differ.	$E_2(KJ)$	differ.	$U_2(mm)$	differ.	$F_2(KN)$	differ.	$E_2(KJ)$	differ.	$U_2(mm)$	differ.	$F_2(KN)$	differ.	$E_2(KJ)$	differ.	$U_2(mm)$	differ.
-	-	-	-	-	-	852.0	15.5%	106.9	-7.4%	184.3	0.0%	912.2	22.2%	115.2	0.1%	184.3	0.0%
2-FB																	
Experiment																	
$F_2(KN)$						$E_2(KJ)$						$U_2(mm)$					
729.7						115.1						184.3					

D.2 ST-3-BW, ST-3-OW, ST-4-BW and ST-4-OW models-(Paik et al. 1999)

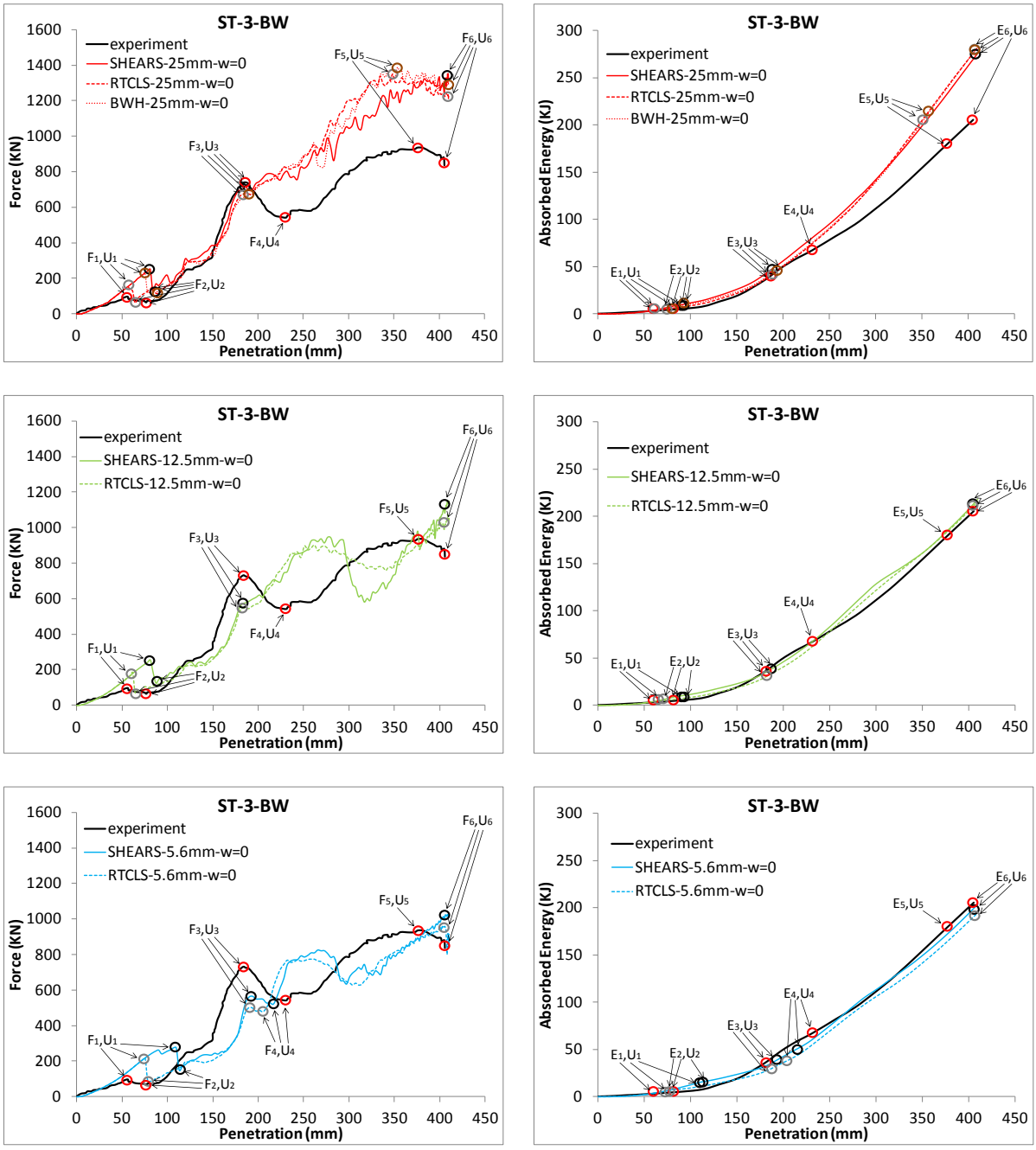

Figure D.4. ST-3-BW model. Force and absorbed energy-penetration curves.
Definition of force peaks and troughs for each element size and rupture criterion and comparison with the corresponding experimental values
(red circle: experiment, black circle: SHEARS, grey circle: RTCLS, brown circle: BWH)

Table D.4. ST-3-BW model. Numerical values of force, energy and penetration depth for each element size and rupture criterion at the selected peaks and troughs and comparison with the corresponding experimental values

SHEARS																	
l_e (mm)																	
5.6						12.5						25					
l_e/t = 2						l_e/t = 4.5						l_e/t = 8.9					
$F_1(KN)$	differ.	$E_1(KJ)$	differ.	$U_1(mm)$	differ.	$F_1(KN)$	differ.	$E_1(KJ)$	differ.	$U_1(mm)$	differ.	$F_1(KN)$	differ.	$E_1(KJ)$	differ.	$U_1(mm)$	differ.
275.6	96.7%	15.2	140.4%	109.5	64.0%	254.8	90.6%	8.6	105.5%	81.1	35.9%	251.2	89.5%	8.3	103.3%	81.1	35.9%
RTCLS																	
l_e (mm)																	
5.6						12.5						25					
l_e/t = 2						l_e/t = 4.5						l_e/t = 8.9					
$F_1(KN)$	differ.	$E_1(KJ)$	differ.	$U_1(mm)$	differ.	$F_1(KN)$	differ.	$E_1(KJ)$	differ.	$U_1(mm)$	differ.	$F_1(KN)$	differ.	$E_1(KJ)$	differ.	$U_1(mm)$	differ.
218.3	77.9%	6.6	84.5%	75.2	28.6%	184.2	63.1%	4.4	48.2%	61.5	8.7%	153.9	46.5%	3.3	22.4%	56.4	0.0%
BWH																	
l_e (mm)																	
5.6						12.5						25					
l_e/t = 2						l_e/t = 4.5						l_e/t = 8.9					
$F_1(KN)$	differ.	$E_1(KJ)$	differ.	$U_1(mm)$	differ.	$F_1(KN)$	differ.	$E_1(KJ)$	differ.	$U_1(mm)$	differ.	$F_1(KN)$	differ.	$E_1(KJ)$	differ.	$U_1(mm)$	differ.
-	-	-	-	-	-	-	-	-	-	-	-	230.2	82.4%	6.9	89.2%	75.2	28.6%
ST-3-BW																	
Experiment																	
$F_1(KN)$						$E_1(KJ)$						$U_1(mm)$					
95.9						2.7						56.4					

continued on next page

continued from previous page

SHEARS																	
l_e (mm)																	
5.6						12.5						25					
l_e/t = 2						l_e/t = 4.5						l_e/t = 8.9					
$F_2(KN)$	differ.	$E_2(KJ)$	differ.	$U_2(mm)$	differ.	$F_2(KN)$	differ.	$E_2(KJ)$	differ.	$U_2(mm)$	differ.	$F_2(KN)$	differ.	$E_2(KJ)$	differ.	$U_2(mm)$	differ.
149.4	81.0%	15.9	116.4%	112.8	38.1%	125.6	66.0%	9.7	79.3%	87.1	12.6%	122.9	64.0%	8.9	71.7%	84.0	9.1%
RTCLS																	
l_e (mm)																	
5.6						12.5						25					
l_e/t = 2						l_e/t = 4.5						l_e/t = 8.9					
$F_2(KN)$	differ.	$E_2(KJ)$	differ.	$U_2(mm)$	differ.	$F_2(KN)$	differ.	$E_2(KJ)$	differ.	$U_2(mm)$	differ.	$F_2(KN)$	differ.	$E_2(KJ)$	differ.	$U_2(mm)$	differ.
86.8	31.4%	7.0	49.9%	78.1	1.8%	71.0	11.5%	4.7	10.9%	64.2	-17.8%	62.3	-1.5%	4.3	2.1%	64.2	-17.8%
BWH																	
l_e (mm)																	
5.6						12.5						25					
l_e/t = 2						l_e/t = 4.5						l_e/t = 8.9					
$F_2(KN)$	differ.	$E_2(KJ)$	differ.	$U_2(mm)$	differ.	$F_2(KN)$	differ.	$E_2(KJ)$	differ.	$U_2(mm)$	differ.	$F_2(KN)$	differ.	$E_2(KJ)$	differ.	$U_2(mm)$	differ.
-	-	-	-	-	-	-	-	-	-	-	-	111.4	55.1%	9.0	73.0%	90.1	16.1%
ST-3-BW																	
Experiment																	
$F_2(KN)$						$E_2(KJ)$						$U_2(mm)$					
63.3						4.2						76.7					

continued on next page

continued from previous page

SHEARS																	
l_e (mm)																	
5.6						12.5						25					
l_e/t = 2						l_e/t = 4.5						l_e/t = 8.9					
$F_3(KN)$	differ.	$E_3(KJ)$	differ.	$U_3(mm)$	differ.	$F_3(KN)$	differ.	$E_3(KJ)$	differ.	$U_3(mm)$	differ.	$F_3(KN)$	differ.	$E_3(KJ)$	differ.	$U_3(mm)$	differ.
565.6	-25.5%	39.1	5.2%	193.5	5.4%	577.7	-23.4%	37.7	1.4%	185.8	1.3%	717.7	-1.8%	46.0	21.2%	185.8	1.3%
RTCLS																	
l_e (mm)																	
5.6						12.5						25					
l_e/t = 2						l_e/t = 4.5						l_e/t = 8.9					
$F_3(KN)$	differ.	$E_3(KJ)$	differ.	$U_3(mm)$	differ.	$F_3(KN)$	differ.	$E_3(KJ)$	differ.	$U_3(mm)$	differ.	$F_3(KN)$	differ.	$E_3(KJ)$	differ.	$U_3(mm)$	differ.
501.2	-37.3%	31.0	-18.0%	189.6	3.4%	546.5	-28.8%	30.7	-18.9%	182.0	-0.7%	676.2	-7.7%	40.3	8.2%	185.8	1.3%
BWH																	
l_e (mm)																	
5.6						12.5						25					
l_e/t = 2						l_e/t = 4.5						l_e/t = 8.9					
$F_3(KN)$	differ.	$E_3(KJ)$	differ.	$U_3(mm)$	differ.	$F_3(KN)$	differ.	$E_3(KJ)$	differ.	$U_3(mm)$	differ.	$F_3(KN)$	differ.	$E_3(KJ)$	differ.	$U_3(mm)$	differ.
-	-	-	-	-	-	-	-	-	-	-	-	675.0	-7.9%	44.2	17.3%	189.7	3.4%
ST-3-BW																	
Experiment																	
$F_3(KN)$						$E_3(KJ)$						$U_3(mm)$					
730.6						37.1						183.3					

continued on next page

continued from previous page

SHEARS																	
l_e (mm)																	
5.6						12.5						25					
l_e/t = 2						l_e/t = 4.5						l_e/t = 8.9					
$F_4(KN)$	differ.	$E_4(KJ)$	differ.	$U_4(mm)$	differ.	$F_4(KN)$	differ.	$E_4(KJ)$	differ.	$U_4(mm)$	differ.	$F_4(KN)$	differ.	$E_4(KJ)$	differ.	$U_4(mm)$	differ.
521.0	-3.7%	51.6	-25.2%	216.5	-6.3%	Not captured						Not captured					
RTCLS																	
l_e (mm)																	
5.6						12.5						25					
l_e/t = 2						l_e/t = 4.5						l_e/t = 8.9					
$F_4(KN)$	differ.	$E_4(KJ)$	differ.	$U_4(mm)$	differ.	$F_4(KN)$	differ.	$E_4(KJ)$	differ.	$U_4(mm)$	differ.	$F_4(KN)$	differ.	$E_4(KJ)$	differ.	$U_4(mm)$	differ.
478.4	-12.2%	38.5	-53.3%	205.0	-11.7%	Not captured						Not captured					
BWH																	
l_e (mm)																	
5.6						12.5						25					
l_e/t = 2						l_e/t = 4.5						l_e/t = 8.9					
$F_4(KN)$	differ.	$E_4(KJ)$	differ.	$U_4(mm)$	differ.	$F_4(KN)$	differ.	$E_4(KJ)$	differ.	$U_4(mm)$	differ.	$F_4(KN)$	differ.	$E_4(KJ)$	differ.	$U_4(mm)$	differ.
-	-	-	-	-	-	-	-	-	-	-	-	Not captured					
ST-3-BW																	
Experiment																	
$F_4(KN)$						$E_4(KJ)$						$U_4(mm)$					
540.7						66.5						230.6					

continued on next page

continued from previous page

SHEARS																		
l_e (mm)																		
5.6						12.5						25						
l_e/t = 2						l_e/t = 4.5						l_e/t = 8.9						
$F_5(KN)$	differ.	$E_5(KJ)$	differ.	$U_5(mm)$	differ.	$F_5(KN)$	differ.	$E_5(KJ)$	differ.	$U_5(mm)$	differ.	$F_5(KN)$	differ.	$E_5(KJ)$	differ.	$U_5(mm)$	differ.	
Not captured						Not captured						Not captured						
RTCLS																		
l_e (mm)																		
5.6						12.5						25						
l_e/t = 2						l_e/t = 4.5						l_e/t = 8.9						
$F_5(KN)$	differ.	$E_5(KJ)$	differ.	$U_5(mm)$	differ.	$F_5(KN)$	differ.	$E_5(KJ)$	differ.	$U_5(mm)$	differ.	$F_5(KN)$	differ.	$E_5(KJ)$	differ.	$U_5(mm)$	differ.	
Not captured						Not captured						1350.6	36.3%	202.3	12.5%	348.5	-7.6%	
BWH																		
l_e (mm)																		
5.6						12.5						25						
l_e/t = 2						l_e/t = 4.5						l_e/t = 8.9						
$F_5(KN)$	differ.	$E_5(KJ)$	differ.	$U_5(mm)$	differ.	$F_5(KN)$	differ.	$E_5(KJ)$	differ.	$U_5(mm)$	differ.	$F_5(KN)$	differ.	$E_5(KJ)$	differ.	$U_5(mm)$	differ.	
-	-	-	-	-	-	-	-	-	-	-	-	1388.2	38.9%	207.4	15.0%	353.6	-6.1%	
ST-3-BW																		
Experiment																		
$F_5(KN)$						$E_5(KJ)$						$U_5(mm)$						
935.8						178.4						375.9						

continued on next page

continued from previous page

SHEARS																	
l_e (mm)																	
5.6						12.5						25					
l_e/t = 2						l_e/t = 4.5						l_e/t = 8.9					
$F_6(KN)$	differ.	$E_6(KJ)$	differ.	$U_6(mm)$	differ.	$F_6(KN)$	differ.	$E_6(KJ)$	differ.	$U_6(mm)$	differ.	$F_6(KN)$	differ.	$E_6(KJ)$	differ.	$U_6(mm)$	differ.
1004.7	18.3%	199.3	-2.9%	405.4	0.0%	1082.9	25.7%	213.4	3.9%	405.4	0.0%	1238.9	38.8%	269.2	26.9%	405.4	0.0%

RTCLS																	
l_e (mm)																	
5.6						12.5						25					
l_e/t = 2						l_e/t = 4.5						l_e/t = 8.9					
$F_6(KN)$	differ.	$E_6(KJ)$	differ.	$U_6(mm)$	differ.	$F_6(KN)$	differ.	$E_6(KJ)$	differ.	$U_6(mm)$	differ.	$F_6(KN)$	differ.	$E_6(KJ)$	differ.	$U_6(mm)$	differ.
959.3	13.7%	190.2	-7.7%	405.4	0.0%	1014.9	19.3%	211.3	2.9%	405.4	0.0%	1230.8	38.2%	275.4	29.2%	405.4	0.0%

BWH																	
l_e (mm)																	
5.6						12.5						25					
l_e/t = 2						l_e/t = 4.5						l_e/t = 8.9					
$F_6(KN)$	differ.	$E_6(KJ)$	differ.	$U_6(mm)$	differ.	$F_6(KN)$	differ.	$E_6(KJ)$	differ.	$U_6(mm)$	differ.	$F_6(KN)$	differ.	$E_6(KJ)$	differ.	$U_6(mm)$	differ.
-	-	-	-	-	-	-	-	-	-	-	-	1291.5	42.8%	276.2	29.5%	405.4	0.0%

ST-3-BW		
Experiment		
$F_6(KN)$	$E_6(KJ)$	$U_6(mm)$
836.1	205.3	405.4

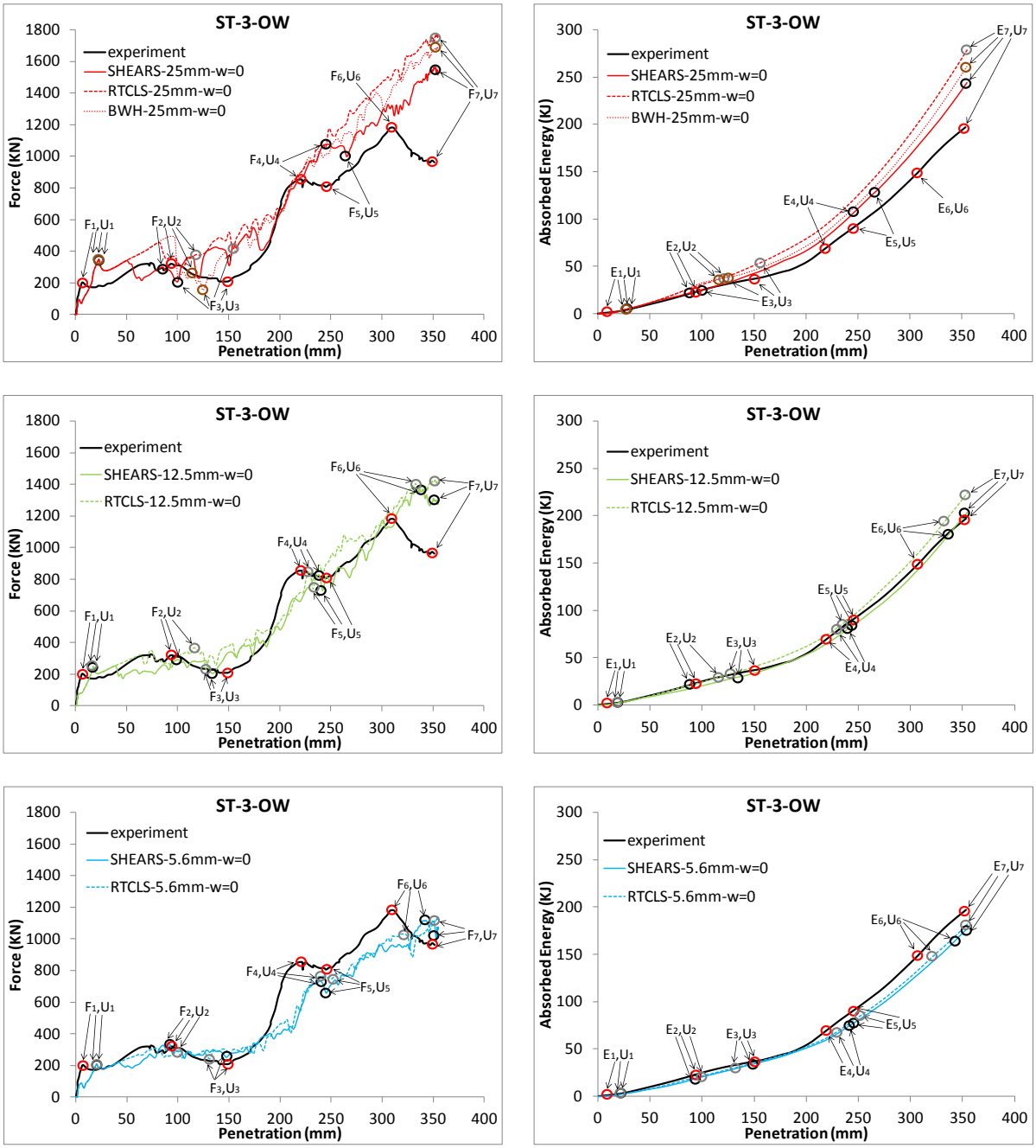

Figure D.5. ST-3-OW model. Force and absorbed energy-penetration curves.
Definition of force peaks and troughs for each element size and rupture criterion and comparison with the corresponding experimental values
(red circle: experiment, black circle: SHEARS, grey circle: RTCLS, brown circle: BWH)

Table D.5. ST-3-OW model. Numerical values of force, energy and penetration depth for each element size and rupture criterion at the selected peaks and troughs and comparison with the corresponding experimental values

SHEARS																	
$l_e\ (mm)$																	
5.6						12.5						25					
l_e/t = 2						l_e/t = 4.5						l_e/t = 8.9					
$F_1(KN)$	differ.	$E_1(KJ)$	differ.	$U_1(mm)$	differ.	$F_1(KN)$	differ.	$E_1(KJ)$	differ.	$U_1(mm)$	differ.	$F_1(KN)$	differ.	$E_1(KJ)$	differ.	$U_1(mm)$	differ.
208.0	3.3%	2.0	83.6%	20.6	99.6%	248.5	20.9%	2.1	85.6%	17.9	89.0%	347.1	53.2%	3.8	127.8%	23.4	109.0%
RTCLS																	
$l_e\ (mm)$																	
5.6						12.5						25					
l_e/t = 2						l_e/t = 4.5						l_e/t = 8.9					
$F_1(KN)$	differ.	$E_1(KJ)$	differ.	$U_1(mm)$	differ.	$F_1(KN)$	differ.	$E_1(KJ)$	differ.	$U_1(mm)$	differ.	$F_1(KN)$	differ.	$E_1(KJ)$	differ.	$U_1(mm)$	differ.
208.6	3.5%	2.0	83.6%	20.6	99.6%	248.5	20.9%	2.1	85.6%	17.9	89.0%	347.1	53.2%	3.8	127.8%	23.4	109.0%
BWH																	
$l_e\ (mm)$																	
5.6						12.5						25					
l_e/t = 2						l_e/t = 4.5						l_e/t = 8.9					
$F_1(KN)$	differ.	$E_1(KJ)$	differ.	$U_1(mm)$	differ.	$F_1(KN)$	differ.	$E_1(KJ)$	differ.	$U_1(mm)$	differ.	$F_1(KN)$	differ.	$E_1(KJ)$	differ.	$U_1(mm)$	differ.
-	-	-	-	-	-	-	-	-	-	-	-	347.3	53.2%	3.8	127.8%	23.4	109.0%
ST-3-OW																	
Experiment																	
$F_1(KN)$						$E_1(KJ)$						$U_1(mm)$					
201.3						0.8						6.9					

continued on next page

continued from previous page

SHEARS																	
l_e (mm)																	
5.6						12.5						25					
l_e/t = 2						l_e/t = 4.5						l_e/t = 8.9					
$F_2(KN)$	differ.	$E_2(KJ)$	differ.	$U_2(mm)$	differ.	$F_2(KN)$	differ.	$E_2(KJ)$	differ.	$U_2(mm)$	differ.	$F_2(KN)$	differ.	$E_2(KJ)$	differ.	$U_2(mm)$	differ.
341.8	7.7%	18.3	-22.5%	91.9	-3.8%	291.8	-8.1%	20.7	-10.3%	100.6	5.3%	297.4	-6.2%	21.5	-6.4%	86.3	-10.1%
RTCLS																	
l_e (mm)																	
5.6						12.5						25					
l_e/t = 2						l_e/t = 4.5						l_e/t = 8.9					
$F_2(KN)$	differ.	$E_2(KJ)$	differ.	$U_2(mm)$	differ.	$F_2(KN)$	differ.	$E_2(KJ)$	differ.	$U_2(mm)$	differ.	$F_2(KN)$	differ.	$E_2(KJ)$	differ.	$U_2(mm)$	differ.
288.8	-9.1%	22.0	-4.3%	100.6	5.3%	364.5	14.1%	29.6	25.4%	115.8	19.2%	378.9	18.0%	37.6	48.5%	118.9	21.9%
BWH																	
l_e (mm)																	
5.6						12.5						25					
l_e/t = 2						l_e/t = 4.5						l_e/t = 8.9					
$F_2(KN)$	differ.	$E_2(KJ)$	differ.	$U_2(mm)$	differ.	$F_2(KN)$	differ.	$E_2(KJ)$	differ.	$U_2(mm)$	differ.	$F_2(KN)$	differ.	$E_2(KJ)$	differ.	$U_2(mm)$	differ.
-	-	-	-	-	-	-	-	-	-	-	-	255.8	-21.2%	36.8	46.5%	115.8	19.3%
ST-3-OW																	
Experiment																	
$F_2(KN)$						$E_2(KJ)$						$U_2(mm)$					
316.4						22.9						95.4					

continued on next page

continued from previous page

SHEARS																	
l_e (mm)																	
5.6						12.5						25					
l_e/t = 2						l_e/t = 4.5						l_e/t = 8.9					
$F_3(KN)$	differ.	$E_3(KJ)$	differ.	$U_3(mm)$	differ.	$F_3(KN)$	differ.	$E_3(KJ)$	differ.	$U_3(mm)$	differ.	$F_3(KN)$	differ.	$E_3(KJ)$	differ.	$U_3(mm)$	differ.
250.9	18.2%	33.9	-7.5%	147.7	-1.7%	203.4	-2.7%	29.8	-20.5%	134.7	-10.9%	208.6	-0.2%	25.2	-36.9%	100.7	-39.5%

RTCLS																	
l_e (mm)																	
5.6						12.5						25					
l_e/t = 2						l_e/t = 4.5						l_e/t = 8.9					
$F_3(KN)$	differ.	$E_3(KJ)$	differ.	$U_3(mm)$	differ.	$F_3(KN)$	differ.	$E_3(KJ)$	differ.	$U_3(mm)$	differ.	$F_3(KN)$	differ.	$E_3(KJ)$	differ.	$U_3(mm)$	differ.
242.4	14.8%	30.3	-18.7%	131.5	-13.3%	227.5	8.5%	33.8	-8.0%	128.3	-15.7%	408.6	64.6%	53.2	37.1%	154.3	2.7%

BWH																	
l_e (mm)																	
5.6						12.5						25					
l_e/t = 2						l_e/t = 4.5						l_e/t = 8.9					
$F_3(KN)$	differ.	$E_3(KJ)$	differ.	$U_3(mm)$	differ.	$F_3(KN)$	differ.	$E_3(KJ)$	differ.	$U_3(mm)$	differ.	$F_3(KN)$	differ.	$E_3(KJ)$	differ.	$U_3(mm)$	differ.
-	-	-	-	-	-	-	-	-	-	-	-	152.3	-31.4%	38.8	5.8%	125.2	-18.2%

ST-3-OW		
Experiment		
$F_3(KN)$	$E_3(KJ)$	$U_3(mm)$
209.0	36.6	150.2

continued on next page

continued from previous page

SHEARS																	
l_e (mm)																	
5.6						12.5						25					
l_e/t = 2						l_e/t = 4.5						l_e/t = 8.9					
$F_4(KN)$	differ.	$E_4(KJ)$	differ.	$U_4(mm)$	differ.	$F_4(KN)$	differ.	$E_4(KJ)$	differ.	$U_4(mm)$	differ.	$F_4(KN)$	differ.	$E_4(KJ)$	differ.	$U_4(mm)$	differ.
734.4	-15.0%	73.1	2.9%	239.2	7.9%	824.3	-3.5%	79.9	11.7%	239.2	7.9%	1074.0	22.9%	106.1	39.6%	245.4	10.4%
RTCLS																	
l_e (mm)																	
5.6						12.5						25					
l_e/t = 2						l_e/t = 4.5						l_e/t = 8.9					
$F_4(KN)$	differ.	$E_4(KJ)$	differ.	$U_4(mm)$	differ.	$F_4(KN)$	differ.	$E_4(KJ)$	differ.	$U_4(mm)$	differ.	$F_4(KN)$	differ.	$E_4(KJ)$	differ.	$U_4(mm)$	differ.
764.7	-10.9%	77.8	9.2%	242.3	9.2%	847.6	-0.7%	81.9	14.3%	229.9	3.9%	Not captured					
BWH																	
l_e (mm)																	
5.6						12.5						25					
l_e/t = 2						l_e/t = 4.5						l_e/t = 8.9					
$F_4(KN)$	differ.	$E_4(KJ)$	differ.	$U_4(mm)$	differ.	$F_4(KN)$	differ.	$E_4(KJ)$	differ.	$U_4(mm)$	differ.	$F_4(KN)$	differ.	$E_4(KJ)$	differ.	$U_4(mm)$	differ.
-	-	-	-	-	-	-	-	-	-	-	-	Not captured					
ST-3-OW																	
Experiment																	
$F_4(KN)$						$E_4(KJ)$						$U_4(mm)$					
853.3						71.0						221.1					

continued on next page

continued from previous page

SHEARS																	
l_e (mm)																	
5.6						12.5						25					
l_e/t = 2						l_e/t = 4.5						l_e/t = 8.9					
$F_5(KN)$	differ.	$E_5(KJ)$	differ.	$U_5(mm)$	differ.	$F_5(KN)$	differ.	$E_5(KJ)$	differ.	$U_5(mm)$	differ.	$F_5(KN)$	differ.	$E_5(KJ)$	differ.	$U_5(mm)$	differ.
657.8	-20.2%	77.4	-16.2%	245.4	0.0%	727.5	-10.2%	82.3	-10.2%	242.3	-1.2%	996.6	21.2%	127.9	33.6%	265.9	8.1%

RTCLS																	
l_e (mm)																	
5.6						12.5						25					
l_e/t = 2						l_e/t = 4.5						l_e/t = 8.9					
$F_5(KN)$	differ.	$E_5(KJ)$	differ.	$U_5(mm)$	differ.	$F_5(KN)$	differ.	$E_5(KJ)$	differ.	$U_5(mm)$	differ.	$F_5(KN)$	differ.	$E_5(KJ)$	differ.	$U_5(mm)$	differ.
749.3	-7.2%	84.7	-7.3%	251.4	2.4%	738.4	-8.7%	84.4	-7.6%	233.0	-5.2%	Not captured					

BWH																	
l_e (mm)																	
5.6						12.5						25					
l_e/t = 2						l_e/t = 4.5						l_e/t = 8.9					
$F_5(KN)$	differ.	$E_5(KJ)$	differ.	$U_5(mm)$	differ.	$F_5(KN)$	differ.	$E_5(KJ)$	differ.	$U_5(mm)$	differ.	$F_5(KN)$	differ.	$E_5(KJ)$	differ.	$U_5(mm)$	differ.
-	-	-	-	-	-	-	-	-	-	-	-	Not captured					

ST-3-OW		
Experiment		
$F_5(KN)$	$E_5(KJ)$	$U_5(mm)$
805.4	91.1	245.3

continued on next page

continued from previous page

SHEARS																	
l_e (mm)																	
5.6						12.5						25					
l_e/t = 2						l_e/t = 4.5						l_e/t = 8.9					
$F_6(KN)$	differ.	$E_6(KJ)$	differ.	$U_6(mm)$	differ.	$F_6(KN)$	differ.	$E_6(KJ)$	differ.	$U_6(mm)$	differ.	$F_6(KN)$	differ.	$E_6(KJ)$	differ.	$U_6(mm)$	differ.
1118.6	-5.3%	164.3	5.0%	342.7	9.5%	1369.5	14.9%	180.5	14.4%	337.1	7.9%	Not captured					
RTCLS																	
l_e (mm)																	
5.6						12.5						25					
l_e/t = 2						l_e/t = 4.5						l_e/t = 8.9					
$F_6(KN)$	differ.	$E_6(KJ)$	differ.	$U_6(mm)$	differ.	$F_6(KN)$	differ.	$E_6(KJ)$	differ.	$U_6(mm)$	differ.	$F_6(KN)$	differ.	$E_6(KJ)$	differ.	$U_6(mm)$	differ.
1032.7	-13.3%	147.9	-5.4%	321.9	3.3%	1405.8	17.5%	193.9	21.5%	333.1	6.7%	Not captured					
BWH																	
l_e (mm)																	
5.6						12.5						25					
l_e/t = 2						l_e/t = 4.5						l_e/t = 8.9					
$F_6(KN)$	differ.	$E_6(KJ)$	differ.	$U_6(mm)$	differ.	$F_6(KN)$	differ.	$E_6(KJ)$	differ.	$U_6(mm)$	differ.	$F_6(KN)$	differ.	$E_6(KJ)$	differ.	$U_6(mm)$	differ.
-	-	-	-	-	-	-	-	-	-	-	-	Not captured					
ST-3-OW																	
Experiment																	
$F_6(KN)$						$E_6(KJ)$						$U_6(mm)$					
1179.3						156.2						311.6					

continued on next page

continued from previous page

SHEARS																	
l_e (mm)																	
5.6						12.5						25					
l_e/t = 2						l_e/t = 4.5						l_e/t = 8.9					
$F_7(KN)$	differ.	$E_7(KJ)$	differ.	$U_7(mm)$	differ.	$F_7(KN)$	differ.	$E_7(KJ)$	differ.	$U_7(mm)$	differ.	$F_7(KN)$	differ.	$E_7(KJ)$	differ.	$U_7(mm)$	differ.
1095.7	13.1%	173.9	-12.8%	351.5	0.0%	1295.2	29.7%	199.5	0.9%	351.5	0.0%	1558.6	47.5%	238.6	18.7%	351.5	0.0%

RTCLS																	
l_e (mm)																	
5.6						12.5						25					
l_e/t = 2						l_e/t = 4.5						l_e/t = 8.9					
$F_7(KN)$	differ.	$E_7(KJ)$	differ.	$U_7(mm)$	differ.	$F_7(KN)$	differ.	$E_7(KJ)$	differ.	$U_7(mm)$	differ.	$F_7(KN)$	differ.	$E_7(KJ)$	differ.	$U_7(mm)$	differ.
1107.1	14.2%	178.0	-10.5%	351.5	0.0%	1420.7	38.6%	219.5	10.4%	351.5	0.0%	1715.7	56.4%	272.6	31.8%	351.5	0.0%

BWH																	
l_e (mm)																	
5.6						12.5						25					
l_e/t = 2						l_e/t = 4.5						l_e/t = 8.9					
$F_7(KN)$	differ.	$E_7(KJ)$	differ.	$U_7(mm)$	differ.	$F_7(KN)$	differ.	$E_7(KJ)$	differ.	$U_7(mm)$	differ.	$F_7(KN)$	differ.	$E_7(KJ)$	differ.	$U_7(mm)$	differ.
-	-	-	-	-	-	-	-	-	-	-	-	1674.5	54.2%	255.4	25.4%	351.5	0.0%

ST-3-OW		
Experiment		
$F_7(KN)$	$E_7(KJ)$	$U_7(mm)$
960.7	197.7	351.6

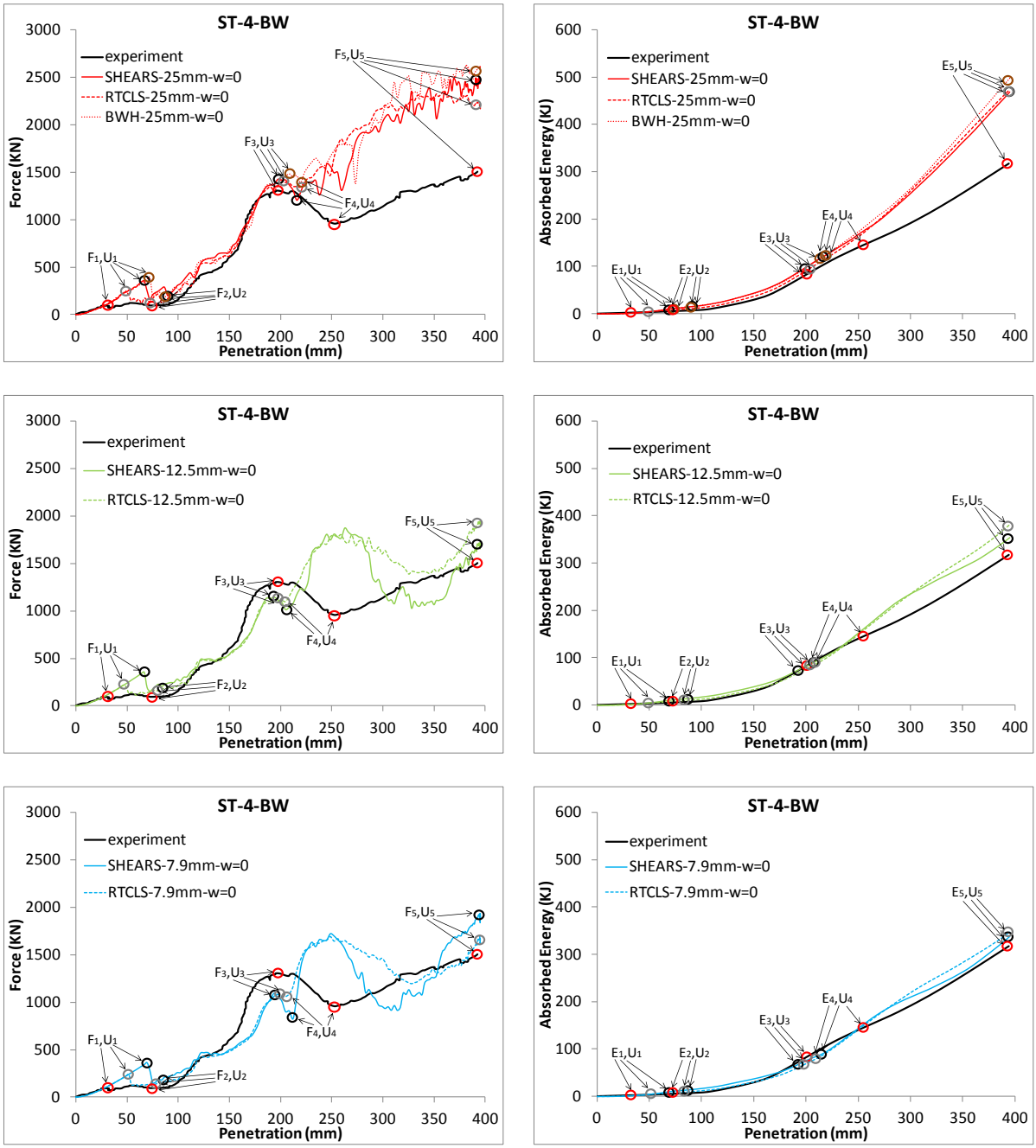

Figure D.6. ST-4-BW model. Force and absorbed energy-penetration curves.
Definition of force peaks and troughs for each element size and rupture criterion and comparison with the corresponding experimental values
(red circle: experiment, black circle: SHEARS, grey circle: RTCLS, brown circle: BWH)

Table D.6. ST-4-BW model. Numerical values of force, energy and penetration depth for each element size and rupture criterion at the selected peaks and troughs and comparison with the corresponding experimental values

SHEARS																	
l_e (mm)																	
7.9						12.5						25					
l_e/t = 2						l_e/t = 3.2						l_e/t = 6.3					
$F_1(KN)$	differ.	$E_1(KJ)$	differ.	$U_1(mm)$	differ.	$F_1(KN)$	differ.	$E_1(KJ)$	differ.	$U_1(mm)$	differ.	$F_1(KN)$	differ.	$E_1(KJ)$	differ.	$U_1(mm)$	differ.
363.1	121.8%	10.3	147.3%	69.7	73.8%	353.2	120.1%	9.8	145.0%	67.1	70.4%	351.6	119.8%	9.6	144.1%	67.1	70.4%
RTCLS																	
l_e (mm)																	
7.9						12.5						25					
l_e/t = 2						l_e/t = 3.2						l_e/t = 6.3					
$F_1(KN)$	differ.	$E_1(KJ)$	differ.	$U_1(mm)$	differ.	$F_1(KN)$	differ.	$E_1(KJ)$	differ.	$U_1(mm)$	differ.	$F_1(KN)$	differ.	$E_1(KJ)$	differ.	$U_1(mm)$	differ.
239.1	92.2%	5.0	104.1%	52.0	47.2%	219.3	85.3%	4.1	90.1%	47.4	38.3%	239.3	92.3%	4.6	97.9%	49.7	42.8%
BWH																	
l_e (mm)																	
7.9						12.5						25					
l_e/t = 2						l_e/t = 3.2						l_e/t = 6.3					
$F_1(KN)$	differ.	$E_1(KJ)$	differ.	$U_1(mm)$	differ.	$F_1(KN)$	differ.	$E_1(KJ)$	differ.	$U_1(mm)$	differ.	$F_1(KN)$	differ.	$E_1(KJ)$	differ.	$U_1(mm)$	differ.
-	-	-	-	-	-	-	-	-	-	-	-	391.3	126.4%	11.6	152.5%	72.5	77.1%
ST-4-BW																	
Experiment																	
$F_1(KN)$						$E_1(KJ)$						$U_1(mm)$					
88.2						1.6						32.1					

continued on next page

continued from previous page

SHEARS																	
l_e (mm)																	
7.9						12.5						25					
l_e/t = 2						l_e/t = 3.2						l_e/t = 6.3					
$F_2(KN)$	differ.	$E_2(KJ)$	differ.	$U_2(mm)$	differ.	$F_2(KN)$	differ.	$E_2(KJ)$	differ.	$U_2(mm)$	differ.	$F_2(KN)$	differ.	$E_2(KJ)$	differ.	$U_2(mm)$	differ.
180.0	64.7%	13.3	81.8%	83.9	14.6%	204.4	75.8%	13.3	81.8%	83.9	14.6%	198.4	73.2%	15.2	92.4%	89.9	21.4%
RTCLS																	
l_e (mm)																	
7.9						12.5						25					
l_e/t = 2						l_e/t = 3.2						l_e/t = 6.3					
$F_2(KN)$	differ.	$E_2(KJ)$	differ.	$U_2(mm)$	differ.	$F_2(KN)$	differ.	$E_2(KJ)$	differ.	$U_2(mm)$	differ.	$F_2(KN)$	differ.	$E_2(KJ)$	differ.	$U_2(mm)$	differ.
136.0	38.5%	8.5	41.8%	78.1	7.4%	159.5	53.7%	8.6	42.8%	78.1	7.4%	136.5	38.9%	8.2	38.4%	72.5	0.0%
BWH																	
l_e (mm)																	
7.9						12.5						25					
l_e/t = 2						l_e/t = 3.2						l_e/t = 6.3					
$F_2(KN)$	differ.	$E_2(KJ)$	differ.	$U_2(mm)$	differ.	$F_2(KN)$	differ.	$E_2(KJ)$	differ.	$U_2(mm)$	differ.	$F_2(KN)$	differ.	$E_2(KJ)$	differ.	$U_2(mm)$	differ.
-	-	-	-	-	-	-	-	-	-	-	-	185.4	67.3%	15.0	91.5%	86.8	18.0%
ST-4-BW																	
Experiment																	
$F_2(KN)$						$E_2(KJ)$						$U_2(mm)$					
92.0						5.6						72.5					

continued on next page

continued from previous page

SHEARS																	
l_e (mm)																	
7.9						12.5						25					
l_e/t = 2						l_e/t = 3.2						l_e/t = 6.3					
$F_3(KN)$	differ.	$E_3(KJ)$	differ.	$U_3(mm)$	differ.	$F_3(KN)$	differ.	$E_3(KJ)$	differ.	$U_3(mm)$	differ.	$F_3(KN)$	differ.	$E_3(KJ)$	differ.	$U_3(mm)$	differ.
1096.5	-17.1%	69.1	-13.4%	193.8	-2.4%	1144.3	-12.9%	75.5	-4.5%	193.8	-2.4%	1424.1	9.0%	95.0	18.4%	197.5	-0.5%

RTCLS																	
l_e (mm)																	
7.9						12.5						25					
l_e/t = 2						l_e/t = 3.2						l_e/t = 6.3					
$F_3(KN)$	differ.	$E_3(KJ)$	differ.	$U_3(mm)$	differ.	$F_3(KN)$	differ.	$E_3(KJ)$	differ.	$U_3(mm)$	differ.	$F_3(KN)$	differ.	$E_3(KJ)$	differ.	$U_3(mm)$	differ.
1082.0	-18.5%	66.5	-17.2%	197.5	-0.5%	1110.2	-15.9%	77.7	-1.7%	201.2	1.4%	1395.0	6.9%	92.4	15.7%	201.2	1.4%

BWH																	
l_e (mm)																	
7.9						12.5						25					
l_e/t = 2						l_e/t = 3.2						l_e/t = 6.3					
$F_3(KN)$	differ.	$E_3(KJ)$	differ.	$U_3(mm)$	differ.	$F_3(KN)$	differ.	$E_3(KJ)$	differ.	$U_3(mm)$	differ.	$F_3(KN)$	differ.	$E_3(KJ)$	differ.	$U_3(mm)$	differ.
-	-	-	-	-	-	-	-	-	-	-	-	1481.3	12.9%	109.5	32.4%	208.6	5.0%

ST-4-BW		
Experiment		
$F_3(KN)$	$E_3(KJ)$	$U_3(mm)$
1302.0	79.0	198.4

continued on next page

continued from previous page

SHEARS																	
l_e (mm)																	
7.9						12.5						25					
l_e/t = 2						l_e/t = 3.2						l_e/t = 6.3					
$F_4(KN)$	differ.	$E_4(KJ)$	differ.	$U_4(mm)$	differ.	$F_4(KN)$	differ.	$E_4(KJ)$	differ.	$U_4(mm)$	differ.	$F_4(KN)$	differ.	$E_4(KJ)$	differ.	$U_4(mm)$	differ.
827.3	-14.3%	87.0	-48.6%	212.3	-17.7%	1012.8	5.9%	87.7	-47.8%	204.9	-21.2%	1203.4	23.0%	120.2	-17.2%	216.0	-16.0%
RTCLS																	
l_e (mm)																	
7.9						12.5						25					
l_e/t = 2						l_e/t = 3.2						l_e/t = 6.3					
$F_4(KN)$	differ.	$E_4(KJ)$	differ.	$U_4(mm)$	differ.	$F_4(KN)$	differ.	$E_4(KJ)$	differ.	$U_4(mm)$	differ.	$F_4(KN)$	differ.	$E_4(KJ)$	differ.	$U_4(mm)$	differ.
1057.8	10.2%	74.3	-63.0%	204.9	-21.2%	1096.2	13.8%	81.8	-54.3%	204.9	-21.2%	1342.8	33.8%	117.7	-19.2%	219.7	-14.3%
BWH																	
l_e (mm)																	
7.9						12.5						25					
l_e/t = 2						l_e/t = 3.2						l_e/t = 6.3					
$F_4(KN)$	differ.	$E_4(KJ)$	differ.	$U_4(mm)$	differ.	$F_4(KN)$	differ.	$E_4(KJ)$	differ.	$U_4(mm)$	differ.	$F_4(KN)$	differ.	$E_4(KJ)$	differ.	$U_4(mm)$	differ.
-	-	-	-	-	-	-	-	-	-	-	-	1390.1	37.1%	125.5	-12.8%	219.7	-14.3%
ST-4-BW																	
Experiment																	
$F_4(KN)$						$E_4(KJ)$						$U_4(mm)$					
954.9						142.8						253.5					

continued on next page

continued from previous page

SHEARS																	
l_e (mm)																	
7.9						12.5						25					
l_e/t = 2						l_e/t = 3.2						l_e/t = 6.3					
$F_5(KN)$	differ.	$E_5(KJ)$	differ.	$U_5(mm)$	differ.	$F_5(KN)$	differ.	$E_5(KJ)$	differ.	$U_5(mm)$	differ.	$F_5(KN)$	differ.	$E_5(KJ)$	differ.	$U_5(mm)$	differ.
1888.2	22.7%	333.4	5.8%	392.5	0.1%	1704.1	12.5%	348.7	10.3%	392.5	0.1%	2379.5	45.1%	462.4	38.0%	392.5	0.1%
RTCLS																	
l_e (mm)																	
7.9						12.5						25					
l_e/t = 2						l_e/t = 3.2						l_e/t = 6.3					
$F_5(KN)$	differ.	$E_5(KJ)$	differ.	$U_5(mm)$	differ.	$F_5(KN)$	differ.	$E_5(KJ)$	differ.	$U_5(mm)$	differ.	$F_5(KN)$	differ.	$E_5(KJ)$	differ.	$U_5(mm)$	differ.
1644.2	8.9%	342.6	8.5%	392.5	0.1%	1907.8	23.7%	376.5	17.9%	392.5	0.1%	2235.7	39.2%	467.8	39.1%	392.5	0.1%
BWH																	
l_e (mm)																	
7.9						12.5						25					
l_e/t = 2						l_e/t = 3.2						l_e/t = 6.3					
$F_5(KN)$	differ.	$E_5(KJ)$	differ.	$U_5(mm)$	differ.	$F_5(KN)$	differ.	$E_5(KJ)$	differ.	$U_5(mm)$	differ.	$F_5(KN)$	differ.	$E_5(KJ)$	differ.	$U_5(mm)$	differ.
-	-	-	-	-	-	-	-	-	-	-	-	2596.3	53.3%	491.7	43.9%	392.5	0.1%
ST-4-BW																	
Experiment																	
$F_5(KN)$						$E_5(KJ)$						$U_5(mm)$					
1503.4						314.7						392.3					

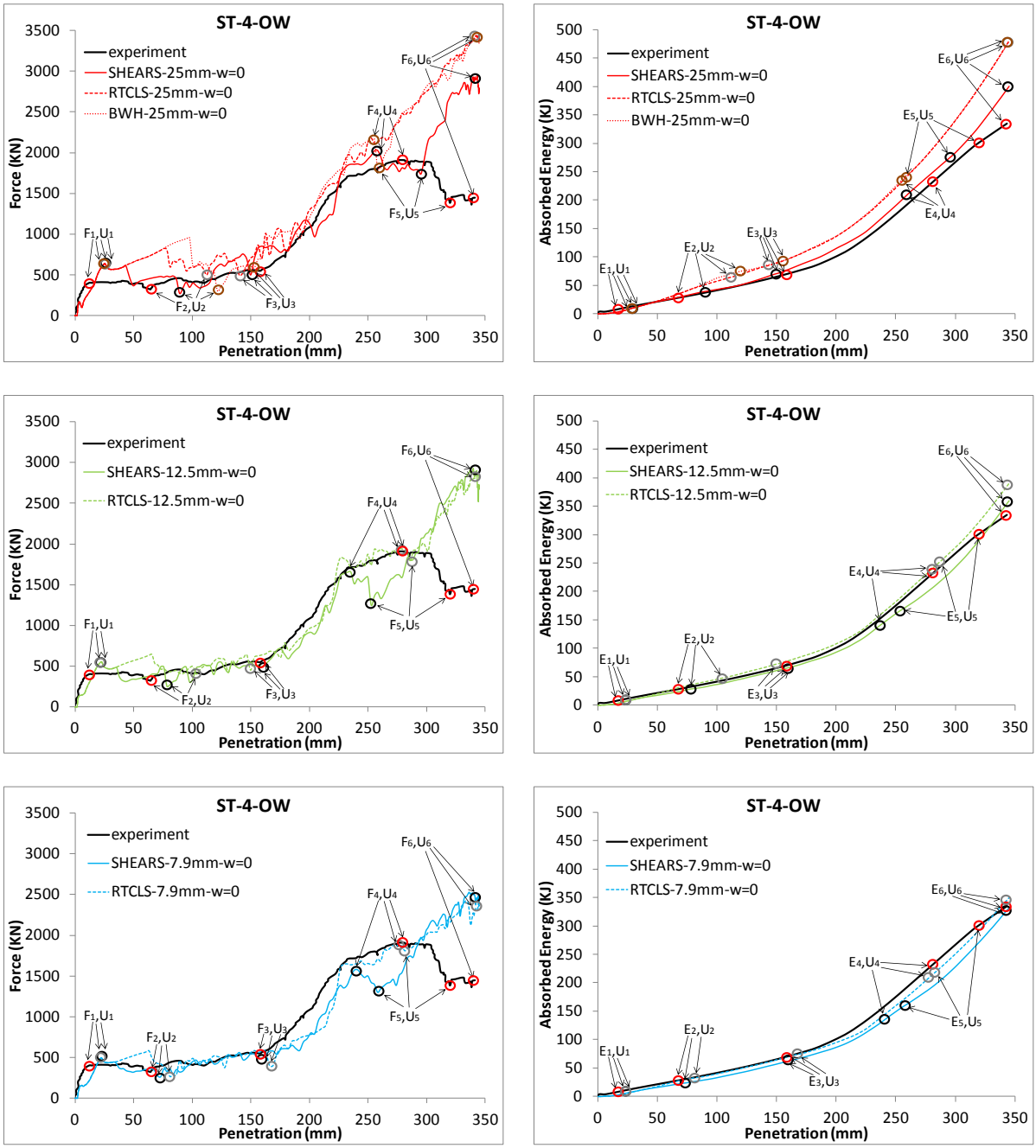

Figure D.7. ST-4-OW model. Force and absorbed energy-penetration curves.
Definition of force peaks and troughs for each element size and rupture criterion and comparison with the corresponding experimental values
(red circle: experiment, black circle: SHEARS, grey circle: RTCLS, brown circle: BWH)

Table D.7. ST-4-OW model. Numerical values of force, energy and penetration depth for each element size and rupture criterion at the selected peaks and troughs and comparison with the corresponding experimental values

SHEARS																	
l_e (mm)																	
7.9						12.5						25					
l_e/t = 2						l_e/t = 3.2						l_e/t = 6.3					
$F_1(KN)$	differ.	$E_1(KJ)$	differ.	$U_1(mm)$	differ.	$F_1(KN)$	differ.	$E_1(KJ)$	differ.	$U_1(mm)$	differ.	$F_1(KN)$	differ.	$E_1(KJ)$	differ.	$U_1(mm)$	differ.
495.7	21.2%	5.4	21.9%	22.7	42.5%	553.9	32.1%	6.5	39.6%	22.7	42.5%	640.3	46.0%	8.3	62.5%	25.7	54.0%
RTCLS																	
l_e (mm)																	
7.9						12.5						25					
l_e/t = 2						l_e/t = 3.2						l_e/t = 6.3					
$F_1(KN)$	differ.	$E_1(KJ)$	differ.	$U_1(mm)$	differ.	$F_1(KN)$	differ.	$E_1(KJ)$	differ.	$U_1(mm)$	differ.	$F_1(KN)$	differ.	$E_1(KJ)$	differ.	$U_1(mm)$	differ.
498.1	21.6%	5.4	21.9%	22.7	42.5%	553.9	32.1%	6.5	39.6%	22.7	42.5%	640.3	46.0%	8.3	62.5%	25.7	54.0%
BWH																	
l_e (mm)																	
7.9						12.5						25					
l_e/t = 2						l_e/t = 3.2						l_e/t = 6.3					
$F_1(KN)$	differ.	$E_1(KJ)$	differ.	$U_1(mm)$	differ.	$F_1(KN)$	differ.	$E_1(KJ)$	differ.	$U_1(mm)$	differ.	$F_1(KN)$	differ.	$E_1(KJ)$	differ.	$U_1(mm)$	differ.
-	-	-	-	-	-	-	-	-	-	-	-	639.4	45.9%	8.3	62.5%	25.7	54.0%
ST-4-OW																	
Experiment																	
$F_1(KN)$						$E_1(KJ)$						$U_1(mm)$					
400.8						4.3						14.8					

continued on next page

continued from previous page

SHEARS																	
l_e (mm)																	
7.9						12.5						25					
l_e/t = 2						l_e/t = 3.2						l_e/t = 6.3					
$F_2(KN)$	differ.	$E_2(KJ)$	differ.	$U_2(mm)$	differ.	$F_2(KN)$	differ.	$E_2(KJ)$	differ.	$U_2(mm)$	differ.	$F_2(KN)$	differ.	$E_2(KJ)$	differ.	$U_2(mm)$	differ.
264.5	-19.1%	23.8	-0.5%	73.3	13.1%	253.6	-23.2%	28.8	18.2%	78.5	19.9%	272.6	-16.1%	39.3	48.6%	89.3	32.6%

RTCLS																	
l_e (mm)																	
7.9						12.5						25					
l_e/t = 2						l_e/t = 3.2						l_e/t = 6.3					
$F_2(KN)$	differ.	$E_2(KJ)$	differ.	$U_2(mm)$	differ.	$F_2(KN)$	differ.	$E_2(KJ)$	differ.	$U_2(mm)$	differ.	$F_2(KN)$	differ.	$E_2(KJ)$	differ.	$U_2(mm)$	differ.
265.5	-18.7%	32.9	31.4%	81.1	23.2%	404.3	23.2%	47.4	65.7%	103.6	46.8%	499.6	43.8%	65.1	92.4%	112.5	54.6%

BWH																	
l_e (mm)																	
7.9						12.5						25					
l_e/t = 2						l_e/t = 3.2						l_e/t = 6.3					
$F_2(KN)$	differ.	$E_2(KJ)$	differ.	$U_2(mm)$	differ.	$F_2(KN)$	differ.	$E_2(KJ)$	differ.	$U_2(mm)$	differ.	$F_2(KN)$	differ.	$E_2(KJ)$	differ.	$U_2(mm)$	differ.
-	-	-	-	-	-	-	-	-	-	-	-	306.0	-4.5%	76.0	104.1%	121.6	61.7%

ST-4-OW		
Experiment		
$F_2(KN)$	$E_2(KJ)$	$U_2(mm)$
320.2	24.0	64.3

continued on next page

continued from previous page

SHEARS																	
l_e (mm)																	
7.9						12.5						25					
l_e/t = 2						l_e/t = 3.2						l_e/t = 6.3					
$F_3(KN)$	differ.	$E_3(KJ)$	differ.	$U_3(mm)$	differ.	$F_3(KN)$	differ.	$E_3(KJ)$	differ.	$U_3(mm)$	differ.	$F_3(KN)$	differ.	$E_3(KJ)$	differ.	$U_3(mm)$	differ.
489.7	-11.3%	62.0	-8.2%	159.6	0.9%	493.1	-10.6%	66.1	-1.8%	159.6	0.9%	499.2	-9.4%	71.0	5.3%	149.9	-5.3%

RTCLS																	
l_e (mm)																	
7.9						12.5						25					
l_e/t = 2						l_e/t = 3.2						l_e/t = 6.3					
$F_3(KN)$	differ.	$E_3(KJ)$	differ.	$U_3(mm)$	differ.	$F_3(KN)$	differ.	$E_3(KJ)$	differ.	$U_3(mm)$	differ.	$F_3(KN)$	differ.	$E_3(KJ)$	differ.	$U_3(mm)$	differ.
402.1	-30.8%	73.6	8.9%	166.0	4.9%	451.7	-19.3%	72.4	7.4%	149.9	-5.3%	496.1	-10.0%	83.8	21.8%	140.4	-11.9%

BWH																	
l_e (mm)																	
7.9						12.5						25					
l_e/t = 2						l_e/t = 3.2						l_e/t = 6.3					
$F_3(KN)$	differ.	$E_3(KJ)$	differ.	$U_3(mm)$	differ.	$F_3(KN)$	differ.	$E_3(KJ)$	differ.	$U_3(mm)$	differ.	$F_3(KN)$	differ.	$E_3(KJ)$	differ.	$U_3(mm)$	differ.
-	-	-	-	-	-	-	-	-	-	-	-	586.2	6.7%	92.5	31.6%	153.1	-3.2%

ST-4-OW		
Experiment		
$F_3(KN)$	$E_3(KJ)$	$U_3(mm)$
548.4	67.3	158.1

continued on next page

continued from previous page

SHEARS																	
l_e (mm)																	
7.9						12.5						25					
l_e/t = 2						l_e/t = 3.2						l_e/t = 6.3					
$F_4(KN)$	differ.	$E_4(KJ)$	differ.	$U_4(mm)$	differ.	$F_4(KN)$	differ.	$E_4(KJ)$	differ.	$U_4(mm)$	differ.	$F_4(KN)$	differ.	$E_4(KJ)$	differ.	$U_4(mm)$	differ.
1575.4	-19.1%	136.3	-52.9%	241.4	-15.2%	1657.2	-14.1%	138.8	-51.1%	235.5	-17.7%	2026.2	6.0%	207.7	-12.0%	258.4	-8.4%
RTCLS																	
l_e (mm)																	
7.9						12.5						25					
l_e/t = 2						l_e/t = 3.2						l_e/t = 6.3					
$F_4(KN)$	differ.	$E_4(KJ)$	differ.	$U_4(mm)$	differ.	$F_4(KN)$	differ.	$E_4(KJ)$	differ.	$U_4(mm)$	differ.	$F_4(KN)$	differ.	$E_4(KJ)$	differ.	$U_4(mm)$	differ.
1890.1	-0.9%	207.4	-12.1%	276.8	-1.5%	1941.8	1.8%	237.8	1.5%	279.3	-0.6%	Not captured					
BWH																	
l_e (mm)																	
7.9						12.5						25					
l_e/t = 2						l_e/t = 3.2						l_e/t = 6.3					
$F_4(KN)$	differ.	$E_4(KJ)$	differ.	$U_4(mm)$	differ.	$F_4(KN)$	differ.	$E_4(KJ)$	differ.	$U_4(mm)$	differ.	$F_4(KN)$	differ.	$E_4(KJ)$	differ.	$U_4(mm)$	differ.
-	-	-	-	-	-	-	-	-	-	-	-	2167.0	12.7%	237.7	1.5%	255.7	-9.5%
ST-4-OW																	
Experiment																	
$F_4(KN)$						$E_4(KJ)$						$U_4(mm)$					
1908.0						234.2						281.1					

continued on next page

continued from previous page

SHEARS																	
l_e (mm)																	
7.9						12.5						25					
l_e/t = 2						l_e/t = 3.2						l_e/t = 6.3					
$F_5(KN)$	differ.	$E_5(KJ)$	differ.	$U_5(mm)$	differ.	$F_5(KN)$	differ.	$E_5(KJ)$	differ.	$U_5(mm)$	differ.	$F_5(KN)$	differ.	$E_5(KJ)$	differ.	$U_5(mm)$	differ.
1299.4	-6.2%	161.2	-61.0%	258.4	-21.2%	1250.6	-10.0%	165.6	-58.5%	252.9	-23.4%	1737.8	22.8%	275.2	-9.5%	295.4	-7.9%

RTCLS																	
l_e (mm)																	
7.9						12.5						25					
l_e/t = 2						l_e/t = 3.2						l_e/t = 6.3					
$F_5(KN)$	differ.	$E_5(KJ)$	differ.	$U_5(mm)$	differ.	$F_5(KN)$	differ.	$E_5(KJ)$	differ.	$U_5(mm)$	differ.	$F_5(KN)$	differ.	$E_5(KJ)$	differ.	$U_5(mm)$	differ.
1808.2	26.7%	216.5	-33.2%	281.7	-12.7%	1785.8	25.5%	251.4	-18.5%	286.4	-11.0%	Not captured					

BWH																	
l_e (mm)																	
7.9						12.5						25					
l_e/t = 2						l_e/t = 3.2						l_e/t = 6.3					
$F_5(KN)$	differ.	$E_5(KJ)$	differ.	$U_5(mm)$	differ.	$F_5(KN)$	differ.	$E_5(KJ)$	differ.	$U_5(mm)$	differ.	$F_5(KN)$	differ.	$E_5(KJ)$	differ.	$U_5(mm)$	differ.
-	-	-	-	-	-	-	-	-	-	-	-	1805.5	26.5%	243.2	-21.8%	258.4	-21.2%

ST-4-OW		
Experiment		
$F_5(KN)$	$E_5(KJ)$	$U_5(mm)$
1382.6	302.7	319.8

continued on next page

continued from previous page

SHEARS																	
l_e (mm)																	
7.9						12.5						25					
l_e/t = 2						l_e/t = 3.2						l_e/t = 6.3					
$F_6(KN)$	differ.	$E_6(KJ)$	differ.	$U_6(mm)$	differ.	$F_6(KN)$	differ.	$E_6(KJ)$	differ.	$U_6(mm)$	differ.	$F_6(KN)$	differ.	$E_6(KJ)$	differ.	$U_6(mm)$	differ.
2495.9	53.2%	322.3	-3.4%	341.1	0.0%	2824.6	64.5%	349.3	4.6%	341.1	0.0%	2898.7	66.8%	389.2	15.4%	341.1	0.0%
RTCLS																	
l_e (mm)																	
7.9						12.5						25					
l_e/t = 2						l_e/t = 3.2						l_e/t = 6.3					
$F_6(KN)$	differ.	$E_6(KJ)$	differ.	$U_6(mm)$	differ.	$F_6(KN)$	differ.	$E_6(KJ)$	differ.	$U_6(mm)$	differ.	$F_6(KN)$	differ.	$E_6(KJ)$	differ.	$U_6(mm)$	differ.
2274.0	44.4%	341.1	2.3%	341.1	0.0%	2810.0	64.0%	379.4	12.9%	341.1	0.0%	3410.2	80.8%	467.7	33.5%	341.1	0.0%
BWH																	
l_e (mm)																	
7.9						12.5						25					
l_e/t = 2						l_e/t = 3.2						l_e/t = 6.3					
$F_6(KN)$	differ.	$E_6(KJ)$	differ.	$U_6(mm)$	differ.	$F_6(KN)$	differ.	$E_6(KJ)$	differ.	$U_6(mm)$	differ.	$F_6(KN)$	differ.	$E_6(KJ)$	differ.	$U_6(mm)$	differ.
-	-	-	-	-	-	-	-	-	-	-	-	3385.8	80.2%	467.0	33.3%	341.1	0.0%
ST-4-OW																	
Experiment																	
$F_6(KN)$						$E_6(KJ)$						$U_6(mm)$					
1447.8						333.5						341.1					

D.3 US, LS, TS and OS models-(Paik and Tak 1995)

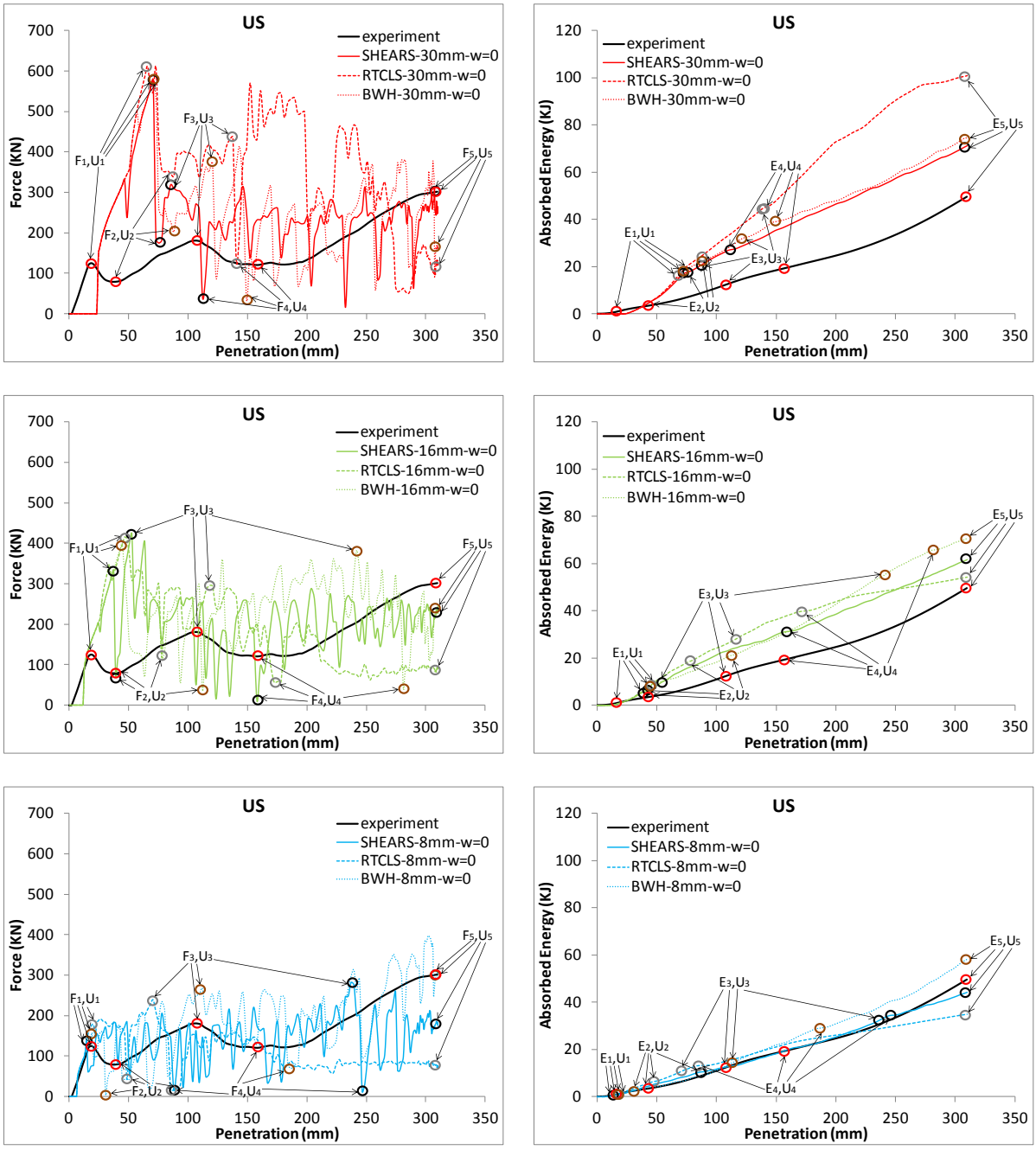

Figure D.8. US model. Force and absorbed energy-penetration curves.
Definition of force peaks and troughs for each element size and rupture criterion and comparison with the corresponding experimental values
(red circle: experiment, black circle: SHEARS, grey circle: RTCLS, brown circle: BWH)

Table D.8. US model. Numerical values of force, energy and penetration depth for each element size and rupture criterion at the selected peaks and troughs and comparison with the corresponding experimental values

SHEARS																	
$l_e\ (mm)$																	
8						16						30					
l_e/t = 1.1						l_e/t = 2.3						l_e/t = 4.3					
$F_1(KN)$	differ.	$E_1(KJ)$	differ.	$U_1(mm)$	differ.	$F_1(KN)$	differ.	$E_1(KJ)$	differ.	$U_1(mm)$	differ.	$F_1(KN)$	differ.	$E_1(KJ)$	differ.	$U_1(mm)$	differ.
138.3	10.1%	0.7	-49.5%	14.6	-25.7%	332.4	90.7%	5.3	128.0%	37.2	65.2%	577.8	128.9%	16.2	173.5%	70.5	115.5%
RTCLS																	
$l_e\ (mm)$																	
8						16						30					
l_e/t = 1.1						l_e/t = 2.3						l_e/t = 4.3					
$F_1(KN)$	differ.	$E_1(KJ)$	differ.	$U_1(mm)$	differ.	$F_1(KN)$	differ.	$E_1(KJ)$	differ.	$U_1(mm)$	differ.	$F_1(KN)$	differ.	$E_1(KJ)$	differ.	$U_1(mm)$	differ.
178.8	35.4%	1.4	22.2%	19.2	1.4%	415.9	107.6%	9.1	154.9%	46.5	84.5%	611.7	132.1%	14.8	171.2%	65.8	110.8%
BWH																	
$l_e\ (mm)$																	
8						16						30					
l_e/t = 1.1						l_e/t = 2.3						l_e/t = 4.3					
$F_1(KN)$	differ.	$E_1(KJ)$	differ.	$U_1(mm)$	differ.	$F_1(KN)$	differ.	$E_1(KJ)$	differ.	$U_1(mm)$	differ.	$F_1(KN)$	differ.	$E_1(KJ)$	differ.	$U_1(mm)$	differ.
156.9	22.7%	1.3	12.8%	19.2	1.4%	397.9	104.4%	8.0	149.9%	44.6	80.9%	578.4	128.9%	16.9	174.4%	70.5	115.5%
US																	
Experiment																	
$F_1(KN)$						$E_1(KJ)$						$U_1(mm)$					
125.0						1.2						18.9					

continued on next page

continued from previous page

SHEARS																	
l_e (mm)																	
8						16						30					
l_e/t = 1.1						l_e/t = 2.3						l_e/t = 4.3					
$F_2(KN)$	differ.	$E_2(KJ)$	differ.	$U_2(mm)$	differ.	$F_2(KN)$	differ.	$E_2(KJ)$	differ.	$U_2(mm)$	differ.	$F_2(KN)$	differ.	$E_2(KJ)$	differ.	$U_2(mm)$	differ.
16.2	-132.2%	10.5	107.8%	87.9	74.6%	72.3	-9.6%	5.6	56.3%	39.0	-2.9%	174.5	74.8%	17.6	139.2%	75.3	61.0%
RTCLS																	
l_e (mm)																	
8						16						30					
l_e/t = 1.1						l_e/t = 2.3						l_e/t = 4.3					
$F_2(KN)$	differ.	$E_2(KJ)$	differ.	$U_2(mm)$	differ.	$F_2(KN)$	differ.	$E_2(KJ)$	differ.	$U_2(mm)$	differ.	$F_2(KN)$	differ.	$E_2(KJ)$	differ.	$U_2(mm)$	differ.
42.0	-61.8%	6.5	69.3%	48.5	19.0%	117.5	38.6%	18.5	142.0%	77.8	63.9%	339.7	124.1%	24.6	154.6%	87.9	74.6%
BWH																	
l_e (mm)																	
8						16						30					
l_e/t = 1.1						l_e/t = 2.3						l_e/t = 4.3					
$F_2(KN)$	differ.	$E_2(KJ)$	differ.	$U_2(mm)$	differ.	$F_2(KN)$	differ.	$E_2(KJ)$	differ.	$U_2(mm)$	differ.	$F_2(KN)$	differ.	$E_2(KJ)$	differ.	$U_2(mm)$	differ.
7.2	-166.7%	2.7	-14.7%	30.5	-27.3%	35.9	-75.6%	21.1	148.0%	112.1	94.6%	202.1	87.0%	22.1	150.2%	87.9	74.6%
US																	
Experiment																	
$F_2(KN)$						$E_2(KJ)$						$U_2(mm)$					
79.5						3.1						40.1					

continued on next page

continued from previous page

SHEARS																	
l_e (mm)																	
8						16						30					
l_e/t = 1.1						l_e/t = 2.3						l_e/t = 4.3					
$F_3(KN)$	differ.	$E_3(KJ)$	differ.	$U_3(mm)$	differ.	$F_3(KN)$	differ.	$E_3(KJ)$	differ.	$U_3(mm)$	differ.	$F_3(KN)$	differ.	$E_3(KJ)$	differ.	$U_3(mm)$	differ.
282.6	44.0%	32.4	91.9%	237.1	76.1%	422.4	80.2%	9.2	-26.1%	52.6	-67.6%	318.7	55.3%	20.1	50.2%	85.3	-22.0%
RTCLS																	
l_e (mm)																	
8						16						30					
l_e/t = 1.1						l_e/t = 2.3						l_e/t = 4.3					
$F_3(KN)$	differ.	$E_3(KJ)$	differ.	$U_3(mm)$	differ.	$F_3(KN)$	differ.	$E_3(KJ)$	differ.	$U_3(mm)$	differ.	$F_3(KN)$	differ.	$E_3(KJ)$	differ.	$U_3(mm)$	differ.
239.6	28.1%	10.7	-12.1%	70.5	-40.6%	295.4	48.2%	28.4	80.9%	117.6	10.0%	437.0	83.0%	44.2	114.5%	137.6	25.6%
BWH																	
l_e (mm)																	
8						16						30					
l_e/t = 1.1						l_e/t = 2.3						l_e/t = 4.3					
$F_3(KN)$	differ.	$E_3(KJ)$	differ.	$U_3(mm)$	differ.	$F_3(KN)$	differ.	$E_3(KJ)$	differ.	$U_3(mm)$	differ.	$F_3(KN)$	differ.	$E_3(KJ)$	differ.	$U_3(mm)$	differ.
266.9	38.5%	14.1	15.7%	112.1	5.2%	382.1	71.6%	55.6	128.9%	241.8	77.8%	373.1	69.5%	31.6	89.8%	120.5	12.4%
US																	
Experiment																	
$F_3(KN)$						$E_3(KJ)$						$U_3(mm)$					
180.7						12.0						106.4					

continued on next page

continued from previous page

SHEARS																	
l_e (mm)																	
8						16						30					
l_e/t = 1.1						l_e/t = 2.3						l_e/t = 4.3					
$F_4(KN)$	differ.	$E_4(KJ)$	differ.	$U_4(mm)$	differ.	$F_4(KN)$	differ.	$E_4(KJ)$	differ.	$U_4(mm)$	differ.	$F_4(KN)$	differ.	$E_4(KJ)$	differ.	$U_4(mm)$	differ.
12.9	-161.4%	34.4	55.7%	246.5	43.5%	10.3	-168.5%	31.1	46.4%	157.9	-0.3%	42.1	-96.4%	27.2	33.5%	112.1	-34.3%
RTCLS																	
l_e (mm)																	
8						16						30					
l_e/t = 1.1						l_e/t = 2.3						l_e/t = 4.3					
$F_4(KN)$	differ.	$E_4(KJ)$	differ.	$U_4(mm)$	differ.	$F_4(KN)$	differ.	$E_4(KJ)$	differ.	$U_4(mm)$	differ.	$F_4(KN)$	differ.	$E_4(KJ)$	differ.	$U_4(mm)$	differ.
15.8	-153.7%	13.1	-38.6%	85.3	-60.0%	56.3	-72.5%	39.7	68.7%	172.4	8.4%	131.7	9.0%	45.0	79.5%	140.5	-12.0%
BWH																	
l_e (mm)																	
8						16						30					
l_e/t = 1.1						l_e/t = 2.3						l_e/t = 4.3					
$F_4(KN)$	differ.	$E_4(KJ)$	differ.	$U_4(mm)$	differ.	$F_4(KN)$	differ.	$E_4(KJ)$	differ.	$U_4(mm)$	differ.	$F_4(KN)$	differ.	$E_4(KJ)$	differ.	$U_4(mm)$	differ.
70.0	-53.0%	29.1	39.8%	186.7	16.4%	40.9	-98.7%	65.7	108.8%	281.1	55.8%	33.6	-112.7%	39.1	67.3%	149.2	-6.0%
US																	
Experiment																	
$F_4(KN)$						$E_4(KJ)$						$U_4(mm)$					
120.5						19.4						158.4					

continued on next page

continued from previous page

SHEARS																	
l_e (mm)																	
8						16						30					
l_e/t = 1.1						l_e/t = 2.3						l_e/t = 4.3					
$F_5(KN)$	differ.	$E_5(KJ)$	differ.	$U_5(mm)$	differ.	$F_5(KN)$	differ.	$E_5(KJ)$	differ.	$U_5(mm)$	differ.	$F_5(KN)$	differ.	$E_5(KJ)$	differ.	$U_5(mm)$	differ.
181.1	-49.8%	44.0	-11.7%	309.5	0.0%	233.1	-25.5%	61.6	21.7%	309.5	0.0%	258.0	-15.4%	71.1	35.9%	309.5	0.0%
RTCLS																	
l_e (mm)																	
8						16						30					
l_e/t = 1.1						l_e/t = 2.3						l_e/t = 4.3					
$F_5(KN)$	differ.	$E_5(KJ)$	differ.	$U_5(mm)$	differ.	$F_5(KN)$	differ.	$E_5(KJ)$	differ.	$U_5(mm)$	differ.	$F_5(KN)$	differ.	$E_5(KJ)$	differ.	$U_5(mm)$	differ.
77.6	-118.0%	34.8	-35.0%	309.5	0.0%	90.7	-107.4%	54.1	8.8%	309.5	0.0%	129.8	-79.5%	100.8	68.3%	309.5	0.0%
BWH																	
l_e (mm)																	
8						16						30					
l_e/t = 1.1						l_e/t = 2.3						l_e/t = 4.3					
$F_5(KN)$	differ.	$E_5(KJ)$	differ.	$U_5(mm)$	differ.	$F_5(KN)$	differ.	$E_5(KJ)$	differ.	$U_5(mm)$	differ.	$F_5(KN)$	differ.	$E_5(KJ)$	differ.	$U_5(mm)$	differ.
297.5	-1.2%	58.1	16.1%	309.5	0.0%	236.6	-24.0%	70.6	35.2%	309.5	0.0%	168.3	-56.6%	74.7	40.6%	309.5	0.0%
US																	
Experiment																	
$F_5(KN)$						$E_5(KJ)$						$U_5(mm)$					
301.1						49.5						309.6					

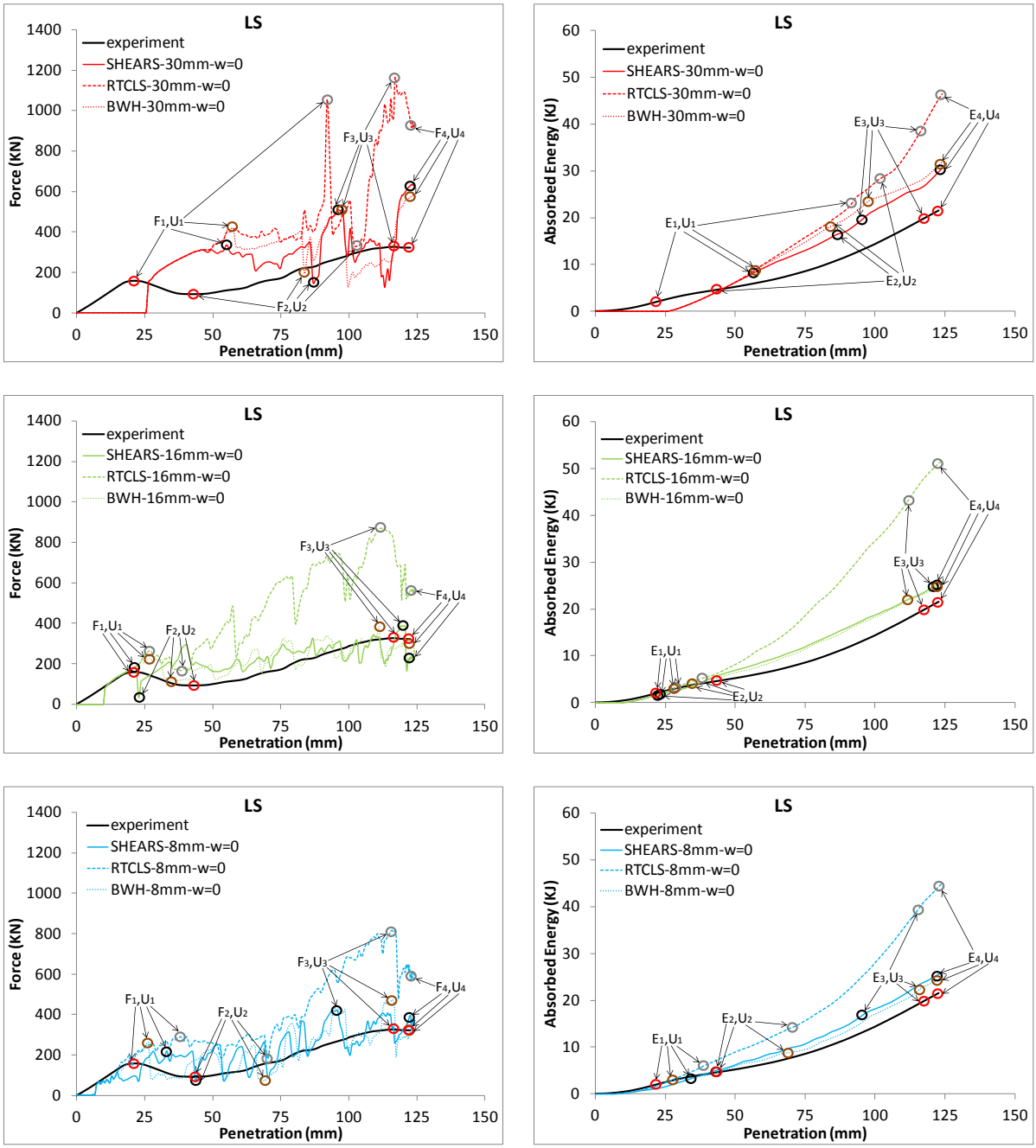

Figure D.9. LS model. Force and absorbed energy-penetration curves.
Definition of force peaks and troughs for each element size and rupture criterion and comparison with the corresponding experimental values
(red circle: experiment, black circle: SHEARS, grey circle: RTCLS, brown circle: BWH)

Table D.9. LS model. Numerical values of force, energy and penetration depth for each element size and rupture criterion at the selected peaks and troughs and comparison with the corresponding experimental values

SHEARS																	
l_e (mm)																	
8						16						30					
l_e/t = 1.1						l_e/t = 2.3						l_e/t = 4.3					
$F_1(KN)$	differ.	$E_1(KJ)$	differ.	$U_1(mm)$	differ.	$F_1(KN)$	differ.	$E_1(KJ)$	differ.	$U_1(mm)$	differ.	$F_1(KN)$	differ.	$E_1(KJ)$	differ.	$U_1(mm)$	differ.
219.1	31.7%	3.1	43.8%	33.1	41.2%	182.8	13.9%	1.5	-26.3%	21.1	-3.5%	335.5	71.3%	7.7	118.9%	55.0	86.5%
RTCLS																	
l_e (mm)																	
8						16						30					
l_e/t = 1.1						l_e/t = 2.3						l_e/t = 4.3					
$F_1(KN)$	differ.	$E_1(KJ)$	differ.	$U_1(mm)$	differ.	$F_1(KN)$	differ.	$E_1(KJ)$	differ.	$U_1(mm)$	differ.	$F_1(KN)$	differ.	$E_1(KJ)$	differ.	$U_1(mm)$	differ.
288.7	57.9%	5.9	99.5%	38.3	54.9%	264.2	49.6%	2.9	38.7%	27.3	22.3%	1054.8	147.6%	23.2	168.8%	91.9	123.3%
BWH																	
l_e (mm)																	
8						16						30					
l_e/t = 1.1						l_e/t = 2.3						l_e/t = 4.3					
$F_1(KN)$	differ.	$E_1(KJ)$	differ.	$U_1(mm)$	differ.	$F_1(KN)$	differ.	$E_1(KJ)$	differ.	$U_1(mm)$	differ.	$F_1(KN)$	differ.	$E_1(KJ)$	differ.	$U_1(mm)$	differ.
261.5	48.7%	2.7	31.8%	26.3	18.8%	226.1	34.8%	2.6	27.3%	26.3	18.8%	418.5	89.8%	9.0	128.0%	57.4	89.8%
LS																	
Experiment																	
$F_1(KN)$						$E_1(KJ)$						$U_1(mm)$					
159.1						2.0						21.8					

continued on next page

continued from previous page

SHEARS																	
l_e (mm)																	
8						16						30					
l_e/t = 1.1						l_e/t = 2.3						l_e/t = 4.3					
$F_2(KN)$	differ.	$E_2(KJ)$	differ.	$U_2(mm)$	differ.	$F_2(KN)$	differ.	$E_2(KJ)$	differ.	$U_2(mm)$	differ.	$F_2(KN)$	differ.	$E_2(KJ)$	differ.	$U_2(mm)$	differ.
66.4	-33.6%	5.1	11.3%	43.7	0.9%	33.2	-94.8%	1.8	-88.8%	22.8	-62.2%	146.9	44.7%	16.5	113.6%	86.8	66.8%
RTCLS																	
l_e (mm)																	
8						16						30					
l_e/t = 1.1						l_e/t = 2.3						l_e/t = 4.3					
$F_2(KN)$	differ.	$E_2(KJ)$	differ.	$U_2(mm)$	differ.	$F_2(KN)$	differ.	$E_2(KJ)$	differ.	$U_2(mm)$	differ.	$F_2(KN)$	differ.	$E_2(KJ)$	differ.	$U_2(mm)$	differ.
179.9	63.5%	14.2	102.8%	70.1	47.3%	167.3	56.9%	5.2	14.2%	38.3	-12.3%	329.6	111.8%	28.4	144.9%	102.1	80.9%
BWH																	
l_e (mm)																	
8						16						30					
l_e/t = 1.1						l_e/t = 2.3						l_e/t = 4.3					
$F_2(KN)$	differ.	$E_2(KJ)$	differ.	$U_2(mm)$	differ.	$F_2(KN)$	differ.	$E_2(KJ)$	differ.	$U_2(mm)$	differ.	$F_2(KN)$	differ.	$E_2(KJ)$	differ.	$U_2(mm)$	differ.
71.6	-26.2%	8.8	63.7%	69.0	45.7%	117.0	22.6%	4.0	-11.8%	34.1	-23.7%	195.3	70.8%	18.0	119.2%	83.6	63.4%
LS																	
Experiment																	
$F_2(KN)$						$E_2(KJ)$						$U_2(mm)$					
93.2						4.5						43.3					

continued on next page

continued from previous page

SHEARS																	
l_e (mm)																	
8						16						30					
l_e/t = 1.1						l_e/t = 2.3						l_e/t = 4.3					
$F_3(KN)$	differ.	$E_3(KJ)$	differ.	$U_3(mm)$	differ.	$F_3(KN)$	differ.	$E_3(KJ)$	differ.	$U_3(mm)$	differ.	$F_3(KN)$	differ.	$E_3(KJ)$	differ.	$U_3(mm)$	differ.
420.2	24.9%	16.9	-13.9%	95.8	-19.3%	388.5	17.1%	24.6	23.6%	120.4	3.5%	509.7	43.6%	19.8	2.1%	95.8	-19.3%
RTCLS																	
l_e (mm)																	
8						16						30					
l_e/t = 1.1						l_e/t = 2.3						l_e/t = 4.3					
$F_3(KN)$	differ.	$E_3(KJ)$	differ.	$U_3(mm)$	differ.	$F_3(KN)$	differ.	$E_3(KJ)$	differ.	$U_3(mm)$	differ.	$F_3(KN)$	differ.	$E_3(KJ)$	differ.	$U_3(mm)$	differ.
815.9	85.5%	39.7	68.6%	115.8	-0.4%	869.0	90.6%	43.2	75.9%	111.8	-3.9%	1163.5	112.2%	39.0	67.0%	116.8	0.5%
BWH																	
l_e (mm)																	
8						16						30					
l_e/t = 1.1						l_e/t = 2.3						l_e/t = 4.3					
$F_3(KN)$	differ.	$E_3(KJ)$	differ.	$U_3(mm)$	differ.	$F_3(KN)$	differ.	$E_3(KJ)$	differ.	$U_3(mm)$	differ.	$F_3(KN)$	differ.	$E_3(KJ)$	differ.	$U_3(mm)$	differ.
474.9	36.8%	22.2	13.4%	115.8	-0.4%	381.6	15.3%	21.6	10.7%	111.2	-4.5%	509.7	43.6%	23.5	19.0%	97.7	-17.4%
LS																	
Experiment																	
$F_3(KN)$						$E_3(KJ)$						$U_3(mm)$					
327.3						19.4						116.3					

continued on next page

continued from previous page

SHEARS																	
l_e (mm)																	
8						16						30					
l_e/t = 1.1						l_e/t = 2.3						l_e/t = 4.3					
$F_4(KN)$	differ.	$E_4(KJ)$	differ.	$U_4(mm)$	differ.	$F_4(KN)$	differ.	$E_4(KJ)$	differ.	$U_4(mm)$	differ.	$F_4(KN)$	differ.	$E_4(KJ)$	differ.	$U_4(mm)$	differ.
394.2	19.9%	25.5	16.9%	122.6	-0.1%	222.0	-37.0%	25.2	15.7%	122.6	-0.1%	632.0	64.8%	29.7	32.0%	122.6	-0.1%
RTCLS																	
l_e (mm)																	
8						16						30					
l_e/t = 1.1						l_e/t = 2.3						l_e/t = 4.3					
$F_4(KN)$	differ.	$E_4(KJ)$	differ.	$U_4(mm)$	differ.	$F_4(KN)$	differ.	$E_4(KJ)$	differ.	$U_4(mm)$	differ.	$F_4(KN)$	differ.	$E_4(KJ)$	differ.	$U_4(mm)$	differ.
565.8	54.7%	44.2	69.0%	122.6	-0.1%	566.9	54.9%	51.1	81.5%	122.6	-0.1%	937.5	97.6%	45.2	71.1%	122.6	-0.1%
BWH																	
l_e (mm)																	
8						16						30					
l_e/t = 1.1						l_e/t = 2.3						l_e/t = 4.3					
$F_4(KN)$	differ.	$E_4(KJ)$	differ.	$U_4(mm)$	differ.	$F_4(KN)$	differ.	$E_4(KJ)$	differ.	$U_4(mm)$	differ.	$F_4(KN)$	differ.	$E_4(KJ)$	differ.	$U_4(mm)$	differ.
315.3	-2.3%	24.3	12.3%	122.6	-0.1%	300.5	-7.1%	24.8	14.2%	122.6	-0.1%	571.5	55.6%	31.1	36.5%	122.6	-0.1%
LS																	
Experiment																	
$F_4(KN)$						$E_4(KJ)$						$U_4(mm)$					
322.7						21.5						122.7					

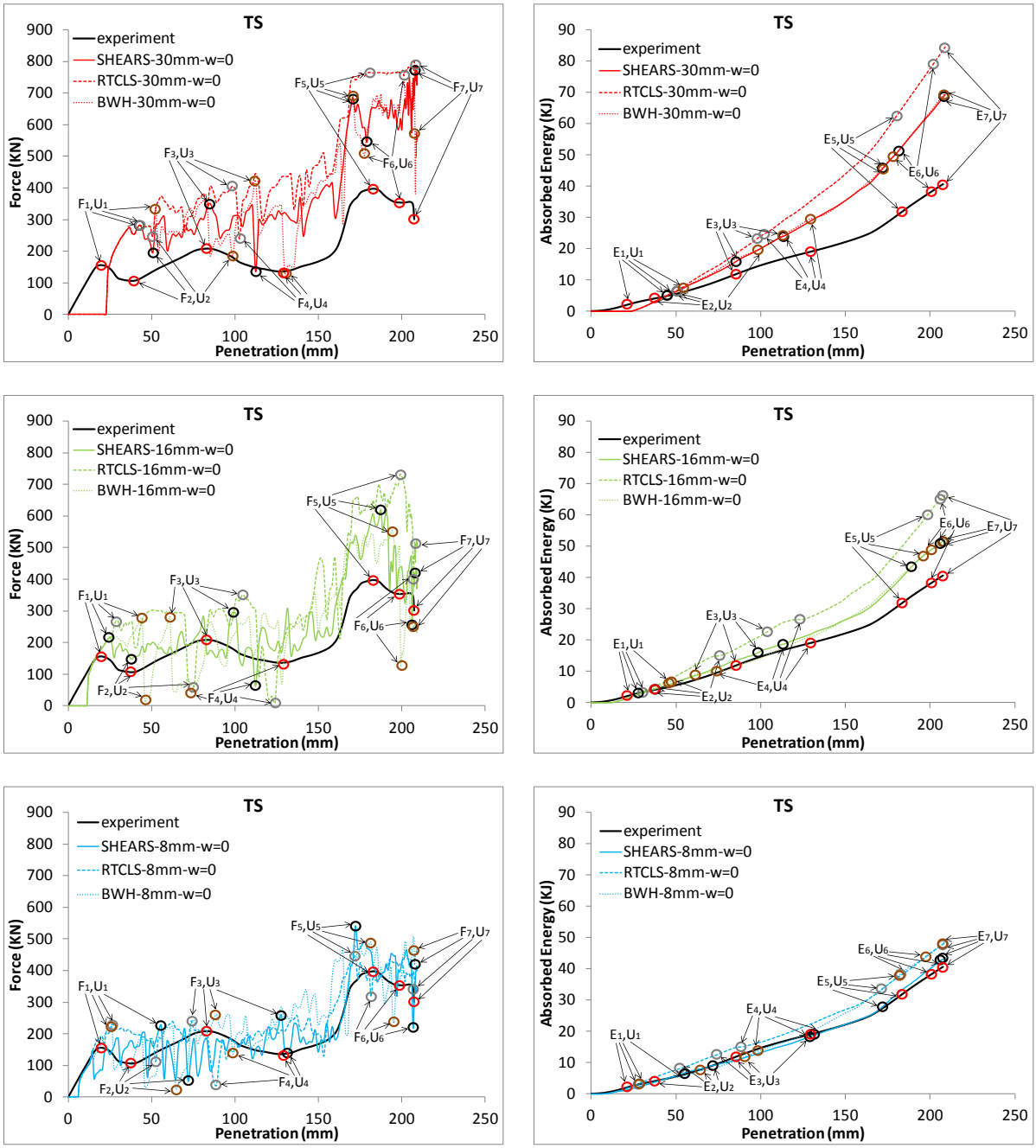

Figure D.10. TS model. Force and absorbed energy-penetration curves.
Definition of force peaks and troughs for each element size and rupture criterion and comparison with the corresponding experimental values
(red circle: experiment, black circle: SHEARS, grey circle: RTCLS, brown circle: BWH)

Table D.10. TS model. Numerical values of force, energy and penetration depth for each element size and rupture criterion at the selected peaks and troughs and comparison with the corresponding experimental values

SHEARS																	
l_e (mm)																	
8						16						30					
l_e/t = 1.1						l_e/t = 2.3						l_e/t = 4.3					
$F_1(KN)$	differ.	$E_1(KJ)$	differ.	$U_1(mm)$	differ.	$F_1(KN)$	differ.	$E_1(KJ)$	differ.	$U_1(mm)$	differ.	$F_1(KN)$	differ.	$E_1(KJ)$	differ.	$U_1(mm)$	differ.
226.5	37.1%	6.9	118.1%	55.8	95.4%	217.5	33.1%	2.2	20.7%	25.1	23.7%	281.6	57.6%	4.5	87.7%	42.8	73.7%
RTCLS																	
l_e (mm)																	
8						16						30					
l_e/t = 1.1						l_e/t = 2.3						l_e/t = 4.3					
$F_1(KN)$	differ.	$E_1(KJ)$	differ.	$U_1(mm)$	differ.	$F_1(KN)$	differ.	$E_1(KJ)$	differ.	$U_1(mm)$	differ.	$F_1(KN)$	differ.	$E_1(KJ)$	differ.	$U_1(mm)$	differ.
229.1	38.2%	2.9	48.5%	26.3	28.3%	269.5	53.6%	3.1	53.3%	28.8	37.1%	281.6	57.6%	4.5	87.7%	42.8	73.7%
BWH																	
l_e (mm)																	
8						16						30					
l_e/t = 1.1						l_e/t = 2.3						l_e/t = 4.3					
$F_1(KN)$	differ.	$E_1(KJ)$	differ.	$U_1(mm)$	differ.	$F_1(KN)$	differ.	$E_1(KJ)$	differ.	$U_1(mm)$	differ.	$F_1(KN)$	differ.	$E_1(KJ)$	differ.	$U_1(mm)$	differ.
227.9	37.7%	2.8	44.0%	26.3	28.3%	277.1	56.1%	6.5	113.9%	44.4	76.7%	336.1	73.4%	7.2	121.0%	52.5	90.5%
TS																	
Experiment																	
$F_1(KN)$						$E_1(KJ)$						$U_1(mm)$					
155.7						1.8						19.8					

continued on next page

continued from previous page

SHEARS																	
l_e (mm)																	
8						16						30					
l_e/t = 1.1						l_e/t = 2.3						l_e/t = 4.3					
$F_2(KN)$	differ.	$E_2(KJ)$	differ.	$U_2(mm)$	differ.	$F_2(KN)$	differ.	$E_2(KJ)$	differ.	$U_2(mm)$	differ.	$F_2(KN)$	differ.	$E_2(KJ)$	differ.	$U_2(mm)$	differ.
51.4	-69.1%	9.1	75.1%	71.8	60.0%	147.9	33.3%	4.5	8.8%	38.4	-0.8%	195.1	59.5%	6.5	43.6%	50.8	27.1%
RTCLS																	
l_e (mm)																	
8						16						30					
l_e/t = 1.1						l_e/t = 2.3						l_e/t = 4.3					
$F_2(KN)$	differ.	$E_2(KJ)$	differ.	$U_2(mm)$	differ.	$F_2(KN)$	differ.	$E_2(KJ)$	differ.	$U_2(mm)$	differ.	$F_2(KN)$	differ.	$E_2(KJ)$	differ.	$U_2(mm)$	differ.
112.5	6.3%	8.1	64.7%	52.4	30.2%	61.1	-53.5%	15.0	113.3%	75.6	64.6%	247.7	80.4%	6.7	47.4%	50.8	27.1%
BWH																	
l_e (mm)																	
8						16						30					
l_e/t = 1.1						l_e/t = 2.3						l_e/t = 4.3					
$F_2(KN)$	differ.	$E_2(KJ)$	differ.	$U_2(mm)$	differ.	$F_2(KN)$	differ.	$E_2(KJ)$	differ.	$U_2(mm)$	differ.	$F_2(KN)$	differ.	$E_2(KJ)$	differ.	$U_2(mm)$	differ.
25.9	-121.3%	7.4	56.9%	64.5	50.2%	14.4	-152.0%	6.7	47.0%	46.0	17.2%	182.5	53.3%	19.8	130.7%	98.6	87.4%
TS																	
Experiment																	
$F_2(KN)$						$E_2(KJ)$						$U_2(mm)$					
105.7						4.1						38.7					

continued on next page

continued from previous page

SHEARS																	
l_e (mm)																	
8						16						30					
l_e/t = 1.1						l_e/t = 2.3						l_e/t = 4.3					
$F_3(KN)$	differ.	$E_3(KJ)$	differ.	$U_3(mm)$	differ.	$F_3(KN)$	differ.	$E_3(KJ)$	differ.	$U_3(mm)$	differ.	$F_3(KN)$	differ.	$E_3(KJ)$	differ.	$U_3(mm)$	differ.
258.6	21.7%	18.1	44.8%	127.8	41.3%	296.4	35.1%	16.1	33.3%	98.6	16.0%	350.4	51.0%	15.8	31.5%	85.0	1.2%

RTCLS																	
l_e (mm)																	
8						16						30					
l_e/t = 1.1						l_e/t = 2.3						l_e/t = 4.3					
$F_3(KN)$	differ.	$E_3(KJ)$	differ.	$U_3(mm)$	differ.	$F_3(KN)$	differ.	$E_3(KJ)$	differ.	$U_3(mm)$	differ.	$F_3(KN)$	differ.	$E_3(KJ)$	differ.	$U_3(mm)$	differ.
240.2	14.4%	12.4	8.0%	73.7	-13.1%	351.4	51.3%	22.8	66.1%	104.5	21.7%	405.2	64.3%	23.5	68.7%	98.6	16.0%

BWH																	
l_e (mm)																	
8						16						30					
l_e/t = 1.1						l_e/t = 2.3						l_e/t = 4.3					
$F_3(KN)$	differ.	$E_3(KJ)$	differ.	$U_3(mm)$	differ.	$F_3(KN)$	differ.	$E_3(KJ)$	differ.	$U_3(mm)$	differ.	$F_3(KN)$	differ.	$E_3(KJ)$	differ.	$U_3(mm)$	differ.
260.7	22.5%	11.5	0.0%	88.9	5.6%	279.1	29.2%	9.0	-24.5%	61.0	-31.7%	422.3	68.0%	24.2	71.4%	112.3	28.8%

TS		
Experiment		
$F_3(KN)$	$E_3(KJ)$	$U_3(mm)$
208.0	11.5	84.0

continued on next page

continued from previous page

SHEARS																	
l_e (mm)																	
8						16						30					
l_e/t = 1.1						l_e/t = 2.3						l_e/t = 4.3					
$F_4(KN)$	differ.	$E_4(KJ)$	differ.	$U_4(mm)$	differ.	$F_4(KN)$	differ.	$E_4(KJ)$	differ.	$U_4(mm)$	differ.	$F_4(KN)$	differ.	$E_4(KJ)$	differ.	$U_4(mm)$	differ.
139.0	2.8%	18.8	0.1%	131.6	2.8%	61.9	-74.5%	18.6	-1.0%	112.3	-13.0%	134.4	-0.6%	23.8	23.6%	112.3	-13.0%
RTCLS																	
l_e (mm)																	
8						16						30					
l_e/t = 1.1						l_e/t = 2.3						l_e/t = 4.3					
$F_4(KN)$	differ.	$E_4(KJ)$	differ.	$U_4(mm)$	differ.	$F_4(KN)$	differ.	$E_4(KJ)$	differ.	$U_4(mm)$	differ.	$F_4(KN)$	differ.	$E_4(KJ)$	differ.	$U_4(mm)$	differ.
37.1	-113.9%	15.1	-21.9%	88.9	-36.0%	9.8	-172.9%	26.6	34.4%	124.0	-3.1%	238.7	55.3%	24.9	28.1%	102.6	-22.0%
BWH																	
l_e (mm)																	
8						16						30					
l_e/t = 1.1						l_e/t = 2.3						l_e/t = 4.3					
$F_4(KN)$	differ.	$E_4(KJ)$	differ.	$U_4(mm)$	differ.	$F_4(KN)$	differ.	$E_4(KJ)$	differ.	$U_4(mm)$	differ.	$F_4(KN)$	differ.	$E_4(KJ)$	differ.	$U_4(mm)$	differ.
137.2	1.4%	13.7	-30.9%	98.6	-25.9%	39.2	-110.1%	10.0	-61.3%	73.7	-53.8%	128.6	-5.0%	29.6	44.8%	129.7	1.4%
TS																	
Experiment																	
$F_4(KN)$						$E_4(KJ)$						$U_4(mm)$					
135.2						18.8						127.9					

continued on next page

continued from previous page

SHEARS																	
l_e (mm)																	
8						16						30					
l_e/t = 1.1						l_e/t = 2.3						l_e/t = 4.3					
$F_5(KN)$	differ.	$E_5(KJ)$	differ.	$U_5(mm)$	differ.	$F_5(KN)$	differ.	$E_5(KJ)$	differ.	$U_5(mm)$	differ.	$F_5(KN)$	differ.	$E_5(KJ)$	differ.	$U_5(mm)$	differ.
540.9	30.5%	27.9	-13.2%	172.1	-6.5%	620.3	43.7%	42.4	28.5%	187.4	2.0%	683.5	52.9%	44.7	33.4%	170.7	-7.4%
RTCLS																	
l_e (mm)																	
8						16						30					
l_e/t = 1.1						l_e/t = 2.3						l_e/t = 4.3					
$F_5(KN)$	differ.	$E_5(KJ)$	differ.	$U_5(mm)$	differ.	$F_5(KN)$	differ.	$E_5(KJ)$	differ.	$U_5(mm)$	differ.	$F_5(KN)$	differ.	$E_5(KJ)$	differ.	$U_5(mm)$	differ.
444.4	11.1%	33.7	5.7%	172.1	-6.5%	723.1	58.1%	60.8	62.5%	199.9	8.4%	765.5	63.2%	62.5	64.9%	180.2	-1.9%
BWH																	
l_e (mm)																	
8						16						30					
l_e/t = 1.1						l_e/t = 2.3						l_e/t = 4.3					
$F_5(KN)$	differ.	$E_5(KJ)$	differ.	$U_5(mm)$	differ.	$F_5(KN)$	differ.	$E_5(KJ)$	differ.	$U_5(mm)$	differ.	$F_5(KN)$	differ.	$E_5(KJ)$	differ.	$U_5(mm)$	differ.
489.3	20.6%	37.8	17.0%	181.5	-1.2%	552.8	32.6%	46.4	37.1%	194.4	5.6%	689.5	53.7%	45.2	34.7%	170.7	-7.4%
TS																	
Experiment																	
$F_5(KN)$						$E_5(KJ)$						$U_5(mm)$					
397.7						31.9						183.7					

continued on next page

continued from previous page

SHEARS																	
l_e (mm)																	
8						16						30					
l_e/t = 1.1						l_e/t = 2.3						l_e/t = 4.3					
$F_6(KN)$	differ.	$E_6(KJ)$	differ.	$U_6(mm)$	differ.	$F_6(KN)$	differ.	$E_6(KJ)$	differ.	$U_6(mm)$	differ.	$F_6(KN)$	differ.	$E_6(KJ)$	differ.	$U_6(mm)$	differ.
217.0	-47.8%	42.7	11.4%	206.7	3.0%	258.7	-30.9%	51.0	29.0%	206.0	2.7%	543.5	42.4%	49.8	26.6%	179.0	-11.4%
RTCLS																	
l_e (mm)																	
8						16						30					
l_e/t = 1.1						l_e/t = 2.3						l_e/t = 4.3					
$F_6(KN)$	differ.	$E_6(KJ)$	differ.	$U_6(mm)$	differ.	$F_6(KN)$	differ.	$E_6(KJ)$	differ.	$U_6(mm)$	differ.	$F_6(KN)$	differ.	$E_6(KJ)$	differ.	$U_6(mm)$	differ.
317.4	-10.7%	37.4	-1.8%	181.5	-10.0%	396.4	11.5%	65.1	52.4%	206.7	3.0%	754.4	72.4%	78.5	69.3%	201.2	0.3%
BWH																	
l_e (mm)																	
8						16						30					
l_e/t = 1.1						l_e/t = 2.3						l_e/t = 4.3					
$F_6(KN)$	differ.	$E_6(KJ)$	differ.	$U_6(mm)$	differ.	$F_6(KN)$	differ.	$E_6(KJ)$	differ.	$U_6(mm)$	differ.	$F_6(KN)$	differ.	$E_6(KJ)$	differ.	$U_6(mm)$	differ.
233.7	-40.8%	43.0	12.0%	195.2	-2.7%	128.0	-93.6%	48.7	24.3%	199.2	-0.7%	505.0	35.3%	49.2	25.4%	177.6	-12.1%
TS																	
Experiment																	
$F_6(KN)$						$E_6(KJ)$						$U_6(mm)$					
353.4						38.1						200.6					

continued on next page

continued from previous page

SHEARS																	
l_e (mm)																	
8						16						30					
l_e/t = 1.1						l_e/t = 2.3						l_e/t = 4.3					
$F_7(KN)$	differ.	$E_7(KJ)$	differ.	$U_7(mm)$	differ.	$F_7(KN)$	differ.	$E_7(KJ)$	differ.	$U_7(mm)$	differ.	$F_7(KN)$	differ.	$E_7(KJ)$	differ.	$U_7(mm)$	differ.
329.4	9.0%	43.0	5.9%	207.7	0.1%	413.3	31.4%	51.7	24.1%	207.7	0.1%	748.2	85.2%	68.3	51.1%	207.7	0.1%
RTCLS																	
l_e (mm)																	
8						16						30					
l_e/t = 1.1						l_e/t = 2.3						l_e/t = 4.3					
$F_7(KN)$	differ.	$E_7(KJ)$	differ.	$U_7(mm)$	differ.	$F_7(KN)$	differ.	$E_7(KJ)$	differ.	$U_7(mm)$	differ.	$F_7(KN)$	differ.	$E_7(KJ)$	differ.	$U_7(mm)$	differ.
335.3	10.7%	47.9	16.6%	207.7	0.1%	518.9	53.1%	65.6	47.2%	207.7	0.1%	778.9	88.5%	83.5	69.3%	207.7	0.1%
BWH																	
l_e (mm)																	
8						16						30					
l_e/t = 1.1						l_e/t = 2.3						l_e/t = 4.3					
$F_7(KN)$	differ.	$E_7(KJ)$	differ.	$U_7(mm)$	differ.	$F_7(KN)$	differ.	$E_7(KJ)$	differ.	$U_7(mm)$	differ.	$F_7(KN)$	differ.	$E_7(KJ)$	differ.	$U_7(mm)$	differ.
433.6	36.1%	48.1	17.0%	207.7	0.1%	260.1	-14.6%	50.8	22.6%	207.7	0.1%	696.4	79.2%	69.1	52.1%	207.7	0.1%
TS																	
Experiment																	
$F_7(KN)$						$E_7(KJ)$						$U_7(mm)$					
301.1						40.5						207.6					

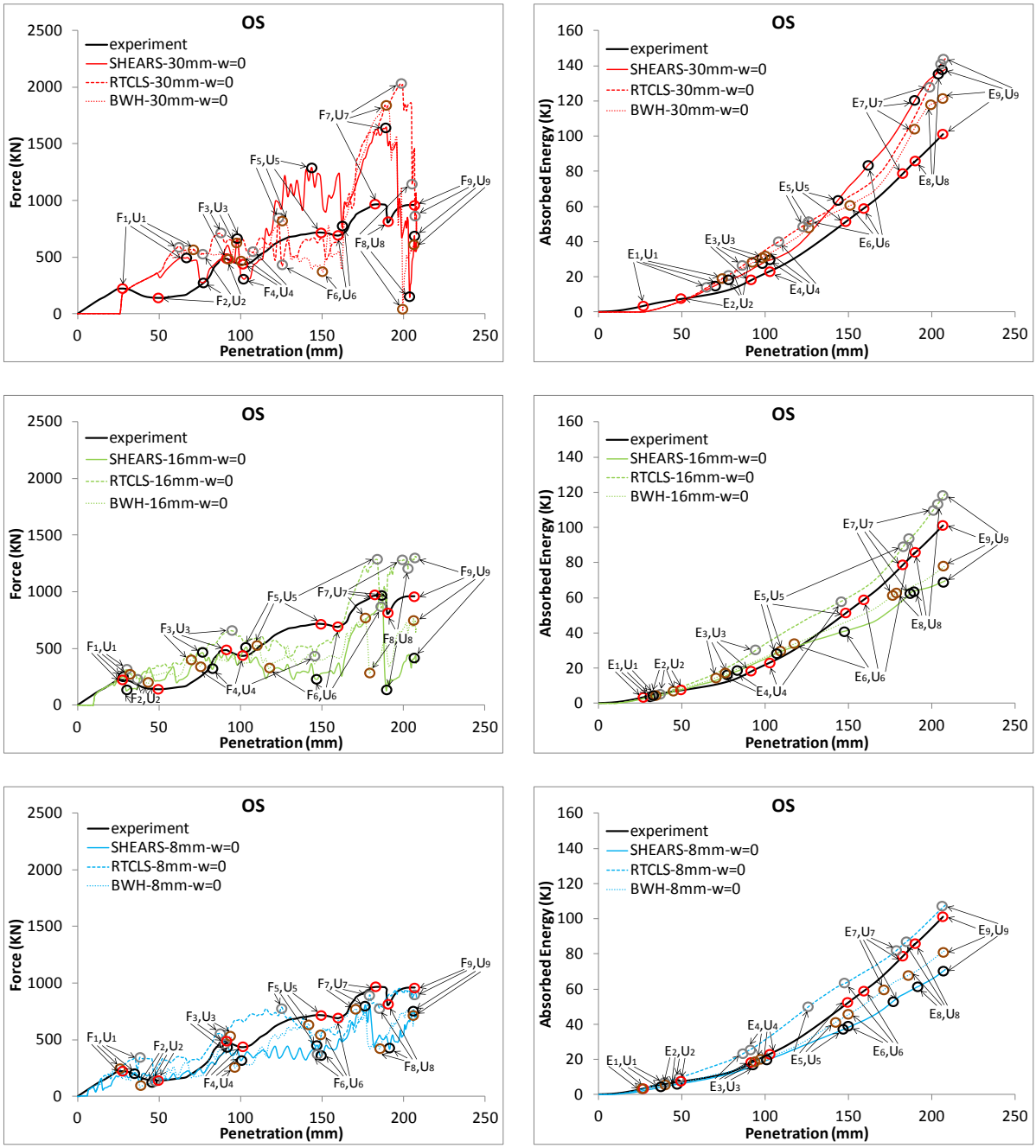

Figure D.11. OS model. Force and absorbed energy-penetration curves.
Definition of force peaks and troughs for each element size and rupture criterion and comparison with the corresponding experimental values
(red circle: experiment, black circle: SHEARS, grey circle: RTCLS, brown circle: BWH)

Table D.11. OS model. Numerical values of force, energy and penetration depth for each element size and rupture criterion at the selected peaks and troughs and comparison with the corresponding experimental values

SHEARS																	
l_e (mm)																	
8						16						30					
l_e/t = 1.1						l_e/t = 2.3						l_e/t = 4.3					
$F_1(KN)$	differ.	$E_1(KJ)$	differ.	$U_1(mm)$	differ.	$F_1(KN)$	differ.	$E_1(KJ)$	differ.	$U_1(mm)$	differ.	$F_1(KN)$	differ.	$E_1(KJ)$	differ.	$U_1(mm)$	differ.
211.6	-4.6%	3.8	18.3%	35.3	28.7%	254.0	13.6%	3.2	-0.2%	28.6	7.9%	492.7	75.9%	14.0	126.1%	67.8	87.8%
RTCLS																	
l_e (mm)																	
8						16						30					
l_e/t = 1.1						l_e/t = 2.3						l_e/t = 4.3					
$F_1(KN)$	differ.	$E_1(KJ)$	differ.	$U_1(mm)$	differ.	$F_1(KN)$	differ.	$E_1(KJ)$	differ.	$U_1(mm)$	differ.	$F_1(KN)$	differ.	$E_1(KJ)$	differ.	$U_1(mm)$	differ.
342.4	42.8%	6.6	69.9%	38.2	36.2%	321.9	36.9%	3.8	17.4%	29.9	12.3%	595.3	91.5%	12.5	118.9%	62.5	81.0%
BWH																	
l_e (mm)																	
8						16						30					
l_e/t = 1.1						l_e/t = 2.3						l_e/t = 4.3					
$F_1(KN)$	differ.	$E_1(KJ)$	differ.	$U_1(mm)$	differ.	$F_1(KN)$	differ.	$E_1(KJ)$	differ.	$U_1(mm)$	differ.	$F_1(KN)$	differ.	$E_1(KJ)$	differ.	$U_1(mm)$	differ.
248.5	11.4%	3.1	-3.8%	26.2	-1.1%	273.6	21.0%	4.3	29.1%	32.6	20.7%	562.1	86.9%	17.1	137.3%	71.5	92.0%
OS																	
Experiment																	
$F_1(KN)$						$E_1(KJ)$						$U_1(mm)$					
221.6						3.2						26.5					

continued on next page

continued from previous page

SHEARS																	
l_e (mm)																	
8						16						30					
l_e/t = 1.1						l_e/t = 2.3						l_e/t = 4.3					
$F_2(KN)$	differ.	$E_2(KJ)$	differ.	$U_2(mm)$	differ.	$F_2(KN)$	differ.	$E_2(KJ)$	differ.	$U_2(mm)$	differ.	$F_2(KN)$	differ.	$E_2(KJ)$	differ.	$U_2(mm)$	differ.
118.1	-16.0%	5.7	-24.6%	45.7	-8.3%	129.3	-7.0%	3.4	-71.9%	29.9	-49.7%	273.1	65.3%	17.9	84.3%	77.1	43.1%
RTCLS																	
l_e (mm)																	
8						16						30					
l_e/t = 1.1						l_e/t = 2.3						l_e/t = 4.3					
$F_2(KN)$	differ.	$E_2(KJ)$	differ.	$U_2(mm)$	differ.	$F_2(KN)$	differ.	$E_2(KJ)$	differ.	$U_2(mm)$	differ.	$F_2(KN)$	differ.	$E_2(KJ)$	differ.	$U_2(mm)$	differ.
134.9	-2.7%	9.5	26.6%	47.3	-4.9%	237.8	52.7%	5.7	-23.9%	36.7	-30.0%	527.7	116.8%	20.6	95.8%	77.1	43.1%
BWH																	
l_e (mm)																	
8						16						30					
l_e/t = 1.1						l_e/t = 2.3						l_e/t = 4.3					
$F_2(KN)$	differ.	$E_2(KJ)$	differ.	$U_2(mm)$	differ.	$F_2(KN)$	differ.	$E_2(KJ)$	differ.	$U_2(mm)$	differ.	$F_2(KN)$	differ.	$E_2(KJ)$	differ.	$U_2(mm)$	differ.
84.8	-48.2%	5.3	-30.9%	38.2	-26.3%	193.2	32.9%	6.6	-9.0%	42.6	-15.3%	467.5	108.5%	28.0	117.6%	92.3	60.0%
OS																	
Experiment																	
$F_2(KN)$						$E_2(KJ)$						$U_2(mm)$					
138.6						7.3						49.7					

continued on next page

continued from previous page

SHEARS																	
l_e (mm)																	
8						16						30					
l_e/t = 1.1						l_e/t = 2.3						l_e/t = 4.3					
$F_3(KN)$	differ.	$E_3(KJ)$	differ.	$U_3(mm)$	differ.	$F_3(KN)$	differ.	$E_3(KJ)$	differ.	$U_3(mm)$	differ.	$F_3(KN)$	differ.	$E_3(KJ)$	differ.	$U_3(mm)$	differ.
432.9	-11.4%	16.3	-8.3%	92.3	1.1%	461.6	-5.0%	16.0	-10.6%	77.1	-16.9%	662.8	30.9%	27.6	43.6%	98.2	7.3%
RTCLS																	
l_e (mm)																	
8						16						30					
l_e/t = 1.1						l_e/t = 2.3						l_e/t = 4.3					
$F_3(KN)$	differ.	$E_3(KJ)$	differ.	$U_3(mm)$	differ.	$F_3(KN)$	differ.	$E_3(KJ)$	differ.	$U_3(mm)$	differ.	$F_3(KN)$	differ.	$E_3(KJ)$	differ.	$U_3(mm)$	differ.
553.7	13.2%	23.3	27.0%	86.5	-5.3%	657.5	30.1%	30.2	51.9%	94.3	3.2%	706.5	37.1%	26.4	39.1%	86.5	-5.3%
BWH																	
l_e (mm)																	
8						16						30					
l_e/t = 1.1						l_e/t = 2.3						l_e/t = 4.3					
$F_3(KN)$	differ.	$E_3(KJ)$	differ.	$U_3(mm)$	differ.	$F_3(KN)$	differ.	$E_3(KJ)$	differ.	$U_3(mm)$	differ.	$F_3(KN)$	differ.	$E_3(KJ)$	differ.	$U_3(mm)$	differ.
524.1	7.7%	19.4	8.8%	94.3	3.2%	399.0	-19.5%	14.3	-21.2%	69.7	-26.9%	637.5	27.1%	31.2	55.0%	98.2	7.3%
OS																	
Experiment																	
$F_3(KN)$						$E_3(KJ)$						$U_3(mm)$					
485.2						17.7						91.3					

continued on next page

continued from previous page

SHEARS																	
l_e (mm)																	
8						16						30					
l_e/t = 1.1						l_e/t = 2.3						l_e/t = 4.3					
$F_4(KN)$	differ.	$E_4(KJ)$	differ.	$U_4(mm)$	differ.	$F_4(KN)$	differ.	$E_4(KJ)$	differ.	$U_4(mm)$	differ.	$F_4(KN)$	differ.	$E_4(KJ)$	differ.	$U_4(mm)$	differ.
318.4	-31.0%	19.3	-17.0%	100.1	-2.5%	317.2	-31.4%	18.2	-22.6%	82.7	-21.5%	303.9	-35.6%	29.3	24.5%	102.1	-0.6%
RTCLS																	
l_e (mm)																	
8						16						30					
l_e/t = 1.1						l_e/t = 2.3						l_e/t = 4.3					
$F_4(KN)$	differ.	$E_4(KJ)$	differ.	$U_4(mm)$	differ.	$F_4(KN)$	differ.	$E_4(KJ)$	differ.	$U_4(mm)$	differ.	$F_4(KN)$	differ.	$E_4(KJ)$	differ.	$U_4(mm)$	differ.
461.7	5.9%	25.3	10.2%	90.4	-12.7%	423.5	-2.7%	58.0	86.8%	145.5	34.6%	539.9	21.5%	39.8	54.1%	107.9	5.0%
BWH																	
l_e (mm)																	
8						16						30					
l_e/t = 1.1						l_e/t = 2.3						l_e/t = 4.3					
$F_4(KN)$	differ.	$E_4(KJ)$	differ.	$U_4(mm)$	differ.	$F_4(KN)$	differ.	$E_4(KJ)$	differ.	$U_4(mm)$	differ.	$F_4(KN)$	differ.	$E_4(KJ)$	differ.	$U_4(mm)$	differ.
256.7	-51.6%	20.1	-12.7%	96.2	-6.4%	345.6	-22.9%	16.5	-32.6%	75.2	-30.9%	463.6	6.3%	32.3	34.0%	100.1	-2.5%
OS																	
Experiment																	
$F_4(KN)$						$E_4(KJ)$						$U_4(mm)$					
435.2						22.9						102.6					

continued on next page

continued from previous page

SHEARS																	
l_e (mm)																	
8						16						30					
l_e/t = 1.1						l_e/t = 2.3						l_e/t = 4.3					
$F_5(KN)$	differ.	$E_5(KJ)$	differ.	$U_5(mm)$	differ.	$F_5(KN)$	differ.	$E_5(KJ)$	differ.	$U_5(mm)$	differ.	$F_5(KN)$	differ.	$E_5(KJ)$	differ.	$U_5(mm)$	differ.
450.2	-45.7%	37.3	-32.7%	147.3	-1.4%	507.9	-34.1%	27.3	-62.2%	104.0	-35.8%	1290.1	57.1%	63.7	20.6%	143.8	-3.9%

RTCLS																	
l_e (mm)																	
8						16						30					
l_e/t = 1.1						l_e/t = 2.3						l_e/t = 4.3					
$F_5(KN)$	differ.	$E_5(KJ)$	differ.	$U_5(mm)$	differ.	$F_5(KN)$	differ.	$E_5(KJ)$	differ.	$U_5(mm)$	differ.	$F_5(KN)$	differ.	$E_5(KJ)$	differ.	$U_5(mm)$	differ.
786.8	9.3%	49.5	-4.5%	125.3	-17.6%	1285.0	56.7%	89.4	53.2%	183.1	20.2%	851.9	17.2%	49.4	-4.7%	123.4	-19.1%

BWH																	
l_e (mm)																	
8						16						30					
l_e/t = 1.1						l_e/t = 2.3						l_e/t = 4.3					
$F_5(KN)$	differ.	$E_5(KJ)$	differ.	$U_5(mm)$	differ.	$F_5(KN)$	differ.	$E_5(KJ)$	differ.	$U_5(mm)$	differ.	$F_5(KN)$	differ.	$E_5(KJ)$	differ.	$U_5(mm)$	differ.
640.0	-11.4%	41.0	-23.2%	142.0	-5.1%	531.4	-29.7%	30.5	-51.8%	109.8	-30.5%	821.4	13.6%	47.3	-9.2%	125.3	-17.6%

OS		
Experiment		
$F_5(KN)$	$E_5(KJ)$	$U_5(mm)$
717.0	51.8	149.4

continued on next page

continued from previous page

SHEARS																	
l_e (mm)																	
8						16						30					
l_e/t = 1.1						l_e/t = 2.3						l_e/t = 4.3					
$F_6(KN)$	differ.	$E_6(KJ)$	differ.	$U_6(mm)$	differ.	$F_6(KN)$	differ.	$E_6(KJ)$	differ.	$U_6(mm)$	differ.	$F_6(KN)$	differ.	$E_6(KJ)$	differ.	$U_6(mm)$	differ.
358.1	-63.3%	38.0	-43.4%	149.0	-6.8%	229.1	-100.3%	41.0	-36.0%	147.3	-8.0%	767.0	10.6%	83.9	34.9%	162.3	1.7%
RTCLS																	
l_e (mm)																	
8						16						30					
l_e/t = 1.1						l_e/t = 2.3						l_e/t = 4.3					
$F_6(KN)$	differ.	$E_6(KJ)$	differ.	$U_6(mm)$	differ.	$F_6(KN)$	differ.	$E_6(KJ)$	differ.	$U_6(mm)$	differ.	$F_6(KN)$	differ.	$E_6(KJ)$	differ.	$U_6(mm)$	differ.
366.9	-61.1%	63.1	6.8%	147.3	-8.0%	859.1	21.9%	93.3	45.0%	186.5	15.5%	430.3	-46.3%	50.6	-15.2%	125.3	-24.1%
BWH																	
l_e (mm)																	
8						16						30					
l_e/t = 1.1						l_e/t = 2.3						l_e/t = 4.3					
$F_6(KN)$	differ.	$E_6(KJ)$	differ.	$U_6(mm)$	differ.	$F_6(KN)$	differ.	$E_6(KJ)$	differ.	$U_6(mm)$	differ.	$F_6(KN)$	differ.	$E_6(KJ)$	differ.	$U_6(mm)$	differ.
541.0	-24.2%	45.0	-26.9%	149.0	-6.8%	321.2	-72.9%	33.8	-54.2%	117.6	-30.3%	369.7	-60.4%	60.5	2.4%	150.8	-5.7%
OS																	
Experiment																	
$F_6(KN)$						$E_6(KJ)$						$U_6(mm)$					
689.8						59.0						159.6					

continued on next page

continued from previous page

SHEARS																	
l_e (mm)																	
8						16						30					
l_e/t = 1.1						l_e/t = 2.3						l_e/t = 4.3					
$F_7(KN)$	differ.	$E_7(KJ)$	differ.	$U_7(mm)$	differ.	$F_7(KN)$	differ.	$E_7(KJ)$	differ.	$U_7(mm)$	differ.	$F_7(KN)$	differ.	$E_7(KJ)$	differ.	$U_7(mm)$	differ.
806.9	-18.1%	53.0	-39.6%	176.8	-3.7%	978.4	1.2%	62.2	-24.1%	186.5	1.6%	1644.5	51.9%	120.0	40.9%	189.6	3.3%
RTCLS																	
l_e (mm)																	
8						16						30					
l_e/t = 1.1						l_e/t = 2.3						l_e/t = 4.3					
$F_7(KN)$	differ.	$E_7(KJ)$	differ.	$U_7(mm)$	differ.	$F_7(KN)$	differ.	$E_7(KJ)$	differ.	$U_7(mm)$	differ.	$F_7(KN)$	differ.	$E_7(KJ)$	differ.	$U_7(mm)$	differ.
895.1	-7.7%	82.6	4.2%	179.4	-2.2%	1283.7	28.1%	109.1	31.7%	200.2	8.7%	2029.3	70.9%	127.4	46.6%	198.2	7.7%
BWH																	
l_e (mm)																	
8						16						30					
l_e/t = 1.1						l_e/t = 2.3						l_e/t = 4.3					
$F_7(KN)$	differ.	$E_7(KJ)$	differ.	$U_7(mm)$	differ.	$F_7(KN)$	differ.	$E_7(KJ)$	differ.	$U_7(mm)$	differ.	$F_7(KN)$	differ.	$E_7(KJ)$	differ.	$U_7(mm)$	differ.
770.2	-22.7%	59.7	-28.1%	171.3	-6.9%	763.7	-23.5%	61.5	-25.2%	176.8	-3.7%	1836.7	62.0%	104.6	27.6%	189.6	3.3%
OS																	
Experiment																	
$F_7(KN)$						$E_7(KJ)$						$U_7(mm)$					
967.0						79.2						183.4					

continued on next page

continued from previous page

SHEARS																	
l_e (mm)																	
8						16						30					
l_e/t = 1.1						l_e/t = 2.3						l_e/t = 4.3					
$F_8(KN)$	differ.	$E_8(KJ)$	differ.	$U_8(mm)$	differ.	$F_8(KN)$	differ.	$E_8(KJ)$	differ.	$U_8(mm)$	differ.	$F_8(KN)$	differ.	$E_8(KJ)$	differ.	$U_8(mm)$	differ.
416.9	-63.8%	61.3	-33.1%	191.6	0.8%	129.3	-144.8%	64.1	-28.7%	189.6	-0.3%	142.7	-139.9%	135.9	45.4%	203.9	7.0%
RTCLS																	
l_e (mm)																	
8						16						30					
l_e/t = 1.1						l_e/t = 2.3						l_e/t = 4.3					
$F_8(KN)$	differ.	$E_8(KJ)$	differ.	$U_8(mm)$	differ.	$F_8(KN)$	differ.	$E_8(KJ)$	differ.	$U_8(mm)$	differ.	$F_8(KN)$	differ.	$E_8(KJ)$	differ.	$U_8(mm)$	differ.
777.4	-3.8%	87.5	2.2%	185.4	-2.5%	1203.4	39.3%	112.6	27.2%	203.0	6.5%	1138.4	34.0%	140.7	48.7%	205.4	7.7%
BWH																	
l_e (mm)																	
8						16						30					
l_e/t = 1.1						l_e/t = 2.3						l_e/t = 4.3					
$F_8(KN)$	differ.	$E_8(KJ)$	differ.	$U_8(mm)$	differ.	$F_8(KN)$	differ.	$E_8(KJ)$	differ.	$U_8(mm)$	differ.	$F_8(KN)$	differ.	$E_8(KJ)$	differ.	$U_8(mm)$	differ.
419.6	-63.3%	67.6	-23.5%	185.4	-2.5%	283.9	-96.0%	62.9	-30.5%	179.4	-5.8%	40.1	-181.1%	118.2	31.9%	199.6	4.9%
OS																	
Experiment																	
$F_8(KN)$						$E_8(KJ)$						$U_8(mm)$					
808.0						85.6						190.1					

continued on next page

continued from previous page

SHEARS																	
l_e (mm)																	
8						16						30					
l_e/t = 1.1						l_e/t = 2.3						l_e/t = 4.3					
$F_9(KN)$	differ.	$E_9(KJ)$	differ.	$U_9(mm)$	differ.	$F_9(KN)$	differ.	$E_9(KJ)$	differ.	$U_9(mm)$	differ.	$F_9(KN)$	differ.	$E_9(KJ)$	differ.	$U_9(mm)$	differ.
698.8	-31.6%	70.3	-35.9%	207.1	0.0%	422.1	-78.0%	69.4	-37.2%	207.1	0.0%	571.7	-50.8%	137.3	30.3%	207.1	0.0%
RTCLS																	
l_e (mm)																	
8						16						30					
l_e/t = 1.1						l_e/t = 2.3						l_e/t = 4.3					
$F_9(KN)$	differ.	$E_9(KJ)$	differ.	$U_9(mm)$	differ.	$F_9(KN)$	differ.	$E_9(KJ)$	differ.	$U_9(mm)$	differ.	$F_9(KN)$	differ.	$E_9(KJ)$	differ.	$U_9(mm)$	differ.
900.6	-6.5%	107.0	5.6%	207.1	0.0%	1308.2	30.6%	117.8	15.2%	207.1	0.0%	835.1	-14.1%	142.9	34.2%	207.1	0.0%
BWH																	
l_e (mm)																	
8						16						30					
l_e/t = 1.1						l_e/t = 2.3						l_e/t = 4.3					
$F_9(KN)$	differ.	$E_9(KJ)$	differ.	$U_9(mm)$	differ.	$F_9(KN)$	differ.	$E_9(KJ)$	differ.	$U_9(mm)$	differ.	$F_9(KN)$	differ.	$E_9(KJ)$	differ.	$U_9(mm)$	differ.
676.7	-34.8%	81.5	-21.5%	207.1	0.0%	733.9	-26.8%	77.5	-26.5%	207.1	0.0%	610.0	-44.7%	121.7	18.4%	207.1	0.0%
OS																	
Experiment																	
$F_9(KN)$						$E_9(KJ)$						$U_9(mm)$					
961.4						101.1						207.0					

D.4 COLLISION STATIC and COLLISION DYNAMIC models-(ASIS 1993 reported in ISSC 2003)

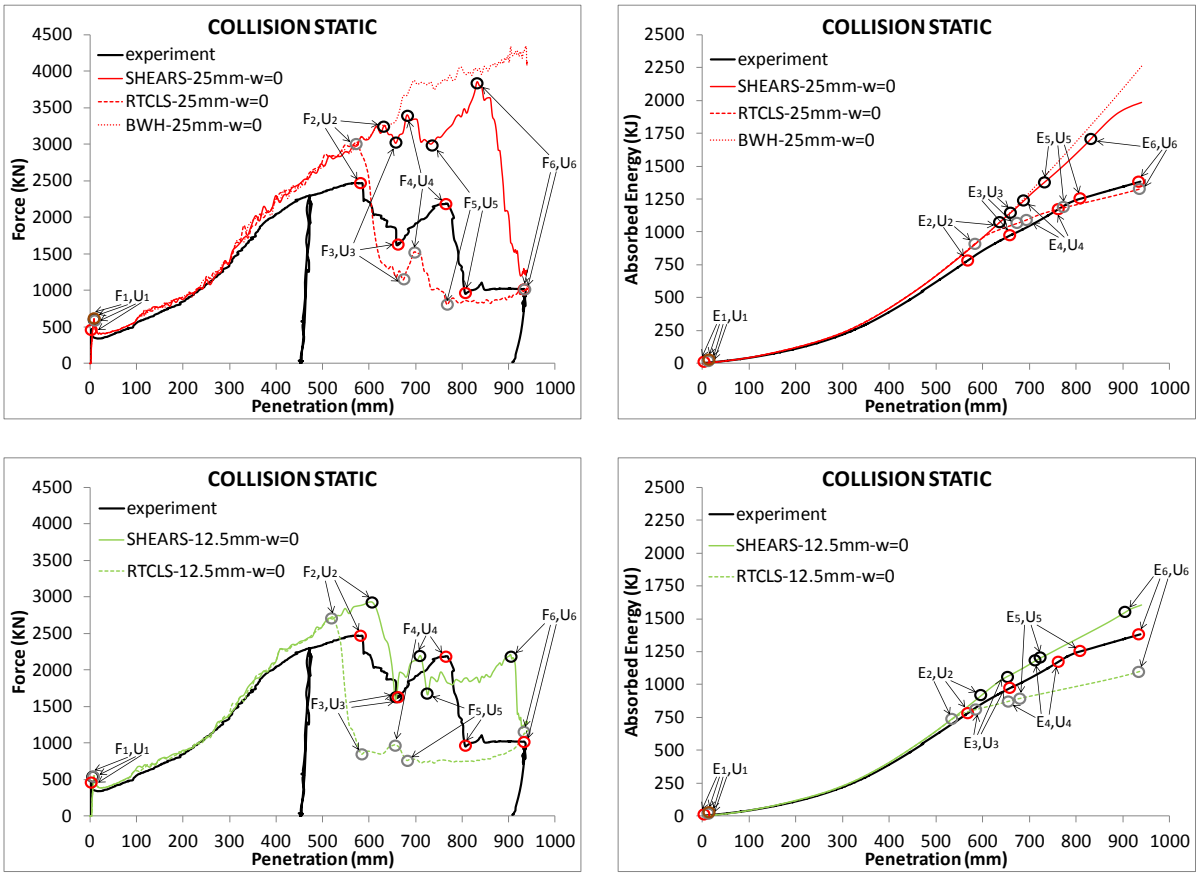

Figure D.12. COLLISION STATIC model. Force and absorbed energy-penetration curves. Definition of force peaks and troughs for each element size and rupture criterion and comparison with the corresponding experimental values
(red circle: experiment, black circle: SHEARS, grey circle: RTCLS, brown circle: BWH)

Table D.12. COLLISION STATIC model. Numerical values of force, energy and penetration depth for each element size and rupture criterion at the selected peaks and troughs and comparison with the corresponding experimental values

SHEARS, RTCLS and BWH												
$l_e\ (mm)$												
12.5						25						
l_e/t = 1.5						l_e/t = 3						
$F_1(KN)$	differ.	$E_1(KJ)$	differ.	$U_1(mm)$	differ.	$F_1(KN)$	differ.	$E_1(KJ)$	differ.	$U_1(mm)$	differ.
551.2	18.8%	1.7	100.5%	9.2	114.0%	612.1	29.1%	2.7	129.8%	9.2	114.1%
COLLISION STATIC												
Experiment												
$F_1(KN)$				$E_1(KJ)$				$U_1(mm)$				
456.7				0.6				2.5				

SHEARS											
$l_e\ (mm)$											
12.5						25					
l_e/t = 1.5						l_e/t = 3					
$F_2(KN)$	differ.	$E_2(KJ)$	differ.	$U_2(mm)$	differ.	$F_2(KN)$	differ.	$E_2(KJ)$	differ.	$U_2(mm)$	differ.
2928.0	17.1%	928.2	16.5%	600.2	5.3%	3259.7	27.7%	1063.5	29.9%	633.5	10.7%
RTCLS											
$l_e\ (mm)$											
12.5						25					
l_e/t = 1.5						l_e/t = 3					
$F_2(KN)$	differ.	$E_2(KJ)$	differ.	$U_2(mm)$	differ.	$F_2(KN)$	differ.	$E_2(KJ)$	differ.	$U_2(mm)$	differ.
2722.8	9.8%	706.2	-10.8%	522.8	-8.5%	3026.7	20.3%	886.2	11.9%	574.8	0.9%
COLLISION STATIC											
Experiment											
$F_2(KN)$				$E_2(KJ)$				$U_2(mm)$			
2467.7				786.6				569.4			

continued on next page

continued from previous page

SHEARS											
$l_e\ (mm)$											
12.5						25					
l_e/t = 1.5						l_e/t = 3					
$F_3(KN)$	differ.	$E_3(KJ)$	differ.	$U_3(mm)$	differ.	$F_3(KN)$	differ.	$E_3(KJ)$	differ.	$U_3(mm)$	differ.
1594.8	-1.7%	1072.1	9.5%	657.7	-0.2%	3014.9	60.1%	1139.6	15.5%	657.7	-0.2%

RTCLS											
$l_e\ (mm)$											
12.5						25					
l_e/t = 1.5						l_e/t = 3					
$F_3(KN)$	differ.	$E_3(KJ)$	differ.	$U_3(mm)$	differ.	$F_3(KN)$	differ.	$E_3(KJ)$	differ.	$U_3(mm)$	differ.
851.2	-62.3%	808.6	-18.7%	583.3	-12.2%	1142.2	-34.7%	1065.7	8.9%	673.5	2.2%

COLLISION STATIC		
Experiment		
$F_3(KN)$	$E_3(KJ)$	$U_3(mm)$
1621.8	975.3	658.9

SHEARS											
$l_e\ (mm)$											
12.5						25					
l_e/t = 1.5						l_e/t = 3					
$F_4(KN)$	differ.	$E_4(KJ)$	differ.	$U_4(mm)$	differ.	$F_4(KN)$	differ.	$E_4(KJ)$	differ.	$U_4(mm)$	differ.
2190.3	0.2%	1180.1	-0.1%	711.6	-7.2%	3397.2	43.4%	1214.3	2.8%	681.3	-11.5%

RTCLS											
$l_e\ (mm)$											
12.5						25					
l_e/t = 1.5						l_e/t = 3					
$F_4(KN)$	differ.	$E_4(KJ)$	differ.	$U_4(mm)$	differ.	$F_4(KN)$	differ.	$E_4(KJ)$	differ.	$U_4(mm)$	differ.
974.7	-76.7%	875.0	-29.7%	657.7	-15.0%	1520.0	-36.0%	1096.3	-7.4%	696.6	-9.3%

COLLISION STATIC		
Experiment		
$F_4(KN)$	$E_4(KJ)$	$U_4(mm)$
2186.5	1180.7	764.5

continued on next page

continued from previous page

SHEARS											
$l_e\ (mm)$											
12.5						25					
l_e/t = 1.5						l_e/t = 3					
$F_5(KN)$	differ.	$E_5(KJ)$	differ.	$U_5(mm)$	differ.	$F_5(KN)$	differ.	$E_5(KJ)$	differ.	$U_5(mm)$	differ.
1659.6	54.1%	1208.4	-3.5%	726.2	-10.5%	3003.5	103.7%	1380.5	9.8%	733.3	-9.5%

RTCLS											
$l_e\ (mm)$											
12.5						25					
l_e/t = 1.5						l_e/t = 3					
$F_5(KN)$	differ.	$E_5(KJ)$	differ.	$U_5(mm)$	differ.	$F_5(KN)$	differ.	$E_5(KJ)$	differ.	$U_5(mm)$	differ.
762.5	-22.2%	895.7	-33.2%	681.3	-16.8%	805.9	-16.7%	1179.6	-6.0%	767.5	-5.0%

COLLISION STATIC		
Experiment		
$F_5(KN)$	$E_5(KJ)$	$U_5(mm)$
952.9	1252.0	806.7

SHEARS											
$l_e\ (mm)$											
12.5						25					
l_e/t = 1.5						l_e/t = 3					
$F_6(KN)$	differ.	$E_6(KJ)$	differ.	$U_6(mm)$	differ.	$F_6(KN)$	differ.	$E_6(KJ)$	differ.	$U_6(mm)$	differ.
2210.2	77.0%	1551.3	11.4%	904.8	-3.5%	3854.9	118.8%	1709.9	21.1%	832.5	-11.8%

RTCLS											
$l_e\ (mm)$											
12.5						25					
l_e/t = 1.5						l_e/t = 3					
$F_6(KN)$	differ.	$E_6(KJ)$	differ.	$U_6(mm)$	differ.	$F_6(KN)$	differ.	$E_6(KJ)$	differ.	$U_6(mm)$	differ.
1146.2	15.5%	1100.9	-22.8%	937.1	0.0%	1006.3	2.5%	1328.2	-4.1%	937.1	0.0%

COLLISION STATIC		
Experiment		
$F_6(KN)$	$E_6(KJ)$	$U_6(mm)$
981.6	1384.1	936.8

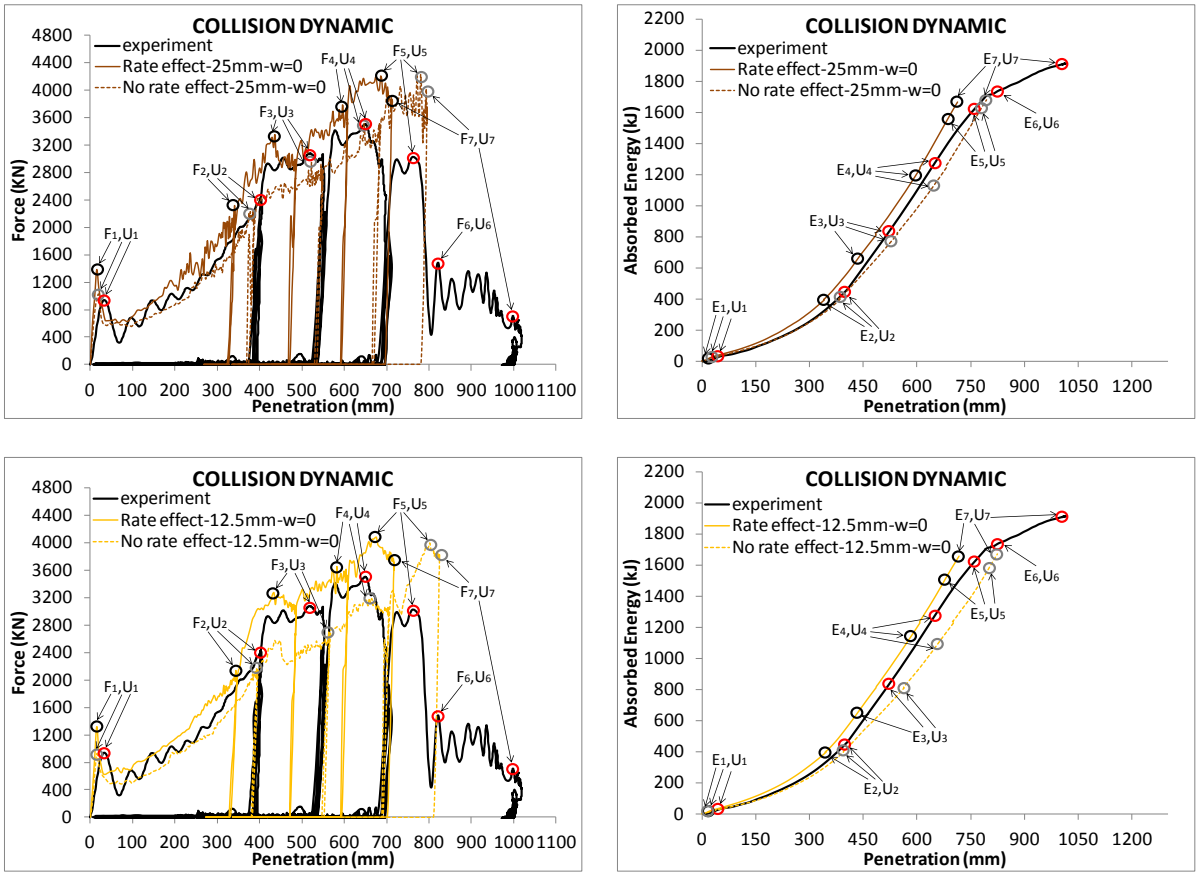

Figure D.13. COLLISION DYNAMIC model. Force and absorbed energy-penetration curves. Definition of force peaks and troughs for each element size in the cases with and without strain-rate effect and no damage and comparison with the corresponding experimental values (red circle: experiment, black circle: rate effect, grey circle: no rate effect)

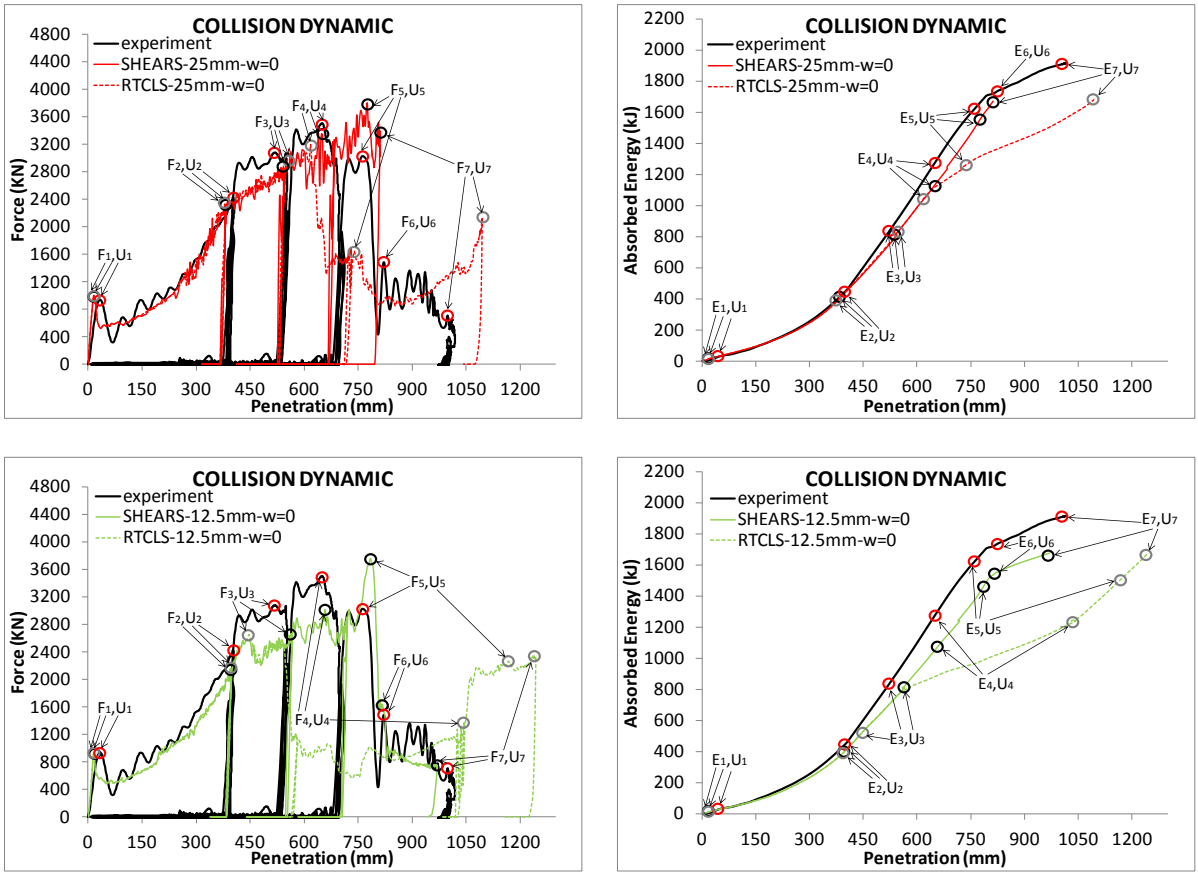

Figure D.14. COLLISION DYNAMIC model. Force and absorbed energy-penetration curves. Definition of force peaks and troughs for each element size for each rupture criterion without strain-rate effect and comparison with the corresponding experimental values
(red circle: experiment, black circle: SHEARS, grey circle: RTCLS)

Table D.13. COLLISION DYNAMIC model. Numerical values of force, energy and penetration depth for each element size in the cases with and without strain rate effect and no damage and in the case with damage and without strain rate effect at the selected peaks and troughs and comparison with the corresponding experimental values

No Damage-with strain rate effect											
$l_e\ (mm)$											
12.5						25					
l_e/t = 1.5						l_e/t = 3					
$F_1(KN)$	differ.	$E_1(KJ)$	differ.	$U_1(mm)$	differ.	$F_1(KN)$	differ.	$E_1(KJ)$	differ.	$U_1(mm)$	differ.
1317.8	33.7%	9.6	-63.6%	15.2	-77.2%	1382.5	38.4%	11.4	-47.5%	15.2	-77.3%
No Damage-without strain rate effect											
$l_e\ (mm)$											
12.5						25					
l_e/t = 1.5						l_e/t = 3					
$F_1(KN)$	differ.	$E_1(KJ)$	differ.	$U_1(mm)$	differ.	$F_1(KN)$	differ.	$E_1(KJ)$	differ.	$U_1(mm)$	differ.
938.6	0.1%	6.7	-94.3%	15.2	-77.1%	994.8	6.0%	8.4	-75.6%	15.2	-77.2%
SHEARS-without strain rate effect											
$l_e\ (mm)$											
12.5						25					
l_e/t = 1.5						l_e/t = 3					
$F_1(KN)$	differ.	$E_1(KJ)$	differ.	$U_1(mm)$	differ.	$F_1(KN)$	differ.	$E_1(KJ)$	differ.	$U_1(mm)$	differ.
938.6	0.1%	6.7	-94.3%	15.2	-77.1%	994.8	6.0%	8.4	-75.6%	15.2	-77.2%
RTCLS-without strain rate effect											
$l_e\ (mm)$											
12.5						25					
l_e/t = 1.5						l_e/t = 3					
$F_1(KN)$	differ.	$E_1(KJ)$	differ.	$U_1(mm)$	differ.	$F_1(KN)$	differ.	$E_1(KJ)$	differ.	$U_1(mm)$	differ.
938.6	0.1%	6.7	-94.3%	15.2	-77.1%	994.8	6.0%	8.4	-75.6%	15.2	-77.2%
COLLISION DYNAMIC											
Experiment											
$F_1(KN)$				$E_1(KJ)$				$U_1(mm)$			
937.3				18.6				34.4			

continued on next page

continued from previous page

No Damage-with strain rate effect											
l_e (mm)											
12.5						25					
l_e/t = 1.5						l_e/t = 3					
$F_2(KN)$	differ.	$E_2(KJ)$	differ.	$U_2(mm)$	differ.	$F_2(KN)$	differ.	$E_2(KJ)$	differ.	$U_2(mm)$	differ.
2136.1	-12.7%	390.7	-15.5%	344.1	-15.7%	2319.2	-4.5%	392.3	-15.0%	340.9	-16.7%
No Damage-without strain rate effect											
l_e (mm)											
12.5						25					
l_e/t = 1.5						l_e/t = 3					
$F_2(KN)$	differ.	$E_2(KJ)$	differ.	$U_2(mm)$	differ.	$F_2(KN)$	differ.	$E_2(KJ)$	differ.	$U_2(mm)$	differ.
2170.4	-11.1%	391.9	-15.1%	393.1	-2.5%	2251.8	-7.4%	393.2	-14.8%	384.1	-4.8%
SHEARS-without strain rate effect											
l_e (mm)											
12.5						25					
l_e/t = 1.5						l_e/t = 3					
$F_2(KN)$	differ.	$E_2(KJ)$	differ.	$U_2(mm)$	differ.	$F_2(KN)$	differ.	$E_2(KJ)$	differ.	$U_2(mm)$	differ.
2128.5	-13.0%	389.0	-15.9%	394.3	-2.2%	2325.7	-4.2%	394.1	-14.6%	382.0	-5.3%
RTCLS-without strain rate effect											
l_e (mm)											
12.5						25					
l_e/t = 1.5						l_e/t = 3					
$F_2(KN)$	differ.	$E_2(KJ)$	differ.	$U_2(mm)$	differ.	$F_2(KN)$	differ.	$E_2(KJ)$	differ.	$U_2(mm)$	differ.
2153.3	-11.9%	387.9	-16.2%	393.9	-2.3%	2326.8	-4.2%	388.1	-16.1%	379.2	-6.1%
COLLISION DYNAMIC											
Experiment											
$F_2(KN)$				$E_2(KJ)$				$U_2(mm)$			
2425.6				456.1				403.0			

continued on next page

continued from previous page

No Damage-with strain rate effect											
l_e (mm)											
12.5						25					
l_e/t = 1.5						l_e/t = 3					
$F_3(KN)$	differ.	$E_3(KJ)$	differ.	$U_3(mm)$	differ.	$F_3(KN)$	differ.	$E_3(KJ)$	differ.	$U_3(mm)$	differ.
3268.3	6.1%	648.3	-25.1%	434.3	-17.8%	3355.7	8.7%	664.2	-22.7%	436.4	-17.3%
No Damage-without strain rate effect											
l_e (mm)											
12.5						25					
l_e/t = 1.5						l_e/t = 3					
$F_3(KN)$	differ.	$E_3(KJ)$	differ.	$U_3(mm)$	differ.	$F_3(KN)$	differ.	$E_3(KJ)$	differ.	$U_3(mm)$	differ.
2703.6	-12.9%	806.5	-3.4%	563.4	8.2%	2949.9	-4.2%	751.3	-10.5%	521.9	0.5%
SHEARS-without strain rate effect											
l_e (mm)											
12.5						25					
l_e/t = 1.5						l_e/t = 3					
$F_3(KN)$	differ.	$E_3(KJ)$	differ.	$U_3(mm)$	differ.	$F_3(KN)$	differ.	$E_3(KJ)$	differ.	$U_3(mm)$	differ.
2673.1	-14.0%	806.9	-3.3%	564.7	8.4%	2855.1	-7.4%	786.9	-5.8%	536.0	3.2%
RTCLS-without strain rate effect											
l_e (mm)											
12.5						25					
l_e/t = 1.5						l_e/t = 3					
$F_3(KN)$	differ.	$E_3(KJ)$	differ.	$U_3(mm)$	differ.	$F_3(KN)$	differ.	$E_3(KJ)$	differ.	$U_3(mm)$	differ.
2650.4	-14.8%	520.0	-46.4%	447.0	-14.9%	2891.3	-6.2%	809.4	-3.0%	542.4	4.4%
COLLISION DYNAMIC											
Experiment											
$F_3(KN)$				$E_3(KJ)$				$U_3(mm)$			
3075.4				834.2				519.2			

continued on next page

continued from previous page

No Damage-with strain rate effect											
l_e (mm)											
12.5						25					
l_e/t = 1.5						l_e/t = 3					
$F_4(KN)$	differ.	$E_4(KJ)$	differ.	$U_4(mm)$	differ.	$F_4(KN)$	differ.	$E_4(KJ)$	differ.	$U_4(mm)$	differ.
3650.9	4.2%	1137.8	-10.3%	582.8	-10.8%	3789.4	7.9%	1194.8	-5.4%	596.2	-8.6%
No Damage-without strain rate effect											
l_e (mm)											
12.5						25					
l_e/t = 1.5						l_e/t = 3					
$F_4(KN)$	differ.	$E_4(KJ)$	differ.	$U_4(mm)$	differ.	$F_4(KN)$	differ.	$E_4(KJ)$	differ.	$U_4(mm)$	differ.
3192.8	-9.2%	1095.3	-14.1%	659.2	1.5%	3521.1	0.6%	1125.7	-11.3%	646.3	-0.5%
SHEARS-without strain rate effect											
l_e (mm)											
12.5						25					
l_e/t = 1.5						l_e/t = 3					
$F_4(KN)$	differ.	$E_4(KJ)$	differ.	$U_4(mm)$	differ.	$F_4(KN)$	differ.	$E_4(KJ)$	differ.	$U_4(mm)$	differ.
3022.2	-14.7%	1076.0	-15.8%	659.1	1.4%	3349.7	-4.4%	1132.2	-10.8%	649.2	-0.1%
RTCLS-without strain rate effect											
l_e (mm)											
12.5						25					
l_e/t = 1.5						l_e/t = 3					
$F_4(KN)$	differ.	$E_4(KJ)$	differ.	$U_4(mm)$	differ.	$F_4(KN)$	differ.	$E_4(KJ)$	differ.	$U_4(mm)$	differ.
1366.9	-87.7%	1237.9	-1.8%	1044.0	46.6%	3193.7	-9.2%	1038.7	-19.3%	617.9	-5.0%
COLLISION DYNAMIC											
Experiment											
$F_4(KN)$				$E_4(KJ)$				$U_4(mm)$			
3501.5				1261.0				649.7			

continued on next page

continued from previous page

No Damage-with strain rate effect											
l_e (mm)											
12.5						25					
l_e/t = 1.5						l_e/t = 3					
$F_5(KN)$	differ.	$E_5(KJ)$	differ.	$U_5(mm)$	differ.	$F_5(KN)$	differ.	$E_5(KJ)$	differ.	$U_5(mm)$	differ.
4076.2	29.7%	1498.5	-8.0%	676.5	-11.9%	4208.4	32.8%	1562.0	-3.9%	686.3	-10.5%
No Damage-without strain rate effect											
l_e (mm)											
12.5						25					
l_e/t = 1.5						l_e/t = 3					
$F_5(KN)$	differ.	$E_5(KJ)$	differ.	$U_5(mm)$	differ.	$F_5(KN)$	differ.	$E_5(KJ)$	differ.	$U_5(mm)$	differ.
4001.9	27.9%	1585.2	-2.4%	802.4	5.1%	4225.6	33.2%	1624.3	0.0%	779.4	2.2%
SHEARS-without strain rate effect											
l_e (mm)											
12.5						25					
l_e/t = 1.5						l_e/t = 3					
$F_5(KN)$	differ.	$E_5(KJ)$	differ.	$U_5(mm)$	differ.	$F_5(KN)$	differ.	$E_5(KJ)$	differ.	$U_5(mm)$	differ.
3763.4	21.8%	1456.0	-10.9%	784.6	2.9%	3790.4	22.5%	1557.5	-4.2%	776.4	1.8%
RTCLS-without strain rate effect											
l_e (mm)											
12.5						25					
l_e/t = 1.5						l_e/t = 3					
$F_5(KN)$	differ.	$E_5(KJ)$	differ.	$U_5(mm)$	differ.	$F_5(KN)$	differ.	$E_5(KJ)$	differ.	$U_5(mm)$	differ.
2263.3	-28.7%	1500.4	-7.9%	1167.3	42.0%	1639.3	-59.3%	1262.1	-25.0%	738.6	-3.2%
COLLISION DYNAMIC											
Experiment											
$F_5(KN)$				$E_5(KJ)$				$U_5(mm)$			
3022.7				1623.5				762.4			

continued on next page

continued from previous page

No Damage-with strain rate effect											
l_e (mm)											
12.5						25					
l_e/t = 1.5						l_e/t = 3					
$F_6(KN)$	differ.	$E_6(KJ)$	differ.	$U_6(mm)$	differ.	$F_6(KN)$	differ.	$E_6(KJ)$	differ.	$U_6(mm)$	differ.
Not captured											
No Damage-without strain rate effect											
l_e (mm)											
12.5						25					
l_e/t = 1.5						l_e/t = 3					
$F_6(KN)$	differ.	$E_6(KJ)$	differ.	$U_6(mm)$	differ.	$F_6(KN)$	differ.	$E_6(KJ)$	differ.	$U_6(mm)$	differ.
Not captured											
SHEARS-without strain rate effect											
l_e (mm)											
12.5						25					
l_e/t = 1.5						l_e/t = 3					
$F_6(KN)$	differ.	$E_6(KJ)$	differ.	$U_6(mm)$	differ.	$F_6(KN)$	differ.	$E_6(KJ)$	differ.	$U_6(mm)$	differ.
1644.3	10.5%	1544.1	-11.4%	817.6	-0.5%	Not captured					
RTCLS-without strain rate effect											
l_e (mm)											
12.5						25					
l_e/t = 1.5						l_e/t = 3					
$F_6(KN)$	differ.	$E_6(KJ)$	differ.	$U_6(mm)$	differ.	$F_6(KN)$	differ.	$E_6(KJ)$	differ.	$U_6(mm)$	differ.
Not captured											
COLLISION DYNAMIC											
Experiment											
$F_6(KN)$			$E_6(KJ)$			$U_6(mm)$					
1480.1			1731.4			821.8					

continued on next page

continued from previous page

No Damage-with strain rate effect											
l_e (mm)											
12.5						25					
l_e/t = 1.5						l_e/t = 3					
$F_7(KN)$	differ.	$E_7(KJ)$	differ.	$U_7(mm)$	differ.	$F_7(KN)$	differ.	$E_7(KJ)$	differ.	$U_7(mm)$	differ.
3717.3	136.1%	1657.6	-13.9%	717.7	-32.7%	3833.4	137.7%	1665.4	-13.4%	712.3	-33.5%

No Damage-without strain rate effect											
l_e (mm)											
12.5						25					
l_e/t = 1.5						l_e/t = 3					
$F_7(KN)$	differ.	$E_7(KJ)$	differ.	$U_7(mm)$	differ.	$F_7(KN)$	differ.	$E_7(KJ)$	differ.	$U_7(mm)$	differ.
3829.6	137.7%	1672.6	-13.0%	825.1	-19.0%	3697.4	135.8%	1682.1	-12.4%	794.9	-22.7%

SHEARS-without strain rate effect											
l_e (mm)											
12.5						25					
l_e/t = 1.5						l_e/t = 3					
$F_7(KN)$	differ.	$E_7(KJ)$	differ.	$U_7(mm)$	differ.	$F_7(KN)$	differ.	$E_7(KJ)$	differ.	$U_7(mm)$	differ.
743.8	5.1%	1677.0	-12.7%	971.0	-2.8%	3322.7	129.8%	1672.4	-13.0%	811.8	-20.6%

RTCLS-without strain rate effect											
l_e (mm)											
12.5						25					
l_e/t = 1.5						l_e/t = 3					
$F_7(KN)$	differ.	$E_7(KJ)$	differ.	$U_7(mm)$	differ.	$F_7(KN)$	differ.	$E_7(KJ)$	differ.	$U_7(mm)$	differ.
2283.2	105.4%	1669.0	-13.2%	1243.5	21.9%	2133.4	100.5%	1679.4	-12.6%	1094.1	9.1%

COLLISION DYNAMIC		
Experiment		
$F_7(KN)$	$E_7(KJ)$	$U_7(mm)$
706.8	1904.3	998.5

D.5 OUTER SHELL and INNER SHELL models-(Gong et al. 2013)

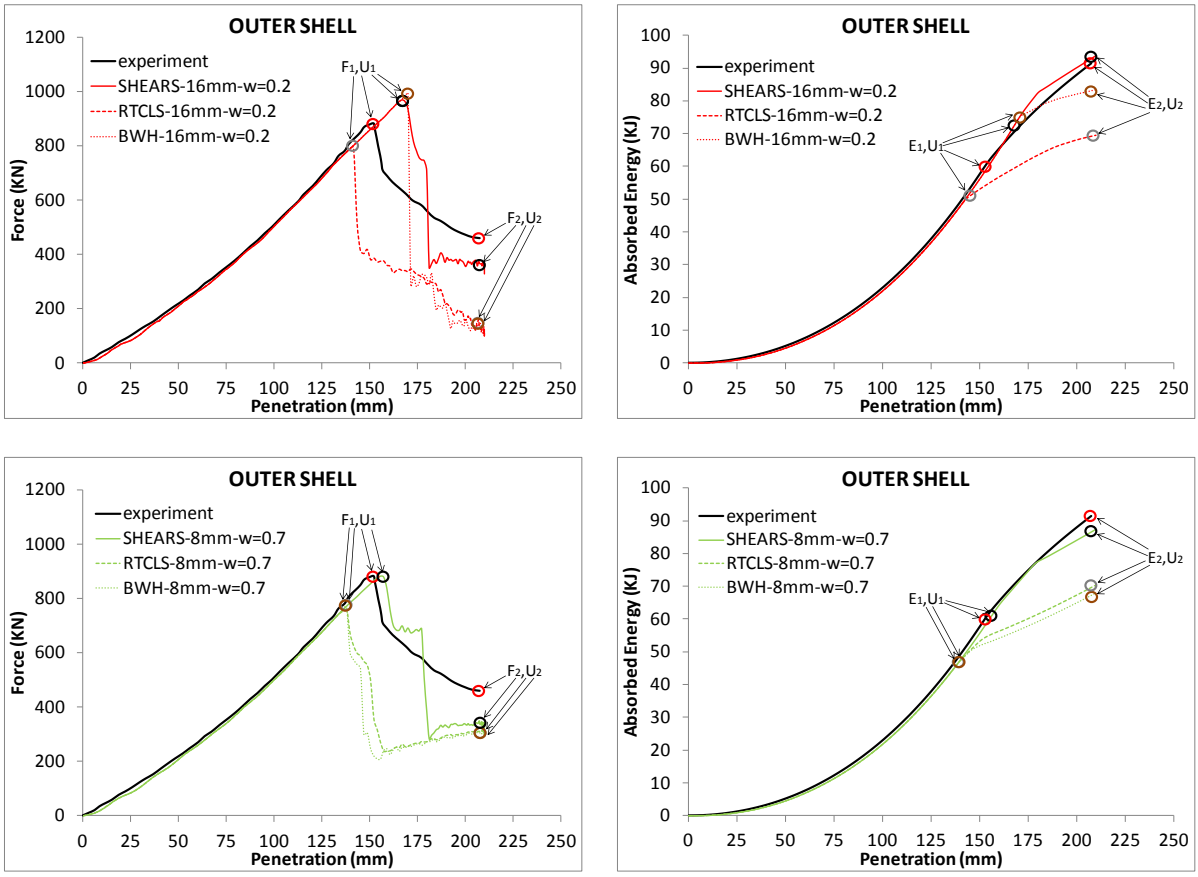

Figure D.15. OUTER SHELL model. Force and absorbed energy-penetration curves.
Definition of force peaks and troughs for each element size and rupture criterion and comparison with the corresponding experimental values
(red circle: experiment, black circle: SHEARS, grey circle: RTCLS, brown circle: BWH)

Table D.14. OUTER SHELL model. Numerical values of force, energy and penetration depth for each element size and rupture criterion at the selected peaks and troughs and comparison with the corresponding experimental values

SHEARS											
l_e (mm)											
8						16					
l_e/t = 2						l_e/t = 4					
$F_1(KN)$	differ.	$E_1(KJ)$	differ.	$U_1(mm)$	differ.	$F_1(KN)$	differ.	$E_1(KJ)$	differ.	$U_1(mm)$	differ.
880.9	-0.1%	60.5	1.8%	155.6	2.3%	969.2	9.4%	71.6	18.6%	167.0	9.3%
RTCLS											
l_e (mm)											
8						16					
l_e/t = 2						l_e/t = 4					
$F_1(KN)$	differ.	$E_1(KJ)$	differ.	$U_1(mm)$	differ.	$F_1(KN)$	differ.	$E_1(KJ)$	differ.	$U_1(mm)$	differ.
767.6	-13.9%	45.8	-25.9%	137.8	-9.8%	793.5	-10.6%	49.1	-19.1%	141.5	-7.2%
BWH											
l_e (mm)											
8						16					
l_e/t = 2						l_e/t = 4					
$F_1(KN)$	differ.	$E_1(KJ)$	differ.	$U_1(mm)$	differ.	$F_1(KN)$	differ.	$E_1(KJ)$	differ.	$U_1(mm)$	differ.
770.2	-13.5%	45.8	-25.9%	137.8	-9.8%	992.5	11.8%	74.6	22.7%	170.0	11.1%
OUTER SHELL											
Experiment											
$F_1(KN)$				$E_1(KJ)$				$U_1(mm)$			
882.0				59.4				152.1			

continued on next page

continued from previous page

SHEARS											
l_e (mm)											
8						16					
l_e/t = 2						l_e/t = 4					
$F_2(KN)$	differ.	$E_2(KJ)$	differ.	$U_2(mm)$	differ.	$F_2(KN)$	differ.	$E_2(KJ)$	differ.	$U_2(mm)$	differ.
336.4	-30.9%	86.7	-5.4%	207.6	0.1%	366.2	-22.5%	93.0	1.7%	207.6	0.1%
RTCLS											
l_e (mm)											
8						16					
l_e/t = 2						l_e/t = 4					
$F_2(KN)$	differ.	$E_2(KJ)$	differ.	$U_2(mm)$	differ.	$F_2(KN)$	differ.	$E_2(KJ)$	differ.	$U_2(mm)$	differ.
310.7	-38.6%	69.7	-27.0%	207.6	0.1%	129.6	-112.0%	69.3	-27.6%	207.6	0.1%
BWH											
l_e (mm)											
8						16					
l_e/t = 2						l_e/t = 4					
$F_2(KN)$	differ.	$E_2(KJ)$	differ.	$U_2(mm)$	differ.	$F_2(KN)$	differ.	$E_2(KJ)$	differ.	$U_2(mm)$	differ.
304.8	-40.4%	67.2	-30.6%	207.6	0.1%	146.6	-103.2%	83.2	-9.5%	207.6	0.1%
OUTER SHELL											
Experiment											
$F_2(KN)$				$E_2(KJ)$				$U_2(mm)$			
459.3				91.4				207.5			

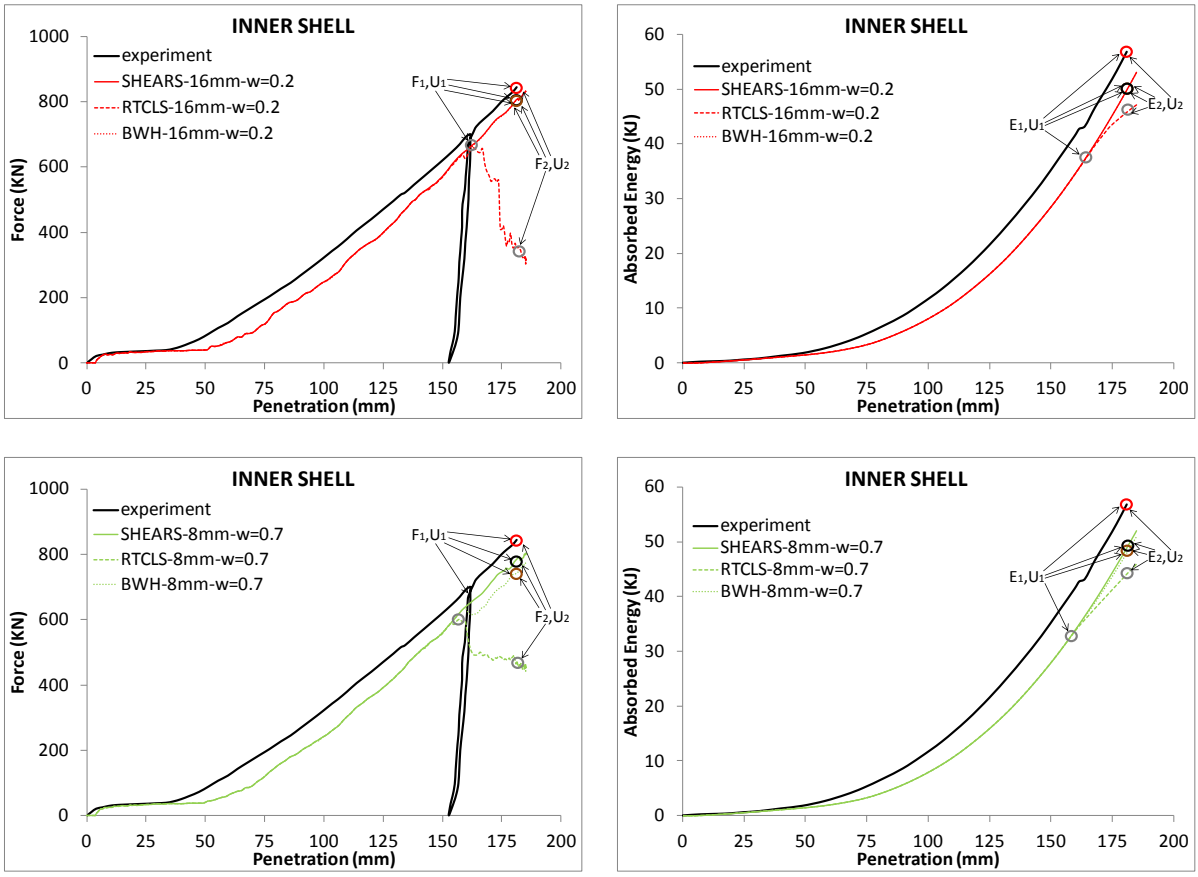

Figure D.16. INNER SHELL model. Force and absorbed energy-penetration curves.
Definition of force peaks and troughs for each element size and rupture criterion and comparison with the corresponding experimental values
(red circle: experiment, black circle: SHEARS, grey circle: RTCLS, brown circle: BWH)

Table D.15. INNER SHELL model. Numerical values of force, energy and penetration depth for each element size and rupture criterion at the selected peaks and troughs and comparison with the corresponding experimental values

SHEARS											
$l_e\ (mm)$											
8						16					
l_e/t = 2						l_e/t = 4					
$F_1(KN)$	differ.	$E_1(KJ)$	differ.	$U_1(mm)$	differ.	$F_1(KN)$	differ.	$E_1(KJ)$	differ.	$U_1(mm)$	differ.
786.8	-7.0%	49.1	-18.7%	181.3	0.0%	806.2	-4.5%	50.0	-16.8%	181.3	0.0%
RTCLS											
$l_e\ (mm)$											
8						16					
l_e/t = 2						l_e/t = 4					
$F_1(KN)$	differ.	$E_1(KJ)$	differ.	$U_1(mm)$	differ.	$F_1(KN)$	differ.	$E_1(KJ)$	differ.	$U_1(mm)$	differ.
601.7	-33.5%	32.1	-59.4%	157.2	-14.2%	658.4	-24.7%	36.3	-47.9%	162.8	-10.7%
BWH											
$l_e\ (mm)$											
8						16					
l_e/t = 2						l_e/t = 4					
$F_1(KN)$	differ.	$E_1(KJ)$	differ.	$U_1(mm)$	differ.	$F_1(KN)$	differ.	$E_1(KJ)$	differ.	$U_1(mm)$	differ.
742.0	-12.8%	48.2	-20.5%	181.3	0.0%	807.0	-4.4%	50.0	-16.8%	181.3	0.0%
INNER SHELL											
Experiment											
$F_1(KN)$				$E_1(KJ)$				$U_1(mm)$			
843.7				59.2				181.2			

continued on next page

continued from previous page

SHEARS											
l_e (mm)											
8						16					
l_e/t = 2						l_e/t = 4					
$F_2(KN)$	differ.	$E_2(KJ)$	differ.	$U_2(mm)$	differ.	$F_2(KN)$	differ.	$E_2(KJ)$	differ.	$U_2(mm)$	differ.
786.8	-7.0%	49.1	-18.7%	181.3	0.0%	806.2	-4.5%	50.0	-16.8%	181.3	0.0%

RTCLS											
l_e (mm)											
8						16					
l_e/t = 2						l_e/t = 4					
$F_2(KN)$	differ.	$E_2(KJ)$	differ.	$U_2(mm)$	differ.	$F_2(KN)$	differ.	$E_2(KJ)$	differ.	$U_2(mm)$	differ.
474.4	-56.0%	44.2	-29.1%	181.3	0.0%	356.9	-81.1%	45.9	-25.4%	181.3	0.0%

BWH											
l_e (mm)											
8						16					
l_e/t = 2						l_e/t = 4					
$F_2(KN)$	differ.	$E_2(KJ)$	differ.	$U_2(mm)$	differ.	$F_2(KN)$	differ.	$E_2(KJ)$	differ.	$U_2(mm)$	differ.
742.0	-12.8%	48.2	-20.5%	181.3	0.0%	807.0	-4.4%	50.0	-16.8%	181.3	0.0%

INNER SHELL		
Experiment		
$F_2(KN)$	$E_2(KJ)$	$U_2(mm)$
843.7	59.2	181.2

D.6 FLAT SPECIMEN and KNIFE SPECIMEN models-(Villavicencio 2012 and Villavicencio et al. 2013)

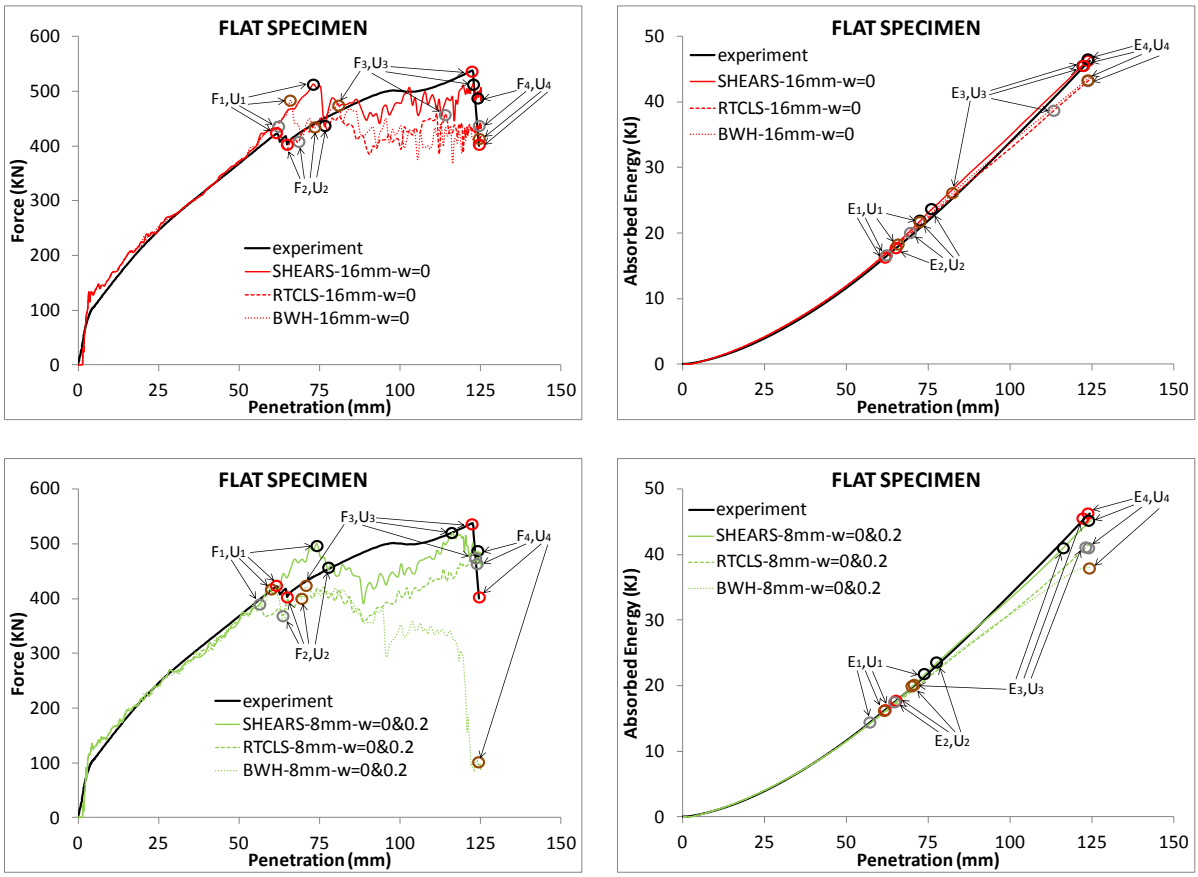

Figure D.17. FLAT SPECIMEN model. Force and absorbed energy-penetration curves. Definition of force peaks and troughs for each element size and rupture criterion and comparison with the corresponding experimental values
(red circle: experiment, black circle: SHEARS, grey circle: RTCLS, brown circle: BWH)

Table D.16. FLAT SPECIMEN model. Numerical values of force, energy and penetration depth for each element size and rupture criterion at the selected peaks and troughs and comparison with the corresponding experimental values

SHEARS											
$l_e\ (mm)$											
8						16					
l_e/t = 2						l_e/t = 4					
$F_1(KN)$	differ.	$E_1(KJ)$	differ.	$U_1(mm)$	differ.	$F_1(KN)$	differ.	$E_1(KJ)$	differ.	$U_1(mm)$	differ.
500.1	16.9%	21.9	29.7%	74.1	18.3%	512.9	19.4%	22.1	30.8%	73.0	16.8%
RTCLS											
$l_e\ (mm)$											
8						16					
l_e/t = 2						l_e/t = 4					
$F_1(KN)$	differ.	$E_1(KJ)$	differ.	$U_1(mm)$	differ.	$F_1(KN)$	differ.	$E_1(KJ)$	differ.	$U_1(mm)$	differ.
388.2	-8.4%	14.0	-14.3%	56.7	-8.5%	433.9	2.7%	17.1	5.2%	62.5	1.3%
BWH											
$l_e\ (mm)$											
8						16					
l_e/t = 2						l_e/t = 4					
$F_1(KN)$	differ.	$E_1(KJ)$	differ.	$U_1(mm)$	differ.	$F_1(KN)$	differ.	$E_1(KJ)$	differ.	$U_1(mm)$	differ.
417.0	-1.3%	15.5	-4.7%	60.2	-2.5%	483.2	13.4%	18.7	14.2%	66.0	6.8%
FLAT SPECIMEN											
Experiment											
$F_1(KN)$				$E_1(KJ)$				$U_1(mm)$			
422.3				16.2				61.7			

continued on next page

continued from previous page

SHEARS											
$l_e\ (mm)$											
8						16					
l_e/t = 2						l_e/t = 4					
$F_2(KN)$	differ.	$E_2(KJ)$	differ.	$U_2(mm)$	differ.	$F_2(KN)$	differ.	$E_2(KJ)$	differ.	$U_2(mm)$	differ.
453.3	11.8%	23.5	28.9%	77.6	17.7%	436.4	8.0%	23.8	30.2%	76.4	16.2%

RTCLS											
$l_e\ (mm)$											
8						16					
l_e/t = 2						l_e/t = 4					
$F_2(KN)$	differ.	$E_2(KJ)$	differ.	$U_2(mm)$	differ.	$F_2(KN)$	differ.	$E_2(KJ)$	differ.	$U_2(mm)$	differ.
368.8	-8.8%	16.7	-5.2%	63.7	-2.0%	406.5	1.0%	19.5	10.3%	68.4	5.1%

BWH											
$l_e\ (mm)$											
8						16					
l_e/t = 2						l_e/t = 4					
$F_2(KN)$	differ.	$E_2(KJ)$	differ.	$U_2(mm)$	differ.	$F_2(KN)$	differ.	$E_2(KJ)$	differ.	$U_2(mm)$	differ.
400.6	-0.5%	19.1	8.7%	69.5	6.8%	432.9	7.2%	21.7	21.4%	73.0	11.7%

FLAT SPECIMEN		
Experiment		
$F_2(KN)$	$E_2(KJ)$	$U_2(mm)$
402.7	17.6	65.0

continued on next page

continued from previous page

SHEARS											
l_e (mm)											
8						16					
l_e/t = 2						l_e/t = 4					
$F_3(KN)$	differ.	$E_3(KJ)$	differ.	$U_3(mm)$	differ.	$F_3(KN)$	differ.	$E_3(KJ)$	differ.	$U_3(mm)$	differ.
520.0	-3.4%	41.0	-10.1%	116.2	-5.3%	512.9	-4.7%	45.9	1.2%	122.8	0.2%
RTCLS											
l_e (mm)											
8						16					
l_e/t = 2						l_e/t = 4					
$F_3(KN)$	differ.	$E_3(KJ)$	differ.	$U_3(mm)$	differ.	$F_3(KN)$	differ.	$E_3(KJ)$	differ.	$U_3(mm)$	differ.
474.7	-12.5%	41.4	-9.0%	124.1	1.3%	459.0	-15.8%	38.9	-15.2%	114.0	-7.2%
BWH											
l_e (mm)											
8						16					
l_e/t = 2						l_e/t = 4					
$F_3(KN)$	differ.	$E_3(KJ)$	differ.	$U_3(mm)$	differ.	$F_3(KN)$	differ.	$E_3(KJ)$	differ.	$U_3(mm)$	differ.
421.8	-24.2%	19.6	-79.2%	70.7	-53.7%	476.5	-12.1%	25.4	-56.5%	80.9	-40.9%
FLAT SPECIMEN											
Experiment											
$F_3(KN)$				$E_3(KJ)$				$U_3(mm)$			
537.8				45.4				122.5			

continued on next page

continued from previous page

SHEARS											
l_e (mm)											
8						16					
l_e/t = 2						l_e/t = 4					
$F_4(KN)$	differ.	$E_4(KJ)$	differ.	$U_4(mm)$	differ.	$F_4(KN)$	differ.	$E_4(KJ)$	differ.	$U_4(mm)$	differ.
476.4	17.4%	45.1	-2.5%	124.5	0.0%	500.0	22.2%	46.8	1.0%	124.5	0.0%

RTCLS											
l_e (mm)											
8						16					
l_e/t = 2						l_e/t = 4					
$F_4(KN)$	differ.	$E_4(KJ)$	differ.	$U_4(mm)$	differ.	$F_4(KN)$	differ.	$E_4(KJ)$	differ.	$U_4(mm)$	differ.
470.0	16.1%	41.7	-10.5%	124.5	0.0%	435.8	8.6%	43.5	-6.2%	124.5	0.0%

BWH											
l_e (mm)											
8						16					
l_e/t = 2						l_e/t = 4					
$F_4(KN)$	differ.	$E_4(KJ)$	differ.	$U_4(mm)$	differ.	$F_4(KN)$	differ.	$E_4(KJ)$	differ.	$U_4(mm)$	differ.
97.0	-122.0%	38.1	-19.4%	124.5	0.0%	420.8	5.1%	43.8	-5.5%	124.5	0.0%

FLAT SPECIMEN		
Experiment		
$F_4(KN)$	$E_4(KJ)$	$U_4(mm)$
400.0	46.3	124.5

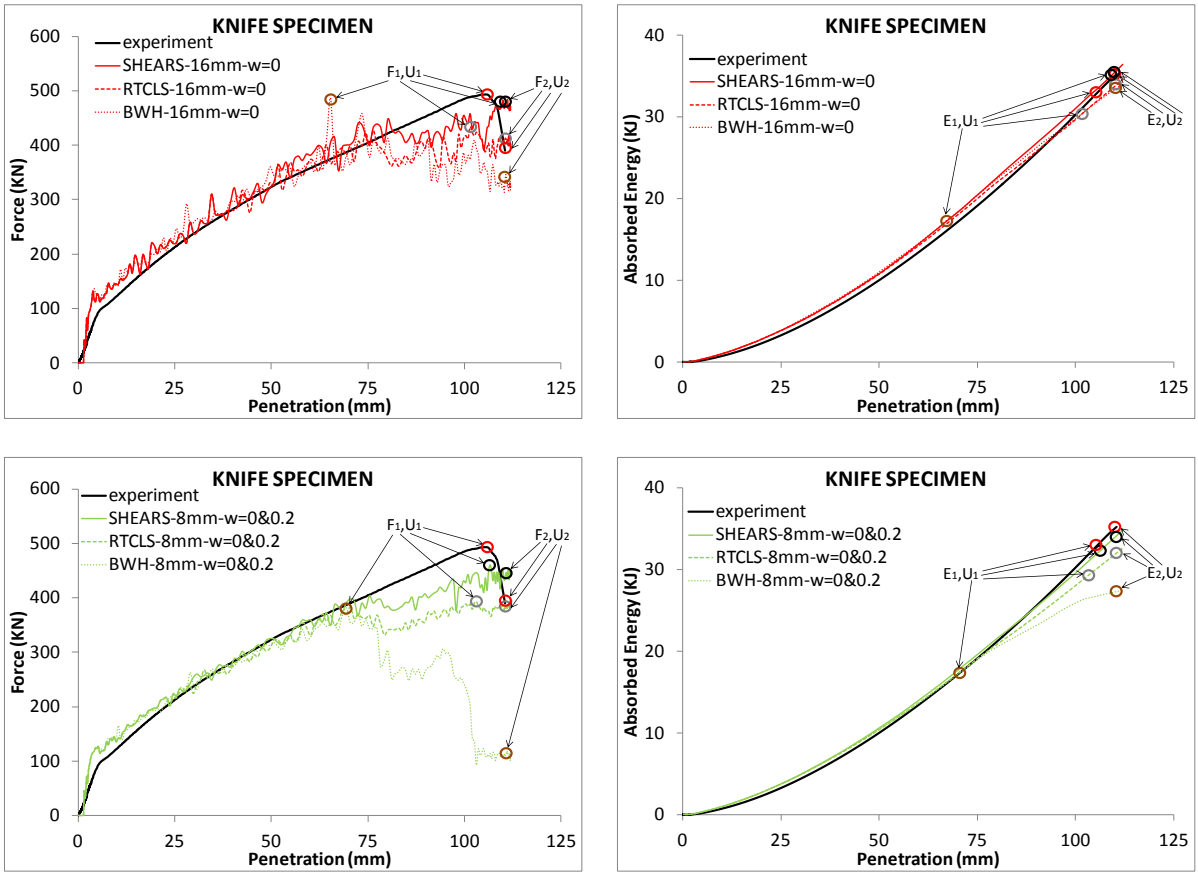

Figure D.18. KNIFE SPECIMEN model. Force and absorbed energy-penetration curves.
Definition of force peaks and troughs for each element size and rupture criterion and comparison with the corresponding experimental values
(red circle: experiment, black circle: SHEARS, grey circle: RTCLS, brown circle: BWH)

Table D.17. KNIFE SPECIMEN model. Numerical values of force, energy and penetration depth for each element size and rupture criterion at the selected peaks and troughs and comparison with the corresponding experimental values

SHEARS											
l_e (mm)											
8						16					
l_e/t = 2						l_e/t = 4					
$F_1(KN)$	differ.	$E_1(KJ)$	differ.	$U_1(mm)$	differ.	$F_1(KN)$	differ.	$E_1(KJ)$	differ.	$U_1(mm)$	differ.
461.2	-6.7%	32.5	-1.2%	106.7	1.2%	483.5	-2.0%	35.5	7.4%	110.0	4.2%
RTCLS											
l_e (mm)											
8						16					
l_e/t = 2						l_e/t = 4					
$F_1(KN)$	differ.	$E_1(KJ)$	differ.	$U_1(mm)$	differ.	$F_1(KN)$	differ.	$E_1(KJ)$	differ.	$U_1(mm)$	differ.
393.0	-22.6%	29.3	-11.6%	103.2	-2.2%	433.6	-12.8%	30.4	-8.1%	101.6	-3.8%
BWH											
l_e (mm)											
8						16					
l_e/t = 2						l_e/t = 4					
$F_1(KN)$	differ.	$E_1(KJ)$	differ.	$U_1(mm)$	differ.	$F_1(KN)$	differ.	$E_1(KJ)$	differ.	$U_1(mm)$	differ.
381.0	-25.6%	17.0	-64.0%	69.5	-41.1%	486.4	-1.4%	16.6	-66.0%	65.4	-46.9%
KNIFE SPECIMEN											
Experiment											
$F_1(KN)$				$E_1(KJ)$				$U_1(mm)$			
493.1				32.9				105.5			

continued on next page

continued from previous page

SHEARS											
l_e (mm)											
8						16					
l_e/t = 2						l_e/t = 4					
$F_2(KN)$	differ.	$E_2(KJ)$	differ.	$U_2(mm)$	differ.	$F_2(KN)$	differ.	$E_2(KJ)$	differ.	$U_2(mm)$	differ.
434.5	10.9%	34.2	-3.0%	110.6	0.0%	473.2	19.4%	35.7	1.3%	110.6	0.0%
RTCLS											
l_e (mm)											
8						16					
l_e/t = 2						l_e/t = 4					
$F_2(KN)$	differ.	$E_2(KJ)$	differ.	$U_2(mm)$	differ.	$F_2(KN)$	differ.	$E_2(KJ)$	differ.	$U_2(mm)$	differ.
385.8	-1.0%	32.1	-9.4%	110.6	0.0%	411.3	5.4%	34.0	-3.6%	110.6	0.0%
BWH											
l_e (mm)											
8						16					
l_e/t = 2						l_e/t = 4					
$F_2(KN)$	differ.	$E_2(KJ)$	differ.	$U_2(mm)$	differ.	$F_2(KN)$	differ.	$E_2(KJ)$	differ.	$U_2(mm)$	differ.
105.9	-114.6%	27.3	-25.3%	110.6	0.0%	330.6	-16.4%	33.5	-5.0%	110.6	0.0%
KNIFE SPECIMEN											
Experiment											
$F_2(KN)$				$E_2(KJ)$				$U_2(mm)$			
389.7				35.3				110.6			

D.7 CE-1 and CE-2 models-(Tautz et al. 2013 and Fricke et al. 2014)

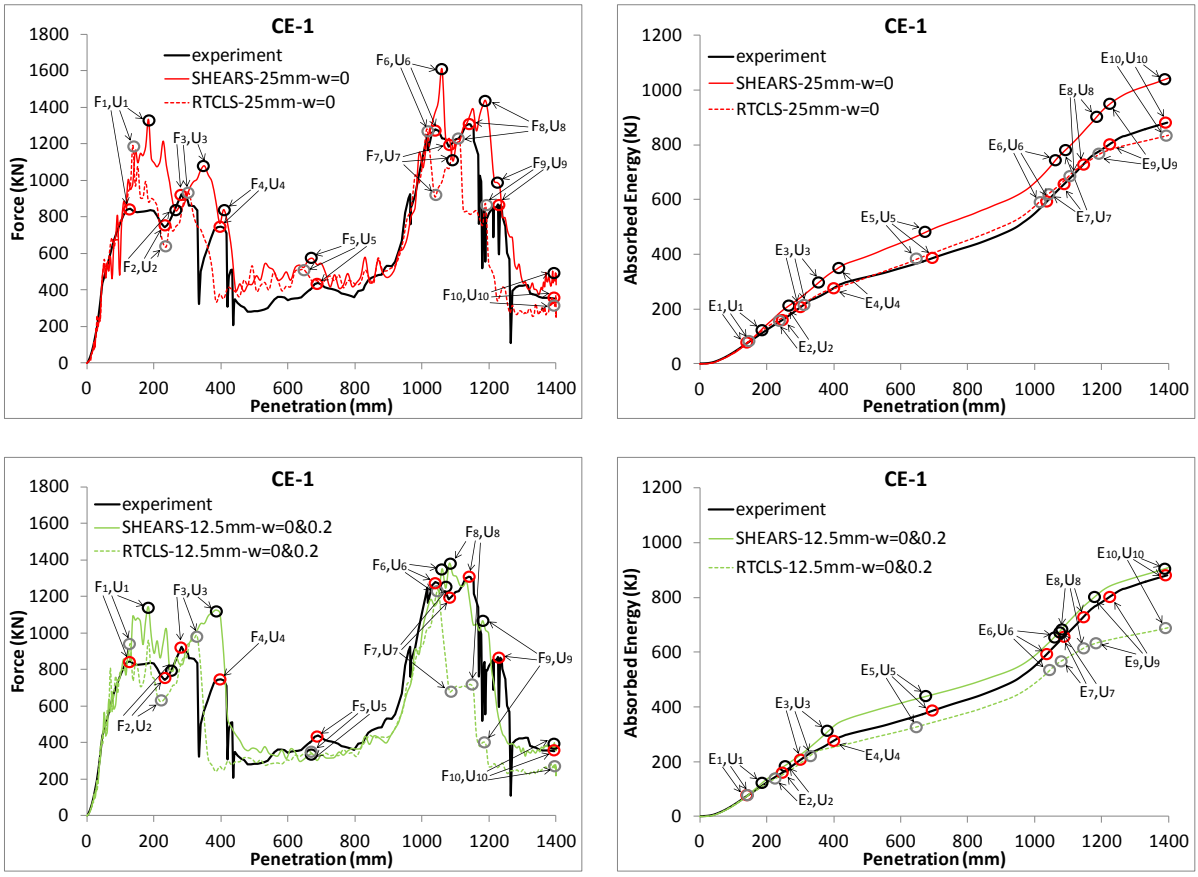

Figure D.19. CE-1 model. Force and absorbed energy-penetration curves.
Definition of force peaks and troughs for each element size and rupture criterion and comparison with the corresponding experimental values
(red circle: experiment, black circle: SHEARS, grey circle: RTCLS)

Table D.18. CE-1 model. Numerical values of force, energy and penetration depth for each element size and rupture criterion at the selected peaks and troughs and comparison with the corresponding experimental values

SHEARS											
$l_e\ (mm)$											
12.5						25					
l_e/t = 2.3						l_e/t = 4.7					
$F_1(KN)$	differ.	$E_1(KJ)$	differ.	$U_1(mm)$	differ.	$F_1(KN)$	differ.	$E_1(KJ)$	differ.	$U_1(mm)$	differ.
1142.3	29.8%	120.0	60.0%	184.3	34.5%	1332.7	44.7%	124.3	63.1%	184.3	34.5%
RTCLS											
$l_e\ (mm)$											
12.5						25					
l_e/t = 2.3						l_e/t = 4.7					
$F_1(KN)$	differ.	$E_1(KJ)$	differ.	$U_1(mm)$	differ.	$F_1(KN)$	differ.	$E_1(KJ)$	differ.	$U_1(mm)$	differ.
938.2	10.3%	65.6	1.4%	130.6	0.4%	1191.6	33.9%	73.4	12.7%	137.6	5.7%
CE-1											
Experiment											
$F_1(KN)$				$E_1(KJ)$				$U_1(mm)$			
846.0				64.7				130.0			

SHEARS											
$l_e\ (mm)$											
12.5						25					
l_e/t = 2.3						l_e/t = 4.7					
$F_2(KN)$	differ.	$E_2(KJ)$	differ.	$U_2(mm)$	differ.	$F_2(KN)$	differ.	$E_2(KJ)$	differ.	$U_2(mm)$	differ.
791.2	6.0%	187.3	22.8%	256.9	9.7%	832.6	11.1%	212.3	35.1%	266.7	13.5%
RTCLS											
$l_e\ (mm)$											
12.5						25					
l_e/t = 2.3						l_e/t = 4.7					
$F_2(KN)$	differ.	$E_2(KJ)$	differ.	$U_2(mm)$	differ.	$F_2(KN)$	differ.	$E_2(KJ)$	differ.	$U_2(mm)$	differ.
625.3	-17.5%	134.1	-10.5%	219.1	-6.1%	637.7	-15.5%	161.5	8.1%	237.7	2.0%
CE-1											
Experiment											
$F_2(KN)$				$E_2(KJ)$				$U_2(mm)$			
745.0				148.9				233.0			

continued on next page

continued from previous page

SHEARS											
l_e (mm)											
12.5						25					
l_e/t = 2.3						l_e/t = 4.7					
$F_3(KN)$	differ.	$E_3(KJ)$	differ.	$U_3(mm)$	differ.	$F_3(KN)$	differ.	$E_3(KJ)$	differ.	$U_3(mm)$	differ.
1126.2	19.5%	313.0	48.8%	385.3	30.6%	1078.6	15.2%	292.6	42.4%	351.3	21.5%
RTCLS											
l_e (mm)											
12.5						25					
l_e/t = 2.3						l_e/t = 4.7					
$F_3(KN)$	differ.	$E_3(KJ)$	differ.	$U_3(mm)$	differ.	$F_3(KN)$	differ.	$E_3(KJ)$	differ.	$U_3(mm)$	differ.
986.2	6.3%	221.3	15.1%	329.2	15.1%	941.5	1.7%	207.8	8.8%	297.3	4.9%
CE-1											
Experiment											
$F_3(KN)$			$E_3(KJ)$			$U_3(mm)$					
926.0			190.2			283.0					

SHEARS											
l_e (mm)											
12.5						25					
l_e/t = 2.3						l_e/t = 4.7					
$F_4(KN)$	differ.	$E_4(KJ)$	differ.	$U_4(mm)$	differ.	$F_4(KN)$	differ.	$E_4(KJ)$	differ.	$U_4(mm)$	differ.
Not captured						839.5	11.5%	345.6	22.4%	408.6	2.1%
RTCLS											
l_e (mm)											
12.5						25					
l_e/t = 2.3						l_e/t = 4.7					
$F_4(KN)$	differ.	$E_4(KJ)$	differ.	$U_4(mm)$	differ.	$F_4(KN)$	differ.	$E_4(KJ)$	differ.	$U_4(mm)$	differ.
Not captured											
CE-1											
Experiment											
$F_4(KN)$			$E_4(KJ)$			$U_4(mm)$					
748.0			276.0			400.0					

continued on next page

continued from previous page

SHEARS											
l_e (mm)											
12.5						25					
l_e/t = 2.3						l_e/t = 4.7					
$F_5(KN)$	differ.	$E_5(KJ)$	differ.	$U_5(mm)$	differ.	$F_5(KN)$	differ.	$E_5(KJ)$	differ.	$U_5(mm)$	differ.
337.2	-26.4%	438.0	13.2%	673.8	-2.4%	572.3	26.1%	480.3	22.4%	673.8	-2.4%
RTCLS											
l_e (mm)											
12.5						25					
l_e/t = 2.3						l_e/t = 4.7					
$F_5(KN)$	differ.	$E_5(KJ)$	differ.	$U_5(mm)$	differ.	$F_5(KN)$	differ.	$E_5(KJ)$	differ.	$U_5(mm)$	differ.
340.5	-25.5%	326.8	-16.0%	647.6	-6.3%	510.8	14.9%	382.5	-0.3%	647.6	-6.3%
CE-1											
Experiment											
$F_5(KN)$				$E_5(KJ)$				$U_5(mm)$			
440.0				383.6				690.0			

SHEARS											
l_e (mm)											
12.5						25					
l_e/t = 2.3						l_e/t = 4.7					
$F_6(KN)$	differ.	$E_6(KJ)$	differ.	$U_6(mm)$	differ.	$F_6(KN)$	differ.	$E_6(KJ)$	differ.	$U_6(mm)$	differ.
1351.5	5.4%	656.0	9.2%	1059.8	1.9%	1606.6	22.6%	739.6	21.1%	1059.8	1.9%
RTCLS											
l_e (mm)											
12.5						25					
l_e/t = 2.3						l_e/t = 4.7					
$F_6(KN)$	differ.	$E_6(KJ)$	differ.	$U_6(mm)$	differ.	$F_6(KN)$	differ.	$E_6(KJ)$	differ.	$U_6(mm)$	differ.
1233.2	-3.8%	537.5	-10.8%	1048.7	0.8%	1281.4	0.0%	592.6	-1.0%	1014.7	-2.5%
CE-1											
Experiment											
$F_6(KN)$				$E_6(KJ)$				$U_6(mm)$			
1281.0				598.6				1040.0			

continued on next page

continued from previous page

SHEARS											
l_e (mm)											
12.5						25					
l_e/t = 2.3						l_e/t = 4.7					
$F_7(KN)$	differ.	$E_7(KJ)$	differ.	$U_7(mm)$	differ.	$F_7(KN)$	differ.	$E_7(KJ)$	differ.	$U_7(mm)$	differ.
1245.8	4.9%	670.2	3.3%	1070.8	-0.9%	1104.6	-7.1%	780.7	18.5%	1092.2	1.1%
RTCLS											
l_e (mm)											
12.5						25					
l_e/t = 2.3						l_e/t = 4.7					
$F_7(KN)$	differ.	$E_7(KJ)$	differ.	$U_7(mm)$	differ.	$F_7(KN)$	differ.	$E_7(KJ)$	differ.	$U_7(mm)$	differ.
679.6	-54.3%	568.6	-13.1%	1081.6	0.1%	914.6	-25.8%	617.7	-4.8%	1037.5	-4.0%
CE-1											
Experiment											
$F_7(KN)$				$E_7(KJ)$				$U_7(mm)$			
1186.0				648.2				1080.0			

SHEARS											
l_e (mm)											
12.5						25					
l_e/t = 2.3						l_e/t = 4.7					
$F_8(KN)$	differ.	$E_8(KJ)$	differ.	$U_8(mm)$	differ.	$F_8(KN)$	differ.	$E_8(KJ)$	differ.	$U_8(mm)$	differ.
1381.6	5.3%	684.4	-5.5%	1081.6	-5.3%	1435.1	9.1%	907.9	22.7%	1189.9	4.3%
RTCLS											
l_e (mm)											
12.5						25					
l_e/t = 2.3						l_e/t = 4.7					
$F_8(KN)$	differ.	$E_8(KJ)$	differ.	$U_8(mm)$	differ.	$F_8(KN)$	differ.	$E_8(KJ)$	differ.	$U_8(mm)$	differ.
719.0	-58.3%	611.9	-16.6%	1143.1	0.3%	1223.9	-6.8%	686.7	-5.1%	1102.7	-3.3%
CE-1											
Experiment											
$F_8(KN)$				$E_8(KJ)$				$U_8(mm)$			
1310.0				722.9				1140.0			

continued on next page

continued from previous page

SHEARS											
l_e (mm)											
12.5						25					
l_e/t = 2.3						l_e/t = 4.7					
$F_9(KN)$	differ.	$E_9(KJ)$	differ.	$U_9(mm)$	differ.	$F_9(KN)$	differ.	$E_9(KJ)$	differ.	$U_9(mm)$	differ.
1067.6	20.4%	803.3	-0.4%	1180.9	-3.8%	988.0	12.7%	948.2	16.2%	1224.0	-0.2%
RTCLS											
l_e (mm)											
12.5						25					
l_e/t = 2.3						l_e/t = 4.7					
$F_9(KN)$	differ.	$E_9(KJ)$	differ.	$U_9(mm)$	differ.	$F_9(KN)$	differ.	$E_9(KJ)$	differ.	$U_9(mm)$	differ.
401.3	-73.7%	631.6	-24.3%	1180.9	-3.8%	868.9	-0.1%	764.1	-5.4%	1189.9	-3.1%
CE-1											
Experiment											
$F_9(KN)$				$E_9(KJ)$				$U_9(mm)$			
870.0				806.2				1227.0			

SHEARS											
l_e (mm)											
12.5						25					
l_e/t = 2.3						l_e/t = 4.7					
$F_{10}(KN)$	differ.	$E_{10}(KJ)$	differ.	$U_{10}(mm)$	differ.	$F_{10}(KN)$	differ.	$E_{10}(KJ)$	differ.	$U_{10}(mm)$	differ.
399.3	12.0%	907.0	2.8%	1394.7	0.0%	450.8	24.1%	1041.5	16.6%	1394.7	0.0%
RTCLS											
l_e (mm)											
12.5						25					
l_e/t = 2.3						l_e/t = 4.7					
$F_{10}(KN)$	differ.	$E_{10}(KJ)$	differ.	$U_{10}(mm)$	differ.	$F_{10}(KN)$	differ.	$E_{10}(KJ)$	differ.	$U_{10}(mm)$	differ.
279.5	-23.5%	688.0	-24.7%	1394.7	0.0%	328.7	-7.4%	834.4	-5.5%	1394.7	0.0%
CE-1											
Experiment											
$F_{10}(KN)$				$E_{10}(KJ)$				$U_{10}(mm)$			
354.0				881.8				1395.0			

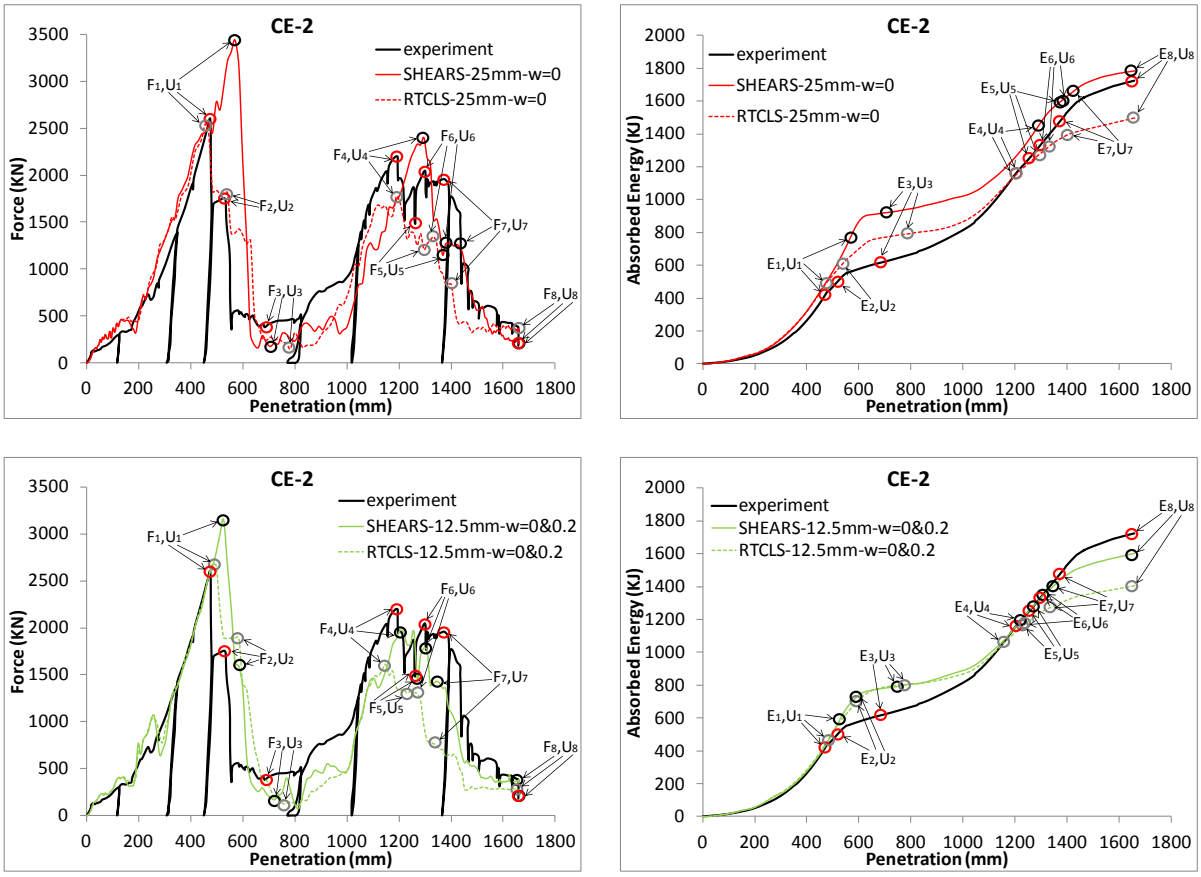

Figure D.20. CE-2 model. Force and absorbed energy-penetration curves.
Definition of force peaks and troughs for each element size and rupture criterion and comparison with the corresponding experimental values
(red circle: experiment, black circle: SHEARS, grey circle: RTCLS)

Table D.19. CE-2 model. Numerical values of force, energy and penetration depth for each element size and rupture criterion at the selected peaks and troughs and comparison with the corresponding experimental values

SHEARS											
l_e (mm)											
12.5						25					
l_e/t = 2.6						l_e/t = 5.3					
$F_1(KN)$	differ.	$E_1(KJ)$	differ.	$U_1(mm)$	differ.	$F_1(KN)$	differ.	$E_1(KJ)$	differ.	$U_1(mm)$	differ.
3150.5	19.0%	589.2	31.9%	527.0	10.6%	3436.3	27.6%	777.7	58.2%	570.5	18.5%
RTCLS											
l_e (mm)											
12.5						25					
l_e/t = 2.6						l_e/t = 5.3					
$F_1(KN)$	differ.	$E_1(KJ)$	differ.	$U_1(mm)$	differ.	$F_1(KN)$	differ.	$E_1(KJ)$	differ.	$U_1(mm)$	differ.
2678.6	2.9%	474.3	10.5%	484.5	2.2%	2542.7	-2.3%	448.8	4.9%	456.8	-3.6%
CE-2											
Experiment											
$F_1(KN)$			$E_1(KJ)$			$U_1(mm)$					
2603.0			427.2			473.7					

SHEARS											
l_e (mm)											
12.5						25					
l_e/t = 2.6						l_e/t = 5.3					
$F_2(KN)$	differ.	$E_2(KJ)$	differ.	$U_2(mm)$	differ.	$F_2(KN)$	differ.	$E_2(KJ)$	differ.	$U_2(mm)$	differ.
1595.5	-9.5%	718.5	32.8%	585.2	10.4%	Not captured					
RTCLS											
l_e (mm)											
12.5						25					
l_e/t = 2.6						l_e/t = 5.3					
$F_2(KN)$	differ.	$E_2(KJ)$	differ.	$U_2(mm)$	differ.	$F_2(KN)$	differ.	$E_2(KJ)$	differ.	$U_2(mm)$	differ.
1892.4	7.6%	685.3	28.1%	585.2	10.4%	1812.8	3.3%	615.5	17.5%	541.4	2.6%
CE-2											
Experiment											
$F_2(KN)$			$E_2(KJ)$			$U_2(mm)$					
1754.5			516.3			527.6					

continued on next page

continued from previous page

SHEARS											
$l_e\ (mm)$											
12.5						25					
l_e/t = 2.6						l_e/t = 5.3					
$F_3(KN)$	differ.	$E_3(KJ)$	differ.	$U_3(mm)$	differ.	$F_3(KN)$	differ.	$E_3(KJ)$	differ.	$U_3(mm)$	differ.
170.7	-75.8%	786.7	24.5%	721.4	5.3%	177.1	-72.6%	920.6	39.9%	706.0	3.1%
RTCLS											
$l_e\ (mm)$											
12.5						25					
l_e/t = 2.6						l_e/t = 5.3					
$F_3(KN)$	differ.	$E_3(KJ)$	differ.	$U_3(mm)$	differ.	$F_3(KN)$	differ.	$E_3(KJ)$	differ.	$U_3(mm)$	differ.
133.4	-95.9%	798.8	26.1%	752.3	9.4%	152.8	-85.1%	790.6	25.0%	783.3	13.5%
CE-2											
Experiment											
$F_3(KN)$				$E_3(KJ)$				$U_3(mm)$			
378.9				614.7				684.4			

SHEARS											
$l_e\ (mm)$											
12.5						25					
l_e/t = 2.6						l_e/t = 5.3					
$F_4(KN)$	differ.	$E_4(KJ)$	differ.	$U_4(mm)$	differ.	$F_4(KN)$	differ.	$E_4(KJ)$	differ.	$U_4(mm)$	differ.
1972.1	-10.7%	1157.4	1.5%	1203.2	0.7%	2398.7	8.9%	1459.3	24.6%	1295.1	8.1%
RTCLS											
$l_e\ (mm)$											
12.5						25					
l_e/t = 2.6						l_e/t = 5.3					
$F_4(KN)$	differ.	$E_4(KJ)$	differ.	$U_4(mm)$	differ.	$F_4(KN)$	differ.	$E_4(KJ)$	differ.	$U_4(mm)$	differ.
1609.5	-30.8%	1038.6	-9.3%	1147.3	-4.0%	1772.1	-21.3%	1126.4	-1.2%	1189.4	-0.4%
CE-2											
Experiment											
$F_4(KN)$				$E_4(KJ)$				$U_4(mm)$			
2195.2				1139.9				1194.6			

continued on next page

continued from previous page

SHEARS											
$l_e\ (mm)$											
12.5						25					
l_e/t = 2.6						l_e/t = 5.3					
$F_5(KN)$	differ.	$E_5(KJ)$	differ.	$U_5(mm)$	differ.	$F_5(KN)$	differ.	$E_5(KJ)$	differ.	$U_5(mm)$	differ.
1459.5	-1.6%	1280.9	1.4%	1269.6	0.5%	1149.3	-25.3%	1586.2	22.7%	1366.9	7.9%

RTCLS											
$l_e\ (mm)$											
12.5						25					
l_e/t = 2.6						l_e/t = 5.3					
$F_5(KN)$	differ.	$E_5(KJ)$	differ.	$U_5(mm)$	differ.	$F_5(KN)$	differ.	$E_5(KJ)$	differ.	$U_5(mm)$	differ.
1302.3	-13.0%	1156.6	-8.8%	1230.2	-2.6%	1207.2	-20.5%	1278.0	1.2%	1295.1	2.5%

CE-2		
Experiment		
$F_5(KN)$	$E_5(KJ)$	$U_5(mm)$
1482.7	1263.4	1262.7

SHEARS											
$l_e\ (mm)$											
12.5						25					
l_e/t = 2.6						l_e/t = 5.3					
$F_6(KN)$	differ.	$E_6(KJ)$	differ.	$U_6(mm)$	differ.	$F_6(KN)$	differ.	$E_6(KJ)$	differ.	$U_6(mm)$	differ.
1784.9	-13.5%	1323.3	-1.0%	1295.1	-0.4%	1271.4	-46.6%	1613.9	18.8%	1389.3	6.6%

RTCLS											
$l_e\ (mm)$											
12.5						25					
l_e/t = 2.6						l_e/t = 5.3					
$F_6(KN)$	differ.	$E_6(KJ)$	differ.	$U_6(mm)$	differ.	$F_6(KN)$	differ.	$E_6(KJ)$	differ.	$U_6(mm)$	differ.
1325.7	-42.6%	1174.1	-13.0%	1243.5	-4.5%	1344.4	-41.2%	1325.2	-0.9%	1331.8	2.4%

CE-2		
Experiment		
$F_6(KN)$	$E_6(KJ)$	$U_6(mm)$
2042.8	1336.7	1300.8

continued on next page

continued from previous page

SHEARS											
$l_e\ (mm)$											
12.5						25					
l_e/t = 2.6						l_e/t = 5.3					
$F_7(KN)$	differ.	$E_7(KJ)$	differ.	$U_7(mm)$	differ.	$F_7(KN)$	differ.	$E_7(KJ)$	differ.	$U_7(mm)$	differ.
1433.2	-30.9%	1398.6	-5.4%	1343.7	-2.2%	1262.5	-43.1%	1654.2	11.3%	1421.3	3.4%
RTCLS											
$l_e\ (mm)$											
12.5						25					
l_e/t = 2.6						l_e/t = 5.3					
$F_7(KN)$	differ.	$E_7(KJ)$	differ.	$U_7(mm)$	differ.	$F_7(KN)$	differ.	$E_7(KJ)$	differ.	$U_7(mm)$	differ.
764.9	-87.6%	1268.2	-15.2%	1331.8	-3.1%	836.5	-80.2%	1393.9	-5.8%	1400.2	1.9%
CE-2											
Experiment											
$F_7(KN)$				$E_7(KJ)$				$U_7(mm)$			
1956.3				1476.6				1373.6			

SHEARS											
$l_e\ (mm)$											
12.5						25					
l_e/t = 2.6						l_e/t = 5.3					
$F_8(KN)$	differ.	$E_8(KJ)$	differ.	$U_8(mm)$	differ.	$F_8(KN)$	differ.	$E_8(KJ)$	differ.	$U_8(mm)$	differ.
375.6	69.8%	1604.0	-7.2%	1659.0	0.0%	225.2	21.7%	1782.9	3.4%	1659.0	0.0%
RTCLS											
$l_e\ (mm)$											
12.5						25					
l_e/t = 2.6						l_e/t = 5.3					
$F_8(KN)$	differ.	$E_8(KJ)$	differ.	$U_8(mm)$	differ.	$F_8(KN)$	differ.	$E_8(KJ)$	differ.	$U_8(mm)$	differ.
269.7	39.3%	1402.8	-20.5%	1659.0	0.0%	349.5	63.4%	1497.9	-14.0%	1659.0	0.0%
CE-2											
Experiment											
$F_8(KN)$				$E_8(KJ)$				$U_8(mm)$			
181.2				1723.0				1658.8			

D.8 P1-15, P2-15, S1-20 and S2-20 models-(DNV 1993)

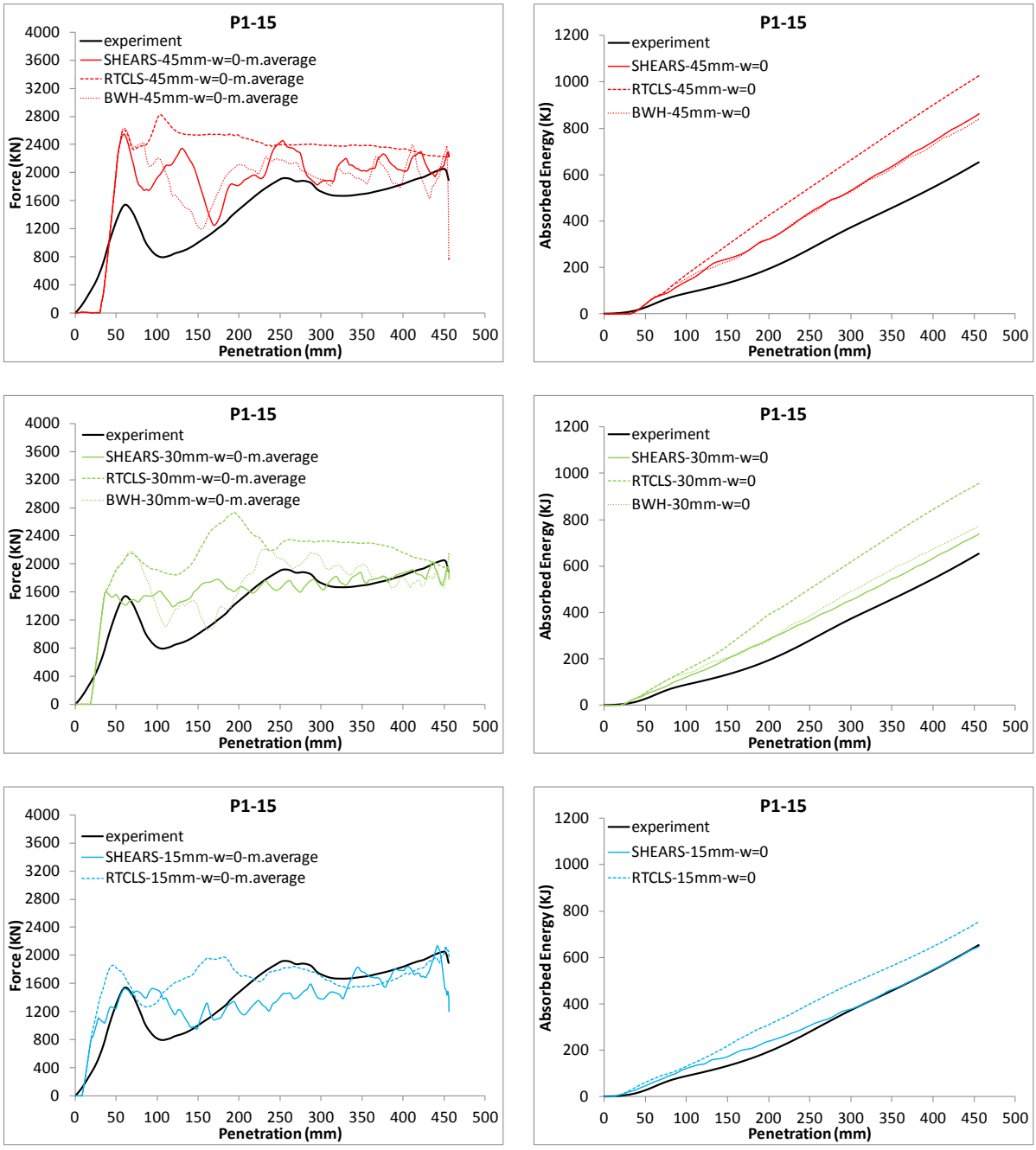

Figure D.21. P1-15 model. Force and absorbed energy-penetration curves using the moving average method and a period equal to ten force values for each element size and rupture criterion

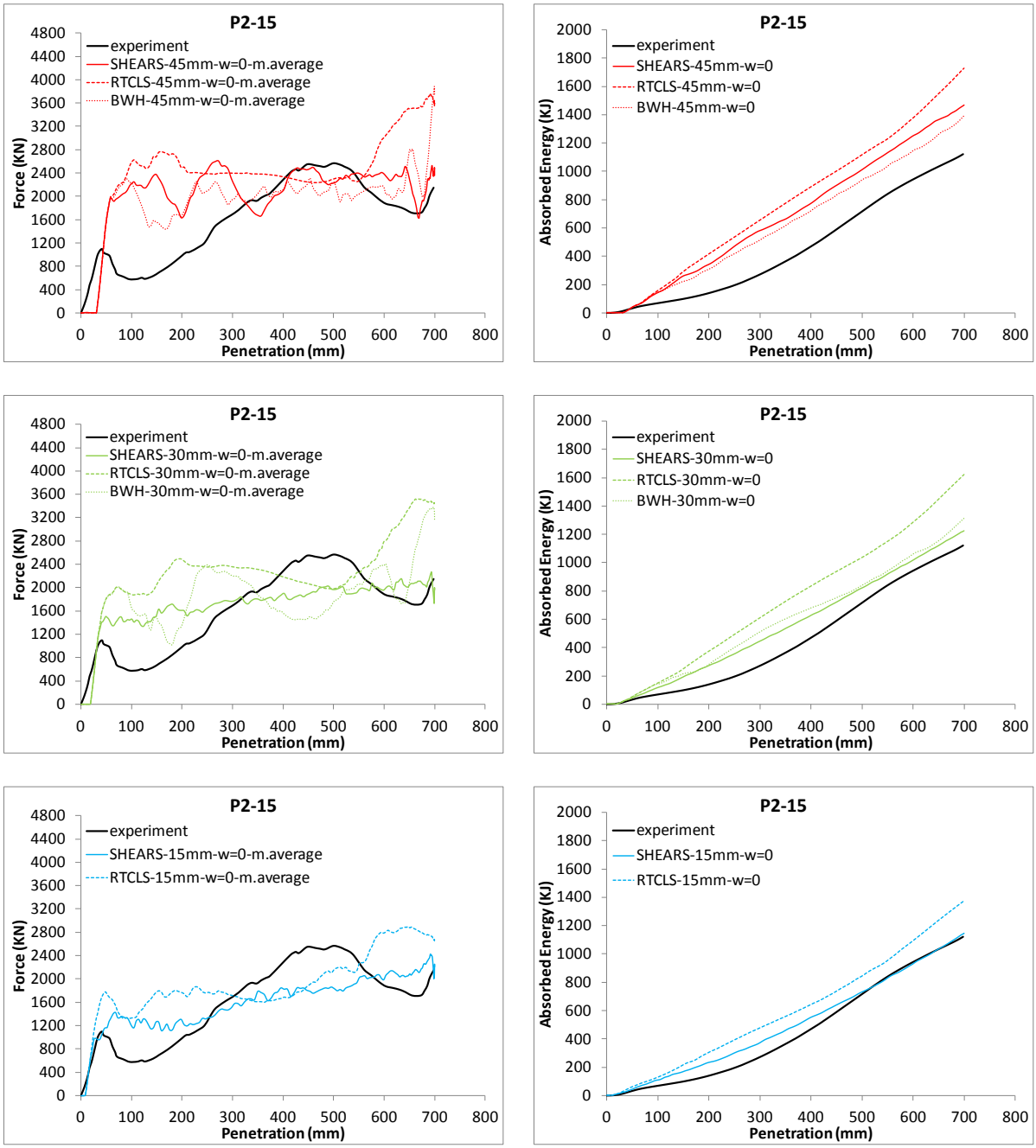

Figure D.22. P2-15 model. Force and absorbed energy-penetration curves using the moving average method and a period equal to ten force values for each element size and rupture criterion

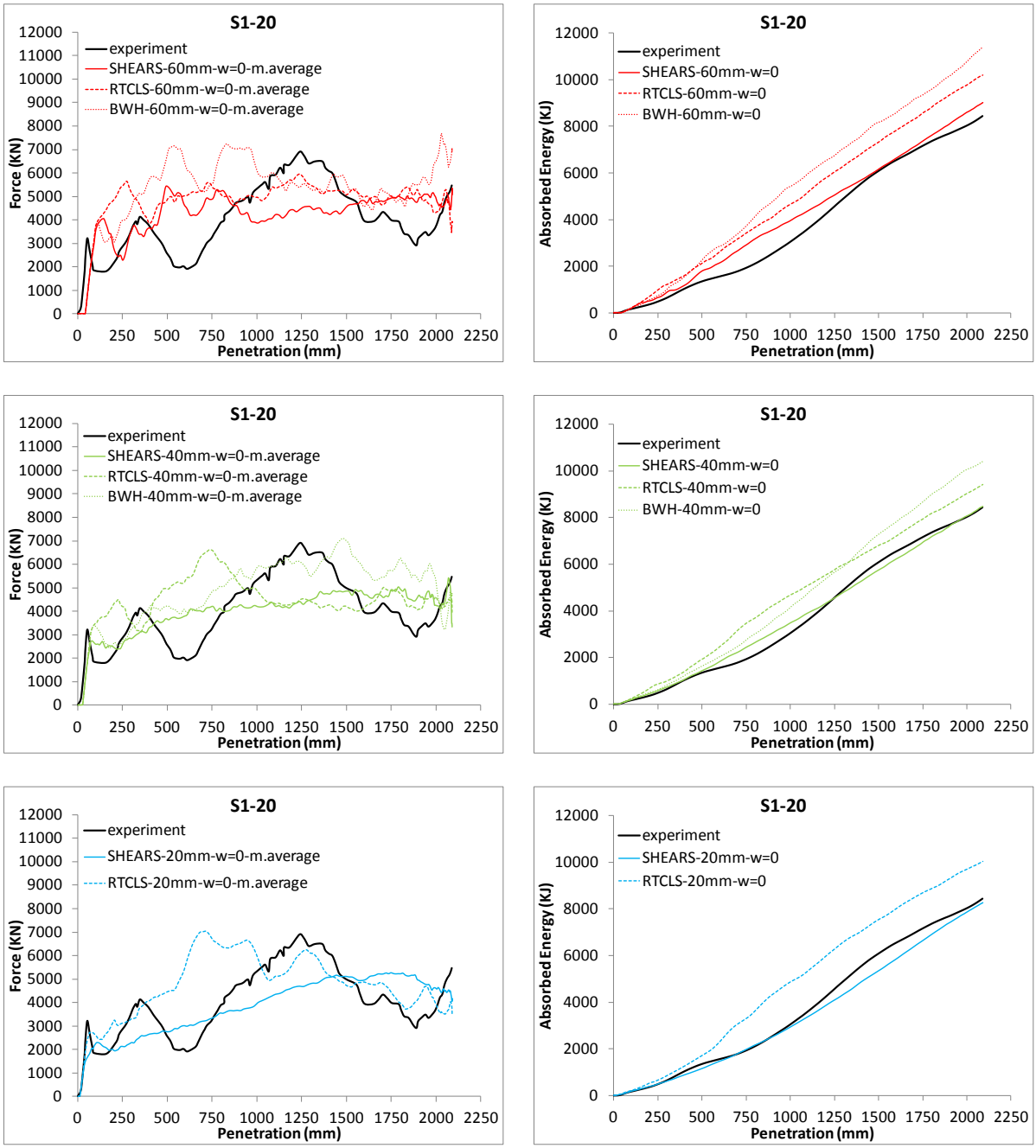

Figure D.23. S1-20 model. Force and absorbed energy-penetration curves using the moving average method and a period equal to ten force values for each element size and rupture criterion

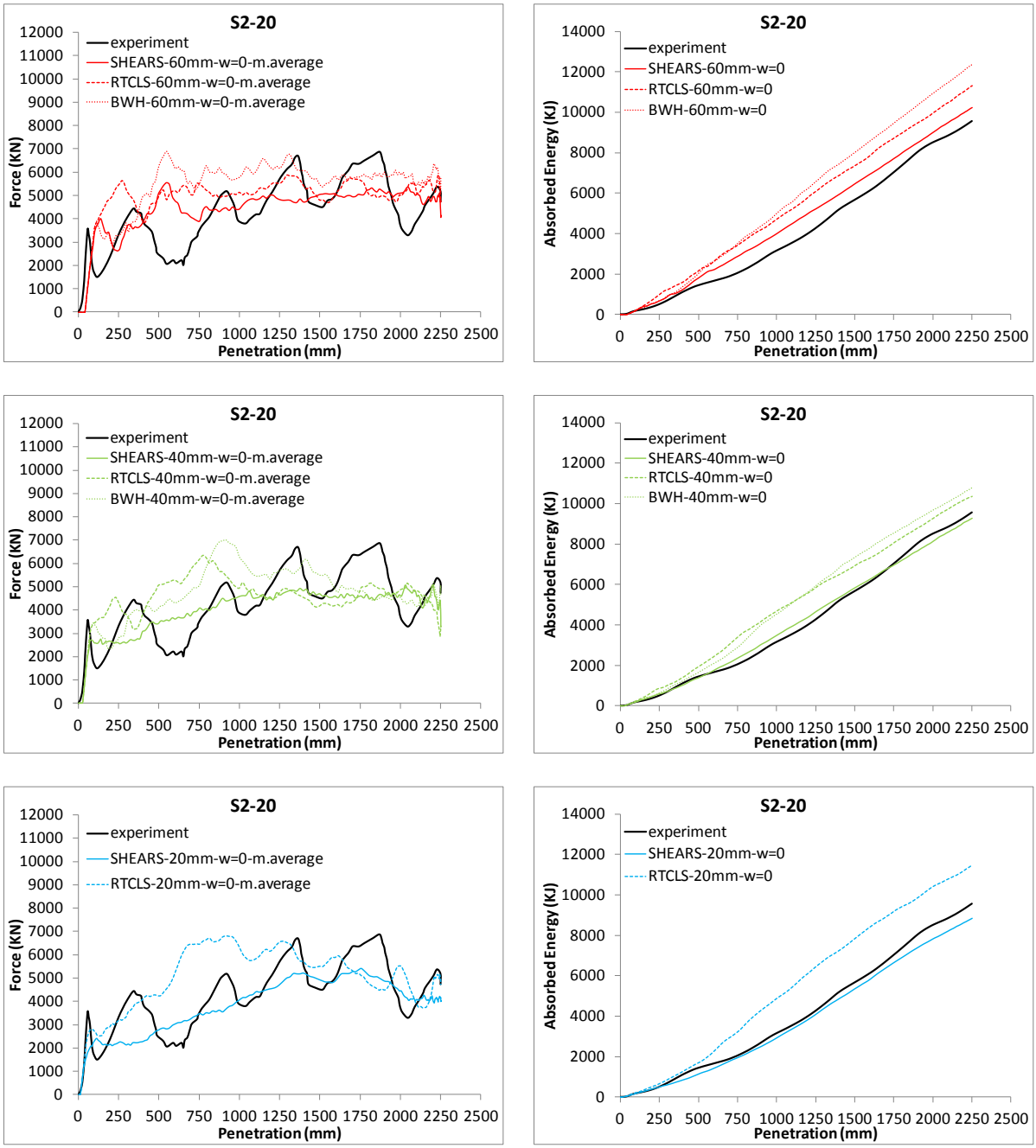

Figure D.24. S2-20 model. Force and absorbed energy-penetration curves using the moving average method and a period equal to ten force values for each element size and rupture criterion